

Adhesion and Adhesives: Fundamental and Applied Aspects

ADVANCES IN CONTACT ANGLE, WETTABILITY AND ADHESION

Volume Two



Advances in Contact Angle, Wettability and Adhesion

Scrivener Publishing
100 Cummings Center, Suite 541J
Beverly, MA 01915-6106

Adhesion and Adhesives: Fundamental and Applied Aspects

The topics to be covered include, but not limited to, basic and theoretical aspects of adhesion; modeling of adhesion phenomena; mechanisms of adhesion; surface and interfacial analysis and characterization; unraveling of events at interfaces; characterization of interphases; adhesion of thin films and coatings; adhesion aspects in reinforced composites; formation, characterization and durability of adhesive joints; surface preparation methods; polymer surface modification; biological adhesion; particle adhesion; adhesion of metallized plastics; adhesion of diamond-like films; adhesion promoters; contact angle, wettability and adhesion; superhydrophobicity and superhydrophilicity. With regards to adhesives, the Series will include, but not limited to, green adhesives; novel and high-performance adhesives; and medical adhesive applications.

Series Editor: Dr. K.L. Mittal
1983 Route 52,
P.O. Box 1280, Hopewell Junction, NY 12533, USA
Email: usharmittal@gmail.com

Publishers at Scrivener
Martin Scrivener(martin@scrivenerpublishing.com)
Phillip Carmical (pcarmical@scrivenerpublishing.com)

Advances in Contact Angle, Wettability and Adhesion

Volume 2

Edited by

K.L. Mittal



WILEY

Copyright © 2015 by Scrivener Publishing LLC. All rights reserved.

Co-published by John Wiley & Sons, Inc. Hoboken, New Jersey, and Scrivener Publishing LLC, Salem, Massachusetts.

Published simultaneously in Canada.

No part of this publication may be reproduced, stored in a retrieval system, or transmitted in any form or by any means, electronic, mechanical, photocopying, recording, scanning, or otherwise, except as permitted under Section 107 or 108 of the 1976 United States Copyright Act, without either the prior written permission of the Publisher, or authorization through payment of the appropriate per-copy fee to the Copyright Clearance Center, Inc., 222 Rosewood Drive, Danvers, MA 01923, (978) 750-8400, fax (978) 750-4470, or on the web at www.copyright.com. Requests to the Publisher for permission should be addressed to the Permissions Department, John Wiley & Sons, Inc., 111 River Street, Hoboken, NJ 07030, (201) 748-6011, fax (201) 748-6008, or online at <http://www.wiley.com/go/permission>.

Limit of Liability/Disclaimer of Warranty: While the publisher and author have used their best efforts in preparing this book, they make no representations or warranties with respect to the accuracy or completeness of the contents of this book and specifically disclaim any implied warranties of merchantability or fitness for a particular purpose. No warranty may be created or extended by sales representatives or written sales materials. The advice and strategies contained herein may not be suitable for your situation. You should consult with a professional where appropriate. Neither the publisher nor author shall be liable for any loss of profit or any other commercial damages, including but not limited to special, incidental, consequential, or other damages.

For general information on our other products and services or for technical support, please contact our Customer Care Department within the United States at (800) 762-2974, outside the United States at (317) 572-3993 or fax (317) 572-4002.

Wiley also publishes its books in a variety of electronic formats. Some content that appears in print may not be available in electronic formats. For more information about Wiley products, visit our web site at www.wiley.com.

For more information about Scrivener products please visit www.scrivenerpublishing.com.

Cover design by Exeter Premedia Services

Library of Congress Cataloging-in-Publication Data:

ISBN 978-1-119-11698-1

Printed in the United States of America

10 9 8 7 6 5 4 3 2 1

Contents

Preface	xv
Part 1: Fundamental and General Aspects	
1 Wetting of Solid Walls and Spontaneous Capillary Flow	3
<i>Jean Berthier and Kenneth A. Brakke</i>	
1.1 Introduction: Capillary Flows and Contact Angles	3
1.2 A General Condition for Spontaneous Capillary Flow (SCF)	5
1.2.1 Theoretical Condition	6
1.2.2 Comparison Between Theory and Numerical Approach	10
1.2.3 Discussion	13
1.2.4 Conclusion	14
1.3 The Dynamics of SCF	15
1.3.1 Open and Confined Systems	15
1.3.2 The Lucas-Washburn-Rideal (LWR) Law for Confined Cylindrical Channels	15
1.3.3 Generalization of the Lucas-Washburn-Rideal Law to Composite, Confined Microchannels of Arbitrary Cross Section	17
1.3.4 Experimental Results for Confined Channels	28
1.3.5 Capillary Flow in Open Microchannels: The Example of Suspended Microflows	31
1.4 Conclusion	41
References	42

2	A Review of “Ordered Water Monolayer That Does Not Completely Wet Water” at Room Temperature	47
	<i>Chunlei Wang and Haiping Fang</i>	
2.1	Introduction	47
2.2	“Ordered Water Monolayer that Does Not Completely Wet Water” at Room Temperature	49
2.3	Effect of Surface Point Defects on the Ordered Water Monolayer	55
2.4	Thermal Properties of Ordered Water Monolayer	56
2.5	Simulation or Experimental Observations on the Phenomenon of Water Droplets on Water Monolayers on Real Solid Surfaces at Room Temperature	59
2.6	“Ordered Ethanol Monolayer that does not Completely Wet Ethanol” at Room Temperature	61
2.7	Discussion	64
2.8	Summary	65
	Acknowledgements	66
	References	66
3	Cheerios Effect and its Control by Contact Angle Modulation	73
	<i>Junqi Yuan and Sung Kwon Cho</i>	
3.1	Introduction	74
3.2	Theoretical Models	76
3.2.1	Model for Two Infinite Vertical Plates	77
3.2.2	Model of Two Vertical Cylinders	82
3.2.3	Model of Two Floating Spherical Particles	89
3.2.4	Model of Floating Spherical Particle and Vertical Wall	93
3.3	Control of Cheerios Effect	102
3.4	Concluding Remarks and Outlook	105
	Acknowledgement	107
	References	107
4	Recent Mathematical Analysis of Contact Angle Hysteresis	111
	<i>Xianmin Xu and Xiaoping Wang</i>	
4.1	Introduction	111
4.2	The Physical Principle and Mathematical Method	113
4.2.1	The Physical Principle	113
4.2.2	Homogenization	114

4.3	The Wenzel's and Cassie's Equations	114
4.4	The Modified Cassie Equation	118
4.5	Contact Angle Hysteresis	119
4.5.1	Quasistatic Process of a Two-dimensional Problem	120
4.5.2	Three-dimensional Case	122
4.6	Conclusion and Outlook	124
	Acknowledgments	125
	References	125
5	Computational Analysis of Wetting on Hydrophobic Surfaces: Application to Self-Cleaning Mechanisms	129
	<i>Muhammad Osman and Roger A. Sauer</i>	
5.1	Introduction	130
5.2	Basic Relations in Differential Geometry	131
5.3	System Model	133
5.4	Governing Equations	134
5.4.1	Droplet Membrane	134
5.4.2	Surface Contact	136
5.4.3	Line Contact	137
5.5	Force Analysis	139
5.6	Results and Discussion	140
5.6.1	Wetting on Rough Surface	140
5.6.2	Adhesion Between Droplet Surface and a Contaminant Particle	142
5.7	Conclusions	145
	Acknowledgement	146
	References	146
6	Bubble Adhesion to Superhydrophilic Surfaces	149
	<i>Ridvan Ozbay, Ali Kibar and Chang-Hwan Choi</i>	
6.1	Introduction	150
6.2	Theoretical Models	151
6.3	Experimental	154
6.4	Results and Discussion	155
6.5	Conclusions	161
	Acknowledgement	162
	References	162

7 Relationship Between the Roughness and Oleophilicity of Functional Surfaces	165
<i>Luisa Coriand, Markus Rettenmayr and Angela Duparré</i>	
7.1 Introduction	165
7.2 Basics and Experimental	166
7.2.1 Preparation of Rough Steel Surfaces	166
7.2.2 Roughness	166
7.2.3 Wettability	168
7.2.4 Roughness Measurements	168
7.2.5 CA Measurements	169
7.3 Results and Discussion	170
7.3.1 Preliminary Investigation: Influence of Temperature and Effect of Pre-wetted Surface	170
7.3.2 Relationship Between Roughness and Oleophilicity	172
7.4 Summary	175
Acknowledgements	176
References	176
8 Liquid Repellent Amorphous Carbon Nanoparticle Networks	179
<i>Ilker S. Bayer, Alexander J. Davis and Eric Loth</i>	
8.1 Introduction	180
8.2 Templates for Liquid Repellent Surfaces	180
8.3 Synthesis Without Flames	184
8.4 Synthesis by Combustion of Terpenoids	189
8.5 Amorphous Carbon Networks on 3-D Porous Materials for Liquid Filtration	191
8.6 Towards Robust Carbonaceous Films on Micro-textured Polymer Surfaces	193
8.7 Conclusions	208
References	209
9 Recent Progress in Evaluating Mechanical Durability of Liquid Repellent Surfaces	211
<i>Athanasios Milionis, Ilker S. Bayer and Eric Loth</i>	
9.1 Introduction	211
9.2 Durability to Tangential Shear	218
9.2.1 Linear Abrasion	219
9.2.2 Circular Abrasion	224
9.2.3 Blade/Knife Test	225

9.2.4	Pencil Test	227
9.2.5	Oscillating Steel Ball	228
9.2.6	Oscillating Steel Ring	230
9.2.7	Finger Rubbing	231
9.3	Durability to Dynamic Impact	233
9.3.1	Solid Particle Impact	233
9.3.2	Liquid Jet/Droplet Impact	236
9.3.3	Gas Pressure Impact	238
9.4	Durability under Vertical Compression/Expansion	239
9.4.1	Tape Peeling	239
9.4.2	Compression Followed by Tension	242
9.5	Wear in Liquid Baths	242
9.5.1	Laundry Test	243
9.5.2	Ultrasonication	247
9.5.3	Rotary Slurry Test	248
9.6	Inherently Durable Liquid Repellent Materials	249
9.6.1	Bulk Materials that are Inherently Liquid Repellent	249
9.6.2	Materials that become Liquid Repellent with Mechanical Wear	251
9.7	Future Directions for Investigating Mechanical Durability	251
	References	253
10	Superhydrophobic and Superoleophobic Biobased Materials	259
	<i>Ilker S. Bayer</i>	
10.1	Introduction	260
10.2	Advances in Liquid Repellent Cellulose Fiber Networks	260
10.3	Liquid Repellent Materials: Cellulose Derivatives	270
10.4	Liquid Repellent Thermoplastic Starch and Biopolyesters	277
10.5	Conclusions	281
	References	282
 Part 2: Wettability Modification		
11	Laser Ablated Micro/Nano-Patterned Superhydrophobic Stainless Steel Substrates	287
	<i>Sona Moradi, Saeid Kamal and Savvas G. Hatzikiriakos</i>	
11.1	Introduction	288

11.2	Materials and Experimental Methods	290
11.2.1	Materials	290
11.2.2	Surface Laser Irradiation	290
11.2.3	Surface Analysis	292
11.3	Experimental Details	292
11.4	Results and Discussion	293
11.4.1	Surface Morphology	293
11.4.2	Surface Wettability	297
11.4.3	The Effect of Overlap on Surface Wettability	300
11.5	Conclusions	301
	Acknowledgement	302
	References	302
12	RF Plasma Treatment of Neptune Grass (<i>Posidonia oceanica</i>): A Facile Method to Achieve Superhydrophilic Surfaces for Dye Adsorption from Aqueous Solutions	305
	<i>Hernando S. Salapare III, Ma. Gregoria Joanne P. Tiquio and Henry J. Ramos</i>	
12.1	Introduction	306
12.1.1	Surfaces and Wetting	306
12.1.2	Plasma Surface Modification	311
12.1.3	<i>Posidonia oceanica</i>	314
12.2	Experimental Details	315
12.2.1	Materials and Experimental Procedures	315
12.2.2	Characterizations	317
12.2.3	Dye Adsorption	318
12.3	Results and Discussion	319
12.3.1	Plasma Treatment of <i>Posidonia oceanica</i>	319
12.3.2	Dye Adsorption by <i>Posidonia oceanica</i> from Aqueous Solutions	324
12.4	Conclusions	328
	References	329
13	Highly Liquid Repellent Technical Textiles Obtained by Means of Photo-chemical and Laser Surface Modifications	333
	<i>Thomas Bahnners and Jochen S. Gutmann</i>	
13.1	Introduction	334
13.2	Background of the Conceptual Approach	335
13.2.1	Surface Free Energy and Liquid Repellence	335

13.2.2	Enhancing Liquid Repellence through Surface Roughness	336
13.2.3	Peculiarities of Textile Substrates and their Relevance to Wetting	337
13.2.4	The Concept of Roughness Formation by Laser Irradiation	342
13.2.5	Introducing Low Surface Energy to the Roughened Surface	346
13.3	Application of Combined Laser and Photo-chemical Modifications to Technical Textiles	347
13.3.1	Increasing Water Repellence of Technical Fabrics Made of PET and Aramids	349
13.3.2	Increased Oil Repellence of Technical PET Fabrics	354
13.4	Summary	358
	Acknowledgement	360
	References	360
14	Modification of Paper/Cellulose Surfaces to Control Liquid Wetting and Adhesion	365
	<i>Victor Breedveld and Dennis W. Hess</i>	
14.1	Introduction	366
14.2	Plasma Processing	366
14.3	Sticky vs. Roll-off Superhydrophobic Surfaces	367
14.4	Local Wetting/Adhesion Control	369
14.5	Superamphiphobic/Superomniphobic Paper	372
14.6	Summary and Conclusions	374
	Acknowledgments	375
	References	375
 Part 3: Surface Free Energy and Adhesion		
15	Surface Free Energy of Superhydrophobic Materials Obtained by Deposition of Polymeric Particles on Glass	381
	<i>Konrad Terpilowski</i>	
	List of Notations	382
15.1	Introduction	382
15.2	Experimental	385
15.2.1	Materials and Methods	385

15.2.2	Preparation of Superhydrophobic Layers Deposited on the Glass Surface	385
15.2.3	Contact Angle Measurements	386
15.2.4	Photographs of PS Layers	386
15.2.5	Imaging the PS Layer Surface with an Optical Profilometer	387
15.3	Results and Discussion	387
15.3.1	Contact Angles Measured on Glass Plates Covered with Pure PS Layers	387
15.3.2	Apparent Surface Free Energy Calculated for Glass Plates Covered with Pure PS Layers	388
15.3.3	Contact Angles Measured on Glass Plates Covered with the PS Layers with Embedded Polymer Fillers	388
15.3.4	Apparent Surface Free Energy Calculated for the Glass Plates Covered with the PS/ Filler Layers	389
15.3.5	Optical Photographs of the PS Layers with Embedded Polymers Particles	390
15.3.6	Images of the Superhydrophobic Layers Using Optical Profilometry	392
15.3.7	Tadmor's Equilibrium Contact Angles	392
15.4	Conclusions	394
	References	394
16	Tablet Tensile Strength: Role of Surface Free Energy	397
	<i>Frank M. Etzler and Sorana Pisano</i>	
16.1	Introduction	398
16.1.1	Overview	398
16.1.2	Densification of Powders under Pressure	399
16.1.3	Measurement of Tablet Tensile Strength	399
16.1.4	The Ryshkewitch-Duckworth Equation	400
16.1.5	Surface Science of Adhesion	401
16.1.6	A Model to Predict the Tensile Strength of Tablets from Individual Components	402
16.2	Applicability of the Proposed Model to Pharmaceutical Materials	404
16.2.1	Experimental Details	404
16.2.2	Ryshkewitch-Duckworth Equation as a Predictor of the Tensile Strength of Binary Mixtures	406

16.2.3	Dependence on Processing Parameters	407
16.2.4	Direct Evidence for the Role of Surface Free Energy	412
16.3	Discussion	414
16.4	Summary	415
	Acknowledgements	416
	References	416
17	Why Test Inks Cannot Tell the Whole Truth About Surface Free Energy of Solids	419
	<i>Ming Jin, Frank Thomsen, Thomas Skrivanek and Thomas Willers</i>	
17.1	Introduction	419
17.2	Background	420
17.3	Materials and Methods	424
17.3.1	Solid Samples Investigated	424
17.3.2	Sample Preparation	424
17.3.3	Test Inks Used	424
17.3.4	Contact Angle Measurement	426
17.3.5	Plasma Treatment	426
17.4	Results and Interpretation	426
17.4.1	SFE Determination for Untreated Samples	426
17.4.2	Interpretation Based on Interfacial Tension	427
17.4.3	Measurements on Plasma-treated Samples	430
17.4.4	Characterization of Test Inks	434
17.5	Advantages and Drawbacks of Contact Angle Measurement in Practice	435
17.6	Summary	437
	References	438
	Index	439

Preface

The express purpose of this book series, *Advances in Contact Angle, Wettability and Adhesion*, is to provide a continuous state-of-the-art critical look at the current knowledge and latest developments in the arena of contact angle, wettability and adhesion.

Some historical facts related to the primordial study and evolution of contact angles and wetting phenomena were described in the Preface to Volume 1. Here I would like to supplement that information by mentioning some other significant milestones in the same vein. First, it is interesting to note that the titans of science like Einstein, Schrödinger and Bohr—all Nobel Laureates—evinced keen interest in capillarity (related to contact angle) and devoted part of their research to this topic. Next, the discovery of electrocapillarity, which in essence signifies manipulation/modulation of wettability (contact angle) by application of electric field, is attributed to the seminal and trailblazing work of Gabriel Lippmann (Nobel Laureate for Physics 1908) as part of his Ph.D. thesis. Electrowetting (EW) or modern electrowetting EWOD (electrowetting on dielectric) was developed from the phenomenon of electrocapillarity investigated in detail by Lippmann. So Gabriel Lippmann can aptly be called the father of electrowetting. Since the discovery of electrocapillarity, the ability to manipulate properties at the phase boundary by applied electric field has been vigorously pursued. The high tempo of research in EW stems from the fact that EWOD can be employed for a broad range of applications involving manipulations of liquids and requiring miniaturization of system size and improving its effectiveness. Lab-on-a-chip is a prime example of the application of EWOD. Lab-on-a-chip has been used in biomedical and analytical devices. Next, the work of the College de France, Paris, a world-renowned research school headed by Pierre-Gilles de Gennes (Nobel Laureate in Physics 1991), deserves special mention for its tremendous contribution towards understanding and explaining wetting phenomena (dynamics of wetting). Therefore, one can see that five Nobel Laureates have contributed to and brought glamour to the fascinating field of contact angles and wetting phenomena.

These days there is an overwhelming interest in biomimetics. According to Wikipedia, biomimetics or biomimicry is the imitation of the models, systems and elements of Nature for the purpose of solving complex human problems. Nature is a great teacher and the old adage, “Nature does not waste time in making frivolous or useless things,” is dead true; in this context, the lotus leaf is a classic paradigm. Even a cursory look at the literature will evince that currently there is a proliferation of research activity in all facets/ramifications of contact angles and wetting phenomena, and all signals indicate that this accelerated pace will be maintained.

The 17 research and review chapters comprising this book are divided into three parts – Part 1: Fundamental and General Aspects; Part 2: Wettability Modification; and Part 3: Surface Free Energy and Adhesion. The topics covered include: wetting of solid walls and spontaneous capillary flow; “ordered water monolayer that does not completely wet water” at room temperature; Cheerios effect and its control by contact angle modulation; mathematical analysis of contact angle hysteresis; computational analysis of wetting and application to self-cleaning mechanisms; bubble adhesion to superhydrophilic surfaces; relationship between the roughness and oleophilicity of surfaces; liquid repellent amorphous carbon nanoparticle networks; mechanical durability of liquid repellent surfaces; superhydrophobic and superoleophobic biobased materials; laser ablation to render stainless steel superhydrophobic; RF plasma treatment of Neptune grass (*Posidonia oceanica*) to achieve superhydrophilic surfaces; combined photochemical and laser surface modifications to achieve liquid repellent textile surfaces; modification of paper/cellulose to control liquid wetting and adhesion; surface free energy of superhydrophobic materials; role of surface free energy in pharmaceutical tablet strength; and why test inks cannot tell the whole truth about surface free energy of solids.

As for this volume, it is essentially based on the written accounts of papers presented at the Ninth International Symposium on Contact Angle, Wettability and Adhesion held at Lehigh University, Bethlehem, PA, on June 16–18, 2014, under the auspices of MST Conferences. It should be recorded for posterity that all manuscripts submitted for this book were rigorously peer reviewed, suitably revised (some twice or thrice) and properly edited before inclusion in this book. As a matter of fact, some manuscripts are not included as they did not pass muster. So this book is not a mere collection of unreviewed and unedited papers, rather it represents articles which have passed rigorous peer scrutiny. Concomitantly, these articles are of archival value and their standard is as high as any journal or even higher than many journals.

It is quite manifest from the topics covered that the 17 chapters written by top-notch researchers which comprise this book address many aspects and ramifications of contact angles and wettability. The book provides a commentary on the current research being actively pursued in this domain and summarizes the research results of many active researchers in this field. Yours truly hopes that anyone wishing to stay abreast of the latest developments and prospects within the purview of contact angle, wettability and adhesion will find this book of great interest and value. In essence, Volume 2 supplements the information consolidated in its predecessor, Volume 1. In closing, I hope the information presented in this volume will spur further research and will serve as the provenance for new ideas. As we learn more about the wettability behavior of surfaces, new and exciting application vistas will emerge. All signals indicate that the high tempo of research in this field will continue unabated.

Now it is my pleasant duty to thank all those who contributed in many different ways in bringing this book to fruition. First and foremost, I am beholden to the authors for their enthusiasm, cooperation and contribution, without which this book would not have seen the light of day. Second, I would like to profusely thank the reviewers for their time and efforts in providing invaluable comments and suggestions which definitely improved the quality of articles included in this book. The comments from peers are a prerequisite for maintaining the highest standards of any publication. Last, but not least, my sincere appreciation goes to Martin Scrivener, publisher, for his unwavering support of this project and for giving this book a body form.

Kash Mittal
P.O. Box 1280
Hopewell Jct., NY 12533
E-mail: ushaRmittal@gmail.com
May 28, 2015

Part 1

FUNDAMENTAL AND GENERAL ASPECTS

Wetting of Solid Walls and Spontaneous Capillary Flow

Jean Berthier^{1,*} and Kenneth A. Brakke²

¹CEA-LETI, CEA/University Grenoble-Alpes, Department of Technology for Life Sciences and Health Care, Grenoble, France

²Department of Mathematics, Susquehanna University, Selinsgrove, PA, USA

Abstract

Spontaneous capillary flows are of great importance in space and biophysics. In space, the gravitational forces are negligible and capillary forces govern liquid motion. In modern biotechnology, the scale of fluidic systems is so small that gravity can be neglected in comparison to capillary forces. In this chapter, we first derive the condition for onset of spontaneous capillary flow in open or confined microchannels; then we present an analysis of the dynamics of the capillary flow that generalizes the Lucas-Washburn-Rideal law to channels of arbitrary section. Finally, we illustrate the theoretical approach by considering the case of suspended capillary microflows.

Keywords: Spontaneous capillary flow (SCF), Gibbs free energy, Lucas-Washburn-Rideal (LWR) law, suspended microflows

1.1 Introduction: Capillary Flows and Contact Angles

At the macroscale, capillary forces seldom have a noticeable effect on physical phenomena. The reason is that their magnitude is much smaller than that of the usual macroscopic forces, such as gravity. However, in two cases capillary forces may become important: in space where gravity is

*Corresponding author: jean.berthier@cea.fr

negligible, and at the micro and nano-scale. In this chapter, we focus on the role and effect of capillarity at the microscale for microflows. More specifically, the relation between the wetting of the walls and the capillary flow is investigated, first from a static or quasi-static point of view, and then from a dynamic point of view.

Biotechnology, biology and medicine are domains where capillarity is now widely used. Let us recall that in all these domains, the concepts of point-of-care (POC) and home care are of increasing interest [1-5]. These systems allow for self-testing and telemedicine. Three main types of tests are targeted: first, the search for metabolites—such as cholesterol, glucose, and thyroid hormones; second, the search for viral load—such as viruses and bacteria; and third, blood monitoring—such as the measure of INR (international normalized ratio), coagulation time, prothrombin (PR) time, or blood cell counts. Monitoring at home or at the doctor's office is an important improvement for the patient: frequent testing, immediate response, no visit to the hospital, and monitoring by telemedicine or directly by the doctor. Such systems must be low-cost, easily portable, sensitive, and robust.

In these domains where biological and chemical targets are transported by liquids, capillary actuation of liquids does not require bulky pumps or syringes, or any auxiliary energy sources. The energy source for the flow is the surface energy of the microchannel walls. On the other hand, conventional forced flow laboratory systems require the help of bulky equipment, which is expensive and not portable.

By definition, a spontaneous capillary flow (SCF) occurs when a liquid volume is moved spontaneously by the effect of capillary forces—without the help of auxiliary devices such as pumps or syringes. Capillary systems can be either confined or open, i.e. the liquid moves inside a closed channel or in a channel partially open to the air. On the other hand, composite channels—sometimes partly open or with apertures—are increasingly used, and spontaneous capillary flow is a convenient method to move liquids in such geometries. Some examples of SCF are shown in Figure 1.1.

In this chapter, we first investigate the conditions for spontaneous capillary flow in open or confined microchannels, composite or not, and we show that a generalized Cassie angle governs the onset of SCF [6]. Then we present the dynamics of the capillary flow with a generalized Lucas-Washburn-Rideal expression for the flow velocity and travel distance [7-9]. Finally, we focus on the particular effect of precursor capillary filaments—sometimes called Concus-Finn filaments [10,11]—that sometimes exist in sharp corners, depending on the wettability of the walls.

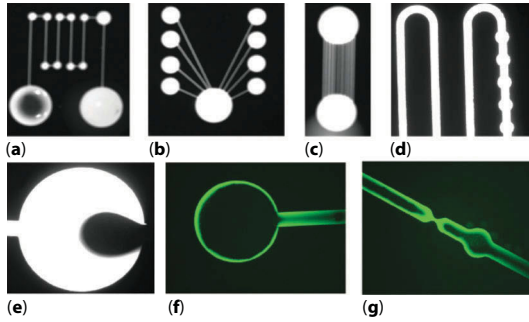


Figure 1.1 Different examples of spontaneous capillary flows (SCF) in open-surface microchannels (channels etched in silicon and coated by an SiO_2 layer): (a) serial SCF; (b) parallel SCF; (c) parallel channels; (d) winding channels crossing wells; (e) filling of a cylindrical cavity; (f) capillary filaments in a cylindrical well; (g) capillary filaments in corners. Photographs by N. Villard, D. Gosselin and J. Berthier (CEA-Leti).

1.2 A General Condition for Spontaneous Capillary Flow (SCF)

In this section, we analyze the conditions for the onset of SCF, i.e. the equilibrium state that is the limit for a capillary flow. Any change in these conditions results either in an advancing SCF, or in the receding of the liquid in the channel. We shall see that SCF depends on the wetting angle of the liquid with the walls, and on the geometry of the channel. Geometry has a profound influence on the channel's ability to allow for a capillary flow. Geometries facilitating the establishment of capillary flows in confined or open channels have been experimentally and numerically investigated [12-20].

From a theoretical standpoint, a first approach valid for confined or open channels with a single wall contact angle (uniform surface energy) has been recently proposed [21]. Later a general condition for SCF in confined or open microchannels, composite or not, was established based on the Gibbs free energy expression [6,22]. It is this latter condition—the most general—that we present next.

Let us consider the general case of a channel of uniform cross section, with a boundary with the surrounding air, and composite walls of different nature as sketched in Figure 1.2. We show that the condition for SCF onset is simply that the generalized Cassie angle for the composite surface be smaller than 90° . Let us recall that the generalized Cassie angle θ^* is the average contact angle defined in the appropriate way, i.e.

$$\cos \theta^* = \sum_i (f_i \cos \theta_i), \quad (1.1)$$

where the θ_i are the Young contact angles with each component i , and the f_i are the areal fraction of each component i in a cross section of the flow (Figure 1.2). The free interface with air is denoted by the index F .

1.2.1 Theoretical Condition

Our starting point is the Gibbs thermodynamic equation [22]

$$dG = \sum_i \gamma_i dA_i - p dV - S dT, \quad (1.2)$$

where G is the Gibbs free energy, A_i the liquid contact areas with the different boundary materials, γ_i the liquid interface tensions with the different boundary materials, V the liquid volume, p the liquid pressure, S the entropy and T the temperature. Generally in biotechnology (except for the very special cases where heating is used, such as for polymerase chain reaction PCR), the temperature is kept constant and the last term of (1.2) vanishes. Assuming a constant temperature, we consider the two following cases: first, the liquid volume is constant, as for a drop with negligible or slow evaporation, and second, an increasing volume of liquid. In the first case, (1.2) reduces to

$$dG = \sum_i \gamma_i dA_i \quad (1.3)$$

The equilibrium position of the droplet is obtained by finding the minimum of the Gibbs free energy. In this case, the minimization of the Gibbs free energy is equivalent to the minimization of the liquid surface area.

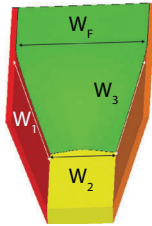


Figure 1.2 Cross section of a partly open composite microchannel: the lengths w_i stand for the wetted perimeters and w_F for free perimeter. The areal fractions are

$$f_i = w_i / \left(\sum_k w_k + w_F \right) \text{ and } f_F = w_F / \left(\sum_k w_k + w_F \right).$$

The second case—that of an SCF—is different: the volume of liquid is not constant in the system ($dV \neq 0$), and the system evolves in the direction of lower energy. Hence

$$\sum_i \gamma_i dA_i - p dV < 0. \quad (1.4)$$

The morphology of the free surface is such that it evolves to reduce the Gibbs free energy G . For simplicity, we first consider a uniform channel with a single contact angle and open to the air. The liquid (L) then has contact with solid (S) and air (G) as sketched in Figure 1.3.

Let us first investigate the upstream conditions. The upstream condition is most of the time given by the pressure condition of a reservoir of liquid. If we suppose that the reservoir is sufficiently large, as did Bruus [23], then the upstream pressure is constant and approximately equal to the atmospheric pressure (zero pressure difference), and the mean curvature of its free surface is small and nearly constant.

SCF occurs as long as the pressure at the flow front is smaller than that of the reservoir ($p \sim 0$), i.e., recalling that pressure may be regarded as the rate of change of energy with respect to volume,

$$\sum_i \gamma_i \frac{dA_i}{dV} < 0, \quad (1.5)$$

where the index i scans all the surfaces A_i (with surface tension γ_i of the liquid). Equation (1.5) can be written in the form

$$\sum_i \gamma_i \frac{dA_i}{dV} = \gamma_{SG} \frac{dA_{SG}}{dV} + \gamma_{SL} \frac{dA_{SL}}{dV} + \gamma_{LG} \frac{dA_{LG}}{dV} < 0. \quad (1.6)$$

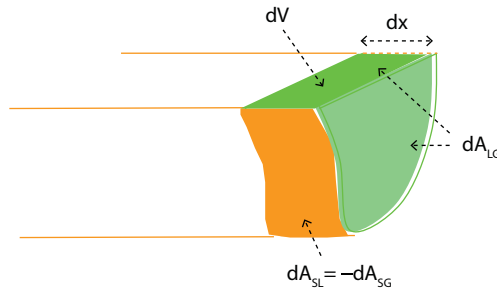


Figure 1.3 Sketch of the liquid front advancing along the solid surface by capillarity.

Considering that any change in A_{SL} is made at the expense of A_{SG} , and using Young's equation $\gamma_{LG} \cos \theta = \gamma_{SG} - \gamma_{SL}$, (1.6) becomes

$$\frac{dA_{LG}}{dV} < \cos \theta \frac{dA_{SL}}{dV}, \quad (1.7)$$

where θ is the Young contact angle. In other words, SCF occurs when

$$\frac{dA_{LG}}{dA_{SL}} < \cos \theta. \quad (1.8)$$

If we denote by w_s the wetted perimeter, i.e. the length of the contact line between the solid and the liquid in a cross section, and w_f the free perimeter, i.e. the length of the front not in contact with the walls in the same cross section, (1.8) yields the condition [21]

$$\frac{w_f}{w_s} < \cos \theta. \quad (1.9)$$

Condition (1.9) is a universal criterion for SCF, which is very simple to use and is confirmed by numerical and experimental results.

Now consider the general case of composite, non-homogeneous channel walls, as in Figure 1.2. The condition (1.6) becomes

$$\sum_i \gamma_i \frac{dA_i}{dV} = \sum_i \left(\gamma_{SG,i} \frac{dA_{SG,i}}{dV} + \gamma_{SL,i} \frac{dA_{SL,i}}{dV} \right) + \gamma_{LG} \frac{dA_{LG}}{dV} < 0. \quad (1.10)$$

Again, using Young's law, and keeping in mind that any change in $A_{SL,i}$ is made at the expense of $A_{SG,i}$ we derive

$$\sum_i \left(-\cos \theta_i \frac{dA_{SL,i}}{dV} \right) + \frac{dA_{LG}}{dV} < 0, \quad (1.11)$$

where the angles θ_i are the Young contact angles with each solid. Because (1.11) is valid for any dV , we obtain the general formula

$$\sum_i \left(-\cos \theta_i dA_{SL,i} \right) + dA_{LG} < 0. \quad (1.12)$$

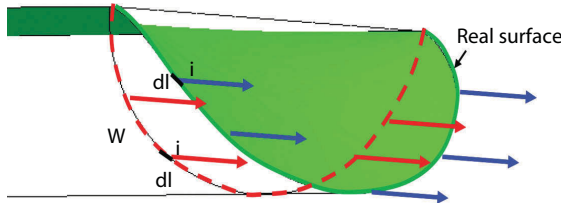


Figure 1.4 Sketch of the real surface and the w line.

Even if the real surfaces A are not flat surfaces, there is no loss of generality in writing

$$dA_{SL,i} = dx w_i, \quad (1.13)$$

where dx is an infinitesimal progression of the liquid front along the axial direction of the channel (Figure 1.3). This property just stems from the fact that the capillary force is identical along any contour traced by the triple line (Figure 1.4). Indeed,

$$\int_w \gamma \cos \theta_i \cdot d\vec{l} = \int_{\text{real surface}} \gamma \cos \theta_i \cdot d\vec{l}. \quad (1.14)$$

Assuming the channel is long compared to its width, the deformation of the free surface near the tip of the flow does not affect substantially the surface energy. Hence the surface in the “open” part of the cross section can be considered of constant shape independently of position along the channel. Then we can approximate

$$dA_{LG} \approx dx w_F. \quad (1.15)$$

A discussion about this hypothesis will be given later in the text. It will be shown that the hypothesis underlying (1.15) is nearly always satisfied, except when the contact angle is very small. Upon substitution of (1.13) and (1.15) in (1.12) we obtain

$$\sum_i (-\cos \theta_i w_i) + w_F < 0. \quad (1.16)$$

Relation (1.16) can be rewritten as

$$\sum_i \left(\cos \theta_i \frac{w_i}{L} \right) + \cos \pi \frac{w_F}{L} > 0, \quad (1.17)$$

where $L = \sum_i w_i + w_F$. By analogy, upon introduction of the generalized Cassie angle θ^* defined by

$$\cos \theta^* = \sum_i (f_i \cos \theta_i), \quad (1.18)$$

where the f_i are the fractional areas of each component ($f_i = w_i / L$, $f_F = w_F / L$), and using the convention that the contact angle with air is 180° , equation (1.18) reduces to the condition

$$\cos \theta^* > 0, \quad (1.19)$$

or

$$\theta^* = \arccos \left(\sum_i (\cos \theta_i f_i) \right) < \frac{\pi}{2}. \quad (1.20)$$

We find that the condition for SCF in a composite channel is simply that the generalized Cassie angle is smaller than 90° , i.e. the Cassie angle must be less than $\pi/2$. It is straightforward to see that the relation (1.20) reduces to the usual criterion for confined homogeneous channels.

1.2.2 Comparison Between Theory and Numerical Approach

In this section, we present a numerical approach based on the Surface Evolver numerical program [24]. Note that the Surface Evolver does not describe the dynamics of the motion, but iteratively relocates the interface to lower the energy. In the case of SCF, no equilibrium location exists, but we can still use Evolver to predict the direction of motion in SCF (but not the precise velocity of the motion).

In fact, Surface Evolver calculates the “static” shape of the advancing interface, which depends on the geometry and contact angles with the walls. This shape corresponds to a Laplace pressure. Assuming that the upstream condition is zero pressure (large reservoir), if the front end of the flow has a negative Laplace pressure, the flow will continue; if it has a zero curvature, the flow is stopped, if it has a positive Laplace pressure, the flow will recede. On one hand, at the onset of SCF, the velocities are

theoretically zero, and a static approach is valid. On the other hand, the quasi-static approach is not far from reality during the liquid progression in the channel since the capillary number is small. Indeed, the capillary number Ca , expressed by

$$Ca = \frac{V\mu}{\gamma}, \quad (1.21)$$

where V is the average liquid velocity, μ the dynamic viscosity of the liquid and γ the surface tension, characterizes the ratio between the viscous and the capillary forces. In the case of the aqueous solutions we have used here, $\mu \sim 0.001\text{--}0.1$ Pa.s, $\gamma \sim 0.030\text{--}0.072$ N/m and $V \sim 1\text{--}5$ mm/s (from measurements), thus $Ca \sim 1 \cdot 10^{-5} - 2 \cdot 10^{-2}$. Hence the surface tension forces are predominant in this problem.

Moreover, the interface relaxation time, characterized by the Tomotika time, is very small. Let us recall that the Tomotika time—or capillary time—noted $\tau_{capillary}$, is the time taken by a distorted liquid-air interface to regain its equilibrium shape against the action of the viscosity [25–28]. It is given by the ratio

$$\tau_{capillary} = \frac{\mu w}{\gamma}. \quad (1.22)$$

At the microscale, using our typical numerical values, we obtain $\tau_{capillary} \approx 10^{-5} - 10^{-6}$ seconds. The capillary time is much smaller than the time taken by the flow to fill even a small distance of the channel. In summary, even if the quasi-static approach does not account for the dynamics, it produces plausible results because the capillary number is much smaller than unity and the Tomotika time much smaller than the flow time scale in the channel. Hence Evolver produces a realistic succession of steady-state location of the interface, but does not account for the flow velocity.

SCF in two different types of composite channels is investigated: first a confined, rectangular microchannel, and second two different geometries of “open” channels, i.e. channels having a boundary with the surrounding air.

1.2.2.1 Composite Confined Channel

Let us start with the SCF in a confined rectangular microchannel of dimensions 250×150 μm with three different solid walls: the top plate has a contact angle of 45° with the liquid while the bottom plate has a contact angle of 120° and the vertical walls a contact angle of 100° (Figure 1.5a). Substitution in (1.18) shows that $\cos \theta^* \sim 0.02$, or $\theta^* \sim 89.2^\circ$. Using Evolver

we find that it is the onset of SCF. A comparison between Evolver results and the theoretical formula is shown in Figure 1.5b for varying top and bottom contact angles.

1.2.2.2 Composite Open Channel

Open channels with virtual walls have appeared recently in the literature. In such geometries, the liquid is partly in contact with the surrounding air, and partly in contact with different solid walls. Some open channels are simply rails, i.e. a channel wall with air gaps on both sides [29]. Other open channels are more complex, such as open rectangular U-grooves with circular apertures in the bottom plate [30].

In the geometry used by Satoh and colleagues [29], two parallel, horizontal plates—the rails—are used to guide the SCF; the capillary flow is

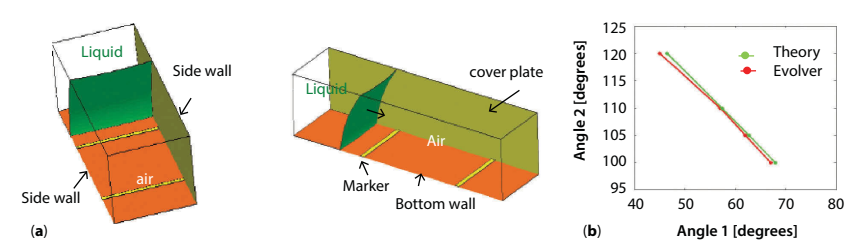


Figure 1.5 (a) SCF in a confined microchannel with three different solid walls (bottom, cover and side walls). Yellow lines are just markers to gauge the motion of the interface; some walls have been removed for visualization. (b) Comparison between theoretical criterion (green curve) and Evolver (red curve) for SCF onset in the case of a rectangular channel with three different contact angles with the liquid. Angles 1 and 2 are, respectively, the top and bottom plate contact angles.

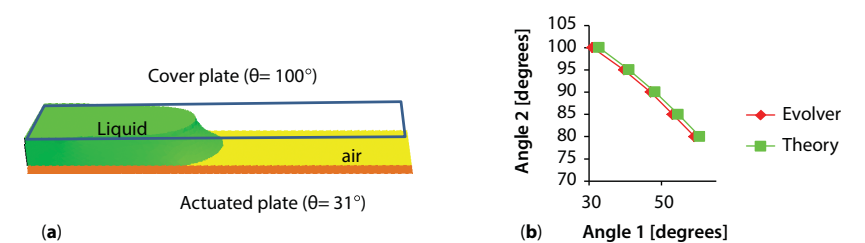


Figure 1.6 (a) SCF onset in a two-rail situation; (b) Comparison between theoretical criterion and Evolver for SCF. Angles 1 and 2 are, respectively, the bottom and top plate contact angles.

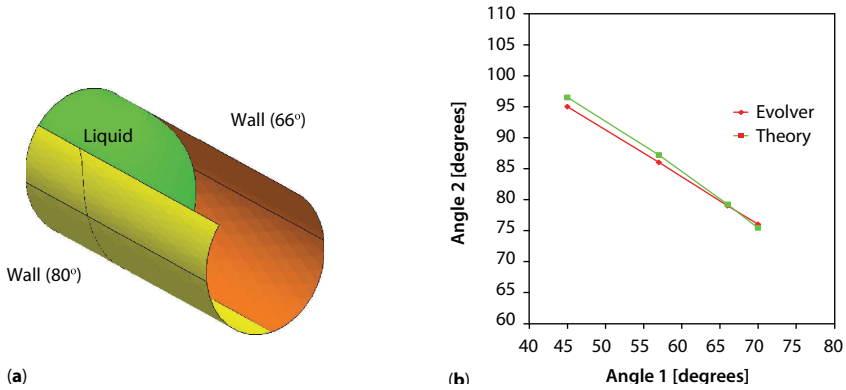


Figure 1.7 (a) Composite cylindrical channel; (b) comparison between theoretical criterion and Evolver for SCF onset in the case of the composite cylinder.

triggered by electrowetting, i.e. the contact angle with the bottom rail is adjusted by a proper level of the electric potential in the electrodes embedded in the rail. The width of the rails is $60\text{ }\mu\text{m}$ and the vertical gap $20\text{ }\mu\text{m}$. The contact angle with the top plate is 100° , and we find with Evolver that the actuated contact angle with the bottom plate for SCF onset should be 31° (Figure 1.6a). Substitution of these values in (1.18) produces the value $\theta^* \sim 89.5^\circ$. A more detailed comparison is shown in Figure 1.6b, where the SCF onset has been plotted versus the two contact angles with the solid walls. The discrepancy between the two curves—theoretical and numerical—is less than a few degrees.

Finally, we investigate the case of a partly open cylinder, with two different wall materials (Figure 1.7a). The radius of the cylinder is $200\text{ }\mu\text{m}$ and the width of the opening is $280\text{ }\mu\text{m}$. Using contact angles of 66° and 80° with the walls, we find $\theta^* \sim 90^\circ$. Again, the value predicted by (1.18) corresponds to the SCF onset found with Evolver. A more detailed comparison is shown in Figure 1.7b, where the SCF onset has been plotted versus the two contact angles with the solid walls. The discrepancy between the two curves—theoretical and Evolver—is again less than a few degrees.

1.2.3 Discussion

Let us come back to the assumption used for equation (1.15): $dA_{LG} \approx dx w_F$. This assumption is linked to a planar top interface and seems to fail when this top interface is distorted. In the following we consider an example

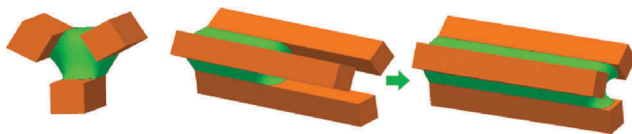


Figure 1.8 SCF between three parallel, square rods. Left: front view of the advancing liquid; middle and right: perspective views of the advancing SCF: The liquid (in green) is advancing, guided by the three rods.

where the top interface is not planar and assess the effect of the distortion on the SCF condition. It is concluded that relation (1.15) has a very wide range of validity.

Consider first the case of three parallel square rods shown in Figure 1.8. When the rods are close enough to each other, SCF occurs even for moderate contact angles (when the rods touch, a theoretical contact angle of 90° is sufficient to obtain SCF). When the rods are at a larger distance, small contact angles are needed to establish SCF. The inter-rod distance corresponding to the onset of SCF has been plotted versus the contact angles in Figure 1.9. The discrepancy between the two curves—theoretical and Evolver—is small for contact angles larger than 30° . Below this value, the relative discrepancy (relative distance between the two curves) is of the order of 5%. The approximation (1.15) can be considered valid.

1.2.4 Conclusion

Composite channels with walls of different nature, and sometimes with virtual walls, i.e. open boundaries, are increasingly used in modern biotechnology. In such designs, capillarity is used to move the liquid through the system. In particular, spontaneous capillary flow (SCF) is especially interesting since it does not require any pressure to move the liquid.

In order to be able to correctly design such systems, the ability to predict the occurrence of SCF is a necessity. A criterion for the establishment of SCF in such composite channels has been derived. This criterion is very simple: the corresponding generalized Cassie angle must be smaller than 90° . For confined microchannels, the result is straightforward, since the capillary line force is the product of the surface tension and the cosine of the contact angle. It is interesting to see that the result is also valid for open channels where the boundary of the liquid flow directly contacts the surrounding air.

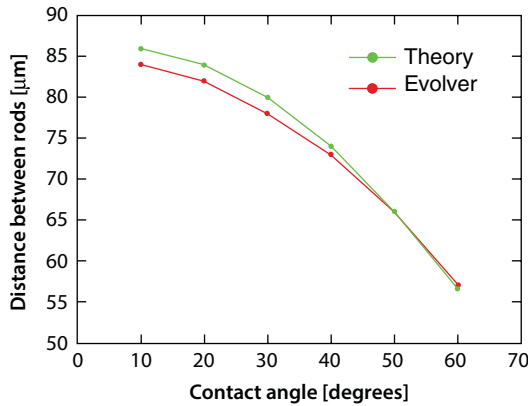


Figure 1.9 Comparison between theoretical criterion and Evolver for SCF onset in the case of three parallel rods. The agreement between the two approaches is good for contact angles larger than 30° and a little less accurate for contact angles smaller than 30° .

1.3 The Dynamics of SCF

For applications in medicine and biotechnology, it is of utmost importance to determine the sample liquid velocities in capillary systems. Especially it is essential to know if sufficiently high velocities can be reached in micro and nanochannels. It is also of importance to know if a system can be totally filled by the sample liquid in a reasonable time span (Figure 1.10).

In this section, the dynamics of spontaneous capillary flows in open or confined microchannels, composite or not, are investigated.

1.3.1 Open and Confined Systems

As we have seen previously, capillary microsystems can be confined or open, i.e. the liquid moves inside a closed channel or in a channel open to the air. Many different geometries of capillary channels exist (Figure 1.11). Of course, the most usual are those whose microfabrication is the easiest, such as rectangular and trapezoidal confined channels and open channels such as rectangular U and triangular V-grooves.

1.3.2 The Lucas-Washburn-Rideal (LWR) Law for Confined Cylindrical Channels

The study of the dynamics of capillary flows started as early as the 1910s with the developments made by Bell, Cameron, Lucas, Washburn and Rideal

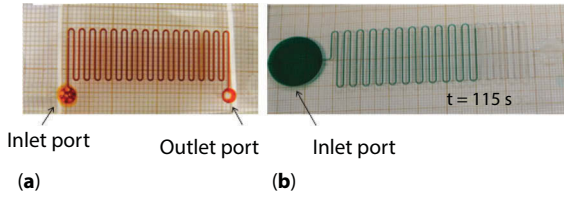


Figure 1.10 (a) capillary flow of red-dyed water in a suspended microchannel (no top cover and no bottom plate); (b) capillary flow of green-dyed water in a rectangular U-shaped microchannel. The channels are etched in PMMA (poly (methyl methacrylate)) in case (a) and COC (cyclic olefin copolymer) in case (b) in all cases, $w=300\text{ }\mu\text{m}$, $h=1000\text{ }\mu\text{m}$. The PMMA channel is 35 cm long and is filled in less than 100 seconds, and the COC channel is 60 cm long and is filled in less than 220 seconds. Photographs by N. Villard, D. Gosselin and J. Berthier (CEA-Leti).

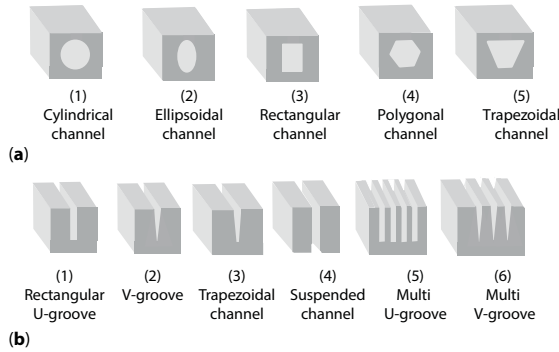


Figure 1.11 Different morphologies of capillary channels. (a) confined (closed) channels. (b) open channels.

[7-9] for cylindrical channels. In general, at the scale of microsystems, inertia is negligible. Indeed, the Reynolds number is usually small. Let us recall that the Reynolds number Re is the ratio of the inertial forces to the viscous forces, $Re = V w / \nu$, where V is the velocity, w a characteristic geometric scale and ν the kinematic viscosity of the liquid. Then a closed-form expression for the travel distance—the distance between channel entrance and the front meniscus of the liquid at a given time—can be derived. This expression is now commonly called the Lucas-Washburn-Rideal (LWR) law

$$z = \sqrt{\frac{\gamma \cos \theta R t}{2 \mu}}, \quad (1.23)$$

where R is the channel radius, μ the dynamic viscosity of the liquid, γ the surface tension, z the travel distance and t the time.

The reasoning behind (1.23) is straightforward: let us consider the two forces acting on the liquid, i.e. the capillary force F_{cap} and the drag force F_{drag} . If the inertial force is negligible, the motion is determined by the balance between these two forces, and using a Poiseuille flow profile for the calculation of the drag force, one can write

$$F_{cap} = 2\pi R \gamma \cos \theta = F_{drag} = 8\pi \mu z V. \quad (1.24)$$

Upon substitution of $V = dz/dt$, and integration, one obtains (23). This expression, valid for a cylinder, has been frequently used for other shapes of channels by replacing the radius R by the hydraulic radius R_H . The hydraulic radius is the half of the hydraulic diameter that is defined $D_H = 4S_C/p$ where S_C is the cross-sectional area, and p the perimeter. In our case, the hydraulic diameter is simply defined by

$$D_H = 4 \frac{S_C}{w}, \quad (1.25)$$

where S_C is the cross-sectional surface area and w is the wetted perimeter of the cross section. However, the use of the hydraulic diameter introduces a bias if the channel is not circular, as we shall see in the following section.

1.3.3 Generalization of the Lucas-Washburn-Rideal Law to Composite, Confined Microchannels of Arbitrary Cross Section

In this section, the general expression for the determination of the velocities of spontaneous capillary flows in composite, confined microchannels of arbitrary shapes is presented. This expression generalizes the conventional Lucas-Washburn-Rideal model, which is valid for cylindrical channels. It will be shown that the use of an equivalent hydraulic diameter in the Lucas-Washburn-Rideal model introduces a bias when the shape of the channel cross section differs notably from a circle.

1.3.3.1 Theory

Let us consider a confined composite channel of uniform cross section, of arbitrary shape, composed of different walls, i.e. walls of different surface energies, as depicted in Figure 1.12.

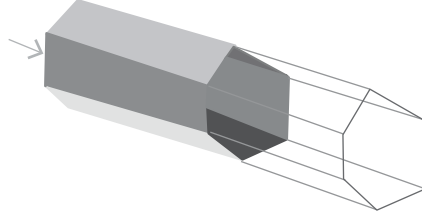


Figure 1.12 Sketch of a composite microchannel with 6 different solid surfaces.

It has been shown that the capillary force is

$$F_{cap} = \gamma \sum_{i=1,n} w_i \cos \theta_i, \quad (1.26)$$

where γ is the surface tension between the liquid and air, and w_i and θ are, respectively, the wetted perimeters and dynamic contact angles in a cross section of the channel—which comprises n different wall surfaces. If we denote by f_i the fraction of the wetted perimeter related to the wall i

$$f_i = \frac{w_i}{L}, \quad (1.27)$$

where L is the cross-sectional perimeter, and using the Cassie notation $\cos \theta^* = \sum_{i=1,n} f_i \cos \theta_i$, relation (1.26) can be recast as:

$$F_{cap} = \gamma L \cos \theta^*. \quad (1.28)$$

From a dynamic standpoint, the velocity of the capillary flow can be determined using the balance between capillary forces and drag force with walls. The drag force is

$$F_{drag} = \int_S \tau ds = \left(\int_{\Gamma} \tau dl \right) z(t) = \bar{\tau} L z(t), \quad (1.29)$$

where τ is the local wall friction, S the wetted surface between the origin and the front end of the liquid flow, Γ the wetted contour of the cross section, $\bar{\tau} = (1/L) \int_{\Gamma} \tau dl$, and z the distance of the interface from inlet, which depends on the time t . The force balance on the liquid flow is then

$$\frac{d(mV)}{dt} = F_{cap} - F_{drag}, \quad (1.30)$$

where m is the (increasing) mass of the liquid in the channel, $m = \rho z(t)S_c$, and V the average velocity. The mass of liquid being proportional to the penetration distance z , (1.30) can be written in the form

$$\rho S_c \left(z \frac{dV}{dt} + V^2 \right) = \gamma L \cos \theta^* - \bar{\tau} L z(t), \quad (1.31)$$

where S_c is the cross-sectional area and ρ the density of the liquid. The Reynolds number of the liquid being small, the flow is fully laminar. The friction τ then depends on the geometry of the channel and on the average velocity V . Locally, the wall friction is

$$\tau = \mu \frac{\partial V}{\partial y} = \frac{\mu V}{\lambda}, \quad (1.32)$$

where λ is a local friction length and ρ the coordinate perpendicular to the wall. A sketch of the friction length λ is shown in Figure 1.13.

Conceptually, the friction can be averaged over a whole wetted cross section,

$$\bar{\tau} = \frac{1}{L} \int_{\Gamma} \tau dl = \frac{1}{L} \int_{\Gamma} \frac{\mu V}{\lambda} dl = \frac{\mu V}{\bar{\lambda}}, \quad (1.33)$$

where $\frac{1}{\bar{\lambda}} = \frac{1}{L} \int_{\Gamma} \frac{1}{\lambda} dl$ is by definition the average friction length. Note that the derivation of (1.33) assumes a constant value of the viscosity, which occurs only for Newtonian liquids. The case of non-Newtonian liquids is

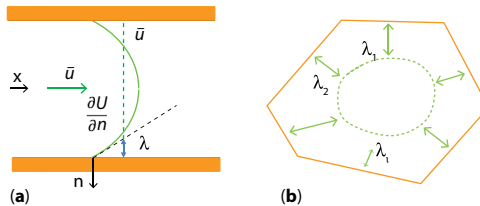


Figure 1.13 (a) Sketch of the local friction length λ between two parallel plates and (b) of the different friction lengths in a channel cross section.

more complex and is not treated here; in fact, the dynamics of capillary flows of non-Newtonian liquids is still in its infancy. Using the relation

$$V = \frac{dz}{dt}, \quad (1.34)$$

and substituting in (1.31) yields the differential equation

$$\rho S_c \frac{1}{2} \frac{d^2 z^2}{dt^2} = \gamma L \cos \theta^* - \bar{\tau} L z(t). \quad (1.35)$$

Substituting (1.33) in (1.35) yields

$$\rho S_c \frac{1}{2} \frac{d^2 z^2}{dt^2} = \gamma L \cos \theta^* - \mu \frac{L}{2 \bar{\lambda}} \frac{dz^2}{dt}. \quad (1.36)$$

Most of the time in capillary microsystems, inertia can be neglected because the Reynolds number is small, i.e.

$$\text{Re} = V w / \nu \leq O(1), \quad (1.37)$$

where w is a characteristic dimension of the channel, ν the kinematic viscosity, and $O(1)$ means “order of 1”. Hence, the left hand side term in (1.36) is most of the time negligible. In fact, equation (1.36) is a differential equation in z^2 ; denoting $A = \mu L / (2 \bar{\lambda} \rho S_c)$ and $B = \gamma L \cos \theta^* / (\rho S_c)$, and using the intermediate variables $Z = z^2$ and $U = dZ/dt$, equation (1.36) can be integrated twice and we find

$$z^2 = \frac{1}{A} \left[Bt + C \left(1 - e^{-At} \right) \right], \quad (1.38)$$

where $C = B/A$. Note that (1.38) implies an infinite velocity at $z = 0$, because $dz/dt = V \sim C/z$ at $t=0$. In reality, there is a very small time lapse before flow establishment, and (1.38) is not valid for $z = 0$. Note also that the value of A is usually high, because of the term S_c at the denominator, and the second term on the right side of (1.38) is negligible, after the time $t > 2/A$.

Neglecting inertia, a closed-form expression for the travel distance z is then

$$z = \sqrt{\frac{\gamma}{\mu}} \sqrt{\cos \theta^*} \sqrt{2 \bar{\lambda} t} . \quad (1.39)$$

The travel distance varies as the square root of the time, in agreement with the Lucas-Washburn-Rideal (LWR) model for capillary flows inside cylinders [7-9]. The liquid velocity can be readily derived from (1.39)

$$V = \sqrt{\frac{\gamma}{\mu}} \sqrt{\cos \theta^*} \sqrt{\frac{\bar{\lambda}}{2t}} . \quad (1.40)$$

In this form, the liquid velocity is the product of the square root of a “physical” velocity $\sqrt{\gamma/\mu}$ —related to the physical properties of the materials—the square root of a “geometrical” velocity $\sqrt{\bar{\lambda}/2t}$, and the cosine of the generalized Cassie angle $\cos \theta^* = \sum_i f_i \cos \theta_i$.

On the other hand, because dz exponent $d z^2/dt=2zV$, relation (1.38) immediately produces a relation between the velocity and the travel distance,

$$V = \frac{\gamma \bar{\lambda}}{\mu} \cos \theta^* \frac{1}{z} . \quad (1.41)$$

Relation (1.41) can be transformed to (1.42) by multiplying both sides in (1.41) by L and dividing by the cross-sectional area S_c

$$\mu \frac{Lz}{\bar{\lambda} S_c} V = \frac{\gamma L \cos \theta^*}{S_c} = \frac{\gamma \sum_{i=1,n} w_i \cos \theta_i}{S_c} . \quad (1.42)$$

We observe that the right hand side is the capillary force F_{cap} divided by the cross-sectional area S_c , i.e. the Laplace pressure at the advancing interface. Hence we obtain the formula

$$\Delta P = \frac{\gamma L \cos \theta^*}{S_c} = \mu \frac{Lz}{\bar{\lambda} S_c} V = \tilde{R}_H z V . \quad (1.43)$$

In the case of confined channels, relation (1.43) is just the translation of the usual pressure drop over a distance z for forced laminar flows to the case of capillary flows,

$$\Delta P = R_H V = \tilde{R}_H z V, \quad (1.44)$$

where \tilde{R}_H is the hydraulic resistance per unit length. Note that the hydraulic resistance R_H that we use here is the ratio of the pressure drop to the average liquid velocity $R_H = \Delta P/V$; some authors consider the ratio of the pressure drop to the volumic flow rate. The definitions are nearly identical; they just differ by a constant, which is the channel cross section. The resistance \tilde{R}_H is the same in (1.43) and (1.44): in both cases, the laminar flow obeys the same Stokes equation, which is the fundamental basis for formula (1.44) [31,32]. The difference pertains to the boundary conditions: forced microflows usually have a pressure or a flow rate imposed at the back end of the flow, except in the case of aspiration, while capillary flows are driven by capillary forces at the front end of the flow.

An interesting application of the formula (1.43) is the direct deduction of the average friction length $\bar{\lambda}$ —and consequently the capillary velocity—when the hydraulic resistance \tilde{R}_H is known, according to

$$\bar{\lambda} = \mu \frac{L}{\tilde{R}_H S_c}. \quad (1.45)$$

The friction length $\bar{\lambda}$ can be related to the hydraulic diameter $D_H = 4S_c/L$. Substitution of the expression for the hydraulic diameter (1.25) in (1.45) yields

$$\bar{\lambda} = \mu \frac{4}{\tilde{R}_H D_H}. \quad (1.46)$$

Let us recall that tables for such resistances as a function of the shape and dimensions of the channels have been reported in the literature for many different confined channels [28,33-36]. In the following section, we deduce velocity expressions for different usual geometrical shapes of the channel cross section. We then propose a simple method to determine the capillary velocity in an arbitrary cross section channel. Finally, we investigate the conditions for obtaining large velocities in capillary-based systems.

1.3.3.2 Expression for the Capillary Velocity

Consider first the case of confined cylindrical channels. This was the first configuration studied. Lucas, Washburn and Rideal gave a non-inertial solution as early as 1921 [7–9]. In (1.46), the value of $\bar{\lambda}$ can be determined by considering the value of the hydraulic resistance per unit length $\tilde{R}_H = 8\mu/R^2$, the wetted perimeter $P_w = 2\pi R$, and the cross-sectional surface area $S_c = \pi R^2$, and using (1.45). One obtains $\bar{\lambda} = R/4$. After substituting this value in (1.39), it is easily seen that relation (1.39) produces exactly the LWR equation.

The method can be extended to the different shapes reported in the literature. We just indicate in Table 1.1 the values of $\bar{\lambda}$ for a few geometries [28,33–36].

Tables for laminar pressure drops are often expressed as a function of the Poiseuille number Po [34]

$$Po = \frac{f Re}{4} = \frac{1}{\mu} \frac{\partial P}{\partial z} \frac{D_H^2}{2V}, \quad (1.47)$$

where Re is the Reynolds number and f the Fanning coefficient. Relation (1.47) can be cast in the form

$$\Delta P = \tilde{R}_H z V = \left(\frac{\mu f Re}{2D_H^2} \right) z V, \quad (1.48)$$

where ΔP is the pressure drop in the length z in the channel. In this form, we see that the average friction length given by relation (1.46) is related to the hydraulic diameter by

$$\bar{\lambda} = \frac{8D_H}{f Re}. \quad (1.49)$$

Table 1.2, taken from [34], shows some expressions for the Poiseuille number together with the friction length. Using Tables 1.1 and 1.2, the travel distances and flow velocities can be easily determined. For a confined channel with a single contact angle, relation (1.39) yields

$$z = 4 \sqrt{\frac{\gamma}{\mu}} \sqrt{\cos \theta} \sqrt{\frac{D_H}{f Re}} t, \quad (1.50)$$

Table 1.1 Values of the average friction length for different geometries.

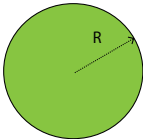

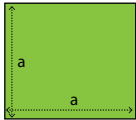
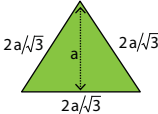
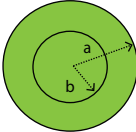
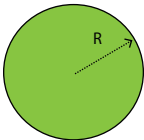

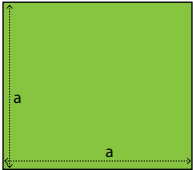
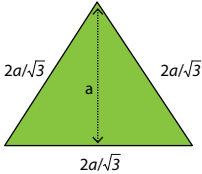
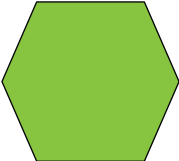
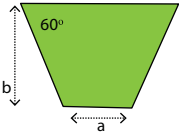
Cross Section	Hydraulic Resistance (Per Unit Length)	Cross-Sectional Area S_c and Wetted Perimeter P_w	Average Friction Length, $\bar{\lambda}$
	$\tilde{R}_H = \frac{8\mu}{R^2}$	$S_c = \pi R^2$ $p_w = 2\pi R$	$\bar{\lambda} = \frac{R}{4}$
	$\tilde{R}_H = \frac{4\mu}{h^2} \frac{1}{q(\varepsilon)},$ $\varepsilon = h/w$ $q(\varepsilon) = \frac{1}{3} - \frac{64}{\pi^5} \varepsilon \tanh\left(\frac{\pi}{2\varepsilon}\right)$	$S_c = hw$ $p_w = 2(w+h)$	$\bar{\lambda} = \frac{\varepsilon q(\varepsilon)(w+h)}{2}$
	$\tilde{R}_H = \frac{28.3\mu}{a^2}$	$S_c = a^2$ $p_w = 4a$	$\bar{\lambda} = \frac{a}{7.1}$
	$\tilde{R}_H = \frac{60\mu}{a^2}$	$S_c = a^2/\sqrt{3}$ $p_w = 6a/\sqrt{3}$	$\bar{\lambda} = \frac{a}{15\sqrt{3}}$
	$\tilde{R}_H = \frac{8\mu}{a^2} \frac{1}{\beta}$ $\varepsilon = b/a$ $\beta = \varepsilon^2 - 1 + \frac{2\ln(1/\varepsilon) + \varepsilon^2 - 1}{\ln(1/\varepsilon)}$	$S_c = \pi(a^2 - b^2)$ $p_w = 2\pi(a+b)$	$\bar{\lambda} = \frac{\beta}{4} \frac{a^2}{(a-b)}$

Table 1.2 Values of the average friction length $\bar{\lambda}$ for different geometries, using the Poiseuille number [32].

Cross Section	$f Re$	Hydraulic Diameter, D_H	Average Friction Length, $\bar{\lambda}$
	64	$D_H = 2R$	$\bar{\lambda} = \frac{R}{4}$
 $h \ll w$	96	$D_H \approx 2h$	$\bar{\lambda} \approx \frac{h}{6}$
	56.92	$D_H = a$	$\bar{\lambda} = \frac{a}{7.1}$
	120	$D_H = \frac{a}{\sqrt{3}}$	$\bar{\lambda} = \frac{a}{15\sqrt{3}}$
	60	$D_H = a\sqrt{3}$	$\bar{\lambda} = \frac{a}{4.33}$
	b/a 4 55.66 2 55.22 1 56.60 0.5 62.77	$D_H = \frac{2b(a\sqrt{3} + b)}{\sqrt{3}(a + b\sqrt{3})}$	$\bar{\lambda} = D_H/6.96$ $\bar{\lambda} = D_H/6.90$ $\bar{\lambda} = D_H/7.07$ $\bar{\lambda} = D_H/7.85$

and relation (1.40) yields

$$V = 2\sqrt{\frac{\gamma}{\mu}}\sqrt{\cos\theta}\sqrt{\frac{D_H}{(f\text{Re})t}}. \quad (1.51)$$

Expressions (1.50) and (1.51) easily produce the travel distance and velocity as a function of time in capillary channels, as long as the Poiseuille number is known. On the one hand, the hydraulic diameter is easy to obtain from the value of the cross-sectional area and the wetted perimeter. On the other hand, the values of the Poiseuille numbers for complicated geometries not described in the literature can be obtained either by experimentation or by numerical methods, such as finite element models [37].

Note that LWR expression (1.23)—in which the radius R is replaced by the hydraulic radius—is often used in the literature to calculate the travel distance. The difference in the travel distances obtained by this method and those obtained with expression (1.50) is

$$\begin{aligned} \Delta z &= \sqrt{\frac{\gamma}{\mu}}\sqrt{\cos\theta}\sqrt{t}\left(\sqrt{\frac{16D_H}{f\text{Re}}} - \sqrt{\frac{D_H}{4}}\right) \\ &= \sqrt{\frac{\gamma}{\mu}}\sqrt{\cos\theta}\sqrt{\frac{16D_H}{f\text{Re}}t}\left(1 - \sqrt{\frac{f\text{Re}}{64}}\right) \end{aligned} \quad (1.52)$$

For “regular” shapes, such as squares or hexagons, or even some trapezes, the value of $f\text{Re}$ is close to 64 (Table 1.2). However, for “irregular” shapes, such as slender rectangles, or triangles, a systematic error is made. This systematic relative error E is

$$E = \left|\frac{\Delta z}{z}\right| = \left|1 - \sqrt{\frac{f\text{Re}}{64}}\right|. \quad (1.53)$$

For the values $f\text{Re} = \{57, 60, 64, 96, 120\}$, respectively corresponding to square, hexagonal, circular, rectangular and triangular shapes, the relative errors are $E = \{6\%, 3\%, 0\%, 22\%, 37\%\}$. The error is large for very irregular shapes.

1.3.3.3 Magnitude of Capillary Velocities

Obtaining sufficiently high velocities is a major issue for capillary systems. It is essential to reach sufficiently high velocities in order to fill a capillary system in a short time span. Also, high velocities are useful for the dissolution, mixing and dispersion of dried or lyophilized reagents often used in capillary devices.

In Figure 1.14, the travel distances and liquid velocities for water ($\mu=1$ cP, $\gamma=72$ mN/m) have been plotted for 6 channels of the same cross-sectional area ($S_c=0.0314$ mm²), but different shapes: circle, square, hexagon, equilateral triangle, slender rectangles of aspect ratio $w/h=10$ and 50. In all cases, the dynamic advancing contact angle is 45°. The velocity expression (1.51) derived in the preceding section shows that relatively high velocities can be obtained, of the order of 3 to 7 mm/s—which is very high for micro-systems—and that large travel distances (~200–300 mm) can be achieved in less than one minute.

It appears from Figure 1.14, that the highest velocities are obtained for channel shapes close to a circle, whereas angular and/or elongated shapes correspond to smaller velocities. Concave shapes are more detrimental to capillary velocity. This result is consistent with the observations already made by Zimmermann *et al.* [15] and Safavieh and Juncker [38], who used constricted channels as flow resistances to reduce the capillary flow velocity (Figure 1.15).

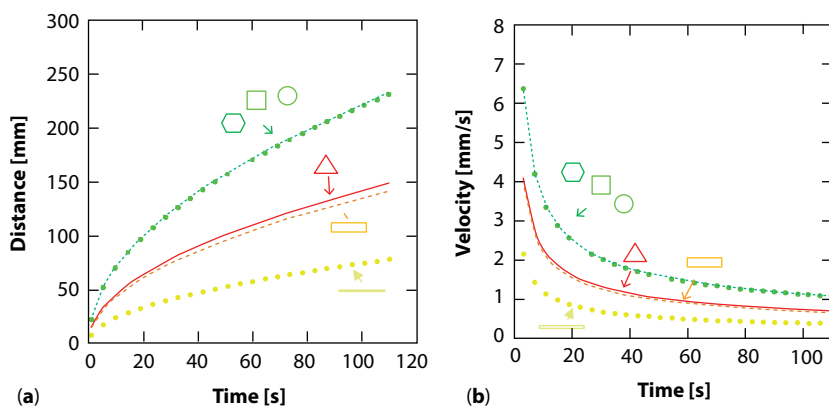


Figure 1.14 (a) Travel distance vs. time for 6 different channel shapes; (b) velocity vs. time for 6 different channel shapes.

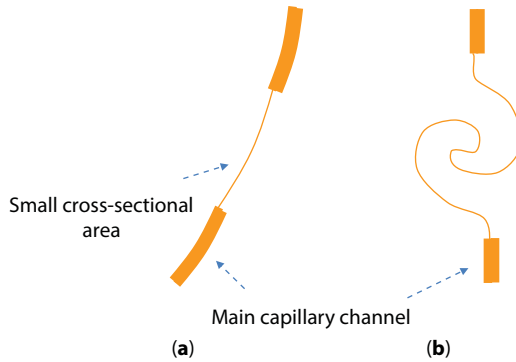


Figure 1.15 View from top: two types of flow resistors, from [15,38]. The main channel is interrupted by a section of very small width. In (a) the narrow section is short and produces a small hydraulic resistance, while in (b) the long, narrow section produces a high hydraulic resistance.

In their case, the cross section is decreased by a reduction of the channel width, the etch depth being unchanged. According to Table 1.2, the value of the friction length for the nominal square channels is $\bar{\lambda}_0 \approx w_0/7.1$, and inside the rectangular constricted channels the friction length is $\bar{\lambda} \approx w/6$. The friction length is then reduced by $\bar{\lambda}/\bar{\lambda}_0 \approx 0.8 (w/w_0)$. The length of the constricted channel also contributes to the flow resistance (difference between A and B in Figure 1.15). On the other hand, high values of the velocity are achieved by etching a channel of dimensions $w=h$, according to Figure 1.14.

1.3.4 Experimental Results for Confined Channels

It was remarked above that equation (1.50) satisfies the Washburn kinetics for cylindrical channels. Let us consider now rectangular cross section channels.

1.3.4.1 Rectangular Channels

We consider first the results obtained by Han and coworkers [39] for nano-channels of approximately rectangular cross section, and coated by a SiO_2 layer (Figure 1.16a). The nanochannels are 900 nm wide with three different depths: 27, 50 and 73 nm. Four different liquids were used: water, a 40% ethanol solution, pure ethanol, and isopropanol. The physical properties of the liquids are tabulated in the literature [40]. In all cases the Washburn

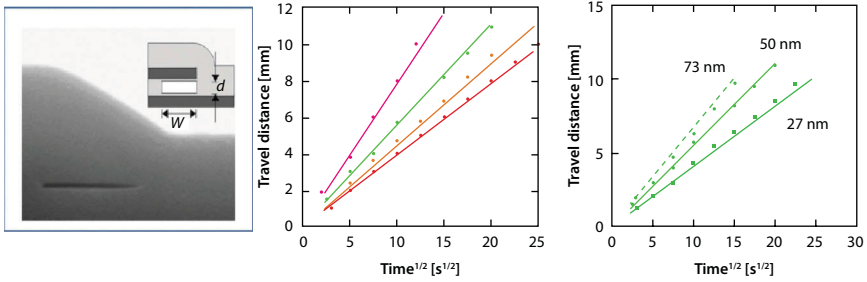


Figure 1.16 (a) View of the horizontal slot ($d = 50$ nm, $w = 900$ nm) [39]; reprinted with permission © Elsevier, 2006. (b) Comparison between experimental results (dots) and model (50) for the travel distance as a function of the square root of time for the four liquids (red-isopropanol, orange-40% ethanol, green-ethanol, and violet-water) in the 50 nm deep channel. (c) travel distances vs. square root of time for ethanol in the three channels (27 nm, 50 nm and 73 nm).

kinetics is obeyed, i.e. the travel distance is proportional to the square root of time.

In their approach the authors directly use the Washburn formula for a cylindrical tube, replacing the radius by the hydraulic radius, and calculate the dynamic contact angle by fitting the curves. It can be observed that this approach with the hydraulic radius yields different contact angles for ethanol—respectively 46, 50 and 55°—in the three channels of different depths—respectively 27, 50 and 73 nm. The reason for the change in contact angle with the change in depth is unclear. The same approach can be repeated using relation (1.50), and using the distance $\bar{\lambda}$. One obtains the results plotted in Figure 1.16b and c. The dynamic contact angle for ethanol is nearly identical in the three cases (43°, 44° and 44° for the 27, 50 and 73 nm depth channels).

As Han and coworkers observed, no change in the advancing contact angle was found with the velocity decrease during the capillary flow. The plots of the travel distance as function of the square root of time are linear with a very small standard deviation. This is in agreement with the observations of Sobolev and colleagues for nanocapillaries [41]. It is also consistent with the investigations of Hamraoui and colleagues [42], who obtained the following expression for the dynamic contact angle:

$$\gamma(\cos \theta_0 - \cos \theta) = \beta V^n, \quad (1.54)$$

where θ_0 and θ are, respectively, the static and dynamic contact angles, β a coefficient of the order of 0.1 to 0.4 and n a coefficient of the order of 1.

Joos and colleagues [43] have proposed a similar expression. In the configurations examined here the flow velocity is less than a few millimeter per second—except at the very beginning of the flow—and the dynamic contact angle is equal to the static contact angle.

1.3.4.2 Trapezoidal Channel

We now relate experiments performed in a winding trapezoidal channel (Figure 1.17). The channel was formed by hot roll embossing of a plastic (PMMA) substrate. The substrate was then treated with O_2 plasma in order to obtain a hydrophilic surface. The channel was covered by a plastic film. The shape of the channel is close to a trapezoid with slightly concave sides, due to the roll embossing (Figure 1.17). The dimensions of the cross section are $a=400\text{ }\mu\text{m}$, $b=800\text{ }\mu\text{m}$, $h\sim 110\text{ }\mu\text{m}$. The corresponding hydraulic diameter is then $D_H\sim 93\text{ }\mu\text{m}$. Water dyed with yellow food coloring was introduced with a pipette in an inlet port (large cylindrical well). The static contact angle of the liquid on the surface was measured with a Krüss device, with a value 28° . The contact angle with the cover film was 120° . Due to the glycol contained in the food coloring, the liquid had a viscosity of 3.5 cP , and a surface tension of 42 mN/m . A finite element model was set up to determine the hydraulic resistance of the trapezoidal channel. A Poiseuille number of $Po=14.25$ was found, corresponding to $fRe=57$. This value is consistent with the values in Table 1.2 (bottom row).

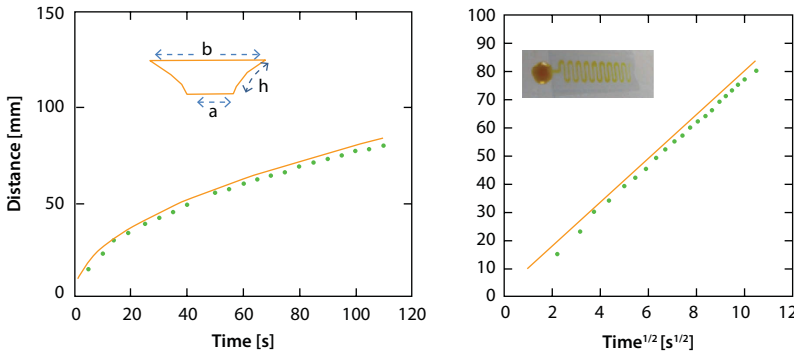


Figure 1.17 Comparison between experiments (green dots) and present model (continuous orange line) for a trapezoidal channel. Left: travel distance as a function of time. Right: travel distance as a function of the square root of time. The photo represents a view of the liquid (yellow tinted water) flowing in the winding channel. The \sqrt{t} law fits well the experiments, with the constant value of the static contact angle.

Photographs of the channel were taken every 5 seconds. A comparison between the experimental results and the present model is shown in Figure 1.17. We observe that the \sqrt{t} law fits well the experiments, with the constant value of the static contact angle. A small overshoot is observed but it is not significant. It is within the error margin of the uncertainties of measurement of the surface tension, viscosity and contact angle.

1.3.4.3 Conclusion

In this section, the capillary velocities in confined, composite channels of arbitrary shapes were investigated. Closed-form expressions for the travel distances and velocities have been worked out, showing respectively dependencies as \sqrt{t} and $\sqrt{1/t}$, in agreement with the Lucas-Washburn-Rideal approach. It is shown that, for any geometry and composite wall, the square of the capillary velocity is the product of a “physical” velocity and a “geometrical” velocity. Moreover, the coefficient appearing in the formula is the cosine of the generalized Cassie angle.

It is also shown that the conventional Lucas-Washburn-Rideal expression is only valid for cylindrical ducts and that the use of an equivalent hydraulic diameter, as is sometimes done in the literature, introduces a systematic bias when the shape of the channel cross section differs notably from a circle.

No change in the dynamic contact angle is observed during the velocity decrease of the capillary flow. This observation is related to the small capillary and Reynolds numbers associated to an inertialess flow. In fact, using the expression for the dynamic contact angle, it is shown that the dynamic contact angle is nearly equal to the static contact angle.

Nevertheless, there are two restrictions to the present developments: First, the liquids have been chosen to have a Newtonian behavior, with a constant viscosity during the flow. The non-Newtonian aspect is still to be investigated since biological liquids often have a shear-thinning behavior, and their viscosity increases with the decrease of the velocity in the capillary channel. Second, capillary filaments may form in sharp corners, as was shown by Concus and Finn [10], and their entrainment effect on the bulk of the flow is still unknown.

1.3.5 Capillary Flow in Open Microchannels: The Example of Suspended Microflows

Amongst the systems based on capillarity, open systems—i.e. microflows with a free surface—are of increasing interest because of their great

accessibility, robustness, functionality, inexpensive fabrication and versatility. However, the physics of open capillary flows is complicated because of the free, deformable interface with air. A formulation equivalent to the generalized Lucas-Washburn-Rideal expression for confined capillary flows is still to be found.

Let us take the example of a subcategory of open microflows called “suspended microflows” which has recently emerged. By definition, a suspended microflow is a flow that uses surface tension to fill and maintain the liquid in microscale structures devoid of a ceiling and floor. A sketch of a typical suspended channel between parallel, vertical walls is shown in Figure 1.18a. A suspended channel drilled through a PMMA plate is shown in Figure 1.18b, and different configurations of suspended flows are shown in Figures 1.18c, d and e.

So far there have been only a few publications on suspended microfluidics [28,45,46]. Below we examine the case of a spontaneous capillary flow in suspended microchannels with parallel, vertical walls. First, we theoretically derive the conditions for SCF onset using an approach based on the Gibbs free energy [4]. Next, we verify the onset of SCF using the Surface Evolver numerical program. The dynamics of the liquid motion is then analyzed, using analytical arguments based on a force balance between the

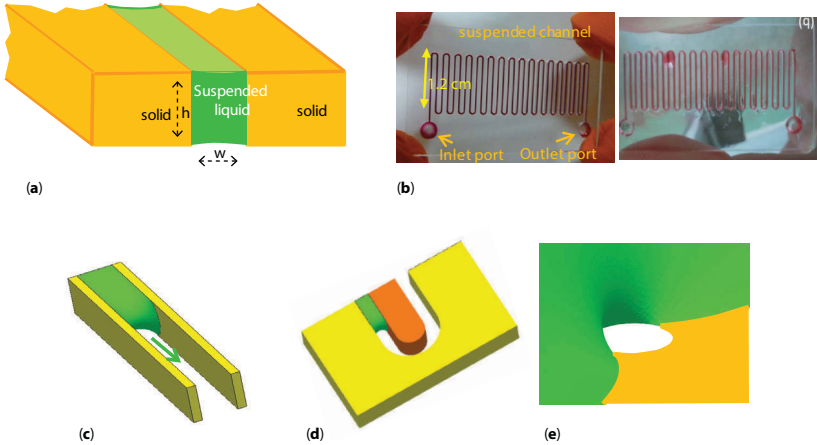


Figure 1.18 (a) Sketch of a suspended microflow between two parallel, vertical walls; (b) photographs of a suspended channel drilled in a PMMA plate ($w=300\ \mu\text{m}$, $h=1000\ \mu\text{m}$); (c) Evolver view of a suspended flow between parallel, vertical walls; (d) Evolver calculation of a suspended capillary flow in a winding channel; (e) Evolver calculation of a capillary flow blocked by a hole in the bottom plate. Photographs by N. Villard and D. Gosselin (CEA-Leti).

capillary forces—which drive the flow—and viscous friction at the walls, which resists the motion of the liquid. Experiments using tinted aqueous solutions of alginate confirm the feasibility of capillary motion even over large distances. Even very viscous liquids can be moved in suspended channels if the capillary forces are sufficient: a suspended channel longer than 37 cm can be filled with diluted or whole blood, or with viscous polymeric alginate solutions.

1.3.5.1. Gravity and Suspended Microflows

In this section, we first analyze the conditions for SCF in a suspended channel with vertical walls. In our analysis, gravity is neglected because the dimension of the device—here the distance between the vertical walls, denoted w —is smaller than the capillary length, i.e.

$$w < l = \sqrt{\frac{\gamma'}{\rho g}}. \quad (1.55)$$

For water, the capillary length is $l=2.7$ mm. It can be shown by using the Surface Evolver that if the distance between the two walls is less than the capillary length, gravity has a negligible effect. Figure 1.19 shows there would be a noticeable downward deformation of the free bottom interface for horizontal distances w larger than 3 mm. In the following, we only consider channel widths smaller than 500 μm , far below the limit determined in (1.55).

1.3.5.2 Condition for SCF

Spontaneous capillary flow results when the energy reduction from wetting walls outweighs the energy increase from extending the free surface. Using Gibbs' thermodynamic equation, it has been shown that the general

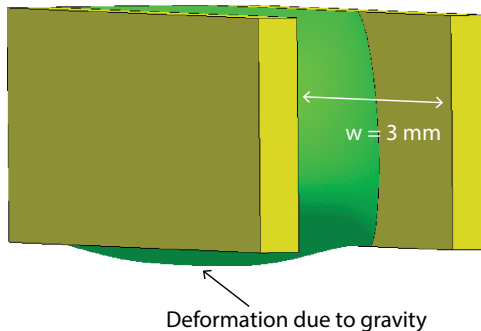


Figure 1.19 Bottom interface of a suspended flow deformed by gravity for $w=3$ mm.

condition for SCF in composite systems is that the generalized Cassie angle must be less than 90° [4], as stated by relation (1.18). Let us recall that, for open microflows, the virtual contact angle with air is 180° .

In the case where the walls are composed of a single material (with the same functionalization), relation (1.9) yields

$$\frac{w_F}{w} < \cos \theta, \quad (1.56)$$

where w_F , w are, respectively, the free—in contact with air—and wetted—in contact with wall—perimeters in a cross section of the channel [21]. If we consider a suspended channel with vertical, parallel walls, such as the one drawn in Figure 1.18a, where d is the distance between the walls and h the height of the walls, the condition for the onset of SCF is then

$$\frac{d}{h} < \cos \theta, \quad (1.57)$$

or

$$\theta < \arccos\left(\frac{d}{h}\right). \quad (1.58)$$

The domain of suspended SCF is plotted in Figure 1.20a. It is delimited by the line corresponding to relation (1.57).

Note that if the channel aspect ratio $e=d/h$ goes to zero, a contact angle approaching 90° can theoretically be sufficient for SCF (we shall see later that in such case the velocity of the flow is extremely small). On the other

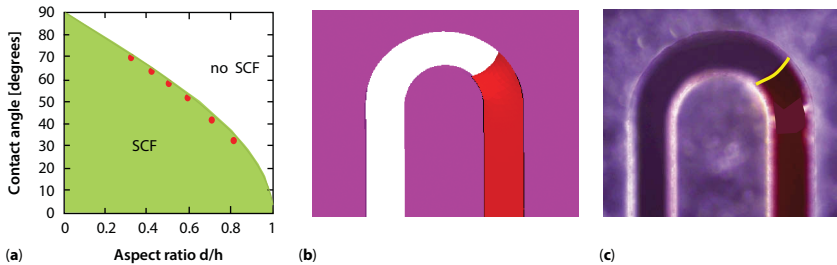


Figure 1.20 (a) SCF domain, and relation between the contact angle and the aspect ratio d/h according to (1.57). The red dots are the results obtained with the Surface Evolver; (b) whole-blood suspended microflow calculated with Surface Evolver; (c) experiments performed with blood (the interface has been visualized with a yellow line).

hand, when the aspect ratio increases to 1 ($d=h$) the contact angle must be zero to ensure a SCF (again, in this particular case we shall demonstrate that the velocity of the flow is extremely small). If the aspect ratio is larger than 1 ($d>h$) no SCF can be observed. For an aspect ratio of 1/3, the maximum contact angle that allows for SCF is approximately 70° .

1.3.5.3 Quasi-static Approach

The SCF onset can be checked by using the Surface Evolver [24]. A discussion of the possibilities of Evolver concerning the modeling of the capillary flow has already been presented above, in section 1.2.2. As an example, Figures 1.20b and c show a comparison of a Surface Evolver calculation and an experimental result using whole blood.

We can use the Surface Evolver to study the SCF onset in the geometry of two parallel vertical walls. In the calculation, the inlet pressure is the atmospheric pressure, which can be obtained by a sufficiently large reservoir (Figure 1.18b). It is the low Laplace pressure—smaller than the inlet pressure—at the tip of the liquid segment that drives the flow. Figure 1.21 shows a SCF calculation corresponding to the conditions $d=40\text{ }\mu\text{m}$, $h=50\text{ }\mu\text{m}$, $d/h=0.8$, $\theta=20^\circ$, $\gamma=72\text{ mN/m}$.

Using Evolver, starting from a geometrical configuration where SCF occurs, we can increase the contact angle to reach the limit where the flow does not progress anymore. The limit of SCF is then obtained for a given aspect ratio. The domain for suspended SCF is plotted in Figure 1.20a. The two limits—theoretical and numerical—are very similar.

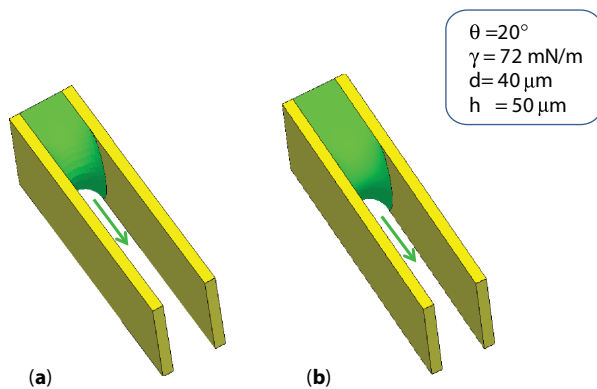


Figure 1.21 SCF for suspended microflow predicted by Evolver ($d=40\text{ }\mu\text{m}$, $h=50\text{ }\mu\text{m}$, $d/h=0.8$, $\theta=20^\circ$)

1.3.5.4 Dynamic Approach

Even if there are good arguments for the validity of the quasi-static Evolver approach concerning the interface shape, it cannot predict the value of the velocity of the flow. A dynamic approach is required to predict the flow velocity.

Let us first start from Newton's law, already stated in (1.30),

$$\frac{d(mV)}{dt} = F_{cap} - F_{drag}. \quad (1.59)$$

Assuming that the advancing contact angle is close to the Young contact angle, the capillary force is given by

$$F_{cap} = w \gamma \cos \theta - w_F \gamma = 2 \gamma (h \cos \theta - d). \quad (1.60)$$

where $w = 2h$ is the wetted perimeter in a cross section. On the other hand, assuming a uniform Poiseuille flow between the vertical walls, such as depicted in Figure 1.22, the wall drag force is approximately

$$F_{drag} \approx 6 \mu \frac{V}{d} z(t) w = 12 \mu \frac{h}{d} z(t) V(t), \quad (1.61)$$

where $V(t)$ is the average velocity at location $z(t)$. Substitution of relations (1.60) and (1.61) into equation (1.59) yields

$$\rho S_c \left(z \frac{dV}{dt} + V^2 \right) = 2 \gamma (h \cos \theta - d) - 12 \mu \frac{h}{d} z(t) V. \quad (1.62)$$

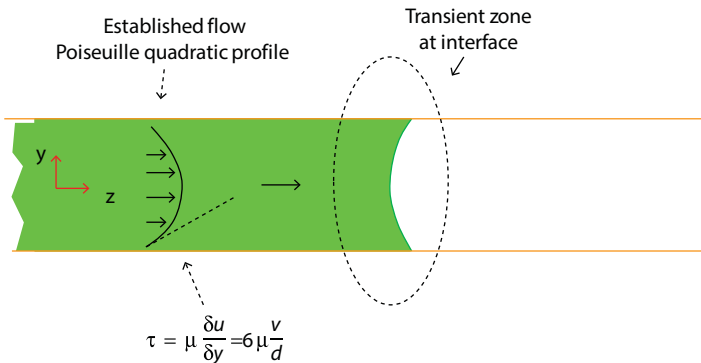


Figure 1.22 Sketch of the top view of the suspended channel: with the exception of the front end of the flow near the interface where the flow is not established, the velocity profile is close to the Poiseuille quadratic profile.

Using the relations

$$\begin{aligned} V &= \frac{dz}{dt} \\ S_C &\approx dh \end{aligned} \quad (1.63)$$

we finally obtain the differential equation

$$\frac{d^2 z^2}{dt^2} + \frac{12\mu}{\rho d^2} \frac{dz^2}{dt} - \frac{4\gamma(\cos\theta - d/h)}{\rho d} = 0. \quad (1.64)$$

Equation (1.64) is a differential equation in z^2 ; denoting $A = 12\mu/(\rho d^2)$ and $B = 4\gamma(\cos\theta - d/h)/(\rho d)$, and using the intermediate variables $Z = z^2$ and $U = dZ/dt$, equation (1.64) can be integrated twice and we find

$$z^2 = \frac{1}{A} \left[Bt + C(1 - e^{-At}) \right], \quad (1.65)$$

where $C = B/A$. Note that (1.65) implies an infinite velocity at $z = 0$, because $dz/dt = V \sim C/z$ at $t = 0$. In reality, there is a very small time lapse before flow establishment, and (1.65) is not valid for $z = 0$. Note also that the value of A is usually high, because of the term d^2 , and the second term on the right side of (1.65) is negligible, after the time $t > 2/A$.

Neglecting inertia, a closed-form expression for the travel distance z is then

$$z^2 = \frac{B}{A} t. \quad (1.66)$$

Replacing A and B in (1.66), the travel distance z is

$$z = \sqrt{\frac{\gamma d (\cos\theta - d/h)}{3\mu}} \sqrt{t}. \quad (1.67)$$

The velocity of the flow is readily deduced from (1.67)

$$V = \sqrt{\frac{\gamma d (\cos\theta - d/h)}{12\mu}} \sqrt{\frac{1}{t}}. \quad (1.68)$$

Expression (1.68) shows the same dependency with time as the well-known Washburn-Lucas-Rideal model for capillary flows inside cylindrical tubes. Note that the term $\cos \theta - d/h$ must be positive in order to obtain a SCF, in agreement with the theoretical condition (1.57).

Finally, the relation between the velocity V and the distance z is obtained by elimination of the time between relations (1.67) and (1.68):

$$V = \frac{\gamma d (\cos \theta - d/h)}{6 \mu} \frac{1}{z}. \quad (1.69)$$

The velocity V decreases as $1/z$. Note that the model predicts that the velocity of the flow decreases but the liquid never stops moving as long as the contact angle satisfies the SCF relation (1.57).

Relation (1.69) can be cast in the general form proposed by Rye *et al.* for spontaneous capillary flows in V-grooves [18]:

$$V = \frac{\gamma}{\mu} \frac{h}{z} F_{geom} = \frac{\gamma}{\mu} \frac{h}{z} \frac{[e (\cos \theta - e)]}{6} \quad (1.70)$$

where the geometrical function F_{geom} depends on the contact angle and on the suspended channel aspect ratio $e = d/h$.

A comparison between the complete (differential) analytical model (Equation 1.65) which includes inertia and the simplified inertialess expression (equation 1.67) is shown in Figure 1.23a. The two expressions are nearly indistinguishable. This was expected since the flow Reynolds number is small, of the order of 1. Considering the velocity to be $V \sim 0.01$ m/s, one finds a value of the Reynolds number $Re \sim 3$.

1.3.5.5 Channel Characteristics for Maximum Velocities

It is interesting to obtain an approximation for the highest velocities that can be obtained in such suspended devices. Relation (1.68) shows that the velocity in a suspended channel is a function of the width d and the height h of the channel. Assuming a constant thickness of the plate, i.e. h is constant, we search for the aspect ratio and contact angle that will provide the maximum velocities. The maximum velocity is obtained by writing

$$\frac{\partial V}{\partial d} = 0. \quad (1.71)$$

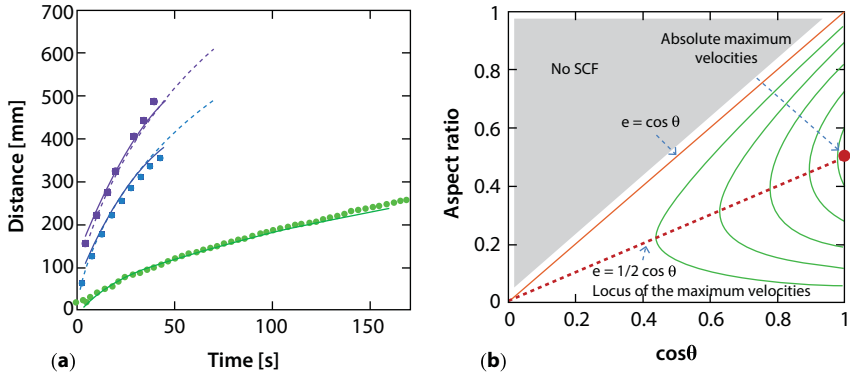


Figure 1.23 (a) Penetration distance as a function of time for the cases of three different aqueous liquids with different viscosities and surface tensions (violet, blue and green tinted water with different food coloring concentration). (b) Plot of the locus of the maximum velocities as a function of the contact angle θ and the aspect ratio e ; the red dotted line, locus of the maximum velocities, corresponds to the relation $e = 1/2 \cos \theta$, and the absolute maximum of the velocities is obtained for $\theta = 0$ ($\cos \theta = 1$) and $e = 1/2$. The red continuous line $e = \cos \theta$ corresponds to the limit of the SCF. The green curves are contour plots of the velocity V . The minimum velocities are obtained in the vicinity of the lines $e = \cos \theta$ and $e = 0$, where the velocity vanishes.

Substitution of (1.70) in (1.71) yields the relation

$$e = \frac{d}{h} = \frac{\cos \theta}{2}. \quad (1.72)$$

Hence, the aspect ratio $e = d/h$ providing the highest velocity is half the aspect ratio corresponding to SCF onset—determined by relation (1.57). Upon substitution of (1.72) in (1.68), we obtain the expression for the maximum velocity in a suspended channel of thickness h :

$$V_{\max} = \frac{\cos \theta}{2} \sqrt{\frac{\gamma h}{12 \mu}} \sqrt{\frac{1}{t}}. \quad (1.73)$$

The maximum velocity is proportional to the cosine of the contact angle, and to the square root of the channel height. Keeping in mind that relation (1.73) is valid if the channel aspect ratio e satisfies (1.72), the maximum velocity increases by increasing the dimensions of the channel

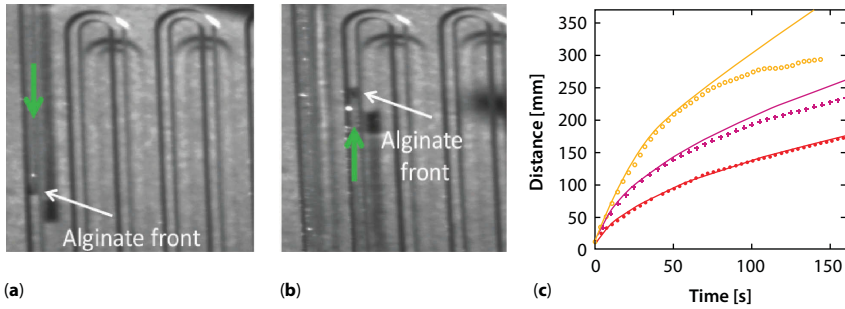


Figure 1.24 (a) and (b) 1wt % alginate spontaneous capillary flow in a suspended winding channel (contact angle $\sim 30^\circ$); in (a) the liquid starts its motion, while in (b) the liquid interface continues its motion further down in the channel; (c) comparison of the flow kinetics between theory and experiments for three liquids: alginate solution is plotted in orange, two SCFs of whole blood, with two different contact angles after recent (15 minutes) or ancient (two hours) O₂ plasma treatment, are respectively plotted in violet and red. Photographs by N. Villard and J. Berthier.

(width and height) by the same factor, until the limit where gravity effects become non-negligible ($d \sim 1$ mm). Relation (1.73) can be cast in a non-dimensional form

$$V_{\max} = \frac{\cos \theta}{4\sqrt{3}} \sqrt{\frac{\gamma}{\mu}} \sqrt{\frac{h}{t}}, \quad (1.74)$$

showing that the maximum velocity is the product of the square root of a “physical” velocity $\sqrt{\gamma/\mu}$ and of a “geometrical” velocity $\sqrt{h/t}$. The locus of the maximum velocities is plotted in Figure 1.23b as a function of the aspect ratio and the contact angle.

Typically, we have the following values: $h=1$ mm, $d=300$ μm , $\theta=20^\circ$, $\mu \sim 1\text{--}5$ cP, and $\gamma \sim 10\text{--}70$ mN/m. An approximation of the maximum velocity is $15\sqrt{1/t} > V_{\max} > 6\sqrt{1/t}$ mm/s. Assuming that the flow is established in less than one second, velocities of the order of a few millimeters per second can be obtained in such suspended channels.

1.3.5.6 Biological Liquids

Liquids used in biology and medicine have a complex rheology. They are usually more viscous than pure water and they frequently are non-Newtonian. This is for example the case of alginate solutions that are commonly

used in cell encapsulation [47] and of whole blood [48-51]. This is also often the case in food-processing engineering [52]. Even if these liquids are much more viscous than water, they can be moved by capillarity. Figure 1.24 shows the spontaneous capillary flow of a 1% alginate solution in the winding, suspended device of Figure 1.18b.

We observe that these liquids obey the square root law at the beginning of the motion, but after a while the experimental points are located below the square root law curve. A fit with the square root law—in the region where the fit is valid—produces the values $\gamma = 29$ mN/m and $\mu = 4.0 \cdot 10^{-3}$ Pa.s for whole blood, and $\gamma = 62$ mN/m and $\mu = 7.0 \cdot 10^{-3}$ Pa.s for the diluted alginate solution.

The behavior at later times may be explained by the shear-thinning rheology of the two liquids: as predicted by (1.69), the velocity of the capillary flow decreases with the penetration distance, consequently the shear-rate decreases and the viscosity increases. Hence a coupling is established between viscosity and velocity, leading to the reduction of the velocity of the capillary motion.

From a physical standpoint, at small velocities, the polymeric chains of the alginate have a random orientation, increasing the viscosity, while under a sufficient shear they align with the flow, and the viscosity is reduced. Different laws exist for the viscosity of alginate solutions; the Carreau-Yasuda law is often used to describe the viscosity of semi-dilute alginate solutions. Similarly, at small velocities, red blood cells form stacks that considerably increase the viscosity. These stacks are dispersed at sufficiently high velocity. Usually blood viscosity is modeled by Casson's law, and an asymptotic value of $4.0 \cdot 10^{-3}$ Pa.s for the viscosity is obtained when the cells are dispersed.

Note that in the case of non-Newtonian liquids, the deceleration of the liquid progressing in the channel has the effect to increase the viscosity, resulting in an increased deceleration of the liquid. In the present chapter, this feedback of the viscosity on the velocity is not presented, for the mere reason that it is presently a subject of investigation.

1.4 Conclusion

The general condition for spontaneous capillary flow onset has been presented in this chapter; it shows that SCF occurs when both geometrical and wetting conditions are met. In the case of composite channels, capillary flow may take place even if some of the walls are not hydrophilic, under the conditions that the other walls counterbalance their hydrophobicity. In the

case of open-surface geometry, i.e. open microflows, the air behaves like a superhydrophobic medium, with a contact angle of 180° . Again, spontaneous capillary flow is observed if some of the walls exert a sufficient capillary force.

The dynamics of capillary flow in confined channels, is now well known in the case of composite walls. In the case of a cylindrical channel, the Lucas-Washburn-Rideal (LWR) expression produces the relation between the travel distance or velocity with the time. But using an equivalent hydraulic diameter for describing the motion in an arbitrary cross section channel introduces a bias, which is important if the cross-section differs notably from the circle. An expression generalizing the LWR expression has been derived, which details the dynamics of the capillary flow under the condition that inertia is negligible, which is often the case at the microscale. In such a case, the advancing contact angle has been found to be constant, and close to the static value.

The dynamics of open-surface capillary microflows is still a subject of investigations. The difficulty is linked to the open boundary that introduces a surface tension force that opposes the motion, but does not provide wall friction. Finding the velocity profile in a cross section is the main task to determine the dynamics of the flow.

Two challenges are remaining: the first one pertains to the capillary flow of non-Newtonian liquids, which are frequent in biology, biotechnology and medicine. The expression for the wall friction in complicated geometries of such flows is difficult and requires numerical modeling and/or experiments. The second challenge is the study of dynamics of the capillary filaments that sometimes occur in corners, ahead of the flow. Their implication in the dynamics of the bulk flow is still to be determined.

References

1. G.J. Kost, *Principles and Practice of Point-of-Care Testing*, Lippincott Williams & Wilkins, Baltimore, MD (2002).
2. P. Yager, T. Edwards, E. Fu, K. Helton, K. Nelson, M.R. Tam and B.H. Weigl, Microfluidic diagnostic technologies for global public health, *Nature* 442, 412–418 (2006).
3. A.W. Martinez, S.T. Phillips, and G.M. Whitesides, Diagnostics for the developing world: Microfluidic paper-based analytical devices, *Anal. Chem.* 82, 3–10 (2010).
4. L. Gervais, N. de Rooij, and E. Delamarche, Microfluidic chips for point-of-care immunodiagnosics, *Adv. Mater.* 23, H151–H176 (2011).

5. L. Gervais and E. Delamarche, Toward one-step point-of-care immunodiagnostics using capillary-driven microfluidics and PDMS substrates, *Lab Chip* 9, 3330–3337 (2009).
6. J. Berthier, K.A. Brakke and E. Berthier, A general condition for spontaneous capillary flow in uniform cross-section microchannels, *Microfluid. Nanofluid.* 16, 779–785 (2014).
7. R. Lucas, Ueber das Zeitgesetz des Kapillaren Aufstiegs von Flüssigkeiten, *Kolloid Z.*, 23, 15–22 (1918).
8. E.W. Washburn, The dynamics of capillary flow. *Phys. Rev.* 17, 273–283 (1921).
9. E.K. Rideal, On the flow of liquids under capillary pressure. *Philos. Mag. Ser.* 6, 1152–1159 (1922).
10. P. Concus and R. Finn, On the behavior of a capillary surface in a wedge, *Proc. Natl. Acad. Sci. (USA)* 63, 292–299 (1969).
11. P. Concus and R. Finn, Capillary surfaces in a wedge—differing contact angles, *Microgravity Sci. Technol.* 7, 152–155 (1994).
12. D. Juncker, Capillary microfluidic systems for bio/chemistry, PhD thesis, University of Neuchatel, Neuchatel, Switzerland (2002).
13. M. Kitron-Belinkov, A. Marmur, T. Trabold and G.V. Dadheech, Groovy-drops: Effect of groove curvature on spontaneous capillary flow, *Langmuir* 23, 8406–8410 (2007).
14. Yongkang Chen, L. S. Melvin, S. Rodriguez, D. Bell and M.M. Weislogel, Capillary driven flow in micro scale surface structures, *Microelec. Eng.* 86, 1317–1320 (2009).
15. M. Zimmerman, H. Schmid, P. Hunziker and E. Delamarche, Capillary pumps for autonomous capillary systems, *Lab Chip* 7, 119–125 (2007).
16. L. Gervais and E. Delamarche, Toward one-step point-of-care immunodiagnostics using capillary-driven microfluidics and PDMS substrates, *Lab Chip* 9, 3330–3337 (2009).
17. F.F. Ouali, G. McHale, H. Javed, C. Trabi, N.J. Shirtcliffe and M. I. Newton, Wetting considerations in capillary rise and imbibition in closed square tubes and open rectangular cross-section channels, *Microfluid. Nanofluid.* 15, 309–326 (2013).
18. R.R. Rye, F.G. Yost and J. Mann, Wetting kinetics in surface capillary grooves, *Langmuir* 12, 4625–4627 (1996).
19. F.G. Yost, R.R. Rye and J.A. Mann, Solder wetting kinetics in narrow V-grooves, *Acta Materialia* 45, 5337–5345 (1997).
20. L.A. Romero and F.G. Yost, Flow in an open channel capillary, *J. Fluid Mech.* 322, 109–129 (1996).
21. J. Berthier and K. Brakke, *The Physics of Microdroplets*, Scrivener-Wiley Publishing, Beverly, MA, (2012).
22. J.W. Gibbs, A method of geometrical representation of the thermodynamic properties of substances by means of surfaces, *Trans. Connecticut Academy Arts Sciences* 2, 382–404 (1873).

23. H. Bruus, *Theoretical Microfluidics*, Oxford University Press, Oxford, UK (2007).
24. K. Brakke, The Surface Evolver, *Expl. Math.* 1, 141–165 (1992).
25. B. Steinhaus, A. Q. Shen and R. Sureshkumar, Dynamics of viscoelastic fluid filaments in microfluidic devices, *Phys. Fluids*, 19, 073103 (2007).
26. J. Eggers, Nonlinear dynamics and breakup of free-surface flows, *Rev. Modern Phys.* 69, 865–929 (1997).
27. S.H. Spiegelberg, D.C. Ables and G.H. McKinley, The role of end effects on measurements of extensional viscosity in filament stretching rheometers, *J. Non-Newtonian Fluid Mech.* 64, 229–267 (1996).
28. J. Berthier and P. Silberzan, *Microfluidics for Biotechnology*, 2nd edition, Artech House publishing, Norwood, MA (2012).
29. W. Satoh, H. Hosono, and H. Suzuki, On-chip microfluidic transport and mixing using electrowetting and incorporation of sensing functions, *Anal. Chem.* 77, 6857–6863 (2005).
30. B.P. Casavant, E. Berthier, A.B. Theberge, J. Berthier, S.I. Montanez-Sauri, L.L. Bishel, K.A. Brakke, C.J. Hedman, W. Bushman, N.P. Keller and D.J. Beebe, Suspended microfluidics, *Proc. Natl. Acad. Sci. (USA)* 110, 10111–10116 (2013).
31. A. Bejan, *Convection Heat Transfer*, 4th Edition, John Wiley and Sons, Hoboken, NJ (2013).
32. M. M. Weislogel, Y. Chen, and D. Bolleddula, A better nondimensionalization scheme for slender laminar flows: The Laplacian operator scaling method, *Physics of Fluids* 20, 093602 (2008).
33. R.K. Shah and A.L. London, Laminar flow forced convection in ducts, *Advances in Heat Transfer series*, Supp. 1, Academic Press, New York (1978).
34. K.V. Sharp, R.J. Adrian, J.G. Santiago and J.I. Molho, *Liquid flows in micro-channels*, in *MEMS : Introduction and Fundamentals*, M. Gad-El-Hak (Ed.), CRC Press, Boca Raton, FL (2005).
35. M. Bahrami, M. M. Yovanovich and J. R. Culham, A novel solution for pressure drop in singly connected microchannels of arbitrary cross-section, *Intl. J. Heat Mass Transfer* 50, 2492–2502 (2007).
36. J.P. McHale and S.V. Garimella, Heat transfer in trapezoidal microchannels of various aspect ratios, *Intl. J. Heat Mass Transfer* 53, 365–375 (2010).
37. J. Berthier, R. Renaudot, P. Dalle, G. Blanco-Gomez, F. Rivera, V. Agache and P. Caillat, COMSOL assistance for the determination of pressure drops in complex microfluidic channels, *Proceedings of the 2010 European COMSOL Conference*, Paris, France (2010).
38. R. Safaviieh and D. Juncker, Capillaries: Pre-programmed, self-powered microfluidic circuits built from capillary elements, *Lab-Chip*, 13, 4180–4189 (2013).
39. A. Han, G. Mondin, N. G. Hegelbach, N. F. de Rooij and U. Staufer, Filling kinetics of liquids in nanochannels as narrow as 27 nm by capillary force, *J. Colloid Interface Sci.* 293, 151–157 (2006).
40. Encyclopedia Britannica, <http://www.global.britannica.com> (2014).

41. V. D. Sobolev, N. V. Churaev, M. G. Velarde, and Z. M. Zorin, Surface tension and dynamic contact angle of water in thin quartz capillaries, *J. Colloid Interface Sci* 222, 51–54 (2000).
42. A. Hamraoui, K. Thuresson, T. Nylander, and V. Yaminsky, Can a dynamic contact angle be understood in terms of a friction coefficient? *J. Colloid Interface Sci.* 226, 199–204 (2000).
43. P. Joos, P. Van Remoortere and M. Bracke, The kinetics of wetting in a capillary, *J. Colloid Interface Sci.* 136, 189–197 (1990).
44. M.M. Weislogel and S. Lichter, Capillary flow in interior corners, *J. Fluid Mech.* 373, 349–378 (1998).
45. E. Berthier, A.B. Theberge, B.P. Casavant, Guo Chunjun, C. Wang, D.J. Beebe and N.P. Keller, Suspended microfluidics: An open and user-friendly technology platform for high-throughput metabolic studies, Proceedings of the 2012 MicroTas Conference, Okinawa, Japan, (2012).
46. J. Berthier, K.A. Brakke, D. Gosselin, A-G. Bourdat, G. Nonglaton, N. Villard, G. Laffite, F. Boizot, G. Costa and G. Delapierre, Suspended microflows between vertical parallel walls, *Microfluid. Nanofluid.* DOI 10.1007/s10404-014-1482-z, (2014).
47. J. Berthier, S. Le Vot, P. Tiquet, F. Rivera and P. Caillat, On the behavior of non-Newtonian fluids in microsystems for biotechnology, Proceedings of the Nanotech International Conference, Houston, TX, USA (2009).
48. E.W. Merrill, Rheology of blood, *Physiological Reviews* 49, 863–888 (1969).
49. A.R. Pries, T.W. Secomb and P. Gaetgens, Biophysical aspects of blood flow in the microvasculature, *Cardiovascular Res.* 32, 654–667 (1996).
50. L. Dintenfass, Viscometry of human blood for shear rates of 0–100,000 sec⁻¹, *Nature* 211, 632–633 (1966).
51. S.S. Shibeshi and W. E. Collins, The rheology of blood flow in a branched arterial system, *Appl Rheol.* 15, 398–405 (2005).
52. J.F. Steffe, *Rheological Methods in Food Process Engineering*, second edition, Freeman Press, Asheville, NC (1982).

A Review of “Ordered Water Monolayer That Does Not Completely Wet Water” at Room Temperature

Chunlei Wang and Haiping Fang*

Division of Interfacial Water and Key Laboratory of Interfacial Physics and Technology, Shanghai Institute of Applied Physics, Chinese Academy of Sciences, Shanghai, China

Abstract

Viewed macroscopically at room temperature, water always completely wets other water due to the formation of hydrogen bonds. In 2009, based on molecular dynamics simulations, we predicted the phenomenon of a liquid water droplet on a water monolayer, which has been termed as “ordered water monolayer that does not completely wet water” at room temperature. Recently, this room temperature phenomenon has been observed on many real surfaces in numerical simulations or experiments by research groups worldwide. In this review, we summarize the recent advances in the understanding of this wetting behavior, including the underlying mechanisms and the possible applications.

Keywords: Ordered water monolayer, room temperature, molecular dynamics simulations, hydrogen bonds, hydrophobicity/hydrophilicity, ethanol molecules

2.1 Introduction

The interfacial water [1-10], which is usually regarded as the key in understanding various processes, such as solvation process of particles/molecules in water [11-16], adsorption/desorption at surfaces [17-22], electrochemical reactions [23,24], protein stability and folding [25], molecular

*Corresponding author: fanghaiping@sinap.ac.cn

self-assembly [26], rearrangement of immunodeficiency virus [27], the nano- toxicity of aggregated gases [28], graphene [29,30] or Al ions [31], and even the asymmetrical diffusion of solvated particles [32], has drawn extensive attention. The molecular structure and dynamics of these interfacial water molecules are usually different from those in the bulk water. Recently, ordered water structures confined to one or two dimensions have been found and extensively studied by experimental or theoretical methods. In one-dimensional systems, such as the nano-channels of nanotubes [33–41] and aquaporins [42], the water molecules were found to form a single-file structure due to the connecting of hydrogen bonds among water molecules. The permeation of water molecules across the channels showed novel behaviors, such as extra-high permeability rate [43,44], excellent on–off gating behavior in response to the external mechanical and electrical signals and noises [35,45]. On two-dimensional (2D) solid surfaces, the room temperature ordered structure of interfacial water was first found on the mica surface [46] in 1995 by Hu *et al.* Subsequent works [47] by simulations showed that the ordered structures of interfacial water on the mica surface formed a 2D hydrogen-bonded network matching with the mica lattice, and there was no dangling OH bond in the first contact layer on the mica surface. More interestingly, ordered water has been found near the biological molecules, such as the antifreeze protein [48], where the ordered water may affect the dynamics of the freezing process.

It has been realized that this novel ordered water affects various surface properties, such as the surface electrochemical property, catalysis, surface corrosion, surface wetting behavior and surface friction, etc. In 2005, at extremely low temperatures, Kimmel *et al.* [49] experimentally found hydrophobic-like ice monolayers on metal Pt(111) surfaces, and attributed this to no dangling OH bonds existing in the ice monolayer. Like the superconductor or the Bose–Einstein condensate, the physical results obtained at cryogenic temperature could usually not be transferred directly to room temperature due to the larger thermal fluctuations at the room temperature. Analogously, the hydrophobic-like ice monolayer observed at cryogenic temperature cannot be extended to room temperature since the thermal fluctuations will break the H-bond networks and provide more opportunities to form hydrogen bonds between the monolayer and water molecules above the monolayer. This thus makes the water monolayer at room temperature more hydrophilic and accounts for the room temperature behavior that when water contacts water monolayer, it will spread out and finally both mix together due to the formation of hydrogen bonds. However, in 2009, based on molecular dynamics simulations, we predicted a clear liquid water droplet on the water monolayer

[50–55], termed as “ordered water monolayer that does not completely wet water” at room temperature. Clearly, this room temperature wetting behavior is much more important and applicable in many scientific fields, since liquid water is essential for various processes, particularly many biological activities. It should be noted that in contrast to the previous studies of no dangling OH bonds in the ordered water monolayer on mica surface [47,56] at room temperature and on Pt (111) surface at very low temperature [49], we predicted that there remained a considerable number of dangling OH bonds in the room temperature water monolayer. Recently, several experimental or simulation works have observed the phenomenon “ordered water monolayer that does not completely wet water” on real solid surfaces at room temperature, suggesting the generality of this wetting behavior. In this review, we summarize these advances on the understanding of the wetting phenomenon mentioned above and discuss the possible applications related to this phenomenon. The review is organized as follows. In sections 2.2 and 2.3, we have presented the underlying mechanism of the peculiar phenomenon with a stable liquid water droplet on water monolayer, and the effect of defects on the ordered water. The thermal property of the ordered water is discussed in section 2.4. In section 2.5, we discuss the recent simulation or experimental observations for the phenomenon “ordered water monolayer that does not completely wet water” observed on real solid surfaces at room temperature. In section 2.6, we have presented the similar phenomenon of an ethanol droplet on an ethanol monolayer at room temperature. A short discussion on the possible applications of this phenomenon “ordered water monolayer that does not completely wet water” is presented in section 2.7. In the last section, we make a short summary.

2.2 “Ordered Water Monolayer that Does Not Completely Wet Water” at Room Temperature

In Figure 2.1(a), based on molecular dynamics simulations, we have presented our prediction of the liquid water droplet on a water monolayer with a thickness of 0.4 nm, termed as “ordered water monolayer that does not completely wet water” on a model surface at room temperature [50–55]. In Figure 2.1(b), we have shown the theoretical model surface with a planar hexagonal structure. The two-dimensional structure of the surface contains positive and negative charges q in certain positions while the surface in total is neutral. This surface charge or dipole distribution is similar to existing surfaces, such as InSb(110), suggesting both unrecognized possibilities

associated with existing materials and potential for new materials that possess this property.

In the simulations, as charge q increases from 0 e to 0.5 e, the water molecules gradually spread over the surfaces. However, when $q \geq 0.5\text{e}$, we found that the water molecules began to assemble in a water droplet on top of a water monolayer. We have calculated the contact angles of liquid water droplets as a function of the charge q and the results are shown in Figure 2.2. Clearly, as charge q increases, the contact angle of the droplets increases, contrary to our common sense that the contact angle should decrease as the surface charge q increases.

To account for this phenomenon, we have calculated the average number of hydrogen bonds (H-bonds) formed by each water molecule in the

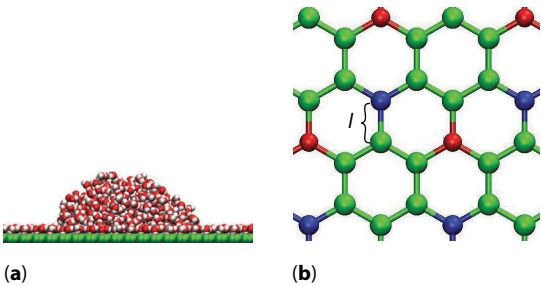


Figure 2.1 (a) A stable water droplet on a water monolayer on a model solid surface. (b) Structure of the model solid surface. Red and blue spheres represent the atoms of the solid with positive and negative charges, respectively, while the green spheres represent neutral solid atoms (reprinted from ref. 50, Copyright 2009 American Physical Society).

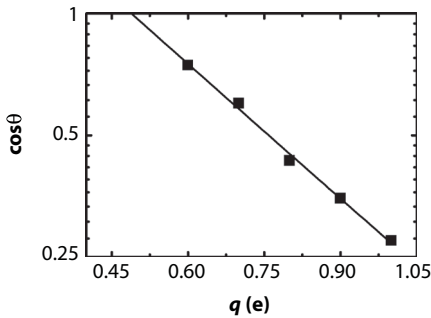


Figure 2.2 Relationship between the cosine values of the contact angle θ and the charge value q . An exponential function $\cos\theta \approx 3.5 \cdot \exp(-q/0.38)$ was fitted to the data (black line) (reprinted from ref. 50, Copyright 2009 American Physical Society).

monolayer under the droplet connecting with its neighboring water molecules in the same layer, namely, within-monolayer H-bonds, and the average number of hydrogen bonds formed by each water molecule in the monolayer connecting with the water molecules above this monolayer, namely, between-droplet-monolayer H-bonds. As shown in Figure 2.3, as q becomes larger, the number of within-monolayer H-bonds increases, which in return reduces the number of between-droplet-monolayer H-bonds. Note that the former is always larger than the latter, and the sum of the two slowly decreases and finally reaches a constant 2.9. Thus, we have found a competition occurring for H-bond formation between within-monolayer H-bonds and between-droplet-monolayer H-bonds. This decrease of H-bond number between the monolayer and water droplet greatly reduces the water-water attraction between water monolayer and the contacting water above, and thus results in the unexpected phenomenon termed “ordered water monolayer that does not completely wet water” at room temperature. The number of H-bonds per water molecule in the monolayer outside the droplet, namely, outside-droplet-monolayer H-bonds, is almost constant at 2.6, which is considerably smaller than the total value of 2.9 H-bonds per water molecule for $q > 0.8e$ in the monolayer under the droplet. This result suggests that there are at least 0.3 free positions at which H bonds can form for each water molecule in the monolayer outside the droplet. We have also performed numerical simulations of solid surface covered with a monolayer of ice at $T = 135$ K, conditions under which the crystalline hydrophobic-like ice monolayer formed on a Pt(111) surface. We have found that the number of H-bonds per water molecule is 2.9 if surface charge $q = 0.3$ e, which is ~ 0.3 larger than the number of H-bonds per water molecule in the monolayer outside the droplet when $q \geq 0.6e$ at room temperature. However, this value of 2.9 equals the total H-bonds per water molecule when $q \geq 0.8e$ at room temperature in the monolayer under the droplet (see Figure 2.3). These results imply that there may be no dangling OH bonds in the ice monolayer at this cryogenic temperature. However, dangling OH bonds still exist in this ordered water monolayer at room temperature.

We have also found that the surface charge or dipoles arrangement is important for the formation of the 2D ordered water structure as well as the water droplet on the water monolayer. Figure 2.4(a) displays a snapshot of the water structures together with the H-bonds (in green lines) in the monolayer outside the droplet for $q = 1.0$ e. To describe the ordered water structures, a parameter φ is defined as the angle between the projection onto the x-y plane of a water molecule dipole orientation and a crystallographic direction. As shown in Figure 2.4(b), when q is

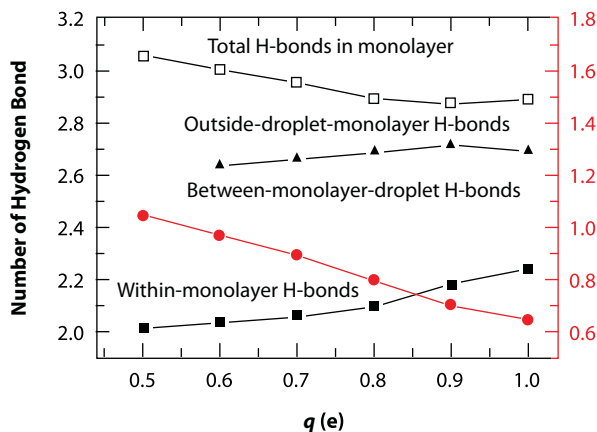


Figure 2.3 Relationship between the number of H-bonds formed by each water molecule of the monolayer under the droplet with other neighboring water molecules in the same monolayer (solid squares), and the H-bonds formed by each water molecule of the monolayer under the droplet with the water molecules above the monolayer (solid red circles corresponding to the right axis), and charge value q . The sum of the two is represented by empty squares. The average number of H-bonds formed by each water molecule of the water monolayer outside the droplet is represented by black solid triangles (reprinted from ref. 50, Copyright 2009 American Physical Society).

sufficiently large (1.0 e), the three peaks at $\varphi = 0^\circ$, 120° and 240° of probability distribution with angle φ are found. These three peaks show the clearly hexagonal ordered water structure (see Figure 2.4(a)). When q is as small as 0.5 e, the peaks cannot be clearly seen. Correspondingly, the droplet on the monolayer cannot be observed. Only when q is equal or larger than 0.6 e, water droplets on water monolayers appear and there are three clear dipole orientation preferences for the water molecules in monolayer with three peaks at $\varphi = 0^\circ$, 120° and 240° . Thus, we have found that there is a tight relationship between the ordered/disordered water structures and appearance/disappearance of the water droplet on the monolayer. Although the heights of the distribution associated with the monolayer under the droplet are lower than the heights for the monolayer outside the droplet, the water molecules in the monolayer under the droplet still retain a good 2D ordered hexagonal structure when q is large. In addition, the solid surface structures are critical for the formation of ordered water structures. To study the effect of solid surface structures on the surface water structures, we have adjusted the neighboring atom bond length l from 0.142 nm to 0.17 nm. We have

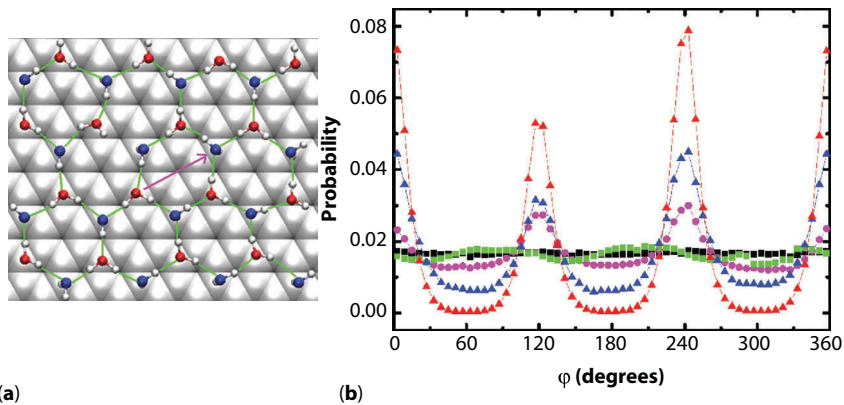


Figure 2.4 (a) Top view of water molecules in the monolayer on the solid surface with regular 2D ordered hexagons. The H-bonds formed between neighboring water molecules are labeled with green lines and the pink arrow represents the direction we used as the crystallographic direction to compute the angle ϕ . (b) Probability distribution of the angle ϕ . Black empty squares and magenta circles correspond to the case when $q = 0.5$ e and $q = 0.6$ e, respectively, with a bond length $l = 0.142$ nm. We use red triangles and blue stars to represent the water monolayer outside the droplet and the monolayer molecules under the droplet, respectively, for $q = 1.0$ e and $l = 0.142$ nm. Solid squares represent the case for a larger neighboring bond length $l = 0.17$ nm with $q = 1.0$ e (reprinted from ref. 50, Copyright 2009 American Physical Society).

found that there is no clear peak in the probability distribution of angle ϕ , although q has quite a large value of 1.0 e when $l = 0.17$ nm. In this case, there is no clear water droplet above the monolayer. If l decreases to 0.12 nm, neither the water droplets nor the ordered water monolayer can be seen. Clearly, the solid surface structure, i.e., the bond parameter l , plays an important role in the formation of the ordered water monolayer, resulting in the emergence of the water droplet on this monolayer. In 2013, Zhu *et al.* [57] also showed that the lattice structure played an important role in surface microscopic wetting, where an unexpected non-monotonic relationship between the water contact angle and surface lattice constant was found.

To gain a deeper understanding of the ordered water monolayer, we have calculated the relaxation dynamics of the H-bonds in the ordered water monolayer under the water droplet. Again, we focus on the hydrogen bonds formed within the monolayer under the droplet, namely, within-monolayer H-bonds, and hydrogen bonds formed between the droplet and the monolayer under the water droplet, namely, between-droplet-monolayer

H-bonds. The relaxation time of hydrogen bonds is characterized by the hydrogen bond autocorrelation function [58,59]

$$C(t) = \frac{\langle h(0)h(t) \rangle}{\langle h(0)h(0) \rangle}, \quad (2.1)$$

where $h(t) = 1$ if the tagged water pair is continuously hydrogen bonded from time 0 to time t , and $h(t) = 0$ otherwise. $C(t)$ describes the probability of a pair of water molecules being hydrogen bonded at time $t = 0$ and continuously hydrogen bonded at time t .

Figure 2.5(a) shows the autocorrelation function of within-monolayer H-bonds (black lines) and between-droplet-monolayer H-bonds (red line) when $q = 0.6$ e, 0.8 e and 1.0 e. The autocorrelation function decays exponentially with time. Through fitting the data of the autocorrelation function by a double exponential decay function [60] at the time interval [0.5 ps, 15 ps], we can obtain the relaxation time of hydrogen bonds using the larger τ . In Figure 2.5(b), the results of the relaxation time of within-monolayer H-bonds (black lines) and between-droplet-monolayer H-bonds (red lines) are presented. With the increase of charge q , the stability of water molecules near the surface is enhanced, thus relaxation times of both within-monolayer H-bonds and between-droplet-monolayer H-bonds increase. However, it should be noted that the relaxation time of the former is always 2–3 times of the latter. This larger relaxation time

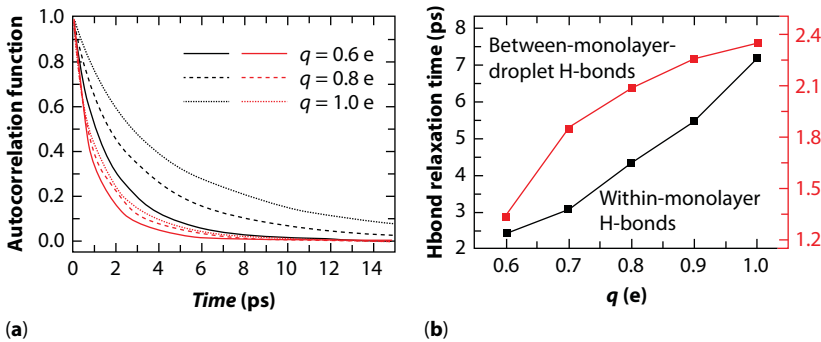


Figure 2.5 (a) Hydrogen bond autocorrelation function $C(t)$ when $q = 0.6$ e (solid lines), 0.8 e (dashed lines) and 1.0 e (dotted lines) for within-monolayer H-bonds (black line) and between-monolayer-droplet H-bonds (red line). (b) Average relaxation time τ of within-monolayer H-bonds (black line) and between-monolayer-droplet H-bonds (red line) vs. q .

of hydrogen bonds within the monolayer is mainly attributed to the fact that the water molecules in the monolayer prefer to form hydrogen bonds with the water molecules in the monolayer, rather than between monolayer and the water molecule above. This is quite consistent with the larger number of hydrogen bonds formed within the monolayer compared to the number of hydrogen bonds formed between water monolayer and droplet as shown in Figure 2.3.

2.3 Effect of Surface Point Defects on the Ordered Water Monolayer

We have shown that the well-defined charge distribution of the solid surface is responsible for the phenomenon “ordered water monolayer that does not completely wet water” in the previous section. However, when practical materials are fabricated, defects always exist [61]. Defects usually have an essential impact on the properties of materials, such as optical absorption [62], photocatalysis [63], ice growth [64] and wettability [65]. Here, we consider the impact of point defects on the ordered water structures and the wetting phenomenon. We have systematically varied the surface defect ratio from 1% to 30% for $q = 1.0$ e and $l = 0.142$ nm. Here the defects are created by randomly eliminating a dipole pair from the hexagons on the solid surface, and still maintaining the charge neutrality over the entire surface. The snapshots of simulations are shown in Figures. 2.6(a) through (d). The water monolayer on the solid surface is gradually covered by the water molecules of the irregularly-shaped droplet above this monolayer when the defect ratio increases. Considering that the profiles of the water droplets are irregular, we have defined a parameter termed as coverage ratio [51] to characterize the behavior of a water droplet on a defect-covered surface rather than the contact angle due to the fact that contact angle is unsuitable for characterizing the hydrophobicity of a surface with defects. This coverage ratio is defined as the ratio of the number of water molecules of the second layer that cover the water monolayer to the number of water molecules in the water monolayer. As shown in Figure 2.6(e), the coverage ratio increases as the defect ratio increases, indicating that the hydrophobicity of the water monolayer decreases. This can be attributed to the fact that the presence of surface defects greatly affects and disrupts the stability of the ordered water monolayer. As shown in Figure 2.6(f), the water monolayer becomes disordered when the defect ratio is high, and the water monolayer becomes more hydrophilic compared to a surface without any surface defect.

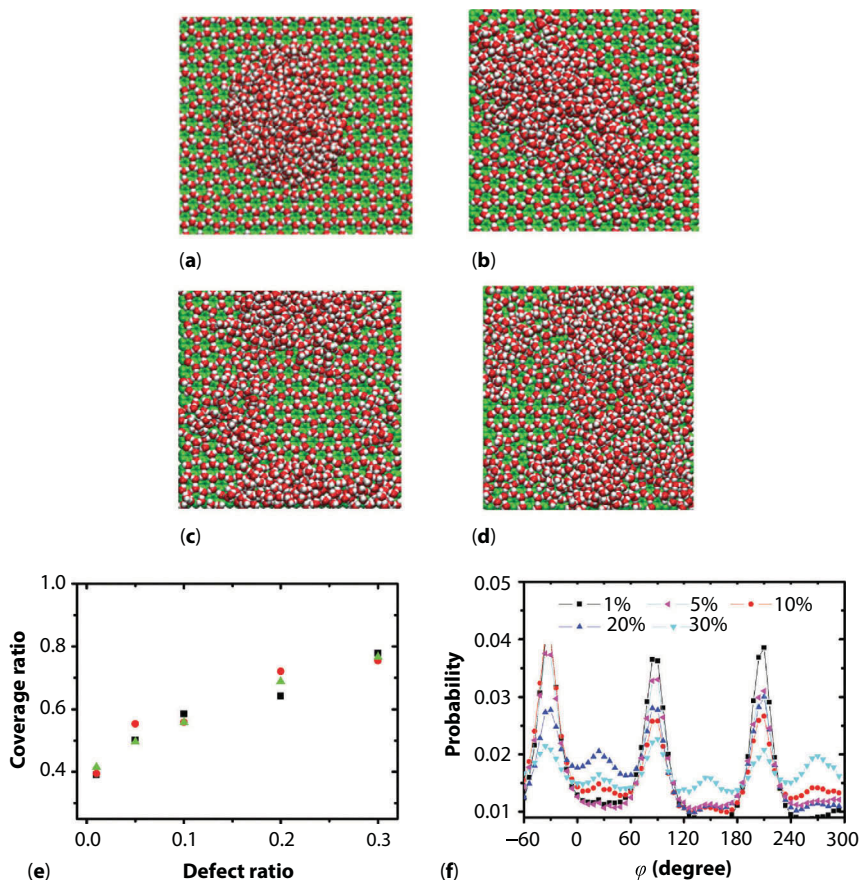


Figure 2.6 Top view snapshots of water droplet profiles on a solid surface with various defect ratios (a) 1%, (b) 10%, (c) 20%, (d) 30%, respectively, for $q = 1.0$ e and $l = 0.142$ nm. (e) Relationship between the surface defect ratio and the coverage ratio for $q = 1.0$ e and $l = 0.142$ nm. (f) Probability distribution of the angle φ under different surface defect ratios from 1% to 30% (reprinted from ref. 51 Copyright 2011, American Chemical Society).

2.4 Thermal Properties of Ordered Water Monolayer

The ordered structure of the water monolayer is the key in understanding the phenomenon “ordered water monolayer that does not completely wet water” at room temperature. Then the question arises: Is the ordered water similar to ice or liquid water? Based on the thermal analysis method, we investigated the thermal property of the ordered water and found that this

ordered water is similar to ice, rather than the liquid water. To measure the thermal conductivity of the monolayer water, we built a steady temperature gradient [66] for the water monolayer on the solid surface as shown in Figure 2.7(a). We first performed at least 1 ns relaxation time to thermalize the monolayer water to a given temperature of 300 K. In this case, the stable ordered water monolayer with hexagonal pattern is equilibrated. Next, we performed the thermal conduction process on the basis of the Muller-Plathe algorithm, which is also termed as a reverse non-equilibrium molecular dynamics (RNEMD) algorithm [67]. The water monolayer has been divided into 100 slabs. Here, we set the first and the last slab as heat sinks while the middle slab as the heat source. The hottest water molecules in the first heat sink exchange their velocities with the coldest water molecules in the heat source. This finally results in a symmetric temperature profile, which is computed by averaging events in a time interval (here for instance 100 ps):

$$T_i(\text{slab}) = \frac{2}{3N_i k_B} \sum_j \frac{p_j^2}{2m} \quad (2.2)$$

where $T_i(\text{slab})$ represents the temperature of the i th slab, N_i represents the number of water molecules in this slab, k_B represents the Boltzmann constant and p_j represents the momentum of the j th atom in this slab and m is the mass of atom.

After a steady temperature gradient is established with the heat flux running from the heat source to the heat sink, we can calculate the thermal conductivity κ using the Fourier's law as:

$$\kappa = \frac{J / (W * H)}{2dT / dL}, \quad (2.3)$$

where J represents the heat flux transferred between the heat source and heat sink, W represents the width of the monolayer water, H represents the height of the monolayer water, dT / dL represents the temperature gradient corresponding to the heat flux.

As shown in Figure 2.7(b) and Figure 2.7(c), we have found that the thermal conductivity of the monolayer water is close to that of ice (2.2 W/mK) rather than the liquid water, for a charge range from 0.6 to 1.0 e at room temperature. The higher thermal conductivity is always observed in

a zig-zag direction, which clearly shows that the thermal conduction process is chirality-dependent.

In order to further investigate the thermal property of ordered water monolayer, we investigated excitation propagation in the ordered water monolayer as shown in Figure 2.7(d) and the kinetic energy

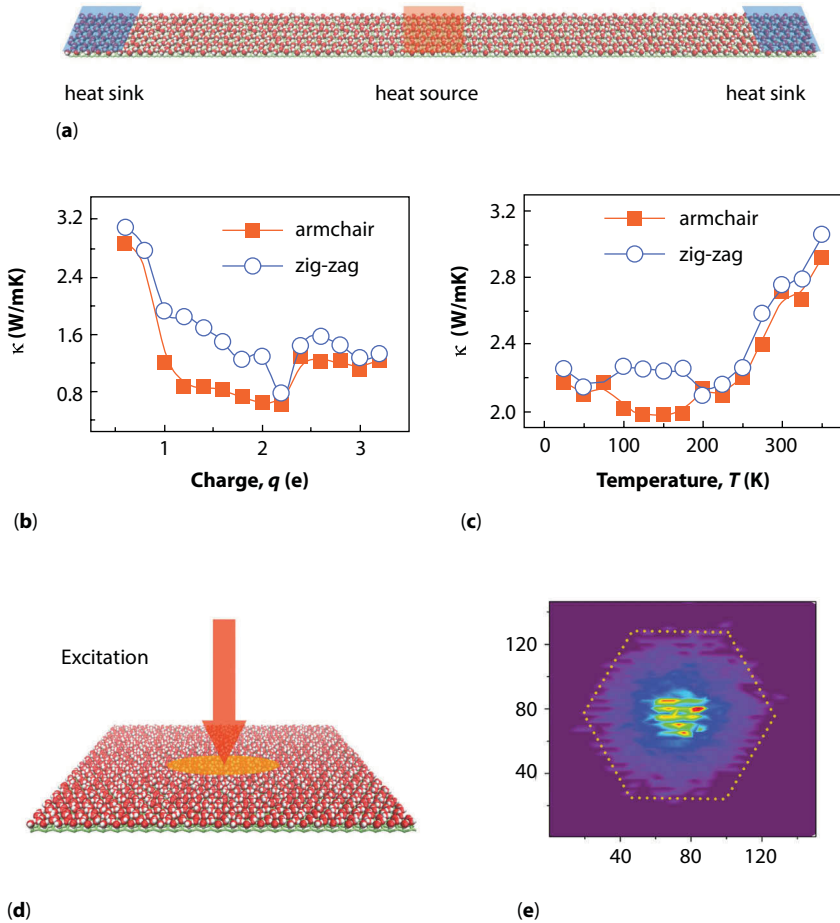


Figure 2.7 (a) Setup of thermal conduction process on the monolayer water with the heat source in the center and heat sink on the edge. (b, c) Thermal conductivity of the monolayer water k with respect to charge q and temperature T on the substrates. (d, e) Kinetic energy excitation propagation in the ordered water monolayer and kinetic energy transportation density at $t = 24$ ps. The center of the monolayer water marked by red arrow is excited. The outer edge of the excitation is marked by a dotted line (reprinted from ref. 66, Copyright 2013 IOP).

transportation density at $t = 24$ ps is shown in Figure 2.7(e). We found a roughly hexagonal pattern in the monolayer water appearing at the outer edge of the transportation density. Therefore, the transport thermal energy is anisotropic in the water monolayer. This is consistent with the chirality-dependent thermal conductivity observed in Figure 2.7(b) and Figure 2.7(c).

2.5 Simulation or Experimental Observations on the Phenomenon of Water Droplets on Water Monolayers on Real Solid Surfaces at Room Temperature

Besides our prediction of the phenomenon of water droplets on water monolayers, there are more observations on real surfaces to support the existence of this phenomenon at room temperature. Recently, several simulation or experimental works have observed the phenomenon of water droplets on water monolayers on some real solid surfaces. All of these results provide solid evidence that this room temperature wetting phenomenon generally exists in the nature.

In 2011, Rotenberg *et al.* [68] found that the talc surface is hydrophobic at high humidity while it is hydrophilic at low humidity using molecular dynamics simulations. More interestingly, the phenomenon of a water droplet coexisting with a water monolayer appears on the surface once the polarity of the modified talc surface becomes large enough (see Figure 2.8(a)). They have proposed that the competition between adhesion (water-surface interactions) and cohesion (water-water interactions) should be responsible for this phenomenon. They have found that water molecules in the monolayer tend to form hydrogen bonds with the solid surface rather than with the water molecules above the monolayer. Later, Phan *et al.* [69] observed the phenomenon of a water droplet on a water monolayer on hydroxylated Al_2O_3 surfaces (see Figure 2.8(b)) and hydroxylated SiO_2 (see Figure 2.8(c)) utilizing molecular dynamics simulations. They found that the water molecules in the first monolayer were strongly influenced by the $-\text{OH}$ implanted on the solid surface. They argued that the phenomenon was attributed to the fewer hydrogen bonds formed between the water monolayer and the droplet above this monolayer. In 2013, Limmer *et al.* [23] performed simulation of water molecules on Pt(100) and Pt(111) surfaces at room temperature. They also refined the phenomenon of a water droplet on a water monolayer on the Pt(100) surface (see Figure 2.8(d)).

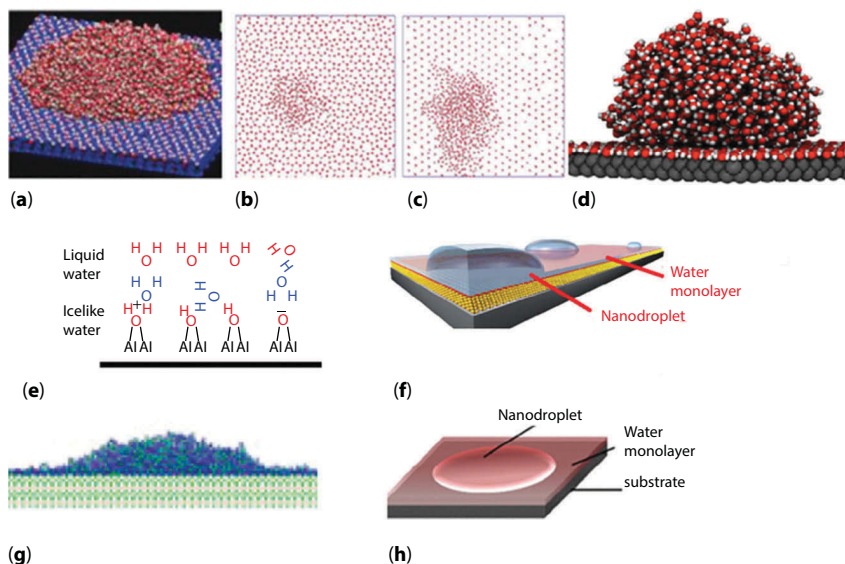


Figure 2.8 Simulation or experimental observations for the phenomenon of water droplets on water monolayers observed on real solid surfaces at room temperature. (a) talc surface (Reprinted with permission from J. Am. Chem. Soc. 133, 20521 (2011), Copyright 2011 American Chemical Society), (b) Al_2O_3 and (c) SiO_2 (Reprinted with permission from J. Phys. Chem. C 116, 15962 (2012), Copyright 2012 American Chemical Society), (d) Pt(100) surface (Reprinted with permission from Proc. Natl. Acad. Sci. USA 110, 4200–4205 (2013), Copyright 2013 National Academy of Sciences), (e) sapphire surface (Reprinted with permission from Adv. Colloid Interface Sci. 157, 61–74 (2010), Copyright 2010 Elsevier), (f) self-assembled monolayer (SAM) surface with a $-\text{COOH}$ terminal (Reprinted with permission from Soft Matter 7, 5309–5318 (2011), Copyright 2011 RSC), (g) titania surface (Reprinted with permission from Proc. Natl. Acad. Sci. USA 111, 5784 (2014), Copyright 2014 National Academy of Sciences), and (h) BSA(bovine serum albumin)- Na_2CO_3 membrane (reprinted from Sci. Rep. 3, 3505 (2013), Copyright 2013, Nature Publishing Group).

However, it should be noted that the water molecules with a square lattice in this monolayer preferred to form about four hydrogen bonds with four neighboring molecules, which is different from our model that each water molecule of the hexagonal lattice prefers to form three hydrogen bonds with three neighbors [50–53]. In addition, their results showed that this phenomenon could not be observed on the Pt(111) surface.

For a comparison between these simulation results, we have analyzed the distribution density of adsorption sites on the talc surface, hydroxylated SiO_2 , hydroxylated Al_2O_3 , Pt(100) and our model surface, which are 4.2 nm^{-2} , 4.5 nm^{-2} , 15.0 nm^{-2} and 12.6 nm^{-2} and 9.5 nm^{-2} respectively. Even

though there are different distribution densities of adsorption sites, the phenomenon of “ordered water monolayer that does not completely wet water” still can be observed on various surfaces, which may inspire more similar investigations.

Besides the simulations, Lützenkirchen *et al.* [70] experimentally found an ice-like configuration of water molecules, which was distinct from liquid water, on the sapphire c-plane surface (see Figure 2.8(e)). They further inferred that this water monolayer might show unexpected hydrophobicity to some extent. Furthermore, James *et al.* [71,72] experimentally found the phenomenon of small water droplets coexisting with a dense and continuous water monolayer of only 5.7 Å in thickness spreading all over the self-assembled monolayer (SAM) surface with a –COOH terminal. Finally, the larger drops formed due to the assembly of small drops (see Figure 2.8(f)). They argued that their finding may be attributed to the structure of the ordered water layer, which reduced the possibility of hydrogen bond formation between water molecules in the monolayer and the water molecules above this monolayer. Interestingly, similarly to our simulations of the irregular [51] (non-circular) water droplets on surfaces with surface defects, James *et al.* [71,72] also found numerous irregularly shaped water droplets on their SAM surfaces with a –COOH terminal using AFM techniques. Lee *et al.* [73] experimentally observed superwetting under light illumination on the titania surfaces. Their results based on molecular dynamics simulations clearly showed that such superwetting phenomenon was attributed to the mechanism termed as “water wets water”. However, they found that when there was only 1 or 2 monolayers of water on the titania surfaces, the phenomenon of a clear nano-droplet on the 1 or 2 water monolayers was observed (see Figure 2.8(g)). In 2013, Wang *et al.* [74] experimentally found the phenomenon of nanoscale water droplet on the solid-like water nanofilm (see Figure 2.8(h)) on BSA (bovine serum albumin) -Na₂CO₃ membrane when the imaging base was sealed at a low RH (15–25%) at room temperature. They attributed this phenomenon to the fact that there were very few hydrogen bonds existing between the first ordered water layer and the droplet above.

2.6 “Ordered Ethanol Monolayer that does not Completely Wet Ethanol” at Room Temperature

Unlike the water molecule, the ethanol molecule can be regarded as amphiphilic, with one hydrophobic nonpolar tail –CH₂CH₃, and a polar head –OH that can form hydrogen bonds. This may give rise to more

complex adsorption behavior of ethanol molecules than that of water molecules when they adsorb on polar solid surfaces. However, very recently, based on molecular dynamics simulations, we have predicted a similar phenomenon at room temperature “ordered ethanol monolayer that does not completely wet ethanol” on polar solid surfaces [75]. As shown in Figure 2.9(a), highly polar surfaces with positive and negative charges of the same magnitude q with the dipole length in the range from 0.162 nm to 0.282 nm are designed and then ethanol molecules in a cuboid shape are placed on the solid surfaces. Our simulation results show that when $l = 0.202$ nm or 0.162 nm, only ethanol droplets with contact angles of 39° or 75° appear on the solid surfaces, respectively. When $l = 0.242$ nm or $l = 0.282$ nm, an ethanol monolayer almost covers the entire solid surface; however, to our surprise, an ethanol droplet with the same contact angle of 71° forms on the ordered ethanol monolayer (see Figure 2.9(b)). This phenomenon is similar to the room temperature phenomenon of “ordered water monolayer does not completely wet water” [50–55] as described in section 2.2.

To further understand the phenomenon, we have plotted the probability distributions of the C atom in the $-\text{CH}_3$ group and O atom in the $-\text{OH}$ group of the ethanol molecules on the surfaces versus the z axis for various dipole length values. The results are shown in Figure 2.9(c). When $l = 0.242$ nm or $l = 0.282$ nm, the same peaks at $z = 0.25$ nm in the O atom distribution profile of $-\text{OH}$ and the same peaks at $z = 0.45$ nm in the C atom distribution profile of $-\text{CH}_3$ are observed. The distance between these two peaks is 0.2 nm, which is close to the distance (0.24 nm) between the O atom of $-\text{OH}$ and the C atom of $-\text{CH}_3$. Clearly, there is upright orientation of ethanol molecules in the monolayer forming with the $-\text{OH}$ group pointing towards the solid surface (see also lower part of Figure 2.9(b)). Similar orientation of ethanol molecules have been found on the calcite surfaces by Wu *et al* [76]. Interestingly, we have found that the second peak of the C atom of $-\text{CH}_3$ appears close to the first peak (see the insert of Figure 2.9(c)), which indicates that a face-to-face orientation of methyl group is formed between the ethanol monolayer and ethanol molecules above the monolayer. This upright structure and orientation of ethanol molecules in the monolayer make it impossible to form hydrogen bonds between the ordered ethanol monolayer and ethanol molecules above the monolayer and lead to the phenomenon of an ethanol droplet on an ethanol monolayer. When $l = 0.162$ nm or 0.202 nm, a peak at $z = 0.3$ nm in the C atom distribution profile of $-\text{CH}_3$ and a peak at $z = 0.45$ nm in the O atom distribution profile of $-\text{OH}$ are observed. This indicates that the ethanol molecules in the first layer lie parallel to the solid surfaces, which is consistent with the results shown in the upper part of Figure 2.9(b).

This is attributed to the steric exclusion effect when the charge dipole length is very short, which prevents the -OH head from attaching to the surface charges. In this case, weak van der Waals interactions dominate the surface-ethanol interactions because the surface-ethanol electrostatic interactions can be neglected.

We have also calculated the distributions of the number of hydrogen bonds for different orientations of ethanol molecules in the first layer as shown in Figure 2.9(d). Here, we focus on the number of hydrogen bonds

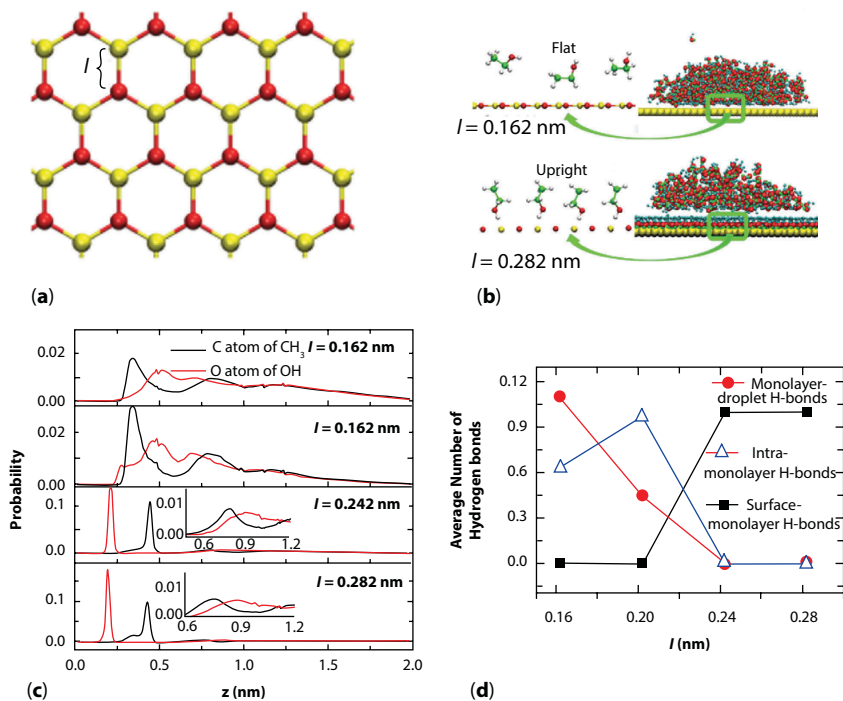


Figure 2.9 (a) Structure of model surface. The red and yellow spheres represent the atoms on the solid surface with positive charges and negative charges, respectively. (b) Side view snapshot of the flat ($l = 0.162 \text{ nm}$) and upright ($l = 0.282 \text{ nm}$) orientations of ethanol molecules and wetting phenomenon. (c) Probability distributions of the -CH_3 and -OH groups of the ethanol molecules versus the z axis for various l values. (d) Average number of hydrogen bonds formed between ethanol molecules and between ethanol molecules and the surfaces for various l values with $q = 1.0$ e. Black solid squares, open blue triangles, and red solid circles correspond to the number of hydrogen bonds formed between surface and ethanol molecules in the monolayer (surface-monolayer H-bonds), between ethanol molecules in the monolayer (intra-monolayer H-bonds), and between ethanol molecules in the monolayer and the droplet (monolayer-droplet H-bonds), respectively.

formed between the surface and the ethanol monolayer, namely, surface-monolayer H-bonds, hydrogen bonds formed between the ethanol molecules in the monolayer, namely, intra-monolayer H-bonds, and hydrogen bonds formed between the molecules in the monolayer and the droplet, namely, surface-monolayer H-bonds. When $l = 0.242$ nm or 0.282 nm, the three values are 1, 0, and 0, respectively. This is in consistent with the upright orientation of ethanol molecules in the monolayer with the $-OH$ groups buried beneath the monolayer, which excludes the possibility of forming hydrogen bonds between the ethanol molecules in the monolayer and ethanol molecules in contact with the monolayer, as well as the hydrogen bonds formed between the neighboring ethanol molecules in the monolayer. When $l = 0.162$ nm, the average number of hydrogen bonds formed between the monolayer and the droplet molecules, and between the neighboring ethanol molecules in the monolayer are 1.1 and 0.63, respectively, while when $l = 0.202$ nm, the average number of hydrogen bonds formed between the monolayer and the droplet molecules, and between the neighboring ethanol molecules in the monolayer are 0.45 and 0.97, respectively. However, no hydrogen bonds formed between the solid surface and the ethanol molecules in both cases.

We have analyzed the difference between the similar wetting phenomenon of water and ethanol molecules on the surfaces. The first difference is that a hexagonal hydrogen bonding network is induced by the elaborate binding of both surface positive and negative charges while the ordered ethanol monolayer is mainly induced by the surface negative charges. The second difference is that there are still hydrogen bonds formed between water monolayer and water droplet, while no hydrogen bonds are formed between ethanol monolayer molecules and ethanol droplet. However, both phenomena highlight the roles of matching/mismatching effect between surface lattice structures and adsorbed molecules in the surface wettability.

2.7 Discussion

Despite several experimental evidences [70–74], we note that a direct experimental demonstration of the ordered water is still lacking at room temperature, which may be attributed to the lack of the resolution accuracy in current techniques. Even the previous works that directly observed the water droplets coexisting with water monolayer on the SAM surface with a terminal $-COOH$ [71] and the water droplet on the BSA surface [74], there is still lack of consistent theoretical work. Very recently, the coexistence of water monolayer and a small water droplet was observed in simulations

[77] on the SAM surface with the terminal $-\text{COOH}$ studied by James *et al.* [71]. We also note that no direct evidence of the phenomenon “ordered ethanol monolayer that does not completely wet ethanol” is present on any real solid surfaces as far as we know.

Solid surfaces with especially ordered water monolayers may have broad applications in physical, environmental and biological systems. For example, this kind of material may be expected in the applications of anti-fouling surfaces that can prevent the non-specific protein adsorption [52], the friction reduction on the super-hydrophilic materials [78] and the artificial precipitation technologies [79]. In addition, the ordered water has also been found near the biological antifreeze protein molecules [48], which may affect the dynamics of the freezing process and even the diffusion behavior of these biological molecules. Considering that talc, SiO_2 , and Al_2O_3 are the key constituents of the soil and rocks, the mechanism we revealed here may have important implications in soil moisture retention, oil prospecting, and mining of the shale. Moreover, the ordered water on the Pt metal and TiO_2 may be of great importance in understanding the processes of surface electrochemistry, surface catalysis, self-cleaning surfaces, air and water purification systems.

2.8 Summary

In this review, we have summarized the recent advances in the phenomenon “ordered water monolayer that does not completely wet water” at room temperature. In contrast to observations of “no dangling OH bonds” in the hydrophobic-like water monolayer at cryogenic temperatures, we have found that there remain a considerable number of dangling OH bonds in the ordered water monolayer at room temperature. The key to this room temperature behavior is the ordered water structure induced by the appropriate charge quantity and distribution of solid surfaces, which provides strong and appropriate Coulomb interactions that counteract the effects of thermal fluctuations. Such ordered water with hexagonal hydrogen bond network reduces the possibility of the formation of the hydrogen bonds and the corresponding interactions between the monolayer and the water molecule above, thus resulting in the phenomenon “ordered water monolayer that does not completely wet water”. Thermal dynamics analysis has shown that this ordered water monolayer is similar to ice rather than liquid water. We have also found that the charge quantity, surface unit cell size and the surface defects all have great effects on the water molecular behaviors in the monolayer. More interestingly, several simulation or

experimental works have observed the room temperature phenomenon “ordered water monolayer that does not completely wet water” on some real solid surfaces, which provide rather solid evidence that the wetting phenomenon may generally exist in nature. Very recently, similar phenomenon of “ordered ethanol monolayer that does not completely wet ethanol” has been observed based on molecular dynamics simulations. However, a direct experimental evidence for this novel phenomenon of ethanol molecules at room temperature is still called for. These works provide a new perspective to understand the microscopic wetting behavior, which greatly depends particularly on the adsorbed molecular structures and orientations due to the interactions between surface and small molecules (water or amphiphilic ethanol molecules). More importantly, this coexistence of the hydrophilicity at a molecular level of water or ethanol monolayer and the macroscopic hydrophobicity, like with clear water or ethanol droplets, enriches the new concept of “molecular-scale hydrophilicity” we have proposed [80].

Acknowledgements

We gratefully thank Dr. Yi Gao for helpful discussions. This work was supported by the National Science Foundation of China (Grant Nos. 11290164, 11204341), the Key Research Program of the Chinese Academy of Sciences (grant no. KJZD-EW-M03), the Knowledge Innovation Program of the Chinese Academy of Sciences, the Youth Innovation Promotion Association CAS, Shanghai Supercomputer Center of China, Deepcomp 7000 and ScGrid of Supercomputing Center, Computer Network Information Center of the Chinese Academy of Sciences.

References

1. V. Ostroverkhov, G. A. Waychunas and Y. R. Shen, New information on water interfacial structure revealed by phase-sensitive surface spectroscopy. *Phys. Rev. Lett.* 94, 046102 (2005).
2. G. Stirnemann, S. Castrillon, J. Hynes, P. Rossky, P. Debenedetti and D. Laage, Non-monotonic dependence of water reorientation dynamics on surface hydrophilicity: Competing effects of the hydration structure and hydrogen-bond strength. *Phys. Chem. Chem. Phys.* 13, 19911–19917 (2011).
3. N. Giovambattista, P. G. Debenedetti and P. J. Rossky, Enhanced surface hydrophobicity by coupling of surface polarity and topography. *Proc. Natl. Acad. Sci. USA* 106, 15181–15185 (2009).

4. N. Giovambattista, P. G. Debenedetti and P. J. Rossky, Effect of surface polarity on water contact angle and interfacial hydration structure. *J. Phys. Chem. B* 111, 9581–9587 (2007).
5. R. Godawat, S. N. Jamadagni and S. Garde, Characterizing hydrophobicity of interfaces by using cavity formation, solute binding, and water correlations. *Proc. Natl. Acad. Sci. USA* 106, 15119–15124 (2009).
6. Q. Z. Yuan and Y. P. Zhao, Precursor film in dynamic wetting, electrowetting, and electro-elasto-capillarity. *Phys. Rev. Lett.* 104, 246101 (2010).
7. G. Shi, J. Liu, C. L. Wang, B. Song, Y. S. Tu, J. Hu and H. P. Fang, Ion enrichment on the hydrophobic carbon-based surface in aqueous salt solutions due to cation- π interactions. *Sci. Rep.* 3, 3436 (2013).
8. M. Sovago, R. Campen, G. Wurpel, M. Müller, H. Bakker and M. Bonn, Vibrational response of hydrogen-bonded interfacial water is dominated by intramolecular coupling. *Phys. Rev. Lett.* 100, 173901 (2008).
9. J. M. Zanotti, M. C. Bellissent-Funel and S. H. Chen, Experimental evidence of a liquid-liquid transition in interfacial water. *EPL (Europhysics Letters)* 71, 91–97 (2005).
10. M. P. Goertz, J. E. Houston and X. Y. Zhu, Hydrophilicity and the viscosity of interfacial water. *Langmuir* 23, 5491–5497 (2007).
11. D. Chandler, Interfaces and the driving force of hydrophobic assembly. *Nature* 437, 640–647 (2005).
12. K. Lum, D. Chandler and J. D. Weeks, Hydrophobicity at small and large length scales. *J. Phys. Chem. B* 103, 4570–4577 (1999).
13. L. Maibaum, A. R. Dinner and D. Chandler, Micelle formation and the hydrophobic effect. *J. Phys. Chem. B* 108, 6778–6781 (2004).
14. A. Pan, B. Naskar, G. K. S. Prameela, B. V. N. Kumar, A. B. Mandal, S. C. Bhattacharya and S. P. Moulik, Amphiphile behavior in mixed solvent media I: Self-aggregation and ion association of sodium dodecylsulfate in 1,4-dioxane– water and methanol–water media. *Langmuir* 28, 13830–13843 (2012).
15. N. Patra and P. Král, Controlled self-assembly of filled micelles on nanotubes. *J. Am. Chem. Soc.* 133, 6146–6149 (2011).
16. S. Prestipino, A. Laio and E. Tosatti, Systematic improvement of classical nucleation theory. *Phys. Rev. Lett.* 108, 225701 (2012).
17. S. Meng, L. F. Xu, E. G. Wang and S. W. Gao, Vibrational recognition of hydrogen-bonded water networks on a metal surface. *Phys. Rev. Lett.* 89, 176104 (2002).
18. H. Ogasawara, B. Brena, D. Nordlund, M. Nyberg, A. Pelmenschikov, L. G. M. Pettersson and A. Nilsson, Structure and bonding of water on Pt(111). *Phys. Rev. Lett.* 89, 276102 (2002).
19. K. Andersson, A. Nikitin, L. G. M. Pettersson, A. Nilsson, and H. Ogasawara, Water dissociation on Ru(001): An activated process. *Phys. Rev. Lett.* 93, 196101 (2004).
20. J. J. Yang, S. Meng, L. F. Xu and E. G. Wang, Water adsorption on hydroxylated silica surfaces studied using the density functional theory. *Phys. Rev. B* 71, 035413 (2005).

21. A. Michaelides and K. Morgenstern, Ice nanoclusters at hydrophobic metal surfaces. *Nature Materials* 6, 597–601 (2007).
22. X. L. Hu and A. Michaelides, Water on the hydroxylated (001) surface of kaolinite: From monomer adsorption to a flat 2D wetting layer. *Surf. Sci.* 602, 960–974 (2008).
23. D. T. Limmer, A. P. Willard, P. Madden and D. Chandler, Hydration of metal surfaces can be dynamically heterogeneous and hydrophobic. *Proc. Natl. Acad. Sci. USA* 110, 4200–4205 (2013).
24. A. P. Willard, D. T. Limmer, P. A. Madden and D. Chandler, Characterizing heterogeneous dynamics at hydrated electrode surfaces. *J. Chem. Phys.* 138, 184702–184705 (2013).
25. G. Hummer, S. Garde, A. E. García and L. R. Pratt, New perspectives on hydrophobic effects. *Chem. Phys.* 258, 349–370 (2000).
26. L. Zhao, C.L. Wang, J. Liu, B. H. Wen, Y. S. Tu, Z.W. Wang and H. P. Fang, Reversible state transition in nanoconfined aqueous solutions. *Phys. Rev. Lett.* 112, 078301 (2014).
27. D. M. York, T. A. Darden, L. G. Pedersen and M. W. Anderson, Molecular dynamics simulation of HIV-1 protease in a crystalline environment and in solution. *Biochemistry* 32, 3196–3196 (1993).
28. M. Zhang, G. H. Zuo, J. X. Chen, Y. Gao and H. P. Fang, Aggregated gas molecules: Toxic to protein? *Sci. Rep.*, 3, 1660 (2013).
29. Y.S. Tu, M. Lv, P. Xiu, T. Huynh, M. Zhang, M. Castelli, Z. R. Liu, Q. Huang, C.H. Fan, H.P. Fang and R. H. Zhou, Destructive extraction of phospholipids from *E. Coli* membrane by a graphene nanosheet, *Nature Nanotechnol.*, 8, 594–601 (2013).
30. J.R. Yang, G.S. Shi, Y.S. Tu and H.P. Fang, High correlation between oxidation loci on graphene oxide, *Angew. Chem. Int. Ed.* 53, 10190–10194 (2014).
31. B. Song, Q. Sun, H. Li, B. Ge, J. S. Pan, A. T. Wee, Y. Zhang, S. Huang, R. Zhou, X. Gao, F. Huang and H. Fang Irreversible denaturation of proteins through aluminum-induced formation of backbone ring structures. *Angew. Chem. Int. Ed.* 53, 6358–6363 (2014).
32. N. Sheng, Y. S. Tu, P. Guo, R.Z. Wan and H. P. Fang, Asymmetrical free diffusion with orientation-dependence of molecules in finite timescales, *Sci China-Phys Mech Astron* 56, 1047–1052 (2013).
33. X. J. Gong, J. Y. Li, H. Zhang, R. Z. Wan, H. J. Lu, S. Wang and H. P. Fang, Enhancement of water permeation across a nanochannel by the structure outside the channel. *Phys. Rev. Lett.* 101, 257801 (2008).
34. G. Hummer, J. C. Rasaiah and J. P. Noworyta, Water conduction through the hydrophobic channel of a carbon nanotube. *Nature* 414, 188–190 (2001).
35. J. Y. Li, X. J. Gong, H. J. Lu, D. Li, H. P. Fang and R. H. Zhou, Electrostatic gating of a nanometer water channel. *Proc. Natl. Acad. Sci. USA* 104, 3687–3692 (2007).
36. R. Wan, J. Li, H. Lu and H. Fang, Controllable water channel gating of nanometer dimensions. *J. Am. Chem. Soc.* 127, 7166–7170 (2005).

37. R. Z. Wan, H. J. Lu, J. Y. Li, J. D. Bao, J. Hu and H. P. Fang, Concerted orientation induced unidirectional water transport through nanochannels. *Phys. Chem. Chem. Phys.* 11, 9898–9902 (2009).
38. Y. S. Tu, P. Xiu, R. Z. Wan, J. Hu, R. H. Zhou and H.P. Fang, Water-mediated signal multiplication with Y-shaped carbon nanotubes. *Proc. Natl. Acad. Sci. USA* 106, 18120–18124 (2009).
39. Y. S. Tu, R. H. Zhou and H. P. Fang, Signal transmission, conversion and multiplication by polar molecules confined in nanochannels. *Nanoscale* 2, 1976–1983 (2010).
40. H.J. Lu, J.Y. Li, X. J. Gong, R. Z. Wan, L. Zeng and H. P. Fang, Water permeation and wavelike density distributions inside narrow nanochannels. *Phys. Rev. B* 77, 174115 (2008).
41. H. J. Lu, X. J. Gong, C. L. Wang, H. P. Fang and R. Z. Wan, Effect of vibration on water transport through carbon nanotubes. *Chin. Phys. Lett.* 25, 1145–1148 (2008).
42. B. L. de Groot and H. Grubmuller, Water permeation across biological membranes: Mechanism and dynamics of aquaporin-1 and GlpF. *Science* 294, 2353–2357 (2001).
43. S. Joseph and N. R. Aluru, Why are carbon nanotubes fast transporters of water? *Nano Lett.* 8, 452–458 (2008).
44. M. Whitby and N. Quirke, Fluid flow in carbon nanotubes and nanopipes. *Nature Nanotechnol.* 2, 87–94 (2007).
45. H. J. Lu, X. Y. Zhou, F. M. Wu and Y. S. Xu, Effect of charge on water filling/emptying transitions of nanochannel. *J. Phys. Chem. B* 112, 16777–16781 (2008).
46. J. Hu, X. D. Xiao, D. F. Ogletree and M. Salmeron, Imaging the condensation and evaporation of molecularly thin-films of water with nanometer resolution. *Science* 268, 267–269 (1995).
47. M. Odelius, M. Bernasconi and M. Parrinello, Two dimensional ice adsorbed on mica surface. *Phys. Rev. Lett.* 78, 2855–2858 (1997).
48. Y.-C. Liou, A. Tocilj, P. L. Davies and Z. Jia, Mimicry of ice structure by surface hydroxyls and water of a [beta]-helix antifreeze protein. *Nature* 406, 322–324 (2000).
49. G. A. Kimmel, N. G. Petrik, Z. Dohnalek and B. D. Kay, Crystalline ice growth on Pt(111): Observation of a hydrophobic water monolayer. *Phys. Rev. Lett.* 95, 166102 (2005).
50. C. L. Wang, H. J. Lu, Z. G. Wang, P. Xiu, B. Zhou, G. H. Zuo, R. Z. Wan, J. Hu and H. P. Fang, Stable liquid water droplet on a water monolayer formed at room temperature on ionic model substrates. *Phys. Rev. Lett.* 103, 137801 (2009).
51. C. L. Wang, B. Zhou, P. Xiu and H. P. Fang, Effect of surface morphology on the ordered water layer at room temperature. *J. Phys. Chem. C* 115, 3018–3024 (2011).
52. C. L. Wang, Y. Yang and H. Fang, Recent advances on “ordered water monolayer that does not completely wet water” at room temperature. *Sci. China-Phys. Mech. Astron.* 57, 802–809 (2014).

53. C. L. Wang, J. Y. Li and H. P. Fang, Ordered water monolayer at room temperature. *Rend. Fis. Acc. Lincei.* 22, 1–12 (2011).
54. S. J. Shao, L. Zhao, P. Guo and C. L. Wang, Ordered water monolayer on ionic model substrates studied by molecular dynamics simulations. *Nuclear Sci. Techniques* 25, 020502 (2014).
55. X. P. Ren, B. Zhou, L. T. Li and C. L. Wang, Structure and dynamics of ordered water in a thick nanofilm on ionic surfaces. *Chin. Phys. B* 22, 016801 (2013).
56. Miranda, L. Xu, Y. R. Shen and M. Salmeron, Icelike water monolayer adsorbed on mica at room temperature. *Phys. Rev. Lett.* 81, 5876–5879 (1998).
57. C. Zhu, H. Li, Y. Huang, X. C. Zeng and S. Meng, Microscopic insight into surface wetting: Relations between interfacial water structure and the underlying lattice constant. *Phys. Rev. Lett.* 110, 126101 (2013).
58. S. Pal, S. Balasubramanian and B. Bagchi, Dynamics of bound and free water in an aqueous micellar solution: Analysis of the lifetime and vibrational frequencies of hydrogen bonds at a complex interface. *Phys. Rev. E* 67, 061502 (2003).
59. S. Balasubramanian, S. Pal and B. Bagchi, Hydrogen-bond dynamics near a micellar surface: Origin of the universal slow relaxation at complex aqueous interfaces. *Phys. Rev. Lett.* 89, 115505 (2002).
60. V. A. Makarov, B. K. Andrews, P. E. Smith and B. M. Pettitt, Residence times of water molecules in the hydration sites of myoglobin. *Biophys. J.* 79, 2966–2974 (2000).
61. A. Hashimoto, K. Suenaga, A. Gloter, K. Urita and S. Iijima, Direct evidence for atomic defects in graphene layers. *Nature* 430, 870–873 (2004).
62. H. J. Queisser and E. E. Haller, Defects in semiconductors: Some fatal, some vital. *Science* 281, 945–950 (1998).
63. Y. Li and Y. Gao, Interplay between water and anatase (101) surface with sub-surface oxygen vacancy. *Phys. Rev. Lett.* 112, 206101 (2014).
64. L. G. Rosa, J. Xiao, Y. B. Losovyj, Y. Gao, I. N. Yakovkin, X. C. Zeng and P. A. Dowben, Crystalline ice grown on the surface of the ferroelectric polymer poly (vinylidene fluoride) (70%) and trifluoroethylene (30%), *J. Am. Chem. Soc.*, 127, 17261–17265 (2005).
65. J. M. DiMeglio, Contact-angle hysteresis and interacting surface-defects. *Europhys. Lett.* 17, 607–612 (1992).
66. J. Cheh, Y. Gao, C. L. Wang, H. Zhao and H. P. Fang, Ice or water: Thermal properties of monolayer water adsorbed on a substrate. *J. Stat. Mech.* P06009 (2013).
67. F. Müller-Plathe, A simple nonequilibrium molecular dynamics method for calculating the thermal conductivity. *J. Chem. Phys.* 106, 6082–6085 (1997).
68. B. Rotenberg, A. J. Patel and D. Chandler, Molecular explanation for why talc surfaces can be both hydrophilic and hydrophobic. *J. Am. Chem. Soc.* 133, 20521–20527 (2011).
69. A. Phan, T. A. Ho, D. R. Cole and A. Striolo, Molecular structure and dynamics in thin water films at metal oxide surfaces: Magnesium, aluminum, and silicon oxide surfaces. *J. Phys. Chem. C* 116, 15962–15973 (2012).

70. J. Lutzenkirchen, R. Zimmermann, T. Preocanin, A. Filby, T. Kupcik, D. Kuttner, A. Abdelmonem, D. Schild, T. Rabung, M. Plaschke, F. Brandenstein, C. Werner and H. Geckeis, An attempt to explain bimodal behaviour of the sapphire c-plane electrolyte interface. *Adv. Colloid Interface Sci.* 157, 61–74 (2010).
71. M. James, T. A. Darwish, S. Ciampi, S. O. Sylvester, Z. M. Zhang, A. Ng, J. J. Gooding and T. L. Hanley, Nanoscale condensation of water on self-assembled monolayers. *Soft Matter* 7, 5309–5318 (2011).
72. M. James, A. Darwish, S. Ciampi, S. Sylvester, Z. M. Zhang, A. Ng, J. Gooding and T. Hanley, Nanoscale water condensation on click-functionalized self-assembled monolayers. *Langmuir* 27, 10753–10762 (2011).
73. K. Lee, Q. Kim, S. An, J. An, J. Kim, B. Kim and W. Jhe, Superwetting of TiO₂ by light-induced water-layer growth via delocalized surface electrons. *Proc. Natl. Acad. Sci. USA* 111, 5784–5789 (2014).
74. N. Wang, Z. G. Duan and D. Fan, An ion diffusion method for visualising a solid-like water nanofilm. *Sci. Rep.* 3, 3505 (2013).
75. C. L. Wang, L. Zhao, D. H. Zhang, J. Chen, G. S. Shi and H. P. Fang, Upright or flat orientations of the ethanol molecules on surface with charge dipoles and the implication on the wetting behavior. *J. Phys. Chem. C* 118, 1873–1878 (2014).
76. D. Wu and A. Navrotsky, Probing the energetics of organic–nanoparticle interactions of ethanol on calcite, *Proc. Nat. Acad. Sci. (USA)*, 112, 5314–5318, 2015.
77. P. Guo and H. P. Fang, Water droplet on the self-assembled monolayer (SAM) surface modified by –COOH, in preparation.
78. C.L. Wang, B.H. Wen, Y. S. Tu, R. Z. Wan, Friction Reduction at a Superhydrophilic Surface: Role of Ordered Water, *J. Phys. Chem. C*, 119, 11679–11684. (2015).
79. S. V. Shevkunov, Structure of water in microscopic fractures of a silver iodide crystal, *Russ. J. Phys. Chem. A*, 88, 313–319 (2014).
80. G. S. Shi, Y. Shen, J. Liu, C. L. Wang, Y. Wang, B. Song, J. Hu and H. P. Fang, Molecular-scale hydrophilicity induced by solute: Molecular-thick charged pancakes of aqueous salt solution on hydrophobic carbon-based surfaces, *Sci. Rep.* 4, 6793 (2014).

Cheerios Effect and its Control by Contact Angle Modulation

Junqi Yuan and Sung Kwon Cho*

*Department of Mechanical Engineering and Materials Science,
University of Pittsburgh, Pittsburgh, PA, USA*

Abstract

This paper reviews theoretical models of the Cheerios effect for four different physical configurations (between two infinite vertical plates, between two vertical cylinders, between two spherical particles, and between a spherical particle and a vertical wall). The Cheerios effect is also generally known as lateral capillary force. A common understanding of the Cheerios effect is that the capillary forces between two vertical walls and between two vertical cylinders are attractive when they have similar wettability (hydrophilic-hydrophilic or hydrophobic-hydrophobic) and is repulsive when they have opposite wettability (hydrophilic-hydrophobic) and are not very close to each other. However, this statement is not applicable for the configurations with floating objects (i.e., between two floating spheres and between a sphere and a vertical wall). Additional parameters (for example, the size and the density of floating objects) are crucially important to determine the lateral capillary force. The effect of the floating object density is emphasized in the latter two configurations. The theoretical predictions of the lateral capillary force agree well with experimental results for large separation between the objects. However, there exists discrepancy for small separation, which could be caused by the increasing nonlinear effect as the two objects come close. In the last part of this paper, we introduce electrowetting-on-dielectric (EWOD) to control the Cheerios effect. By simply turning on/off the EWOD electrode, the contact angle on the plate is modulated. As a result, the capillary force between the plate and the floating object can be reversed in a controlled manner.

Keywords: Lateral capillary force, wettability, electrowetting-on-dielectric (EWOD), Cheerios effect

*Corresponding author: skcho@pitt.edu

3.1 Introduction

The Cheerios effect is an everyday phenomenon named after observations of cereal flakes floating in milk tending to aggregate and stick to the sidewall of the bowl [1,2]. This phenomenon is not restricted to cereal flakes only. In fact, most small floating objects (even bubbles and foams in Figure 3.1(a)) have a tendency to move away from or toward the sidewall depending on the surface hydrophobicity and other properties. In the presence of the floating objects, the air-liquid interface is distorted from its original shape, which generates a lateral force enabling the floating objects to move. Surprisingly, some water-dwelling creatures harness this phenomenon to climb up the inclined meniscus forming at the water bank [3,4]. By using only typical propulsion methods such as sliding their limbs, these creatures are unable to climb the slippery meniscus [5]. Instead, these small animals have developed special tricks where they change their posture and distort the adjacent interfaces to generate a lateral force. In Figure 3.1(b), for example, the waterlily leaf beetle simply bends its back and distorts the adjacent interfaces to climb the slippery meniscus [4]. In addition, the Cheerios effect governs a variety of interaction behaviors between floating objects in the processes of 2-dimensional array or monolayer self-assembly on the fluid-fluid interface [6–8].

Current studies have been performed to understand this phenomenon in different configurations. Four common physical configurations are interactions between (1) two infinite vertical walls, (2) two vertical circular cylinders, (3) two spheres, and (4) a sphere and a vertical wall. The Cheerios effect is also generally known as lateral capillary force. A simple and common understanding in these configurations is that attraction or repulsion solely depends on the surface wetting property [8–11]. For example, objects with similar wettability (i.e., both interacting objects are

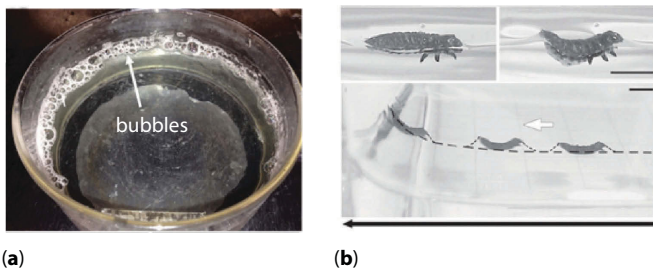


Figure 3.1 Examples of Cheerios effect. (a) Bubbles migrate to the sidewall [1]; and (b) A waterlily leaf beetle climbs the inclined air-water interface by arching its back [4].

hydrophobic or hydrophilic) attract each other; otherwise, they repel away. However, this understanding is true for the case where two infinite vertical walls or vertical cylinders are not very close to each other. It may not be true for other configurations, such as interaction between a floating object and a vertical wall or between two floating objects. Vella and Mahadevan [1] challenged this theory with a simple experiment. By maintaining a similar surface wettability of two floating objects but changing the weight of one object, it was shown that the force between the objects could be reversed.

To better understand the Cheerios effect in these configurations, many theoretical models have been reported. One of the simplest model may be for the configuration between two infinite vertical walls [1,12]. Since the walls are infinitely wide and high, the calculation is relatively simple with no vertical forces considered. When two vertical cylinders are submerged into a liquid, a 3-dimensional model is needed to describe the contact line on the cylinders. Using the Young-Laplace equation and the matched asymptotic expansions [13], Kralchevsky *et al.* [14] obtained an asymptotic solution for the capillary force. The solution reduces to a simple expression when the separation distance is large. In this model, the vertical force balance is not required either. When two spherical objects are floating at the interface, the vertical force balance becomes important. Although the contact angle is fixed, the running slope angle (the angle between the interface near the spheres and horizontal plane, which is critical to calculating the lateral force) can be different depending on the contact line position. Once the contact line position is determined from the vertical force balance, the calculation of the capillary force using the Nicolson superposition approximation is quite similar to that in case of the two vertical cylinders [14–16]. Direct measurements of the lateral capillary force between vertical cylinders and between spheres agree well with theory [17,18]. A theoretical model for the capillary interaction between a single spherical particle floating in the vicinity of an infinite vertical wall (which is the closest model to many Cheerios effect observations) was also developed [19]. The real interaction can be considered equivalent to the interaction between the particle and its mirror image with respect to the wall. This theory was partially verified by measuring the equilibrium position of the floating particle [20]. Moreover, Mansfield *et al.* [21] studied mutual attraction or repulsion of 2-dimensional strips. Some researchers [16,22,23] studied the configuration of horizontally floating two infinite cylinders where the vertical force balance becomes important to determine the contact line around the cylinder surfaces, although the capillary interaction can be described by a 2-dimensional model. The interaction between small floating horizontal cylinders with a finite length was also investigated [24]. Kralchevsky and

Nagayama [25,26] reviewed the latter three configurations (between two vertical cylinders, between two spherical particles, and between a spherical particle and a vertical wall) but did not extensively discuss the parameters that can affect the lateral capillary force.

In this article, theoretical models for the capillary interactions (Cheerios effect) in the four configurations of (1) two infinite vertical walls, (2) two vertical cylinders, (3) two floating spheres, and (4) a floating sphere and a vertical wall are reviewed. In particular, we added our numerical calculations for the case of two cylinders at small separation and compare them with an asymptotic solution and experimental data. For the third and fourth configurations, we have a particular interest in the effect of the density. A theoretical analysis reveals that when the vertical force balance comes into play, it is not safe to conclude that objects with similar surface wettability (hydrophilic-hydrophilic or hydrophobic-hydrophobic) attract while objects with the opposite surface wettability repel. In addition, we will introduce an on-demand controlling method for Cheerios effect in which the electrowetting-on-dielectric (EWOD) principle is used to alter wettability. The contact angle on the wall is controlled by applying a DC voltage, resulting in modulation of Cheerios effect. Finally, we will conclude this article with a summary and outlook on Cheerios effect.

3.2 Theoretical Models

The Cheerios effect is due to the horizontal component of the capillary force generated by the interface distortion. In order to find the horizontal component, the shape of the air-liquid interface deformed by objects or walls needs to be determined. Let ζ be a function describing the shape (vertical position) of the interface:

$$z = \zeta(x, y). \quad (3.1)$$

The interface shape obeys the Young-Laplace equation:

$$\nabla_{\Pi} \left(\frac{\nabla_{\Pi} \zeta}{\sqrt{1 + |\nabla_{\Pi} \zeta|^2}} \right) = \frac{\Delta P}{\sigma} \quad (3.2)$$

where $\nabla_{\Pi} \equiv \frac{\partial}{\partial x} \mathbf{e}_x + \frac{\partial}{\partial y} \mathbf{e}_y$ is the two-dimensional gradient operator, ΔP is the pressure difference across the air-liquid interface, and σ the air-liquid interfacial tension. For a small interfacial slope

$$|\nabla_{\Pi} \zeta|^2 \ll 1, \quad (3.3)$$

Eqn. (3.2) can be linearized to yield [27]

$$\nabla_{\Pi}^2 \zeta = \frac{\Delta \rho g}{\sigma} \zeta = q^2 \zeta, \quad (3.4)$$

where the density difference is $\Delta \rho = \rho_l - \rho_a \approx \rho_l$ and $q^{-1} = L_c \approx \sqrt{\sigma / \rho_l g}$ is the characteristic capillary length. Here, subscripts l and a denote liquid and air. For the air-water interface at room temperature, L_c is about 2.7 mm.

Once the interface shape is determined from Eqn. (3.4) along with the boundary conditions, the capillary force can be calculated by integrating the interfacial tension along the contact line and the hydrostatic pressure on the object:

$$F = F^{(\sigma)} + F^{(P)}, \quad (3.5)$$

where

$$F^{(\sigma)} = \oint_L \sigma dl, \quad F^{(P)} = - \oint_L P ds. \quad (3.6)$$

3.2.1 Model for Two Infinite Vertical Plates

Figure 3.2 illustrates the configuration of two infinite vertical plates at the air-liquid interface [1,12]. The plate thickness is neglected for simplicity. The presence of the plates distorts the air-liquid interface. The plates have contact angles θ_1 and θ_2 and are apart in a horizontal distance L . The three regions divided by the two plates are labeled as $i = 1, 2$, and 3 . Note that the liquid in the three regions is connected. Equation (3.4) can be simplified to a 2-dimensional equation [1]

$$\frac{d^2 \zeta}{dx^2} = q^2 \zeta. \quad (3.7)$$

A general solution of Eqn. (3.7) is:

$$\zeta_i(x) = A_i e^{x/L_c} + B_i e^{-x/L_c}. \quad (3.8)$$

In regions 1 and 3, the interface level as $x \rightarrow \pm \infty$ is 0, i.e.,

$$\zeta_1(-\infty) = \zeta_3(\infty) = 0. \quad (3.9)$$

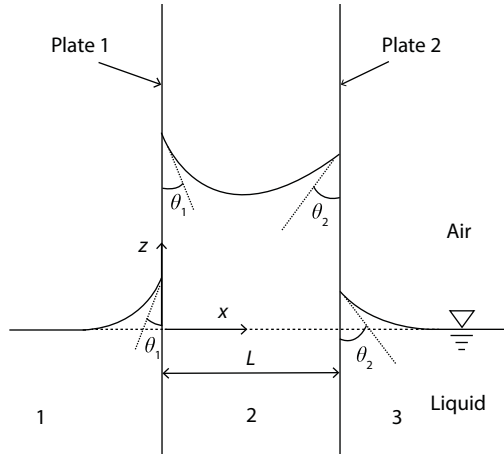


Figure 3.2 Configuration of two infinite vertical plates partially submerged in liquid [1]. The contact angles on the two plates are θ_1 and θ_2 . The separation distance between the two plates is L .

The boundary conditions at the plate walls are given by the contact angles as

$$\xi'_1(0) = \cot \theta_1, \quad \xi'_3(L) = -\cot \theta_2. \quad (3.10)$$

Combining Eqns. (3.8), (3.9) and (3.10), one can obtain the interface profiles in regions 1 and 3 as

$$\xi_1(x) = L_c \cot \theta_1 e^{x/L_c}, \quad (3.11)$$

$$\xi_3(x) = L_c \cot \theta_2 e^{(L-x)/L_c}. \quad (3.12)$$

In region 2, the boundary conditions at the walls are

$$\xi'_2(0) = -\cot \theta_1, \quad \xi'_2(L) = \cot \theta_2, \quad (3.13)$$

which give an interface profile between the two plates as:

$$\xi_2(x) = L_c \frac{\cot \theta_1 \cosh \frac{L-x}{L_c} + \cot \theta_2 \cosh \frac{x}{L_c}}{\sinh \frac{L}{L_c}}. \quad (3.14)$$

Due to the same contact angles on both sides of each plate, the horizontal components of the interface force on both sides of the plate cancel out ($F^{(\sigma)} = 0$). So the horizontal force is caused by only the hydrostatic pressure difference across the plate. The horizontal force acting on each plate can be calculated according to Eqn. (3.6) by integrating the hydrostatic pressure on the plate [1,11]. For example, the force on the left plate in Figure 3.2 is given as:

$$\begin{aligned} F_x &= \int_{-\infty}^{\xi_1^{(0)}} \rho_l g y dy - \int_{-\infty}^{\xi_2^{(0)}} \rho_l g y dy = \int_{\xi_2^{(0)}}^{\xi_1^{(0)}} \rho_l g y dy \\ &= \frac{1}{2} \rho_l g \left[\xi_1^{(0)^2} - \xi_2^{(0)^2} \right]. \end{aligned} \quad (3.15)$$

By substituting Eqns. (3.11) and (3.14) into (3.15), one has the horizontal force as:

$$F_x = -\frac{\sigma}{2} \left[\frac{\left(\cot \theta_1 \cosh \frac{L}{L_c} + \cot \theta_2 \right)^2}{\sinh^2 \left(\frac{L}{L_c} \right)} - \cot^2 \theta_1 \right]. \quad (3.16)$$

Figure 3.3 shows the calculated interface profiles and horizontal force when both plates are hydrophilic or hydrophobic. In Figure 3.3(a), both plates are hydrophilic with contact angles θ_1 and θ_2 ($\theta_1 < 90^\circ$ and $\theta_2 < 90^\circ$). The air-liquid interface (liquid level) in region 2 is higher than that at infinity ($x \rightarrow \pm \infty$), i.e., $h_2 > 0$. The liquid weight in region 2 is balanced by the upward vertical component of the capillary force at the contact line. This phenomenon is commonly known as capillary action or capillarity. Using the Young-Laplace equation, one can easily find that the liquid pressure P between the plates is smaller than the atmospheric pressure P_a . In region 2, the liquid surface is higher ($h_2(0) > h_1(0)$ and $h_2(L) > h_3(L)$) and the pressure is smaller ($P < P_a$), so the plates are pushed toward each other (attract each other). In Figure 3.3(b), on the contrary, the interface in region 2 is lower than the zero level ($h_2 < 0$) when both plates are hydrophobic ($\theta_1 > 90^\circ$ and $\theta_2 > 90^\circ$). The cavity between the plates creates an upward buoyancy-like force that is balanced by the downward vertical component of the capillary force at the contact line. Similarly to the hydrophilic case in region 2, can be obtained from the Young-Laplace equation. Since the liquid level in region 2 is lower ($h_2(0) < h_1(0)$ and $h_2(L) < h_3(L)$) and the pressure in regions 1 and 3 is greater than P_a ($P > P_a$), the two plates also attract each other. Figure 3.3(c) shows the horizontal

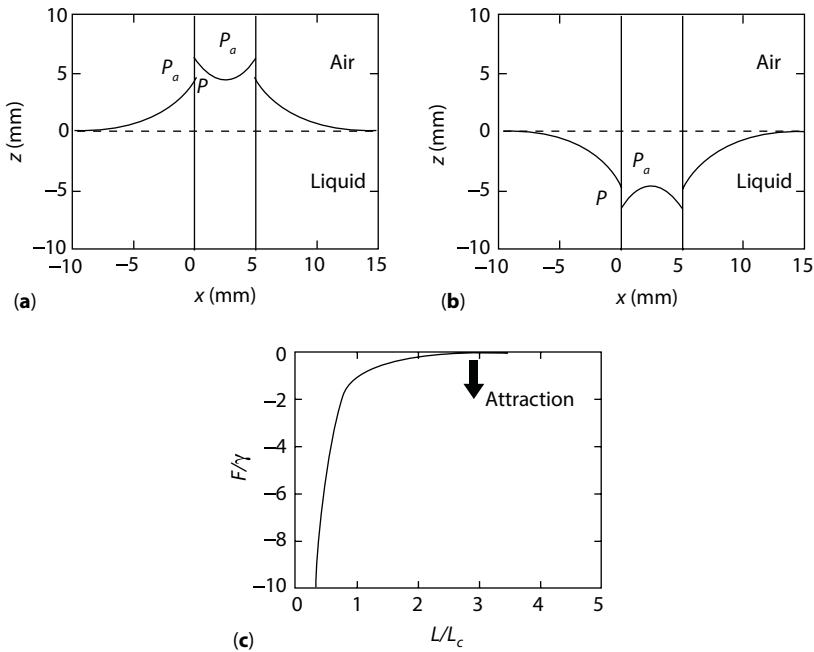


Figure 3.3 Two vertical plates with similar wettability. (a) Interface profiles near two hydrophilic plates; and (b) two hydrophobic plates. (c) Horizontal component of the dimensionless force between the plates vs. separation ($\theta_1 = 45^\circ$ and $\theta_2 = 60^\circ$). In (a) and (b), the thick solid lines represent the plates; the black dashed line denotes the liquid level at infinity; and the thin solid lines denote the air-liquid interface.

force vs. the separation for the plates with similar wettability, which is calculated from Eqn. (3.16). Positive means repulsive while negative means attractive. No matter what the separation distance is, the force is always attractive. In particular, it increases quickly as the two plates come closer.

For the plates with opposite wettability (i.e., one plate is hydrophilic and the other is hydrophobic), the force behavior is much more complicated. Figure 3.4(a) shows the interface profiles for $\theta_1 < 90^\circ$, $\theta_2 > 90^\circ$ and $\theta_1 + \theta_2 < 180^\circ$ when the two plates are a moderate distance apart. The left contact line in region 2 is a little lower than the contact line in region 1 ($h_2(0) < h_1(0)$) but the right contact line is higher than the contact line in region 3 ($h_2(L) > h_3(L)$). One can easily find that $P_a > P_1$ and $P_{2d} > P_a$. On the left plate, in the small vertical gap between $h_1(0)$ and $h_2(0)$, P_1 is smaller than P_a . This generates a net force toward the left. Similarly on the right plate, P_{2d} is larger than P_a such that a net force toward the right is generated. As a result, the two plates repel each other. When two plates become very

close (Figure 3.4(b)), the interface in region 2 becomes much higher ($h_2(0) > h_1(0)$ and $h_2(L) > h_3(L)$). The two plates push each other because the pressures in regions 1 and 3 are larger than the pressure between the plates ($P_a > P_2$). Note that when the two plates have opposite wettability and $\theta_1 + \theta_2 > 180^\circ$, the interface in region 2 will be lowered. This results in repulsion at a large separation and attraction at a small separation. Figure 3.4(c) is the force curve for the plates with opposite wettability ($\theta_1 < 90^\circ$, $\theta_2 > 90^\circ$ and $\theta_1 + \theta_2 \neq 180^\circ$). In the large separation, the force is repulsive and small. It increases as the separation L decreases. Once the repulsive force reaches a peak, it decreases rapidly and becomes attractive when the distance becomes very small. There exists a zero force point at $L = L_0$, which depends on the contact angles on the two plates.

$\theta_1 + \theta_2 = 180^\circ$ is a special case where the middle point of the interface in region 2 always stays at the zero level no matter how close the two plates are (Figure 3.5(a)). Because the pressure in region 2 is always greater than that

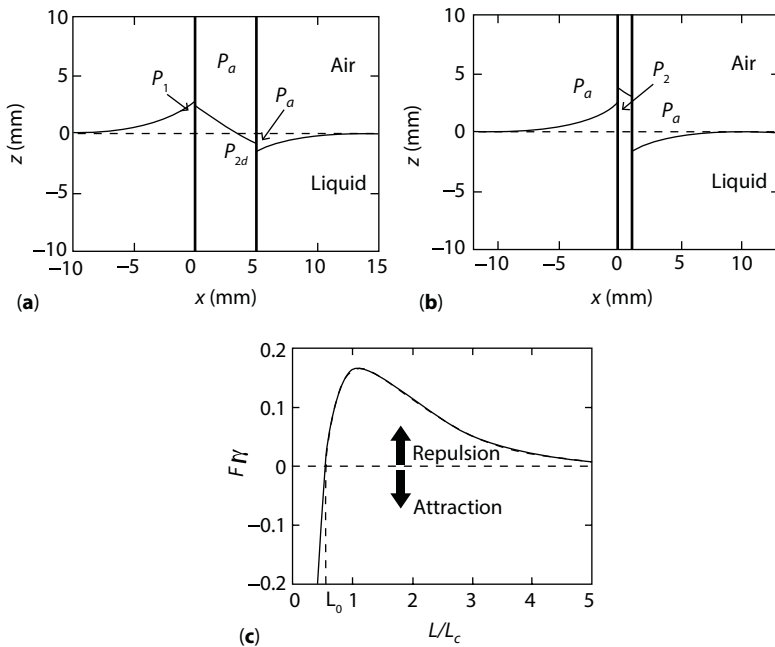


Figure 3.4 Two vertical plates with opposite surface wettability and $\theta_1 + \theta_2 \neq 180^\circ$. Interface profiles for (a) a moderate separation; and (b) a small separation between the plates; (c) horizontal component of the dimensionless force between the plates vs. separation ($\theta_1 = 45^\circ$ and $\theta_2 = 120^\circ$). In (a) and (b), the thick solid lines represent the plates; the black dashed line indicates the liquid level at infinity; and the thin solid lines denote the air-liquid interface.

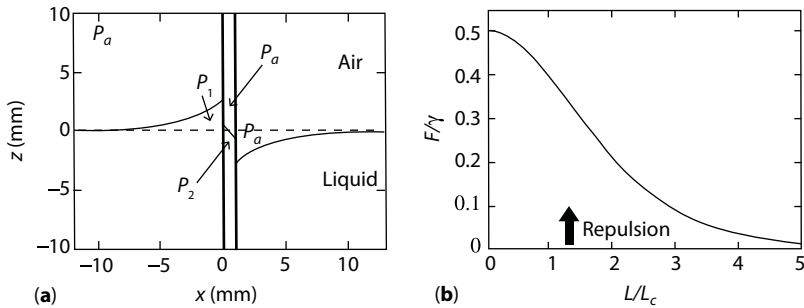


Figure 3.5 Two vertical plates with opposite surface wettability and $\theta_1 + \theta_2 = 180^\circ$. (a) Interface profile; (b) horizontal component of the dimensionless force vs. separation ($\theta_1 = 45^\circ$ and $\theta_2 = 135^\circ$). In (a), the thick solid lines represent the plates; the black dashed line indicates the liquid level at infinity; and the thin solid lines denote the air-liquid interface.

in regions 1 and 3 ($P_a > P_1$ for the left plate and $P_2 > P_a$ for the right plate), the plates always repel each other (Figure 3.5(b)). The repulsive force is small when the two plates are far apart. It increases as the separation L becomes smaller. However, it does not change the sign of the force even when L approaches zero. In summary, two infinite plates attract each other when both of them are hydrophilic or hydrophobic, while they repel each other when the surface wettability is opposite and the distance between plates is not very small.

3.2.2 Model of Two Vertical Cylinders

When two cylinders are submerged into liquid, as shown in Figure 3.6(a), Eqn. (3.4) can be written as

$$\frac{d^2 \xi}{dx^2} + \frac{d^2 \xi}{dy^2} = q^2 \xi. \quad (3.17)$$

Due to the capillary interaction between the cylinders, the contact lines on the cylinders are not horizontal. Otherwise, no horizontal force could be generated because the integrals in Eqn. (3.6) would be zero. The capillary force calculation can be performed in the following two regimes divided based on the separation distance between the cylinders: small or moderate separation and large separation.

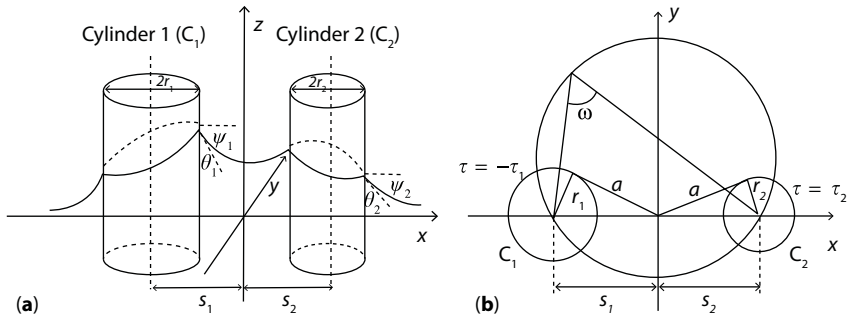


Figure 3.6 (a) Configuration of two vertical cylinders partially submerged in liquid [14]; (b) Bipolar coordinates on plane xy [13].

3.2.2.1 Cylinders Spaced at a Small or Moderate Separation

The geometry of the system suggests to use the bipolar coordinates (τ, ω, z) ([13], Figure 3.6(b)):

$$x = a \frac{\sinh \tau}{\cosh \tau - \cos \omega}, \quad y = a \frac{\sin \omega}{\cosh \tau - \cos \omega}, \quad (3.18)$$

where

$$a^2 = s_1^2 - r_1^2 = s_2^2 - r_2^2. \quad (3.19)$$

In the bipolar coordinates, Eqn. (3.17) is converted to

$$(\cosh \tau - \cos \omega)^2 \left(\frac{\partial^2 \xi}{\partial \tau^2} + \frac{\partial^2 \xi}{\partial \omega^2} \right) = (qa)^2 \xi(\tau, \omega). \quad (3.20)$$

Note that τ is mathematically defined in Eqn. (3.18), though it is not easy to show it graphically in Figure 3.6. Since only the interface profiles on the cylinder surfaces are required to calculate the lateral capillary force, one can only look for a solution of Eqn. (3.20) in the region close to the cylinders with ignoring the far field.

When two cylinders are spaced at a small or moderate distance $((qa)^2 \ll 1)$, the following mathematical description is valid [14]:

$$(\cosh \tau - \cos \omega)^2 \gg (qa)^2. \quad (3.21)$$

Now Eqn. (3.20) reduces to

$$\frac{\partial^2 \xi}{\partial \tau^2} + \frac{\partial^2 \xi}{\partial \omega^2} = 0. \quad (3.22)$$

On the cylinder surfaces, the boundary conditions in the bipolar coordinates can be expressed as [13]

$$\begin{aligned} \left. \frac{\partial \xi}{\partial \tau} \right|_{\tau=-\tau_1} &= - \left. \frac{a}{\cosh \tau - \cos \omega} \right|_{\tau=-\tau_1} \sin \psi_1, \\ \left. \frac{\partial \xi}{\partial \tau} \right|_{\tau=\tau_2} &= - \left. \frac{a}{\cosh \tau - \cos \omega} \right|_{\tau=\tau_2} \sin \psi_2. \end{aligned} \quad (3.23)$$

where ψ_i is the slope angle. For the vertical cylinders, ψ_i equals $\left(\frac{\pi}{2} - \theta_i \right)$ which is positive when $\theta_i < 90^\circ$ and is negative when $\theta_i > 90^\circ$. One can obtain a solution of Eqn. (3.22) with Eqn. (3.23) in the form of Fourier series [14]:

$$\begin{aligned} \xi_i(\tau, \omega) &= C_0 + Q_i \ln(2 \cosh \tau - 2 \cos \omega) \\ &\quad + \sum_{n=1}^{\infty} C_n^{(i)} \cosh n \left[\tau - (-1)^i \tau_i \right] \cos n \omega, \quad i = 1, 2 \end{aligned} \quad (3.24)$$

where

$$C_0 = (Q_1 - Q_2)A - (Q_1 + Q_2) \ln(\gamma_e q a) \quad (3.25)$$

$$A = \sum_{n=1}^{\infty} \frac{1}{n} \frac{\sinh n(\tau_1 - \tau_2)}{\sinh n(\tau_1 + \tau_2)} \quad (3.26)$$

$$Q_i = r_i \sin \psi_i \quad (3.27)$$

$$C_n^{(i)} = \frac{2(Q_2 - Q_1)}{n} \frac{(-1)^i \sinh n \tau_j}{\sinh n(\tau_1 + \tau_2)}, \quad i, j = 1, 2; i \neq j, n = 1, 2, 3, \dots \quad (3.28)$$

In Eqn. (3.25) the Euler-Mascheroni constant is $\gamma_e = 1.781 \dots$ [28].

As shown in Figure 3.7 [14], let $z = \xi(\varphi)$ be the vertical position of the contact line on the cylinder surface, where φ is the azimuthal angle on the xy plane. The position vector to the contact line is

$$\mathbf{R}(\varphi) = r_i \cos \varphi \mathbf{e}_x + r_i \sin \varphi \mathbf{e}_y + \xi(\varphi) \mathbf{e}_z. \quad (3.29)$$

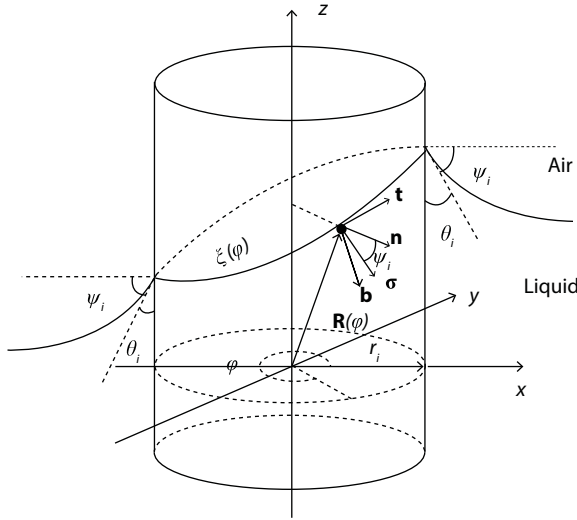


Figure 3.7 Contact line on the left cylinder when the separation between the two cylinders is small [14]. The second cylinder is located on the right (not shown).

In the bipolar coordinates, τ is constant on the cylinder surface. ω and φ are related as

$$\tan \omega = \frac{\sin \varphi}{r_i / (s_1 + s_2) - \cos \varphi}. \quad (3.30)$$

The line element along the contact line is

$$dl = \chi d\varphi, \text{ where } \chi = \left| \frac{d\mathbf{R}}{d\varphi} \right| = \sqrt{r_i^2 + \left(\frac{d\zeta}{d\varphi} \right)^2}. \quad (3.31)$$

The unit vector tangential to the contact line is described as

$$\mathbf{t} = \frac{1}{\chi} \frac{d\mathbf{R}}{d\varphi} = \frac{1}{\chi} \left(-r_i \sin \varphi \mathbf{e}_x + r_i \cos \varphi \mathbf{e}_y + \frac{d\zeta}{d\varphi} \mathbf{e}_z \right), \quad (3.32)$$

the unit vector normal to the cylinder surface is

$$\mathbf{n} = \cos \varphi \mathbf{e}_x + \sin \varphi \mathbf{e}_y, \quad (3.33)$$

and the unit vector \mathbf{b} that is normal to the nt plane can be defined as

$$\mathbf{b} = \mathbf{t} \times \mathbf{n}. \quad (3.34)$$

The vector form of surface tension σ , which is placed on the bn plane, can be written as

$$\boldsymbol{\sigma} = \sigma(\sin \psi_i \mathbf{b} + \cos \psi_i \mathbf{n}). \quad (3.35)$$

Then, the horizontal surface tension is

$$\sigma_x = \boldsymbol{\sigma} \cdot \mathbf{e}_x = \sigma \left(\cos \varphi \cos \psi_i - \frac{1}{\chi} \frac{d\zeta}{d\varphi} \sin \varphi \sin \psi_i \right). \quad (3.36)$$

Substituting Eqn. (3.36) into Eqn. (3.6), one can derive

$$F_x^{(\sigma)} = -2\sigma \sin \psi_i \int_0^\pi \frac{d\zeta}{d\varphi} \sin \varphi d\varphi + 2\sigma \cos \psi_i \int_0^\pi \chi \cos \varphi d\varphi. \quad (3.37)$$

A numerical calculation shows that for small cylinders ($(qr_i)^2 \ll 1$), the second integral on the right-hand side of Eqn. (3.37) is much smaller than the first integral [14]. By substituting Eqn. (3.24) into Eqn. (3.37), one may obtain $F_x^{(\sigma)}$ for the small or moderate separation. The force due to hydrostatic pressure $F_x^{(P)}$ also needs to be calculated in order to obtain the total horizontal force. The hydrostatic pressure is given as

$$P = P_a - \rho_l g \zeta. \quad (3.38)$$

where P_a is the atmospheric pressure. Substituting Eqn. (3.38) into Eqn. (3.6), one can obtain

$$F_x^{(P)} = -\rho_l g r_i \int_0^\pi \zeta^2(\varphi) \cos \varphi d\varphi. \quad (3.39)$$

Finally, the horizontal force between two vertical cylinders can be expressed as:

$$\begin{aligned} F_x = & -2\sigma \sin \psi_i \int_0^\pi \frac{d\zeta}{d\varphi} \sin \varphi d\varphi \\ & + 2\sigma \cos \psi_i \int_0^\pi \chi \cos \varphi d\varphi - \rho_w g r_i \int_0^\pi \zeta^2(\varphi) \cos \varphi d\varphi. \end{aligned} \quad (3.40)$$

Kralchevsky *et al.* [14] compared the contributions of both hydrostatic pressure and surface tension, and concluded that for small cylinders ($(qr_i)^2 \ll 1$), the ratio below is small:

$$F_x^{(P)} / F_x^{(\sigma)} \ll 1. \quad (3.41)$$

3.2.2.2 Cylinders spaced at a large separation

When two cylinders are apart at a large separation, the capillary interaction between the two cylinders is weak. One can assume that the interface on the cylinder surface is modeled by a linear equation and is a superposition of the interfaces distorted by the two isolated cylinders [15]:

$$\zeta = \zeta_1 + \zeta_2. \quad (3.42)$$

When a single cylinder is isolated and submerged into liquid, the interface profile can be obtained by solving Eqn. (3.4), which yields a modified Bessel function in the cylindrical coordinates as

$$\zeta_i = Q_i K_0(qr), \quad (3.43)$$

where K_0 is the modified Bessel function of zeroth order and r is the distance from the cylinder axis. When $r = r_i$, ζ_{i0} denotes the contact line on the cylinder surface. When the two cylinders are far from each other,

$$a \gg r_i \text{ and } s_i \gg r_i. \quad (3.44)$$

Thus,

$$s_1 \approx s_2 = s = \frac{L}{2}. \quad (3.45)$$

So the interface profile on a single cylinder surface (for example, for cylinder 2) is

$$\zeta_2 = \zeta_{20} + Q_1 K_0(2qr), \quad (3.46)$$

where ζ_{20} is the elevation of the contact line on cylinder 2 for the infinite separation distance and r the distance from the axis of cylinder 1. On the cylinder surface, one can derive

$$\frac{d\zeta}{d\varphi} = 2qr_1 r_2 \sin \varphi_1 K_1(2qs) \sin \varphi. \quad (3.47)$$

By substituting Eqn. (3.47) into Eqn. (3.40) and neglecting $F_x^{(P)}$, an expression for $F_x^{(\sigma)}$ for small cylinders ($(qr_i)^2 \ll 1$) can be obtained as [16]:

$$F_x \approx F_x^{(\sigma)} \approx -2\pi\sigma q Q_1 Q_2 K_1(2qs). \quad (3.48)$$

Figures 3.8 and 3.9 show comparisons between experimental results [17] and numerical calculations based on Eqns. (3.24), (3.40) and (3.48). As capillary interactions between the two hydrophilic cylinders partially submerged into water are shown in Figure 3.8, the numerical calculation from Eqn. (3.48) fits perfectly at the large separation, and deviates as the separation decreases. The results from Eqns. (3.24) and (3.40), which are obtained with the assumption of small separation distances, fit better when the two cylinders are close to each other. In Figure 3.8(b), however, when the two cylinders are in an 8×10^{-2} M sodium dodecyl sulfate (SDS) solution $\sigma_{\text{SDS}} = 36.8$ mN/m, and $\rho_{\text{SDS}} = 1.01$ g/cm³, Eqn. (3.48) works only for the large separation and Eqns. (3.24) and (3.40) do not fit very well. Velev *et al.* suggested that this large deviation with the 8×10^{-2} M SDS solution may be caused by a nonlinear effect associated with the dimensionless radii qr_p , which are larger than those in pure water [17].

Figure 3.9 shows force-separation curves for the two cylinders having opposite wettability ($\theta_1 = 0^\circ$ and $\theta_2 = 99^\circ$). Eqn. (3.48) agrees well with the experimental data for the large separation. Velev *et al.* found that the measured horizontal force decreases at the small separation and predicted that the force might change from repulsion to attraction at a much smaller separation [17]. However, Eqn. (3.48) does not change sign at any separation because it uses a linear approximation and neglects the contact line elevation caused by the capillary interaction between the cylinders. The

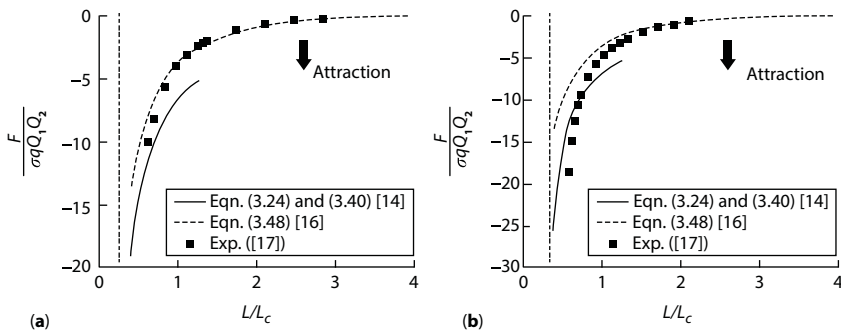


Figure 3.8 Comparison of theoretical predictions with experimental data for the dimensionless horizontal force between two vertical cylinders. Both cylinders are hydrophilic (a) Both cylinders are partially submerged in water; (b) Both cylinders are partially submerged in an 8×10^{-2} M SDS solution. The dash-dot lines show the lower limit for possible separation between the cylinder centers. ($\theta_1 = \theta_2 = 0^\circ$, $r_1 = 370$ μm , $r_2 = 315$ μm , $\sigma_{\text{water}} = 72.4$ mN/m, $\rho_{\text{water}} = 1.0$ g/cm³, $\sigma_{\text{SDS}} = 36.8$ mN/m, and $\rho_{\text{SDS}} = 1.01$ g/cm³)

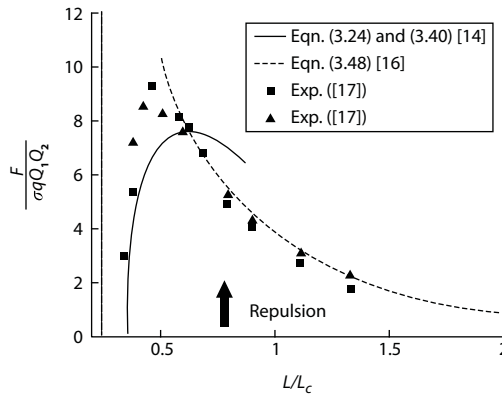


Figure 3.9 Comparison of theoretical predictions and experimental data for the horizontal force between two vertical cylinders partially submerged in water. The two cylinders have the opposite wettability. The dash-dot line shows the lower limit for possible separation between the cylinder centers. ($\theta_1 = 0^\circ$, $\theta_2 = 99^\circ$, $r_1 = 370 \mu\text{m}$, $r_2 = 315 \mu\text{m}$, $\sigma_{\text{water}} = 72.4 \text{ mN/m}$).

numerical calculation using Eqns. (3.24) and (3.40) fairly predicts the capillary force at small separation. Furthermore, the calculation predicts that the force direction is reversed when the two cylinders come very close to each other.

Comparing Figure 3.8 with Figure 3.3(c) and Figure 3.9 with Figure 3.4(c), one finds that the overall trends for the vertical walls model and vertical cylinders model are very similar: objects with similar wettability (hydrophilic-hydrophilic or hydrophobic-hydrophobic) attract each other; objects with opposite wettability repel each other at large separation but attract at small or moderate separation. Similar to the results shown in Figure 3.5(b), the numerical calculation shows that when $\theta_1 + \theta_2 = 180^\circ$ the force between the two cylinders is always repulsive and does not change its direction no matter how close the two cylinders are.

3.2.3 Model of Two Floating Spherical Particles

Consider two small spherical particles with radii of R_1 and R_2 floating at the air-liquid interface ([14], Figure 3.10(a)). The radii of the contact lines on the particle surfaces are r_1 and r_2 . Similar to the aforementioned two-cylinder model, $F_x^{(P)} / F_x^{(\sigma)}$ is small for small spheres ($(qR_i)^2 \ll 1$), so $F_x^{(P)}$ can be neglected. If two spherical particles generate the same contact line shape as the cylinders do, the horizontal forces generated by the spherical

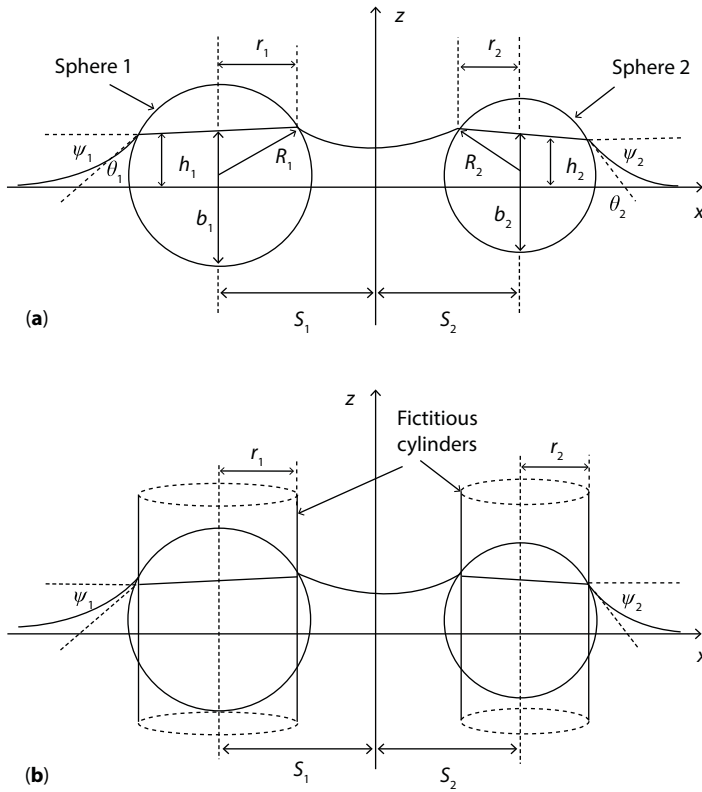


Figure 3.10 (a) Configuration of two small spherical particles floating at the interfaces [14]; (b) The two fictitious cylinders generate the same interface profiles [14].

particles will equal those generated by the cylinders because $F_x^{(\sigma)}$ depends solely on the interface shape close to the cylinders.

In this case, we can imagine that the two spherical particles are replaced by two vertical fictitious cylinders with radii r_1 and r_2 ([14], Figure 3.8(b)). As shown in the two-cylinder model, the contact lines are not horizontal. The inclination of the contact line is significant when the two cylinders are close to each other, even though it becomes small at large separation, because the contact lines have a large room to move vertically. However, the inclination of the contact lines for small spherical particles would not be large since it is restricted by the size and curvature of the particles. One can infer that Eqn. (3.48), which is used to calculate the capillary force between the cylinders at large separation, is suitable for calculating the

horizontal force between the two floating spherical particles in the entire range of separation distance, as follows:

$$F_x \approx -2\pi\sigma q Q_1 Q_2 K_1(2qs). \quad (3.49)$$

Kralchevsky et al. [14] also proved from the energy method that Eqn. (3.49) is valid for calculating the horizontal force between the two floating spherical particles. Since r_i is always positive, the sign of capillary charge Q_i depends solely on ψ_i . If both particles have the same sign of ψ_i , the lateral capillary force between the two floating spheres is attractive; otherwise, the force is repulsive.

Since the contact line moves on the curved surface of the sphere, either r_i or ψ_i is not constant. In order to calculate the capillary charge Q_i in Eqn. (3.49), one needs to use the vertical force balance. Because the inclination of the contact line is not significant, the contact line can be assumed horizontal to obtain geometric relations. The volume of the lower part of the sphere immersed in liquid is

$$V_l^{(i)} = \pi b_i^2 (R_i - b_i / 3). \quad (3.50)$$

where b_i is the height of the submerged part in liquid. R_i and b_i are related as

$$\frac{b_i - R_i}{R_i} = \cos(\psi_i + \theta_i). \quad (3.51)$$

Using $\beta_i = \psi_i + \theta_i$ and substituting Eqn. (3.51) into Eqn. (3.50) yields

$$V_l^{(i)} = \frac{1}{3} \pi R_i^3 (2 + 3 \cos \beta_i - \cos^3 \beta_i). \quad (3.52)$$

The radius of the contact line can be expressed as

$$r_i = \sqrt{b_i (2R_i - b_i)}. \quad (3.53)$$

According to the vertical force balance, the vertical component of capillary force at the contact line is counterbalanced by the gravitational force, i.e.,

$$F_g^{(i)} = 2\pi\sigma r_i \sin \psi_i. \quad (3.54)$$

The gravitational force can be expressed as [29]

$$F_g^{(i)} = g \left[(\rho_l - \rho_i) V_l^{(i)} + (\rho_a - \rho_i) V_u^{(i)} - (\rho_l - \rho_a) \pi r_i^2 h_i \right], \quad (3.55)$$

where ρ_i is the particle density, $V_u^{(i)}$ the volume of the non-submerged part of the sphere, and h_i the contact line elevation with respect to the interface level at infinity ($x \rightarrow \pm\infty$). The relation for the sphere volume is:

$$V_l^{(i)} + V_u^{(i)} = V^{(i)} = \frac{4}{3} \pi R_i^3. \quad (3.56)$$

Because $\rho_i \gg \rho_a$, Eqn. (3.54) and Eqn. (3.55) can be combined and transformed to yield

$$Q_i = r_i \sin \psi_i \approx \frac{q^2}{2\pi} \left[V_l^{(i)} - D_i V^{(i)} - \pi r_i^2 h_i \right], \quad (3.57)$$

where the density correlation D_i is defined as

$$D_i = \frac{\rho_i - \rho_a}{\rho_l - \rho_a}. \quad (3.58)$$

For the small particles ($(qR_i)^2 \ll 1$), the term $\pi r_i^2 h_i$ in Eqn. (57) is small compared to $V_l^{(i)}$ and $D_i V^{(i)}$, so it can be neglected. By substituting Eqns. (3.52) and (3.56) into Eqn. (3.57), Eqn. (3.57) can be further expressed as

$$Q_i \approx \frac{q^2 R_i^3}{6} (2 - 4D_i + 3 \cos \beta_i - \cos^3 \beta_i). \quad (3.59)$$

Due to extremely small weight (note that the particle weight is proportional to the cube of radius), the interface deformation with small particles is very small. Kralchevsky and Nagayama [26] estimated that particles with radius less than 10 μm cannot deform the interface and, as a result, do not generate any horizontal force, i.e., ψ_i is small and $\beta_i \approx \theta_i$. Eqn. (3.59) finally becomes

$$Q_i \approx \frac{q^2 R_i^3}{6} (2 - 4D_i + 3 \cos \theta_i - \cos^3 \theta_i). \quad (3.60)$$

Combining Eqn. (3.48) with Eqn. (3.60), the horizontal capillary force vs. distance between particles can be calculated. Experimental measurements agree well with this calculation [18,30].

In Eqn. (3.60), the contact angle θ_i , the particle radius R_i and the density correlation D_i are the parameters to determine the lateral capillary force. Here, D_i is more important than R_i because it may affect both magnitude and sign of the capillary force while R_i changes only the magnitude. When

the contact angle and size of particles are fixed, Q_i may change its sign depending on the particle density. This leads to a direction change in the horizontal force F_x . Figure 3.11 shows the force vs. separation for three pairs of spherical particles with different density combinations. The particle size and the contact angle are kept constant in calculation ($R_i = 100 \mu\text{m}$, $\theta_i = 60^\circ$). The solid line ($\rho_1 = \rho_2 = 2 \text{ g/cm}^3$) and dash-dot line ($\rho_1 = \rho_2 = 0.5 \text{ g/cm}^3$) show attraction between the two identical particles. However, between a heavy particle and a light particle ($\rho_1 = 2 \text{ g/cm}^3$ and $\rho_2 = 0.5 \text{ g/cm}^3$), the force becomes repulsive due to the opposite signs of capillary charges.

3.2.4 Model of Floating Spherical Particle and Vertical Wall

The last configuration for Cheerios effect in this article is a spherical particle with capillary charge Q floating in vicinity of an infinite vertical wall. In order to find the horizontal capillary force between the wall and particle, one may consider a simple case where the contact angle at the wall is fixed at $\theta_w = 90^\circ$, i.e., the boundary condition is

$$\xi'_0(0) = 0 \quad (3.61)$$

Due to the zero slope at the wall, the mirror image method can be used to find the capillary force: the second identical particle (mirror image) floats at the distance $2s$ from the original one ([19], Figure 3.12(a)). In

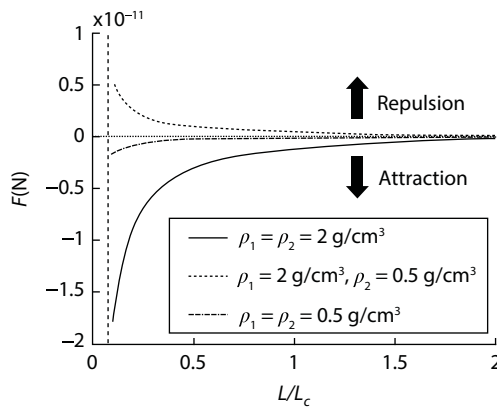


Figure 3.11 Force vs. separation for three pairs of spherical particles with different densities. The particle sizes and contact angles are kept constant in calculation ($R_1 = R_2 = 100 \mu\text{m}$, $\theta_1 = \theta_2 = 60^\circ$). The dash-dot line shows the lower limit of possible separation between the centers of the particles.

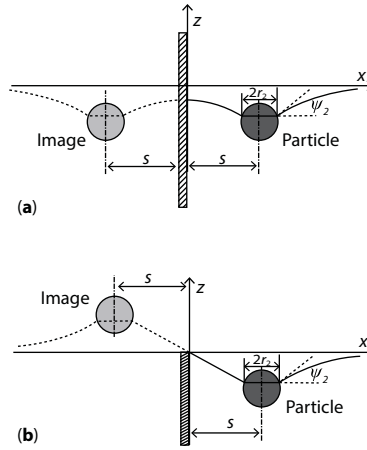


Figure 3.12 Capillary image force between the floating particle and its image [19]. (a) Fixed contact angle at the wall ($\theta_w = \pi/2$); (b) Fixed contact line at the wall ($\xi_0(0) = 0$).

case the vertical wall is removed in Figure 3.12(a), the interface should not change. Since the two particles (real and imaginary) are identical, the capillary charges of the two particles are also equal to each other ($Q_1 = Q_2 = Q$). As derived in the two-particle model, the capillary force between these two particles is attractive:

$$F_x = -2\pi\sigma q Q^2 K_1(2qs). \quad (3.62)$$

The capillary charge Q can be calculated by Eqn. (3.57). Since the interface elevation caused by the wall is zero and the elevation caused by the floating particle is negligibly small, the term $\pi r_i^2 h_i$ can be ignored. In addition, ψ_i is small due to the small size and weight of the particle. As a result, Eqn. (3.57) can be reduced to Eqn. (3.60).

One may ask if the capillary force can become repulsive for the wall-particle interaction. When the boundary condition becomes

$$\xi_0(0) = 0, \quad (3.63)$$

which means the contact line at the wall is pinned to the zero elevation, the force becomes repulsive. In practice, this boundary condition can be realized when the contact line is attached to the edge of a vertical plate or to the boundary between hydrophilic and hydrophobic regions on the surface of the wall [19]. Using the symmetry, one can imagine that the

second particle (image) with the opposite capillary charge ($Q_1 = -Q_2 = Q$) is located at the distance $2s$ from the original one (Figure 3.12(b)). Similar to the previous case, the interface should not change when the vertical wall is removed. The capillary force becomes repulsive:

$$F_x = 2\pi\sigma q Q^2 K_1(2qs). \quad (3.64)$$

The above two cases are rare and special in reality, which are simply described by 'Capillary Image Force' [19]. The above method cannot be directly used for general and realistic conditions where the contact angle is not fixed just to 90° but can be any angle over a wide range and the contact line is positioned to an arbitrary elevation.

The following discussion shows how to find solutions for more general boundary conditions: (1) fixed contact angle at the arbitrary value and (2) fixed contact line at the arbitrary position. Since the current scope is limited to the small interface slope, the Young-Laplace equation can be linearized (Eqn. (3.4)). For the inclined interface, one can seek a superposed solution:

$$\xi = \xi_0 + \xi_1, \quad (3.65)$$

where ξ_0 is the deformation of interface created by the particle when $\theta_w = 90^\circ$ or $\xi_0(0) = 0$ and ξ_1 is the deformation of interface formed near the wall in the absence of the floating particle.

For the fixed contact angle at the wall, the boundary conditions are:

$$\xi_0'(0) = 0, \quad \xi_1(0) = -\tan\psi_1. \quad (3.66)$$

Similarly, the boundary conditions for the fixed contact line at the wall are

$$\xi_0(0) = 0, \quad \xi_1'(0) = H. \quad (3.67)$$

Then the interfaces formed by the wall without the floating particle can be expressed as:

$$\xi_1(x) = q^{-1} \tan\psi_1 e^{-qx} \quad (\text{Fixed contact angle}); \quad (3.68)$$

$$\xi_1(x) = H e^{-qx} \quad (\text{Fixed contact line}). \quad (3.69)$$

We can use the concept of the fictitious cylinder with the radius r_2 that is submerged in liquid (Figure 3.13). The angle ψ between the centerline of the cylinder and the z axis is the local slope angle of the wall. We can

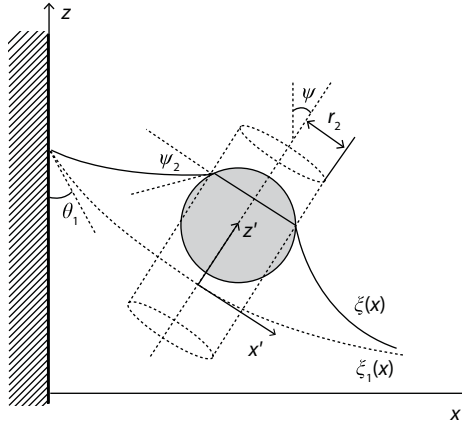


Figure 3.13 Configuration of the spherical particle and vertical wall [19]. The particle can be modeled and analyzed using the fictitious cylinder.

introduce a new coordinate system (x', y', z') where the z' axis coincides with the cylinder axis:

$$\begin{aligned} \mathbf{e}'_x &= \cos \psi \mathbf{e}_x - \sin \psi \mathbf{e}_z; \\ \mathbf{e}'_y &= \mathbf{e}_y; \\ \mathbf{e}'_z &= \cos \psi \mathbf{e}_x + \sin \psi \mathbf{e}_z. \end{aligned} \quad (3.70)$$

Assume that the contact line on the cylinder surface is parallel to the x' axis. Similarly to the deriving procedure from Eqn. (3.29) to Eqn. (3.36), one can obtain σ_x in the (x', y', z') system as [19]:

$$\sigma_x = \sigma \left[\cos \psi \left(\cos \varphi \cos \psi_2 - \frac{1}{\chi} \frac{d\xi_0}{d\varphi} \sin \varphi \sin \psi_2 \right) - \frac{1}{\chi} \sin \psi \sin \psi_2 \right], \quad (3.71)$$

where ψ_2 is the slope angle around the particle in the (x', y', z') coordinate. Substituting Eqn. (3.71) into Eqn. (3.6), one obtains

$$\begin{aligned} F_x^{(\sigma)} &= -2\pi\sigma r_2 \sin \psi_2 \sin \psi \\ &\quad - 2\sigma \sin \psi_2 \int_0^\pi \frac{d\xi_0}{d\varphi} \sin \varphi d\varphi + 2\sigma \cos \psi \cos \psi_2 \int_0^\pi \chi \cos \varphi d\varphi. \end{aligned} \quad (3.72)$$

The last term in Eqn. (3.72) is negligible for large separation [19]. Eqn. (3.72) becomes

$$F_x^{(\sigma)} \approx -2\pi\sigma r_2 \sin \psi_2 \sin \psi - 2\sigma \sin \psi_2 \int_0^\pi \frac{d\xi_0}{d\varphi} \sin \varphi d\varphi. \quad (3.73)$$

For a small interface elevation,

$$\sin \psi \approx \tan \psi = -\left. \frac{d\xi_1}{dx} \right|_{x=s}. \quad (3.74)$$

Substituting Eqns. (3.68) and (3.69) into Eqn. (3.74), $\sin \psi$ in Eqn. (3.73) becomes

$$\sin \psi \approx \tan \psi_1 e^{-qs} \quad (\text{Fixed contact angle}); \quad (3.75)$$

$$\sin \psi \approx qHe^{-qs} \quad (\text{Fixed contact line}). \quad (3.76)$$

To estimate the horizontal force due to the hydrostatic pressure $F_x^{(P)}$, one can use the approximation [19]

$$\xi(\varphi) \approx h_2 + \frac{dh_2}{ds} r_2 \cos \varphi \quad (3.77)$$

and substitute it into Eqn. (3.39) to obtain

$$F_x^{(P)} \approx \pi\sigma(qr_2)^2 h_2 \frac{dh_2}{ds}. \quad (3.78)$$

We still need to find ξ_0 , which is the interface deformation created by the floating particle when the imaginary particle floats at $2s$ separation. Eventually, this information allows finding the contact line elevation h_2 and the total capillary force after substituting h_2 into Eqns. (3.73) and (3.78). r_2 and $\sin \psi_2$ are also required for finding the total horizontal force.

3.2.4.1 Fixed Contact Angle at the Wall

If the elevation of the contact line is zero at the wall, Eqn. (3.60) is valid to calculate the capillary charge Q . For the typical inclined interface near the wall, however, the elevation of the contact line on the particle h_2 is no longer small. The term $\pi r_i^2 h_2$ cannot be neglected. Eqn. (3.57) can be used to calculate the capillary charge Q of the particle. The elevation of the contact line on the particle surface h_2 can be given as:

$$h_2 = q^{-1} \tan \psi_1 e^{-qs} + h_{20}, \quad (3.79)$$

where h_{20} is the mean elevation of the contact line for a single particle floating at the flat air-liquid interface:

$$h_{20} = \frac{1}{2\pi r_2} \oint_{C_2} \xi_0^z dl. \quad (3.80)$$

For the two particles with capillary charges Q_1 and Q_2 , Eqn. (3.24) is used to compute the interface deformation close to the particles for small or moderate inter-particle separation ($(qa)^2 \ll 1$). By setting $Q_1 = Q_2$ in Eqn. (3.24) and using the relations of the bipolar coordinates, one obtains [19]

$$\xi_0^{in}(\omega) = Q_2 \left[\ln \frac{2}{\gamma_e q r_2} + \ln \frac{2}{\gamma_e 2qa^2 / (s - r_2 \cos \omega)} \right], \quad (3.81)$$

where superscript 'in' denotes the solution in the inner region (close to the particle, $(qa)^2 \ll 1$). Substituting Eqn. (3.81) into Eqn. (3.80) yields

$$h_{20}^{in} = Q_2 \left[\ln \frac{2}{\gamma_e q r_2} + \ln \frac{2}{\gamma_e q (s + a)} \right]. \quad (3.82)$$

For the large inter-particle separation ($(qa)^2 \gg 1$), the superposition and approximation [15] are used to derive the interface shape for the two identical particles, i.e.,

$$\xi_0^{out}(\omega) = Q_2 \left[K_0(qd_r) + K_0(qd_l) \right], \quad (3.83)$$

where d_r is the horizontal distance from the center of the right particle and d_l denotes the horizontal distance from the center of the left particle. Because the modified Bessel function can be written as

$$K_0(x) \approx \ln \frac{2}{\gamma_e x}, \quad (3.84)$$

the inner asymptote ($a \rightarrow 0$) of Eqn. (3.83) for small x is

$$\left(\xi_0^{out} \right)^{in} \approx Q_2 \left[\ln \frac{2}{\gamma_e q d_r} + \ln \frac{2}{\gamma_e q d_l} \right]. \quad (3.85)$$

By substituting Eqn. (3.83) into Eqn. (3.80), one can derive

$$h_{20}^{out} = h_{2\infty} + Q_2 K_0(2qs); \quad h_{2\infty} = Q_2 \ln \frac{2}{\gamma_e q r_2}. \quad (3.86)$$

By comparing Eqn. (3.81) with Eqn. (3.85), one obtains a compound expression for ξ_0 :

$$\xi_0 = h_{2\infty} + Q_2 K_0 \left(\frac{2qa^2}{s - r_2 \cos \omega} \right). \quad (3.87)$$

Similarly, the compound expression for h_{20} can be obtained by comparing Eqns. (3.82) and (3.86):

$$h_{20} = h_{2\infty} + Q_2 K_0(2q(s+a)). \quad (3.88)$$

Then, h_2 becomes:

$$h_2 = q^{-1} \tan \psi_1 e^{-qs} + h_{2\infty} + Q_2 K_0(2q(s+a)). \quad (3.89)$$

From Eqn. (3.57), one can calculate the capillary charge of particle Q_2 as

$$Q_2 = \frac{q^2}{6} \left[(3R_2 - b_2)b_2^2 - 4D_2 R_2^3 - 3r_2^2 h_2 \right]. \quad (3.90)$$

Combining Eqns. (3.73), (3.75), (3.78), (3.87), (3.89), and (3.90), one can obtain the horizontal force for the fixed contact angle as [19]

$$F_x = -\pi\sigma \left[2qQ_2^2 K_1(2qs) + 2Q_2 \tan \psi_1 e^{-qs} + q \left(r_2 \tan \psi_1 e^{-qs} \right)^2 \right]. \quad (3.91)$$

3.2.4.2 Fixed Contact Line at the Wall

Similarly to the fixed contact angle at the wall, when the contact line is fixed to an arbitrary position at the wall,

$$h_2 = He^{-qs} + h_{20}; \quad h_{20} = \frac{1}{2\pi r_2} \oint_{C_2} \xi_0 dl. \quad (3.92)$$

For the small separation ($(qa)^2 \ll 1$), by setting $Q_1 = -Q_2$, Eqn. (3.24) becomes

$$\xi_0^{in}(\omega) = Q_2 \tilde{\tau}_2(\omega), \quad (3.93)$$

where

$$\tilde{\tau}_2(\omega) = \tau_2 + 2 \sum_{n=1}^{\infty} \frac{1}{n} \tanh n \tau_2 e^{-n \tau_2} \cos n \omega. \quad (3.94)$$

Similarly to Eqn. (3.81), we can rewrite Eqn. (3.93) in the form [19]:

$$\xi_0^{in}(\omega) = Q_2 \left[\ln \frac{2}{\gamma_e q r_2} - \ln \frac{2}{\gamma_e q r_2 e^{\tilde{\tau}_2}} \right]. \quad (3.95)$$

Substituting Eqn. (3.95) into Eqn. (3.92), one obtains

$$h_{20}^{in} = Q_2 \tau_2^*, \quad (3.96)$$

where

$$\tau_2^* = \tau_2 + 2 \sum_{n=1}^{\infty} \frac{1}{n} e^{-2n \tau_2} \tanh n \tau_2. \quad (3.97)$$

Equation (3.96) can be rewritten in the form [19]

$$h_{20}^{in} = Q_2 \left[\ln \frac{2}{\gamma_e q r_2} - \ln \frac{2}{\gamma_e q r_2 e^{\tau_2^*}} \right]. \quad (3.98)$$

When the inter-particle separation is large ($(qa)^2 \gg 1$), again by using the superposition approximation [15], one obtains

$$\xi_0^{out}(\omega) = h_{2\infty} - Q_2 K_0(2qs). \quad (3.99)$$

From Eqn. (3.92), one derives

$$h_{20}^{out} = h_{2\infty} - Q_2 K_0(2qs). \quad (3.100)$$

Similarly to the fixed contact angle, we can compare Eqn. (3.95) with Eqn. (3.99) to obtain

$$\xi_0 = h_{2\infty} - Q_2 K_0(qr_2 e^{\tilde{\tau}_2}) \quad (3.101)$$

and compare Eqn. (3.98) with Eqn. (3.100) to find

$$h_{20} = h_{2\infty} - Q_2 K_0(qr_2 e^{\tau_2^*}). \quad (3.102)$$

From Eqn. (3.92), h_2 is

$$h_2 = He^{-qs} + h_{2\infty} - Q_2 K_0 \left(qr_2 e^{\tau_2^*} \right). \quad (3.103)$$

Combining Eqns. (3.73), (3.76), (3.78), (3.90), (3.101), and 3.103), the horizontal force for the fixed contact line is finally obtained as [19]

$$F_x = -\pi\sigma \left[-2qQ_2^2 K_1(2qs) + 2Q_2 q H e^{-qs} + q \left(r_2 q H e^{-qs} \right)^2 \right] \quad (3.104)$$

In Eqns. (3.91) and (3.104), the first term comes from the capillary image force; the second one originates from the buoyancy force; and the last term is the pressure jump across the interface and is typically small for small particles ($(R_2)^2 (qR_2)^2 \ll 1$).

Similarly to the capillary force between the two floating spheres, the wall-particle interaction not only depends on the contact angle but also on the density of the particle. Figure 3.14 shows the force vs. separation for the fixed contact angle and fixed contact line. The particle size and contact angle are fixed in the calculation ($R_2 = 500 \mu\text{m}$, $\theta_2 = 70^\circ$). We have already discussed that the capillary image force is attractive for the fixed contact angle and is repulsive for the fixed contact line. In Figure 3.14(a), the contact angle at the wall θ_1 is fixed at 89° (the wall is slightly hydrophilic). We see that only the particle with the moderate density ($\rho = 1 \text{ g/cm}^3$) is

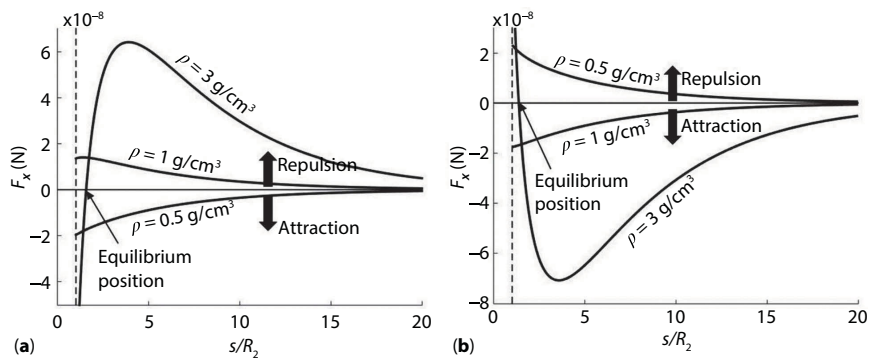


Figure 3.14 Horizontal force vs. separation in the wall-particle capillary interaction for different particle densities. (a) Fixed contact angle on the wall ($R_2 = 500 \mu\text{m}$, $\theta_1 = 89^\circ$, $\theta_2 = 70^\circ$); (b) Fixed contact line ($R_2 = 500 \mu\text{m}$, $H = -50 \mu\text{m}$, $\theta_2 = 70^\circ$). The dashed-dot lines show the smallest separation between the particle center and wall.

repelled by the wall in the entire range of separation due to the strong gravitational force. The force for the light particle ($\rho = 0.5 \text{ g/cm}^3$) is attractive because of the combined effect of the buoyancy force and capillary image force. For the heavy particle ($\rho = 3 \text{ g/cm}^3$), the force is repulsive at large separation because the gravitational force is strong. However, this force becomes attractive at small separation because the capillary image force becomes dominant. Similar results can be found in Figure 3.14(b) where the contact line at the wall is fixed at $H = -50 \text{ }\mu\text{m}$. Now the particle with the moderate density ($\rho = 1 \text{ g/cm}^3$) is attracted. The force of the light particle ($\rho = 0.5 \text{ g/cm}^3$) is repulsive due to the strong buoyancy force. The heavy particle ($\rho = 3 \text{ g/cm}^3$) is attracted towards the wall at large separation but is repelled at small separation.

An interesting observation in Figure 3.14 is that for the heavy particle the horizontal force intersects the x -axis, which means there is a zero force point located close to the wall. For the fixed contact angle, the zero force point is not stable (the particle has tendency to move away from the zero force point), while for the fixed contact line, this point is stable (the particle has tendency to stay at the zero force point). The measurements (Velev *et al.* [20]) of the zero force point for the fixed contact line agree with the theory well. In summary, when the separation is not too small, the lateral capillary force is attractive if the slope angles at the wall ψ_1 and on the floating particle ψ_2 have the same sign, otherwise, the force is repulsive. When the separation is too small, the situation is much more complicated.

3.3 Control of Cheerios Effect

In the previous sections, we reviewed the theoretical models for Cheerios effect for four different configurations. The main parameters are the density of the floating object and the contact angles of the floating object and wall. In this section, we introduce a method to control Cheerios effect [31,32]. Among the parameters, changing the density is much more difficult than the contact angle. The contact angle can be relatively easily changed using many methods such as electrowetting [33], optical methods [34,35], magnetic fields [36] and so on. In this section we will give a brief introduction on how to control Cheerios effect using electrowetting (more exactly electrowetting-on-dielectric or EWOD).

The intrinsic contact angle is determined and fixed by the properties of materials at the three-phase contact line. However, the apparent contact angle can be modulated by applying a voltage to the dielectric-covered electrode, on which the contact line is placed. This is known as

electrowetting-on-dielectric (EWOD) [33]. By controlling the applied voltage, the contact angle can be adjusted and controlled in a certain range, that is, an initially hydrophobic state can be reversibly switched to a hydrophilic state. If this EWOD is implemented to Cheerios effect, the direction of the lateral component of the capillary force can be changed and controlled. This results in reversible switching between attraction and repulsion in Cheerios effect.

Figure 3.15 shows a conceptual sketch how to implement EWOD to control Cheerios effect. In the configuration of the wall and floating object, the EWOD electrode is installed on the wall. Initially, the wall surface of EWOD is hydrophobic, so the slope angle ψ_1 is negative (Figures 3.15(a) and (c)). In this case, as already discussed in the previous section, the

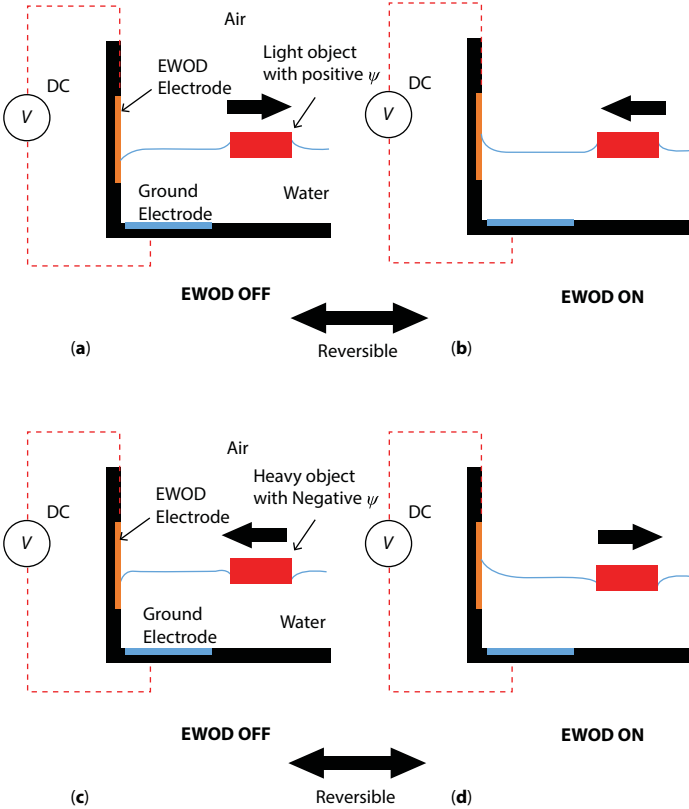


Figure 3.15 Concept of EWOD-controlled Cheerios effect. (a) and (b) Low-density object with positive slope angle ψ . (a) EWOD is OFF; (b) EWOD is ON. (c) and (d) High-density object with negative slope angle ψ . (c) EWOD is OFF. (d) EWOD is ON.

capillary force between the wall and the floating object is repulsive when the slope angle of the floating object ψ_2 is positive (Figure 3.15 (a)) while it is attractive when ψ_2 is negative (Figure 3.15(c)). Once EWOD is turned on, the wall surface becomes hydrophilic and the slope angle at the wall ψ_1 turns positive. Then, the force becomes attractive for the positive ψ_2 (Figure 3.15(b)) and repulsive for the negative ψ_2 (Figure 3.15(d)). By turning EWOD on or off, one can reverse the capillary force and control the movement of the floating objects.

An experimental verification of the above concept is shown in Figure 3.16. The EWOD electrode is attached to the vertical wall and prepared as follows: A DuPont Pyralux® flexible Cu product with an 18- μm Cu layer is coated with a 2.5- μm parylene layer. To make the surface hydrophobic, a thin layer (~ 200 nm) of Teflon AF® is dip-coated on the parylene layer. The

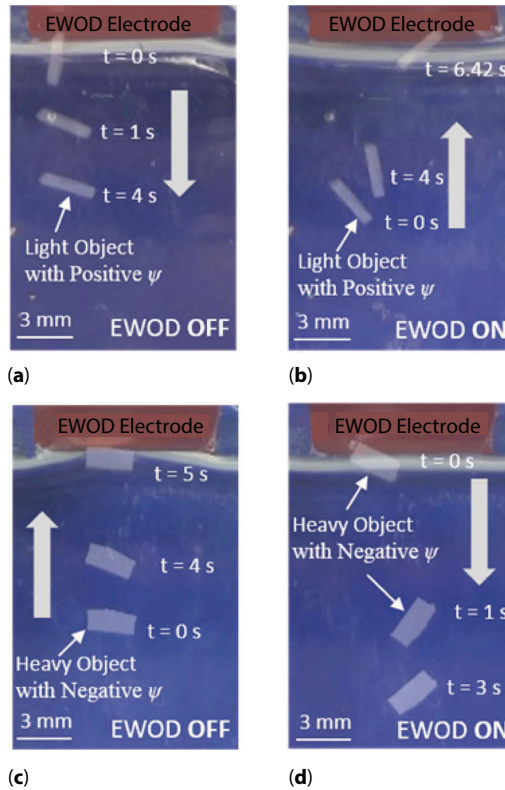


Figure 3.16 Experimental results for EWOD-assisted Cheerios effect (top view). Images are overlapped to show the movement of the object. (a) and (b) Low-density object with positive slope angle ψ and (c) and (d) high-density object with negative slope angle.

low-density floating object with a positive slope angle ψ_2 is pushed away from the wall when EWOD is off (Figure 3.16(a)). However, it is pulled towards the wall when EWOD is on (Figure 3.16(b)). On the contrary, these attraction and repulsion behaviors are reversed when a high-density object with a negative slope angle ψ_2 is placed near the EWOD electrode (Figures 3.16(c) and 3.16(d)).

3.4 Concluding Remarks and Outlook

This paper reviewed theoretical models of the Cheerios effect for four different physical configurations. The horizontal component of the capillary force is the key force to understand and determine attractive and repulsive behaviors between objects on the air-liquid interface. The first configuration consists of two infinite vertical plates, which is two-dimensional and the simplest. The horizontal force is not directly generated from the interfacial tension but by the hydrostatic pressure difference across the plates. Here, the hydrostatic pressure difference, which creates the height difference in the liquid level, originates from the capillary interaction between the plates. The second configuration is composed of two vertical cylinders. Although this configuration needs to solve the Young-Laplace equation in the 3-D space to describe the interface profile, it does not require the analysis for the vertical force balance. Analytical and numerical solutions can be obtained for two different cases: small/moderate separation and large separation between the cylinders. After finding the interface profiles for these two cases, we numerically calculated the lateral capillary force and compared it with the experimental data. The results show that our calculations predict much better for the small separation than the asymptotic solution does. The third configuration is for two floating spherical particles. The interface distortion generated by the floating particles is similar to, yet smaller than, that in the two-cylinder configuration. Due to this reason, a linear approximation for the contact line is used for all separations, and the equation of the interface profiles derived for the two cylinders separated by a large distance is adopted to calculate the lateral capillary force between the two floating spherical particles. The last configuration is a spherical particle floating in the vicinity of a vertical wall. The concept of the image capillary force is introduced. The force is attractive for the contact angle of 90° at the wall but repulsive for the fixed contact line at zero elevation. For the general wall conditions, where the contact angle is an arbitrary value or the contact line is positioned at an arbitrary elevation, the solutions for the interface profiles and the expressions for the lateral capillary force are

derived from the linearized Young-Laplace equation with the assumption of small deformation of the interface profile.

In general, the capillary forces between two vertical walls and between two vertical cylinders are attractive when they have similar wettability (hydrophilic-hydrophilic or hydrophobic-hydrophobic) and are repulsive when they have opposite wettability (hydrophilic-hydrophobic). However, this statement is not applicable for the latter two configurations (i.e., between two floating spheres and between a spherical particle and a vertical wall). Additional parameters (for example, the size and the density of floating objects) are crucially important to determine the lateral component of the capillary force. The effect of the floating object density was particularly discussed for the latter two configurations.

Direct measurements of the horizontal capillary force for the configurations of two vertical cylinders, two spheres, and sphere/plate have been reported [17,30]. The experimental results agree well with the theoretical predictions for the large separation between the objects. However, there is the discrepancy for the small separation, which could be caused by the increasing nonlinear effect as the two objects come close. Numerical calculations with the non-linearized Young-Laplace equation would improve the accuracy of the capillary force, especially when the separation between the objects is small. Moreover, additional parameters such as the size and density of the floating objects are important to determine the horizontal force for the last two configurations. In particular, these parameters may directly affect the vertical elevation of the sphere. In the past experimental measurements of the horizontal force between a sphere and other objects (for example, another sphere or vertical plate), the sphere was supported by an external vertical force and thus confined to the horizontal plane regardless of the contact angle, the particle size and the particle density. As a result, the effects of these parameters could not be detected. This might cause significant measurement errors, especially at small separation where the slope of the interface is substantial. An improvement should be made in the future such that the sphere could move freely in the vertical direction during force measurement. Although theoretical studies on the configurations of two spheres and sphere/wall have been relatively well established, experimental data on them are currently missing. In particular, the density effects of floating objects are not fully verified experimentally as of today.

In order to control the Cheerios effect, we implemented electrowetting-on-dielectric (EWOD) on the vertical plate. By simply turning on/off the EWOD electrode on the plate, we were able to change the contact angle on the plate and reverse the capillary force between the plate and the floating object. This results in reversing of attraction and repulsion behaviors

between the plate and the object. As a future study, the EWOD electrode can be installed in the floating objects, although this involves more complex fabrication and experimentation. In addition, other methods such as optical and magnetic actuations can be utilized to control the contact angle and thus the Cheerios effect.

Acknowledgement

This work was supported in part by the NSF Grant (ECCS-1029318).

References

1. D. Vella and L. Mahadevan, The “Cheerios effect”, *Am. J. Phys.*, 73, 817–825 (2005).
2. J. Walker, *The Flying Circus of Physics*, second edition, Wiley, New York (2007).
3. J.Q. Yuan and S.K. Cho, Bio-inspired micro/mini propulsion at air-water interface: A review, *J. Mech. Sci. Technol.*, 26, 3761–3768 (2012).
4. D.L. Hu and J.W. Bush, Meniscus-climbing insects, *Nature*, 437, 733–736 (2005).
5. R. Baudoin, La physico-chimie des surfaces dans la vie des Arthropodes aeriens des miroirs d’eau, des rivages marins et lacustres et de la zone intercotidale, *Bull. Biol. France Belg.*, 89, 16–164 (1955).
6. S. Biswas and L.T. Drzal, A novel approach to create a highly ordered monolayer film of graphene nanosheets at the liquid-liquid interface, *Nano Lett.*, 9, 167–172 (2009).
7. N. Bowden, F.A. Arias, T. Deng, and G.M. Whitesides, Self-assembly of microscale objects at a liquid/liquid interface through lateral capillary forces, *Langmuir*, 17, 1757–1765 (2001).
8. N. Bowden, A. Terfort, J. Carbeck, and G.M. Whitesides, Self-assembly of mesoscale objects into ordered two-dimensional arrays, *Science*, 276, 233–235 (1997).
9. G.K. Batchelor, *An Introduction to Fluid Dynamics*, Cambridge University Press, Cambridge, U.K. (1967).
10. D.J. Campbell, E.R. Freidinger, J.M. Hastings, and M.K. Querns, Spontaneous assembly of soda straws, *J. Chem. Educ.*, 79, 201–202 (2002).
11. J.C. Berg, *An Introduction to Interfaces & Colloids: The Bridge to Nanoscience*, World Scientific, Singapore (2009).
12. B.V. Derjaguin and V.M. Starov, Capillary interaction between solid bodies, *Colloid J. USSR (Engl. Transl.)*, 39, 383–386 (1977).
13. P.A. Kralchevsky, V.N. Paunov, I.B. Ivanov, and K. Nagayama, Capillary meniscus interactions between colloidal particles attached to a liquid-fluid interface, *J. Colloid Interface Sci.*, 151, 79–94 (1992).

14. P.A. Kralchevsky, V.N. Paunov, N.D. Denkov, I.B. Ivanov, and K. Nagayama, Energetical and force approaches to the capillary interactions between particles attached to a liquid-fluid interface, *J. Colloid Interface Sci.*, 155, 420–437 (1993).
15. M.M. Nicolson, The interaction between floating particles, in: *Mathematical Proceedings of the Cambridge Philosophical Society*, pp. 288–295 (1949).
16. D.Y.C. Chan, J.D. Henry Jr., and L.R. White, The Interaction of colloidal particles collected at fluid interfaces, *J. Colloid Interface Sci.*, 79, 410–418 (1981).
17. O.D. Velev, N.D. Denkov, V.N. Paunov, P.A. Kralchevsky, and K. Nagayama, Direct measurement of lateral capillary forces, *Langmuir*, 9, 3702–3709 (1993).
18. C.D. Dushkin, P.A. Kralchevsky, H. Yoshimura, and K. Nagayama, Lateral capillary forces measured by torsion microbalance, *Phys. Rev. Lett.*, 75, 3454–3457 (1995).
19. P.A. Kralchevsky, V.N. Paunov, N.D. Denkov, and K. Nagayama, Capillary image forces: I. Theory, *J. Colloid Interface Sci.*, 167, 47–65 (1994).
20. O.D. Velev, N.D. Denkov, V.N. Paunov, P.A. Kralchevsky, and K. Nagayama, Capillary image forces: II. Experiment, *J. Colloid Interface Sci.*, 167, 66–73 (1994).
21. E.H. Mansfield, H.R. Sepangi, and E.A. Eastwood, Equilibrium and mutual attraction or repulsion of objects supported by surface tension, *Phil. Trans. R. Soc. Lond. A*, 355, 869–919 (1997).
22. W.A. Gifford and L.E. Scriven, On the attraction of floating particles, *Chem. Eng. Sci.*, 26, 287–297 (1971).
23. C. Allain and M. Cloitre, Interaction between particles trapped at fluid interfaces, I. Exact and asymptotic solutions for the force between horizontal cylinders, *J. Colloid Interface Sci.*, 157, 261–268 (1993).
24. H.N. Dixit and G.M. Homsy, Capillary effects on floating cylindrical particles, *Phys. Fluids*, 24, 122102 (2012).
25. P.A. Kralchevsky and K. Nagayama, Capillary interactions between particles bound to interfaces, liquid films and biomembranes, *Adv. Colloid Interface Sci.*, 85, 145–192 (2000).
26. P.A. Kralchevsky and K. Nagayama, *Particles at Fluid Interfaces and Membranes: Attachment of Colloid Particles and Proteins to Interfaces and Formation of Two-Dimensional Arrays*, Chapters 7 and 8, pp. 287–395, Elsevier, Amsterdam, Netherlands (2001).
27. R. Finn, *Equilibrium Capillary Surfaces*, Springer, New York (1986).
28. G.A. Korn and T.M. Korn, *Mathematical Handbook for Scientists and Engineers*, McGraw-Hill, New York (1968).
29. I.B. Ivanov, P.A. Kralchevsky, and A.D. Nikolov, Film and line tension effects on the attachment of particles to an interface: I. conditions for mechanical equilibrium of fluid and solid particles at a fluid interface, *J. Colloid Interface Sci.*, 112, 97–107 (1986).

30. C.D. Dushkin, P.A. Kralchevsky, V.N. Paunov, H. Yoshimura, and K. Nagayama, Torsion balance for measurement of capillary immersion forces, *Langmuir*, 12, 641–651 (1996).
31. J.Q. Yuan and S.K. Cho, Electrowetting climbing of inclined water surfaces, presented at the 66th Annual Meeting of the American Physical Society Division of Fluid Dynamics, San Diego, California, (2012).
32. J.Q. Yuan and S.K. Cho, Free surface propulsion by electrowetting-assisted ‘Cheerios effect’, in Proc. IEEE 27th International Conference on Micro Electro Mechanical Systems (MEMS), pp. 991–994, San Francisco, CA. (2014).
33. S.K. Cho, H. Moon, and C.J. Kim, Creating, transporting, cutting, and merging liquid droplets by electrowetting-based actuation for digital microfluidic circuits, *J. Microelectromech. Syst.*, 12, 70–80 (2003).
34. W. Zhu, X. Feng, L. Feng, and L. Jiang, UV-manipulated wettability between superhydrophobicity and superhydrophilicity on a transparent and conductive SnO₂ nanorod film, *Chem. Commun.*, 2753–2755 (2006).
35. H.S. Lim, J.T. Han, D. Kwak, M. Jin, and K. Cho, Photoreversibly switchable superhydrophobic surface with erasable and rewritable pattern, *J. Am. Chem. Soc.*, 128, 14458–14459 (2006).
36. Q. Zhou, W.D. Ristenpart, and P. Stroeve, Magnetically induced decrease in droplet contact angle on nanostructured surfaces, *Langmuir*, 27, 11747–11751 (2011).

Recent Mathematical Analysis of Contact Angle Hysteresis

Xianmin Xu^{1,*} and Xiaoping Wang²

¹*The State Key Laboratory of Scientific and Engineering Computing,
Institute of Computational Mathematics and Scientific/Engineering Computing,
Chinese Academy of Sciences, Beijing, China*

²*Department of Mathematics, the Hong Kong University of Science and Technology, Clear
Water Bay, Kowloon, Hong Kong, China*

Abstract

In this paper, we review some recent mathematical results on analysis of wetting phenomena on chemically patterned or rough surfaces. Our analysis shows that the effective contact angles determined from the Wenzel's and Cassie's equations correspond to the global minimum of the total energy of the system. The local minimizers give different static contact angles that can predict the contact angle hysteresis observed in reality. We also review the basic mathematical tools used in our analysis.

Keywords: Wenzel's equation, Cassie's equation, contact angle hysteresis, homogenization

4.1 Introduction

The study of wetting phenomena is of critical importance for many industrial applications [1–4], from oil recovery in petroleum reservoirs to microscopic flows in microfluidics. Generally speaking, wetting is the ability of liquid to maintain contact with or spread on a solid surface. In principle, the wetting property is determined by microscopic molecular interactions of liquid, air and the solid surface, including short-ranged chemical

*Corresponding author: xmxu@lsec.cc.ac.cn, xianmin.xu@gmail.com

interactions and long range van de Waals forces, etc. On a larger scale, wetting could be described by Young's equation [5] (see Equation (4.2) below), a classical model that connects the static contact angle to the surface tensions in the three-phase system.

Although there is a long history in the study of wetting phenomena, there are still some problems that are not fully understood. Among them, an important one is the phenomenon of contact angle hysteresis (CAH). The origin of CAH is attributed to several factors such as surface roughness, chemical contaminants, among others. The contact angle hysteresis proves to be an important quantity that determines the motion and properties of the droplets on the surfaces. Understanding of how the patterning or roughness of the surface affects contact angle and contact angle hysteresis is of critical importance in surface engineering. There have been intensive studies on contact angle hysteresis (see [6–10] among many others). Theoretical models of CAH have focused on how roughness and chemical heterogeneity provide energy barriers to the system.

Wetting on rough or chemically patterned surfaces has also been studied for a long time. Two well-known equations, the Wenzel's equation [11] and the Cassie's equation [12] are introduced to characterize the macroscopic apparent contact angle in terms of surface roughness and inhomogeneity (see Equations (4.6) and (4.7) in Section 4.3). There have been many works on the derivation and validity of these two equations [10,13–17], despite some controversies on their correctness [18–22]. In particular, they cannot describe the contact angle hysteresis and cannot explain some of the experimental observations [18,23]. Various modifications or variations of these two equations are proposed and studied [10,20,24–26].

Static or quasi-static wetting phenomena can be studied by surface energy minimization [10,13,27] where some rigorous mathematical analysis is possible. Furthermore, wetting on chemically patterned or rough surfaces is clearly a multi-scale problem. The macroscopic apparent contact angle is determined by microscopic properties near the contact line of the liquid drop. Notice that there are many mathematical tools for multi-scale analysis [28,29]. We expect that these tools are also useful for the studies of wetting and contact angle hysteresis. On the other hand, the studies on wetting will also stimulate the development of new mathematical or numerical techniques.

In this paper, we review some of our recent mathematical analysis for wetting and contact angle hysteresis phenomena. We concentrate mainly on the illustration of the analysis results and our understanding of wetting, but ignore the technical details, which can be found in our published papers. The outline of the paper is as follows. In Section 4.2, we introduce

the basic physical principles for wetting and some mathematical tools we used. In Section 4.3, we justify the classical Wenzel's and Cassie's equations for a general three-dimensional problem by a variational approach. These two equations are validated by considering convergence of global minimizers of the total energy in the system. In Section 4.4, we derive a modified Cassie equation by asymptotic analysis from the equilibrium equations of a liquid-vapor interface. The modified Cassie equation is different from the classical one in the sense that a line fraction (along the contact line) is used instead of the original area fraction. In Section 4.5, we analyze the contact angle hysteresis by studying quasi-static interface motion in a two-dimensional channel. We then give some examples of the contact angle hysteresis phenomenon in three-dimensional problems using the modified Cassie equation. Finally, we end the paper with some conclusions and outlook.

4.2 The Physical Principle and Mathematical Method

4.2.1 The Physical Principle

In thermodynamic equilibrium, wetting is characterized by two well-known equations, the Young-Laplace equation and the Young equation. The Young-Laplace equation,

$$p_L - p_V = 2\gamma_{LV} \kappa, \quad (4.1)$$

relates the mean curvature of the liquid-vapor interface to the capillary pressure difference across the interface. The Young equation [5],

$$\gamma^{lv} \cos \theta = \gamma^{sv} - \gamma^{sl}. \quad (4.2)$$

on the other hand, relates the static contact angle to the surface tensions in the system. In (4.1) and (4.2), p_L and p_V denote respectively the pressures in the liquid and the vapor. κ is the mean curvature of the interface. γ_{LV} , γ_{SL} and γ_{SV} denote the liquid-vapor, solid-liquid and solid-vapor interfacial tensions respectively. The Young's angle θ_Y is the local contact angle between the liquid and the solid surface.

Equations (4.1) and (4.2) describe force equilibrium state on the interface and the contact line. These equations could be derived when minimizing the total energy in the system. Specifically, the Young's equation (4.2) appears as the transversality condition of the energy minimizing problem of wetting on ideal surfaces [24]. Suppose the size of the liquid drop is smaller than the capillary length $l_c = \gamma / \rho g$, so that gravity is negligible. In

equilibrium, the total energy in the system E is the sum of the interface energies,

$$E = \gamma_{LV} |\Sigma_{LV}| + \gamma_{SL} |\Sigma_{SL}| + \gamma_{SV} |\Sigma_{SV}|, \quad (4.3)$$

where Σ_{LV} , Σ_{SL} and Σ_{SV} are the liquid-vapor, solid-liquid and solid-vapor interfaces, respectively. The norm $|\bullet|$ denotes area of the interface.

4.2.2 Homogenization

The Young equation (4.2) is correct only locally. For homogeneous solid surfaces, the Young's angle is also the apparent contact angle. However, solid surfaces are seldom homogeneous in reality. They are either chemically inhomogeneous or geometrically rough. In these cases, the apparent angle might differ considerably from the local Young angles. This is an obvious multiscale problem. Mathematically, there are some methods to derive macroscopic law from microscopic properties. Among them, an important one is the homogenization method.

The first step of homogenization is asymptotic analysis. For an abstract equation:

$$L_\varepsilon \varphi_\varepsilon = 0, \quad (4.4)$$

where L_ε is a differential operator on the function φ_ε , $\varepsilon \ll 1$ denotes the microscopic spatial scale. Suppose φ_ε has an expansion $\varphi_\varepsilon = \varphi_0 + \varepsilon \varphi_1 + \varepsilon^2 \varphi_2 + \dots$, where φ_0 is taken as the function for macroscopic properties. Substitute the expansion in equation (4.4) and separate the equation into a series of equations according to the order of ε . In general, one could obtain a leading order equation:

$$L_0 \varphi_0 = 0. \quad (4.5)$$

This is called a homogenized equation. It is an effective equation for the macroscopic property φ_0 .

Asymptotic analysis is not rigorous in mathematics. One needs to prove further the convergence of φ_ε to φ_0 , as ε goes to zero. This could be done by some techniques, e.g. the Γ -convergence theory [28], which is a useful tool to prove the convergence of a sequence of variational problems [17].

4.3 The Wenzel's and Cassie's Equations

The roughness-enhanced wetting is described by two famous equations that illustrate the relation between the apparent contact angle θ_a and the

local Young's angle θ_Y . One is the so-called Wenzel's equation for rough surface cases [11]:

$$\cos \theta_a = R \cos \theta_Y, \quad (4.6)$$

with the roughness parameter R being the area ratio between a rough solid surface and the effective smooth surface corresponding to it. The other is the Cassie's equation for a chemically patterned surface (composed of two materials) [12]:

$$\cos \theta_a = \rho \cos \theta_{Y1} + (1 - \rho) \cos \theta_{Y2}, \quad (4.7)$$

where θ_{Y1} and θ_{Y2} are the Young's angles on the two materials, and ρ is the area fraction of material 1 on the solid surface.

The validity of the Wenzel's and Cassie's equations has been investigated for many years. For example, these two equations are derived by considering the transversality condition of the wetting problem of rough and chemically heterogeneous surfaces in [24]. Previous studies consider either a simplified two-dimensional problem or some three-dimensional problems for solid surfaces with very special geometries. In [27], we considered a three-dimensional model with a relatively general solid surface. It is worthwhile to stress that all the validations of the Wenzel's and Cassie's equations are under the condition that the size of the wetting area is much larger than the characteristic spatial scale of the roughness (heterogeneity) of the surface. Otherwise, the notion of an apparent contact angle is meaningless.

In [27], we suppose the solid surface is $x = \varepsilon h(y / \varepsilon, z / \varepsilon)$ (see Figure 4.1), where ε is a small parameter, $h(Y, Z)$ is a given function which is periodic in Y and Z with period 1. The liquid-vapor interface is $z = u(x, y)$, such that $u(1, y) = 0$, and $u(x, y)$ is periodic in y with period ε . The liquid region is given by $\{(x, y, z) \mid z < u(x, y), 0 < x < 1\}$ and the vapor region is given by $\{(x, y, z) \mid z > u(x, y), 0 < x < 1\}$. We consider only partial wetting case, so that $u(x, y)$ is bounded, in other words, there exists an $M > 0$ such that $|u(x, y)| < M$.

We now compute the total interface energy in a bounded domain $(\varepsilon h(y / \varepsilon, z / \varepsilon), 1) \times (0, \varepsilon) \times (-M, M)$. Suppose the liquid-vapor interface Γ_u has a projection B_u in each period on the plain $z = 0$, see Figure 4.1. Similarly, the solid-liquid interface S_u has a projection Π_u in one period on the plain $x = 0$. Thus, after scaling with $1/\varepsilon$, the total energy (4.3) could be written as

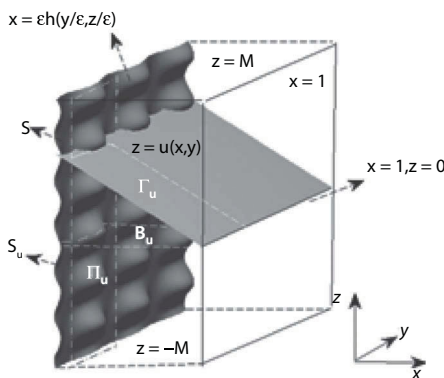


Figure 4.1 A liquid-vapor interface (the grey surface inside the box) intersects a rough solid surface (the left boundary of the box).

$$\begin{aligned} E &= \frac{\gamma_{LV}}{\varepsilon} \int_{B_u} \sqrt{1 + |\nabla u|^2} \, dx dy + \frac{1}{\varepsilon} \int_{\Pi_u} \gamma_{SL} \sqrt{1 + |\nabla h(y/\varepsilon, z/\varepsilon)|^2} \, dy dz \\ &\quad + \frac{1}{\varepsilon} \int_{(0, \varepsilon) \times (-M, M) \setminus \Pi_u} \gamma_{SV} \sqrt{1 + |\nabla h(y/\varepsilon, z/\varepsilon)|^2} \, dy dz \\ &= \frac{\gamma_{LV}}{\varepsilon} \int_{B_u} \sqrt{1 + |\nabla u|^2} \, dx dy + \frac{1}{\varepsilon} \int_{\Pi_u} (\gamma_{SL} - \gamma_{SV}) \\ &\quad \sqrt{1 + |\nabla h(y/\varepsilon, z/\varepsilon)|^2} \, dy dz \end{aligned}$$

with a constant $C = \frac{1}{\mathcal{E}} \int_{(0, \mathcal{E}) \times (-M, M)} \gamma_{SV} \sqrt{1 + |\nabla h(y/\mathcal{E}, z/\mathcal{E})|^2} \, dydz$. The normalized energy could be written as

$$\begin{aligned} \hat{E}^\varepsilon &= \frac{E-C}{\gamma_{LV}} = \frac{1}{\varepsilon} \int_{B_u} \sqrt{1+|\nabla u|^2} dx dy \\ &+ \frac{1}{\varepsilon} \int_{\Pi_u} \cos \theta_Y \sqrt{1+| \nabla h(y/\varepsilon, z/\varepsilon) |^2} dy dz. \end{aligned} \quad (4.8)$$

Here we use the Young's equation (4.2).

In [27], we proved that if θ_Y is a constant, when the scale ε becomes smaller and smaller, the global minimizers u_ε of the energy \hat{E}_ε converge to the function

$$u^*(x, y) = (1 - x) \cos \theta_a,$$

with $\theta_a = \arccos \left(\int_0^1 \int_0^1 \sqrt{1 + |\nabla h(Y, Z)|^2} dY dZ \cos \theta_Y \right)$. This means the apparent contact angle satisfies

$$\cos \theta_a = \int_0^1 \int_0^1 \sqrt{1 + |\nabla h(Y, Z)|^2} dY dZ \cos \theta_Y. \quad (4.9)$$

This equation is the Wenzel's equation with a roughness parameter

$$R = \int_0^1 \int_0^1 \sqrt{1 + |\nabla h(Y, Z)|^2} dY dZ.$$

being the area ratio between the rough surface and the effective smooth surface.

In addition, our method can also be generalized to the case when θ_Y varies on the surface. In this case, the apparent contact angle satisfies

$$\cos \theta_a = \int_0^1 \int_0^1 \sqrt{1 + |\nabla h(Y, Z)|^2} \cos \theta_Y dY dZ, \quad (4.10)$$

For chemically patterned planar surface where $h \equiv 0$, we have

$$\cos \theta_a = \int_0^1 \int_0^1 \cos \theta_Y dY dZ. \quad (4.11)$$

Since the Young's angle θ_Y is equal to either θ_{Y_1} or θ_{Y_2} on the chemically patterned surface, the integral on the right hand side of (4.11) is calculated as

$$\int_0^1 \int_0^1 \cos \theta_Y dY dZ = \rho_1 \cos \theta_{Y_1} + \rho_2 \cos \theta_{Y_2} = \rho_1 \cos \theta_{Y_1} + (1 - \rho_1) \cos \theta_{Y_2}$$

where ρ_1 and ρ_2 are the areas of the two materials in the unit square, respectively. This is the classic Cassie's equation (4.7).

4.4 The Modified Cassie Equation

From the analysis in the previous section, the Wenzel's and Cassie's equations are correct when one considers global minimizers of the total energy in a liquid-vapor system. However, a liquid drop might be in equilibrium when it corresponds to a local minimum of the total energy in the system. This is also the origin of contact angle hysteresis. In this section, we will concentrate on the equilibrium state of the system instead of the completely stable state corresponding to the global minimizers of the total energy.

As in [26], we start from the equilibrium equations (4.1) and (4.2). The setup of a liquid-vapor system is similar to that in the previous section. Here we consider only the chemically patterned surfaces as shown in Figure 4.2. The solid surface is located on the $z = 0$ plane. It is composed of two materials. The pattern of the materials on the surface is periodic in both x and y with period ε and contact angle function

$$\theta_Y(x, y) = \begin{cases} \theta_{Y1}, & \text{if } (x, y) \text{ is in material 1;} \\ \theta_{Y2}, & \text{if } (x, y) \text{ is in material 2.} \end{cases} \quad (4.12)$$

For the above system, we assume the liquid-vapor interface is given by

$$x = f(y, z) = kz + \varepsilon u\left(\frac{y}{\varepsilon}, \frac{z}{\varepsilon}\right). \quad (4.13)$$

Here k is a constant, ε is the period of the pattern along y -axis. The equation (4.13) represents an interface which differs from the plane $x = kz$ only near the bottom surface $z = 0$.

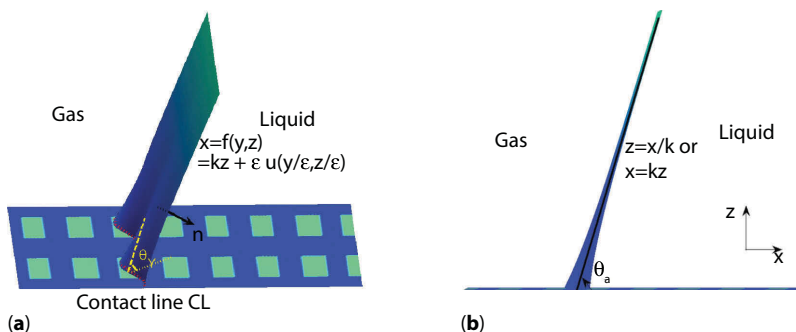


Figure 4.2 The liquid-vapor interface on chemically patterned solid surface[26]. (a) The patterned solid surface and the liquid-vapor interface; (b) The apparent contact angle.

We also suppose the pressures across the liquid-vapor interface are equal. From Equation (4.1) the liquid-vapor interface has zero mean curvature. That is:

$$\nabla \cdot \frac{1}{\sqrt{1 + (\varepsilon \partial_y u)^2 + (k + \varepsilon \partial_z u)^2}} \begin{pmatrix} 1 \\ -\varepsilon \partial_y u \\ -(k + \varepsilon \partial_z u) \end{pmatrix} = 0. \quad (4.14)$$

The contact line, CL , of the liquid-vapor interface and the solid surface is given by

$$\begin{cases} x = \varepsilon u(y / \varepsilon, 0), \\ z = 0. \end{cases}$$

From (4.2) the local contact angle at the contact line is given by $\cos \theta_Y \left(\frac{x}{\varepsilon}, \frac{y}{\varepsilon} \right)$ for $(x, y, 0) \in CL$.

From the asymptotic analysis in [26] when $\varepsilon \rightarrow 0$, the apparent contact angle which is the angle between the plane $x = kz$ and the bottom $z = 0$ (as shown in Figure 4.2) is given by

$$\cos \theta_a = \frac{k}{1 + k^2} = \frac{1}{\varepsilon} \int_0^\varepsilon \cos \theta_Y(x, y) \big|_{x=\varepsilon u(y/\varepsilon, 0)} dy. \quad (4.15)$$

This is the modified Cassie equation where the right hand side term is the integral average of the local Young's angles along the contact line in one period of y . This is different from the traditional Cassie's equation (4.11) where the area average is used. The modified Cassie equation provides an explicit formula to compute the apparent contact angle once we know the patterns of a solid surface and the location of the contact line. Similar results have also been given in [25,30]. The equation is verified by recent experiments [23].

4.5 Contact Angle Hysteresis

In reality, the apparent contact angle of a liquid drop on rough or inhomogeneous surfaces could take a range of values depending on the history of the liquid drop. Among these values, the largest one is called the advancing

angle and the smallest is called the receding angle. This is the so-called contact angle hysteresis phenomenon.

4.5.1 Quasistatic Process of a Two-dimensional Problem

In [9], we studied a two-dimensional wetting problem on chemically patterned surfaces. We show that the advancing angle is the largest Young's angle of a surface, and the receding angle is the smallest one. Consider a channel periodically patterned with materials with different contact angles θ_A (in dark color) and θ_B (in light color) on the solid boundary (see Figure 4.3). The height of the channel is $2h$. The length of the channel is $2L$. The channel is patterned with two materials. We assume that there are k periodic patterns in the interval $[-L/2, L/2]$. In each period, the two materials occupy the same area $\Delta x = L/2k$. Denote Ω_1 and Ω_2 as the domains in the channel which fluid 1 (liquid) and fluid 2 (vapor) occupy, respectively. Let θ be the contact angle of liquid phase (fluid 1).

Define

$$\alpha = |\Omega_1| / 4Lh, \quad (4.16)$$

which is the relative volume of the liquid in the channel. It is easy to see that $0 < \alpha < 1$. The liquid is advancing if α is increasing, while the liquid is receding when α is decreasing.

For quasi-static process, if one ignores the gravity, the pressure on each side of an interface is a constant at any time. This implies that the curvature of the interface is constant (from the Young-Laplace equation). Thus, the interface is a circular arc. From (4.16), it is easy to show that the contact point x is related to θ as,

$$x = \frac{1}{2} \frac{h}{\cos^2 \theta} \left(\left(\frac{\pi}{2} - \theta \right) - \cos \theta \sin \theta \right) + 2\alpha L.$$

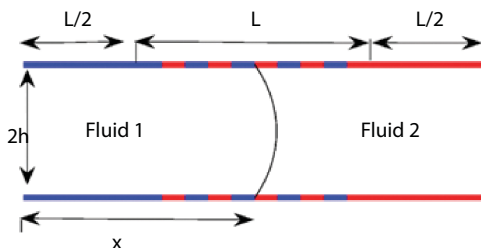


Figure 4.3 The chemically patterned channel ([9])

Equivalently, the relative position of the contact point is given by:

$$\hat{x} = \frac{x-L}{h} = \frac{1}{2\cos^2\theta} \left(\left(\frac{\pi}{2} - \theta \right) - \cos\theta \sin\theta \right) + 2(\alpha-1)\frac{L}{h}. \quad (4.17)$$

From (4.3), the normalized total interface energy can be computed as:

$$\begin{aligned} \hat{E}(\alpha, \theta) &= \frac{\gamma_{LV}|\Sigma_{LV}| + \gamma_{SL}|\Sigma_{SL}| + \gamma_{SV}|\Sigma_{SV}|}{\gamma_{LV}h} \\ &= C_0 + \begin{cases} \frac{\pi-2\theta}{\cos\theta} - 2\hat{x}\cos\theta_A, \\ \frac{\pi-2\theta}{\cos\theta} + \frac{(L-2\Delta x)\cos\theta_A}{h} - \frac{2I_x\Delta x(\cos\theta_A + \cos\theta_B)}{h} \\ \frac{\pi-2\theta}{\cos\theta} - 2\hat{x}\cos\theta_B, \end{cases} \\ &\quad \hat{x} \leq -\frac{L}{2h}; \\ &\quad -2\left(\hat{x} - \frac{(2I_x+1)\Delta x}{h} + \frac{L}{2h} \right) \hat{\beta}, \quad -\frac{L}{2h} \leq \hat{x} \leq \frac{L}{2h}; \\ &\quad \hat{x} \geq \frac{L}{2h}. \end{aligned} \quad (4.18)$$

where $I_x = \left\lfloor \frac{2\hat{x}h+L}{4\Delta x} \right\rfloor$ is the integer part of the number $\frac{2\hat{x}h+L}{4\Delta x} = \frac{x-L/2}{2\Delta x}$, representing the number of complete periods occupied by liquid, and

$$\hat{\beta} = \begin{cases} \cos\theta_A & \text{if } \frac{2\hat{x}h+L}{4\Delta x} - I_x \leq \frac{1}{2}; \\ \cos\theta_B & \text{otherwise.} \end{cases}$$

In the example below, we take $\theta_A = \frac{\pi}{6} = 30^\circ$ and $\theta_B = \frac{5\pi}{6} = 150^\circ$.

We now study the behavior of the quasi-static motion of the interface. The quasi-static states are obtained by computing the local minimizer θ of

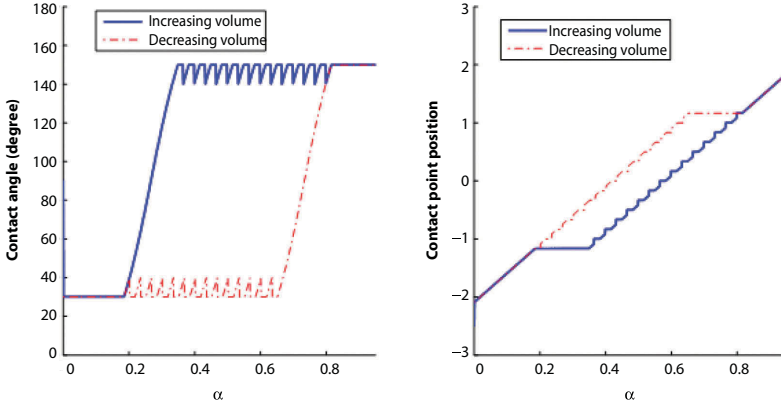


Figure 4.4 The contact angle, contact point and energy as functions of α with $k = 15$. Here the pattern size is small enough so that one observes clear advancing and receding contact angles.

the energy \hat{E} for gradually increasing or decreasing α . The corresponding contact point \hat{x} is then computed from (4.17). Figure 4.4 shows the contact angle θ_s and the contact point \hat{x} plotted as a function of α for $k = 15$. There exists a clear hysteresis phenomenon. Similar results could also be obtained for other k values. We observe that when Δx is small enough, the contact angle oscillates around θ_B (or θ_A) as the interface moves to the right (or the left).

Computations for spreading or shrinking droplets on a chemically patterned surface also give similar results [9]. Therefore, we could conclude that: in two-dimensional case, the advancing angle is the largest one of the Young's angles on a chemically patterned surface while the receding angle is the smallest one. The computations also suggest that the classical Cassie's equation is seldom valid in the quasi-static process.

4.5.2 Three-dimensional Case

As in [26], we now consider contact angle hysteresis for a channel composed of two planes with periodic patterns in both x and y directions, as shown in Figure 4.5. The liquid-vapor interface is lying (almost) parallel to y -direction. We assume that the base material (in dark color) has a contact angle θ_{y1} and the square patch material (in light color) has a contact angle θ_{y2} with $\theta_{y1} < \theta_{y2}$.

From the analysis in Section 4.4, the following conclusions can be drawn. When the period of the chemical patterns goes to zero, the homogenized problem is independent of the y coordinate. It reduces to a two-dimensional

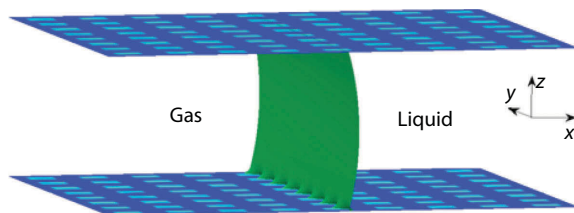


Figure 4.5 The channel composed of chemically patterned solid surfaces.

channel problem similar to that in subsection 4.5.1. Furthermore, from the modified Cassie equation (4.15), we could compute the apparent contact angles as follows. When the contact line is located completely in the dark blue region) the effective contact angle is

$$\theta_{a1} = \theta_{Y1}; \quad (4.19)$$

and when the contact line intersects fully with the array of the square patch in y direction, the effective contact angle is

$$\cos \theta_{a2} = (1 - \lambda) \cos \theta_{Y1} + \lambda \cos \theta_{Y2}. \quad (4.20)$$

with λ being the ratio of the square spot width to one period of the pattern in y direction. When the contact line intersects only partly the array of the square patch the effective contact angle is θ_{ζ} in between so that $\theta_{a1} \leq \theta_{\zeta} \leq \theta_{a2}$. Therefore, from the analysis in subsection 4.5.1, we can see that the advancing contact angle for the channel is θ_{a2} (given by equation (4.20)) and the receding contact angle is θ_{a1} (given by equation (4.19)).

As the end of the section, we show an example given in [19,31]. The following analysis comes from [26]. As shown in Figure 4.6, we consider two configurations of a chemically patterned surface. On the solid surface, the circular spots of radius r are periodically placed with the distance between two nearest spot centers being about $2.693r$. This setup allows each material to occupy half area of the surface. Denote the contact angles for the green area and the red area as θ_{Y1} and θ_{Y2} respectively. Without loss of generality, we suppose $\theta_{Y1} \leq \theta_{Y2}$.

Suppose that the contact line is almost straight as shown in Figure 4.6. From the modified Cassie equation, it is easy to compute the maximum and minimum effective contact angles for the two configurations. For the left one, the minimum effective contact angle, which is also the receding contact angle, is

$$\theta_{rec} = \theta_{Y1};$$

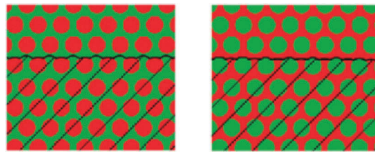


Figure 4.6 Water on two surfaces with 50% surface area of two components with different contact angles(taken from [19]). In the left subfigure, material 1(in green) is the base and material 2(in red) constitutes the circular spots on the base. In the right subfigure, the materials are displayed in an opposite way.

and the maximum effective contact angle, which is also the advancing contact angle, is such that

$$\cos\theta_{adv} = \lambda \cos\theta_{Y1} + (1 - \lambda) \cos\theta_{Y2}.$$

with $\lambda = (2.693r - 2r) / (2.693r) \approx 0.257$. For the right configuration, the receding contact angle is

$$\cos\tilde{\theta}_{rec} = (1 - \lambda) \cos\theta_{Y1} + \lambda \cos\theta_{Y2}.$$

and the advancing contact angle is

$$\tilde{\theta}_{adv} = \theta_{Y2};$$

The two configurations have very different wetting properties, although their area ratios are the same. This is consistent, in principle, with some existing analytical and experimental results [18,19,31]. This example shows clearly how the modified Cassie equation can explain the contact angle hysteresis phenomenon, while the classical Cassie's equation cannot do this.

4.6 Conclusion and Outlook

We have reviewed some mathematical analysis of wetting and contact angle hysteresis phenomena. We concentrate mainly on the static or quasi-static process of wetting. The Wenzel's and Cassie's equations are proven to be correct when one considers the global minimizers of the total energy in the system. A modified Cassie equation is derived which characterizes the apparent contact angle on chemically patterned surfaces. The modified equation corresponds to some local minimizers of the total energy. The equation is further used to explain the contact angle hysteresis phenomenon.

There are some other very interesting unsolved problems. Notice that we only derived the modified Cassie equation for chemically patterned surfaces. We expect that there is a similar relation for chemically homogeneous rough surfaces. Rigorous verification of the modified Cassie equation is also important. One needs to consider the convergence of local minimizers, which is a difficult mathematical problem and requires further study.

Acknowledgments

This publication was based on work supported in part by Award No SA-C0040/UK-C0016, made by King Abdullah University of Science and Technology (KAUST), Hong Kong RGC-CERG grants 603107 and 604209 and by Chinese NSFC project 11001260. We would like to thank Dr. K. L. Mittal and Dr. Robert H. Lacombe for their organization of the conference.

References

1. D. Bonn, J. Eggers, J. Indekeu, J. Meunier, and E. Rolley, Wetting and spreading. *Rev. Mod. Phys.*, 81, 739–805, (2009).
2. P.G. de Gennes, Wetting: Statics and dynamics. *Rev. Mod. Phys.*, 57, 827–863, (1985).
3. P.G. de Gennes, F. Brochard-Wyart, and D. Quere, *Capillarity and Wetting Phenomena*. Springer, Berlin (2003).
4. D. Quere, Wetting and roughness. *Annu. Rev. Mater. Res.*, 38, 71–99, (2008).
5. T. Young, An essay on the cohesion of fluids. *Philos. Trans. R. Soc. London*, 95, 65–87, (1805).
6. R. E. Johnson Jr. and R. H. Dettre, Contact angle hysteresis. iii. Study of an idealized heterogeneous surface. *J. Phys. Chem.*, 68, 1744–1750, (1964).
7. C. W. Extrand, Model for contact angles and hysteresis on rough and ultraphobic surfaces. *Langmuir*, 18, 7991–7999, (2002).
8. L. W. Schwartz and S. Garoff, Contact angle hysteresis on heterogeneous surfaces. *Langmuir*, 1, 219–230, (1985).
9. X. Xu and X. P. Wang, Analysis of wetting and contact angle hysteresis on chemically patterned surfaces. *SIAM J. Appl. Math.*, 71, 1753–1779, (2011).
10. G. Whyman, E. Bormashenko, and T. Stein, The rigorous derivation of Young, Cassie-Baxter and Wenzel equations and the analysis of the contact angle hysteresis phenomenon. *Chem. Phys. Letters*, 450, 355–359, (2008).

11. R. N. Wenzel, Resistance of solid surfaces to wetting by water. *Ind. Eng. Chem.*, 28, 988–994, (1936).
12. A. Cassie and S. Baxter, Wettability of porous surfaces. *Trans. Faraday Soc.*, 40, 546–551, (1944).
13. G. Alberti and A. DeSimone, Wetting of rough surfaces: A homogenization approach. *Proc. R. Soc. A*, London, 451, 79–97, (2005).
14. E. Bormashenko, Young, Boruvka-Neumann, Wenzel and Cassie-Baxter equations as the transversality conditions for the variational problem of wetting. *Colloids Surfaces* 345, 163–165, (2009).
15. N. A. Patankar, On the modeling of hydrophobic angles on rough surfaces. *Langmuir*, 19, 1249–1253, (2003).
16. G. Wolansky and A. Marmur, Apparent contact angles on rough surfaces: The Wenzel equation revisited. *Colloids Surfaces A*, 156, 381–388, (1999).
17. X. Xu and X. P. Wang, Derivation of the Wenzel and Cassie equations from a phase field model for two phase flow on rough surface. *SIAM J. Appl. Math.*, 70, 2929–2941, (2010).
18. L. Gao and T. J. McCarthy, How Wenzel and Cassie were wrong. *Langmuir*, 23, 3762–3765, (2007).
19. L. Gao and T. J. McCarthy, Reply to “comment on how Wenzel and Cassie were wrong by Gao and McCarthy”. *Langmuir*, 23, 13243–13243, (2007).
20. A. Marmur and E. Bittoun, When Wenzel and Cassie are right: Reconciling local and global considerations. *Langmuir*, 25, 1277–1281, (2009).
21. G. McHale, Cassie and Wenzel: Were they really so wrong. *Langmuir*, 23, 8200–8205, (2007).
22. M. V. Panchagnula and S. Vedantam, Comment on how Wenzel and Cassie were wrong by Gao and McCarthy. *Langmuir*, 23, 13242–13242, (2007).
23. C. Priest, R. Sedev, and J. Ralston, A quantitative experimental study of wetting hysteresis on discrete and continuous chemical heterogeneities. *Colloid Polym. Sci.*, 291, 271–277, (2013).
24. E. Bormashenko, A variational approach to wetting of composite surfaces: Is wetting of composite surfaces a one-dimensional or two-dimensional phenomenon? *Langmuir*, 25, 10451–10454, (2009).
25. W. Choi, A. Tuteja, J. M. Mabry, R. E. Cohen, and G. H. McKinley, A modified Cassie-Baxter relationship to explain contact angle hysteresis and anisotropy on non-wetting textured surfaces. *J. Colloid Interface Sci.*, 339, 208–216, (2009).
26. X. Xu and X. P. Wang, The modified Cassie’s equation and contact angle hysteresis. *Colloid Polym. Sci.*, 291, 299–306, (2013).
27. X. Chen, X.-P. Wang, and X. Xu, Effective contact angle for rough boundary. *Physica D*, 242, 54–64, (2013).
28. A. Braids, *Gamma-convergence for Beginners*. Oxford University Press, (2002).
29. J. Nevard and J. B. Keller, Homogenization of rough boundaries and interfaces. *SIAM J. Appl. Math.*, 57, 1660–1686, (1997).

30. R. Raj, R. Enright, Y. Zhu, S. Adera, and E. N. Wang, Unified model for contact angle hysteresis on heterogeneous and superhydrophobic surfaces. *Langmuir*, 28, 15777–15788, (2012).
31. W. Chen, A. Y. Fadeev, M. Hsieh, D. Öner, J. Young, and T. J. McCarthy, Ultrahydrophobic and ultralyophobic surfaces: Some comments and examples. *Langmuir*, 15, 3395–3399, (1999).

Computational Analysis of Wetting on Hydrophobic Surfaces: Application to Self-Cleaning Mechanisms

Muhammad Osman¹ and Roger A. Sauer^{2,*}

¹*Institute of Mechanics, Technical University of Dortmund, Dortmund, Germany*

²*Aachen Institute for Advanced Study in Computational Engineering Science (AICES), RWTH Aachen University, Aachen, Germany*

Abstract

In this work, we present a 3D model capable of describing the detailed interactions involved in self-cleaning mechanisms, which are exhibited by some hydrophobic surfaces. The model is based on a continuum mechanical formulation, and is discretized using the finite element (FE) method. A stabilized FE formulation is used to model the liquid membrane. The microstructure of the surface is modeled by spherical functions, which represent the surface asperities. When these surfaces are wetted by liquid droplets, local contact regions can be captured at the individual asperities. Generally, the contact angle which characterizes the surface has a dominant effect on the wetting behavior. Based on the presented model, the deformation of a 3D droplet in contact with a micro-structured hydrophobic surface can be computed for given droplet and surface parameters. Furthermore, the same model can be adapted to capture the interaction between the droplet and contaminant particles. Knowing the local membrane deformation at each particle, the equilibrium forces acting on the particle can be computed. This can help in providing an answer to the question: Does self-cleaning work for given droplet and particles parameters? Numerical examples are shown for two types of interactions: wetting on rough surfaces represented by spherical functions, and contact of liquid membranes with rigid spherical particles.

Keywords: Self-cleaning mechanism, contact angle, static wetting, nonlinear finite element analysis, droplet membranes.

*Corresponding author: sauer@aices.rwth-aachen.de

5.1 Introduction

Computational treatments of wetting problems provide in many cases explanations for physical phenomena, which are difficult and sometimes even impossible to be obtained through experiments. Therefore, several numerical techniques are utilized to solve such problems, based on mathematical models. Wetting is often modeled by a system of a liquid droplet in contact with a substrate surface with a predefined contact angle. The first mathematical equation which describes the contact angle of a solid flat surface was introduced in 1805 by Young [1]. Wenzel [2] extended Young's equation to model surface roughness, considering that the liquid fills the gaps between the surface asperities, and a non-composite state exists black in the contact region. The composite state, where air fills the gaps between the asperities was first proposed by Cassie and Baxter [3]. They found that the hydrophobicity, i.e. the wetting of a surface is significantly affected by the air-surface area fraction. This conclusion was bolstered by Johnson and Dettre [4] who argued that surfaces of higher roughness are more likely to be in the composite state during wetting.

The multi-scale nature of hydrophobic surfaces is mathematically modeled by Osman *et al.* [5] and Osman and Sauer [6] by considering superposed exponential functions with multiple levels representing different length-scales. Using the finite element method (FEM), these works studied the effect of the contact angle captured locally at the individual asperities on the wetting behavior, considering axisymmetric droplets. Investigations on the effect of surface roughness on wetting at the macro-level are provided by Raeesi *et al.* [7], and at the nano-level by Lee *et al.* [8]. Kavousanakis *et al.* [9] studied the patterns of surface roughness which influence the transition between Cassie-Baxter and Wenzel wetting states.

Numerically, static droplets in contact with flat surfaces were first modeled by Brown *et al.* [10], who derived an FE formulation to solve the Young-Laplace equation. Their Cartesian-based formulation was, however, limited to contact with flat surfaces. In order to capture complex geometries at the contact interface, it is useful to use curvilinear coordinates to describe surfaces and displacements as done by Steigmann *et al.* [11], and Agrawal and Steigmann [12, 13]. A general 3D model for droplets in contact with rough surfaces based on curvilinear coordinates is presented by Sauer *et al.* [14] and Sauer [15]. A stabilized FE formulation for static liquid membranes was used to model the droplet. Here, we employ this model to account for different contact angles representing wetting on rough surfaces. Furthermore, we use the model to describe the interactions

between contaminant particles and liquid membranes, which take place in self-cleaning mechanisms. This work extends the 2D model introduced by Osman and Sauer [16], and provides a general 3D framework for modeling interactions between membrane interfaces and rigid particles. Examples shown here are limited to static contact angles, however the model can be extended to account for the contact angle hysteresis.

This paper is organized as follows: Section 5.2 provides a brief overview on the basic definitions used in differential geometry, on which the droplet membrane model is based. Then the model describing a self-cleaning system is illustrated in Section 5.3, where the following individual sub-models are introduced: the droplet model, the substrate surface model, and the model discussing the particle-droplet interaction. The governing equations of these models are presented in Section 5.4, followed by the force analysis for the last model performed in Section 5.5. Numerical examples are shown in Section 5.6 in order to clarify the theory. In the end, we outline the summary of the presented work in Section 5.7.

5.2 Basic Relations in Differential Geometry

Here, we briefly overview the basic definitions and relations used to describe curvilinear coordinate systems in Euclidean space. These definitions are used to derive the governing equations in Section 5.4. The kinematics of the membrane is also expressed in differential geometry. For further discussion on the topic refer to Carmo [17] and Kreyszig [18]. A two-dimensional surface \mathcal{S} is characterized by a general set of coordinates (ξ^1, ξ^2) as shown in Figure 5.1. The point (ξ^1, ξ^2) in the parameter domain \mathcal{P} and its mapping \mathbf{x} on the surface \mathcal{S} are defined by the vector $\mathbf{x} = \mathbf{x}(\xi^1, \xi^2)$. The associated tangent vectors read

$$\mathbf{a}_\alpha = \frac{\partial \mathbf{x}}{\partial \xi^\alpha}, \alpha = 1, 2. \quad (5.1)$$

These tangents are generally non-orthogonal and are not normalized. Greek indices take values in 1, 2, and repeated indices are summed according to index notation. Equation (5.1) defines the basis for the tangent plane at \mathbf{x} , which is characterized by the metric tensor

$$a_{\alpha\beta} := \mathbf{a}_\alpha \cdot \mathbf{a}_\beta, \quad (5.2)$$

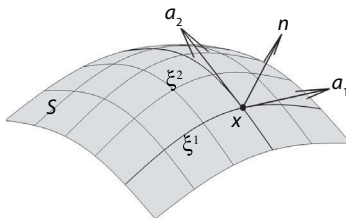


Figure 5.1 2-D Surface in curvilinear coordinates.

with the contra-variant components of the metric tensor defined by

$$a^{\alpha\beta} := [a_{\alpha\beta}]^{-1}. \quad (5.3)$$

The normal vector can then be defined as

$$\mathbf{n} = \frac{\mathbf{a}_1 \times \mathbf{a}_2}{\sqrt{\det[a_{\alpha\beta}]}}, \quad (5.4)$$

The contra-variant pair of tangent vectors can be defined in terms of $a^{\alpha\beta}$

$$\mathbf{a}^\alpha = a^{\alpha\beta} \mathbf{a}_\beta, \quad (5.5)$$

which satisfies $\mathbf{a}^\alpha \cdot \mathbf{a}^\beta = a^{\alpha\beta}$. Then it can be easily shown that

$$\mathbf{a}^\alpha \cdot \mathbf{a}_\beta = \delta_\beta^\alpha, \quad (5.6)$$

where δ_β^α is the Kronecker symbol. From the definitions of $a_{\alpha\beta}$ and $a^{\alpha\beta}$ in Equations (5.2) and (5.3), it follows that

$$a^{\alpha\beta} a_{\alpha\gamma} = \delta_\gamma^\beta. \quad (5.7)$$

The basis $\{\mathbf{a}^1, \mathbf{a}^2, \mathbf{n}\}$ constitutes a dual basis on the tangent plane, with $a^{\alpha\beta}$ as the dual metric.

A vector \mathbf{v} in \mathbb{R}^3 can then be decomposed using both bases $\{\mathbf{a}_1, \mathbf{a}_2, \mathbf{n}\}$ and $\{\mathbf{a}^1, \mathbf{a}^2, \mathbf{n}\}$ as,

$$\mathbf{v} = v^\beta \mathbf{a}_\beta + v_n \mathbf{n} = v_\beta \mathbf{a}^\beta + v_n \mathbf{n}, \quad (5.8)$$

where v_β and v^β are, respectively, the co-variant and contra-variant components of the vector \mathbf{v} , defined as

$$v^\beta = \mathbf{v} \cdot \mathbf{a}^\beta \quad \text{and} \quad v_\beta = \mathbf{v} \cdot \mathbf{a}_\beta. \quad (5.9)$$

The co- and contra-variant components are related by

$$v^\beta = a^{\beta\alpha} v_\alpha \quad \text{and} \quad v_\beta = a_{\beta\alpha} v^\alpha. \quad (5.10)$$

Surface tensors generally take the form

$$\sigma = \sigma^{\alpha\beta} (\mathbf{a}_\alpha \otimes \mathbf{a}_\beta) = \sigma_{\alpha\beta} (\mathbf{a}^\alpha \otimes \mathbf{a}^\beta). \quad (5.11)$$

Using Weingarten formula, the curvature tensor can be expressed in terms of the derivative of \mathbf{n} as

$$b_{\alpha\beta} = -\mathbf{n}_\alpha \cdot \mathbf{a}_\beta. \quad (5.12)$$

The derivative of \mathbf{a}_a can be computed from Equation (5.1) as

$$\mathbf{a}_{\alpha,\beta} = \mathbf{x}_{,\alpha\beta}, \quad (5.13)$$

with $\mathbf{x}_{,\alpha\beta} = \frac{\partial^2 \mathbf{x}}{\partial \xi^\alpha \partial \xi^\beta}$. Next, we introduce the so-called co-variant derivative of \mathbf{a}_α ,

$$\mathbf{a}_{\alpha;\beta} := \mathbf{a}_{\alpha,\beta} - \Gamma_{\alpha\beta}^\gamma \mathbf{a}_\gamma. \quad (5.14)$$

5.3 System Model

We consider the system model depicted in Figure 5.2, which describes the self-cleaning mechanism through the following sub-models; (1) drop-let model, (2) substrate surface model, and (3) particle-droplet interaction model. Since quasi-static conditions are considered in this work, it is convenient to treat the droplet as a hydrostatic bulk and a deformable liquid membrane. The latter is modeled using the stabilized FE formulation introduced by Sauer [15], which captures the in-plane equilibrium of the membranes due to constant surface tension. The multi-scale nature of self-cleaning surfaces can be mathematically modeled as 2D sinusoidal functions as done by Bittoun and Marmur [19], and Iliev and Pesheva [20],

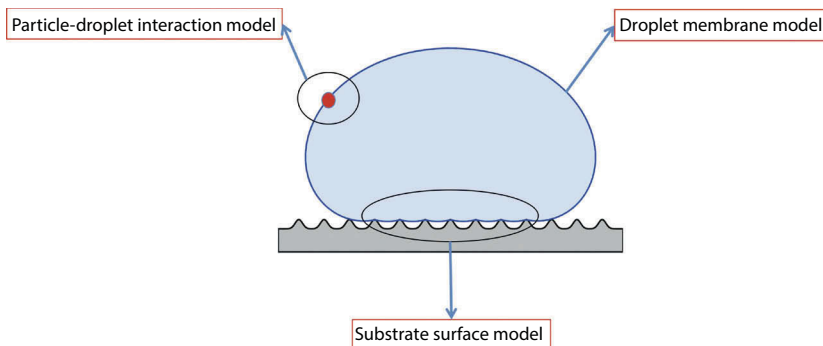


Figure 5.2 Self-cleaning system model comprising: droplet membrane model, substrate surface model, and particle-droplet interaction model.

or as superimposed 2D exponential functions as in Osman and Sauer [6]. Here we introduce a new 3D surface model based on superimposed spherical functions, parameterized by the radii and spacing between neighboring spheres. This model represents the micro-scale level, where only one level of roughness is captured. Surface and line contact algorithms are incorporated in the liquid membrane model, in order to capture wetting on the individual asperities of the rough surface. The third model presented in this work discusses the forces acting on a rigid spherical contaminant particle interacting with the liquid membrane, in order to assess whether the contaminant particle will be lifted towards the droplet or remains attached to the substrate surface. The liquid membrane formulation used in the first model is employed here, and the contact algorithms are adapted to model the interactions with spherical rigid particles.

5.4 Governing Equations

5.4.1 Droplet Membrane

The equilibrium equation of the static membrane surface S_s can be expressed as

$$\mathbf{t}_{;\alpha}^\alpha + \mathbf{f} = \mathbf{0}, \quad (5.15)$$

where $\mathbf{t}_{;\alpha}^\alpha$ is the covariant derivative of the membrane traction \mathbf{t} , and \mathbf{f} is the vector of body forces. The latter can be split into the in-plane and out-of-plane components

$$\mathbf{f} = f^\alpha \mathbf{a}_\alpha + p \mathbf{n}, \quad (5.16)$$

where f^α ($\alpha = 1, 2$) are the tangential components of the traction, and p is the normal pressure. The traction on the surface, normal to \mathbf{a}^α , can be defined in terms of the interface stress σ as

$$\mathbf{t}^\alpha = \sigma \mathbf{a}^\alpha. \quad (5.17)$$

Substituting Equations (5.17) and (5.16) into (5.15), and performing some manipulations yields two balance equations: one in the in-plane direction,

$$\sigma_{;\beta}^{\alpha\beta} + f^\alpha = 0, \quad (5.18)$$

and the other in the out-of-plane direction

$$\sigma^{\alpha\beta} b_{\alpha\beta} + p = 0. \quad (5.19)$$

For liquid membranes, the surface tension is a hydrostatic stress state, $\sigma^{\alpha\beta} = \gamma a^{\alpha\beta}$, and Equation (5.19) becomes the well-known Young-Laplace equation which is often written as

$$2H\gamma + p = 0, \quad (5.20)$$

where H denotes the mean curvature defined by $2H = b_\alpha^\alpha$, while b_β^α are the mixed components of the curvature tensor, and $b_\alpha^\alpha = b_1^1 + b_2^2$. The pressure p is defined w.r.t a predefined reference level and comprises the capillary pressure p_0 and the hydrostatic pressure,

$$p = p_0 + \rho_s g u, \quad (5.21)$$

where u is the surface height w.r.t the reference level. The dimensionless form of Equation (5.20) is obtained through dividing it by γL_0 , where L_0 is a reference length,

$$2\tilde{H} = \lambda + B\tilde{u}, \quad (5.22)$$

where λ is the Lagrange multiplier representing the capillary pressure, $B\tilde{u}$ is the hydrostatic pressure, with $B = \rho_s g L_0^2 / \gamma$ is the so-called Bond number, \tilde{H} and \tilde{u} are respectively the normalized curvature and surface height. ρ_s is the density of the liquid and g is the gravitational force. The covariant derivatives $\sigma_{;\beta}^{\alpha\beta}$ in Equation (5.18) vanish for liquid membranes

with constant surface tension, which means that Equation (5.18) is trivially satisfied for arbitrary values of traction f^a . Physically interpreted, hydrostatic membranes do not naturally support in-plane loads. A stabilization scheme is therefore essential as a numerical treatment for the in-plane stability. Here we use the scheme proposed by Sauer [15], which substitutes $\sigma^{a\beta}$ in Equation (5.18) by the stabilization stress

$$\sigma_{sta}^{\alpha\beta} = \mu / J \left(a_{pre}^{\alpha\beta} - a^{\alpha\beta} \right), \quad (5.23)$$

Where μ is the stabilization parameter, J is the Jacobian, and $a_{pre}^{\alpha\beta}$ is the metric tensor computed in the previous load step. Using this scheme requires very small load steps through which the solution is gradually reached when $\sigma_{sta}^{\alpha\beta}$ eventually vanishes, satisfying Equation (5.18).

5.4.2 Surface Contact

In computational contact mechanics it is conventional to denote two surfaces in contact as master surface S_m (often a rigid surface) and slave surface S_s (usually the deformable surface). The 3D substrate surface S_m is mathematically modeled as a set of spheres representing the physical asperities. The surface is characterized by the radius of the sphere, and the spacing between the neighboring spheres. Both parameters are usually functions of the droplet radius.

We use the closest point projection technique (see Wriggers [21]) to determine contact between the membrane and the substrate surface. We consider a point \mathbf{x}_c which lies on the membrane surface, and find its projection on the substrate surface at \mathbf{x}_p . The impenetrability constraint characterized by the gap between the two surfaces g_n then reads,

$$g_n = (\mathbf{x}_c - \mathbf{x}_p) \cdot \mathbf{n}_p \geq 0, \quad \forall \mathbf{x}_c \in S_s, \quad (5.24)$$

where \mathbf{x}_p is the closest projection of the membrane point \mathbf{x}_c onto the substrate surface S_m in the direction \mathbf{n}_p , normal to S_m . Generally, several projections of \mathbf{x}_c might exist, and therefore an iterative solution is necessary to compute all possible projection points \mathbf{x}_m , satisfying the orthogonality condition,

$$\mathbf{a}_m \cdot (\mathbf{x}_c - \mathbf{x}_m) = 0, \quad (5.25)$$

where \mathbf{a}_m is the surface tangent on S_m at \mathbf{x}_m . In order to find the closest projection point \mathbf{x}_p among the possible solutions, a minimum distance problem has to be solved,

$$\mathbf{x}_p(\mathbf{x}_c) = \min_{\mathbf{x}_m \in S_m} (\mathbf{x}_c - \mathbf{x}_m), \quad \forall \mathbf{x}_c \in S_s. \quad (5.26)$$

Since the substrate surface here is represented by spheres, the projection \mathbf{x}_p , the normal \mathbf{n}_p and the gap g_n can be explicitly determined without any further iterative steps. Knowing the position of the center of the sphere \mathbf{r}_0 , we can define the normal \mathbf{n}_p as

$$\mathbf{n}_p = \frac{\mathbf{x}_c - \mathbf{r}_0}{\|\mathbf{x}_c - \mathbf{r}_0\|}. \quad (5.27)$$

The projection \mathbf{x}_p on the sphere of radius r_s simply lies on the line connecting the center of the sphere and the point \mathbf{x}_c , and can be defined as

$$\mathbf{x}_p = \mathbf{r}_0 + r_s \mathbf{n}_p. \quad (5.28)$$

5.4.3 Line Contact

Wetting is mainly characterized by the contact angle formed at the liquid and solid interfaces at the contact line \mathcal{L}_c , the location at which the three phases meet. In this study, we distinguish two different contact interfaces; 1) the liquid membrane with the substrate surface with contact angle θ_s , and 2) the liquid membrane with the contaminant particle with contact angle θ_p . In both cases, the location of the contact line in a quasi-static framework is maintained by the balance of the interfacial tractions \mathbf{t}_{SG} , \mathbf{t}_{LG} and \mathbf{t}_{SL} at the solid-gas, liquid-gas and solid-liquid interfaces, respectively, through

$$\mathbf{t}_{SG} + \mathbf{t}_{LG} + \mathbf{t}_{SL} + \mathbf{q}_n = \mathbf{0}, \quad (5.29)$$

where $\mathbf{q}_n = q_n \mathbf{n}_c$ is the line load which counterbalances the projection of \mathbf{t}_{LG} onto the normal direction \mathbf{n}_c w.r.t S_m . These tractions are illustrated in Figure 5.3, which depicts one quarter of a droplet resting on a flat surface with contact angle θ_s . Both tractions \mathbf{t}_{SG} and \mathbf{t}_{SL} have opposite directions along the vector \mathbf{m}_c , which is normal to the surface tangent \mathbf{a}_c and lies on the surface S_m . The force $\mathbf{t}_{LG} = \gamma_{LG} \mathbf{a}_m$ is tangent to the liquid membrane at the plane which forms the contact angle θ_s with the master surface S_m . The normal and tangential components of Equation (5.29) w.r.t S_m , respectively read

$$\gamma_{SG} - \gamma_{LG} \cos \theta - \gamma_{SL} = 0, \quad (5.30)$$

$$q_n - \gamma_{LG} \sin \theta = 0, \quad (5.31)$$

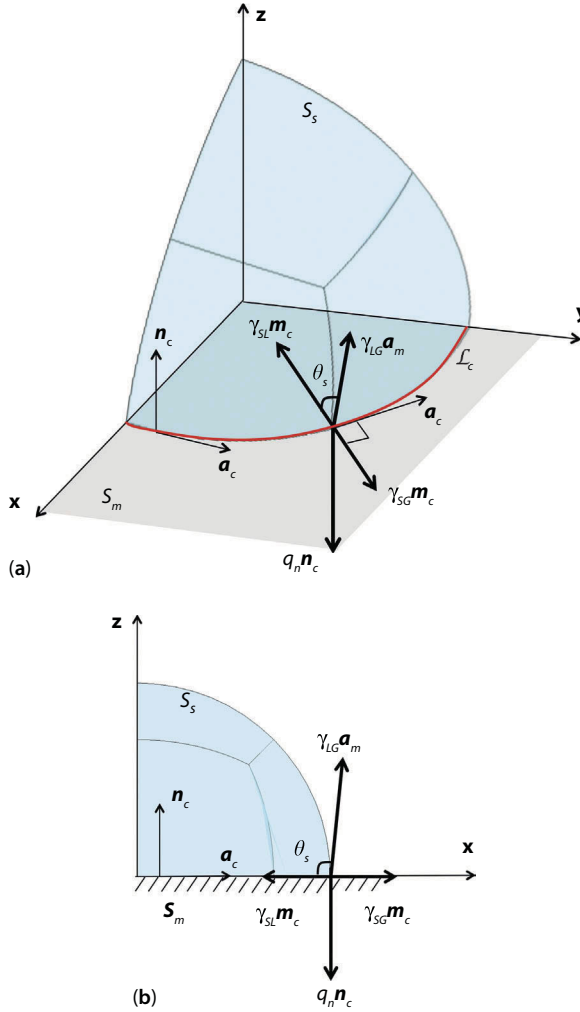


Figure 5.3 Forces along the contact line: (a) 3D view, and (b) 2D side-view.

where γ_{SG} , γ_{LG} and γ_{SL} are the interfacial tensions at the respective interfaces. We note here that $\gamma_{LG} = \gamma$ is used in Section 5.4.1. The above equations hold for interactions on both substrate surfaces $\theta = \theta_s$ and contaminant particles $\theta = \theta_p$. Computationally, the contact angle θ is imposed within the membrane as a kink by applying a certain load q_c at the contact line,

$$q_c = q_n n_c + \gamma_{SG} m_c. \quad (5.32)$$

This load \mathbf{q}_c has to balance the tractions \mathbf{t}_{LG} and \mathbf{t}_{SL} (see Figure 5.3). Therefore, computing \mathbf{q}_c requires determining the vectors \mathbf{n}_c , \mathbf{a}_c , and \mathbf{m}_c . The normal \mathbf{n}_c is computed w.r.t to the known substrate surface at the contact point, by considering the closest point projection as mentioned in the surface contact, while the tangent \mathbf{a}_c is determined at the membrane point \mathbf{x}_c as

$$\mathbf{a}_c = \frac{\partial \mathbf{x}_c}{\partial \xi}. \quad (5.33)$$

The vector \mathbf{m}_c is the cross-product of \mathbf{a}_c and \mathbf{n}_c , defined as

$$\mathbf{m}_c = \frac{\mathbf{a}_c \times \mathbf{n}_c}{\|\mathbf{a}_c \times \mathbf{n}_c\|}. \quad (5.34)$$

For further details we refer to Sauer [15].

5.5 Force Analysis

We consider a rigid spherical contaminant particle of radius r_p and density ρ_p initially resting on a substrate surface and interacting with a liquid droplet under quasi-static conditions (see Figure 5.4). Four forces are involved in this interaction: particle weight \mathbf{F}_G , contact line force \mathbf{F}_{CL} , hydrostatic force \mathbf{F}_H , and buoyancy force \mathbf{F}_B , defined as follows:

$$\mathbf{F}_G = \frac{4}{3} \pi r_p^3 \rho_p \mathbf{g}, \quad (5.35)$$

$$\mathbf{F}_{CL} = \oint_{L_c} \mathbf{t}_{LG} dL_c, \quad (5.36)$$

$$\mathbf{F}_H = \int_{A_s} p \mathbf{n} dA_s \approx p_0 A_s \mathbf{N}, \quad A_s = 2\pi r b, \quad (5.37)$$

$$\mathbf{F}_B = \rho_s g v_s \mathbf{N}, \quad v_s = \frac{\pi b}{6} (3a^2 + b^2), \quad (5.38)$$

where \mathbf{n} is the normal to the wetted area A_s , while v_s is the wetted volume of the particle, \mathbf{N} is the normal to the contact line along the particle axis, and a & b are distances defined in Figure 5.4. In order to define \mathbf{F}_{CL} , the traction \mathbf{t}_{LG} is computed from Equation (5.29). The effective force \mathbf{F}_e is the summation of all forces,

$$\mathbf{F}_e = \mathbf{F}_G + \mathbf{F}_{CL} + \mathbf{F}_H + \mathbf{F}_B. \quad (5.39)$$

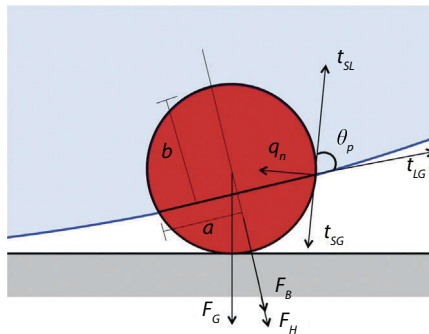


Figure 5.4 Schematic of the forces acting on a particle resting on a flat substrate surface, and in contact with a liquid droplet (Osman and Sauer [16]).

The vertical component of \mathbf{F}_e determines whether the particle is pulled upwards towards the droplet or not. In case a contact angle hysteresis evolves, the dynamic contact angles can be obtained through the tangential equilibrium, i.e the in-plane component of \mathbf{F}_e .

Among the above parameters, the following require computation of the membrane deformation: (1) the location of the contact line \mathcal{L}_C w.r.t the particle (represented by the distances a & b), (2) the traction along the liquid-gas interface t_{LG} , and (3) the internal pressure p_0 . Friction and surface adhesion between the particle and the substrate are not considered in this work. The example shown in Figure 5.4 represents a special case of the general model depicted in Figure 5.2 where the contaminant particle can be initially located anywhere on the droplet surface.

5.6 Results and Discussion

Based on the sub-models described above, we present two numerical examples: (1) wetting of droplets on a rough surface, and (2) adhesion of contaminant particles to a droplet surface. Quasi-static conditions are considered in both examples. We distinguish the parameters for the substrate surface in the first example ($\theta_s, \gamma_{SL}|^s, \gamma_{SG}|^s, \gamma_{LG}, V_s, \rho_s$) from those for the particle in the second example ($\theta_p, \gamma_{SL}|^p, \gamma_{SG}|^p, \gamma_{LG}, V_p, \rho_p$). It should be noted here that the interfacial tension $\gamma_{SL}|^s$ is not necessarily the same as $\gamma_{SL}|^p$.

5.6.1 Wetting on Rough Surface

Superhydrophobic surfaces are characterized by a water contact angle $\theta_s \geq 150^\circ$. This angle is locally captured at the individual asperities at the

micro-scale, where the surface roughness can be visualized. For a flat surface, however, only one global contact angle is observed. In order to distinguish between the two, we consider the examples shown in Figures 5.5, 5.6, and 5.7 for a droplet in contact with a flat surface with $\theta_s = 180^\circ$, rough surface with $\theta_s = 180^\circ$ and with $\theta_s = 150^\circ$, respectively. Load-driven conditions are considered here, where the applied load is simply the gravity $\rho_s g = 2\gamma / 2R^2$ and R is the undeformed droplet radius. Relative to the droplet size, the radii of the spheres representing the surface roughness are chosen to be $r_s = 0.05R$, and the distance between each two neighboring asperities is $\Delta x = 0.2R$. As discussed in Section 5.4.1, numerical instability problems appear while modeling liquid membranes since they do not naturally equilibrate in-plane loads. Therefore, the stabilized finite element formulation introduced by Sauer [15] is employed to model the membrane. The stabilization parameter $\mu = \gamma$ is used in the computations. The penalty parameter used for applying the surface contact constraint is $\varepsilon_n = 10^4 \gamma / R$.

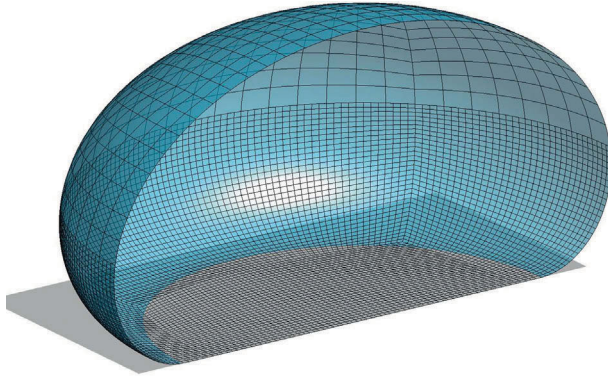


Figure 5.5 FE solution for a droplet in contact with a flat surface, $\theta_s = 180^\circ$.

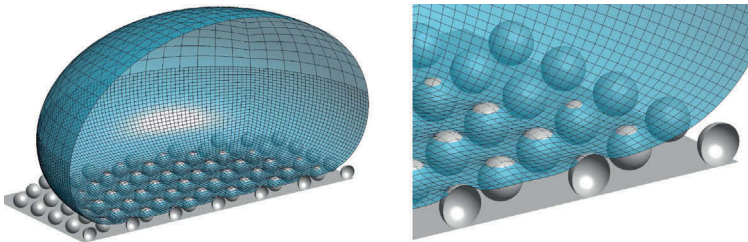


Figure 5.6 Left: FE solution for a droplet in contact with a rough surface, $\theta_s = 180^\circ$. Right: zoom-in view.

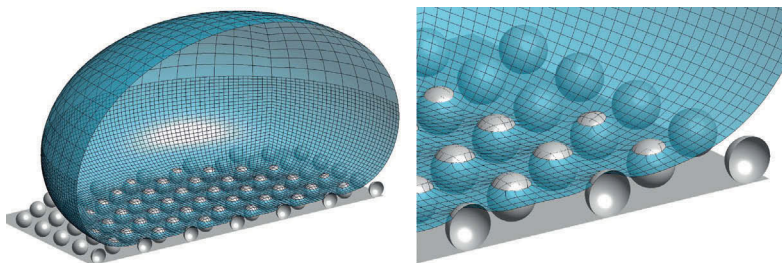


Figure 5.7 Left: FE solution for a droplet in contact with a rough surface, $\theta_s = 150^\circ$. Right: zoom- in view.

As observed in Figures 5.5, 5.6, and 5.7, there is almost no change in the overall droplet deformation due to changing the roughness parameters and the contact angle. Decreasing the contact angle below 150° eventually will lead to a complete wetting (Wenzel state) of the surface, for the given surface parameters. Furthermore, the global contact angle is almost 180° in the three cases, although different local contact angles are captured at the rough surfaces in Figures 5.6 and 5.7. This means that the wetting behavior of superhydrophobic surfaces is independent of the contact angle, as long as the latter is sufficiently large (about 150° in this example), and under partial wetting state (Cassie-Baxter). This observation is only valid when the surface roughness parameters are relatively small compared to the droplet size.

5.6.2 Adhesion Between Droplet Surface and a Contaminant Particle

In self-cleaning applications, contaminant particles are usually so small compared to the liquid droplet such that the surface of the droplet appears almost planar to the particle. This allows reducing the model to a simple square sheet representing the initial configuration of a liquid membrane. In order to avoid boundary effects, the dimensions of the membrane are considered to be large enough so that the undeformed membrane surface at the boundary is approximately flat. An interacting contaminant particle is represented by a sphere of radius r_p , as in Figure 5.8. The membrane can thus be considered fixed at the boundaries. The capillary pressure effect can still be considered in this model by applying a volume constraint on the membrane (Sauer [15]).

Now we employ this model to compute the membrane deformation due to contact with a spherical particle considering a predefined contact angle θ_p . Based on this deformation, we can compute the unknown parameters discussed in Section 5.5, and evaluate the equilibrium forces. In the following example, we consider a square membrane of dimensions $5L_0 \times 5L_0$, in contact with a rigid sphere of radius $r_p = L_0$ (see Figure 5.9). The membrane is deformed under the distributed contact line load \mathbf{q}_c defined in Equation (5.32), applied along the contact line. Due to the symmetry of the system, it is enough to run the computations for one quarter of the system, after

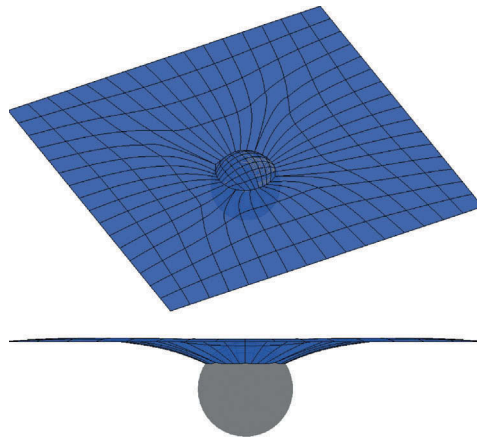


Figure 5.8 Top: 3D view of an FE solution for a liquid membrane in contact with a spherical rigid particle with contact angle $\theta_p = 90^\circ$. Bottom: 2D side-view.

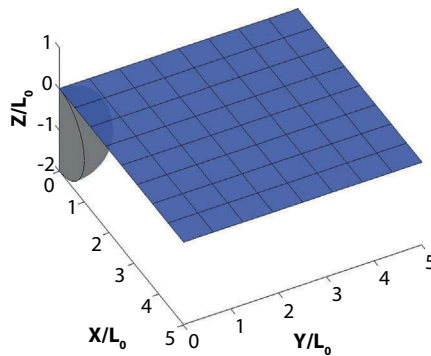


Figure 5.9 Initial configuration of a liquid membrane sheet in contact with a rigid sphere with contact angle $\theta_p = 180^\circ$. Dimensions are normalized by the characteristic length L_0 .

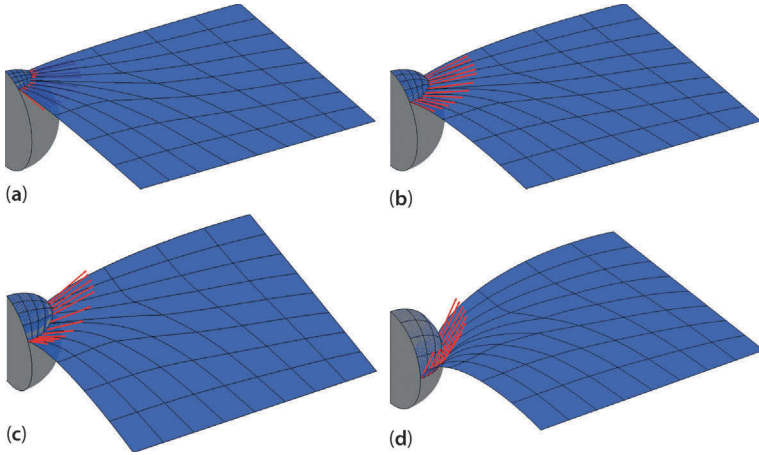


Figure 5.10 FE solution of a deformed liquid membrane in contact with a sphere of contact angle (a) to (d): $\theta_p = 150^\circ, 120^\circ, 90^\circ$ and 30° . The red arrows represent the directions of the distributed contact line traction \mathbf{t}_{LG} .

applying the appropriate boundary conditions. Furthermore, we assume the plane formed by the closed contact line to be horizontal. This assumption is, however, only limited to this example and not to the equations in Section 5.5, which are applied to any orientation of the contact line.

Figure 5.10 shows the membrane deformation for contact with spheres of contact angles $\theta_p = 150^\circ, 120^\circ, 90^\circ$ and 30° . Larger deformations are noticed for lower contact angles, where the net contact line force \mathbf{F}_{CL} points inwards, pulling the sphere towards the liquid membrane. This result agrees with the physical fact that droplets tend to stick to hydrophilic surfaces through maximizing the area of contact. On the other hand, hydrophobic spheres are subjected to repulsive contact line forces pushing them away from the liquid membrane. Based on the obtained results, the forces in Equations (5.36, 5.37) and (5.38) are computed, and the effective force $\mathbf{F}_e \cdot \mathbf{e}_3$ is plotted in Figure 5.11 for spheres of different contact angles. The region where $\mathbf{F}_e \cdot \mathbf{e}_3$ is below zero in Figure 5.11 means that the effective force is not enough to lift the sphere towards the liquid membrane. However, the positive values of $\mathbf{F}_e \cdot \mathbf{e}_3$ indicate a lift off since the contact line force overcomes the other forces. The point at which the effective force flips direction is denoted in Figure 5.11 as a critical point. This indicates when the self-cleaning is activated and the contaminant particle is attached to the droplet. It is important to note here that the direction of the contact line force, plotted in Figure 5.10, is not necessarily the direction of the

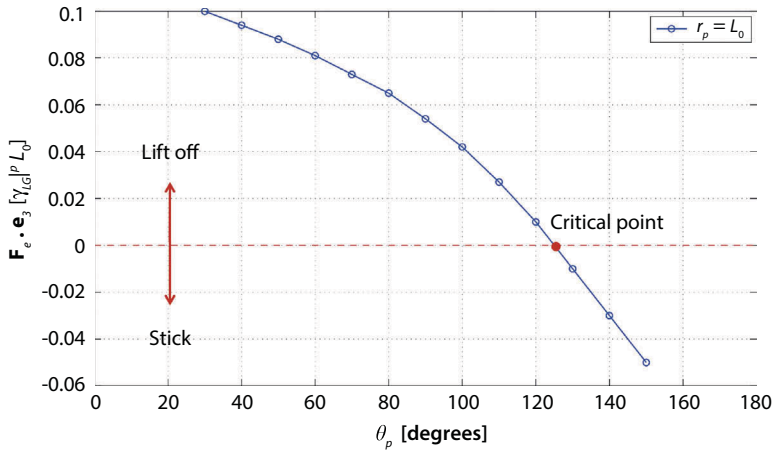


Figure 5.11 Effect of contact angle on the equilibrium force of particles with radii $r_p = L_0$.

effective force, since the other forces (\mathbf{F}_H , \mathbf{F}_G , and \mathbf{F}_B) pointing downwards might dominate, depending on the sphere and membrane parameters. In the above computations the density of the particle ρ_p is chosen to be the same as the density of the liquid ρ_s . Different results can be obtained for different sizes and densities of the spherical particle.

The precision of the computations depends on the number of load steps taken over the contact angle. Detailed discussion on convergence of the numerical scheme used here can be found in Sauer [15]. Penetrations of the liquid membrane into the rigid surface are observed in the contact regions in Figures 5.5, 5.6, 5.7, 5.8 and 5.10 due to the use of the penalty method, which is an approximation method. This problem can be eliminated by using other exact methods to enforce the surface contact constraint, which significantly increase the computational cost.

5.7 Conclusions

Static wetting of hydrophobic surfaces considering surface roughness is computationally studied through an introduced 3D model based on FEM. The same model is adapted to describe the interactions between contaminant particles and droplet surfaces, which are involved in self-cleaning mechanisms. These interactions are analyzed through a force balance to determine whether a contaminant particle in contact with a liquid surface will be lifted off towards it or sticks to the substrate. The

force balance shows that the net contact line force is dominant for relatively small particles w.r.t the droplet. Examples shown in Section 5.6.2 help in explaining the self-cleaning effect through the introduced model. Furthermore, it is shown that super- hydrophobicity is attainable for surfaces with sufficiently large contact angles (approximately 150°), as long as Cassie-Baxter wetting state exists. Such an independence from the contact angle can help in reducing the structural requirements while fabricating artificial superhydrophobic surfaces.

Acknowledgement

The authors are grateful to the German Research Foundation (DFG) for supporting this research under projects SA1822/3-2 and GSC 111.

References

1. T. Young, An essay on the cohesion of fluids, *Phil. Trans. R. Soc. Lond.* 95, 65–87 (1805).
2. R.N. Wenzel, Resistance of solid surfaces to wetting by water, *Ind. Eng. Chem.* 28, 988–994(1936).
3. A.B.D. Cassie and S. Baxter, Wettability of porous surfaces, *Trans. Faraday Soc.* 40, 546–551 (1944).
4. R.E. Johnson, Jr. and R.H. Dettre, Contact angle hysteresis study of an idealized rough surface, *Adv. Chem. Ser.* 43, 112–135 (1964).
5. M. Osman, R. Rasool, and R. A. Sauer, Computational aspects of self-cleaning surface mechanisms, in: *Advances in Contact Angle, Wettability and Adhesion*, Vol.1, K.L. Mittal (Ed.), pp. 109–130, Wiley-Scrivener, Beverly, MA (2013).
6. M. Osman and R. A. Sauer, A parametric study of the hydrophobicity of rough surfaces based on finite element computations, *Colloids Surfaces, A* 461, 119–125 (2014).
7. B. Raeesi, N.R. Morrow, and G.Mason, Effect of surface roughness on wettability and displacement curvature in tubes of uniform cross-section, *Colloids Surfaces, A* 436, 392–401 (2013).
8. S.M. Lee, I.D. Jung, and J.S. Ko, The effect of the surface wettability of nanoprotusions formed on network type microstructures, *J. Micromech. Microeng.* 18, 125007 (7pp) (2008).
9. M.E. Kavousanakis, C.E. Colosquib, and A.G. Papathanasiou, Engineering the geometry of stripe-patterned surfaces toward efficient wettability switching, *Colloids Surfaces, A* 436, 309–317 (2013).

10. R.A. Brown, F.M. Orr, and L.E. Scriven, Static drop on an inclined plate: Analysis by the finite element method, *J. Colloid Interface Sci.* 73, 76–87 (1980).
11. D. Steigmann, E. Baesu, R.R. Rudd, J. Belak, and M. McElfresh, On the variational theory of cell-membrane equilibria, *Interface Free Bound.* 5, 357–366 (2003).
12. A. Agrawal and D.J. Steigmann, Modeling protein-mediated morphology in biomembranes, *Biomech. Model. Mechanobiol.* 8, 371–379 (2009).
13. A. Agrawal and D.J. Steigmann, Boundary value problems in the theory of lipid membranes, *Continuum Mech. Thermodyn.* 21, 57–82 (2009).
14. R. A. Sauer, X.T. Duong, and C.J. Corbett, A computational formulation for constrained solid and liquid membranes considering isogeometric finite elements, *Comput. Method Appl. Mech. Engrg.* 271, 48–68 (2014).
15. R. A. Sauer, Stabilized finite element formulations for liquid membranes and their application to droplet contact, *Int. J. Numer. Meth. Fluids* 75, 519–545 (2014).
16. M. Osman and R. A. Sauer, Quasi-static analysis of self-cleaning surface mechanisms, in Proceedings of the 22nd UK Conference on Computational Mechanics (ACME2014), pp. 324–327 (2014).
17. M.P. Do Carmo, *Differential Geometry of Curves and Surfaces*, Prentice-Hall (1976).
18. E. Kreyszig, *Differential Geometry*, Dover (1991).
19. E. Bittoun and A. Marmur, The role of multiscale roughness in lotus effect: Is it essential for super-hydrophobicity?, *Langmuir* 28, 13933–13942 (2012).
20. S. Iliev and N. Pesheva, Nonaxisymmetric drop shape analysis and its application for determination of local contact angles, *J. Colloid Interface Sci.* 301, 677–684 (2006).
21. P. Wriggers, *Computational Contact Mechanics*, 2nd ed. Springer, Heidelberg (2006).

Bubble Adhesion to Superhydrophilic Surfaces

Ridvan Ozbay¹, Ali Kibar² and Chang-Hwan Choi^{1,*}

¹*Department of Mechanical Engineering, Stevens Institute of Technology,
Hoboken, New Jersey, USA*

²*Department of Mechanical and Material Technologies, Kocaeli University,
Kocaeli, Turkey*

Abstract

This paper reports experimental results and analysis of adhesion forces of captive air bubbles of varying volumes (8–20 μL and Bond number on the order of 1) to superhydrophilic surfaces, and are compared to hydrophilic surfaces. A polished bare silicon substrate and a micropillared silicon substrate with apparent contact angles of sessile water droplets of 40° and 4° were used as the hydrophilic and superhydrophilic surfaces, respectively. Theoretically, the adhesion force of an air bubble to an inclined surface depends on the contact width and the contact angle hysteresis (or the cosine difference of the contact angles between uphill (advancing) and downhill (receding) sides, also called maximum and minimum angles, respectively). The results show that the sliding angle, contact angle hysteresis, and adhesion force are much lower on the micropillared superhydrophilic surface than on the hydrophilic surface, which is due to the entrapped water layer on the micropillared superhydrophilic surface. On both the hydrophilic and superhydrophilic surfaces, the adhesion force slightly decreases with bubble volume. Although the contact width increases with an increase in bubble volume, the contact angle hysteresis decreases more significantly so that the adhesion force is effectively reduced with an increase in bubble volume. This is attributed to the effect of the buoyancy force, which becomes more pronounced with an increase in bubble volume (i.e., larger Bond number) and depends on the shapes of air bubbles formed on the surfaces with different wettabilities.

Keywords: Bubble, superhydrophilic surface, sliding angle, contact angle hysteresis, adhesion force

*Corresponding author: cchoi@stevens.edu

6.1 Introduction

The wetting of solid surfaces by liquid droplets [1–7] and the adhesion between liquid droplets and solid surfaces [8–13] have been studied extensively over the past decade. In contrast, the adhesion and dynamic behaviors of bubbles on solid surfaces submerged in liquid have been studied less [14–18], especially on rough solid surfaces [19, 20]. Bubble behaviors are of great significance in many applications such as thermal/fluid systems, including boiling [21], heat exchangers [22], chemical reactors [23], and microfluidic systems [24]. Bubbles detach easily from hydrophilic surfaces (i.e., $\theta_w < 90^\circ$, where θ_w represents the contact angle of the sessile droplet of water), while they are prone to adhere and spread over hydrophobic (i.e., $\theta_w > 90^\circ$) surfaces. If the surfaces are roughened or patterned, hydrophilic surfaces typically become more hydrophilic (i.e., superhydrophilic with $\theta_w < 10^\circ$) and hydrophobic surfaces become more hydrophobic (i.e., superhydrophobic with $\theta_w > 150^\circ$). Bubbles detach more easily from superhydrophilic surfaces than from hydrophilic surfaces, while they adhere and spread more strongly over superhydrophobic surfaces than over hydrophobic surfaces. On superhydrophilic surfaces, water is typically entrapped within the surface patterns/structures so that bubbles have little contact to the solid surface with an enlarged contact angle of the bubble (i.e., $\theta_b > 150^\circ$, where θ_b represents the contact angle of the bubble) [25]. On superhydrophobic surfaces, in contrast, air is typically entrapped within the surface patterns so that bubbles are merged with the air layer already entrapped on the surface and spread out over the superhydrophobic surfaces with a very small contact angle of the bubble (θ_b) as low as $0\text{--}5^\circ$ [26].

Most of the previous studies of bubble adhesion to solid surfaces were interested in adhesion between air bubbles and mineral surfaces [16, 17]. Most of the analyses of adhesion force between bubbles and solid surfaces were made on the vertical detachment of the bubble. For instance, Janczuk and Bialopiotrowicz [16] showed the relationship between the adhesion force of an air bubble and the bubble size, contact angle, and surface tension in detaching the bubble placed on a horizontal hydrophobic surface. In contrast, in this study, we analyze the lateral adhesion (friction or depinning) forces of air bubbles on hydrophilic and superhydrophilic surfaces on the basis of bubble sliding at inclination. On the other hand, the previous studies of bubbles on patterned superhydrophilic [25] or superhydrophobic [26] surfaces were mainly concerned with the morphology of bubbles and contact angles. The detailed investigation of the effects of surface wettability and patterns, as well as bubble volume on the

contact angle hysteresis, adhesion force, and sliding angle has not been carried out yet. The objective of this study is to investigate the adhesion and dynamic behaviors of a captive bubble on an inclined substrate with a micropillared superhydrophilic surface and compare these with those on a simple (i.e., flat) hydrophilic surface, including the contact angle hysteresis, sliding angle, and adhesion force with systematically varied bubble volume.

6.2 Theoretical Models

The wettability of an ideal (smooth and chemically homogeneous) solid surface, in terms of the contact angle between a gas-liquid interface and a solid surface, can be defined by the Young's equation [27]. Following the Young's equation, the contact angle of a bubble (θ_b) on a solid surface can be described by

$$\cos(180^\circ - \theta_b) = (\gamma_{sg} - \gamma_{sl}) / \gamma_{lg} \quad (6.1)$$

where θ_b represents the contact angle of the bubble, and γ_{sg} , γ_{sl} and γ_{lg} represent the interfacial tensions of solid-gas, solid-liquid, and liquid-gas interfaces, respectively (Figure 6.1). The external forces acting on the bubble can also affect the contact angle, especially when the bubble volume is large (i.e., Bond number is greater than one), including gravity (g : gravitational constant), buoyancy (F_B), and pressure force (F_p). In a quasi-static manner, there is a force balance between the surface tension and the external forces acting on a bubble [18]. The net external force acting on a bubble in the vertical direction ($F_{net/vertical}$) can be expressed as

$$F_{net/vertical} = F_B + F_p \quad (6.2)$$

where F_B represents the buoyancy force and F_p the other pressure-related force such as the Young-Laplace pressure. It was reported that a thin aqueous (wetting) film was likely to be retained between the air bubble and the solid surface, especially if the solid surface was hydrophilic [19, 28, 29]. However, such an aqueous film at the gas-solid interface is likely to be ruptured by the bubble and gets drained over time [29]. When there is no wetting film retained at the interface and the bubble directly attaches to the solid surface, the buoyancy force is not applied to the entire bubble but is only effective for a partial volume of the bubble where the difference of the hydrostatic pressure distribution between upward and downward

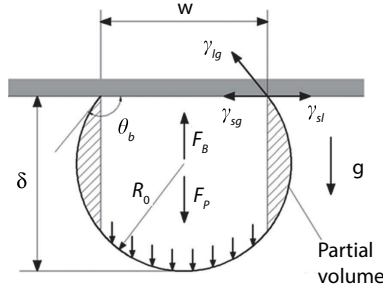


Figure 6.1 Contact angle of a bubble (θ_b) on a solid surface, defined by interfacial tensions γ_{sg} , γ_{sl} and γ_{lg} (s: solid, l: liquid, g: gas) and external forces acting on a bubble including buoyancy force (F_B) and the Laplace pressure force (F_P).

directions is present (Figure 6.1). Then, the effective buoyancy force acting on the partial volume can be approximated as:

$$F_B = (\rho_l - \rho_g)gV_{bubble} - (\rho_l - \rho_g)g\delta A \quad (6.3)$$

where ρ_l and ρ_g are the densities of liquid (e.g., water) and gas bubble (e.g., air), respectively, V_{bubble} is the total volume of the whole gas bubble, δ is the hydrostatic height of the bubble, and A is the surface area of the bubble base contacting the solid surface (i.e., $A = \pi w^2/4$, where w is the contact width or diameter) [18, 19]. Meanwhile, due to the curvature of the gas-liquid interface of the bubble, the Laplace pressure is present across the curved interface, especially at the bottom of the bubble. The force caused by the Laplace pressure can be expressed as

$$F_P = \frac{2\gamma_{lg}}{R_0} A \quad (6.4)$$

where R_0 represents the radius of curvature of the bubble, especially at the bottom part (apex) [18, 30].

Figure 6.2 illustrates the force balance acting on a bubble on an inclined surface. When the solid substrate is tilted (with a tilt angle of α), the bubble deforms due to the net vertical force (Figure 6.2a). In this case, the A in Equations (6.3) and (6.4) represents the horizontally projected surface area of the bubble base, i.e., $A = (\pi w^2/4)\cos\alpha$. If the net vertical force in the tangential direction ($F_{net/vertical} \sin\alpha$) is as large as the adhesion (or static

friction) force of the bubble on the surface (F_{adh}), the bubble will depin from the surface and slide upward (Figure 6.2b). Then, the lateral adhesion force of a bubble (F_{adh}) on an inclined surface can be estimated by

$$F_{adh} = F_{net/vertical} \sin \alpha \quad (6.5)$$

On the other hand, the lateral adhesion force (F_{adh}) can also be described by

$$F_{adh} = kw\gamma_{lg} (\cos \theta_{min} - \cos \theta_{max}) \quad (6.6)$$

where k is the retentive force factor, and θ_{min} and θ_{max} the minimum and maximum contact angles of the bubble on the downhill and uphill sides, respectively (Figure 6.2b). Such an equation was previously developed and used for a liquid droplet on an inclined plane [31], which can also be applied to the case of a bubble. Equation (6.6) indicates that the adhesion force between a bubble and a solid surface is affected by the contact width (w) and the cosine difference of the maximum and minimum contact angles (or contact angle hysteresis), which should be dependent on the bubble volume and the wettability of the surface [32, 33]. In Equation (6.6), the retentive force factor k also depends on the surface wettability, i.e., on the shape and length of the three-phase contact line of the bubble on the surface and it is generally evaluated experimentally [31, 34]. Receding and advancing contact angles are often used for θ_{min} and θ_{max} , respectively, for sliding droplets/bubbles. However, the minimum and maximum angles are not always necessarily the same as the receding and advancing contact angles [35]. From Equations

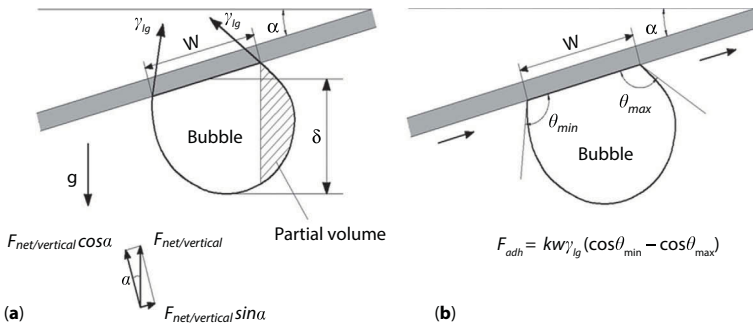


Figure 6.2 Forces acting on a captive bubble on an inclined surface. (a) Vertical net force and its tangential and normal components. (b) Lateral adhesion (static friction) force.

(6.5) and (6.6), the theoretical sliding angle (the critical inclination angle α at which the bubble starts to slide up) can then be described as [32]

$$\sin \alpha = \frac{kw\gamma_g (\cos \theta_{\min} - \cos \theta_{\max})}{F_{\text{net/vertical}}} \quad (6.7)$$

Equation (6.7) is physically the same as the Furmidge equation developed for a sliding liquid droplet on an inclined surface [36]. Equation (6.7) also suggests that the sliding angle is influenced by both the surface wettability (i.e., contact angle hysteresis) and the bubble volume (i.e., by $F_{\text{net/vertical}}$). In this study, we use Equation (6.6) to evaluate the adhesion force of a bubble to a superhydrophilic surface, and compare it to that to a hydrophilic surface. To use Equation (6.6), the contact width and angles (w , θ_{\min} and θ_{\max}) are experimentally measured, and then the best fit of the retentive force factor (k) is obtained from Equation (6.7) by using the experimentally measured sliding angles (α) and $F_{\text{net/vertical}}$ for both hydrophilic and superhydrophilic surfaces.

6.3 Experimental

A bare polished silicon substrate and a micropillared silicon substrate were used as hydrophilic and superhydrophilic surfaces, respectively. A square array of micropillars (5 μm in diameter, 12 μm in height, and 5 μm in spacing) was fabricated using photolithography and deep reactive ion etching (DRIE) techniques [13, 37]. The fabrication process is summarized in the following. First, a clean silicon wafer was spin-coated with a photoresist (SPR 3012, Shipley Megaposit) at 2000 rpm for 1 minute. Then the substrate was exposed to UV light in a soft contact mode to define microdot patterns using a mask aligner (MA-6, SUSS MicroTec, Garching, Germany) and developed in solution (MF-319, Shipley Megaposit) for 1 minute. After the microdot photoresist patterns were transferred to the substrate, the DRIE was applied to create high aspect-ratio micropillar structures on silicon. Finally, the photoresist layer used as the etch mask was removed by piranha solution (mixture of sulfuric acid (H_2SO_4) and hydrogen peroxide (H_2O_2), 3:1 by volume) and the substrate was rinsed with deionized water.

To investigate the adhesion and dynamic behaviors of an air bubble on these surfaces with inclination, the volume (V), width (w), height (δ), radius of curvature (R_0), and minimum/maximum contact angles (θ_{\min} and θ_{\max}) of the bubble and the sliding angle (α) were measured using a goniometer

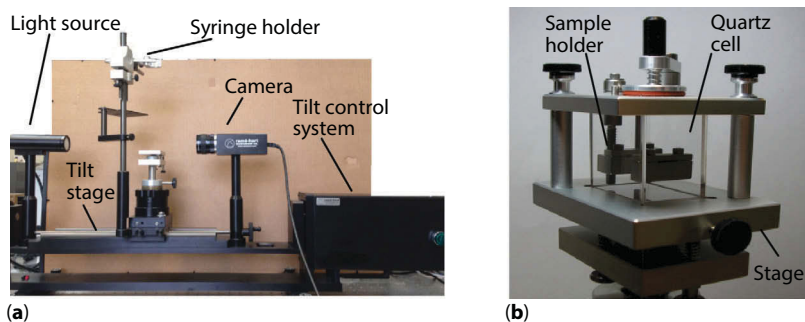


Figure 6.3 Experimental setup. (a) Goniometer. (b) Environmental chamber designed for captive bubble measurements.

system with an automated tilting base (Model 590, Rame-Hart) (Figure 6.3a). An environmental chamber (Figure 6.3b) was integrated into the goniometer system for experimentation with captive bubbles. The square quartz cell of the environmental chamber was filled with distilled water. All substrates were immersed in the water, and then air bubbles were injected beneath the underside of the surface (i.e., hydrophilic or superhydrophilic surface) using an inverted needle with a micro-syringe. The bubbles were left to sit on the surface for a few minutes until the apparent contact angles became constant. In order to measure the sliding angle and adhesion force of the air bubble, the goniometer stage was tilted gradually at a rate of 0.1 deg/s until the bubble started to depin and move upward on the surface. While the stage was tilted at a constant speed, the images of the bubble were captured at ten frames per second (10 fps). The captured images were analyzed to estimate the volume (V), width (w), height (δ), radius of curvature (R_0), and minimum/maximum contact angles (θ_{\min} and θ_{\max}) of the bubble, and the sliding angle (α), using image processing software (Dropimage advanced v2.4, Rame-Hart). The maximum/minimum contact angles were measured from the images showing the air bubble just before moving. In order to study the effect of bubble volume on the adhesion force and sliding angle, the volume of the bubble was varied in the range of 8–20 μL (Bond number, Bo on the order of 1, $Bo = (\rho_l - \rho_g)gL^2/\gamma_{lg}$, where L is a characteristic length, i.e., the diameter of the bubble).

6.4 Results and Discussion

Figure 6.4 shows the scanning electron microscope (SEM) images of the flat (polished and smooth) hydrophilic and the micropillared superhydrophilic

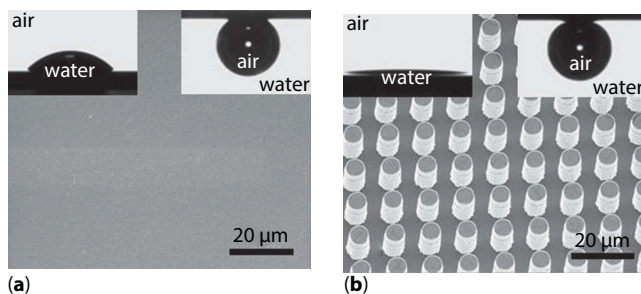


Figure 6.4 SEM images of hydrophilic (a) and superhydrophilic (b) surfaces and their wettabilities for a water droplet (left inset) and an air bubble (right inset). Scale bars are 20 μm .

surfaces. The insets in Figure 6.4 show the optical images of a sessile water droplet in air (left) as well as of a captive air bubble in water (right), a few microliters for both cases, on each surface, revealing different wettabilities of the surfaces. Compared to a flat hydrophilic surface ($\theta_w \cong 40^\circ$), the water droplet on the micropillared superhydrophilic surface shows almost complete wetting ($\theta_w < 10^\circ$). In case of a bubble, the contact angle of the bubble on the micropillared superhydrophilic surface ($\theta_b \cong 170^\circ$) is greater than that on the flat hydrophilic surface ($\theta_b \cong 140^\circ$). In case of the flat hydrophilic surface, the initial contact angle of the bubble was greater than 140° , but gradually decreased for a couple of hours and became stable at $\sim 140^\circ$. This indicates that the bubble gradually ruptured the thin water film initially retained at the gas-solid interface and came in direct contact with the solid surface. In contrast, in case of the micropillared superhydrophilic surface, there was no significant decrease of the initial contact angle of the bubble, suggesting that the thin water film trapped at the gas-solid interface would mostly be retained. Thus, in the case of a micropillared superhydrophilic surface, the effective surface area of the bubble contacting the solid surface (i.e., A in Equation (6.3)) is negligible so that it is ignored in the estimation of the buoyancy force (F_B).

When the substrates were tilted, the captive air bubble sitting on the superhydrophilic surface moved and slid up more easily at a lower sliding angle than on a hydrophilic surface. For example, Figure 6.5 shows the profiles of the air bubbles of the same volume (20 μL) on the hydrophilic and superhydrophilic surfaces, at both the initial horizontal position and the inclination at a sliding angle. When an air bubble sits on the micropillared superhydrophilic surface immersed in water, there is no direct contact between the bottom trench of the micropillared solid surface and

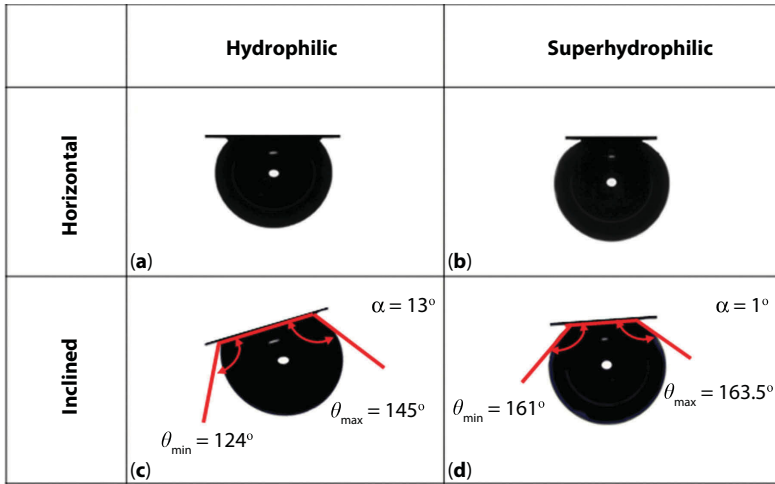


Figure 6.5 (a-b) Profiles of air bubbles on hydrophilic and superhydrophilic surfaces, respectively, in a horizontal position after stabilization. (c-d) Deformation of the air bubble at inclination (at sliding angle) and the change in contact angles. On the hydrophilic surface (c), the air bubble (20 μL) started to slide up at 13° with the maximum/minimum contact angles ($\theta_{\min}/\theta_{\max}$) of 145° and 124° , respectively. On the superhydrophilic surface (d), the air bubble (20 μL) started to slide up at 1° with the maximum/minimum contact angles ($\theta_{\min}/\theta_{\max}$) of 163.5° and 161° , respectively.

the bubble due to the water film trapped within the micropillar structures. Thus, the air bubble does not go into the microstructures and instead rests on the top of the micropillars. The Young-Laplace pressure force formed across the air-water meniscus of the bubble is much less than the capillary force applied by the micropillar structures so that the bubble cannot penetrate into the trenches of the micropillared surface to displace water between the micropillars [25, 38]. With the lubrication effect of the trapped water layer [39], the air bubble then becomes very mobile, and it moves easily with little friction at a lower sliding angle. As shown in Figure 6.5, the deformation of a bubble on the micropillared superhydrophilic surface is less significant with the lower sliding angle than on the flat hydrophilic surface. Thus, the difference between the maximum and the minimum contact angles (or contact angle hysteresis) at the onset of a sliding motion is less on the micropillared superhydrophilic surface than on the flat hydrophilic surface. The low contact angle hysteresis implies low adhesion force of a bubble according to Equation (6.6).

Figure 6.6 shows the experimentally measured values of the contact widths (Figure 6.6a), maximum/minimum contact angles (Figure 6.6b),

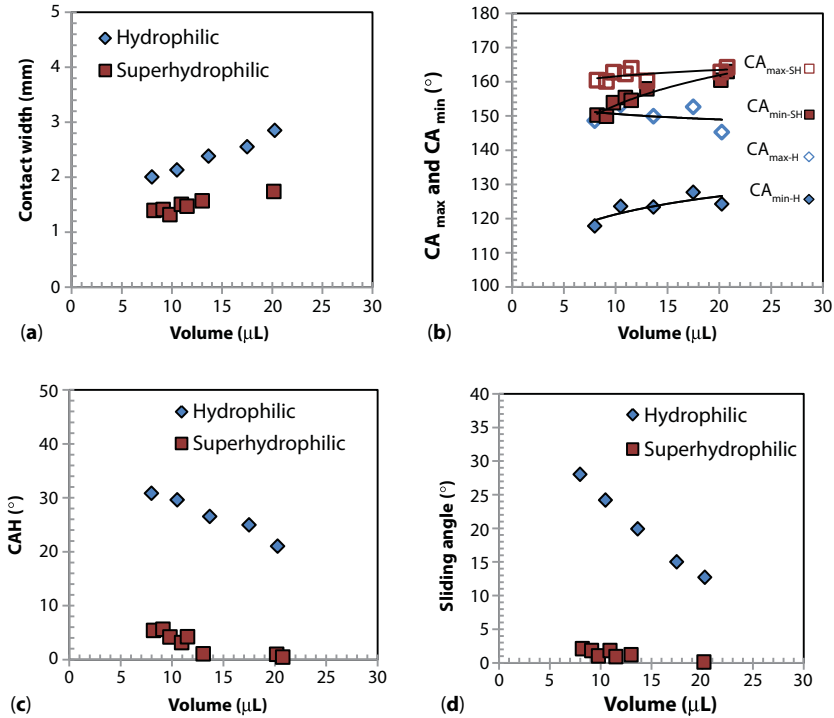


Figure 6.6 Experimental results. (a) Contact width. (b) Maximum and minimum contact angles (CA_{max} and CA_{min} where -SH and -H represent superhydrophilic and hydrophilic surfaces, respectively; the solid lines are drawn to show the trends). (c) Contact angle hysteresis (CAH = CA_{max} - CA_{min} = θ_{\max} - θ_{\min}). (d) Sliding angle.

contact angle hysteresis (CAH, Figure 6.6c), and sliding angles (Figure 6.6d) of the bubbles with different volumes. Figure 6.6a shows that the contact width of a bubble on the superhydrophilic surface is significantly lower than on the hydrophilic surface at the same bubble volume, which is due to the lower wettability (i.e., larger contact angle) of the bubble on the superhydrophilic surface. The contact width increases with the bubble volume for both cases. However, the contact width (w) increases at a slower rate than the increase rate of the volume (V), since $V \sim r^3$ (or w^3), where r is the radius of the bubble. The increase of the contact width with the bubble volume is less pronounced on the superhydrophilic surface due to the larger contact angle of the bubble than on the hydrophilic surface.

Figure 6.6b shows that the maximum contact angle (θ_{\max}) at the uphill (advancing) side does not change much even with the increase of the

bubble volume. However, it shows that the minimum contact angle (θ_{\min}) at the downhill (receding) side increases on both hydrophilic and superhydrophilic surfaces with the bubble volume. Both the maximum and the minimum contact angles on the superhydrophilic surface are greater than those on the hydrophilic surface. Meanwhile, the difference of maximum (or advancing) contact angles between the superhydrophilic and the hydrophilic surfaces is less than the difference of minimum (or receding) contact angles between the two surface types. These results indicate that the bubble adhesion and movement on both the flat hydrophilic and the micropillared superhydrophilic surfaces is mostly dominated by the receding motion of the three-phase contact line at the downhill side. The results also indicate that the bubble volume affects the minimum (or receding) contact angles at the downhill side (θ_{\min}) more than the maximum (or advancing) contact angles at the uphill side (θ_{\max}), agreeing with the previous report by Drelich *et al.* [33].

Moreover, as shown in Figure 6.6c, the difference between the maximum and the minimum contact angles (i.e., contact angle hysteresis) on the superhydrophilic surface is much lower than that on the hydrophilic surface. This implies that the adhesion force of a bubble on the superhydrophilic surface should be lower than that on the hydrophilic surface, according to Equation (6.6). Figure 6.6c further shows that the contact angle hysteresis decreases with the increase of the bubble volume for both hydrophilic and superhydrophilic surfaces. This is due to the more pronounced effect of the inertia force (i.e., buoyancy) on the bubble than that of a surface force (i.e., surface tension or friction) with the increase of the bubble volume. The Bond number ($Bo = \Delta\rho g L^2 / \gamma_{lg}$, where $\Delta\rho = \rho_l - \rho_g$, and L is a characteristic length, i.e., the diameter of the bubble) corresponding to the tested bubble volume of 8–20 μL (the bubble diameter on the order of 1 mm) is on the order of one. The Bond (Bo) number is a measure of the effect of surface tension force compared to body force (i.e., buoyancy or gravity) [30]. With the Bo number on the order of 1, the bubble system should be significantly affected by the buoyancy force as well as the surface tension force. The bubble size (diameter) is also comparable to the capillary length of water/air interface at standard temperature and pressure (~ 2 mm) and thus the buoyancy force can significantly affect the bubble shape (i.e., the maximum and minimum contact angles, or the contact angle hysteresis) along with the surface tension.

Figure 6.6d shows the experimentally measured sliding angles with varying bubble volume. As can be expected from Equation (6.7), the sliding angle on the superhydrophilic surface is much lower than that on the hydrophilic surface due to the lower contact angle hysteresis (CAH) or

lower cosine difference of the maximum and minimum contact angles ($\cos\theta_{\min} - \cos\theta_{\max}$) on the superhydrophilic surface. It also shows that the sliding angle decreases with the bubble volume. The major reason for this is that the contact angle hysteresis decreases with the bubble volume, as shown in Figure 6.6c. Another reason is that the rate of the contact width increase with respect to the bubble volume (i.e., w/V) is less than 1, as shown in Figure 6.6a. Therefore, the greater increase of the buoyancy force with the bubble volume than the increase of the adhesion force with the bubble contact width leads to the decrease of the sliding angle with the bubble volume, according to Equation (6.7). The decrease of the sliding angle with the bubble volume is more pronounced on the hydrophilic surface than on the superhydrophilic surface since the decrease of the contact angle hysteresis with the volume as well as the change of the contact width with the volume are both more significant on the hydrophilic surface than on the superhydrophilic surface.

From the experimental results shown in Figure 6.6, the retentive force factors (k) which best fitted Equation (6.7) were obtained for both hydrophilic and superhydrophilic surfaces. They were 2.1 and 0.4 for the hydrophilic and the superhydrophilic surfaces, respectively. Using these k values in Equation (6.7), Figure 6.7 shows the adhesion forces of bubbles with varying volumes on the superhydrophilic surface, as compared to a hydrophilic surface. As can be expected from Figures 6.6a and 6.6c, the adhesion force of a bubble on the superhydrophilic surface is much lower than that on the hydrophilic surface due to the significantly lower contact width and

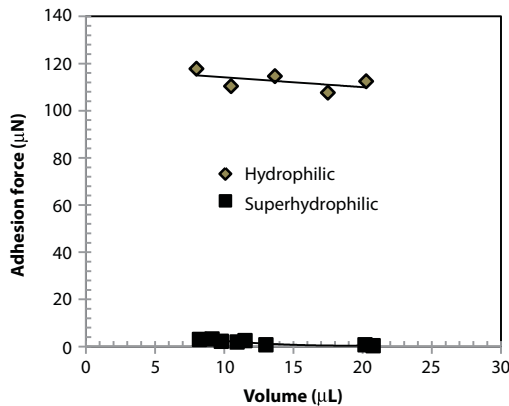


Figure 6.7 Adhesion forces of air bubbles of varying volumes on the hydrophilic and the superhydrophilic surfaces. (The solid lines are drawn to show the trends).

contact angle hysteresis. This also agrees with the result of the lower sliding angle on the superhydrophilic surface than on the hydrophilic surface as shown in Figure 6.6d. It should also be noted in Figure 6.7 that the adhesion force slightly decreases with the bubble volume. When the bubble volume increases, the contact width increases which will lead to increase in the adhesion force according to Equation (6.6) if the cosine difference of the maximum and minimum contact angles is constant. However, as shown in Figures 6.6b and 6.6c, the contact angle hysteresis (i.e., the cosine difference of the maximum and minimum contact angles) significantly decreases with the bubble volume. The effect of the decrease of the contact angle hysteresis (or the cosine difference of the maximum and minimum contact angles) with the bubble volume is more significant to the adhesion force than that of the increase of the contact width. Thus, overall, such opposing effects eventually result in the decrease of the adhesion force with the increase in the bubble volume.

6.5 Conclusions

In this study, the sliding angle and the adhesion force of a captive bubble with varying volume are investigated on a micropillared superhydrophilic surface, and are compared with those on a flat hydrophilic surface. The micropillared superhydrophilic surface shows lower sliding angle as well as lower adhesion force than the flat hydrophilic surface. This is mainly due to the trapped water layer between the micropillars, which reduces the contact width and the contact angle hysteresis on the superhydrophilic surface to a higher extent, compared to those on the hydrophilic surface. The sliding angle and the adhesion force of a bubble on both hydrophilic and the superhydrophilic surfaces decrease with the increase of bubble volume. This is also mainly due to the substantial decrease of the contact angle hysteresis with the increase of bubble volume. The increase of bubble volume makes the influence of the inertia force (i.e., buoyancy) to become important in bubble adhesion and sliding, affecting the shape and the contact angle hysteresis of a captive bubble at inclination significantly. The change in contact angle hysteresis with the bubble volume is greater than the change in the contact width (or area) to affect the adhesion (or static friction) force. Thus, the adhesion force and the sliding angle are eventually reduced with the increase of bubble volume. Especially, the sliding angle on a flat hydrophilic surface is more dependent on the bubble volume than on a micropillared superhydrophilic surface. This work shows that both the surface wettability and the bubble volume significantly affect both the

adhesion force and the sliding angle of a captive bubble. Such new understanding will be of great importance in many scientific and engineering applications dealing with bubbles such as boiling, flotation, nuclear reactors, biotechnology, and microfluidics.

Acknowledgement

This study was carried out, in part, at the Center for Functional Nanomaterials, Brookhaven National Laboratory, which is supported by the U.S. Department of Energy, Office of Basic Energy Sciences, under contract no. DE-AC02-98CH10886.

References

1. P.-G. de Gennes, F. Brochard-Wyart, D. Quéré, and B. Widom, Capillarity and wetting phenomena: Drops, bubbles, pearls, waves, *Phys. Today*, 57, 66-67 (2004).
2. D. Quéré, Wetting and roughness, *Annu. Rev. Mater. Res.*, 38, 71–99 (2008).
3. A. Marmur, Wetting on hydrophobic rough surfaces: To be heterogeneous or not to be?, *Langmuir*, 19, 8343–8348 (2003).
4. A. Marmur, Solid surface characterization by wetting, *Annu. Rev. Mater. Res.*, 39, 473–489 (2009).
5. B. Bhushan and Y. C. Jung, Wetting study of patterned surfaces for superhydrophobicity, *Ultramicroscopy*, 107, 1033–1041 (2007).
6. W. Xu and C.-H. Choi, Experimental studies on evaporation kinetics and wetting dynamics of nanofluid droplets on superhydrophobic surfaces of micro-post patterns, *J. Adhesion Sci. Technol.*, 25, 1305–1321 (2011).
7. Y. Liu and C.-H. Choi, Condensation-induced wetting state and contact angle hysteresis on superhydrophobic lotus leaves, *Colloid Polym. Sci.*, 291, 437–445 (2013).
8. R. Li, A. Alizadeh, and W. Shang, Adhesion of liquid droplets to rough surfaces, *Phys. Rev. E*, 82, 041608 (2010).
9. D. P. Das, Liquid water-droplet adhesion-force measurements on fresh and aged fuel-cell gas-diffusion layers, *J. Electrochem. Soc.*, 159, B489-B496 (2012).
10. C. Antonini, F. J. Carmona, E. Pierce, M. Marengo, and A. Amirfazli, General methodology for evaluating the adhesion force of drops and bubbles on solid surfaces, *Langmuir*, 25, 143–154 (2009).
11. H. Teisala, M. Tuominen, M. Aromaa, M. Stepien, J. M. Mäkelä, J. J. Saarinen, M. Toivakka, and J. Kuusipalo, Nanostructures increase water droplet adhesion on hierarchically rough superhydrophobic surfaces, *Langmuir*, 28, 3138–3145 (2012).

12. C. Jeong and C.-H. Choi, Single-step direct fabrication of pillar-on-pore hybrid nanostructures in anodizing aluminum for superior superhydrophobic efficiency, *ACS Appl. Mater. Interfaces*, 4, 842–848 (2012).
13. W. Xu and C.-H. Choi, From sticky to slippery droplets: Dynamics of contact line de-pinning on superhydrophobic surfaces, *Phys. Rev. Lett.*, 109, 024504 (2012).
14. A. Perron, L. I. Kiss, and S. Poncsák, An experimental investigation of the motion of single bubbles under a slightly inclined surface, *Int. J. Multiphase Flow*, 32, 606–622 (2006).
15. A. S. Najafi, Z. Xu, and J. Masliyah, Measurement of sliding velocity and induction time of a single micro-bubble under an inclined collector surface, *Can. J. Chem. Eng.*, 86, 1001–1010 (2008).
16. B. Jańczuk and T. Białopiotrowicz, Adhesion of air bubbles to Teflon surfaces in water, *J. Colloid Interface Sci.*, 128, 1–6 (1989).
17. B. Jańczuk, Adhesion of air bubbles to mineral surfaces in the presence of liquids, in *Encyclopedia of Surface and Colloid Science*, Vol. 1, A. T. Hubbard (Ed.), CRC Press, Boca Raton, FL (2002).
18. S. Vafaei and D. Wen, Bubble formation in a quiescent pool of gold nanoparticle suspension., *Adv. Colloid Interface Sci.*, 159, 72–93 (2010).
19. N. Hosoda and S. N. Gorb, Underwater locomotion in a terrestrial beetle: Combination of surface de-wetting and capillary forces, *Proc. Biol. Sci.*, 279, 4236–4242 (2012).
20. E. Hirose, H. Mayama, and A. Miyauchi, Does the aquatic invertebrate nipple array prevent bubble adhesion? An experiment using nanopillar sheets, *Biol. Lett.*, 9, 20130552 (2013).
21. H. Jo, H. S. Ahn, S. Kang, and M. H. Kim, A study of nucleate boiling heat transfer on hydrophilic, hydrophobic and heterogeneous wetting surfaces, *Int. J. Heat Mass Transfer*, 54, 5643–5652 (2011).
22. K. Cornwell, The influence of bubbly flow on boiling from a tube in a bundle, *Int. J. Heat Mass Transfer*, 33, 2579–2584 (1990).
23. N. Kantarci, F. Borak, and K. O. Ulgen, Bubble column reactors, *Process Biochem.*, 40, 2263–2283 (2005).
24. M. Vojtišek, M. D. Tarn, N. Hirota, and N. Pamme, Microfluidic devices in superconducting magnets: On-chip free-flow diamagnetophoresis of polymer particles and bubbles, *Microfluidics Nanofluidics*, 13, 625–635 (2012).
25. C. Dorrer and J. Rühle, Superaerophobicity: Repellence of air bubbles from submerged, surface-engineered silicon substrates, *Langmuir*, 28, 14968–14973 (2012).
26. J. Wang, Y. Zheng, F.-Q. Nie, J. Zhai, and L. Jiang, Air bubble bursting effect of lotus leaf, *Langmuir*, 25, 14129–14134 (2009).
27. T. Young, An essay on the cohesion of fluids, *Philos. Trans. R. Soc. London*, 95, 65–87 (1805).
28. A. R. Pushkarova and R. G. Horn, Surface forces measured between an air bubble and a solid surface in water, *Colloids Surfaces A*, 261, 147–152, (2005).

29. A. Nikolov and D. Wasan, Wetting-dewetting films: The role of structural forces, *Adv. Colloid Interface Sci.*, 206, 207–221 (2014).
30. N. S. Kaveh, E. S. J. Rudolph, P. Van Hemert, W. R. Rossen, and K. Wolf, Wettability evaluation of a CO₂/water/Bentheimer sandstone system : Contact angle, dissolution, and bubble size, *Energy Fuels*, 28, 4002–4020 (2014).
31. C. W. Extrand and Y. Kumagai, Liquid drops on an inclined plane: The relation between contact angles, drop shape, and retentive force, *J. Colloid Interface Sci.*, 170, 515–521 (1995).
32. A. Kibar, R. Ozbay, M. A. Sarshar, Y. T. Kang, and C.-H. Choi, Air bubble movement over and under hydrophobic surfaces in water, in: Proceedings of the 8th International Conference on Multiphase Flow, Jeju, Korea, (May 2013).
33. J. Drelich, J. D. Miller, and R. J. Good, The effect of drop (bubble) size on advancing and receding contact angles for heterogeneous and rough solid surfaces as observed with sessile-drop and captive-bubble techniques, *J. Colloid Interface Sci.*, 179, 37–50 (1996).
34. A. I. ElSherbini and A. M. Jacobi, Retention forces and contact angles for critical liquid drops on non-horizontal surfaces, *J. Colloid Interface Sci.*, 299, 841–849 (2006).
35. B. Krasovitski and A. Marmur, Drops down the hill: Theoretical study of limiting contact angles and the hysteresis range on a tilted plate, *Langmuir*, 21, 3881–3885 (2005).
36. C. G. L. Furmidge, Studies at phase interfaces. I. The sliding of liquid drops on solid surfaces and a theory for spray retention, *J. Colloid Sci.*, 17, 309–324 (1962).
37. W. Xu, R. Leeladhar, Y. T. Kang, and C.-H. Choi, Evaporation kinetics of sessile water droplets on micropillared superhydrophobic surfaces, *Langmuir*, 29, 6032–6041 (2013).
38. D. Bartolo, F. Bouamrine, É. Verneuil, A. Buguin, P. Silberzan, and S. Moulinet, Bouncing or sticky droplets: Impalement transitions on superhydrophobic micropatterned surfaces, *Europhys. Lett.*, 74, 299–305 (2006).
39. S. I. Karakashev, K. W. Stckelhuber, R. Tsekov, C. M. Phan, and G. Heinrich, Tribology of thin wetting films between bubble and moving solid surface, *Adv. Colloid Interface Sci.*, 210, 39–46 (2014).

Relationship Between the Roughness and Oleophilicity of Functional Surfaces

Luisa Coriand^{1,*}, Markus Rettenmayr² and Angela Duparré¹

¹*Fraunhofer Institute for Applied Optics and Precision Engineering,
Jena, Germany*

²*Friedrich-Schiller-University, Otto-Schott Institute of Materials Research,
Jena, Germany*

Abstract

We present first approaches and results to extend our measurement and analysis methodology for hydrophobic and hydrophilic wetting systems to oleophilic surfaces.

To investigate the relationship between the surface roughness and oleophilic wetting behavior, robust roughness analysis and apparent contact angle measurements for different environmental conditions are performed. The characterization of the roughness structures based on Power Spectral Density (PSD) functions determined from Atomic Force Microscopy (AFM) and White Light Interferometry (WLI) topography data is presented. Furthermore, our well-established wetting analysis methods are applied, optimized, and extended to the specific wetting situation with oil as the liquid phase.

Keywords: Oleophilic surfaces, contact angle, surface roughness, tribological systems

7.1 Introduction

The resistance to friction and wear of components for tribological systems plays a key role in their functionality and therefore for the application in daily life. For such highly stressed functional components, like motors with

*Corresponding author: luisa.coriand@iof.fraunhofer.de

bearings or gaskets, it is essential to realize optimal solid – solid interactions with minimal friction and without significant wear. Thus, the specific functionality of the system has to be preserved. In most cases, a specific lubricant is used to fulfill the needed requirements. For an efficient utilization of the given resources, it is important to use optimal films of the lubricant with only low amounts of oil. This can be achieved by optimizing the wetting system, especially through a defined functionalization of the relevant components. Here, the wetting properties of the surface can be controlled by the roughness characteristic, besides chemical composition, as it has been known for a long time [1–7].

This research focuses on achieving complete wettability (contact angle $< 5^\circ$) of oil using functional surfaces with specific roughnesses. For a wetting system with only oil as liquid phase and apparent contact angles smaller than 90° , the term “oleophilic” is used, where “oleo” (from Latin) refers to oils and “philic” (from Greek) refers to loving/attracting the liquid [8].

In this paper, we report on a measurement and analysis methodology to characterize the roughness as well as wetting properties. This also includes an approach to extend the methodology to oleophilic surfaces. The aim is to investigate the relationship between roughness and oleophilicity. Examples of rough stainless steel samples are given.

7.2 Basics and Experimental

7.2.1 Preparation of Rough Steel Surfaces

Stainless steel samples with a diameter of 50 mm and a thickness of 5 mm were prepared by different methods. The steel surfaces were polished using a final grain size of $1\ \mu\text{m}$ to achieve a homogeneous surface characteristic of all samples as initial condition for the following steps of treatment. To prepare steel surfaces with graded roughness, polishing processes with varying grain size ($3\ \mu\text{m}$, $15\ \mu\text{m}$, $30\ \mu\text{m}$) or lapping processes with varying so-called grit size (#800, #400) were utilized. The respective photographs are presented in Figure 7.1.

7.2.2 Roughness

A stochastically rough surface with a large diversity of spatial frequencies can be quantitatively described by Power Spectral Density (PSD) functions [9, 10]. The PSD function provides the relative strength of the individual roughness components as a function of the spatial frequencies f_x and f_y in

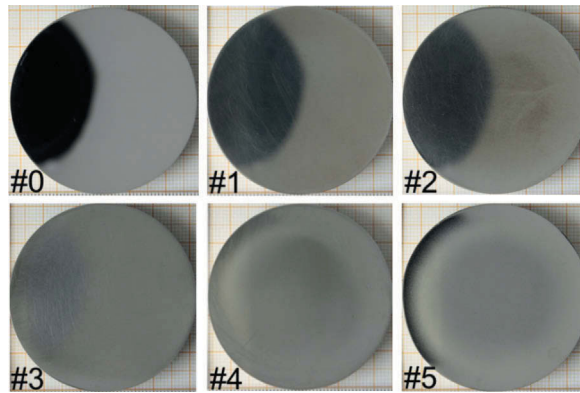


Figure 7.1 Photographs of the steel samples with varying surface finish: #0 (reference) polished (1 μm grain size), #1 ... #3 polished (grain size: 3 μm , 15 μm , 30 μm); #4 and #5 lapped (grit size: #800 and #400).

x and y directions, respectively. The PSD is defined as the squared absolute value of the Fourier Transform FT of the surface topography $z(x,y)$ within a scan range L:

$$PSD(f_x, f_y) = \lim_{L \rightarrow \infty} \frac{1}{L^2} |FT\{z(x, y)\}|^2 \quad (7.1)$$

For surfaces with isotropic roughness characteristics, the $PSD(f_x, f_y)$ can be simplified to a 2D-isotropic PSD by transforming into polar coordinates and averaging over all polar angles. By integration of the PSD, the root mean square roughness R_{rms} is obtained. The R_{rms} is the standard deviation of the surface topography data from the mean value.

In addition to the fact that the PSD function includes the vertical as well as the lateral distribution of surface heights, it also provides a direct link between the roughness characteristics and the wetting behavior of real surfaces. In previous works, a roughness based structural parameter was established, which is derived from the surface PSD by means of a data reduction procedure. This parameter is directly connected to the contact angle (CA) of the wetting system and enables separation of the influences of the roughness properties and of the material chemical properties on the wettability. Therefore, we call this (non-dimensional) quantity “wetting parameter” κ_B . Further information about κ_B as well as an overview of the algorithm developed at the Fraunhofer IOF is given in [11–13].

7.2.3 Wettability

The wettability of an ideal solid surface (smooth, rigid, chemically homogeneous, insoluble, and nonreactive) depends only on the surface and interfacial tensions γ . The relationship between the CA and the corresponding tensions is established by the Young theory [14]:

$$\cos\Theta_Y = \frac{\gamma_s - \gamma'_{sl}}{\gamma_l} \quad (7.2)$$

with the solid surface tension γ_s , the liquid surface tension γ_l , and the solid-liquid interfacial tension γ_{sl} . The Young CA Θ_Y can also be denoted as ideal CA or intrinsic CA. Based on this equation, the wettability of ideal solid surfaces by water drops can be classified into two states: intrinsically hydrophobic or water-repelling ($90^\circ < \Theta_Y < 180^\circ$) and intrinsically hydrophilic or water-attracting ($0^\circ \leq \Theta_Y < 90^\circ$). For a wetting system with oil or fat as the liquid phase, the prefix of the introduced terms will be “oleo” or “lipo”.

Depending on the liquid drop behavior on a rough solid surface, two classical and well-established wetting regimes can be distinguished: homogeneous (liquid completely covers the surface features) and heterogeneous (air situated in roughness structures below the liquid phase) wetting states [5]. For an oleophilic wetting system only the homogeneous situation is relevant, which can be described by the Wenzel equation [15]:

$$\cos\Theta_W = r \cdot \cos\Theta_Y \quad (7.3)$$

where the Wenzel CA (Θ_W) denotes the apparent CA (Θ_{ap}) and r is the roughness ratio (ratio of real solid surface area to its projected area). A detailed consideration of equation (7.3) leads to the conclusion that increasing roughness enhances the intrinsic wetting properties in both directions. For ideal smooth surfaces ($r = 1$), Θ_W is equal to the intrinsic CA Θ_Y .

7.2.4 Roughness Measurements

The roughness components of the treated steel surfaces were analyzed within a wide spatial frequency range using two different measurement techniques. The Atomic Force Microscopy (AFM) for the higher spatial frequency range, and the White Light Interferometry (WLI) for the lower range, were combined to analyze the roughness between the spatial frequency $f = 0.001 \mu\text{m}^{-1}$ and $f = 100 \mu\text{m}^{-1}$. The AFM measurements were

performed with a Dimension 3100 (Digital Instruments Veeco Metrology Group) in the Tapping Mode™ with single crystalline silicon probes (nominal tip radius: 10 nm). The vertical resolution is limited by instrumental noise to R_{rms} value as low as about 0.04 nm. For the WLI examinations an optical profilometer NewView 7300 (Zygo LOT) with a vertical resolution smaller than 0.1 nm was used.

For each sample, several measurements were performed at different positions and with different scan sizes. From these data, R_{rms} and PSD functions were calculated.

7.2.5 CA Measurements

For a comprehensive wetting analysis, e.g. characterization of the whole range of metastable CAs, it is necessary to determine the advancing and receding CAs [15, 16]. However, this method is most suitable for hydrophobic surfaces and becomes complicated for wetting systems with CA smaller than 20° . For such strong wettability the failure of the drop shape analysis increases caused by decreasing contrast between the drop, sample surface, and background with decreasing CA. In case of complete wettability ($CA < 5^\circ$) the determined advancing and receding drop shape contours are non-evaluable. Thus, instead of advancing and receding CA measurements, CAs with a defined volume of 3 μl were determined as a function of the wetting time t_w using a DataPhysics OCA20 measurement system [16]. This means the CA behavior is observed beginning with the first moment of contact between the liquid drop and the solid surface until the oleophilic wetting system reaches its equilibrium and hence a near-constant Θ_{ap} . For this kind of wetting system, three typical CAs for the drop spreading behavior can be defined:

- Θ_0 : Θ_{ap} at $t_w = 0$ s,
- $\Theta_{2.5..10s}$: mean of Θ_{ap} between 2.5 s and 10 s, and
- $\Theta_{50..100s}$: mean of Θ_{ap} between 50 s and 100 s.

Another important issue for the investigation of specific wetting systems is the optimization of the drop shape analysis. The analysis software SCA20 (DataPhysics) offers four different methods to calculate the CA [17]: Circle fitting, ellipse fitting, Laplace-Young fitting, and tangent leaning (Θ_{ap} are the slopes of the tangents which were determined at each contact point of the drop shape). The Laplace-Young fitting is the most exact method, but is not suitable for the analysis of recorded video data because of the large memory capacity requirement [18]. So, for the evaluation of

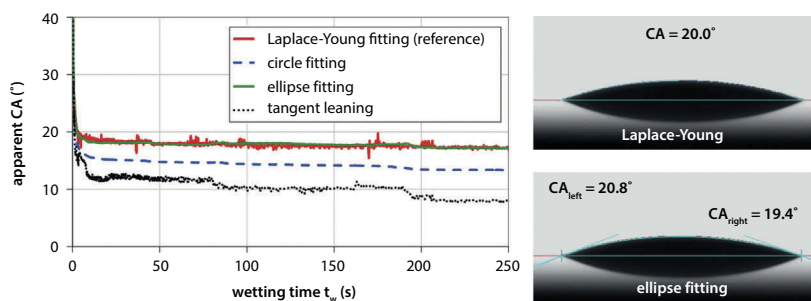


Figure 7.2 Apparent CA behavior as a function of the wetting time t_w (left) of a car engine oil drop on a metal surface determined using Laplace-Young fitting (drop shape and CA in the top right-hand corner); circle fitting; ellipse fitting (drop shape and CA in the bottom right-hand corner); and tangent leaning.

the suitability of the contour analysis methods, the Laplace-Young fitting is used as the reference method. Θ_{ap} of surfaces with different oleophilic wettabilities were observed and analyzed with circle fitting, ellipse fitting, and tangent leaning. This evaluation led to the conclusion that for the specific wetting system “metal surface – oil drop – air”, Θ_{ap} calculated by ellipse fitting shows the smallest deviations from the reference CA determined by the Laplace-Young fitting (see Figure 7.2). For this reason, the ellipse fitting was used to analyze the drop shapes in the case of oleophilic steel surfaces.

For the examination of the oleophilic wettability of steel surfaces conventional car engine oil was utilized.

7.3 Results and Discussion

7.3.1 Preliminary Investigation: Influence of Temperature and Effect of Pre-wetted Surface

Before starting the investigation regarding the relationship between roughness and oleophilicity, it was necessary to perform some preliminary investigation on the new wetting system “metal surface – oil drop – air”: The influence of the temperature on the wettability as well as the effect of a pre-wetted, or oily, surface was examined.

For the study of the influence of temperature, the metal surfaces were gradually heated from 30°C to 140°C in steps of 10°C. The results of the CA measurements are plotted in Figure 7.3. An almost linear decrease of the apparent CA Θ_{ap} with increasing substrate temperature can be clearly seen.

To determine the influence of an already wetted / oily surface on the CA behavior, two metal samples (A and B) with slightly different surface roughnesses were investigated under a clean and under an oily condition. The oily state was realized by wiping the sample surface with a tissue paper saturated with car engine oil. From Figure 7.4 it becomes obvious that a pre-wetted (oily) surface increases the wettability compared to a clean surface. In the case of a first contact with oil, both samples exhibit different CA behaviors depending on the surface characteristic. But for the wettability of oil on a pre-wetted surface, the CA clearly decreases to 5° , and no significant difference between the two samples can be observed.

Nevertheless, for the investigation of the relationship between surface roughness and oleophilicity, investigations were performed at room

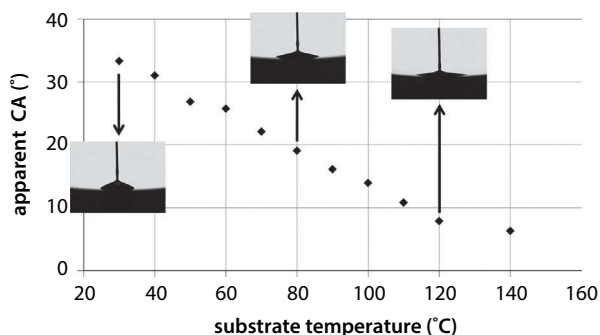


Figure 7.3 Apparent CA behavior of a car engine oil drop on a heated metal surface as a function of the substrate temperature.

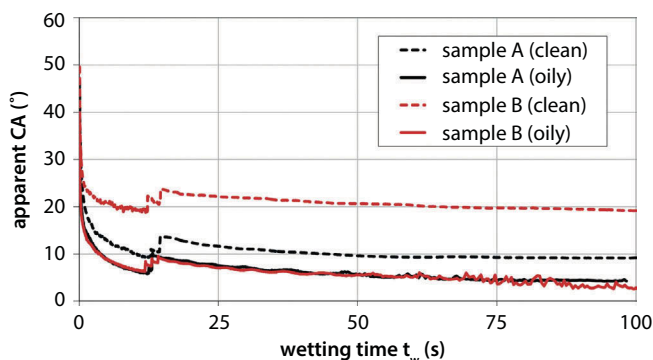


Figure 7.4 Apparent CA behavior of car engine oil drops on “clean” surfaces compared to “oily” surfaces as a function of the wetting time t_w .

temperature ($T = 23^\circ\text{C}$) and with “clean” surfaces. The roughness effect on wettability is much more pronounced for these conditions than for high temperature or oily surfaces.

7.3.2 Relationship Between Roughness and Oleophilicity

Characteristic topography images of selected steel surfaces can be seen in Figure 7.5. The R_{rms} values calculated from the topography data for all samples in each investigated scan area are listed in Table 7.1. These results show that the chosen preparation process leads to a series of samples with graded surface roughness: An increasing grain or grit size during the polishing or lapping (from samples #1 to #5) results in an increasing surfaces roughness. This is confirmed by the PSD functions presented in Figure 7.6.

Furthermore, the PSDs also reveal that the surface roughness depends on the scan area or spatial frequency range: For example, in the high spatial frequency range ($f > 1 \mu\text{m}^{-1}$) sample #1 exhibits higher PSD values than sample #2. This changes for spatial frequency between $0.01 \mu\text{m}^{-1}$ and $0.4 \mu\text{m}^{-1}$, and sample #1 is smoother than sample #2. The same behavior can be observed for the samples #4 and #5.

κ_b values (Table 7.1) were calculated from the PSD functions for four different spatial frequency decades between $0.01 \mu\text{m}^{-1}$ and $100 \mu\text{m}^{-1}$. The samples #4 and #5 exhibit the highest wetting parameter in this sample series, and hence for both samples the best wettability, i.e. the lowest CA, is expected.

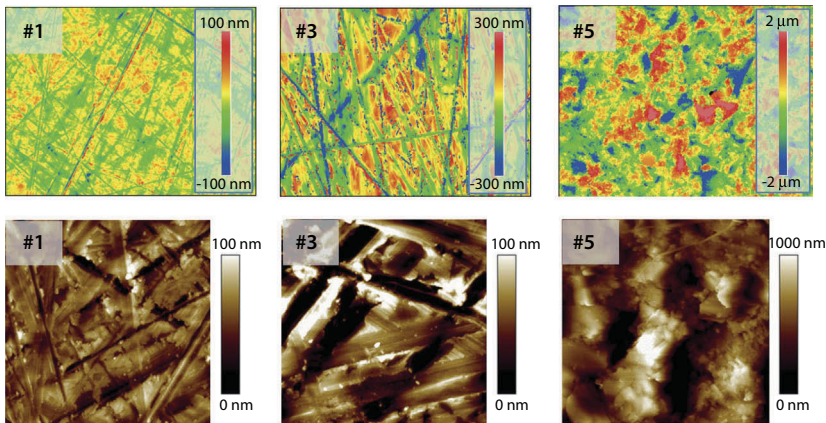


Figure 7.5 Surface topography (upper row: WLI images $140 \mu\text{m} \times 105 \mu\text{m}$; lower row: AFM images $10 \mu\text{m} \times 10 \mu\text{m}$) of selected steel surfaces.

Table 7.1 Root mean square roughness R_{rms} , from at least two individual measurement positions in different scan areas, and wetting parameter κ_B , determined within the investigated spatial frequency range, of the steel samples with graded surface roughness.

Samples	R_{rms} value (nm)						κ_B
	$1 \times 1 \mu\text{m}^2$	$10 \times 10 \mu\text{m}^2$	$50 \times 50 \mu\text{m}^2$	$360 \times 270 \mu\text{m}^2$	$140 \times 105 \mu\text{m}^2$	$35 \times 26 \mu\text{m}^2$	
#0	0.8	0.8	1.9	2.1	5.0	13	0.01
#1	5.5	15	19	22	32	22	0.05
#2	4.4	13	28	48	44	32	0.03
#3	7.4	37	90	117	128	83	0.09
#4	57	129	209	321	318	266	0.30
#5	40	243	> 460	781	783	699	0.28

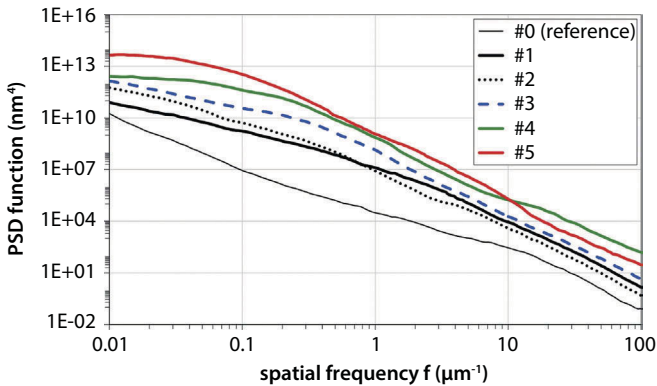


Figure 7.6 PSD functions of the steel surfaces with graded surface roughness.

The results of the CA measurements are given in Figure 7.7. It becomes obvious that a different wetting behavior could be achieved depending on the roughness characteristic (cf. κ_B values). These observations agree with the classical relationships between the roughness properties and the wettability given by the Wenzel equation (see Equation 7.3) and are illustrated by Johnson and Dettre [4] through the simulation of the roughness effect on the wettability using examples of idealized, mono-harmonic

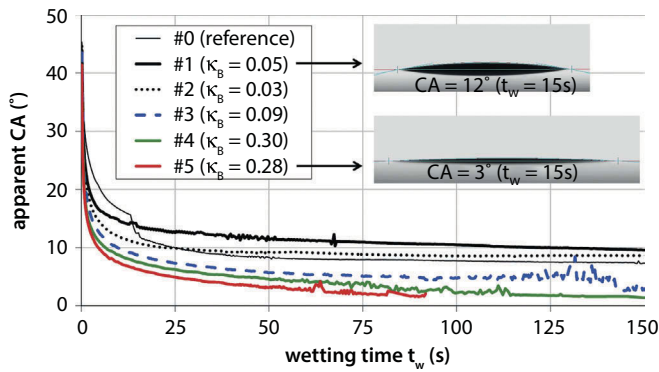


Figure 7.7 Apparent CA behavior of car engine oil drops on steel surfaces with graded surface roughness as a function of the wetting time t_w . Additionally, the wetting parameters κ_B for all samples are listed in the legend.

Table 7.2 Wetting parameters κ_B and apparent CA values for different wetting times t_w of the steel surfaces with graded surface roughness.

Sample	κ_B	Apparent CA (°)		
		$t_w = 0\text{ s}$	$2.5\text{ s} \leq t_w \leq 10\text{ s}$	$50\text{ s} \leq t_w \leq 100\text{ s}$
#0 (reference)	0.01	62 ± 17	19 ± 3	8 ± 3
#1	0.05	54 ± 17	15 ± 3	10 ± 3
#2	0.03	73 ± 21	14 ± 3	9 ± 3
#3	0.09	79 ± 25	12 ± 3	5 ± 3
#4	0.30	55 ± 4	10 ± 3	4 ± 3
#5	0.28	59 ± 5	9 ± 3	3 ± 3

hydrophobic/-philic surfaces. In the case of “-philic” surfaces, an increase of the roughness results in stronger wetting. Moreover, the prediction based on the κ_B -method was confirmed from the lowest CA for the surfaces with the highest roughness (#4, #5). The steel surface #5 shows a pronounced oleophilicity due to the fact that it is not possible to determine the CA over the captured time frame, because the CA is smaller than 3°. Hence, the contrast between the drop, surface, and background is too low to determine exact CA.

By comparing the typical CAs for different time frames with the κ_B values (Table 7.2), in particular for a CA between 2.5 s and 10 s (Figure 7.8),

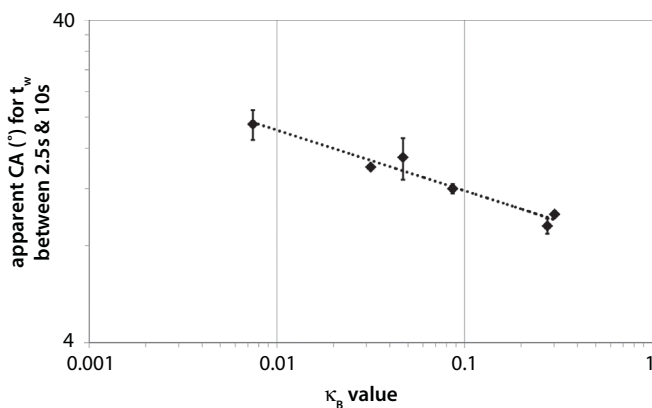


Figure 7.8 Apparent CA behavior of car engine oil drops on steel surfaces with graded surface roughness as a function of the wetting parameter κ_B (calculated within a spatial frequency range of $0.01 \mu\text{m}^{-1}$ to $100 \mu\text{m}^{-1}$).

it can be concluded that the roughness property correlates with the oleophilicity: With increasing surfaces roughness, the CA decreases almost linearly (in logarithmic scale) from $\Theta_{\text{ap}} = 19^\circ$ for the smooth reference sample #0 ($\kappa_B = 0.01$) to nearly 10° for the samples with the highest κ_B values of around 0.3.

7.4 Summary

Our wetting analysis methodology was optimized for the wetting system “metal surface – oil drop – air”. Simultaneously, the influences of the system temperature and surface condition on the wettability were investigated. The results show that the CA behavior clearly depends on these environmental conditions.

After these preliminary examinations, the surface structures of the stainless steel samples with varying surface finish were examined using Atomic Force Microscopy and White Light Interferometry. Utilizing the achieved roughness information, the wetting parameters κ_B were determined and thus first approaches to extend this roughness structure assessment to oleophilic surfaces were performed. Afterwards, the predictions were confirmed by CA measurements. Rough steel surfaces exhibited pronounced oleophilicity with CA smaller than 5° after a wetting time of 50 s.

In conclusion, our investigations of rough stainless steel surfaces revealed that the surface roughness clearly influences the oleophilicity. This means there is a correlation between the roughness and wetting properties.

Acknowledgements

This work has been supported by the Federal Ministry of Education and Research (joint project “SmartSurf”). We gratefully acknowledge the contributions of Dr. Stephanie Lippmann (Friedrich-Schiller-University) and Gilbert Leibeling (Fraunhofer IOF) for the sample preparation as well as Christian Wiede, Nadja Felde (both Fraunhofer IOF) and Erik Forwerk for their experimental investigations.

References

1. E. Wolfram and R. Faust, Liquid drops on a tilted plate: Contact angle hysteresis and the Young contact angle, in: *Wetting, Spreading and Adhesion*, J.F. Padday (Ed.) pp. 213-222, Academic Press, London, UK (1978).
2. R.N. Wenzel, Resistance of solid surfaces to wetting by water, *Ind. Eng. Chem.* 28, 988-994 (1936).
3. A.B.D. Cassie and S. Baxter, Wettability of porous surfaces, *Trans. Faraday Soc.* 40, 546-551 (1944).
4. R.E. Johnson, Jr. and H.R. Dettre, Contact angle hysteresis. I. Study of an idealized rough Surface, in: *Contact Angle, Wettability, and Adhesion*, *Adv. Chem. Ser.* No.43, American Chemical Society, Washington, D.C., pp. 112-135 (1964).
5. A. Marmur, Soft contact: Measurement and interpretation of contact angles, *Soft Matter* 2, 12-17 (2006).
6. Y.C. Jung, B. Bhushan, Contact angle, adhesion and friction properties of micro- and nanopatterned polymers for superhydrophobicity, *Nanotechnology* 17, 4970-4980 (2006).
7. D. Quéré, Wetting and roughness, *Annual Rev. Mater. Res.* 38, 71-99 (2008).
8. A. Marmur, Hydro- hydro- oleo- omni-phobic? Terminology of wettability classification, *Soft Matter* 8, 2867-2870 (2012).
9. J.M. Bennett and L. Mattsson, *Introduction to Surface Roughness and Scattering*. 2nd ed. Optical Society of America, Washington, D.C. (1999).
10. A. Duparré, J. Ferré-Borrull, S. Gliech, G. Notni, J. Steinert, and J. M. Bennett, Surface characterization techniques for determining rms roughness and power spectral densities of optical components, *Appl. Opt.* 41, 154-171 (2002).
11. M. Flemming and A. Duparré, Design and characterization of nanostructured ultrahydrophobic coatings, *Appl. Opt.* 45, 1397-1401 (2006).

12. M. Flemming, L. Coriand, and A. Duparré, Ultra-hydrophobicity through stochastic surface roughness, in: *Superhydrophobic Surfaces*, A. Carré and K.L. Mittal (Eds.) pp.19-38, CRC Press, Boca Raton, FL.(2009)
13. A. Duparré and L. Coriand, Assessment criteria for superhydrophobic surfaces with stochastic roughness, in *Advances in Contact Angle, Wettability and Adhesion*, Vol. 1, K.L. Mittal (Ed.) pp. 197-201, Wiley-Scrivener, Beverly, MA (2013).
14. T. Young, An essay on the cohesion of fluids, *Philos. Trans. Royal Soc.* London 95, 65-87 (1805).
15. A. Marmur, Equilibrium contact angles: Theory and measurement, *Colloids Surfaces A* 116, 55-61 (1996).
16. L. Coriand, M. Mitterhuber, A. Duparré, and A. Tünnermann, Definition of roughness structures for superhydrophobic and hydrophilic optical coatings on glass, *Appl. Opt.* 50, C257-C263 (2011).
17. *DataPhysics Instruments GmbH*, User's manual OCA (2005).
18. *DataPhysics Instruments GmbH*, Determination of contact angles through different methods of the drop shape analysis (2010).

Liquid Repellent Amorphous Carbon Nanoparticle Networks

Ilker S. Bayer^{1,2,*}, Alexander J. Davis¹ and Eric Loth²

¹*Smart Materials, Istituto Italiano di Tecnologia, Genova, Italy*

²*Department of Mechanical and Aerospace Engineering,
University of Virginia, Charlottesville, VA, USA*

Abstract

This chapter aims to present an overview of the use of amorphous carbon nanoparticle films, generally referred to as carbonaceous films, towards liquid repellent technologies. The most common way of producing these films is by impinging a diffusion flame onto a target surface that collects the “soot” particles. Carbon nanoparticles collected in this way are generally amorphous in nature and form a porous nano-textured network having the suitable roughness features for liquid repellency. In fact, such flame synthesized carbonaceous films display superhydrophobicity due to the combination of hydrophobic chemistry of the carbon particles and the sub-micrometer surface texture. However, they display very poor adhesion to the surface they are deposited on and hence cannot be used as liquid repellent surfaces except for the possibility of using their morphology as a template. The number of publications on liquid repellent carbonaceous films is very small as compared to other reported liquid repellent structures made by carbon nanotubes, nanofibers or graphene, mostly due to the aforementioned substrate adhesion problem. However, recently there have been some advances towards rendering them more durable and robust by depositing them on various polymeric surfaces or other micro-textured substrates such that partial melting of the substrate during flame impingement enables good bonding between the substrate and carbon nanoparticles. This chapter will first introduce the recent works related to liquid repellent nano-structured carbon nanoparticle films and their applications and then will present the new concepts and recent works conducted in the authors’ laboratories towards producing more robust liquid repellent carbonaceous films by direct flame impingement and deposition.

*Corresponding author: ilker.bayer@iit.it

Keywords: amorphous carbon, soot, carbon nanoparticles, superhydrophobic, liquid jet impact.

8.1 Introduction

The synthesis of carbonaceous films (porous nanocarbon) is beyond the scope of this chapter. The early work of Dobbins and Megaridis [1] can be consulted on the details related to flame synthesis of carbon nanoparticle agglomerates. Over the past few decades, porous nanocarbons with specific morphology have become attractive due to a number of inherent properties such as sorption ability, chemical stability, low density, suitability for large scale production and their inherent hydrophobicity (particularly from flame synthesis). As such, a number of potential technological applications of the porous nanocarbons can be envisioned in hydrogen storage, electric double-layer capacitors, as well as in fluid management and corrosion control. As an example, a recent study by Wei *et al.* [2] has established cost-efficient, environmentally stable and abundant candle soot (Figure 8.1) as an efficient hole extractor and developed the concept of clamping solar cells by carefully interfacing the candle soot with perovskite ($\text{CH}_3\text{NH}_3\text{PbI}_3$) films. Femtosecond time-resolved photo-luminescence (PL) and distance-dependent PL measurements have confirmed that the improved power conversion efficiency is largely due to the enhanced directional hole extraction at the candle soot/perovskite interface. The soot/perovskite interface that promotes hole extraction and electron blocking by forming a Schottky junction was made by flame deposition of soot on the perovskite layer [2].

The morphology and structure of porous nanocarbons are very sensitive to the synthesis method [3]. Figure 8.2, for example, demonstrates the typical morphology of porous nanocarbon films made up of connected carbon nanoparticle aggregates obtained by a solution synthesis method. This structure is made up of closely packed carbon nanoparticles and differs considerably from the flame synthesized carbonaceous films.

8.2 Templates for Liquid Repellent Surfaces

Candle light soot can also be used to generate nanoporous rough carbonaceous surfaces (*a*-C surfaces) which can be used as templates for fabrication of liquid repellent surfaces as described by Deng *et al.* [4]. The

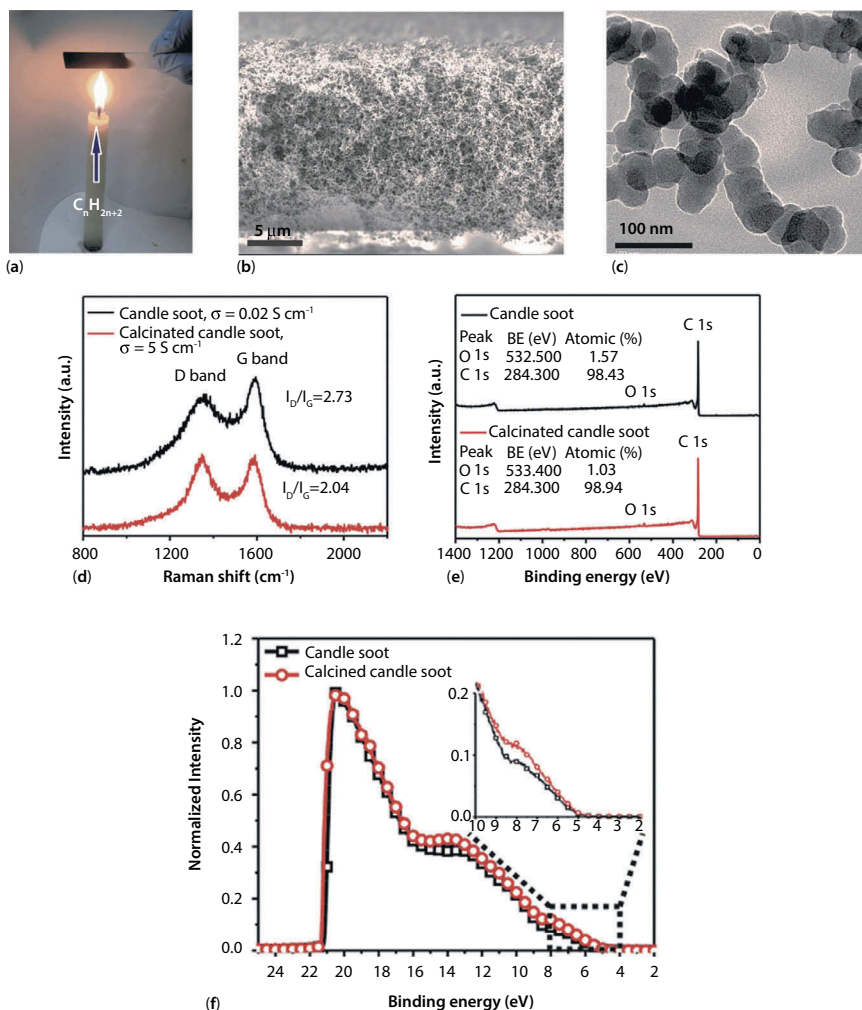


Figure 8.1 Characterization of as-prepared and calcined candle soot. (a) A digital photograph portraying the flame deposition of candle soot. (b) Cross-sectional SEM image of the sponge-like candle soot film. (c) TEM image of the as-prepared bi-continuous network of chain-like candle soot nanoparticles. (d) Raman spectra of the as-prepared and the calcined candle soot. (e) X-ray photoelectron spectra (XPS) and (f) ultraviolet photoelectron spectra (UPS) of the as-prepared and the calcined candle soot. With permission from [2].

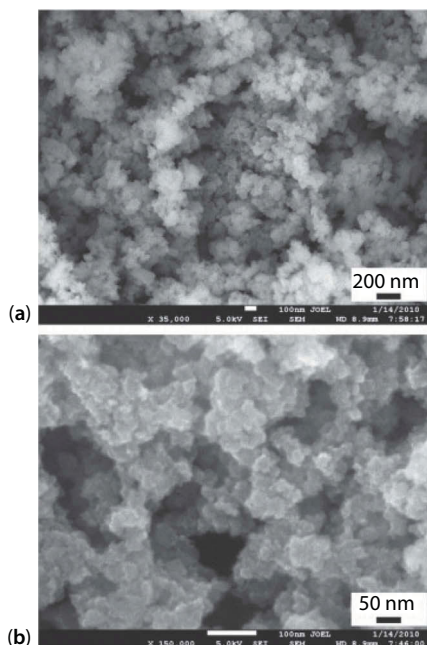


Figure 8.2 SEM micrographs of the amorphous carbon nanoparticles synthesized by a solution based method at different magnifications. With permission from [3].

carbonaceous films can be wetted and coated with silica precursors, for instance, to transfer their porous and hierarchical morphology after calcination and burning away of the carbon. After calcination, a similar morphology (negative image) made up of silica can be obtained which can further be functionalized with fluorinated chemicals for liquid repellency (see Figure 8.3).

Other works such as the one reported by Liu *et al.* [5] also developed methods for the facile synthesis of transparent superhydrophobic materials such as TiO_2 films by using the flame soot layer as a nano-imprint template. After the nano-imprint stage and calcination process, the TiO_2 coating exhibited the inverse roughness structure of the soot layer with high transparency. Subsequent hydrophobic modification with 1H,1H,2H,2H-perfluorodecyltriethoxysilane rendered the transparent surfaces superhydrophobic. The transparency and superhydrophobicity of such TiO_2 coatings could be controlled by adjusting the initial concentration of the TiO_2 suspension. The coatings possess good chemical stability and good mechanical resistance. Moreover, a superhydrophobic–superhydrophilic micrometer scale pattern was further fabricated by

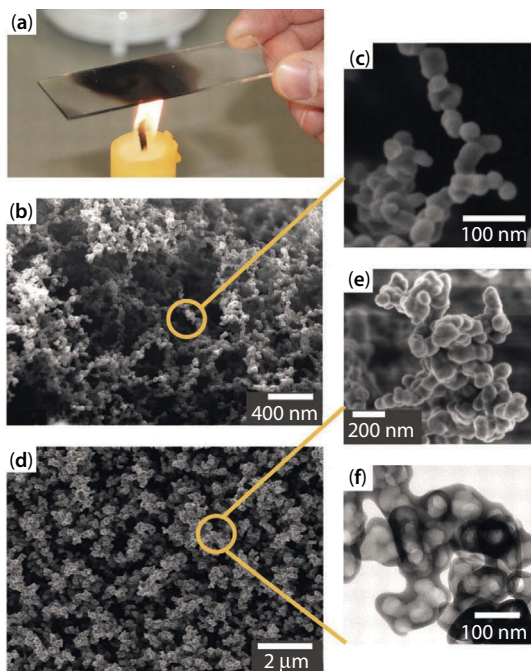


Figure 8.3 (a) A glass slide is held in the flame of a candle until a soot layer a few micrometers thick is deposited. (b) Scanning electron microscope (SEM) image of the soot deposit. (c) High-resolution SEM image showing a single particle chain made up of almost spherical carbon beads 40 ± 10 nm in diameter. (d) SEM image of the deposit after being coated with a silica shell. (e) High-resolution SEM image of a cluster after the carbon core was removed by heating for 2 hours at 600°C . (f) High-resolution TEM image of a cluster after calcination, revealing the silica coating with holes that were previously filled with carbon particles. The silica shell is 20 ± 5 nm thick. With permission from [4].

illumination with ultraviolet light through a photomask (see Figure 8.4). The pattern was immersed in a fluorescent Ag precursor solution. The silver aqueous solution only wetted the super-hydrophilic circular regions (droplets in Figure 8.4b). After several minutes of UV irradiation, Ag precursor droplets resting on the superhydrophilic region changed color to black (Figure 8.4c). After being washed by water and alcohol, brown residues in the superhydrophilic region remained where the Ag nanoparticles attached to the TiO_2 rough surface. It is expected that the wettability pattern might have some potential applications, for example, the fabrication of nanoarray pattern and single-cell analysis in bio-microfluidic research.

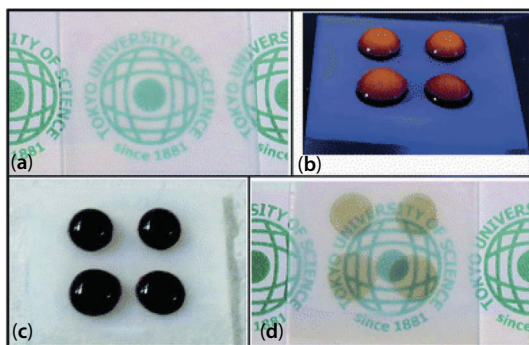


Figure 8.4 (a) Optical micrograph of a superhydrophobic–superhydrophilic pattern, under the visible light. Superhydrophilic zones are invisible under visible light. (b) Aqueous silver precursor droplets deposited on the superhydrophilic zones after immersion in solution, photographed under UV light with excitation at 365 nm (c) After UV illumination the silver solution turns black (reduction of silver salts into metallic silver nanoparticles) (d) Stains (silver nanoparticle deposits) left by the irradiated droplets seen in (c) after removing them from the surface. With permission from [5].

8.3 Synthesis Without Flames

Although flame synthesis appears to be the easiest way of producing amorphous carbon structures, α -C films with nano-structured surfaces can also be deposited on substrates with magnetron sputtering method [6]. The morphologies of the surfaces vary with the deposition parameters. Therefore, these α -C surfaces can be controlled to exhibit different wettability states ranging from hydrophilic to superhydrophobic. For instance, CF_4 plasma treatment would remarkably enhance the phobicity of such films against other liquids including those with acidic and basic nature. Moreover, a superhydrophobic surface of the non-fluorinated α -C film can be reversed to hydrophilic by treatment with H_2 or N_2 plasma as shown in Figure 8.5. These films, however, do not show reasonable resistance to abrasion as even by gentle touching or rubbing they can be removed from the surfaces on which they are deposited.

Similarly, a recent report [7] presents a facile single-step method for fabricating porous carbon nanoparticle (CNP) networks with tunable wettability and absorbability. These materials were prepared by glow discharge deposition at pressures of 100 to 500 mTorr using C_2H_2 and a gas mixture of C_2H_2 and CF_4 as the carbon precursors. Porous CNP network materials were made at high deposition pressures above 200 mTorr at a low temperature ($<50^\circ\text{C}$), facilitating the coating of these materials onto other

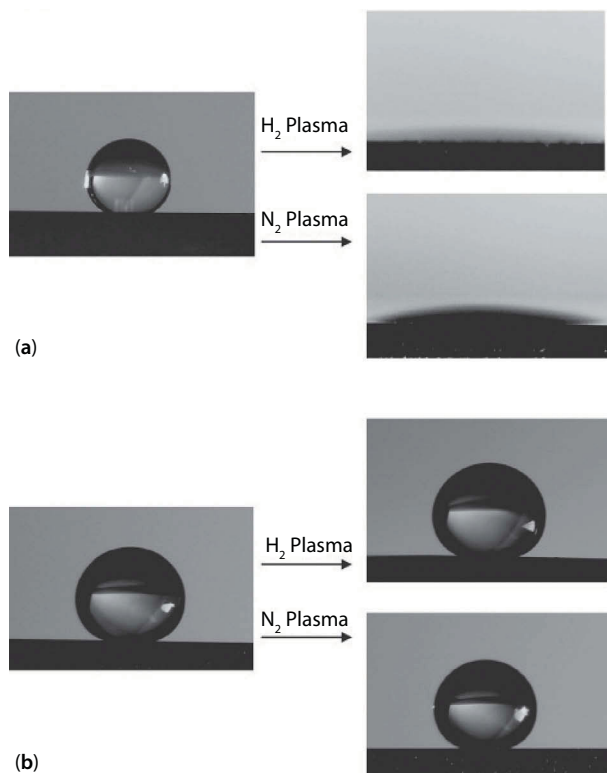


Figure 8.5 The shapes of water droplets on the α -C films before (left) and after (right) H₂ or N₂ plasma treatment, respectively. (a) Superhydrophobic α -C film and (b) superhydrophobic fluorinated α -C film. With permission from [6].

materials such as paper, polymers and metals. Furthermore, the porous CNP network materials with various fluorine contents showed selective repellency and absorption of liquids with different surface tensions enabling their potential use in water filtration, liquid separation or oil-spill (or organics) cleanup. Figure 8.6 shows structural and morphological details (Figures 8.6a, 8.6b, 8.6c and 8.6d) of these CNP network materials along with photographs (Figures 8.6e and 8.6f) depicting liquid repellent properties.

The static CAs and corresponding CAH values measured for the F-porous CNP network materials deposited with various CF₄/C₂H₂ ratios are shown in Figures 8.7a and 8.7b. It should be noted that as the CF₄/C₂H₂ ratio in the gas mixture increased, the static water CA of the fluorinated carbonaceous (F-porous CNP network) coatings increased, whereas the CAH dropped. When the CF₄/C₂H₂ ratio was 16/4, the porous CNP

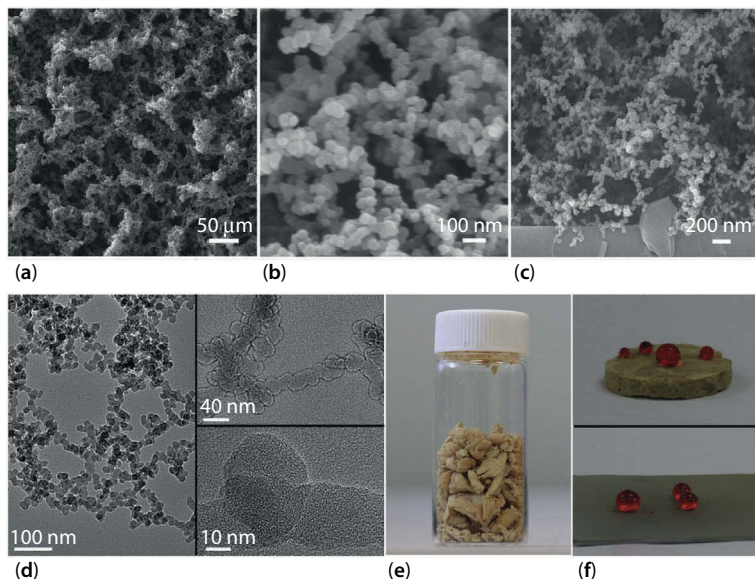


Figure 8.6 (a) SEM images of the sooty nanoporous film; (b) detailed view of the SEM image; (c) cross-sectional view of the carbonaceous film; (d) corresponding TEM image; (e) optical image showing a collection of porous CNP materials deposited for 30 min in a vial measuring 2 cm in diameter; (f) water droplets placed on the porous CNP network coated onto the Si substrate (lower panel) and on the collected porous CNP networks compressed into a solid disk (upper panel). With permission from [7].

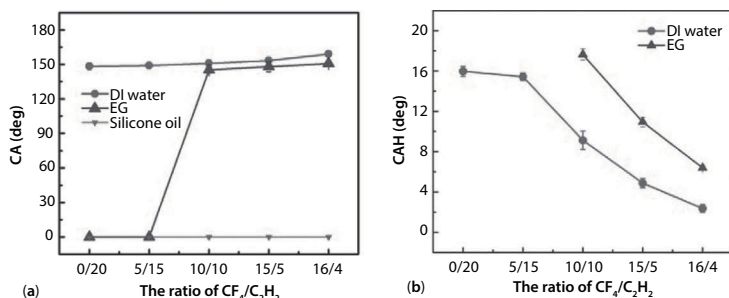


Figure 8.7 (a) Static contact angles and (b) contact angle hysteresis of the as-deposited porous carbonaceous materials as a function of the $\text{CF}_4/\text{C}_2\text{H}_2$ ratio in the precursor; (c) a schematic design of the water/oil separation process on the porous carbonaceous coating/filter paper (top), and photographs of the water/silicone oil mixture placed on the fluorinated (F-porous) carbonaceous coating/filter paper (below); (d) the states of various liquids such as water, ethylene glycol (EG), silicone oil and their mixtures deposited on the surfaces of the filter paper and paper coated with porous carbon and F-porous carbon. The water droplet was dyed red, the silicone oil blue, and ethylene glycol was clear; (e) a layer of silicone oil on the water can be removed by adding superhydrophobic carbonaceous film. With permission from [7]. (*Continued*)

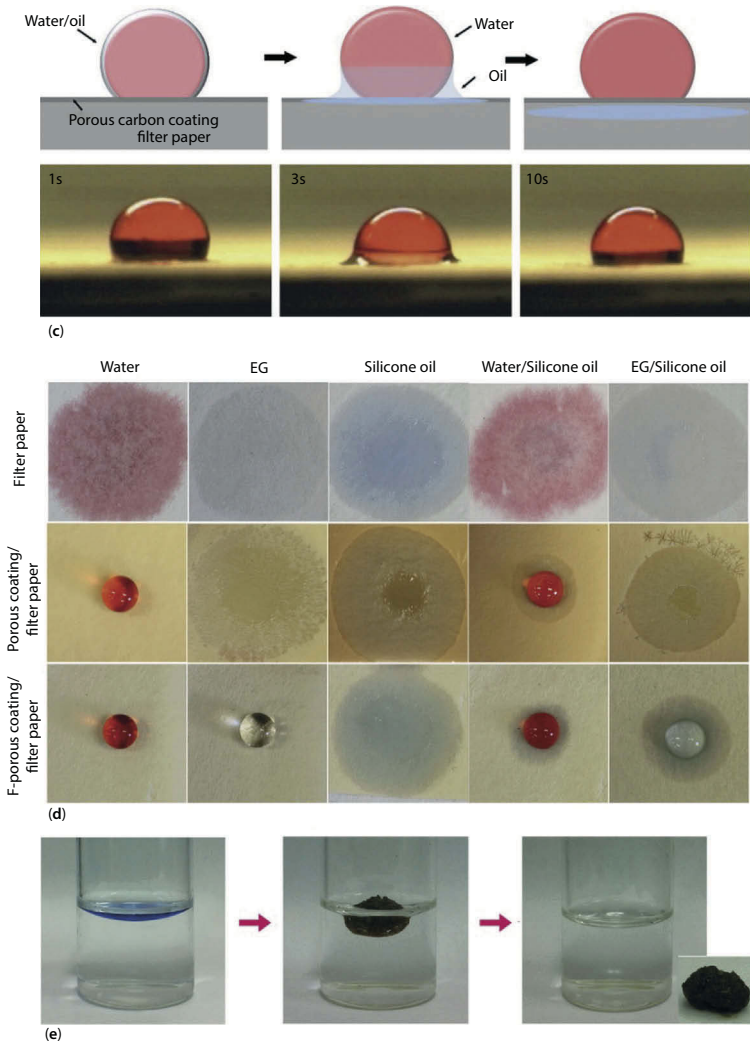


Figure 8.7 (Continued)

coatings presented superhydrophobicity with a high CA of approximately 160° and a low CAH of approximately 2° . Wetting behavior of the F-porous CNP network coatings against different liquids: ethylene glycol and silicone oil, whose surface tensions are 47.7 and 21.2 mN/m at 20°C , respectively, and water (the surface tension of DI water is 72.8 mN/m) was also investigated in this study. For ethylene glycol, the pure porous CNP network coatings as well as the network deposited with a low $\text{CF}_4/\text{C}_2\text{H}_2$ ratio of

5/15 revealed complete wetting behavior, with a CA of approximately 0° ; in particular, ethylene glycol was absorbed by the porous carbon, but at a high $\text{CF}_4/\text{C}_2\text{H}_2$ ratio of 16/4, the porous CNP network coatings showed hydrophobicity, with a CA of approximately 145° . As the $\text{CF}_4/\text{C}_2\text{H}_2$ ratio was increased further, the CA increased monotonously with the decrease in the CAH. When the $\text{CF}_4/\text{C}_2\text{H}_2$ ratio reached 16/4, the CA increased to 150° and the CAH dropped to 7° , indicating superhydrophobicity. This extreme wetting contrast of ethylene glycol on the F-porous CNP networks can be explained by the control of the coating materials with the $\text{CF}_4/\text{C}_2\text{H}_2$ ratio and by the surface roughness of the nanoscale porous structures. However, all samples with F-porous CNP coatings were completely wetted with silicone oil due to the low surface tension of the oil as well as lack of re-entrant sub-micrometer surface texture.

The wettability measurements showed that the pure porous CNP network deposited with only a hydrocarbon precursor can repel water very well and absorb low surface tension liquids (both ethylene glycol and silicone oil) suitable for water cleanup applications. However, the F-porous CNP network with a high content of added fluorine can repel both water and ethylene glycol but not silicone oil, which has the lowest surface tension. This means that one can tune the wettability or absorbability of the porous CNP networks by controlling the amount of CF_4 that is incorporated. Thus, porous CNP networks can be used to separate mixtures of liquids with different surface tensions, such as water/silicone oil and ethylene glycol /silicone oil mixtures as indicated by the authors [7]. To test their liquid separation behavior, the pure porous CNP and F-porous CNP networks were coated onto filter paper, as shown in Figure 8.7c. Using a high-speed camera the authors recorded wetting and impact dynamics, and a water droplet (dyed red) bounced on the porous CNP network material without penetration, while silicone oil (dyed in light blue) was quickly absorbed by the porous network/filter paper. As the water/silicone oil mixture was placed on filter paper coated with a porous CNP network, the silicone oil surrounding the outer surface of the mixture droplet was quickly absorbed by the porous CNP, forming an oil meniscus and leaving only a water droplet on the surface. Figure 8.7d shows the wetting states of the water, ethylene glycol, silicone oil and mixed droplets of these materials on the surfaces of the as-received filter paper and the porous CNP and F-porous CNP networks coated onto filter paper. When each droplet was gently placed on each surface, one minute was allowed to elapse before the optical images were taken. All of the liquid droplets, i.e., those of water, ethylene glycol, silicone oil and their mixtures, were completely absorbed on the bare filter paper due to its hydrophilic and oleophilic nature, as shown

in the first row of Figure 8.7d. For the porous CNP coating/filter paper sample shown in the second row, water droplet was repelled by the porous CNP network coating without penetration, while ethylene glycol and silicone oil were completely absorbed. When the water/silicone oil mixture was deposited, only water remained on the surface, indicating the separation of the water from the silicone oil, whereas the ethylene glycol/silicone oil mixture was completely absorbed. For the F-porous CNP coated onto filter paper, water and ethylene glycol were repelled while silicone oil was completely absorbed, as shown in the images in the last row (Figure 8.7). The porous carbon materials collected from the Si wafers (shown as photo in Figure 8.7e) could also be used directly as absorbents for oil or organic solvents, such as hexane and toluene, as demonstrated in Figure 8.7e. The porous CNP material was immersed into the water/silicone oil mixture and the water/hexane mixture, where only silicone oil and hexane, respectively were quickly absorbed.

8.4 Synthesis by Combustion of Terpenoids

Camphor crystals were also used as a precursor for producing nanostructured carbon networks [8]. Combustion of camphor was carried out in a controlled environment. An in-depth evaluation of the wetting, surface structure and optical properties was carried out on these surfaces. A chain of carbon nanospheres with an average size of 25–60 nm was observed from FESEM micrographs, with interconnected soot particles held together by a fragile network and weak van der Waals bonds. The formation of carbon bead structure was confirmed from the HR-TEM micrographs. It was observed that the fractal dimensions of soot particles were slightly less than the fractal dimensions of soot particles derived from ethylene and hexane. The relation between the superhydrophobicity and surface free energy of camphor soot particles was evaluated for soot particles collected at different heights above the flame. Since these particles were also found to display photoluminescence, applications can be envisioned as superhydrophobic coatings with luminescent properties.

Figure 8.8 depicts the 2D and 3D Atomic Force Microscopy images of camphor soot particles coated over a glass substrate above a flame for 5, 15, 30 and 45 s. With increasing coating time, the surface structures of soot particles illustrate higher extent of roughness. The enhancement of surface roughness occurs due to an increased number of particles adhering to the glass, which enhances the amount of nanopillar formation over the surface, leading to increased roughness. Surface roughness values of 22.25,

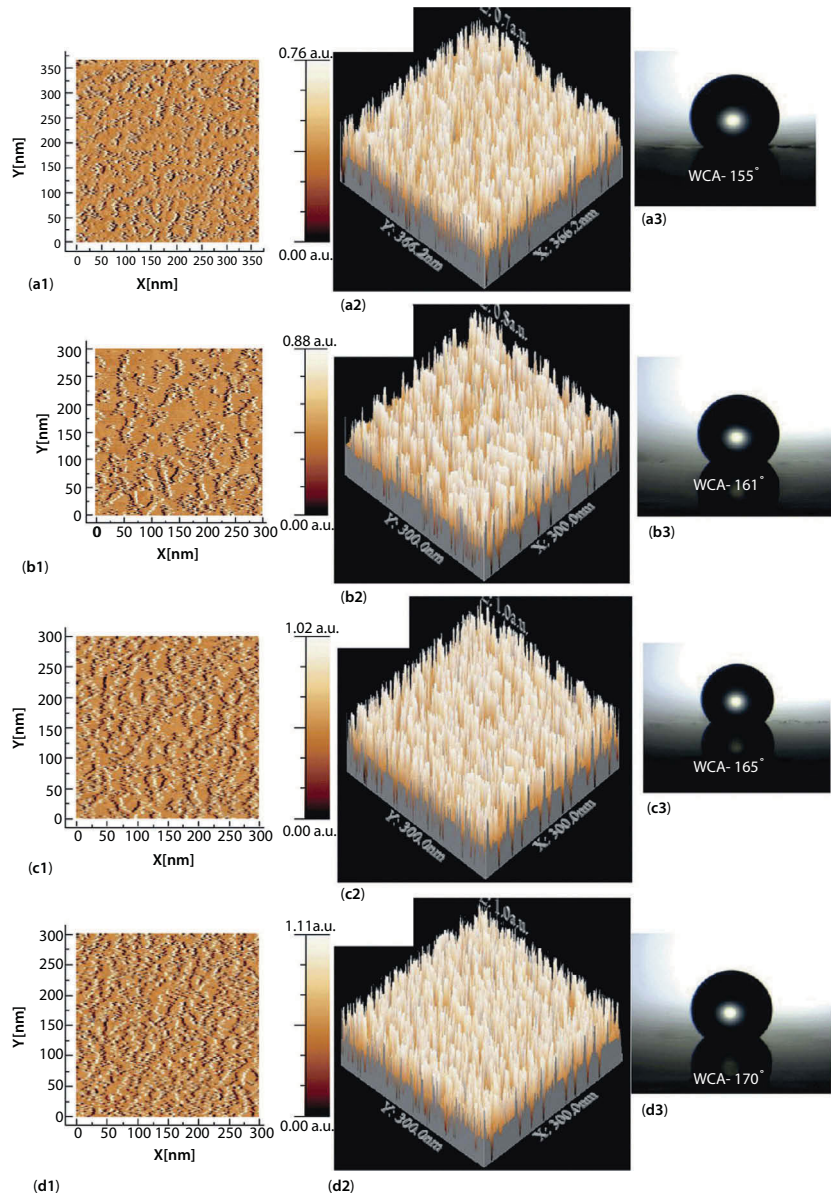


Figure 8.8 AFM images of the soot particles (a) 5 s (b) 15 s (c) 30 s (d) 45 s (a1, a2, a3, b1, b2, b3, c1, c2, c3 and d1, d2, d3 represent the 2D image, the 3D image and the shape of the water droplet from left to right, respectively). With permission from [8].

36.78, 63.56 and 90.57 nm were determined for soot particles coated for 5, 15, 30 and 45 s, respectively. It was found that the water contact angle of soot particles coated for various times increased from 155° to 170°.

8.5 Amorphous Carbon Networks on 3-D Porous Materials for Liquid Filtration

Oil spills in oceans are one of the most serious pollution incidents in the world. The cost of the oil spill, including the damage to the coastal ecosystem and the loss of an entire fishing and tourism season, is very expensive. The ramifications are also long lasting. Although many oil-absorbing materials have been developed for cleanup of oil spill, they all exhibit shortcomings including low separation efficiency, high operation costs, scale up issues and the generation of secondary pollutants. Therefore, facile strategies to synthesize highly efficient and inexpensive oil cleanup materials are indispensable. One recent application of superoleophilicity and superhydrophobicity is the fabrication of 3D materials for oil spill cleanup. Superhydrophobic 3D porous materials are considered as promising high-capacity absorbents due to their larger surface area and well-developed pores. Zhao *et al.* [9] fabricated soot coated metal foams for this purpose. Nickel foam, for instance, is a kind of commercially available 3D porous material, which has been used for fabricating superhydrophobic absorbents aimed at oil spill cleanup. However, the complex synthesis processes involved in creating the reported absorbent materials hamper the use of these materials in large-scale applications. Therefore, it is of great importance to develop a low-cost efficient material for oil/water separation. They reported a facile strategy for the preparation of superhydrophobic and superoleophilic nickel foam surface through candle soot coating and subsequent modification with poly(dimethylsiloxane), PDMS, as shown in Figure 8.9. The as-prepared nickel foam could be used for selective and effective separation of water and oil through simple, time-saving, and inexpensive process without any extra power (see Figure 8.10 for details).

Other researchers [10] have recently demonstrated that soot particles from a diffusion flame can be used for developing a cost-effective absorbent sponge, to remove oil contamination from water. The carbon particles were synthesized by an ethylene-oxygen combustion flame. The soot coated sponge was prepared via a dip-coating method. Without further surface modification and pretreatments, the soot coated sponge demonstrated high absorption capacities (up to 80 times its own weight) for a

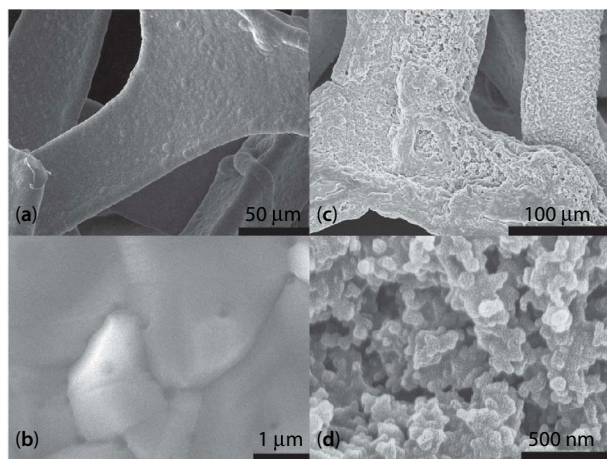


Figure 8.9 Typical FESEM images of pristine nickel foam (a and b) and as-prepared superhydrophobic and superoleophilic nickel foam (c and d) at different magnifications. With permission from [9].

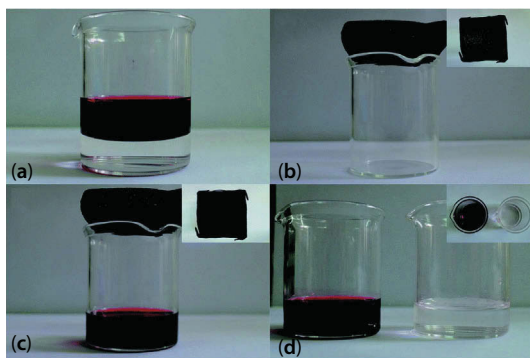


Figure 8.10 Water purification using superhydrophobic and superoleophilic nickel foam: (a) hexane solution colored with oil (red) and water before separation. (b) Foam to be used as a filter (c) colored hexane solution stay in beaker after passing through the nickel foam box. (d) colored hexane solution and water in two separate beakers. With permission from [9].

broad spectrum of oils and organic solvents with a recyclability of more than 10 times as shown in Figure 8.11. Such experimental results show evidence that foams or sponges functionalized with amorphous carbon networks are highly promising in environmental remediation for large-scale, low-cost removal of oils from water.

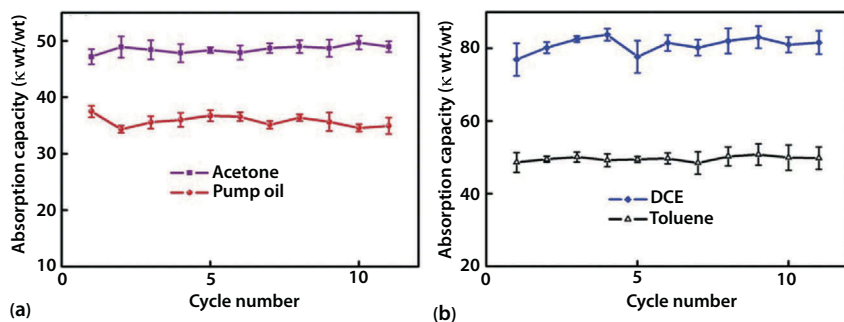


Figure 8.11 Demonstration of absorption recyclability of the amorphous carbon network functionalized sponges. DCE stands for dichloroethane. With permission from [10].

8.6 Towards Robust Carbonaceous Films on Micro-textured Polymer Surfaces

A recent study conducted by Bayer and coworkers [11] showed that when pure perfluorinated acrylic or natural wax-perfluorinated acrylic polymer blend coating surfaces were treated with small diffusion flames for a short duration, deposition of superhydrophobic nanostructured carbonaceous films could be made. The carbonaceous films display a good degree of surface binding which cannot be removed by impinging and rolling water droplets and also with some degree of abrasion. The resultant surfaces had very low droplet roll-off angles and remarkable resistance to complete wetting or saturation (soaking up water into the pores) against fast impacting water streams as well as to disintegration in ultrasonic bath treatment. Particularly, the fluoroacrylic polymer-wax blend films had excellent surface features for collecting and anchoring carbon nanoparticles on their surfaces as shown in Figure 8.12. The micro-structure of the carbonaceous films is demonstrated in Figure 8.12a. Figure 8.12b shows wetting measurements on untreated and flame synthesized amorphous carbon network coated polymeric surfaces. Note that very low water droplet roll-off angles are observed on both polymeric surfaces coated with the carbonaceous films. The micro-morphology of the carbonaceous film along with its surface roughness is depicted in Figure 8.13a.

Melting of the polymer and/or the wax during flame impingement would allow the nanoparticles to get embedded into the polymer film and establish a better binding carbonaceous film compared to a film deposited on a ceramic or metallic surface which can be picked up by

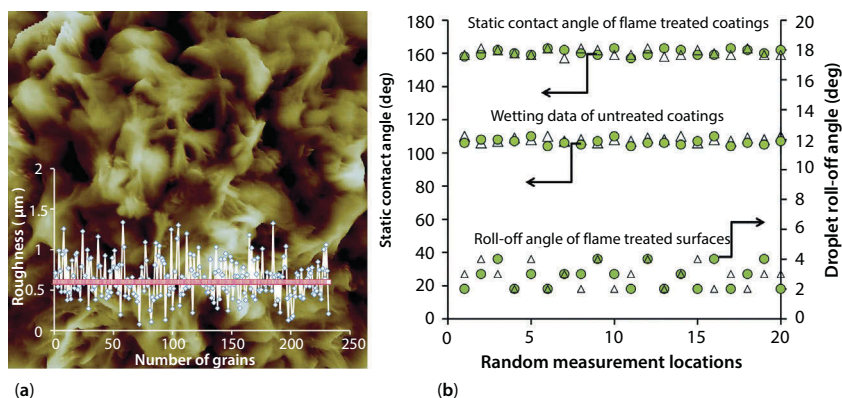


Figure 8.12 (a) AFM morphology and roughness data for a spray cast and thermally cured wax-polymer film. The image is a square $10\ \mu\text{m} \times 10\ \mu\text{m}$ in size. (b) All contact angle data. The uncertainty in contact angle measurements on polymeric films was approximately $\pm 4^\circ$ and in flame treated superhydrophobic surfaces was $\pm 3^\circ$. Filled circles correspond to polymer and unfilled triangles correspond to wax-polymer films for both as deposited and flame treated cases. With permission from [11].

the rolling droplets (self-cleaning). In fact, Figure 8.13b compares the surface roughness measurements on this superhydrophobic surface before and after being placed in an ultrasonic bath using a standard grain analysis. The average surface roughness of both surfaces remained at 174 nm. Although surface roughness of the film before and after sonication remained stable, its superhydrophobicity was lost during sonication. However, once the sample was dried and heat treated in an oven at 120°C for 1/2 hour, the surfaces recovered their superhydrophobic state as well as low droplet roll-off angles. Although no resistance against ultrasonic immersion was observed and the surfaces were saturated (completely wetted during ultrasonic processing), the carbonaceous films on the flame treated coatings were not removed or even cracked by the ultrasonic treatment. This is considered quite satisfactory since the carbonaceous film is an external nanostructured deposit from the diffusion flame. The films show a certain degree of mechanical durability against soft abrasion. Rubbing the surfaces with a material having a Shore A hardness of 70–75 for several times do not degrade the superhydrophobicity, although some of the carbonaceous film is removed. As such, amorphous carbon nanoparticles deposited on hydrophobic polymer surfaces by flame synthesis form saturation resistant (resistance to complete wetting under water with or without sonication or resistance to wetting by water jet impingement) superhydrophobic films which can

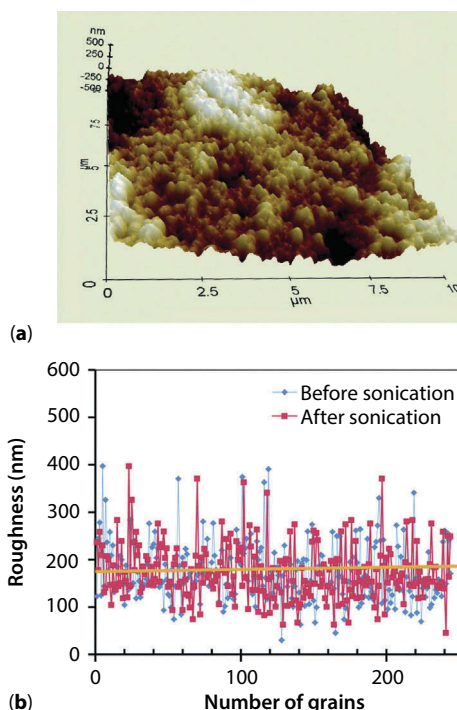


Figure 8.13 (a) Morphology of the carbonaceous superhydrophobic surface deposited on wax-polymer blend coatings after sonication for 20 seconds in an ultrasonic bath. (b) Comparison of roughness grain analysis results of the same superhydrophobic coating as in (a) before and after sonication. As seen, the average roughness (flat yellow line) of the superhydrophobic carbonaceous films remains practically the same at approximately 174 nm. With permission from [11].

withstand impacting water streams as well as ultrasonic bath processing by immersion. Surfaces demonstrate very high sessile droplet contact angles with low droplet roll-off angles after undergoing water stream impacts and sonication. Ultrasonic processing does not remove or crack the nanostructured carbonaceous films indicating strongly bonded nanoparticles to the polymeric films, possibly due to local melting of the polymer during flame impingement.

As mentioned earlier, flame synthesized carbon nanostructures demonstrate superhydrophobicity due to inherent hydrophobicity of carbon as well as the formation of dual-scale roughness during deposition. However, their main drawback is that nanostructured carbon materials do not form a firm bond with the surface upon which they are assembled, considerably reducing their practical applications in liquid repellent surface

technologies. Very recently, in our laboratories we demonstrated a simple, rapid, solvent-free and cost-effective strategy to synthesize hydrodynamically robust nanostructured carbon on randomly micro-textured surfaces. We utilized the concepts of friction induced polymer-particle adhesion (triboelectricity) and diffusion flame synthesis to form superhydrophobic carbonaceous films on surfaces including flexible substrates. These nanostructured carbon surfaces show remarkable resistance to saturation by high-pressure impinging water jets. For simplicity, we use common aluminum oxide sandpaper surfaces as our flexible substrates for deposition of sub-micrometer Teflon particles and subsequent deposition of carbon nanobead films via a simple utility burner (small diffusion flame). A substrate surface roughness between 10 to 50 μm (which correspond to 1500 grit to 500 grit sandpapers respectively) was found to give good performance. The resulting superhydrophobic surfaces displayed remarkable water saturation resistance against impinging water jets. The impinging jet pressure and angle were found to determine the conditions at which superhydrophobic surfaces became saturated (completely wetted by soaking up water into pores). However, even after saturation, the deposited nanocarbon films still remained adhered and could be re-functionalized after drying by a waterborne fluoroacrylic polymer solution to render them superhydrophobic and even oleophobic. Details of the process and results are given in the following.

No surface pretreatment was used prior to the polymer deposition using triboelectric adhesion. To accomplish this adhesion, Teflon powder was brushed onto 500 grit aluminum oxide sandpaper (Figure 8.14a) using a polyurethane foam paint brush. Depending on the initial amount of the Teflon powder to be applied per unit area the thickness of the polymer coating can be varied. Using this technique it is possible to maintain the original micro-texture of the substrate while introducing an overlaid sub-micrometer scale roughness as shown in Figures 8.14a and 8.14b. During deposition of the carbonaceous layer the underlying polymer coating melts enabling good adhesion of the carbon nanoparticles as seen in Figures 14c and 14d. It is also possible to use other micro-textured surfaces such as roughened aluminum foils which are flexible substrates like sandpaper. In Figure 8.15a, an atomic force microscope (AFM) image revealing the topography of the carbonaceous layer deposited on a rough aluminum foil coated with Teflon particles by tribo-adhesion is shown. The corresponding representative surface roughness profile is shown in Figure 8.15b. The morphology of the underlying Teflon film is shown in Figure 8.15c. This morphology was obtained by removing the carbonaceous film. It is seen that there are no longer sub-micrometer particles but rather an

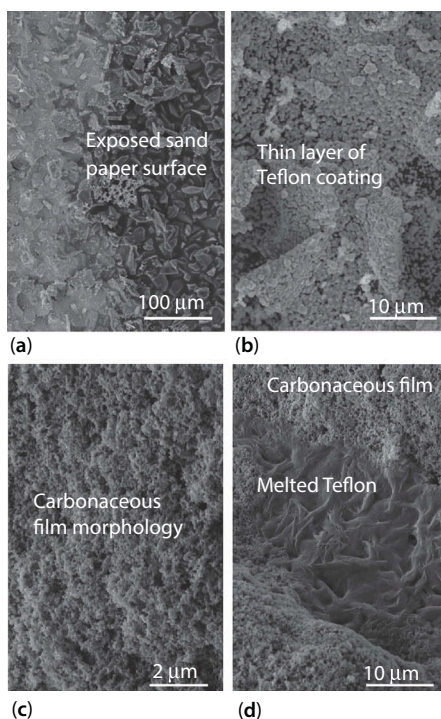


Figure 8.14 (a) SEM image of a sandpaper surface partially coated with a thin layer of Teflon particles using triboelectric adhesion. (b) The thickness of the particulate polymer coating can be tuned by depositing right amount of particles per unit area. In this case the sandpaper roughness features are still visible due to low thickness of the polymer coating. (c) SEM image of the carbonaceous film texture after flame treatment. (d) SEM image of a deliberately scratched region exposing the melted Teflon layer due to heating by the flame.

amorphous film which has a higher roughness than the superhydrophobic carbonaceous film (Figure 8.15d). It must be noted that AFM measurements cannot be conducted if a thin Teflon layer is applied such that the main substrate micro-morphology is not masked as seen in Figures 8.14a and 8.14b due to high roughness scale ($> 10\mu\text{m}$). Moreover, the carbonaceous layer deposited over this thin Teflon film can be easily removed by gentle rubbing. Hence, we have found that the optimum Teflon coating is achieved when the coating is thick enough such that the underlying micro-texture is masked by the Teflon coating.

To test the hydrodynamic robustness of the surface, the samples were exposed to a 3.2 mm in diameter high-speed water jet with varying dynamic pressures. Contact angle measurements were taken at 10 second increments. Samples were exposed until saturation (pores start soaking up

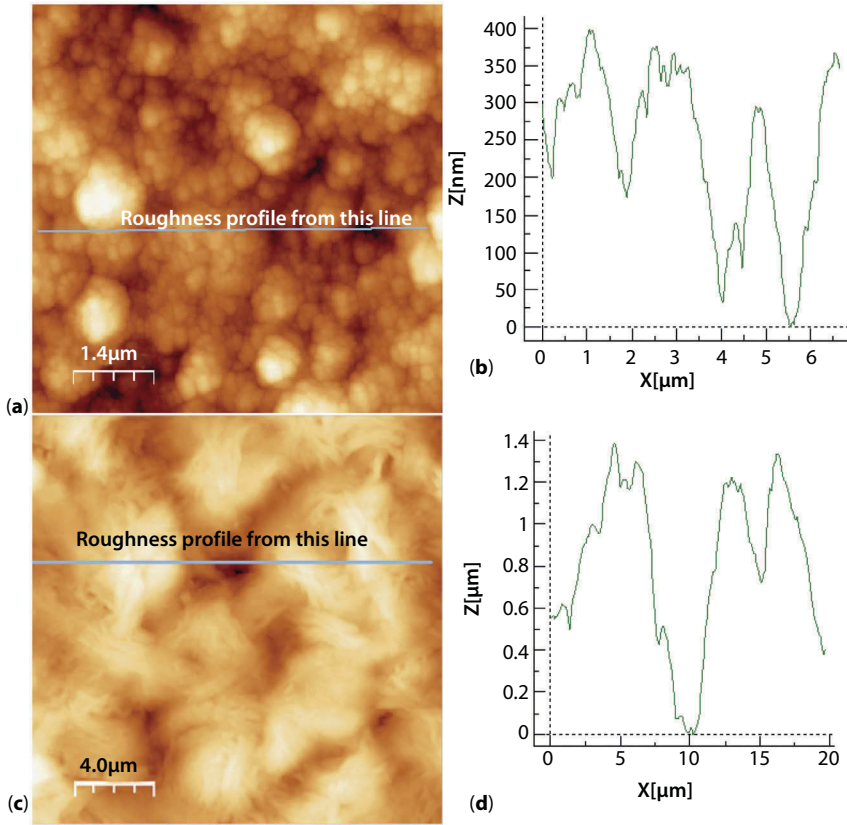


Figure 8.15 (a) AFM topography of the flame deposited carbonaceous layer on the Teflon coated sandpaper surface. The line is an arbitrary section from which the roughness profile is extracted. (b) Roughness profile extracted from the AFM image shown in (a). (c) Topography of the melted Teflon layer under the carbonaceous film. The overlaying carbonaceous film was removed intentionally to inspect the underlying morphology. (d) The roughness profile extracted from the arbitrary line of the AFM image in (c).

water although no visible wetting appears on the surface) occurred, as evidenced by condition when a 10 μL droplet would not roll off the samples. To find the effect of oblique water jet impact, substrates were also tilted by tilt angle β , when exposed to the water jet. A schematic of the experimental setup is shown as inset in Figure 8.16a. The graph of Figure 8.16a illustrates the importance of the triboelectrically deposited Teflon in creating a robust surface. Two samples, one with carbonaceous film deposited on Teflon (Teflon “with soot”), and one having the carbonaceous film directly (“just soot”) deposited on the micro-textured sandpaper were exposed to a 10 kPa water jet impinging at $\beta = 0^\circ$. As seen in Figure 8.16a, the surface

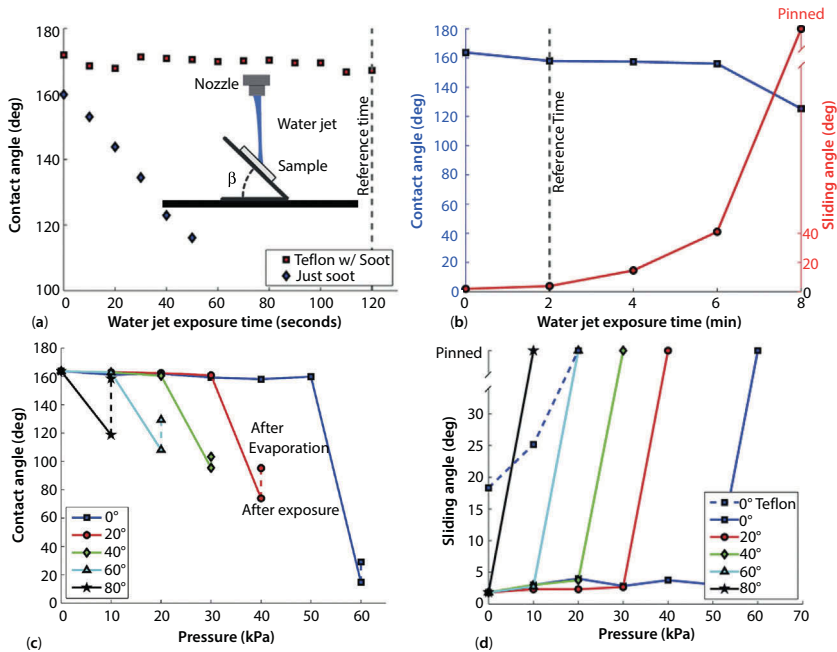


Figure 8.16 (a) Importance of the Teflon sub-layer on the resistance of superhydrophobicity to vertically ($\beta=0$) impacting water streams (at 10 kPa impact pressure) as a function of exposure time. The inset shows the schematic of the water impact tests. The static water contact angle of the carbonaceous films maintains a superhydrophobic value continuously at 10 kPa, whereas the contact angle of the carbonaceous film deposited directly on the micro-textured paper degrades within 10 seconds even if the water impact pressure is much less than 10 kPa. (b) Changes in static contact angle and sliding angle as a function of water jet exposure time. No changes in wettability occur within 2 minutes of tests. Therefore, 2 minutes was chosen as the reference time for all other experiments concerning effect of impact pressure and substrate tilt angle. (c) Effect of water impact pressure on the loss of superhydrophobicity (measured by static water contact angles) under different substrate tilt angles. Vertical dashed lines indicate wetting recovery of the dried surfaces after evaporation. (d) Water droplet pinning tests as function of water impact pressure for each tilt angle studied (expressed as sliding contact angle).

containing the Teflon binder maintained its superhydrophobic state at all times, displaying its robust nature. The surface composed of carbonaceous film deposited onto sandpaper initially showed superhydrophobic performance, with a CA = 160°. However, when it was exposed to a modest water jet (dynamic pressure ~ 1kPa), the carbonaceous film quickly washed off the surface and as a result, contact angle steadily decreased as the surface deteriorated to a CA of 120° in 50 seconds. To find the right experimental

conditions in terms of maximum time allowed before loss of superhydrophobicity, samples were subjected to a 40 kPa water jet impinging vertically at $\beta = 0^\circ$ for exposure times increasing in 2 minute increments. The results of this test, shown in Figure 8.16b, revealed that the contact angle of the exposed samples stayed nearly constant through 6 minutes. However, after 8 minutes, CAs degraded to 125° , falling below superhydrophobicity threshold ($\sim 150^\circ$). A minor decrease in roll-off angle occurred after the first 2 minutes, from 2° to 4° . Increasing exposure times produced a more dramatic degradation in performance, with a pinned state occurring after 8 minutes. Hence, 2 minutes of exposure was chosen as the reference time (set parameter) for all the remaining tests.

Resistance of superhydrophobicity against the water jet for 2 minutes as a function of dynamic pressure and substrate tilt angle is shown in Figure 8.16c. Three clear trends were apparent. First, as substrate tilt angle (β) increased (see Figure 8.16a for the definition and schematic), the dynamic pressure required to degrade superhydrophobic performance decreased. For instance, referring to Figure 8.16c, superhydrophobic performance corresponding to normal water jet impact ($\beta = 0^\circ$) degraded from $P = 60$ kPa to $P = 40$ kPa when the substrate was tilted to $\beta = 20^\circ$.

When the tilt angle was further increased to $\beta = 80^\circ$, superhydrophobicity was lost when the surface was exposed to just 10 kPa. The same trend was observed in the sliding angles (Figure 16d). The more the surface was tilted the less impinging pressure was required to pin the droplets. For instance, water droplets pinned on the $\beta = 80^\circ$ tilt surfaces at 10 kPa impinging liquid pressure. The second trend that was observed was related to the recovery of the contact angle towards its initial value after the impinging water jet tests. Under normal impact, for instance, after saturation and drying under ambient conditions, the surfaces remained in a hydrophilic state with $CA = 40^\circ$. The surfaces were always dried under ambient laboratory conditions without additional heat. Here, saturation of the surfaces means that the surfaces still have considerable amount of adsorbed water on them after drying. As the tilt angle β was increased however, the surfaces could recover towards more hydrophobic wetting state. For instance, at $\beta = 80^\circ$, although the superhydrophobicity was lost at low impinging liquid pressures, CA degraded to only 119° and after drying under ambient conditions the surface was superhydrophobic again. However, for other tilt angles lower than 80° , full superhydrophobic recovery was not possible. The third observation was that anti-wetting performance did not degrade until a clear threshold in dynamic pressure had been reached. It might have been expected that a gradually decreasing trend in CA and droplet roll-off angle would be observed with the increasing water jet pressure. Instead,

for a given tilt angle, CA remained constant at its superhydrophobic state and the superhydrophobicity was instantly lost once the critical pressure was reached. For instance, in Figure 8.16c, under normal impact ($\beta=0^\circ$), gradually increasing impinging jet pressure from 10 kPa to 60 kPa did not at all cause degradation in superhydrophobicity. However, once 60 kPa was reached, sudden surface wetting took place. The justification for the importance of the deposited carbonaceous layer in maintaining superhydrophobicity under high water impact pressures is shown in Figure 8.16d. In the case of a Teflon coated micro-textured surface (as a control sample), when it was exposed to a normal water jet at 20 kPa water droplets started to pin. Interestingly, in this case though, the trend of a “sudden” degradation was not observed. At 10 kPa water impact, sliding angles (droplets did not roll-off but slid instead) slightly increased (an additional $\sim 7^\circ$) but the droplets would still slide off the surfaces unlike for the surfaces with the carbonaceous coating.

Optical microscope images taken immediately after testing as shown in Figure 8.17 revealed that the spot where the water jet impacted (see also the schematic in Figure 8.17), as well as two bands to either side of this spot, had been affected when a sample was tilted to $\beta = 60^\circ$. These regions were covered with either a film or drops of water, indicating that they had saturated and were no longer superhydrophobic. Likewise, photographs of a sample that was tilted to $\beta = 80^\circ$ during testing showed a somewhat

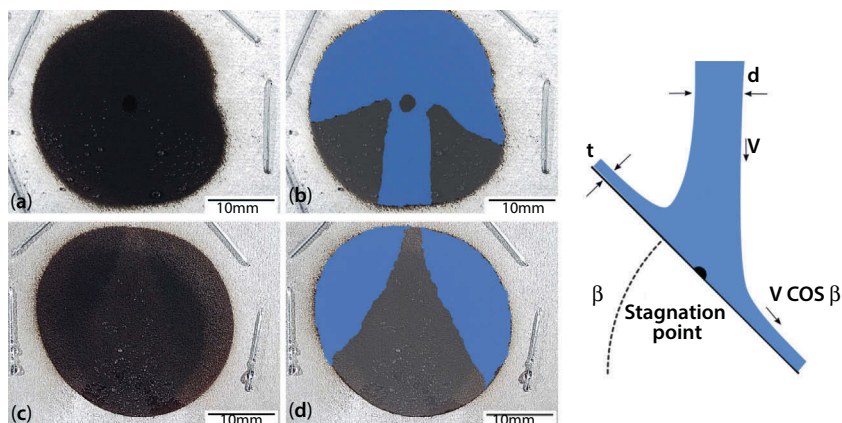


Figure 8.17 Optical microscope images showing surface conditions after (a) 60° and (c) 80° liquid jet impact. Blue regions in images (b) and (d) indicate unsaturated regions of images (a) and (b) for better clarification. The schematic on the right depicts inclined liquid jet impact conditions. V indicates impact velocity of the impinging jet; t thickness of the liquid film and d indicates the thickness of the jet.

different continuous degraded region. Energy-dispersive X-ray spectroscopy (EDS) data collected during SEM imaging (not shown) also revealed a large difference in surface chemistry for regions that saturated (pore wetting causing droplet pinning) and for regions that remained superhydrophobic. Over the saturated regions, a relatively smaller carbon peak was detected, along with more fluorine.

This indicated that some of the carbonaceous layer had been washed away possibly causing saturation of the superhydrophobic surface. It is somewhat contradictory to the notion that more fluorine should ensure higher water repellency but it is highly probable that the surface roughness changes due to partial loss of carbonaceous layer are responsible for the saturation. This observation will be discussed next with the help of AFM and XPS measurements. Since EDX measurements also contain signals from part of the bulk of the material they should be supported with XPS measurements. Figure 8.18 compares the C 1s signals from various regions (unsaturated-blue and saturated-green) designated by the numbers, of a surface tested under 60kPa orthogonal jet impact, obtained from XPS measurements. The region indicated by (1) is the center of the superhydrophobic ring (blue), the region indicated by (2) is the edge of the superhydrophobic ring, the region indicated by (3) is the edge of the superhydrophilic outer ring (green) and the region indicated by (4) is the center of the superhydrophilic ring. The purpose of this measurement was

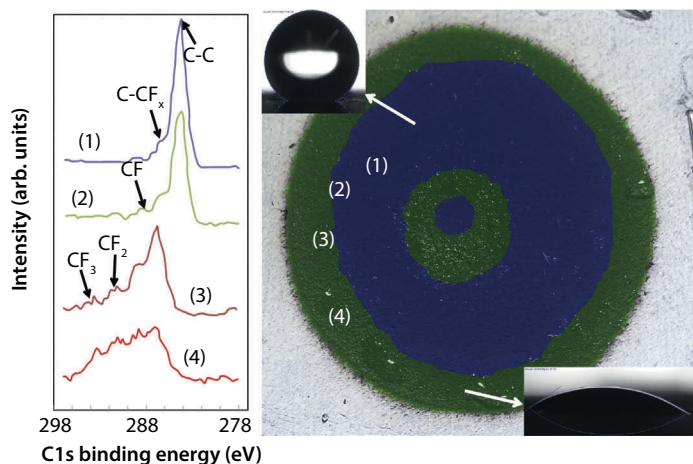


Figure 8.18 XPS C 1s signals from various locations on the surface of a superhydrophobic surface after 60 kPa normal jet impact. The blue regions preserved their superhydrophobic state whereas the green regions saturated (loss of superhydrophobicity in a highly porous, sponge-like surface).

to understand the changes in the chemical composition of the surface as a function of location after loss of superhydrophobicity. The peaks were de-convoluted into five components: C-C or C-H_n, (hydrocarbon) at 285 eV, C-CF_x, at 287 eV, CF at 289 eV, CF₂, at 292 eV, and CF₃, at 294 eV. The increase in the C-F signals and the relative decrease in the C-C signals close to and within the saturated regions (green) indicate presence of more Teflon component confirming the EDX results discussed earlier. The spectrum corresponding to region (4) clearly shows very high contribution from CF_n bonds indicating that a large portion of the underlying Teflon layer is exposed due to jet impact surface alteration. The quantification of the chemical changes before and after saturation is beyond the scope of this study and will be analyzed in a future work.

The shapes of the saturated regions resemble non-circular hydraulic jump patterns formed due to obliquely impinging Newtonian fluids [12,13]. Therefore, it is believed that there could be a relationship between the shape of the region of saturation and the onset of hydraulic jump. However, it is important to consider that saturation (loss of superhydrophobicity of a sponge-like surface) can also be caused by roughness induced shear stress changes due to turbulent to laminar transition before the hydraulic jump occurs. However, more detailed work would be required to distinguish between laminar-turbulent flow transitions and onset of hydraulic jump. Referring to Figures 8.17c and 8.17d, it seems that the hydraulic jump locations are the boundaries of the saturated and unsaturated regions as defined by the edges of the blue zones. As such, regions within the spreading film just before the hydraulic jump occurs would probably preserve their superhydrophobic state. Moreover, the work of Kate *et. al.* [12] showed that the circular hydraulic jumps formed due to normal impinging jets change their shapes, as the jet inclination angle (β) is changed from 90°. They showed that hydraulic jumps with corners occurred under certain inclination angles which closely resemble the shape of saturated regions in Figure 8.17d. Hence, we have made an attempt to interpret the results within the framework of hydraulic jump theory of impinging liquid jets [14]. In the present case, the Weber and Reynolds numbers associated with the liquid jet impingement experiments fall within $5 \times 10^2 < We < 4 \times 10^3$ and $8 \times 10^3 < Re < 3 \times 10^4$ ranges, respectively, where Weber and Reynolds numbers are defined by equations (8.1) and (8.2) below.

$$We = \frac{\rho d U^2}{\sigma} \quad (8.1)$$

$$Re = \frac{\rho d U}{\mu} \quad (8.2)$$

In the equations above, ρ , σ and μ stand for liquid density, surface tension and viscosity respectively, and d and U stand for the diameter of the liquid jet and the velocity of the impinging jet, respectively. The Weber and Reynolds numbers are comparatively high compared to other studies on impinging liquid jets on hydrophobic and superhydrophobic surfaces [15–17]. The radius of the non-circular hydraulic jump, $R_j(\theta, \beta)$, (with reference to the stagnation point) due to an oblique jet impact can be estimated by equation 8.3.

$$R_j(\theta, \beta) = C \left[\frac{U d^2}{8} \frac{\sin^3 \beta}{(1 + \cos \beta \cos \theta)^2} \right]^{\frac{5}{8}} \left(\frac{\mu}{\rho} \right)^{-\frac{3}{8}} g^{-\frac{1}{8}} \quad (8.3)$$

The angle of inclination is β , as schematically shown in Figure 8.19a as inset, and θ is the angular component of the polar coordinates. Here g is the acceleration of gravity. The constant C is a function of the velocity profile of radially spreading film after impingement, upstream of the hydraulic jump. It ranges from 0.73 for a parabolic velocity profile to 0.85 for higher order velocity profiles [12] for the no-slip condition at the wall. From equation 8.3, one can estimate the location of the hydraulic jump as a function of jet impact velocity and the oblique angle (β) at for instance $\theta = 0$ or at $\theta = \pi$ which correspond to the horizontal line of the stagnation point (see Figure 8.19a). In the case of a jet impingement on a superhydrophobic surface, the velocity profile of the spreading film before the hydraulic jump does not have a wall slip due to high contact angles and jet rebound. In this case, the constant C can be approximated by the restitution coefficient for jet rebound on superhydrophobic surfaces [17] which approximately scales with $We^{-1/2}$. Figure 8.19b shows the R_j/d ratio (radius at which the hydraulic jump occurs) at $\theta = \pi$ for the experimental conditions shown in Figure 16 for four different tilt angles and six different jet impact pressures. As seen in the Figure, for all tilt angles, estimated hydraulic jump radius decreases as the impinging jet pressure increases towards 60 kPa. For low tilt angles, for instance at 20° , the jump radius extends out as far as 6 to 7 impinging jet diameters. For high tilt angles, however, such as 80° , the hydraulic jump radius is about twice the diameter of the impinging jet. These estimated jump radii do not directly indicate the location of the saturation of superhydrophobicity but would allow us to

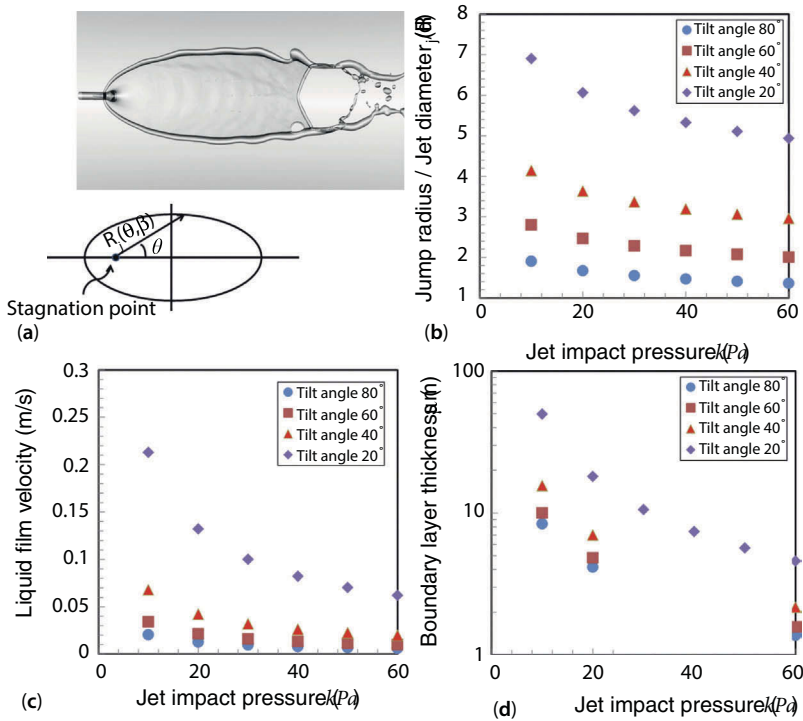


Figure 8.19 (a) Photograph of formation of a hydraulic jump upon liquid jet impingement on a flat surface. The schematic below indicates the stagnation point and the hydraulic jump radius in polar coordinates. (b) Estimated non-dimensional hydraulic jump radius as a function of impact pressure and tilt angle for the experimental conditions studied. Note that the values are calculated for $\theta = \pi$. (c) Estimated liquid film velocity just before the hydraulic jump. (d) Estimated boundary layer thickness as a function of jet impact pressure and substrate tilt angle.

estimate the liquid velocity right at the hydraulic jump and the associated boundary layer thickness just before the jump. As shown by the scaling arguments of Choi and Kim [18] if the estimated boundary layer thickness turns out to be of the order of 10 mm, the fluid experiences an easy slip in Cassie-Baxter mode on the nano-textured superhydrophobic surfaces. As the boundary layer thickness decreases towards single digit micrometer or sub-micrometer levels, the liquid is considered to be no longer in the Cassie-Baxter state but rather flows on a hydrophilic surface with no slip or stick-slip at the wall [18]. From the theory developed by Wang *et al.*, [19], for an oblique liquid jet impingement, the velocity of the liquid film, U_j , just before the hydraulic jump can be estimated by equation 8.4.

$$U_j = \frac{5\sigma(1 - \cos(\alpha))}{3U\rho r_e^2 \sin\beta} R_j \quad (8.4)$$

In Eq. 8.4, the angle α denotes the contact angle (hydrophobicity of the surface), σ is the liquid surface tension and r_e denotes the edge radius of the impingement zone which scales with the jet diameter d . Figure 8.19c shows the calculated film velocities just before the hydraulic jump for all impact pressures and substrate tilt angles studied. It should be noted that since the surface texture of the present superhydrophobic carbonaceous films is random, the scaling arguments developed for lithographically patterned surfaces [18] cannot be directly used here even if it is possible to measure the average roughness of the surfaces (saturated and unsaturated) before and after the liquid jet impingement. Moreover, recent experimental studies on hydraulic jumps on superhydrophobic surfaces also use patterned surfaces with well-defined ribs and cavities [16,17]. The local thickness, h , of the liquid before the hydraulic jump can be estimated by the relationship developed by Liu *et al.* [20] as

$$h = 0.1713 \left(\frac{d^2}{R_j} \right) + \frac{5.147}{Re} \left(\frac{R_j^2}{d} \right) \quad (8.5)$$

hence, one can approximate the effective boundary layer thickness, d_{eff} within the spreading film before the hydraulic jump as

$$\delta_{eff} \sim \frac{U_j}{U} h \quad (8.6)$$

Estimated boundary layer thickness values are shown in Figure 8.19d. As seen in the figure, smaller boundary layer thicknesses are estimated at high tilt angles and at high impact pressures (shaded regions in Figure 8.19d) according to the models used. This in turn, indicates that the liquid flow obeying Cassie-Baxter regime becomes more difficult under these conditions ($\delta_{eff} < 10 \mu\text{m}$) [18–20], which indirectly suggests potential saturation of the surface texture with water. Indeed, as was seen in Figure 8.16c, at high tilt angles partial loss of superhydrophobicity occurs at lower jet impact pressures.

Figure 8.20 demonstrates static contact angle measurements of various liquids on the saturated surfaces functionalized with the fluoroacrylic polymer under 60 kPa jet impact. Two different tilt angles (40° and 80°) were used and the results were compared with the orthogonal impact case

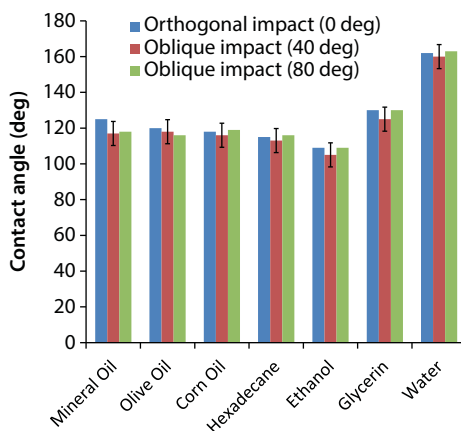


Figure 8.20 Static contact angles of various liquids on fluoropolymer functionalized surfaces that had saturated (superhydrophobicity loss due to internal pore wetting) as a result of water jet impact at 60 kPa.

at the same impact pressure. As seen in the figure, substrate tilt angle does not seem to affect the liquid contact angles once the saturated surfaces (loss of superhydrophobicity due to internal pore wetting) were functionalized. All of the drops except for water pinned and it was not possible to measure droplet roll-off angles. Oil droplets slid off the surfaces leaving a stained trail behind at high tilt angles close to 50° . This can be attributed to the lack of re-entrant surface texture resulting in high liquid retention during sliding [22]. Water droplets rolled off easily at a substrate tilt angle of approximately 5° after functionalization. It was not possible to render the saturated surfaces superoleophobic. It is argued that the reason is the loss of dual-scale re-entrant surface texture [22–23] due to water hammer effect. The re-entrant surface texture is not essential for water repellency due to high surface tension of water [24–25].

Finally, we studied the abrasion resistance of the developed coatings. The coatings could not withstand severe abrasion but under mild abrasion conditions they could maintain their super hydrophobicity even if the surfaces were scratched provided that the coating thickness was sufficient. The coatings were abraded using a vibratory polisher (VibroMet 2, Buehler) in abrasion mode. One micrometer diamond paste (Metadi®, Buehler, Germany) was applied on a soft polishing cloth and the samples were pressed against the cloth using a specimen weight holder corresponding to 532 Pa downward pressure, which is quite mild compared to other studies [26–29]. The maximum abrasion time was 360 minutes. However,

the samples were completely abraded (removal of the carbonaceous layer) after 10 minutes of abrasion with the built-in vibration frequency of 50 Hz. The Teflon layer at the end of this process was still intact. The coatings, however, maintained their superhydrophobic state if the abrasion process was stopped after 2–3 minutes. The samples were found to be partially scratched but droplets still rolled off. Droplet roll-off angles slightly exceeded 10° at this stage.

8.7 Conclusions

This chapter attempted to present the latest research on liquid repellent surfaces made from amorphous carbon nanoparticle networks, sometimes referred to as carbonaceous films. It mostly focused on carbon nanoparticle networks obtained from flame synthesis (in the form of soot) but other interesting synthesis routes such as vacuum deposition from gas precursors or solution routes were also outlined for completeness. As can be deduced, the morphology of these carbonaceous films is ideal for liquid repellent applications, therefore they have been used as templates for making super-repellent surfaces from other materials via precursor application or molding. They were also used extensively for oil-water separation applications by depositing them on 3D structures such as foams or sponges due to ease of their production in large quantities. However, most of these works fail to report the durability of these carbonaceous coatings. Hence, in this chapter, we have included latest work from our laboratories on the fabrication of robust amorphous carbon nanoparticle networks on certain soft polymeric surfaces having micrometer scale texture by flame impingement. We showed that the polymer and micrometer scale texture combination can yield reasonably robust carbonaceous films that can withstand strong water jet hammering as well as mechanical wear.

We anticipate that this chapter would trigger more research efforts towards finding other innovative means to render them more robust as coatings, as these carbonaceous films can be made easily in large quantities and are much less expensive than other nano-structured carbon materials. Potential future directions could be, for instance, synthesis of polymer-carbon nanocomposite surfaces made up of carbon nanotubes, graphene or other carbon nanomaterials as well as flame synthesis of other soft materials which can be thermally triggered to crosslink or polymerize during nanoparticle network deposition.

References

1. R. A. Dobbins and C. M. Megaridis, Morphology of flame-generated soot as determined by thermophoretic sampling, *Langmuir*, 3, 254–259 (1987).
2. Z. Wei, K. Yan, H. Chen, Y. Yi, T. Zhang, X. Long, J. Li, L. Zhang, J. Wang and S. Yang, Cost-efficient clamping solar cells using candle soot for hole extraction from ambipolar perovskites *Energy Environ. Sci.*, 7, 3326–3333 (2014).
3. B. Liu, H. Huang, F. Zhang, Y. Zhou, W. Li and J. Zhang, Agglomerates of amorphous carbon nanoparticles synthesized by a solution-phase method, *Mater Lett* 66, 199–202 (2012).
4. X. Deng, L. Mammen, H.-J. Butt and D. Vollmer, Candle soot as a template for a transparent robust superamphiphobic coating, *Science* 335, 67–70 (2012).
5. S. Liu, M. Sakai, B. Liu, C. Terashima, K. Nakata and A. Fujishima, Facile synthesis of transparent superhydrophobic titania coating by using soot as a nanoimprint template, *RSC Adv.*, 3, 22825–22829 (2013).
6. Y. Zhou, B. Wang, X. Zhang, M. Zhao, E. Li, and H. Yan, The modifications of the surface wettability of amorphous carbon films, *Colloids Surfaces A*, 335, 128–132 (2009).
7. W. Dai, S. J. Kim, W.-K. Seong, S. H. Kim, K.R. Lee, H.-Y. Kim and M.-W. Moon, Porous carbon nanoparticle networks with tunable absorbability, *Scientific Reports* 3, 2524–2527 (2013).
8. B. N. Sahoo and B. Kandasubramanian, Photoluminescent carbon soot particles derived from controlled combustion of camphor for superhydrophobic applications *RSC Adv.*, 4, 11331–11342 (2014).
9. F. Zhao, L. Liu, F. Ma and L. Liu, Candle soot coated nickel foam for facile water and oil mixture separation, *RSC Adv*, 4, 7132–7135 (2014).
10. Y. Gao, Y.S. Zhou, W. Xiong, M. Wang, L. Fan, H. Rabiee-Golgir, L. Jiang, W. Hou, X. Huang, L. Jiang, J.-F. Silvain, and Y. F. Lu, Highly efficient and recyclable carbon soot sponge for oil cleanup *ACS Appl Mater Interfaces* 6, 5924–5929 (2014).
11. I. S. Bayer, A. J. Davis and A. Biswas, Robust superhydrophobic surfaces from small diffusion flame treatment of hydrophobic polymers, *RSC Adv.*, 4, 264–268 (2014).
12. R.P. Kate, P.K. Das and S. Chakraborti, Investigation on non-circular hydraulic jumps formed due to obliquely impinging circular liquid jets, *Experiments in Thermal Fluid Sci*, 32, 1429–1439 (2008).
13. E. A. Martens, S. Watanabe and T. Bohr, Model for polygonal hydraulic jumps, *Phys Rev E*, 85, 036316 (2012).
14. V. J.H. Lienhard, Liquid jet impingement, in: Annual Review of Heat Transfer, Vol.6, C.L.Tien (Ed.), pp.199–270, Begell House, New York (1995).
15. D. Maynes, M. Johnson and B. W. Webb, Free-surface liquid jet impingement on rib patterned superhydrophobic surfaces, *Phys Fluids* 23, 052104, (2011).

16. A. Kibar, H. Karabay, K. S. Yigit, I. O. Ucar and H. Y. Erbil, Experimental investigation of inclined liquid water jet flow onto vertically located superhydrophobic surfaces, *Experiments in Fluids*, 49, 1135–1145 (2010).
17. F. Celestini, R. Kofman, X. Noblin and M. Pellegrin, Water jet rebounds on hydrophobic surfaces: A first step to jet micro-fluidics, *Soft Matter*, 6, 5872–5876 (2010).
18. C-H. Choi and C-J. Kim, Large slip of aqueous liquid flow over a nanoengineered superhydrophobic surface, *Phys Rev Lett*, 96, 066001 (2006).
19. T. Wang, D. Faria, L.J. Stevens, J.S.C. Tan, J.F. Davidson and D.I. Wilson, Flow patterns and draining films created by horizontal and inclined coherent water jets impinging on vertical walls, *Chem. Eng. Sci.* 102, 585–601 (2013).
20. X. Liu, V.J.H. Lienhard and J.S. Lombara, Convective heat transfer by impingement of circular liquid jets, *J. Heat Transfer*, 113, 571–582 (1991).
21. R. Dufour, P. Brunet, M. Harnois, R. Boukherroub, V. Thomy and V. Senez, Zipping effect on omniphobic surfaces for controlled deposition of minute amounts of fluid or colloids. *Small*, 8 1229–1236 (2012).
22. L. Cao, T. P. Price, M. Weiss and D. Gao, Super water- and oil-repellent surfaces on intrinsically hydrophilic and oleophilic porous silicon films, *Langmuir*, 24, 1640–1643 (2008).
23. A. Susarrey-Arce, A. G. Marin, H. Nair, L. Lefferts, J. G. E. Gardeniers, D. Lohse and A. van Houselt, Absence of an evaporation-driven wetting transition on omniphobic surfaces, *Soft Matter*, 8, 9765–9770 (2012).
24. H. Zhao, K-Y. Law and V. Sambhy, Fabrication, surface properties, and origin of superoleophobicity for a model textured surface, *Langmuir* 27, 5927–5935 (2011).
25. B. N. Sahoo and B. Kandasubramanian, Recent progress in fabrication and characterization of hierarchical biomimetic superhydrophobic structures, *RSC Adv.*, 4, 22053–22093 (2014).
26. Q. F. Xu, B. Mondal and A. M. Lyons, Fabricating superhydrophobic polymer surfaces with excellent abrasion resistance by a simple lamination templating method, *ACS Appl. Mater. Interfaces*, 3 , 3508–3514 (2011).
27. I. A. Larmour, G. C. Saunders, and S. E. J. Bell, Compressed metal powders that remain superhydrophobic after abrasion, *ACS Appl. Mater. Interfaces*, 2, 2703–2706, (2010).
28. A. Milionis, R. Ruffilli, and I. S. Bayer, Superhydrophobic nanocomposites from biodegradable thermoplastic starch composites (Mater-Bi®), hydrophobic nano-silica and lycopodium spores, *RSC Adv.*, 4, 34395–34404 (2014).
29. I. S. Bayer, A. Brown, A. Steele and E. Loth, Transforming anaerobic adhesives into highly durable and abrasion resistant superhydrophobic organoclay nanocomposite films: A new hybrid spray adhesive for tough superhydrophobicity. *Appl. Phys. Express*, 2, 125003 (2009).

Recent Progress in Evaluating Mechanical Durability of Liquid Repellent Surfaces

Athanasios Milionis^{1,*}, Ilker S. Bayer^{1,2} and Eric Loth¹

¹*Mechanical and Aerospace Engineering, University of Virginia,
Charlottesville, VA, United States*

²*Smart Materials/Nanophysics, Istituto Italiano di Tecnologia, Genoa, Italy*

Abstract

Following a large number of studies to develop surfaces and coatings that have extreme liquid repellence, researchers have recently focused on improving the mechanical performance of these surfaces as this is the main challenge for their commercialization. In this chapter, we summarize the developments since 2011 on fabrication, design and understanding of mechanically durable liquid repellent surfaces. This includes a review of recently published diagnostic techniques for demonstrating the mechanical durability. In particular, we categorize high-repellency surfaces and coatings by the type of durability testing and we highlight the most successful approaches to produce mechanically robust surfaces. Finally, future prospects towards obtaining a set of standard characterization/evaluation methods are discussed.

Keywords: Mechanical durability, wear, textured surfaces, surface wetting, superhydrophobic

9.1 Introduction

The discovery of the unique self-cleaning properties of the lotus leaf by Barthlott and Neinhuis [1] during 1997 was the beginning of an intensive research on bio-inspired artificial liquid repellent surfaces. In the following years, an enormous number of papers were published regarding different

*Corresponding author: am2vy@virginia.edu

methods to fabricate superhydrophobic [2] and more recently superoleophobic [3], as well as superomniphobic surfaces [4]. Usually, when a liquid droplet is placed on such surfaces, it exhibits apparent contact angle higher than 150° and roll-off angle lower than 10° or 5° . However, recent coatings based on Slippery Liquid Impregnated Porous Surfaces (SLIPS) have shown that extreme shedding can occur with only low roll-off angles independent of the apparent water contact angle [5]. This is also a bio-inspired surface as it follows the concept of the pitcher plant.

If a surface or coating also displays such high liquid repellency for oil droplets, it is referred as superoleophobic. Surfaces that display both superhydrophobicity and superoleophobicity and can also repel most other liquids in the same fashion are generally referred to as superomniphobic. The enormous research interest in liquid repellent surfaces stems from their potential to be incorporated in a vast number of different applications [6–17].

In general, the key element to obtain surfaces with extreme liquid repellency is to use hydrophobic materials to compose a rough surface with micro and/or nano-scale features [17,18]. When liquid droplets are dispensed on surfaces with appropriate combination of chemical (material) and physical (surface texture) properties, air pockets can form at the interface between liquid and solid such that only a small fraction of the liquid surface contacts the solid (while the rest contacts air). In this case, the frictional force for tangential motion of the drops along the surface is due only to the small fraction of liquid-solid contact area. This phenomenon is known as the Cassie-Baxter state, named in honor of the two researchers who first reported it in 1944, and it is present in all the surfaces that exhibit extreme liquid repellency with high apparent contact angles [19]. However, other forms of liquid repellency have been devised that do not necessarily employ the Cassie-Baxter state. In particular, the Slippery Liquid-Infused Porous Surfaces (SLIPS) concept [20] achieves liquid repellency by maintaining a liquid-liquid interface where the liquid of the drop is immiscible with the impregnated liquid. In this case, the frictional force for tangential motion of the drop is based on the liquid-liquid contact area. The surface must generally be textured at micro and/or nano-scale and should have high adhesion to hold the impregnated liquid in place, but this impregnated liquid should also be highly repellent to liquid droplets. Figure 9.1 depicts all the aforementioned cases. In Figure 9.1a is shown a rough surface and a liquid droplet placed on it while air pockets are present in the spacing between the rough features that reduce the solid-liquid adhesion. In Figure 9.1b is shown the Wenzel state, where the liquid penetrates in the spacing between the rough protrusions of the surface, inducing pinning effects that

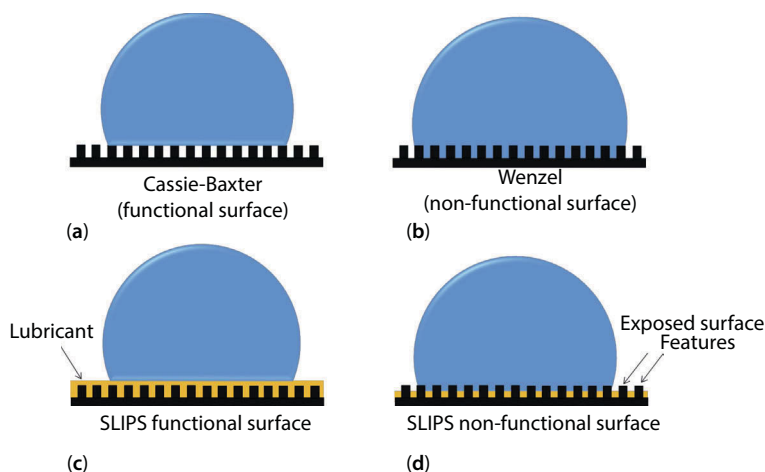


Figure 9.1 (a) Cassie-Baxter state that promotes liquid repellency. (b) Wenzel state where the liquid penetrates in the rough asperities of the surface, increasing the surface-liquid adhesion. (c) SLIPS type of surface where the lubricant covers the surface features. (d) The lubricant leaves exposing some surface features and the adhesion of the droplet to substrate increases.

dramatically increase the solid-liquid adhesion [21]. Figure 9.1c represents the SLIPS concept where the liquid droplet is “floating” on the lubricant layer that fully covers the surface features, while Figure 9.1d depicts a damaged/non-functional SLIPS type of surface due to the uncovering of surface features that again induce pinning effects.

The liquid repellency of a surface can be degraded by different ways including chemical reactions with solvents or gases, UV exposure, particle or bacteria contamination and mechanical wear. In this chapter, the focus will be on “mechanical” durability, i.e. surfaces that are able to retain their liquid repellency after repeated cycles of damage by mechanical forces and motions. The reason for this focus is that wear is the main performance loss mechanism found in most of the liquid repellent surfaces, while other types of degradation (UV exposure, particle contamination, chemical degradation, etc.) are more general topics that apply similarly to a broader range of non-liquid repellent surfaces.

In general, most superhydrophobic, superoleophobic, and superomniphobic surfaces are very fragile (i.e. they will lose liquid repellency if touched or rubbed by human hands) and are not suitable for commercial uses. This mechanical fragility of the surface texture can cause surface defects which leads to collapse of the Cassie-Baxter state. As a result, a subsequent

transition to the energetically more favorable Wenzel state occurs, where the liquid now penetrates in the rough asperities inducing strong pinning effects and eventually increased adhesion of the liquid to the substrate and loss of liquid repellency [21]. This lack of surface mechanical robustness to retain high liquid repellency hinders the possibility of applying such coatings in household products, vehicles, clothing, electronic devices, machinery, aircraft industry, etc. Owing to this, there has recently been an increased scientific effort towards significantly improving the mechanical performance of liquid repellent coatings. The first key review article that emphasized the mechanical durability of superhydrophobic coatings was published in 2011 [22]. The present article builds on this work by surveying many new developments that have occurred in the last few years.

As mentioned before, obtaining a Cassie-Baxter state that promotes liquid repellency requires at least one scale of roughness but the performance is increased if two scales of roughness (usually micro and nano) or more are employed [23]. The role of the micro-rough features is to sustain the droplet on their upper part so that air-pockets are formed on the droplet-substrate interface. However, studies in the literature have demonstrated that the height of micro-features must exceed a threshold value, which can vary for different types of textures, in order to suspend the liquid surface in air between two neighboring surface peaks, to maintain a Cassie-Baxter state [24]. If the height of micro-features is lower than the threshold value then transition to a Wenzel state will occur and the liquid repellency will be lost. Such a height reduction can happen when textured surfaces undergo mechanical wear, i.e. the height of the micro-features progressively decreases until it goes below the threshold for maintaining a Cassie-Baxter state. When this transition to a Wenzel state occurs, the damaged surface cannot perform its function of liquid repellency. This degradation is thus related to a loss in surface topography. Adding additional roughness scales on the order of submicrometer or nanoscale roughness can also change the wetting states from Cassie-Baxter to Wenzel or vice versa, having a dramatic impact on the liquid adhesion as it has been reported in recent studies [17,25,26].

Another mechanism for loss of functionality is the change in the surface chemistry by mechanical wear. This can happen when a liquid repellent surface employs a thin hydrophobic top-coat or simply surface functionalization to induce liquid repellent properties. Very thin monolayers or treatments which are usually on the molecular to nanoscale level tend to be removed very easily by the application of even minor mechanical abrasion, thus gradually uncovering hydrophilic sites from the underlying material that ruin the desired surface properties. This degradation is

thus related to a change in surface chemistry, as described schematically in Figure 9.2a, while Figure 9.2b describes a loss in geometric topology as previously discussed.

In the case of a SLIPS surface, mechanical degradation can have similar mechanisms. The textured coating must have nearly consistent porosity and chemistry throughout to hold the thin layer of infused-liquid. Thus a reduction in roughness height (geometric topology) or change in surface chemistry which inhibits the ability to hold the impregnated liquid in place would thereby reduce the performance. In addition, a third mechanism can occur for SLIPS if mechanical or fluid dynamic forces strip the impregnated liquid from a portion of the surface thereby exposing a portion of the hydrophilic solid surface to the liquid drop, and yielding a Wenzel state that causes loss of liquid drop repellence. Since the first two wear mechanisms are likely to be more common and since these two are strongly tied to those for conventional superhydrophobicity, this survey will focus on the mechanical degradation of surface geometry and chemistry as described in Figure 9.2.

The most common strategy for mechanical durability is to employ surfaces that can withstand structural forces while retaining the micro and nano-scale features associated with the surface topology and the hydrophobic composition associated with the surface chemistry. Two other possible strategies to maintain liquid repellency include self-healing surfaces [27] and easily repairable surfaces [28] although these surfaces are not wear resistant or otherwise mechanically durable. In particular, self-healing

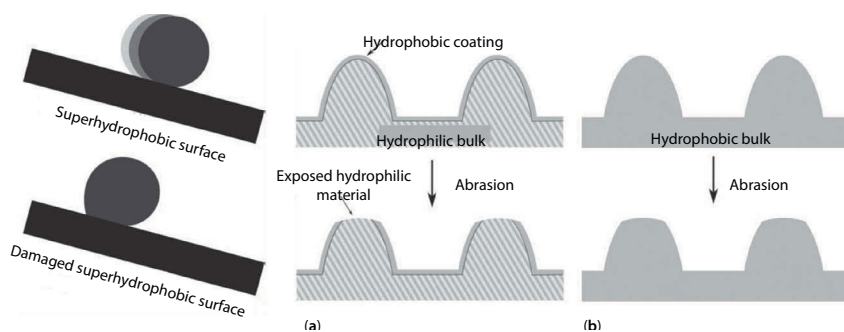


Figure 9.2 Due to the high contact angle and low hysteresis, liquid droplets easily roll off superhydrophobic surfaces. However, damage to the surface often leads to an increased contact angle hysteresis and, consequently, droplets stick to the surface. (a) A hydrophobic surface coating on a roughness pattern may get easily worn off, and hydrophilic bulk material will be exposed as a result. (b) If the roughness features are fabricated of hydrophobic material, wear will not introduce hydrophilic pinning sites [22].

surfaces are able to recover their liquid repellency upon being damaged by mainly two approaches. The first approach is based on encapsulation of the liquid repellent component in the pores of rough nano-porous materials. When damaged, this component quickly migrates to the damaged surface and recovers its surface properties [29]. The second approach is based on spontaneous self-organization of liquid repellent colloidal particles at interfaces [30]. On the other hand, easily repairable surfaces are materials whose liquid repellent properties can easily be repaired by deposition of a new material. This strategy is suitable for applications that require long-term functionality of the surfaces, yet continuous maintenance is required. However, both the self-healing and easily repairable strategies can be problematic. Specifically, self-healing surfaces once slightly damaged need some recovery time to self-heal which is an issue for applications that demand to retain the liquid repellency continuously. Furthermore, if the damage is significant (e.g. at the micro-scale), self-repair may not be possible since this strategy tends to be focused on the first few nanometers of the surface. The strategy of easily repairable coatings can compensate for micro-scale wear but requires accessibility for maintenance. For many applications where the object to be coated is not easily reachable by workers (wind turbine blades, for instance) or the area to be coated is very large, recoating would be prohibitive due to these technical issues.

Physical parameters that have been used in the literature to characterize the mechanical durability of liquid repellent surfaces include the apparent contact angle (APCA), the contact angle hysteresis (CAH), the roll-off angle (ROA) and the shedding angle (SHA). The APCA is a measurement of the equilibrium condition when a liquid droplet is placed on a solid substrate and it is defined as the angle between the tangent to the liquid–fluid interface and the tangent to the solid interface at the contact line between the three phases [31]. For extreme liquid repellent surfaces this value has to be greater than 150° . However, meta-stability can make this parameter difficult to measure as it can be a function of the method of droplet placement, condensation, surface vibration, etc [32]. In contrast, the other parameters mentioned above (CAH, ROA and SHA) quantify the dynamic ability of the liquid to stay adhered on the solid surface. As such, they are a more consistent indicator of liquid repellence from a functional perspective and are defined in more detail below.

The roll-off or sliding angle is simply the maximum angle that the surface can be tilted until the liquid droplet rolls off or starts sliding. This measurement can be influenced by the volume of the liquid droplet, since gravitational effects take place. In other words, the roll-off (ROA) or sliding angle (SA) decrease as the size of the droplet increases [33]. The

terminologies ROA and SA describe different behaviors in that rolling motion occurs when both the receding contact angle (RCA) and advancing contact angle (ACA) are greater than 90° while sliding motion of a droplet on a surface occurs when either RCA or (less likely) ACA is less than 90° . Both ROA and SA are defined by researchers as the substrate tilt angle at which a liquid droplet starts to move at both the advancing and receding contact lines. To avoid misunderstanding and confusion we declare that throughout this chapter we will generally use the terminology that each author provides in his/her paper. The contact angle hysteresis of a surface is the difference between the advancing and receding angles, i.e. $CAH = ACA - RCA$. The greater the difference between the advancing and receding angles, the more adhesive the solid surface is to the liquid under investigation. Finally, the shedding angle (SHA) is defined as the lowest surface angle to the horizontal that allows the droplets to leave the substrate by bouncing or rolling off when released from a given height. If the release height approaches zero, the shedding angle simply reverts to the roll-off or sliding angle.

The shedding angle can be measured by releasing drops from a fixed height for different tilt angles of the substrate. This measurement method was originally developed by Zimmerman *et al.* for overcoming imaging problems in the classic contact angle measurement when using textiles, since the surfaces of the textiles are usually very rough and the boundaries of the water droplets cannot be well distinguished in order to have an accurate measurement [34]. The shedding angle values are also influenced by the dispensing height and the size of the droplets, as the authors describe in their paper. In general, the shedding angle is less than or equal to the roll-off angle.

If an extremely liquid repellent surface is mechanically durable, it should ideally maintain CAH, ROA and SHA values lower than 5° or 10° for repeated mechanical degradation tests of the surface. The reason for this focus on dynamic parameters is that damaged liquid repellent surfaces sometimes maintain a high APCA but the droplets tend to stay “pinned” on the substrates, a phenomenon described in the literature by various researchers as “petal effect” [35]. Furthermore, surfaces such as the SLIPS concept are designed to have low SA values, with little attention paid to the magnitude of the APCA. For these reasons, it is of significant importance to focus on the dynamic repellency characteristics, such as CAH, ROA and SHA.

Having mentioned the parameters that are used to quantify the wetting performance of a surface, the following sections will describe the primary modes of mechanical degradation and the different associated testing for

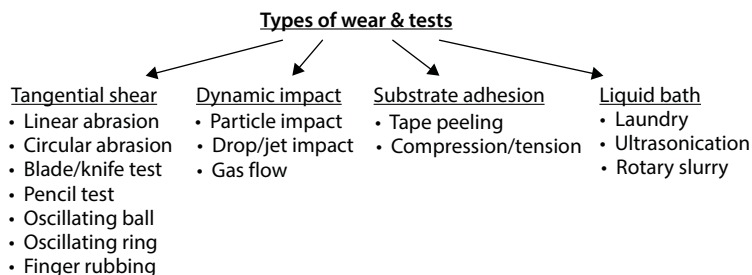


Figure 9.3 Different types of wear and their corresponding tests.

each of these modes as described in the schematic of Figure 9.3. The mode aspect is critical to understanding the mechanisms of wear while the testing aspect is closely related to the practical aspect of commercial development. The mode mechanisms discussed herein include: tangential linear abrasion (shear stress), impact with solid, liquid and gas phase, and normal (compression or tension) stress. Regarding testing, there are many different types of experimental setups, most of them custom-built in-house equipments, that induce mechanical damage and have been reported in the literature such as linear abrasion, sand impact, tape peeling, finger touching, washing cycles, etc. Finally, special cases of liquid repellent surfaces will be presented that are not influenced by mechanical wear (bulk liquid repellent materials) or mechanical wear even enhances their properties instead of degrading them.

9.2 Durability to Tangential Shear

An objective comparison of the abrasion resistance of superhydrophobic surfaces has been hampered by the lack of a single, standardized test method. Likewise, no single measure has been used for characterizing the effect of wear. Moreover, all these different approaches induce very diverse surface topography modifications but at the same time all of them are referred as “mechanical durability” tests. This is very confusing for someone who wants to evaluate how durable is one surface compared to the other. Generally, abrasion resistance is most directly and commonly measured using linear shear abrasion. In this form, shear stress arises from the force vector component parallel to the cross section of the material. The most common approach, based on the number of published papers, for the evaluation of the mechanical durability of liquid repellent surfaces is

to perform tangential (shear) abrasion tests. This has been reported in the literature using many different experimental setups all of them having in common the basic concept of rubbing a solid material to the surface under investigation. This induces wear and subsequently material removal that eventually leads to alteration of the surface characteristics and loss of the liquid repellency. Before we present the work that has been done so far, it is necessary to address some important issues that have to be considered when the mechanical performance of different surfaces is to be compared.

Different materials have been used throughout the literature to perform abrasion. These materials vary from study to study since authors have used as abrasants, e.g. rough sandpapers of different grades, aluminum, A4 paper sheets, poly(dimethylsiloxane) (PDMS), glass, etc. Wu *et al.* prepared superhydrophobic polyester textiles by a dip-coating approach and later they tested their mechanical durability by abrading them linearly with different abrasants (A4 paper sheets and sandpaper) [36]. Due to the difference in the physicochemical characteristics of these two materials (hardness, surface roughness, chemical affinity) they observed very different degradation rates of the water repellency of their samples. Furthermore, Wang *et al.* showed completely different liquid repellency when they abraded their superhydrophobic surfaces by sandpapers of different grades [37]. Interestingly, they were able to show superhydrophobicity only when they used sandpaper of grade in the range 280–400#. For all the other grades used, outside these limits, their surfaces did not exhibit superhydrophobic property. These important observations lead to the conclusion that a mechanical test is heavily influenced by factors such as the surface roughness of the abrasant surface, or its chemical composition and Young's modulus. Other obvious parameters that influence the measurement and also vary from study to study include the applied pressure on the abrasant surface, the type of contact between the two surfaces, the relative speed between them, etc. Thus, in order to evaluate the mechanical durability of a sample surface and compare it with others all these parameters have to be clearly stated.

9.2.1 Linear Abrasion

Figure 9.4a depicts a typical experimental setup for performing a linear abrasion test. Usually it consists of a horizontal arm holding a vertical cylinder that reciprocates in a linear direction while the speed and the length can be adjusted. The bottom end of the cylinder can be fitted with various types of abrasant materials like cloth, sandpapers, rubbers, papers or hard aluminum oxide which produce different type of mechanical wear. The

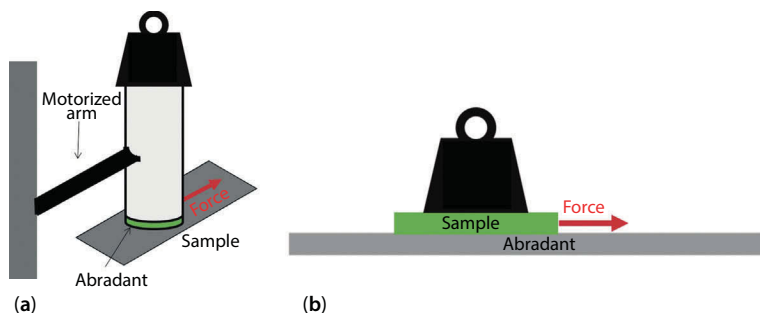


Figure 9.4 Linear abrasion configurations: (a) with motorized arm that moves and rubs the tested sample surface tangentially, and (b) with sample moving on the abrasant surface.

sample to be tested is mounted and aligned parallel and in contact with the bottom part of the cylinder. The pressure applied on the surface to be tested can be adjusted by adding or removing weight on the vertical cylinder. There are a few companies in the market that offer automatized instruments in this configuration and also provide a wide selection of abrasant materials. A common alternative configuration that typically is followed in house-built setups is the one shown in Figure 9.4b. The surface to be tested is fixed at the bottom part of a solid structure of known weight and it performs a linear reciprocating motion on the substrate which in this case is the abrasant material. Linear abrasion setups are the most common and widely accepted method to test the mechanical durability of liquid repellent surfaces.

Wu *et al.* [38] used a similar apparatus as in Figure 9.4a in order to test the durability of superhydrophobic cotton fabric (SCF) obtained by radiation-induced graft polymerization of lauryl methacrylate and n-hexyl methacrylate. Self-healing of the surfaces could be achieved by ironing. Through the steam ironing process, the superhydrophobicity could be regenerated even after the yarns were ruptured during the abrasion test under a load pressure of 44.8 kPa and crocking cloth used as abrasant material. The treated cotton fabric could ultimately withstand at least 24,000 cycles of abrasion with periodic steam ironing. However, the term superhydrophobic was used considering only the APCA since no hysteresis values were reported in this study. Textile surfaces will be analyzed more extensively in one of the following sections since they behave very differently in terms of durability compared with non-fibrous materials.

Tang *et al.* [39] prepared superomniphobic coatings by spray-casting dispersions of polyurethane and MoS₂ nanoparticles. After the spraying

process the surfaces were functionalized by gas-phase silanization with a fluorosilane. The abradant material was stainless steel that was roughened with a sandpaper prior to the abrasion test. The applied pressure on the surface was 0.7 MPa and the water APCA and CAH were measured as a function of the rubbing distance (i.e. the total distance that the abradant covered on the tested surface by rubbing it) and not abrasion cycles like in other studies. The coatings were able to preserve high contact angles ($>150^\circ$) for up to 100 m rubbing distance but the CAH increased significantly with the first 10 m of rubbing distance. This result is a very good example to emphasize the importance of presenting both static and dynamic contact values when mechanical abrasion tests are performed, since the surfaces might appear extremely liquid repellent statically but dynamically (which is also the most practical aspect) their properties might degrade faster.

Steele *et al.* [40] prepared laser-textured titanium surfaces that were rendered superhydrophobic by applying a subsequent fluoropolymer coating. Titanium was selected as the material for surface texturing due its inherent outstanding mechanical durability. In this study, they investigated harsh applied pressure conditions ranging from 108.4 to 433.7 kPa. This surface was able to survive 200 abrasion cycles before it was destroyed and the APCA decreased gradually. For higher applied pressure the reduction of the APCA was faster. Also in this case the CAH increased much faster even only after 10 abrasion cycles. The effect of the wear mechanism from the abradant material was also described in detail. The primary abrasive wear mechanism was found to be the fatigue by repeated plowing, but there was also contribution by the small particles detached from the abradant material during abrasion that caused small striations on the textured titanium substrates (Figure 9.5).

Milionis *et al.* [41] have also investigated the effect of applied pressure on superhydrophobic biodegradable starch-based thermoplastic nanocomposites. The nanocomposites were prepared by spraying colloidal dispersions of bio-plastic Mater Bi® (Novamont, Italy) and surface modified fumed silica and for specific concentrations of particles lotus leaf-type behavior was achieved. Five different pressure values ranging from 1115 Pa to 2123 Pa were applied on the surface of the coatings and the water APCAs and ROAs were recorded for up to 17 abrasion cycles. A solid smooth plastic disk (2 cm in diameter) with Rockwell hardness of M70 (R-scale; ISO 2039-2) similar to polycarbonate was used as an abradant. Again it was observed that increasing the applied pressure on the surfaces gradually decreased the APCAs, a phenomenon that was most intense for the highest pressure used (2123 Pa) since the APCAs dropped below 150° after 10 abrasion cycles. However, the increasing trend of the roll-off angles

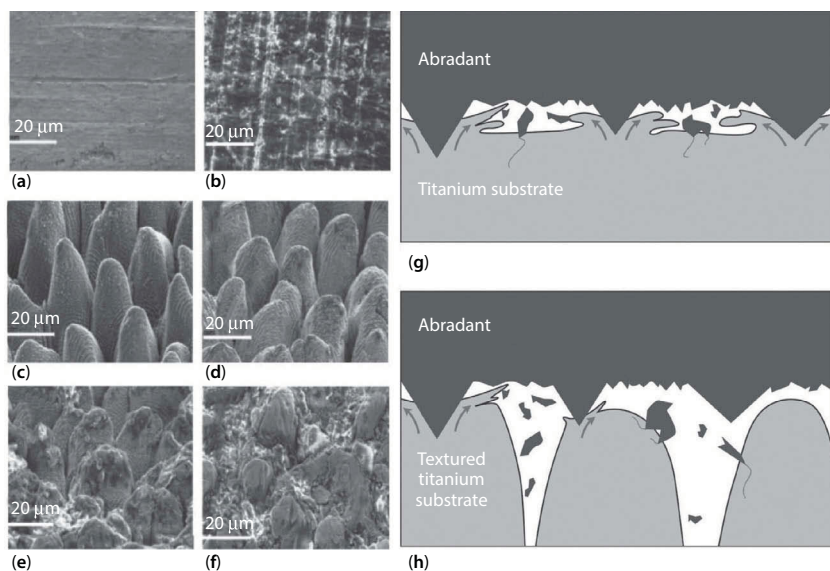


Figure 9.5 Left: SEM images of (a) control titanium with fluoropolymer coating; (b) control titanium with fluoropolymer coating after 200 abrasion cycles at 350 g; (c) as prepared titanium; (d) textured titanium with fluoropolymer coating; (e) textured titanium with fluoropolymer coating after 200 abrasion cycles at 350 g; (f) textured titanium with fluoropolymer coating after 200 abrasion cycles at 1400 g. Right: Schematic of primary abrasive wear mechanism with fatigue by repeated plowing, showing a blend of two-body (significant plowing) and three-body (small striations) wear modes with the direction of abrasion into the page for (g) control titanium and (h) textured titanium substrates [40].

against the number of abrasion cycles was much more evident, especially for applied pressures equal or greater than 1717 Pa. Under 2123 Pa the coatings lost their superhydrophobicity after 5 abrasion cycles.

Zhu *et al.* [42] used a home-made setup similar to Figure 9.4b to test the mechanical durability of their superhydrophobic surfaces prepared by molding ultra-high molecular weight polyethylene and functionalizing the surface with silver and perfluorodecanethiol. The abradant used was a sandpaper (1500 mesh) and the applied pressure was 10 kPa. The resulting surface was able to withstand 10 abrasion cycles under these conditions before eventually starting losing the superhydrophobicity due to the decrease in the fluorine concentration on the surface. However, they were able to easily regenerate their surfaces when the superhydrophobicity was lost by repeating the Ag deposition and surface fluorination with the immersion method.

Zhou *et al.* [43] used the same experimental apparatus to evaluate the mechanical performance of cotton fabric that was rendered superhydrophobic by incorporation of polyaniline and fluorinated alkylsilane via a facile vapor phase deposition process. The applied pressure was 3.68 kPa. The authors demonstrated that their surface could maintain water APCAs greater than 150° for 600 abrasion cycles but they did not mention anything about hysteresis values.

Cho *et al.* [44] prepared superhydrophobic aluminum surfaces by preparing micro- and nano-rough hierarchical structures by a 3-step approach. First, the formation of nanostructured aluminum hydroxide was carried out in a NaOH solution. Subsequently, a microrough surface texture was obtained by sandblasting the aluminum sheet with sand particles and finally the surface was hydrophobized with a fluorosilane. The authors used a similar experimental setup to carry out the mechanical durability tests but with a slightly different approach. Instead of reporting the total number of abrasion cycles until their surface would lose its properties, they performed only one abrasion cycle but they increased every time the weight (or the pressure) applied on the surfaces until eventually they would see loss of superhydrophobicity. Their surfaces were able to withstand up to 100 g with this technique (or otherwise 500 Pa, considering the surface area of their specimens).

Chen *et al.* [45] developed self-repairing superhydrophobic organic/inorganic coatings comprising polystyrene, fluorinated poly(methylsiloxane), fluorinated alkylsilane, modified silica nanoparticles (NPs) and photocatalytic titania NPs that showed self-repairing ability after mechanical damage with the application of UV light. To evaluate the influence of mechanical wear of the superhydrophobic coating, the surface was abraded using a piece of sandpaper under 10 and 20 kPa pressure. The results showed that the surface was still superhydrophobic although a slight decrease in the APCA was observed (from 155° to 150°) after 10 cycles of abrasion under 10 kPa pressure. Nevertheless, when the surface was abraded under 20 kPa pressure, the water contact angle (WCA) declined considerably from 155° to 139° and the SA rose to 70° . However, after UV exposure the samples fully recovered their superhydrophobicity. The authors also performed an accelerated weathering test to demonstrate the suitability of their surfaces to outdoor environment.

Tenjimbayashi and Shiratori [46] developed superhydrophobic coatings by mixing SiO_2 nanoparticles and ethyl alpha cyanoacrylate polymer in acetone and subsequently spraying them while at the same time the distance between spray source and substrate was continuously changing. The change in the distance between spray and substrate was found to be the

key for improving the durability. The durability of the coatings was tested for different applied pressures (10 cycles) with cellulose fiber as abradant. The coatings retained their superhydrophobicity after abrasion testing at 40 kPa. Coatings consisting of only nanoparticles lost their superhydrophobicity upon testing.

9.2.2 Circular Abrasion

Circular abrasion is based on the same concept as linear abrasion and it uses the same experimental apparatus with the only difference being the type of movement that the abradant material performs. In this case the abradant material has the shape of a disk and it performs a rotational motion. The only disadvantage in this case, compared to the linear abrasion, is that different parts of the abradant material move with different speeds. Even if in most of the cases this is not very crucial, we cannot exclude the possibility that this technique can produce diverse surface characteristics in the abraded surfaces. The Martindale method is a common circular abrasion test that is used mainly for evaluating textiles (see also Section 9.5.1).

Kondrashov and Ruhe [47] studied the effect on the mechanical durability of different hierarchical superhydrophobic surfaces with micrometer sized cone and nanoscale grass structures produced by reactive ion etching and subsequent deposition of a fluorinated film. Their setup for testing the mechanical durability consisted of a rheometer where a metal disk (2 cm diameter) was brought into contact with the tested surfaces and performed a rotational motion for 30 s (10 rotations/min) (Figure 9.6). Different forces were applied vertically ranging from 1 to 20 N. The authors did not mention the pressure values applied on the surface since samples with different densities of microstructures were used. The density of the structures varied across the sample and the contact area of the load with the micro- and nanostructures changed with time as some breaking of the micro- and nanostructures occurred. Therefore, it was not possible to calculate the area in contact with the abradant. It was found that the most durable surfaces were the ones with the tallest and densest micrometer sized cone structures that were able to maintain their superhydrophobic characteristics even for 20 N applied force. On the contrary, the nanoscale grass surfaces where they did not have micro-scale roughness were found to be significantly less durable.

Raimundo *et al.* fabricated aluminum alloy surfaces with omniphobic behavior [48]. Functional, hybrid organic–inorganic coatings were obtained by a classic sol–gel route, followed by a controlled dip coating of the substrate in order to achieve surface nanostructures. The surfaces

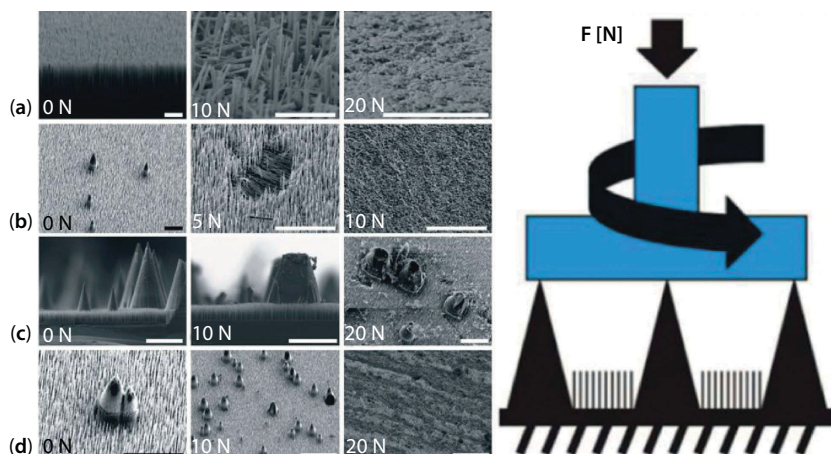


Figure 9.6 SEM images of various superhydrophobic surfaces before and after performing the wear tests with forces given in figure (a) nanograss surface (NS), (b,c,d) microcone and nanograss combinations. Scale bar: 5 μm (a), 20 μm (b–d). On the right there is a sketch depicting the circular abrasion configuration. Reproduced with permission from [47]. Copyright 2014 American Chemical Society.

showed good liquid repellency with APCA higher than 170° and CAH lower than 5° with water, as well APCA about 145° with low-surface tension liquids. The mechanical performance of the surfaces was tested by applying loads as low as 4 N for a short time (30 s) by an abrasive felt disk (diameter of 6 cm) rotating on the test sample at a speed of 60 rpm. The samples retained their liquid repellent characteristic after the aforementioned test was performed.

9.2.3 Blade/Knife Test

Rubbing between two solid surfaces is a common case that can occur in everyday use of liquid repellent materials. However, there are also occasions when surfaces could come into contact with sharper objects (e.g. knives, pens, forks, etc.) that induce much more severe damage. Driven by this problem, a few studies have been published where liquid repellent surfaces undergo blade tests, which are practically linear abrasion tests but instead of a flat abradant material the rubbing is performed by a sharp blade.

Wang *et al.* [49] used both blade and circular abrasion tests and plotted the wetting characteristics of their samples against the number of abrasion cycles. Superomniphobic, surface-treated polyester fabrics were fabricated

by a 2-step dip-coating procedure. The first step involved immersion in a dispersion of fluoroalkyl surface-modified silica nanoparticles and the second in a mixture of fluorinated decyl polyhedral oligomeric silsesquioxane and tridecafluorooctyl triethoxysilane. The blade scratching test was performed on a custom-made setup. The coated fabric sample was placed on a flat smooth plate. A flat blade was mounted vertically on a frame with the blade edge in close contact to the top surface of the fabric sample. A 0.8 kg weight was loaded on the blade, which was adequate load to cut the fabric. The blade was then dragged linearly with 100 drags of the blade being a “cycle”. Water, hexadecane and ethanol were used for contact angle measurements. Only APCA values were reported for the blade test. After 100 scratches were performed, the ethanol APCA reduced to 0° , while the APCA for water and hexadecane reduced to 150° and 120° , respectively. For the circular abrasion tests, a polyester abradant was used under 12 kPa pressure. The APCA of water remained above 150° even after 20000 abrasion cycles. On the other hand, the APCA for hexadecane and ethanol reduced with increasing abrasion cycles, although the hexadecane APCA value was still above 150° after 20000 cycles of abrasion, and the APCA for ethanol reduced to 127° after the abrasion. The SA suffered a larger impact from abrasion testing than the APCA. After 20000 cycles of abrasion, the SA for water and hexadecane increased, respectively, from 2.8° and 18.5° to 12.3° and 68.0° . A larger increase in SA was observed for ethanol, which reached the test limit of 75° after 5000 cycles of abrasion. As can be seen from the results the blade test produces more severe damage on the surfaces.

Jin *et al.* [50] also used the blade test in their surface-treated aerogels. Figure 9.7 shows high and low magnification SEM images of the surface before (Figure 9.7A,B) and after abrasion with sandpaper (Figure 9.7C,D) and a knife (Figure 9.7E,F) as abradants. After performing scratches on their samples with the knife, severe abrasion was observed at macroscale. However, the nanoscale roughness features (Figure 9.7E, F) remained similar to that in the original aerogel surface (Figure 9.7B). This demonstrates that the silica aerogel had a nanoscale topography that was tolerant to damage, as a fresh surface with nanoscale topography was spontaneously exposed upon mechanical damage.

Vogel *et al.* [51] prepared patterned omniphobic lubricated surfaces based on inverse colloidal monolayers following the SLIPS approach. Their surfaces showed very low SA ($< 3^\circ$) for both water and octane. They performed various qualitative tests including the blade test without observing loss of the liquid repellency. Other mechanical durability tests performed included finger rubbing, tape peeling, etc. which will be discussed in the following sections.

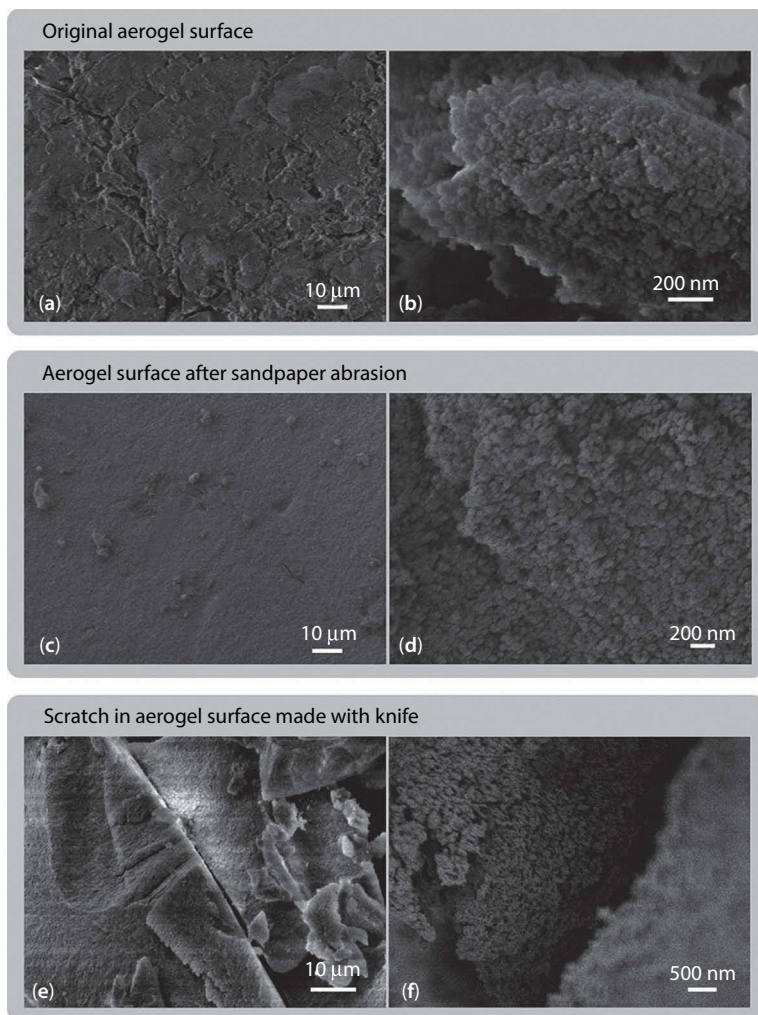


Figure 9.7 SEM micrographs of fluorinated silica aerogel (a, b) before abrasion, (c, d) after abrasion with sandpaper (100 cycles), and (e, f) after scratching with a knife. Images b, d, and f show that after mechanical damage the exposed aerogel surface has a similar nanoscale topography as before abrasion. This is due to the bulk structure of the silica aerogel consisting of a nanoporous framework of silica nanoparticles. Reproduced with permission from [50]. Copyright 2014 American Chemical Society.

9.2.4 Pencil Test

Another mechanical durability test is the pencil hardness test. According to this method a pencil with quantified hardness is dragged on the surface

to be tested. The maximum pencil hardness that the surface can withstand without losing its liquid repellency is associated with its mechanical durability.

Geng and He [52] prepared superomniphobic silica thin films by self-assembly of different sizes of nanoparticles and subsequent chemical vapor deposition (CVD) with tetraethyl orthosilicate (TEOS) to improve the mechanical robustness. Only APCA values were measured for the coatings that reached 171° for water and 152° for ethylene glycol. The pencil hardness test was carried out by holding the pencil firmly against the film at a 45° angle and performing a 6.5 mm stroke at a speed of 0.5 mm/s. The coatings could withstand pencils with hardnesses up to 4H without being destroyed. Figure 9.8 shows the morphology of the surfaces after performing scratches with increasing pencil hardness.

Simovich *et al.* [53] developed a durable and superhydrophobic coating through encapsulating nylon micrometer sized rods in a hydrophobic silica shell. The resultant coating structure resembled a network of highly entangled micrometer sized rods that gave rise to both surface roughness and hydrophobicity, resulting in contact angles greater than 155° . The embedded nylon polymer within the micrometer sized rods imparts significant mechanical durability to the surface, resulting in a coating hardness of 2H using the pencil hardness test.

Hydrophobic nanosilica and nanofluoric particles were mixed with fluoropolyurethane resin in various concentrations to fabricate superhydrophobic coatings that had APCA ranging from 140° to 148° and CAH from 5° to 12° [54]. The hardness of coatings was found to increase by raising the nanoparticle concentrations. By using the appropriate ratios between the two types of particles and the polymer, the maximum pencil hardness that the coatings could withstand was 3H.

9.2.5 Oscillating Steel Ball

Another experimental setup that has been used in the literature by Hensel *et al.* [55] to evaluate the mechanical durability of their omniphobic polymer membranes is the oscillating steel ball. A steel ball with a diameter of 1.5 mm was brought in contact with the sample surface and pressed with a normal load that was stepwise increased until the surface features were damaged. Shear stress was generated by lateral oscillation of the probe: 10 cycles with a speed of 0.05 cm/s and a maximal displacement of 1 mm (Figure 9.9). The mechanical durability of the membranes was compared with pillar-patterned surfaces. The membranes resisted loads of 200 to 500 mN depending on the comb (the hexagonal structure) wall width (Figure 9.9a). In contrast, the mechanical stability of the pillar structures was much lower

compared to the membranes and was able to withstand forces ranging from 1 to 75 mN depending on the pillar diameter (Figure 9.9b).

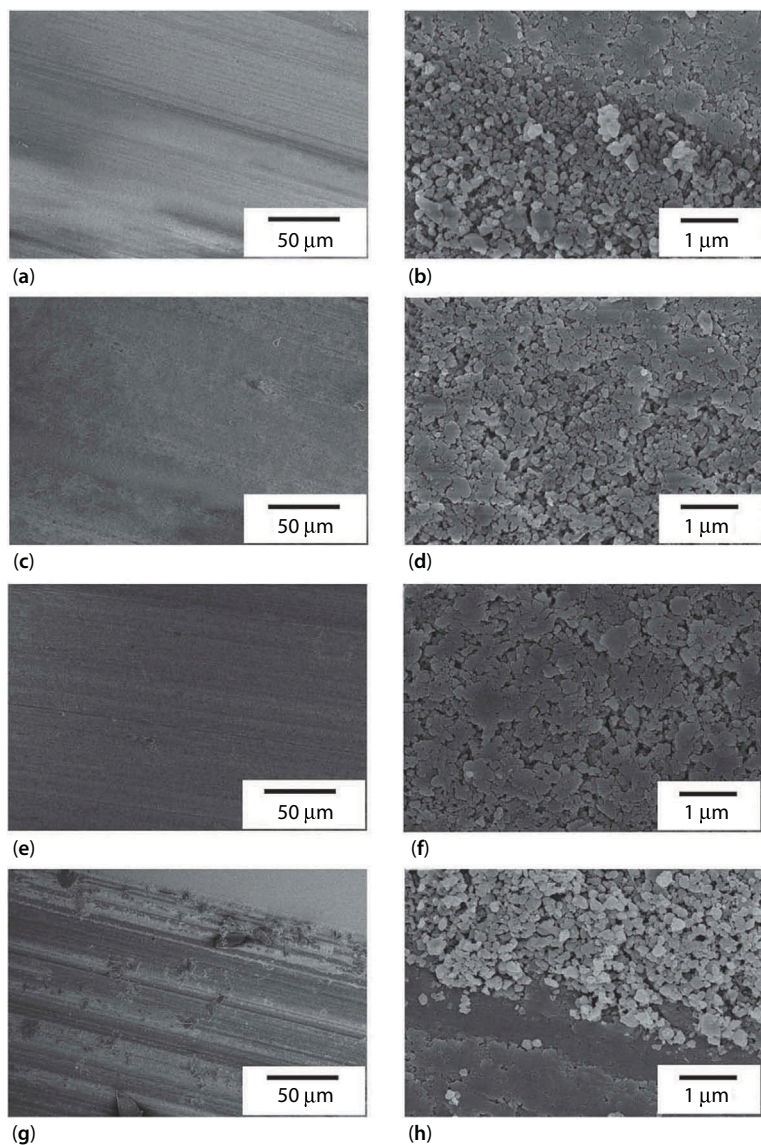


Figure 9.8 SEM images of the coatings treated by tetraethyl orthosilicate chemical vapor deposition (TEOS CVD) for 3 h after 2H (a and b), 3H (c and d), 4H (e and f) and 5H (g and h) pencil scratching tests. Reproduced from [52] with permission of The Royal Society of Chemistry.

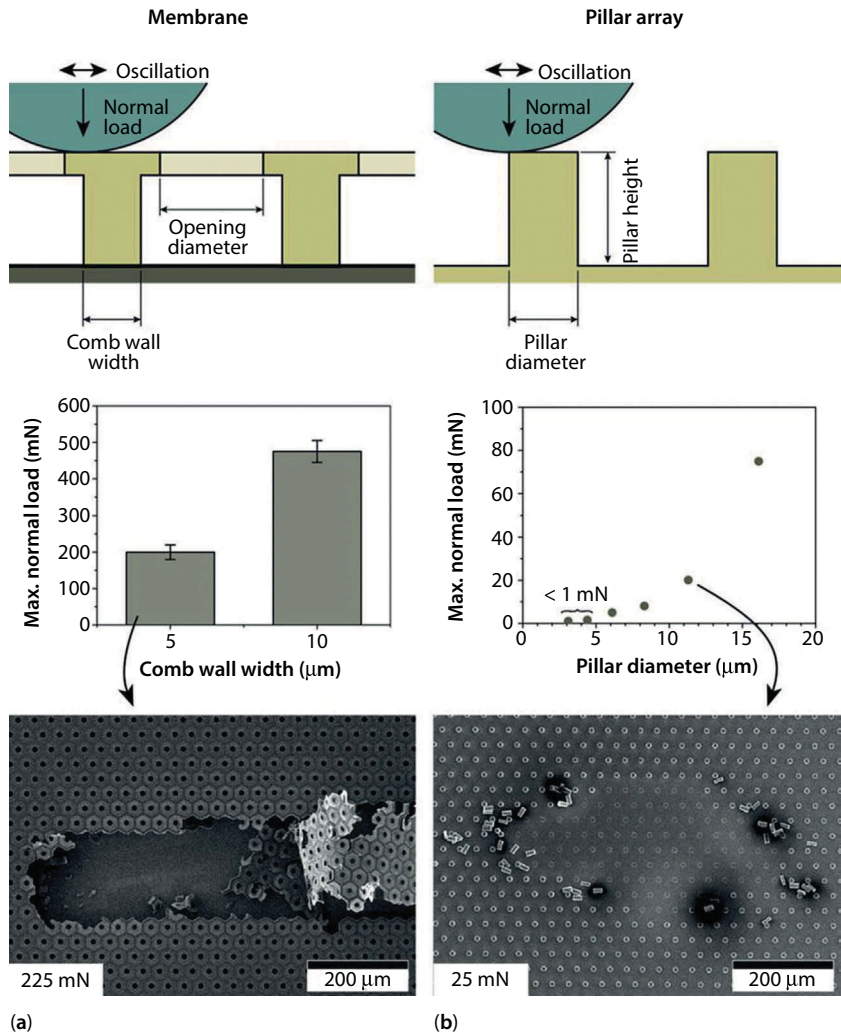


Figure 9.9 Wear tests on (a) polymer membranes in comparison to (b) pillar arrays: Schematic representation of the experimental setup consisting of an oscillating steel ball, pressed onto the structured surfaces. Experimental data on maximum normal loads the surfaces can resist without destruction and SEM images after failure [55].

9.2.6 Oscillating Steel Ring

Instead of an oscillating ball as described in the previous section, an alternative abrasant material could be an oscillating ring. Groten and Ruhe [56] used an experimental setup comprising a steel ring (diameter 2 cm,

thickness 1.5 mm) that was pressed on the tested surfaces with a force perpendicular to the surface plane. The surfaces under investigation were silicon pillars with micro- and nano-roughness. To create shear stress, the ring was oscillated for 30 s on the tested surfaces at a frequency of 20 Hz and a maximal displacement of 4 mm. Parallel alignment of the ring to the tested surface was assured. Whenever force was applied, the ring was automatically (self-) aligned to the surface plane. The force applied on the surfaces ranged from 1 to 20 N. It was found that adding micro-rough pillar structures improved the mechanical performance of the surfaces as they were able to retain better water-repellent characteristic at higher shear forces. However, the surfaces that had only nano-roughness were the only ones that presented CAH values lower than 10° and eventually were destroyed by the abrasion test.

9.2.7 Finger Rubbing

Finally, shear stress measurements on liquid-repellent surfaces have also been performed with more qualitative methods, but still important results could be obtained regarding the applicability of liquid repellent surfaces in commercial, everyday use applications. Such approach involves rubbing the surfaces with a gloved finger. A periodic rubbing motion with the finger can be considered an abrasion cycle and the mechanical performance of surfaces can be evaluated by measuring the wetting parameters before and after the abrasion or for continuous abrasion cycles with the finger.

Xu *et al.* [57] prepared superhydrophobic surfaces using stainless steel meshes as a template to pattern low density polyethylene films by heating them above their glass transition temperature, allowing them to conform to the template's surface, and subsequently cooling them down and peeling them off. The surfaces were rendered superhydrophobic by adjusting mesh dimensions and molding parameters, and no further surface treatment was necessary. In this manner, surfaces with APCA 160° and SA 5° were obtained. Subsequently a manual test was carried out to evaluate the mechanical performance including 4 steps (3 finger rubbing steps and a final ultrasonication step): (1) dry abrading firmly with a gloved finger using a back and forth movement for 50 times, (2) dry abrading firmly with a finger wearing an industrial cotton glove back and forth for 50 times, (3) wet scrubbing manually with a gloved finger for 1 h (20 cycles) with a saturated industrial cleaner solution, and (4) ultrasonication in the same saturated industrial cleaner solution for 5 h. As can be seen from Figure 9.10 the samples preserved their superhydrophobicity. The APCA remained the same while the SA increased to 10° . Additionally, a controlled linear

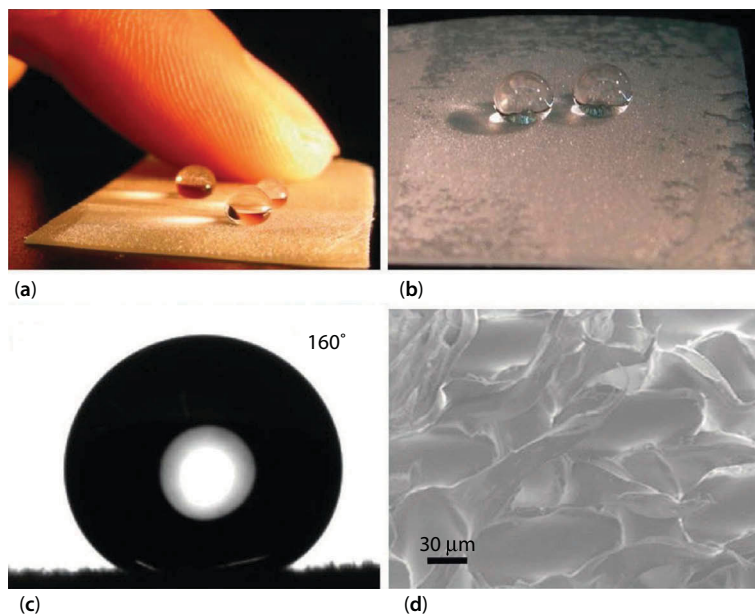


Figure 9.10 Superhydrophobic surface after manual abrasion testing (a) being touched with a bare finger, (b) water droplets on a partly dried surface after the multistep manual test, (c) water contact angle on the surface after the same multistep manual test; the surface was rinsed with water and dried before measuring, (d) SEM image of the surface structure after the same multistep manual test. The surface was rinsed, dried, and coated with gold before imaging. Reproduced with permission from [57]. Copyright 2011 American Chemical Society.

abrasion test was also performed with 32 kPa applied pressure. The APCA remained essentially unchanged at 160° over the first 2520 abrasion cycles and then decreased slowly to 155° with increasing cycles. The SA remained unchanged after 2520 cycles and increased slowly with increasing abrasion cycles. After 5520 cycles, water droplets on the surface still appeared as transparent balls. When the total number of abrasion cycles was increased to 6520, the APCA decreased to 140° and then maintained this level with further abrasion cycles.

Zhang *et al.* [58] developed superhydrophobic aluminum alloys by one-step spray coating of an alcohol solution consisting of hydrophobic silica nanoparticles (15–40 nm) and methyl silicate precursor on etched aluminum alloy with pitted morphology. The as-sprayed metal surface showed APCA of 155° and ROA of 4° . In their study they used many different mechanical durability tests that we will describe in the next section and

they made a video demonstration where they rubbed their surfaces with a gloved finger without losing their water repellency.

Bare finger touch has also been reported in various tests. This is a qualitative test that is performed on liquid repellent surfaces to better mimic human handling. The natural and artificial liquid repellent surfaces are often fragile to hand touch. A bare finger touch on a surface can also cause performance-degrading material addition, e.g. the touch can add salt and oil contaminant to surface, especially if this surface does not repel organic compounds, i.e. is not oleophobic. Natural secretions of sweat from the eccrine glands that are present in epidermal ridges are easily deposited on surfaces (such as glass or metal or plastics) by just touching them. Consequently, touching a liquid repellent surface with a finger can alter its characteristics both physically (by destroying the surface texture) and chemically (by leaving natural secretions), thus degrading its inherent properties. Such qualitative tests have been performed in various studies in the literature [42,57,59–63].

9.3 Durability to Dynamic Impact

Surface durability can also be tested under collisions with solid, liquid or gas phases. In these tests the surfaces are usually placed either horizontally or with a 45° tilt. The surface topography can be significantly altered by these collisions in a way that it is not functional anymore or the hydrophobic component of the surface can be totally removed/destroyed. In this section we will present approaches to evaluate how sensitive is a liquid repellent surface to normal impacts and material removal.

9.3.1 Solid Particle Impact

Solid particle impact is a common test that is performed to evaluate the mechanical robustness of surface finishes. In this test, sand is typically used which is a mixture of micrometer-sized oxide particles with the silicon dioxide being the most dominant. This test can provide information whether a coating is suitable for use in outdoor applications where eventually it has to withstand harsh weather conditions and contamination/degradation of the liquid repellent properties by embedded particles on the surface that can disrupt the surface chemistry by their presence or can cause partial destruction of the surface texture due to the impacts. It is also a common test in aerospace applications (e.g. for helicopters) where they

have to withstand very severe particle collisions during their take-off and landing. A typical experimental setup is depicted in Figure 9.11. The coating under investigation is tilted usually 45° , so that re-deposition of the particles after the impact can be avoided. The sand flows at a constant rate from a container placed at a given height from the surface. With increasing height, the kinetic energy of the particles increases and eventually the probability of damaged surface is higher. The impact energy of a solid particle is given by:

$$W_s = m_s gh = \frac{4\pi}{3} \rho R_s^3 gh$$

Here, ρ is the average density of the particles, g the acceleration of gravity, and R_s the mean radius of the particles.

Deng *et al.* [64] prepared transparent superhydrophobic surfaces composed of hydrophobically surface modified silica shells on glass slides. The surfaces showed APCA of 160° and SA of 5° . Sand grains were impacted on the superhydrophobic surfaces and the minimal height at which the porous silica particles burst was determined. Bursting leads to an increase of the sliding angle and finally to loss of superhydrophobicity. If 100 to 300 μm sized sand grains impacted on a superhydrophobic surface the shells remained intact for impact heights, h , up to 30 cm. After the sand abrasion, the surface remained superhydrophobic, i.e. water droplets placed on the surface would bounce and slide off easily. For h significantly larger than 30 cm, fractured shells were found. The same research group fabricated superomniphobic surfaces consisting of silica shells and carbon particles (candle soot) and the same sand impact test was performed [65]. The APCA and ROA for water were measured to be $165^\circ \pm 1^\circ$ and $1^\circ \pm 1^\circ$ respectively and for diiodomethane the APCA was $161^\circ \pm 1^\circ$ and the ROA

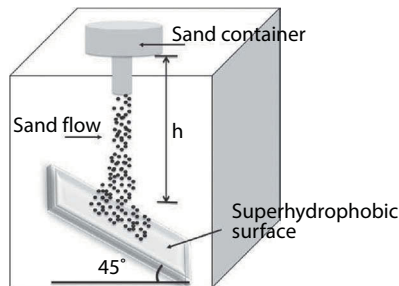


Figure 9.11 Sketch of the setup used to determine the stability of the surface against sand impact.

$2^\circ \pm 1^\circ$. The silica shells were not sufficiently robust to completely resist sand impact and caves formed underneath the impacted area. However, zooming into the caves revealed almost unaltered submicrometer morphology. Owing to the coating's self-similarity, the surface kept its superomniphobicity until the layer was removed after an extended impact. The mechanical stability increased with the thickness of the silica shell, but at the expense of the coating transparency. The surface retained its superomniphobicity for 5 min of sand abrasion from a height of 25 cm (2 m/s). Although the coating could be eroded by wear and abrasion, it kept its superomniphobicity as long as its thickness remained above 2 μm .

Tang *et al.* [66] used a brush-coating approach to fabricate superhydrophobic nanocomposite surfaces by combining calcium carbonate (CaCO_3) nanoparticles (NPs) with either acrylate copolymer or epoxy resin. Without CaCO_3 nanoparticles, the acrylate copolymer exhibited water APCA of 77.1° but with the gradual addition of the CaCO_3 NPs the APCA increased to 152.5° . Similarly, without nano- CaCO_3 , the epoxy surface exhibited water APCA of 84.4° but with the gradual addition of the CaCO_3 NPs the APCA increased to 150° . Sand grains with a diameter of $\sim 200 \mu\text{m}$ impinged on the surface from a height of 15 cm. After sand abrasion for 5 min, the wettability of the surface was re-characterized. The APCA for the acrylate copolymer based nanocomposite decreased slightly to 150° while for the epoxy-based to 146° . No CAH values were reported.

Zhang *et al.* [67] prepared polypropylene (PP)/high density polyethylene (HDPE) composite films by a laminating exfoliation method. The treatments performed resulted in the formation of a rough surface. By varying the ratios between the two polymers they were able to achieve superhydrophobicity. Silica particles with diameters of 100 μm to 300 μm impacting the polymer film surface at a velocity of 2.8 m/s (40 cm) for 30 seconds (10 g of silica particles, impacting area 3 cm \times 3 cm) did not destroy the superhydrophobicity of the film. Likely, this is due to the high flexibility of HDPE polymer nanohairs. Both the APCA and ROA for water remained unaltered.

By spraying polystyrene/ SiO_2 core/shell NPs as a coating skeleton and PDMS as a hydrophobic interconnection between the coating and the substrate, lasting and self-healing superhydrophobic surfaces were fabricated by Xue *et al.* [68]. The abrasion resistance of the coating was evaluated by sand impact. The sample was abraded for different times by impinging the coating surface with 50 g of 300 to 1000 μm diameter sand grains from a height of 40 cm at 45° . It was found that an increase in sand abrasion time resulted in a gradual reduction in the APCAs and an increase in the CAH. However, the thicker samples were able to retain APCAs greater than 160° .

and CAH lower than 10° after 10 sand abrasion cycles. After 15 cycles, the superhydrophobicity in terms of CAH was lost since the value measured was 22.5° while the APCA was still high (158.1°).

Geng and He [52], apart from the pencil test described in Section 9.2.4 used additionally a sand impact setup to test their coatings. In the sand abrasion test, 40 g sand grains with diameters of 100–300 μm were used to impact the coating surface from a height of 30 cm in 1 min. Subsequently, the coating was cleaned with water. The water and ethylene glycol APCAs before and after sand abrasion test showed approximately the same values.

Zhang *et al.* [58] performed also sand impact tests on their superhydrophobic aluminum alloys. Approximately 10 g sea sand particles were dropped onto the 45° tilted substrate surface for 1 min from a height of 30 cm from the substrate. The samples maintained superhydrophobicity (APCA $> 150^\circ$ and ROA $< 10^\circ$) after five cycles.

9.3.2 Liquid Jet/Droplet Impact

Another mechanical impact test which is useful to evaluate the performance of liquid repellent surfaces is the droplet or jet impact test. Such test can mimic exposure to raindrop impacts commonly encountered in outdoor coatings applications. During heavy rain in the thunderstorm, the rain droplets have the maximum diameter of 4–5 mm and could reach a maximum speed $v = 7\text{--}9\text{ m/s}$ when impacting a rigid surface on the ground with a frequency of $3.88 \times 10^5\text{ drops/m}^2\text{h}$ [58]. A typical experimental setup for testing a liquid repellent coating is depicted in Figure 9.12. The setup is very similar to the sand impact apparatus with the only difference being that the liquid dispenser replaces the sand container. Again by increasing the dispensing height, the impact of the ejected liquid on the surface becomes more destructive. In some cases, liquid repellent surfaces are not damaged by drop or jet impacts but gradually a loss of their liquid

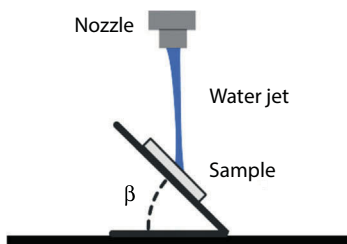


Figure 9.12 Experimental setup for the jet or drop impact test.

repellency is observed due to a Cassie to Wenzel transition. Specifically, penetration of the hierarchical protrusions on the liquid repellent surface is expected during the impact event after repeated tests, and such occurrence probability increases with drop height because of the high instantaneous pressure exerted on the surface.

Xiong *et al.* [69] followed a two-step approach including spray-deposition and UV photopolymerization of thiol-ene resins containing hydrophobic silica nanoparticles. The perfluorinated thiols provided a multiscale topography and low-energy surface that endowed the surface with superomniphobicity for increasing particle concentration. Water drops were repeatedly impinged on the surface of the films from a height of 2.5 and 20 cm. For drops released from $h = 2.5$ cm (impact velocity of 0.7 m/s), the superomniphobic films did not show any sign of water drop penetration even after extended testing (the experiment was ended after 7600 impact events) indicating a robust superhydrophobic wetting state. For drops released from $h = 20$ cm (impact velocity of 1.98 m/s), drop penetration and adhesion to film were observed after 4160 drop impact events, when the superhydrophobic properties of the coating started to degrade. Additionally, a linear abrasion test was performed with sandpaper as abradant and 254 Pa applied pressure. After 200 cycles the water ROA increased to 14° while maintaining APCAs above 150° . On the contrary, the APCA of hexadecane decreased faster. After 100 cycles the initial value of 155° dropped to 116° .

Huang and Lin [70] developed superhydrophobic transparent coatings by following a low temperature (80°C) sol-gel process. The results showed that the coating had water APCA exceeding 160° and SA lower than 10° . The coatings kept their superhydrophobicity even after 20,000 water drop impacts (6 h).

Geng and He performed also a water drop impact test on their superomniphobic surfaces [52]. In this test, about 4500 water droplets (ca. 22 mL) were dropped from a height of 50 cm above the coating. The velocity at which the water droplets impacted the surface was 1 m/s. The water and ethylene glycol APCAs remained unchanged after the water-drop impact test.

Finally, Zhang *et al.* [58] performed a water jet test to evaluate the robustness of their superhydrophobic aluminum alloys. The samples were fixed on a substrate tilted at 45° and placed 5 cm below a water pipe (inner diameter 4 mm), and then jetted for 10 min at different pressures (10–100 kPa). The pressure 25 kPa was selected because according to the authors' calculations it corresponds to a heavy thunderstorm. The water APCA remained greater than 150° up to 75 kPa for 10 min. However,

ROAs increased significantly when the water jetting pressure was greater than 25 kPa. However, in the thunderstorm condition of 25 kPa the coatings retained their superhydrophobicity. Therefore, the films were water jetted at 25 kPa repeatedly up to five times to investigate the cyclic durability. The surface remained superhydrophobic after water jetting up to three cycles. After five cycles of water jetting water APCA still exceeded 150° , although ROA increased to $\sim 19^\circ$.

9.3.3 Gas Pressure Impact

Impact with gas molecules is not a very common test for the degradation of liquid repellent surfaces. However, elevated gas flows could be severe for many coatings. Moreover, this is a test that should be considered for surfaces that target aerospace applications or finishes for outdoor use in regions affected by hurricanes and tornados.

Nahum *et al.* [71] prepared stable superhydrophobic coatings by UV exposure using SiO_2 NPs of various diameters grafted with photoreactive benzophenone (BPh) groups and methylated fumed silica ($\text{SiO}_2\text{@BPh}$) NPs in combination with urethane acrylate base layer and fluorosilane top layer. They tested their surfaces under severe air drag conditions. The air drag test was devised using an air gun with air velocity of 300 km/hr. An anemometer was placed at the end of the sample to measure the velocity of air passing along the sample. The APCAs and SAs were measured before and after the air drag test. FC294, FC156, and FC65 were designated as the coatings containing $\text{SiO}_2\text{@BPh}$ NPs of 294, 156, and 65 nm, respectively. As could be concluded the contact angle measurements showed insignificant changes in all coatings before and after air drag test. However, an increase in sliding angles was observed after air drag. Both FC294 and FC156 kept their superhydrophobicity demonstrating SA smaller than 10° after the air drag test while FC65 exhibited a SA above 30° . These results might be explained by the detachment of the non-bonded hydrophobic methylated fumed silica exposing the hydrophilic $\text{SiO}_2\text{@BPh}$ NPs to the surface. As a result, an increase in contact area between the water drops and polymer substrate was obtained on moving from Cassie to Wenzel state. SEM images (Figure 9.13A,B) showed a slight decrease in surface roughness for FC294 and FC156 containing formulations which explain the slight increase in SA. However, a close look at FC294 containing coating (Figure 9.13D) confirmed that surface roughness was retained and the increase in sliding angle was a consequence of the loss of non-bonded methylated fumed silica in some areas. In FC65 containing coating (Figure 9.13C), cracks could be noticed on the surface that led to the increase in SA.

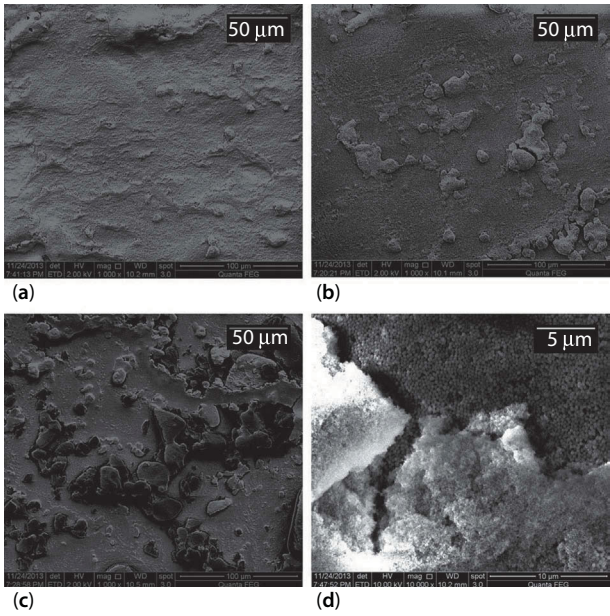


Figure 9.13 SEM topography images of (a) FC294 after air flow test, (b) FC156 after air flow test, (c) FC65 after air flow test, and (d) magnified image of FC294 after air flow test [71].

9.4 Durability under Vertical Compression/Expansion

Applying shear stress is not the only way that a liquid repellent surface can be damaged. Vertical compression or expansion can also lead to degradation of the surface properties. Furthermore, material removal can occur by vertical compression or expansion when two solid surfaces are in contact. In the following section we will describe techniques that apply normal (and not shear) force to the tested surface.

9.4.1 Tape Peeling

Tape peeling is a material removal test that has been used to test the adhesion strength of liquid repellent coatings to substrates. Tapes are classified according to the values of adhesion force to a reference substrate, reported as adhesion to steel in N/m. The higher this parameter is, the more destructive is the tape peeling test to the coating under investigation. The tape is

applied on the surface of the tested material and it is pressed in order to ensure that there is no air entrapment and the entire adhesive surface is in contact with the liquid repellent surface. Subsequently the tape is peeled from one end (typically holding it at 45°).

Steele *et al.* [72] used the tape peeling test to evaluate the adhesion strength and superhydrophobicity of polyurethane/organoclay nanocomposite coatings. They tested six different values of tape adhesion strength ranging from 440 to 3850 N/m (adhesion to steel). The tapes were detached from the coatings at 2 mm/s. Increasing tape adhesion strength was found to degrade faster the anti-wetting performance. After 12 tape tests, the coatings were able to maintain superhydrophobic performance with maximum tape adhesion strength 820 N/m. However, even at the highest tape adhesion strength (3850 N/m) the surfaces retained APCAs higher than 140° and CAH less than 20° while prior to testing the APCA was greater than 160° and the CAH less than 10° .

Cholewinski *et al.* [73] prepared a robust superhydrophobic bilayer coating containing PDMS-functionalized silica particles on top and an epoxy bonding layer at the base. It was fabricated with a facile dip-coating process that embedded micro-scale PDMS-functionalized silica particles with nano-scale roughness into an epoxy layer spin-coated onto a substrate. The APCAs of the coatings remained stable after four tape tests but no CAH values were reported.

Barthwal *et al.* [74] developed superomniphobic surfaces on aluminum with a three-step method including etching with an acidic solution, anodization with sulfuric acid, and fluorination. The durability of the surfaces was tested by performing ten tape peeling attempts. The APCA of water remained above 150° while the oil APCA remained above 150° until the 8th cycle and slightly degraded in the last two cycles. Again no CAH values were reported.

Geng and He [52] used the tape peeling test to compare the adhesion to substrate of their superomniphobic silica thin films before and after the chemical vapor deposition (CVD) process which is used to deposit tetraethyl orthosilicate for improving the mechanical robustness. The water APCA (which initially was measured 171°) decreased to 167° after 10 tape peeling tests, 161° after 20 tests, and 157° after 40 tests. The ethylene glycol APCA (initially 152°) decreased to 145° after 10 tape peeling tests, 145° after 20 tests, and 142° after 40 tests. However, APCAs of water and ethylene glycol on the coating without CVD treatment decreased to 150° and 135° respectively after 10 tape peel tests, indicating that the coating lost its superomniphobicity and that the CVD treatment significantly improved the coating-to-substrate adhesion. No CAH measurements were reported

here also. The same test, but only with one cycle, was performed by Deng *et al.* [64].

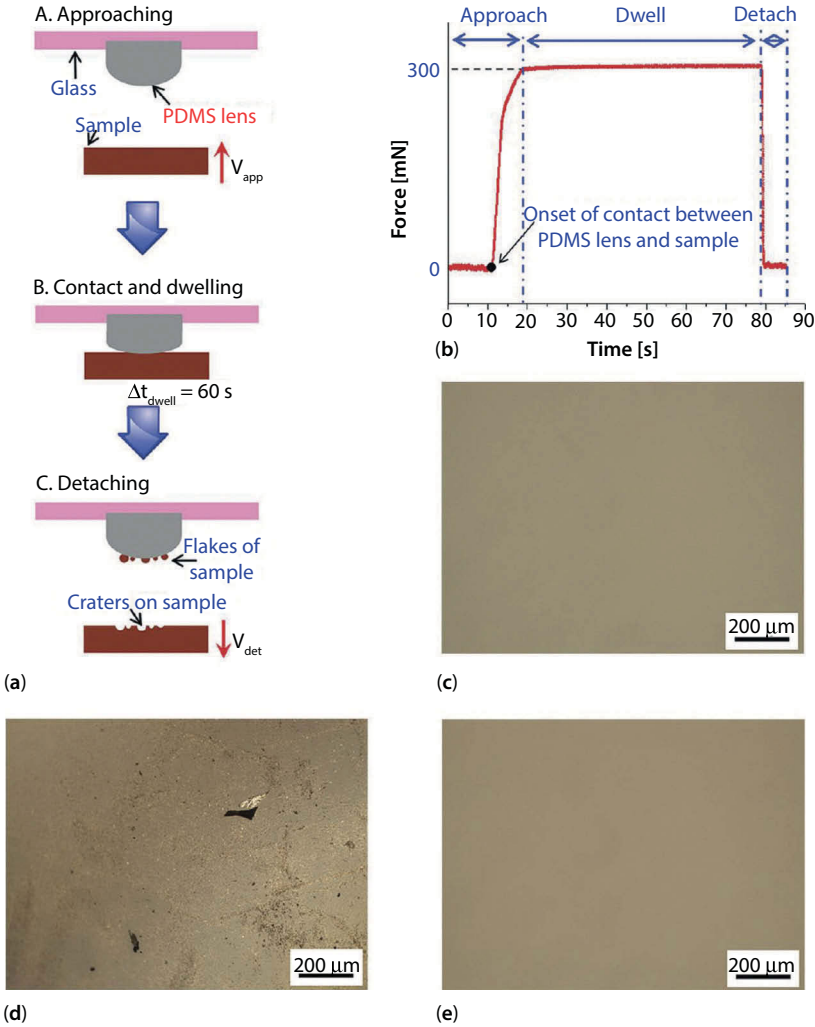


Figure 9.14 Mechanical stability test using a home-built microtribometer. (a and b) The testing procedure and representative force versus time profile during the test. (c–e) Optical micrographs of the PDMS lens surface before testing (c) and after testing of the CuO sample (d) and Cu sample (e). While many flakes were observed on the lens after testing of the CuO slowly cooled sample, the Cu slowly cooled sample was as clear as the PDMS lens surface before testing. Reproduced with permission from [74]. Copyright 2013 American Chemical Society.

9.4.2 Compression Followed by Tension

Another technique that has been used to evaluate the mechanical performance of liquid repellent surfaces is to apply normal force to the substrate. This technique involves a material that comes in contact with the tested surface, compresses it and then it is retracted. This way the maximum load that a surface can withstand can be estimated while at the same time maintaining the surface texture that is responsible for the liquid repellency.

Lee *et al.* [75] used an oxidation-reduction reaction on a bulk copper substrate to alter the surface morphology and obtain superhydrophobic surfaces. Subsequently, they performed a durability test using a home-built setup composed of a PDMS lens that was used as a counterpart material in order to compress the superhydrophobic substrates. As described in Figure 9.14a,b, the sample was moved upward to contact the PDMS lens by controlling the z-axis stage. Then the sample was pressed against the lens until the load reached the predetermined maximum load (300 mN), and contact was maintained for a 60 s dwell time. Subsequently, the sample was detached from the lens at a constant unloading velocity by lowering the z-axis stage. The tested surfaces were composed of copper oxide (CuO) or copper (Cu) nanowires. The surface of the PDMS lens was examined under an optical microscope to examine any worn-off flakes from the counter surfaces. As can be seen in Figure 9.14c,d, while the CuO was found to be mechanically rather weak (Figure 9.14d), the Cu nanowires that were cooled slowly to room temperature appeared to have superior mechanical stability (Figure 9.14e) and showed unchanged superhydrophobic nature. The same samples were also found to be more durable after a tape peeling test was performed.

Barthwal *et al.* [74] used a similar setup to evaluate the mechanical performance of their superomniphobic aluminum surfaces. They applied loads up to 4 N in increments of 1 N on their samples and then tested their performance by measuring the APCAs of various liquids after each compression cycle. Even after 4 cycles, the samples showed only minor changes in the APCA values for all the tested liquid droplets.

9.5 Wear in Liquid Baths

Liquid repellent surfaces have been evaluated in the literature with other types of mechanical durability tests. Such tests are designed to evaluate the performance of the tested surfaces for certain types of applications (e.g. the laundry test for textiles). These include laundry test, ultrasonication, and

particle impact using a rotary slurry of particles. In this section we will give an overview of the studies that have conducted the aforementioned tests.

9.5.1 Laundry Test

Laundry test is a very common test to evaluate the mechanical performance of liquid repellent textiles since it is the main cause of degradation during their practical use. Fabric during washing undergoes mechanical stresses in addition to exposure to chemical agents. The synergistic effect of chemical and physical actions accelerates the detachment of coating layer from fibrous substrates. These tests are simply performed by washing the treated textiles in commercial washing machines for a specific amount of time and then characterizing the wetting properties. In some of the tests also the amount of detergent present in water is mentioned and in some other cases the washing occurs in the presence of steel balls that are introduced in the laundry machine to mimic wear effects that occur in real-world laundry. Other factors that can be varied include the water temperature and the duration of the laundry cycle.

Generally, the fibrous nature of textiles promotes mechanical durability since such surfaces are easily deformed and can withstand better the shear abrasion. Thus, liquid repellent textiles are currently top performing in the mechanical durability tests and are able to maintain their properties for a much greater number of abrasion cycles than any other surface. However, it should be noted that in many studies CAH values are not reported, but only APCA measurements that are stable even after thousands of abrasion cycles. Thus, one has to be very careful when evaluating experimental data since in terms of application the CAH is a more important parameter than the APCA. Moreover, for textiles it is common to measure the SHA which was introduced specifically to avoid difficulties when measuring APCAs on textile surfaces with conventional goniometers [34]. Usually the test involving laundry cycles is accompanied also with abrasion tests. In this section we will mention also the results from the abrasion tests together with the laundry test.

Wang *et al.* [76] prepared self-healing superhydrophobic and superoleophobic polyester fabrics from fluorinated-decyl polyhedral oligomeric silsesquioxane and hydrolyzed fluorinated alkyl silane by a dip-coating method. After 200 cycles of standard laundry machine, the coated fabric was found to still maintain the superhydrophobicity and superoleophobicity in terms of APCAs measured with water and hexadecane respectively. The abrasion durability was evaluated by the circular abrasion method using untreated fabric as abradant to simulate actual damage. During the

test, pressures of 9 kPa and 12 kPa were employed, which are typically used for evaluating the coated fabrics for apparel and heavy-duty upholstery usages, respectively. The coated fabric can withstand at least 6000 cycles of abrasion damages without affecting its super-repellent feature. More abrasion cycles led to a decrease in both water and oil repellency. No CAH measurements were reported.

The same research group used a different formulation and dip-coating approach to produce superhydrophobic polyester fabrics by surface treatment with fluoroalkylsilane (FAS) modified PDMS/silica NP composite (Figure 9.15) [77]. With increasing laundry cycles, the APCA slightly decreased, while the SA had a little increase. Changes in both APCA and SA were less than 5° after 500 washing cycles. The SEM observation revealed that the coating surface still retained its particulate morphology, even after 500 cycles of repeated washing. The abrasion resistance was evaluated with the same setup and applied pressure values (9 to 12 kPa). The APCA remained at 170° after the first 2000 cycles under both pressure conditions. Although the APCA reduced with further increasing the abrasion cycles, the coated polyester fabrics could withstand at least 28000 cycles of abrasion damages without losing their superhydrophobicity. After 28000 abrasion cycles under 12 kPa pressure, water droplets on the fabric surface still showed APCA more than 150° and the nano-scale roughness could still be observed. In comparison to the APCA, the SA was more sensitive to abrasion cycles. After 20000 abrasion cycles, the SA increased slightly above 10° .

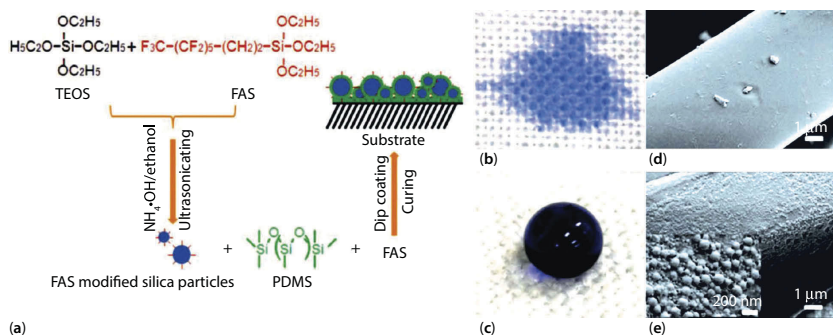


Figure 9.15 (a) Procedure to prepare the coating solution and superhydrophobic fabrics; (b) & (c) The pictures of water drops (10 μ L each) on the (b) untreated and (c) treated polyester fabrics; (d) & (e) SEM images of (d) pure polyester fabric and (e) silica/PDMS/FAS treated fabric [77].

An alternative approach was used by the same group for treating polyester fabrics [78]. Self-healing superomniphobic fabrics were prepared by one-step vapor-phase polymerization of poly(3,4-ethylenedioxythiophene) (PEDOT) in the presence of fluorinated decyl polyhedral oligomeric silsesquioxane (FD-POSS) and FAS. With increasing laundry cycles, the PEDOT/FD-POSS/FAS coated fabric had only a small decrease in both water and hexadecane contact angles. After 500 washing cycles, the superomniphobic property was retained. After 10000 cycles of abrasion (12 kPa), the PEDOT/FD-POSS/FAS coated fabric still retained its superomniphobicity.

Another two-step dip-coating approach was developed by the same group to prepare self-healing superomniphobic polyester fabrics using poly(vinylidene fluoride-co-hexafluoropropylene), fluoroalkyl silane (FAS), and modified silica NPs [79]. Washing and abrasion durabilities of the coated fabrics were evaluated. Washing tests were performed at 49° C for 45 min in presence of a detergent (0.15 wt %) and 50 stainless steel balls. After 600 cycles of standard machine laundry, the coated fabric still maintained its superomniphobicity. Both the APCA and SA underwent a slight decrease with the washing cycles. After 600 cycles of washing, silica particles could be clearly observed on the coating surface, indicating that the particles were immobilized firmly on the fiber surface. Abrasion tests were also performed (circular abrasion, 12 kPa). After 8000 abrasion cycles, the coated fabric showed APCA values of 165°, 152° and 145° respectively for water, soybean oil and hexadecane. Although the SA increased with increasing abrasion cycles, it was still lower than 10° for all the liquids after the fabric was subjected to 8000 abrasion cycles. After 25000 abrasion cycles, the coated fabric still retained its superhydrophobicity, although it lost its oleophobicity. It was also found that the 25000 abrasion cycles led to physical damage to both the fibers and the fabric structure.

The superomniphobic polyester fabrics tested with the blade test by the same group (Zhou *et al.*) were also tested under laundry and circular abrasion [49]. In the machine laundry process, the coated fabric did not show changes in the APCAs of water, hexadecane or ethanol after 200 cycles of washing. However, the SA values increased to 4.5°, 36.7°, and 47.5° for water, hexadecane, and ethanol respectively. After 20000 abrasion cycles nearly no nanoparticles could be observed on the top surface. However, the damaged surface after the abrasion test was healable when the coated fabric was heated at 140° C for 30 min. The APCAs of water and hexadecane recovered to 171° and 152°, respectively. However, the heat treatment could increase the APCA of ethanol only to 127°.

The same group (Zhao *et al.*) investigated the surface modification of cotton fabrics [80]. The method included functionalization of silica NPs with highly photoreactive phenyl azido groups that were utilized as a negatively charged building block for layer-by-layer (LbL) electrostatic assembly to produce a stable silica NP coating. Combined with a FAS post-treatment, the photoreactive LbL multilayers were used as a coating for superhydrophobic modification of cotton fabrics. The superhydrophobic fabric showed reasonable wash durability with CAH remaining lower than 10° after 25 cycles of machine washing, and APCA above 150° after 50 cycles.

Zhang *et al.* [59] developed robust superhydrophobic wool textiles by simply dip coating in a nanocomposite solution of fluorine-free organosilanes. Despite the fact that the APCA remained stable after the laundry test, the water SA increased gradually with increasing laundry cycles but remained below 15° after 10 laundry cycles. The abrasion resistance of the coated fabric was evaluated. No obvious change in contact angle (CA) could be detected after 200 abrasion cycles at 5 kPa using A4 paper as the abradant. SHA increased gradually from 3° to 21° with increasing abrasion cycles at 5 kPa. The increase in abrasion pressure to 9 kPa had no evident influence on SHA. Water droplets remained nearly spherical in shape and could still easily roll off the tilted sample after 200 abrasion cycles. Similar SHA and bouncing of water drops were observed when sandpaper (2000 mesh) was used as the abradant although the wool fabrics were seriously damaged. The same tests were applied also on the superhydrophobic polyester fabrics developed by the same group [36] and the coatings retained their properties for 50 laundry cycles.

Xue *et al.* [81] fabricated superhydrophobic colorful surfaces through chemical etching of poly(ethylene terephthalate) fiber surfaces, followed by diffusion of fluoroalkylsilane into fibers. The laundering durability was evaluated by washing samples at 40°C in the presence of 10 stainless steel balls in the presence of 0.37% soap powder. The APCA remained at 157.3° after 20 cycles, showing a slight decrease from 162.9° . SEM images revealed that the surface retained its rough morphology even after 100 cycles of repeated washing. The abrasion resistance was evaluated using linear abrasion with a common nylon fabric as abradant. The APCA remained at 157.7° after the first 1500 cycles, showing a slight decrease from 161.9° on non-abraded sample. SEM observation revealed that the PET fibers were flattened after 3000 abrasion cycles. However, the CA increased to 162.3° .

Zou *et al.* [82] prepared superhydrophobic cotton fibers from functional diblock copolymers consisting of both poly(glycidyl methacrylate) (PGMA) and poly(2,2,2-trifluoroethyl methacrylate) (PTFEMA) blocks

synthesized via sequential atom transfer radical polymerization. While the PTFEMA block provided the low surface free energy, the PGMA block served as an anchor and formed covalent bonds with the surfaces of cotton fibers. The modified cotton fabrics showed APCA of 163° and SA of 3° . Resistance against mechanical damage was evaluated by laundering samples in water with 0.15 wt% detergent. The superhydrophobicity was maintained, with an APCA of 150° and a SA of 10° after the treated fabrics had been laundered for 50 cycles. The mechanical stability of the samples was also evaluated by linear abrasion with sandpaper at a constant rate under 3.9 kPa. This experiment demonstrated that although the SAs increased to above 10° after the samples were rubbed for 20 cycles, the APCAs remained above 150° even after the samples had been rubbed for 40 cycles.

Liu *et al.* [83] developed a dip-coating approach for fabricating superhydrophobic polyester textiles with polydopamine@octadecylamine nanocapsules. Laundering durability of the coated fabric was evaluated in pure water and in soap solution by both machine and hand washing. After 20 laundry cycles (for 45 min at 25°C), the coated fabric still maintained its static liquid-repellency though the APCA underwent a slight decrease with the increasing washing cycles with an APCA of 144° when it was dried at 80°C for 20 min. After 20 washing cycles, the nanocapsules could be clearly observed on the coating surface, indicating that they were immobilized firmly on the fiber surface. No CAH values were reported for this test. In order to further test the washing durability of the coated fabric, it was washed 5 minutes by hand in an aqueous solution containing soap powder. The coated fabric still retains its hydrophobicity, and liquid droplets could roll off easily from the surface. The change in liquid repellency with abrasion cycles was tested by linear abrasion of the fabric surface (10 kPa). With the increase of abrasion cycles (up to 500), the APCAs of water, juice and coffee decreased only slightly ($\sim 140^\circ$). No CAH values were reported.

9.5.2 Ultrasonication

Ultrasonication is the application of energy by ultrasonic frequency ($> 20\text{ kHz}$) in liquid media. It can operate at various frequencies above this threshold and it is used in colloidal chemistry, cleaning materials, etc. The application of ultrasonic frequencies can physically damage a fragile surface where there is no good chemical bonding with the substrate. For this reason, it has been used as a test to evaluate the mechanical stability of liquid repellent surfaces.

Liu *et al.* [84] evaluated the mechanical strength of their superhydrophobic Cu surfaces by ultrasonic treatment in water. After ultrasonication

for 1 h, the resultant surface exhibited a mean APCA of 165° while no CAH value was measured. Yoo *et al.* [85] applied ultrasonic process to their superhydrophobic fabric in water for more than 4 days and the superhydrophobic film remained intact, which confirmed the strong adhesion between the stacked polymer film and the fabric. The receding contact angle on the fabric after ultrasonication was 156° . Zou *et al.* [82] used the ultrasonication test for their superhydrophobic cotton fabrics in the presence of tetrahydrofuran (THF) or trifluorotoluene (TFT) to evaluate both physical and chemical stability. It was found that the water APCAs and SAs of the coated fabrics changed only slightly after they had been ultrasonicated for 100 min in THF or TFT, thus retaining the superhydrophobicity. Finally, Huang and Lin [70] tested their superomniphobic surfaces with ultrasonication. After two hours of ultrasonic treatment the surfaces retained their superhydrophobicity but the diiodomethane CAH increased significantly to 94° while the APCA remained stable.

9.5.3 Rotary Slurry Test

Jokinen *et al.* [86] introduced another novel type of abrasion test including a rotary slurry (Figure 9.16). The sample to be tested is rotated in slurry and erosion results from direct impacts between the slurry particles and the surface of the sample. The beaker holding the slurry contains stators to prevent the slurry from picking up momentum and flow. The extent of erosion in the slurry test depends on the composition, size, and shape of the eroding particles, their velocity and angle of impact, and the composition and microstructure of the surface being eroded. The set-up comprised a custom sample holder which was connected directly to a motor by a long steel rod. The sample holder was designed to simultaneously hold multiple test pieces. The samples were tilted so that the angle of impact was 73° . The distance of the sample from the rotation

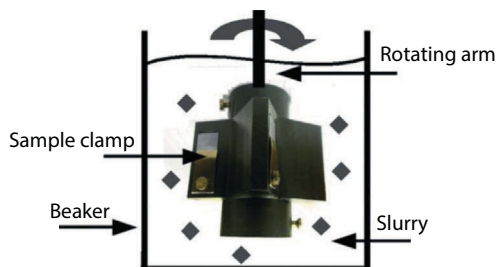


Figure 9.16 Rotary abrasive slurry test setup [86].

axis was 25 mm as measured from the center of the sample. With this device, it was possible to control both the temperature and the rotation rate. In their experiments, the temperature was kept at ambient conditions and the rotation was set at 900 rpm for the main abrasion experiment. The slurry used for the main abrasion experiment consisted of 10% (by weight) suspension of 30 μm alumina particles in water. The slurry was contained in a 500 ml glass beaker.

9.6 Inherently Durable Liquid Repellent Materials

While the above section examined the mechanical durability characterization techniques and the type of damage that each of them induces on the surfaces, it should be noted that there exist a few materials in the literature which are entirely liquid repellent (bulk material) [87,88] or in some cases mechanical degradation improves the liquid repellent performance of a surface [37,38,89]. These are approaches that can be followed when long term liquid repellency is desired but also exhibit some disadvantages. One drawback is that liquid repellent bulk materials can be very fragile since their cohesive forces are very weak. Additionally, the use of such materials could be much more expensive compared to the application of thin coatings on various surfaces where much less quantity of liquid repellent material is required to perform the same function.

9.6.1 Bulk Materials that are Inherently Liquid Repellent

Zhu *et al.* [87] developed a superhydrophobic bulk material by embossing carbon nanotubes (CNTs) on polytetrafluoroethylene mold under high temperature (390° C) and pressure (256 kPa). Both these materials are hydrophobic but the protruding CNTs provide the necessary hierarchical texture required for superhydrophobicity (Figure 9.17a,b). The APCAs for water droplets placed on the bulk material surface varied from 159° in the initial state to 152° after 20 abrasion cycles were performed by rubbing the surface with a sandpaper under a pressure of 5.6 kPa, whereas the corresponding SAs ranged from 3° to 22°. As depicted in Figure 9.17e, the superhydrophobic property is present also in the inner part of the material since the water droplets maintain a spherical shape also when deposited on a piece cut from the bulk. Another quite similar molding approach was followed by Zhang *et al.* [88] where they combined TiO_2 nanorods, hydrophobic SiO_2 nanoparticles (NPs), polypropylene (PP) and a small amount of poly(dimethylsiloxane) that acted

as a binder to improve the adhesion of the inorganic SiO_2 and TiO_2 nano-materials to the PP matrix. The pressure during molding was 35 MPa but no thermal treatment was necessary in this fabrication method. Water droplets exhibited typical spherical shapes with a water APCA about $158^\circ \pm 1^\circ$ and a low sliding angle $1^\circ \pm 0.5^\circ$.

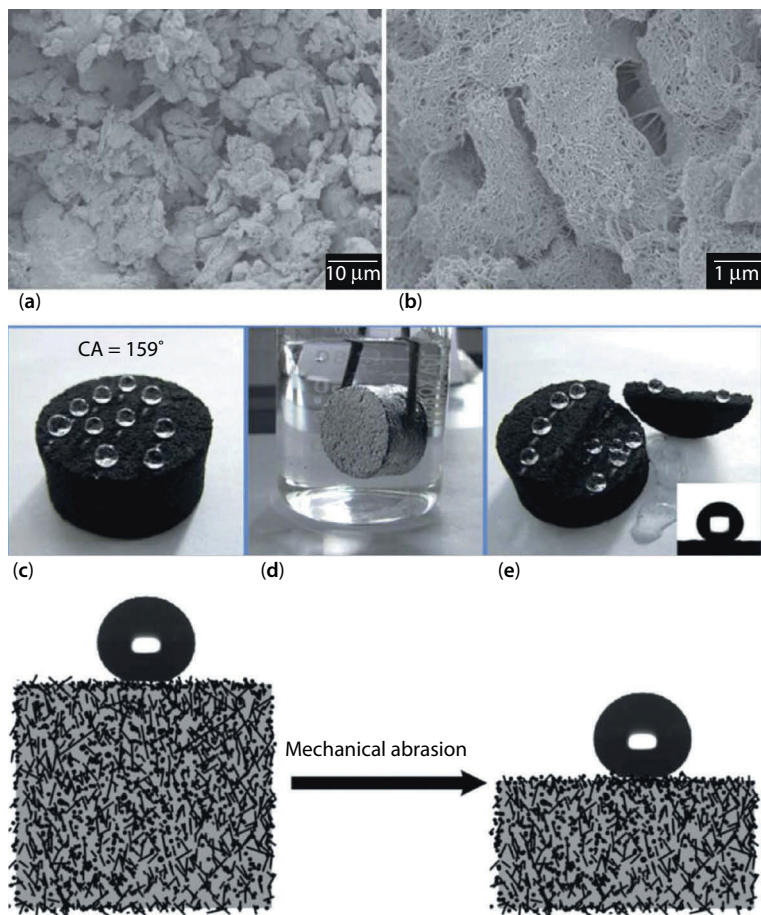


Figure 9.17 Field emission scanning electron microscope images of the bulk material at low (a) and high (b) magnification; (c) water droplets exhibit spherical shape on the surface of the bulk material; (d) mirror-like phenomenon can be observed on the bulk material submerged in water and (e) optical image and contact angle profile of the water droplet placed on the abraded bulk material. Bottom: schematic illustration of a bulk material which can still sustain its superhydrophobicity after mechanical abrasion because of the low surface energy microstructures extending throughout its volume. Reproduced from [87,88] with permission of The Royal Society of Chemistry.

9.6.2 Materials that become Liquid Repellent with Mechanical Wear

Mechanical wear, in some cases, can enhance the anti-wetting performance of a surface. Wang *et al.* [37] prepared superhydrophobic surfaces by abrading with sandpaper poly(tetrafluoroethylene) (PTFE)/room temperature vulcanized silicone rubber composites (RTVSR). The PTFE/RTVSR composites were fabricated by a solution casting method followed by a room temperature curing process. The initial surfaces prior to abrasion were relatively flat. The water APCA for pure RTVSR was measured to be 92.7° and the SA 69.5° while after increasing the volume fraction of PTFE up to 30% the water APCA increased to 108.7° and the SA decreased to 6.5° . Interestingly, after abraded with the sandpaper for 2 min with 10 kPa applied pressure, the surface of the composites showed superhydrophobicity with water APCA 165° and SA 7.3° . This was because the sandpaper abrasion induced surface texture to the bulk material that was composed of hydrophobic constituents. Rough surface microstructures were still observed after abraded with sandpaper or cotton fabric for 100 abrasion cycles. The same authors followed a similar concept to prepare superhydrophobic surfaces by PTFE/poly(vinylidene fluoride) composites with various ratios between the two materials by a simple powder mixing and hot pressing method [89].

Jin *et al.* [50] prepared superomniphobic fluorinated silica aerogels and they abraded their surfaces with a sandpaper. After 100 abrasion cycles the total thickness of the removed material was $660\text{ }\mu\text{m}$. Unlike in most of the cases, a gradual decrease of the CAH with increasing abrasion cycles was observed. This is probably due to the fact that the surfaces become smoother while maintaining their hierarchical type of texture but in some cases very high surface roughness can lead to the formation of valleys that can entrap liquid droplets. The liquid repellency could be preserved after the abrasion due to the nanoporous self-similar aerogel structure that essentially maintained the desired topography even upon abrasion, and in addition by deposition of surfactant in the interior of the aerogel that self-replenished the damaged sites of the surface acting as a self-healing material.

9.7 Future Directions for Investigating Mechanical Durability

During the last years, the amount of published material regarding the development of mechanically durable liquid repellent surfaces has exponentially increased. Various techniques have been demonstrated that can

produce robust surface topographies and bulk materials which can repel liquids after repeated cycles of mechanical wear. Despite substantial scientific progress, research continues to further improve the mechanical characteristics of such surfaces since in most cases the performance does not meet the requirements for commercialization. Considering the huge potential impact that liquid repellent coatings with enhanced durability could have in a vast number of applications, it is expected that in the following years researchers will come up with new techniques and different formulations that will initiate the next generation of mechanically robust liquid repellent surfaces.

It is expected that in the following years, the number of micro- and nano-devices will increase due to the evolution of nanotechnology. The demand for highly precise, selective and fast techniques that efficiently control liquid adhesion (and eventually the degree of liquid repellency) on small components of such devices will increase. Laser-based approaches, for instance, are already excellent candidates for designing ultrafine and highly localized surface textures with precise control of the liquid adhesion both spatially and quantitatively on a wide range of materials [90]. Since the commercialization of these devices would require good mechanical robustness of the fabricated surfaces, evaluating and improving the mechanical performance will be very critical and of significant importance.

Currently, however, quantitative assessment of the mechanical durability of non-wetting surfaces is difficult due to the diversity of wear testing and characterization methods discussed above. Ideally, the evaluation techniques should be more standardized and possibly reduced in number, as this would be beneficial for focused efforts to develop resilient coatings. From all the techniques that we described above, there seem to be some of them that are more commonly accepted. Linear abrasion, for instance, seems to be a very well accepted and is a common method to evaluate the mechanical durability. Sand, water/jet and gas impact are also good techniques to evaluate the stability of the surfaces for outdoor applications. Nevertheless, the range of possible applications for superhydrophobic surfaces may call for specialized mechanical tests like laundry tests, finger touch, etc.

Finally, apart from the standardized test methods that should be used, it is of extreme importance for reasons of consistency that researchers measure both static and dynamic contact angles in their experiments, otherwise it is impossible to compare the performance of a surface to studies published by other researchers. Selecting also standardized physical quantities and materials in the tests would also be beneficial (e.g. applied pressure and abradant materials).

References

1. W. Barthlott and C. Neinhuis. Purity of the sacred lotus, or escape from contamination in biological surfaces. *Planta*, 202, 1–8 (1997).
2. A. Carre and K.L. Mittal (Eds.) *Superhydrophobic Surfaces*, CRC Press, Boca Raton, FL (2009).
3. A.K. Kota, J.M. Mabry and A. Tuteja. Superoleophobic surfaces: Design criteria and recent studies, *Surface Innovations*, 1, 71–83 (2013).
4. A.K. Kota, W. Choi and A. Tuteja. Superomniphobic surfaces: Design and durability. *MRS Bull.*, 38, 383–390 (2013).
5. J.D. Smith, R. Dhiman, E. Reza-Garduno, R.E. Cohen, G.H. McKinley and K.K. Varanasi. Droplet mobility on lubricant-impregnated surfaces. *Soft Matter*, 9, 1772–1780 (2013).
6. I. P. Parkin and R.G. Palgrave. Self-cleaning coatings. *J. Mater. Chem.*, 15, 1689–1695 (2005).
7. P. Tourkine, M. Le Merrer and D. Quere, Delayed freezing on water repellent materials. *Langmuir*, 25, 7214–7216, (2009).
8. J. Chapman and F. Regan. Nanofunctionalized superhydrophobic antifouling coatings for environmental sensor applications - advancing deployment with answers from nature. *Adv. Eng. Mater.*, 14, B175–B184 (2012).
9. C.J. Weng, C.H. Chang, C.W. Peng, S.W. Chen, J.M. Yeh, C.L. Hsu and Y. Wei. Advanced anticorrosive coatings prepared from the mimicked *Xanthosoma Sagittifolium*-leaf-like electroactive epoxy with synergistic effects of superhydrophobicity and redox catalytic capability. *Chem. Mater.*, 23, 2075–2083 (2011).
10. P.A. Charpentier, K. Burgess, L. Wang, R.R. Chowdhury, A.F. Lotus and G. Moula. Nano-TiO₂/polyurethane composites for antibacterial and self-cleaning coatings. *Nanotechnology*, 23, 425606 (2012).
11. Y.A. Dai, H.C. Chang, K.Y. Lai, C.A. Lin, R.J. Chung, G.R. Lin and J.H. He. Subwavelength Si nanowire arrays for self-cleaning antireflection coatings. *J. Mater. Chem.*, 20, 10924–10930 (2010).
12. B. Bhushan and Y.C. Jung. Natural and biomimetic artificial surfaces for superhydrophobicity, self-cleaning, low adhesion, and drag reduction. *Prog. Mater. Sci.*, 56, 1–108 (2011).
13. K. Tsougeni, D. Papageorgiou, A. Tserepi and E. Gogolides. “Smart” polymeric microfluidics fabricated by plasma processing: Controlled wetting, capillary filling and hydrophobic valving. *Lab Chip*, 10, 462–469 (2010).
14. H.K. Webb, J. Hasan, V.K. Truong, R.J. Crawford and E.P. Ivanova. Nature inspired structured surfaces for biomedical applications. *Curr. Med. Chem.*, 18, 3367–3375 (2011).
15. P. Calcagnile, D. Fragouli, I.S. Bayer, G.C. Anyfantis, L. Martiradonna, P.D. Cozzoli, R. Cingolani and A. Athanassiou. Magnetically driven floating foams for the removal of oil contaminants from water. *ACS Nano*, 6, 5413–5419 (2012).

16. A. Millionis, R. Giannuzzi, I.S. Bayer, E.L. Papadopoulou, R. Ruffilli, M. Manca and A. Athanassiou. Self-cleaning organic/inorganic photo-sensors. *ACS Appl. Mater. Interfaces*, 5, 1036–1043 (2013).
17. A. Millionis, D. Fragouli, L. Martiradonna, G.C. Anyfantis, P.D. Cozzoli, I.S. Bayer and A. Athanassiou. Spatially controlled surface energy traps on superhydrophobic surfaces. *ACS Appl. Mater. Interfaces*, 6, 7139–7145 (2014).
18. L. Gao and T.J. McCarthy. The “lotus effect” explained: Two reasons why two length scales of topography are important. *Langmuir*, 22, 2966–2967 (2006).
19. A.B.D. Cassie and S. Baxter. Wettability of porous surfaces. *Trans. Faraday Soc.*, 40, 546–551 (1944).
20. T.S. Wong, S.H. Kang, S.K.Y. Tang, E.J. Smythe, B.D. Hatton, A. Grinthal and J. Aizenberg. Bioinspired self-repairing slippery surfaces with pressure-stable omniphobicity. *Nature*, 477, 443–447 (2011).
21. R.N. Wenzel. Resistance of solid surfaces to wetting by water. *Ind. Eng. Chem.*, 28, 988–994 (1936).
22. T. Verho, C. Bower, P. Andrew, S. Franssila, O. Ikkala and R.H.A. Ras. Mechanically durable superhydrophobic surfaces. *Adv. Mater.*, 23, 673–678 (2011).
23. A. Steele, I. Bayer, S. Moran, A. Cannon, W.P. King and E. Loth. Conformal ZnO nanocomposite coatings on micro-patterned surfaces for superhydrophobicity. *Thin Solid Films*, 518, 5426–5431 (2010).
24. N.A. Patankar. Transition between superhydrophobic states on rough surfaces. *Langmuir*, 20, 7097–7102 (2004).
25. H. Teisala, M. Tuominen, M. Aromaa, M. Stepien, J.M. Saarinen, M. Toivakka and J. Kuusipalo. Nanostructures increase water droplet adhesion on hierarchically rough superhydrophobic surfaces. *Langmuir*, 28, 3138–3145 (2012).
26. A.T. Paxson and K. Varanasi. Self-similarity of contact line depinning from textured surfaces. *Nature Commun.*, 4, 1492 (2013).
27. L. Ionov and A. Synytska. Self-healing superhydrophobic materials. *Phys. Chem. Chem. Phys.*, 14, 10497–10502 (2012).
28. J. Li, X. Liu, Y. Ye, H. Zhou and J. Chen. A simple solution-immersion process for the fabrication of superhydrophobic cupric stearate surface with easy repairable property. *Appl. Surf. Sci.*, 258, 1772–1775 (2011).
29. Y. Li, L. Li and J. Sun. Bioinspired self-healing superhydrophobic coatings. *Angew. Chem. Int. Ed.*, 49, 6129–6133 (2010).
30. N. Pureskiy, G. Stoychev, M. Stamm and L. Ionov. Switchable surfaces based on freely floating colloidal particles. *ACS Appl. Mater. Interfaces*, 2, 2944–2948 (2010).
31. A. Marmur. Soft contact: Measurement and interpretation of contact angles. *Soft Matter*, 2, 12–17 (2006).
32. K.Y. Law. Definitions for hydrophilicity, hydrophobicity, and superhydrophobicity: Getting the basics right. *J. Phys. Chem. Lett.*, 5, 686–688 (2014).
33. E. Pierce, F.J. Carmona and A. Amirfazli. Understanding of sliding and contact angle results in tilted plate experiments. *Colloids Surfaces A*, 323, 73–82 (2008).

34. J. Zimmermann, S. Seeger and F.A. Reifler. Water shedding angle: A new technique to evaluate the water-repellent properties of superhydrophobic surfaces. *Textile Res. J.*, 79, 1565–1570 (2009).
35. L. Feng, Y. Zhang, J. Xi, Y. Zhu, N. Wang, F. Xia and L. Jiang. Petal effect: A superhydrophobic state with high adhesive force. *Langmuir*, 24, 4114–4119 (2008).
36. L. Wu, J. Zhang, B. Li, L. Fan, L. Li and A. Wang. Facile preparation of super durable superhydrophobic materials. *J. Colloid Interface Sci.*, 432, 21–42 (2014).
37. F. Wang, S. Yu, J. Ou, M. Xue and W. Li. Mechanically durable superhydrophobic surfaces prepared by abrading. *J. Appl. Phys.*, 114, 124902 (2013).
38. J. Wu, J. Li, B. Deng, H. Jiang, Z. Wang, M. Yu, L. Li, C. Xing and Y. Li. Self-healing of the superhydrophobicity by ironing for the abrasion durable superhydrophobic cotton fabrics. *Scientific Reports*, 3, 2951 (2013).
39. Y. Tang, J. Yang, L. Yin, B. Chen, H. Tang, C. Liu and C. Li. Fabrication of superhydrophobic polyurethane/MoS₂ nanocomposite coatings with wear-resistance. *Colloids. Surfaces A*, 459, 261–266 (2014).
40. A. Steele, B.N. Nayak, A. Davis, M.C. Gupta and E. Loth. Linear abrasion of a titanium superhydrophobic surface prepared by ultrafast laser microtexturing. *J. Micromech. Microeng.*, 23, 115012 (2013).
41. A. Milionis, R. Ruffilli and I.S. Bayer. Superhydrophobic nanocomposites from biodegradable thermoplastic starch composites (Mater-Bi®), hydrophobic nano-silica and lycopodium spores. *RSC Adv.*, 4, 34395–34404 (2014).
42. X. Zhu, Z. Zhang, X. Men, J. Yang, K. Wang, X. Xu, X. Zhou and Q. Xue. Robust superhydrophobic surfaces with mechanical durability and easy reparability. *J. Mater. Chem.*, 21, 15793–15797 (2011).
43. X. Zhou, Z. Zhang, X. Xu, F. Guo, X. Zhu, X. Men and B. Ge. Robust and durable superhydrophobic cotton fabrics for oil/water separation. *ACS Appl. Mater. Interfaces*, 5, 7208–7214 (2013).
44. H. Cho, D. Kim, C. Lee and W. Hwang. A simple fabrication method for mechanically robust superhydrophobic surface by hierarchical aluminum hydroxide structures. *Current Appl. Phys.*, 13, 762–767 (2013).
45. K. Chen, S. Zhou and L. Wu. Facile fabrication of self-repairing superhydrophobic coatings. *Chem. Commun.*, 50, 11891–11894 (2014).
46. M. Tenjimbayashi and S. Shiratori. Highly durable superhydrophobic coatings with gradient density by movable spray method. *J. Appl. Phys.*, 116, 114310 (2014).
47. V. Kondrashov and J. Ruhe. Microcones and nanoglass: Toward mechanically robust superhydrophobic surfaces. *Langmuir*, 30, 4342–4350 (2014).
48. M. Raimundo, M. Blosi, A. Caldarelli, G. Guarini and F. Veronesi. Wetting behavior and remarkable durability of omniphobic aluminum alloys surfaces in a wide range of environmental conditions. *Chem. Eng. J.*, 258, 101–109 (2014).
49. H. Wang, H. Zhou, A. Gestos, J. Fang and T. Lin. Robust, superomniphobic fabric with multiple self-healing ability against both physical and chemical damages. *ACS Appl. Mater. Interfaces*, 5, 10221–10226 (2013).

50. H. Jin, X. Tian, O. Ikkala and R.H.A. Ras. Preservation of superhydrophobic and superoleophobic properties upon wear damage. *ACS Appl. Mater. Interfaces*, 5, 485–488 (2013).
51. N. Vogel, R.A. Belisle, B. Hatton, T.S. Wong and J. Aizenberg. Transparency and damage tolerance of patternable omniphobic lubricated surfaces based on inverse colloidal monolayers. *Nature Communications*, 4, 2176 (2013).
52. Z. Geng and J. He. An effective method to significantly enhance the robustness and adhesion-to-substrate of high transmittance superomniphobic silica thin films. *J. Mater. Chem. A*, 2, 16601–16607 (2014).
53. T. Simovich, A.H. Wu and R.N. Lamb. Energy efficient one-pot synthesis of durable superhydrophobic coating through nylon micro-rods. *Appl. Surf. Sci.*, 295, 203–206 (2014).
54. S.A. Seyedmehdi, H. Zhang and J. Zhu. Fabrication of superhydrophobic coatings based on nanoparticles and fluoropolyurethane. *J. Appl. Polym. Sci.*, 128, 4136–4140 (2013).
55. R. Hensel, A. Finn, R. Helbig, H.G. Braun, C. Neinhuis, W.J. Fischer and C. Werner. Biologically inspired omniphobic surfaces by reverse imprint lithography. *Adv. Mater.*, 26, 2029–2033 (2014).
56. J. Groten and J. Ruhe. Surfaces with combined microscale and nanoscale structures: A route to mechanically stable superhydrophobic surfaces? *Langmuir*, 29, 3765–3772 (2013).
57. Q.F. Xu, B. Mondal and A.M. Lyons. Fabricating superhydrophobic polymer surfaces with excellent abrasion resistance by a simple lamination templating method. *ACS Appl. Mater. Interfaces*, 3, 3508–3514 (2011).
58. Y. Zhang, D. Ge and S. Yang. Spray-coating of superhydrophobic aluminum alloys with enhanced mechanical robustness. *J. Colloid Interface Sci.*, 423, 101–107 (2014).
59. J. Zhang, B. Li, L. Wu and A. Wang. Facile preparation of durable and robust superhydrophobic textiles by dip coating in nanocomposite solution of organosilanes. *Chem. Commun.*, 49, 11509–11511 (2013).
60. X. Zhang, T. Geng, Y. Guo, Z. Zhang and P. Zhang. Facile fabrication of stable superhydrophobic SiO_2 /polystyrene coating and separation of liquids with different surface tension. *Chem. Eng. J.*, 231, 414–419 (2013).
61. Q. Chu, J. Liang and J. Hao. Facile fabrication of a robust super-hydrophobic surface on magnesium alloy. *Colloids Surfaces A*, 443, 118–122 (2014).
62. J. Ma, X.Y. Zhang, D.P. Wang, D.Q. Zhao, D.W. Ding, K. Liu and W.H. Wang. Superhydrophobic metallic glass surface with superior mechanical stability and corrosion resistance. *Appl. Phys. Lett.*, 104, 173701 (2014).
63. X. Zhu, Z. Zhang, J. Yang, X. Xu, X. Men and X. Zhou. Facile fabrication of a superhydrophobic fabric with mechanical stability and easy-repairability. *J. Colloid Interface Sci.*, 380, 182–186 (2012).
64. X. Deng, L. Mammen, Y. Zhao, P. Lellig, K. Mullen, C. Li, H.J. Butt and D. Vollmer. Transparent, thermally stable and mechanically robust superhydrophobic surfaces made from porous silica capsules. *Adv. Mater.*, 23, 2962–2965 (2011).

65. X. Deng, L. Mammen, H.J. Butt and D. Vollmer. Candle soot as a template for a transparent robust superamphiphobic coating. *Science*, 335, 67–70 (2012).
66. X. Tang, F. Yu, W. Guo, T. Wang, Q. Zhang, Q. Zhu, X. Zhang and M. Pei. A facile procedure to fabricate nano calcium carbonate-polymer-based superhydrophobic surfaces. *New J. Chem.*, 38, 2245–2249 (2014).
67. Z. Zhang, Y. Li, M. Ye, K. Boonkerd, Z. Xin, D. Vollmer, J.K. Kim and X. Deng. Fabrication of superhydrophobic surface by a laminating exfoliation method. *J. Mater. Chem. A*, 2, 1268–1271 (2014).
68. C.H. Xue, Z.D. Zhang, J. Zhang and S.T. Jia. Lasting and self-healing superhydrophobic surfaces by coating of polystyrene/SiO₂ nanoparticles and polydimethylsiloxane. *J. Mater. Chem. A*, 2, 15001–15007 (2014).
69. L. Xiong, L.L. Kendrick, H. Heusser, J.C. Webb, B.J. Sparks, J.T. Goetz, W. Guo, C.M. Stafford, M.D. Blanton, S. Nazarenko and D.L. Patton. Spray-deposition and photopolymerization of organic-inorganic thiol-ene resins for fabrication of superomniphobic surfaces. *ACS Appl. Mater. Interfaces*, 6, 10763–10774 (2014).
70. W.H. Huang and C.S. Lin. Robust superhydrophobic transparent coatings fabricated by a low-temperature sol-gel process. *Appl. Surf. Sci.*, 305, 702–709 (2014).
71. T. Nahum, H. Dodiuk, A. Dotan, S. Kenig and J.P. Lellouche. Superhydrophobic durable coating based on UV-photoreactive silica nanoparticles. *J. Appl. Polym. Sci.*, 131, 41122 (2014).
72. A. Steele, I. Bayer and E. Loth. Adhesion strength and superhydrophobicity of polyurethane/organoclay nanocomposite coatings. *J. Appl. Polym. Sci.*, 125, E445–E452 (2012).
73. A. Cholewinski, J. Trinidad, B. McDonald and B. Zhao. Bio-inspired polydimethylsiloxane-functionalized silica particles – epoxy bilayer as a robust superhydrophobic surface coating. *Surf. Coat. Technol.*, 254, 230–237 (2014).
74. S. Barthwal, Y.S. Kim and S.H. Lim. Mechanically robust superomniphobic aluminum surface with nanopore-embedded microtexture. *Langmuir*, 29, 11966–11974 (2013).
75. S.M. Lee, K.S. Kim, E. Pippel, S. Kim, J.H. Kim and H.J. Lee. Facile route toward mechanically stable superhydrophobic copper using oxidation-reduction induced morphology changes. *J. Phys. Chem. C*, 116, 2781–2790 (2012).
76. H. Wang, Y. Xue, J. Ding, L. Feng, X. Wang and T. Lin. Durable, self-healing superhydrophobic and superoleophobic surfaces from fluorinated-decyl polyhedral oligomeric silsesquioxane and hydrolyzed fluorinated alkyl silane. *Angew. Chem. Int. Ed.*, 50, 11433–11436 (2011).
77. H. Zhou, H. Wang, H. Niu, A. Gestos, X. Wang and T. Lin. Fluoroalkyl silane modified silicone rubber/nanoparticle composite: A super durable, robust superhydrophobic fabric coating. *Adv. Mater.*, 24, 2409–2412 (2012).
78. H. Wang, H. Zhou, A. Gestos, J. Fang, H. Niu, J. Ding and T. Lin. Robust, electro-conductive, self-healing, superomniphobic fabric prepared by one-step vapour-phase polymerisation of poly(3,4-ethylenedioxythiophene) in

- the presence of fluorinated decyl polyhedral oligomeric silsesquioxane and fluorinated alkyl silane. *Soft Matter*, 9, 277–282 (2013).
79. H. Zhou, H. Wang, H. Niu, A. Gestos and T. Lin. Robust, self-healing super-omniphobic fabrics prepared by two-step coating of fluoro-containing polymer, fluoroalkyl silane, and modified silica nanoparticles. *Adv. Funct. Mater.*, 23, 1664–1670 (2013).
 80. Y. Zhao, Z. Xu, H. Wang and T. Lin. Photoreactive azido-containing silica nanoparticle/polycation multilayers: Durable superhydrophobic coating on cotton fabrics. *Langmuir*, 28, 6328–6335 (2012).
 81. C.H. Xue, P. Zhang, J.Z. Ma, P.T. Ji, Y.R. Li and S.T. Jia. Long-lived superhydrophobic colorful surfaces. *Chem. Commun.*, 49, 3588–3590 (2013).
 82. H. Zou, S. Lin, Y. Tu, G. Liu, J. Hu, F. Li, L. Miao, G. Zhang, H. Luo, F. Liu, C. Hou and M. Hu. Simple approach towards fabrication of highly durable and robust superhydrophobic cotton fabric from functional diblock copolymer. *J. Mater. Chem. A*, 1, 11246–11260 (2013).
 83. Y. Liu, Z. Liu, H. Hu, Y. Li, P. Yan, B. Yu and F. Zhou. One-step modification of fabrics with bioinspired polydopamine@octadecylamine nanocapsules for robust and healable self-cleaning performance. *Small*, 11, 426–431 (2014).
 84. L. Liu, F. Xu and L. Ma. Facile fabrication of a superhydrophobic Cu surface via a selective etching of high energy facets. *J. Phys. Chem. C*, 116, 18722–18727 (2012).
 85. Y. Yoo, J.B. You, W. Choi and S.G. Im. A stacked polymer film for robust superhydrophobic fabrics. *Polym. Chem.*, 4, 1664–1671 (2013).
 86. V. Jokinen, P. Suvanto, A.R. Garapaty, J. Lyytinen, J. Koskinen and S. Franssila. Durable superhydrophobicity in embossed CYTOP fluoropolymer micro and nanostructures. *Colloids Surfaces A*, 434, 207–212 (2013).
 87. X. Zhu, Z. Zhang, G. Ren, J. Yang, K. Wang, X. Xu, X. Men and X. Zhou. A novel superhydrophobic bulk material. *J. Mater. Chem.*, 22, 20146–20148 (2012).
 88. X. Zhang, Y. Guo, H. Chen, W. Zhu and P. Zhang. A novel damage-tolerant superhydrophobic and superoleophilic material. *J. Mater. Chem. A*, 2, 9002–9006 (2014).
 89. F.J. Wang, S. Lei, J.F. Ou, M.S. Xue and W. Li. Superhydrophobic surfaces with excellent mechanical durability and easy reparability. *Appl. Surf. Sci.*, 276, 397–400 (2013).
 90. A. Milionis, D. Fragouli, I.S. Bayer and A. Athanassiou, Water adhesion to laser treated surfaces, in: *Laser Surface Modification and Adhesion*, K.L. Mittal and Thomas Bahners (Eds.) pp. 377–413, Wiley-Scrivener, Beverly, MA (2015).

Superhydrophobic and Superoleophobic Biobased Materials

Ilker S. Bayer

Smart Materials, Istituto Italiano di Tecnologia, Genova, Italy

Abstract

Polymers obtained from renewable resources will be more and more important in the future as oil resources will be depleted. Plant based polymers are increasingly being studied in many different applications because of their non-toxic and biodegradation properties. As it is well known, water and liquid repellency requires presence of CH_3 and CF_3 groups at the solid surface-air interfaces along with the right kind of hierarchical surface roughness. By nature, most biopolymers (excluding natural waxes) are not hydrophobic as they are made up of polysaccharide building blocks, or polyester structures. However, this does not dictate that it is impossible to produce liquid repellent surfaces from biopolymers. After all, lotus leaf surface is a composite made up of waxes embedded in a cellulosic matrix as a result of millions of years of natural evolution. In liquid repellent technologies, “mimicking” mostly refers to duplicating the natural surface nanostructures and functionalizing them with synthetic chemicals such as fluorinated silanes. However, recently, there have been attempts to produce liquid repellent materials from biopolymers with minimal use of fluorinated compounds or with fluorinated compounds that would not degrade into perfluorooctanoic acid. The aim of this chapter is to present the latest literature related to liquid repellent materials utilizing biobased resources and discuss the relevant shortcomings and future directions. It is hoped that this chapter will encourage the readers to increase their research efforts towards gradually reducing and eventually eliminating the use of hazardous fluorinated compounds in designing liquid repellent materials.

Keywords: Biopolymers, superhydrophobic, cellulose, starch, hydrophobic cellulose, nanofibers.

Corresponding author: ilker.bayer@iit.it

K.L. Mittal (ed.) *Advances in Contact Angle, Wettability and Adhesion* Volume 2, (259–283)
© 2015 Scrivener Publishing LLC

10.1 Introduction

Biopolymers have increasingly become popular as environmental awareness along with latest developments in sustainable technologies are compelling more research and development efforts towards green materials. Naturally, cellulose is among the most studied biopolymer due to its abundance and low cost. Most of the earlier research pertaining to cellulose has been driven by papermaking industry as paper is a cheap and degradable substrate attractive for many applications ranging from packaging to flexible electronics [1–3]. The main drawback of pure cellulose is that it cannot be melted before it thermally degrades. However, cellulose derivatives also known as modified cellulose such as cellulose acetate, ethyl cellulose and others are commonly used in industry as they can be dissolved in solvents or even melt processed. On the other hand, starch is among the most utilized natural resource for bioplastics. Thermoplastic starch, for instance, is melt processed just like any petroleum based resin but has poor dimensional stability and water resistance. However, with proper additives, compatibilizers and plasticizers thermoplastic starch has been blended with a wide variety of synthetic or bio-based polymers and some of these are commercially available.

The latest advances in bio-based polymers are beyond the scope of this chapter, however, the reader can refer to a number of reviews [4–6] on the synthesis and applications of biopolymers. Instead in this chapter, we will review latest advances in liquid repellent surfaces and materials based on biopolymers starting with cellulose, other polysaccharides such as starch and chitosan, biodegradable polyesters, and plant waxes. It is hoped that this chapter will encourage researchers actively engaged in conventional liquid repellent technologies to explore new techniques and materials based on biodegradable polymers.

10.2 Advances in Liquid Repellent Cellulose Fiber Networks

The recent review by Cunha and Gandini can be consulted on rendering polysaccharides hydrophobic [7]. Paper, paperboard and linerboard are the common packaging materials with reasonable mechanical properties, flexibility and low cost. In many packaging applications paper based materials must resist water. The control of wetting of fibrous surfaces with liquids is important for a number of applications such as filtration

membranes and self-cleaning textiles. Hence, research efforts have intensified towards tuning the resistance of cellulosic materials against liquids for packaging, food storage, medical industry, printing industries, and microfluidics or bioassay devices [8]. Figure 10.1 demonstrates a wetting angle or contact angle map that one can use to classify the state of wetting of a surface. These data are presented by Samyn [8] as compilation of results from various publications on cellulose paper surfaces. Contact angle hysteresis is defined as the difference between advancing and receding contact angles when a droplet moves (by rolling or sliding) on a surface. Since cellulose is highly hydrophilic and water absorbing by nature, rendering it “self-cleaning” (hydrophobic with droplet mobility) is quite challenging unless the fiber surfaces are completely coated which is known as paper sizing in general terms.

Nonetheless, the application potential of functional cellulosic materials such as electromagnetic or antimicrobial has substantially increased the scientific activity in designing new cellulosic nanomaterials, or functionalizing natural cellulose fibers or sheets. For instance, various recent studies use the cellulose fiber networks, such as paper or cotton sheets, as substrates for the deposition of functional materials for the formation of sensors/actuators or lab-on-paper devices, with the main limitation being the possible degradation due to water absorption, resulting in the loss of any incorporated functionality. On the other hand, interesting studies that demonstrate the use of nanomaterials for the functionalization of cellulose fibers follow mostly complicated and sophisticated preparation methods. It is still very challenging to use a universal technique that can provide cellulosic materials such as cellulosic mats, sheets, membranes

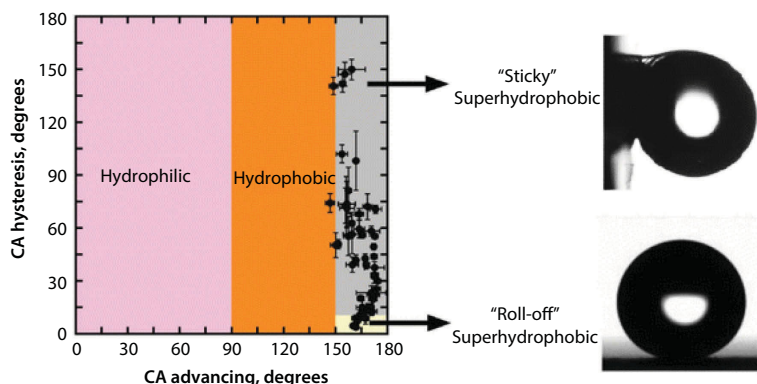


Figure 10.1 A wetting map of water on cellulosic surfaces [8,9].

and paper all with the desired functionalities in an inexpensive and single-step process, and significantly advance its numerous applications. A recent study [10] showed that fiber surfaces can be rendered waterproof with additional functional properties, all in a single-step. The technique is simple, low-cost, scalable, and environmentally friendly and can be applied to any cellulosic material composed of cellulose fiber networks. The approach is based on the impregnation of the cellulose fiber networks with solutions of alkylcyanoacrylate (ACA) monomers and sub-micrometer or nanoscale functional fillers, applied by using drop casting or dip coating, both techniques are suitable for scale-up. These monomers are fully biocompatible and degradable and in biomedical applications come in direct contact with human skin or open wounds. The proposed process relies on moisture-initiated polymerization of ACA on the cellulose fibers, because of hydroxyl groups and environmental moisture existence on them forming a protective polyalkylcyanoacrylate (PACA) layer around each fiber, without changing the structure of entangled fiber network as shown in Figure 10.2. Specifically, ethylcyanoacrylate (ECA) and its polymerized form, polyethylcyanoacrylate (PECA), were used in this study.

The polymeric cyanoacrylate shell formed around the cellulose fibers renders them waterproof. Specifically, Figure 10.3a shows a cellulose sheet (presented in Figure 10.2d) treated with PECA in its central area. Dyed water drops bead up on the treated part, whereas they completely wet the surrounding non-treated region. It is possible to enhance the water repellent character of the treated fiber network by dispersing plant wax or sub-micrometer Teflon particles in the initial ECA solution. In this case, the ECA behaves as a vehicle for the delivery and self-assembly of hydrophobic particles on the fiber's surface. After the application of the ECA/wax or ECA/Teflon solution on the cellulose sheets by drop casting, each fiber becomes decorated by the particles, which get bonded to the surface with the PECA, creating a hydrophobic hierarchical surface morphology. Indeed, the optical microscopy and SEM images b and c in Figure 10.3 show the formation of protruding features onto the surface of the fibers, resulting from dispersed wax and Teflon particles, respectively, in the PECA coating (shell) around the fibers.

In another recent study [11], an industrial waterproof reagent, potassium methyl silicate (PMS), was used for fabricating a superhydrophobic surface on a cellulose-based material (cotton fabric or paper) through a solution-immersion method (Figure 10.4). This method involved a hydrogen bond assembly and a polycondensation process. The silanol group, which was formed by a reaction of PMS aqueous solution with CO_2 , was

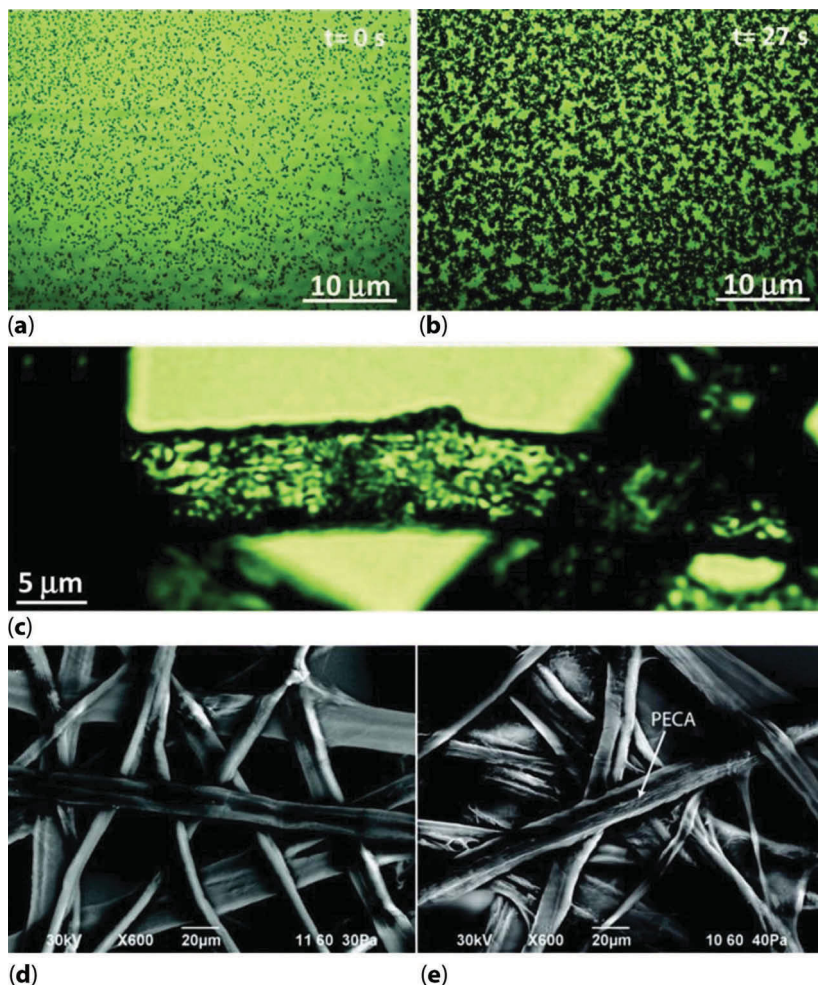


Figure 10.2 (a, b) Optical microscope images taken at the beginning and at the end of the polymerization of ECA monomers deposited on a glass slide from a 5 wt % ECA-acetone solution. To accelerate the polymerization, a small beaker of boiling water was placed in the vicinity of the glass slide to increase the moisture level near the microscope. (c) Optical microscope image of a cellulose fiber wetted by ECA oligomers as they form a network over the fiber surface. SEM images of (d) an untreated cellulosic sheet ($35\ \mu\text{m}$ thick), and (e) a treated sheet revealing the perfectly preserved fiber network after treatment [10].

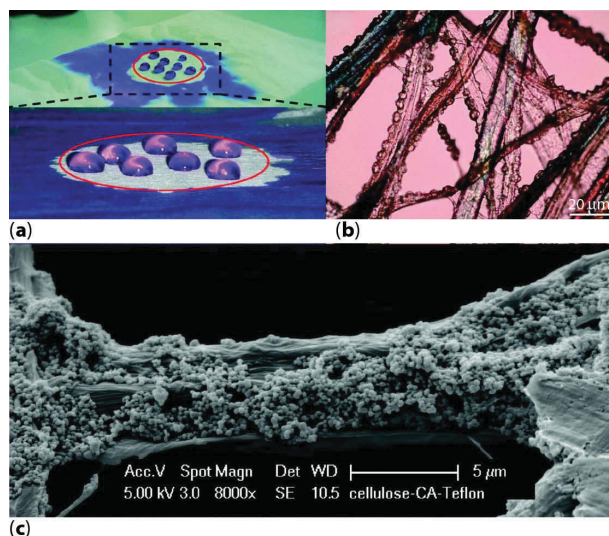


Figure 10.3 (a) Colored water droplets are resting onto the area of a cellulose sheet treated with PECA (defined by the red line (in digital editions only)), whereas they are absorbed in the untreated area. (b) Optical microscope image showing surface roughness generation on cellulose fibers by impregnating them with nanocomposite of 10.0 wt % carnauba wax in PECA to render them highly hydrophobic. (c) SEM image showing the surface of a cellulose fiber roughened by submicrometer (<200 nm) Teflon particles mixed with PECA (20.0 wt % Teflon in PECA) to fabricate super water repellent cellulose sheets [10].

bonded to the cellulose surface via hydrogen bonding. The polymethylsilsesquioxane coatings were prepared by a polycondensation reaction between hydroxyl groups of cellulose and silanol group. Analytical characterization revealed that nanoscale roughness protuberances uniformly covered the surface, thus transforming the cellulose from superhydrophilic to superhydrophobic with a water contact angle of 157° . The superhydrophobic coatings were satisfactory with regard to both chemical and mechanical durability, and because of the transparency of the coatings, the native cotton fabric displayed no changes with regard to either morphology or color.

Zhou *et al.* [12] fabricated an extremely durable superhydrophobic tridecafluorooctyl triethoxysilane modified poly(dimethylsiloxane) (PDMS)/silica nanoparticle composite coating for use on different fabrics (Figure 10.5). Inspiration for the robust composite coating was obtained from a tire, a classic and highly durable nanocomposite material, where the main components are natural rubber and carbon black.

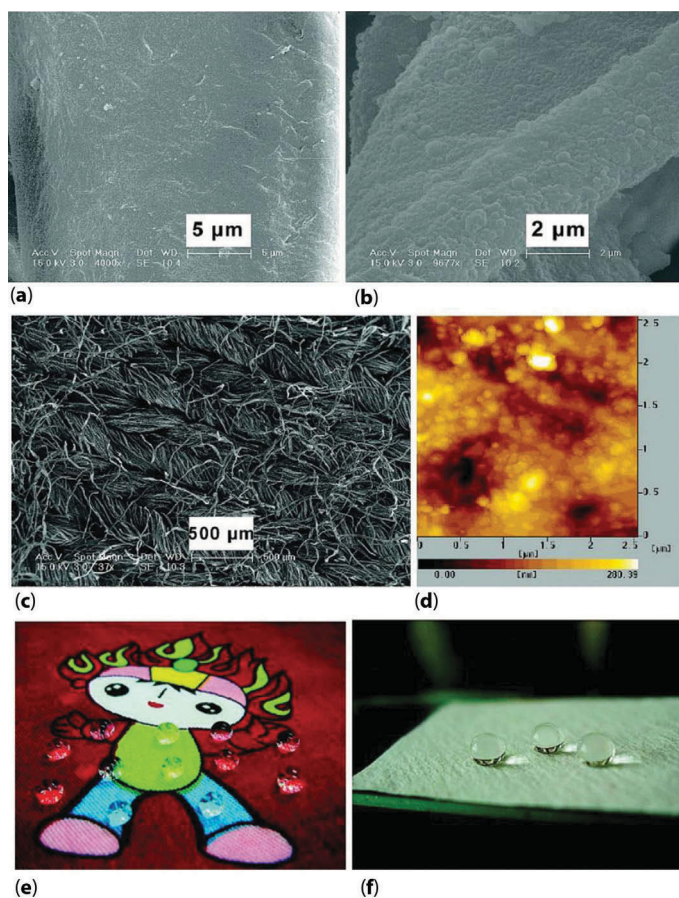


Figure 10.4 FE-SEM images of (a) the native cotton fiber, (b) the modified cotton fiber, and (c) the modified cotton fabric at low magnification. (d) A three-dimensional AFM image of the modified fiber surface, (e) an image of water droplets on the surface of the modified colored cotton fabric, and (f) an image of water droplets on the surface of the modified filter paper [11].

The coating dispersion was applied on the fabrics by dip-coating, after which the samples were dried at room temperature and cured at 135°C for 30 min. The authors highlighted that other coating techniques, e.g., spray-coating and padding, could be used as well. The coating showed excellent mechanical and chemical durability. For example, contact angle and sliding angle for a 5 μ L water droplet on pristine coated cotton were 170° and 3°, respectively, and after 500 wash cycles the corresponding values were nearly unchanged, 165° and 6°, respectively. Similar results

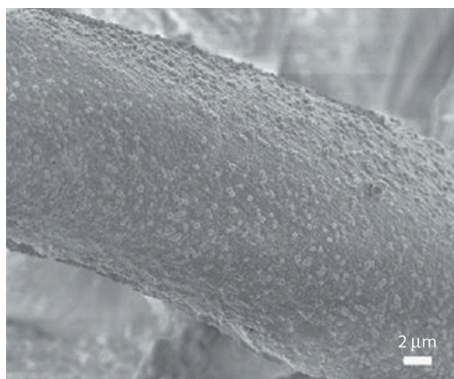


Figure 10.5 SEM image of PDMS/silica nanoparticle coated cotton [13].

were also obtained after treatments with boiling water and acid or base solutions. In addition to the durable superhydrophobicity, the coated fabrics showed good stain resistance and maintained their inherent high air permeability.

Another approach is to assemble nanoparticles on cellulose fiber surfaces from precursors and cover them with polymeric siloxanes containing fluorine groups again from precursors [14]. This combination of different steps made it possible to construct novel features at the resulting surface as shown in Figure 10.6, characterized by both an increase in its roughness induced by amorphous silica particles and a reduction in its surface energy insured by perfluoro moieties, giving rise to water contact angles approaching 150° . The modification calls for an aqueous layer-by-layer system followed by siloxane hydrolysis, both conducted at room temperature in air. The approach is based on the surface modification of cellulose fibers by increasing their surface roughness with silica particles of different sizes and lowering their surface energy through chemical modification with two fluorosiloxanes, viz., 3,3,3-trifluoropropyltrimethoxysilane (FPTS) and 1H,1H,2H,2H-perfluorooctyltriethoxysilane (FOTS), although the latter silane can raise environmental concerns.

A recent study [15] presented a novel method to create superamphiphobic paper by modifying the paper fiber size and structure with plasma etching and fluoropolymer deposition (see Figure 10.7). The heterogeneous nature of the paper structure is drastically different from that of artificially created superamphiphobic surfaces. By refining the wood fibers, smaller diameter fibers (fibrils) were created so that liquid droplets did not get

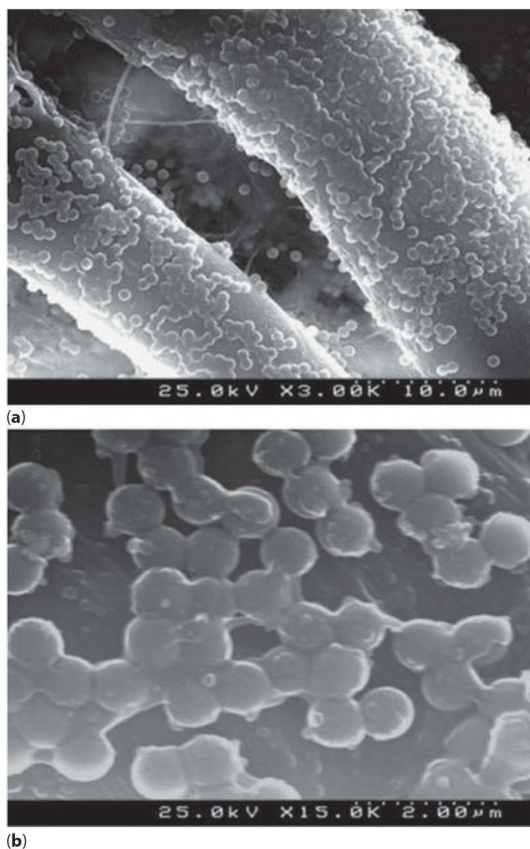


Figure 10.6 Fluorinated silica nanoparticles attached to the cellulose fibers rendering them rough and hydrophobic [14]. (a) Fiber surface with $\times 3000$ magnification and (b) Modified fiber surface details with $\times 15000$ magnification.

absorbed into the paper. After oxygen plasma etching and deposition of a fluoropolymer film, motor oil droplet, contact angles reached $149 \pm 3^\circ$, although these structures readily absorbed *n*-hexadecane. Exchange of water in the pulp solution with sec-butanol provided additional control over fiber spacing to create superamphiphobic substrates with contact angles $>150^\circ$ for water, ethylene glycol, motor oil, and *n*-hexadecane (Figure 10.8).

Moreover, it has been demonstrated that liquid repellent nanocellulose aerogels, consisting of fibrillar networks and aggregates with structures at different length scales, easily float on water while supporting considerable weight [16] and also on oils as inspired by flotation of insects on

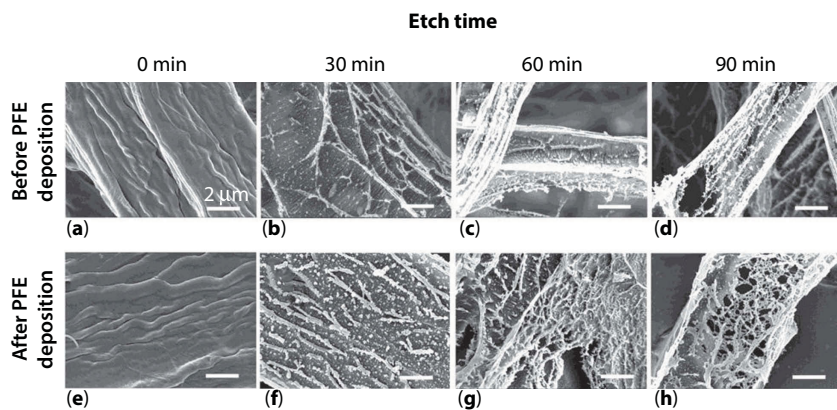


Figure 10.7 SEM images of fibers that have been etched for (a, e) 0, (b, f) 30, (c, g) 60, and (d, h) 90 min, before and after deposition of 400 nm of perfluoroelastomer (PFE) [15].

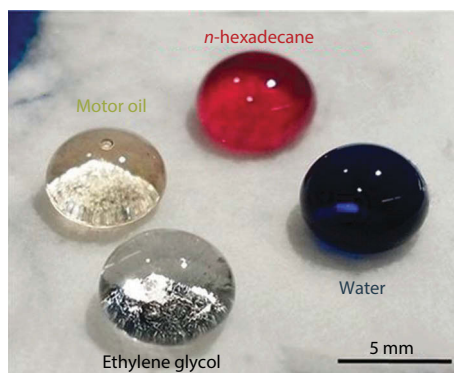


Figure 10.8 Droplets of four test liquids (water-dyed blue), ethylene glycol, motor oil and *n*-hexadecane (dyed red) are shown resting on the treated paper surface exhibiting high contact angles for all liquids [15].

water due to their superhydrophobic legs as depicted in Figure 10.9. These aerogels are capable of supporting a weight nearly 3 orders of magnitude larger than the weight of the aerogel itself (refer to Figure 10.9 caption for further details). The load support is achieved by surface tension acting at different length scales: at the macroscopic scale along the perimeter of the aerogel block, and at the microscopic scale along the cellulose nanofibers by preventing soaking of the aerogel thus ensuring buoyancy. They demonstrated high-adhesive pinning of water and oil droplets, gas permeability, and light reflection at the plastron (a thin film of air held by

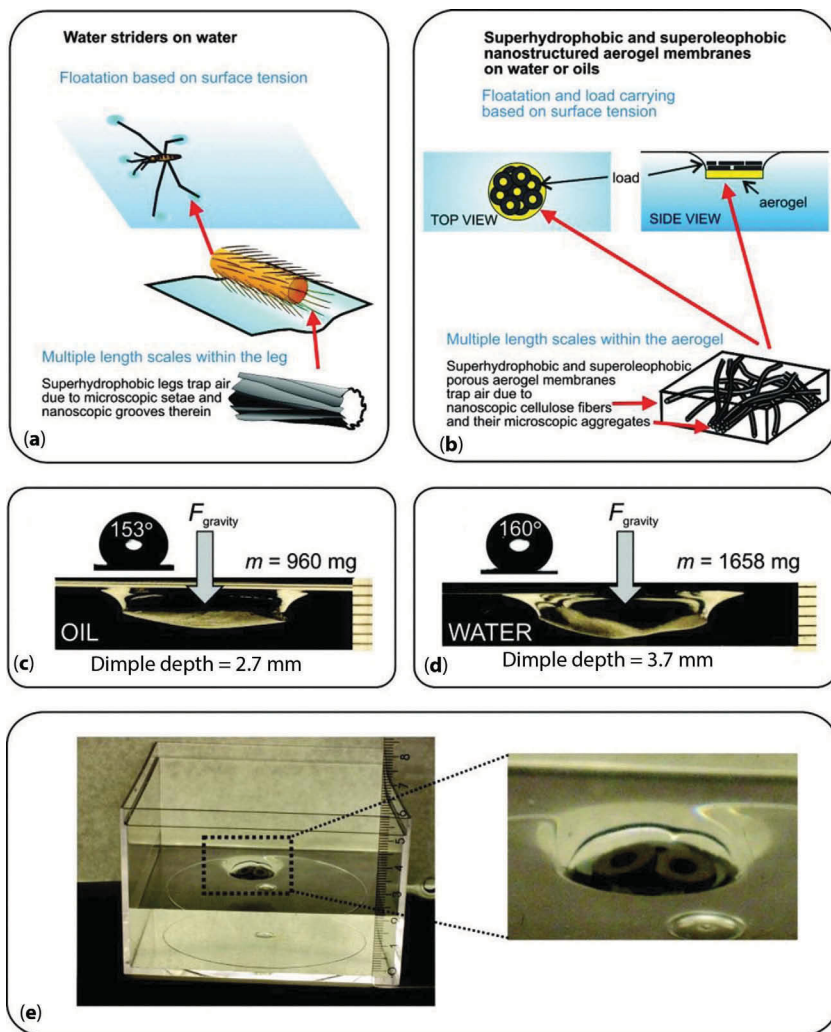


Figure 10.9 Flotation and load carrying on oil and water based on fluorinated nanostructured aerogel working as water striders, a class of insects capable of floating on water based on surface tension, using superhydrophobic legs with fibrillar structures. (b) Cartoon of a fluorinated nanofibrous cellulose aerogel membrane floating on water and oil due to surface tension. The liquid repellency is induced by entangled networks of fibers. (c,d) Contact angle measurement and load carrying experiment on the aerogel on, respectively, paraffin oil and water. The side-view photograph of the aerogel load carrier on paraffin oil and water shows the dimple at maximum supportable weight. The scale markers on the right are in millimeters. (e) Load carrying setup. Metal weights (washers) are loaded on the fluorinated aerogel membrane floating on water (similarly on oil) [16].

water-repellent hairs of some aquatic insects) in water and oil, and viscous drag reduction of the fluorinated aerogel in contact with oil. The potential applications were envisioned to be buoyant, gas permeable, dirt-repellent coatings for miniature sensors and other devices floating on liquid surfaces.

10.3 Liquid Repellent Materials: Cellulose Derivatives

As can be seen, most popular approaches for fabricating liquid repellent surfaces are based on cellulose fiber surface treatment or reducing the size of the fibers and functionalizing the surfaces with nanomaterials or silanes with different chemistries. Alternatively, it is possible to use cellulose derivatives in combination with other polymers and nanofillers to produce liquid repellent coatings. Most cellulose derivatives can be solution processed with common solvents and this would allow one to make polymer/nanoparticle colloidal solutions for applying by simple methods such as spray. Moreover, certain cellulose derivatives such as ethyl cellulose are relatively hydrophobic and waterproof. For instance, inherently superhydrophobic and flexible cellulose nitrate-based bionanocomposites were fabricated from solid stabilized (Pickering) emulsions [17]. Emulsions were formed by dispersing cyclosiloxanes in water stabilized by layered silicate particles and were subsequently modified by blending into a zinc oxide nanoparticle colloidal suspension. The polymer matrix was a blend of cellulose nitrate and fluoroacrylic polymer (with C-8 chemistry) dispersed in a system of co-solvents. Coatings were spray cast onto aluminum substrates from polymer blends dispersed in modified Pickering emulsions. No post-surface treatment was required to induce superhydrophobicity. Effect of antiseptic additives on bionanocomposite superhydrophobicity was also presented. Alternatively, another simple technique was also shown for the fabrication of rubber-toughened cellulose nitrate/organoclay nanocomposite coatings with highly water repellent surface wetting characteristics and strong adhesion to metal surfaces [18]. The technique combines the principles of phase inversion and atomization of multicomponent polymer/organoclay suspensions containing a biolubricant as the non-solvent. The biolubricant was a blend of cyclomethicone/dimethiconol oil with fruit kernel oils. The ternary system of cellulose nitrate/solvent/biolubricant was blended with rubber dispersed organoclay nanofluids. Natural, synthetic, and fluoroacrylic latex rubbers were used for

the purpose. Self-cleaning superhydrophobic coatings were obtained from synthetic and fluoroacrylic rubbers whereas natural rubber containing formulations resulted in sticky superhydrophobic coatings (Figure 10.10).

Anitha *et al.* [19] prepared ZnO nanoparticle embedded cellulose acetate (CA) fibrous membranes with multifunctional properties through electrospinning method (Figure 10.11). They found that the polymer

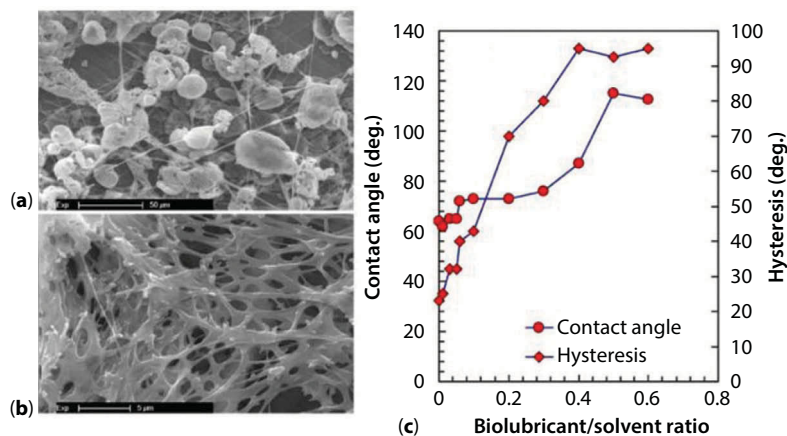


Figure 10.10 Scanning electron microscope images (a) and (b), showing morphology of cellulose nitrate biopolymer spray cast from cellulose nitrate/solvent/biolubricant ternary system (c) measured static water contact angle and hysteresis on the biopolymer coating as a function of biolubricant/solvent weight ratio [18].

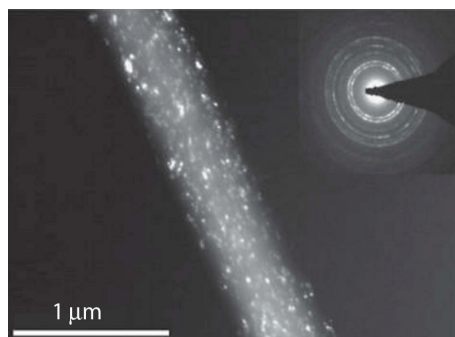
















Figure 10.11 TEM image of the composite fiber and selected area electron diffraction (SAED) pattern (inset in the left top of the Figure). The ZnO nanoparticles are clearly seen on surface of the fibers [19].

concentration in the solution had a significant effect on the morphology of the fibers. The wettability of the pure and composite fibrous membranes was also studied by measuring the contact angle of water on the membranes (see Figure 10.12). It was observed that the embedded ZnO in the CA was responsible for the hydrophobic nature of the surface. The optical property of the sample was tested using Photo Luminescence (PL) spectra. The membranes also demonstrated some degree of anti-bacterial activity.

Contact angle measurements were carried out to evaluate the wetting properties of the fibrous membrane. Most of the previous studies focused on the preparation of hydrophobic and super-hydrophobic surfaces by appropriate surface modification of the sample. Still, it is difficult to achieve a superhydrophobic surface without chemical modification of the cellulose based sample. Figures 10.12 a and b show the contact angle of a water droplet on the fibrous membrane for a duration of 30 s. In the case of pure CA fibrous membrane, the measured contact angle was found to be 47° initially and the contact angle decreases rapidly from 47° to 31° . The observed water contact angle (WCA) on ZnO embedded CA is about 124° , which is much higher than that of the pure CA fibers. The value of the WCA does not change significantly from the observed initial value. As a result, it was concluded that the wetting property of the CA had changed from hydrophilic to hydrophobic when ZnO was impregnated into it. They argued that the Cassie-Baxter type superhydrophobicity could be due to the formation of hierarchical roughness features made up of ZnO nanoparticles embedded in electrospun fiber surface texture.

Ding *et al.* [20] reported a new approach to convert an electrospun nanofibrous cellulose acetate mat surface from super-hydrophilic to super-hydrophobic. Super-hydrophilic cellulose acetate nanofibrous mats were obtained by electrospinning hydrophilic cellulose acetate. The surface property of the fibrous mats was modified from super-hydrophilic to super-hydrophobic with a simple sol-gel coating of decyltrimethoxysilane (DTMS) and tetraethyl orthosilicate (TEOS). The resultant samples were characterized by various spectroscopic techniques. The results showed that the sol-gel (I) coatings were formed on the rough fibrous mats only after immersion in sol-gel. After the sol-gel (I) coating, the cellulose acetate fibrous mats formed in both 8 and 10 wt% cellulose acetate solutions showed the superhydrophobic surface property as shown in Figure 10.13. Additionally, the average sol-gel coating thickness on 10 wt% cellulose acetate fibrous mats was calculated to be 80 nm. The super-hydrophobicity of fibrous mats was attributed to the combined

Time (sec)	CA fibrous membrane	ZnO embedded CA membrane
0	 47.4°	 124.2°
5	 43.2°	 124.1°
10	 41.4°	 123.9°
15	 38.7°	 123.2°
20	 37.3°	 123.1°
25	 37.2°	 122.7°
30	 31.2°	 122.4°

(a) **(b)**

Figure 10.12 Optical photographs of water droplets on (a) pure and (b) ZnO embedded CA fibrous membranes [19].

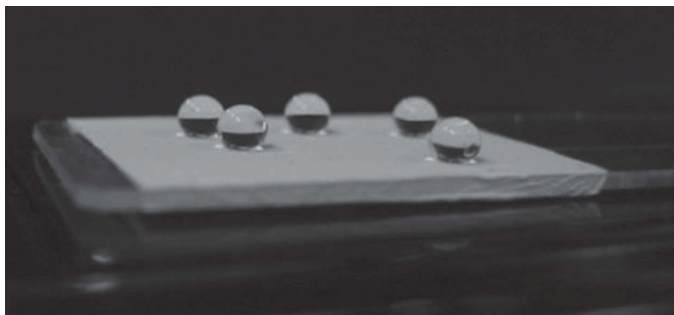


Figure 10.13 Several water droplets placed on the 10 wt% cellulose acetate fibrous mat with the sol-gel (I) coating showing the super-hydrophobicity [20].

effect of the high surface roughness of the electrospun nanofibrous mats and the hydrophobic DTMS sol-gel coating. Additionally, hydrophobic sol-gel nanofilms were found to be transparent according to UV-visible measurements.

Extracts of wood contain cellulose but also substantial amounts of other natural polymers such as hemicellulose and lignin. Any material synthesized directly from wood can be considered as cellulose derivative. Kavalenka *et al.* [21] showed that a lignin-based polymer can be microstructured with a scalable replication technique in a heated mold, resulting in a superhydrophobic/superoleophilic surface covered with microhairs (see Figure 10.14). The microhaired surface is used to clean crude oil spills and to separate oil/water mixtures by absorbing oil. After treating the microhaired surface with argon plasma it can turn into an underwater superoleophobic material necessary for removing water from the oil/water mixtures (see Figure 10.15).

To investigate the ability of the superhydrophobic/superoleophilic wood-based surface to separate crude oil (Total Azolla ZS 10) and water from the oil/water mixture, they dispensed a droplet of water-oil mixture on a tilted microhaired “liquid wood” surface. The experiments showed that the oil/water mixture applied to the microstructured “liquid wood” surface segregated into oil and water, and the oil was absorbed and trapped by the microhaired surface, while the water stayed on the surface of the material in a non-wetting state. Therefore, these results suggest that microhaired wood-based surfaces enable effective separation of oil and water from the oil/water mixtures, and also help to reduce the environmental impacts of oil/water separations by utilizing green materials for their fabrication (Figure 10.15).

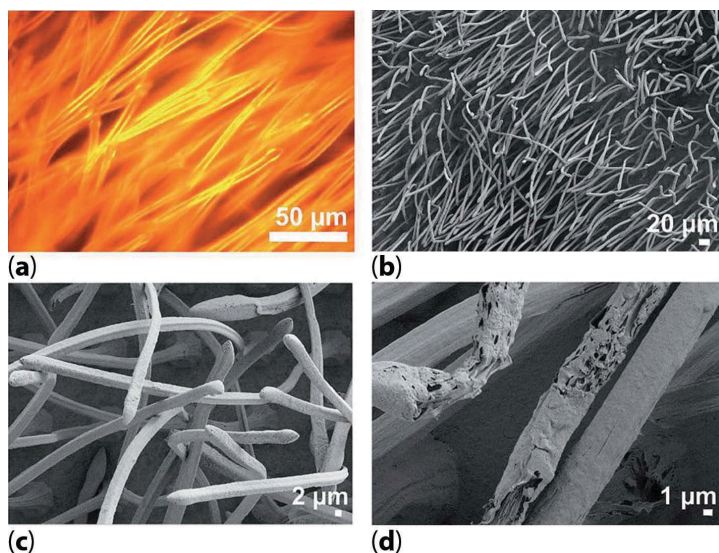


Figure 10.14 Micrographs of wood-based microhairs fabricated in a heated mold. Specifically, the wood-based polymer heated above the melting temperature is pressed into the mold. During the demolding step the mold is cooled and retracted, and the softened microstructures are elongated due to adhesion to the mold cavities, resulting in long microhairs. (a) Optical microscopy image of the microhairs. (b and c) SEM images of the microhairs. Their dimensions are: approximately 5 μm in diameter, >200 μm in length, aspect ratios $\sim 40\text{--}50$. (d) Higher magnification SEM image reveals the submicrometer details of the microhairs. The fibrous structure possibly originates from the processed wood fibers contained in the “liquid wood” polymer [21].

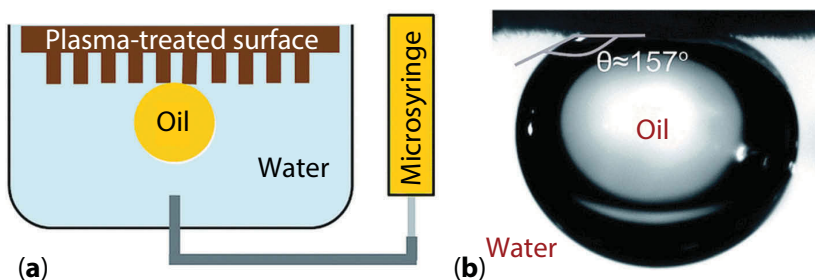


Figure 10.15 Underwater superoleophobicity of the microhaired wood-based surface treated with argon plasma (0.2 mbar, 30 W, 120 s). (a) Schematic of the underwater contact angle measurement. Water trapped between microhairs limits the contact between oil and solid. (b) Photograph of a 7 μl oil droplet deposited under water on the plasma-treated microhaired surface with the oil contact angle of 157° [21].

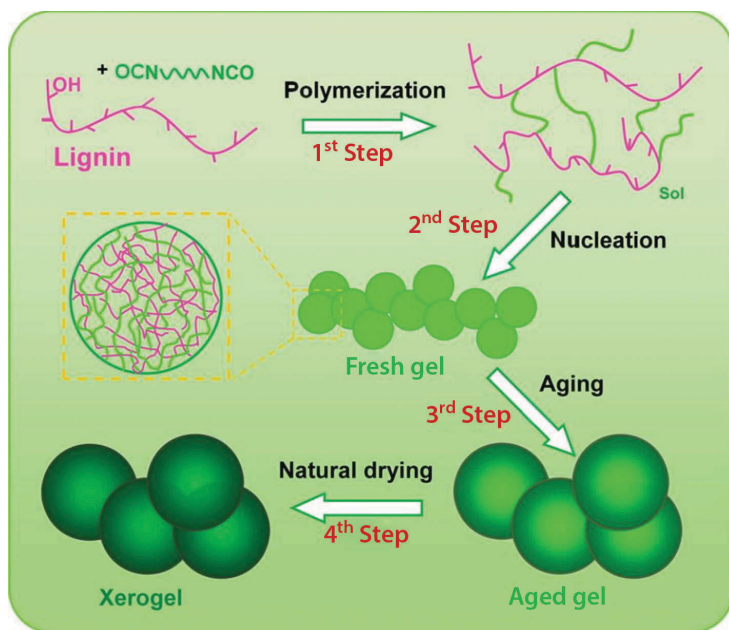


Figure 10.16 Schematic representation of formation of lignin-based xerogels by controlling phase separation in the sol-gel process and subsequent ambient pressure drying. Each steps corresponds to a phase of structural evolution in the sol-gel system, including cross-linking polymerization between lignin and modified isocyanate (1st step), spontaneous nucleation of sol nanoparticles (2nd step), and aging process to form a framework of nanoparticles (3rd step) and drying under ambient conditions (4th step) [22].

Yang *et al.* [22] developed a novel isocyanate-modified lignin xerogel using renewable lignin as precursor via a sol-gel process and ambient pressure drying method. The xerogel demonstrated high performance in self-cleaning and superhydrophobicity with no additional hydrophobic modification. The process is schematically shown in Figure 10.16. They claim that the xerogel obtained can find potential applications in absorbents, coatings, and scaffolds. Specifically, a monolithic polyurethane organogel was made by the condensation polymerization of lignin and modified isocyanate in a tetrahydrofuran (THF) solution, and then ambient pressure drying was applied to the as-prepared organogel resulting in a lignin-based xerogel. Interestingly, the obtained xerogels simultaneously possess low surface energy and good water repellence, exhibiting multifunctional characteristics including self-cleaning and selective oil absorption, demonstrating that they are ideal absorbents for removing oils or organic solvents from water for oil spill cleanup or industrial wastewater purification (see Figure 10.17).

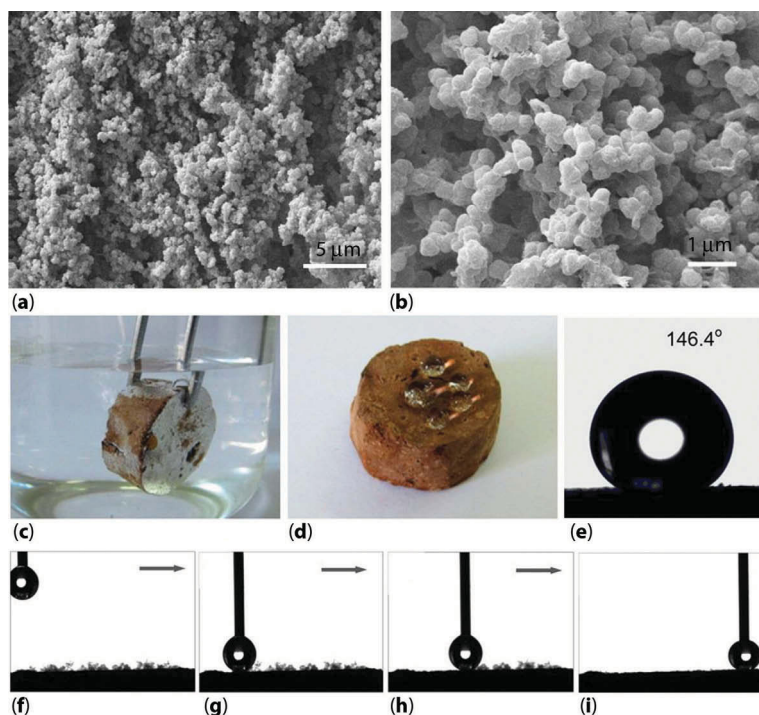


Figure 10.17 (a,b) SEM images of the xerogels at different magnifications. (c) Mirror-like air cushion can be observed on the lignin-based xerogel (submerged in water). (d) Water droplets exhibit spherical shapes on the surface of the xerogel. (e) The water contact angle on the surface of the xerogel. (f–i) Self-cleaning action demonstrated by the removal of silica particles from the surface using a moving water droplet (5 μ L) [22].

10.4 Liquid Repellent Thermoplastic Starch and Biopolyesters

There are only a few recent studies on the fabrication and characterization of stand-alone bio-polymer nanocomposite films or coatings displaying liquid repellent properties. Obeso *et al.* [23] developed a superhydrophobic surface by precipitation of poly(hydroxybutyrate) (PHB) on the surface of cellulose fibers of papers using a phase separation process. The same authors used a similar approach to synthesize biodegradable superhydrophobic poly (L-lactic acid) substrates in order to control cell adhesion. Superhydrophobic/superoleophilic porous poly (L-lactic acid) films were also prepared by Xue *et al.* for water-oil separation applications [24]. Yohe *et al.* [25] prepared 3D superhydrophobic materials from biocompatible

building blocks, where air acts as a barrier component in a porous electrospun mesh to control the rate at which a drug is released. Specifically, they fabricated poly (ϵ -caprolactone), a biopolyester, electrospun meshes containing poly (glycerol monostearate-co- ϵ -caprolactone) as a hydrophobic polymer dopant, which results in meshes with a high apparent contact angle. The apparent contact angle of these meshes dictates the rate at which water penetrates into the porous network and displaces entrapped air. The surface wettability was controlled by hydration which caused a model bioactive agent to penetrate into the pores displacing air. Once the meshes were in contact with an aqueous medium the bioactive agent was slowly released from the pores. It was possible to produce porous electrospun meshes with higher surface area to release drugs more slowly than control nonporous constructs. The drug-loaded meshes were efficacious against cancer cells in vitro for >60 days, thus demonstrating their applicability for long-term drug delivery as schematically depicted in Figure 10.18.

Milionis *et al.* [26] demonstrated an approach in which a commercial thermoplastic starch composite, Materi-Bi® (Novamont SpA, Italy) was compounded with hydrophobic fumed silica nanoparticles and lycopodium spores. They found that both hydrophobic fumed silica and Materi-Bi® have excellent colloidal stability and solubility in chloroform and they can be sprayed onto various surfaces like paper, metals and semiconductors. By varying the concentration of biopolymer to hydrophobic fumed silica, the wetting properties of the nanocomposites were varied (see Figure 10.19). Superhydrophobic nanocomposites displayed raspberry-like surface roughness with water contact angles exceeding 160° with very low water droplet roll-off angles ($\sim 1^\circ$). On the other hand, composites of Materi-Bi® and lycopodium spores displayed adhesive superhydrophobicity (rose petal effect). Superhydrophobic nanocomposites were found to withstand thermal aging at 250°C without loss of properties. Due to the

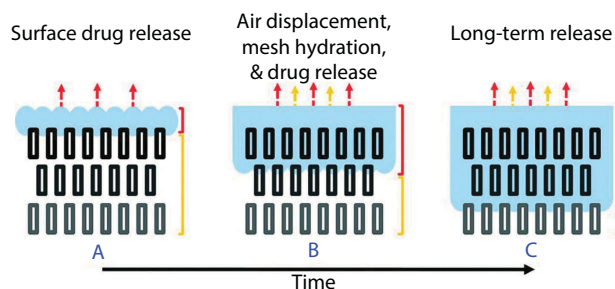


Figure 10.18 Infusion of polymer nanofibers network with water allowing controlled and slow rate drug release [25]. Infusion progresses in time from A to C.

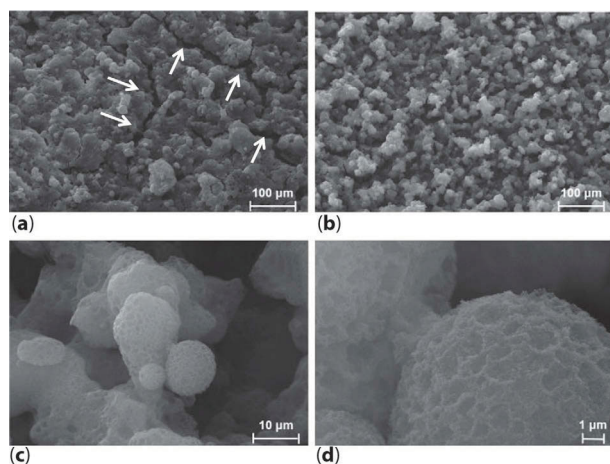
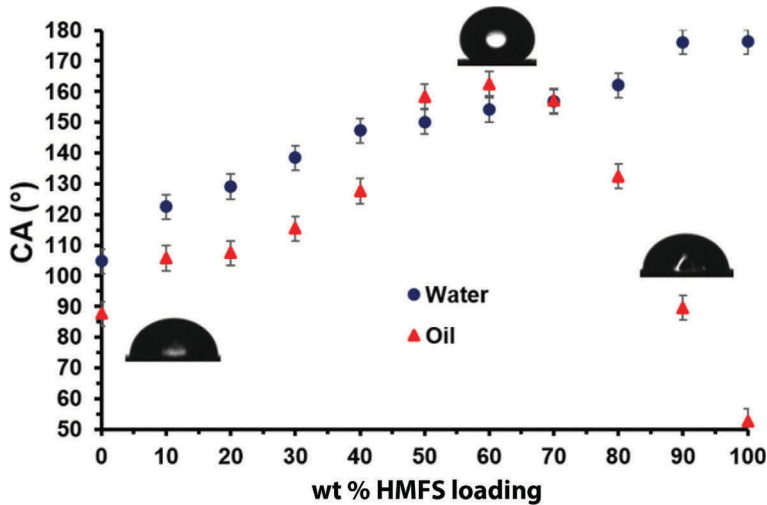


Figure 10.19 Low magnification SEM images of the Mater-Bi® nanocomposite loaded with 60 wt % hydrophobically modified fumed silica (HMFS) nanoparticles before (a) and after (b) the thermal treatment. (c,d) Higher magnification SEM images indicate that the nanoscale roughness from the HMFS is still present in the nanocomposite and is responsible for the superhydrophobicity [26].

resultant micro-morphology of nanocomposites, certain coatings were rendered superoleophobic by functionalizing with a dilute fluoroacrylic polymer solution in acetone. Oil droplet contact angles reached 166° with droplet roll-off angles of approximately 15° .

As mentioned earlier, Mater-Bi®/HMFS composite coatings can also be rendered superoleophobic with a secondary spray layer of diluted fluoroacrylic solution in acetone (C6-chemistry). The fluoroacrylic is available commercially as water dispersion (Capstone™ ST 100, DuPont, USA; 20% polymer by weight). Due to superhydrophobicity of the nanocomposites, wetting their surfaces with the water-based dispersion was not possible. The polymer, however, can be extracted from water and re-dispersed in acetone by using trifluoroacetic acid as a precipitating agent. All the composite surfaces were treated with the dilute fluoroacrylic solution in acetone to study the effect on the water and oil contact angles as a function of surface fluorination.

Note that Mater-Bi® does not swell or dissolve in acetone. All the surfaces with 50% HMFS loading and above retain their super water repellent properties as shown in Figure 10.20. However, as shown in the table of Figure 10.20, relatively high water roll-off angles were observed ranging from 17° to 29.3° without showing a specific trend. This is attributed to the potential partial loss of surface morphology due to the presence of an



wt % HMFS loading	RA (°) water	RA (°) oil
50	29.5	pinned
60	17.0	14.7
70	23.1	pinned
80	28.7	pinned
90	29.3	pinned
100	24.2	pinned

Figure 10.20 Droplet contact angle measurements for water and olive oil droplets plotted as a function of percent HMFS loading. The table lists water and oil droplet roll-off angles (RA) as a function of HMFS loading. Below 50 wt% HMFS loading, all the droplets are pinned [26]. HMFS: Hydrophobically modified fumed silica.

extra polymer layer covering the original topological features. In terms of oleophobicity, the coatings of pure Mater Bi® with the fluoroacrylic cover layer exhibit an oil contact angle (OCA) of 88°. The addition of HMFS gradually increases the OCA due to its contribution to the surface roughness. We observed an increasing trend in the OCA with a maximum value corresponding to the sample with 60% HMFS loading (OCA = 163°). In particular, the condition for superoleophobicity (OCA > 150°) is satisfied for HMFS loadings between 50% and 70%. However, even if these OCAs

are really high, only the coating with 60% HMFS demonstrates rolling off of oil droplets at 14.7° substrate tilt angles. For all other concentrations, the oil droplets remain pinned on the surface. At this particular nanocomposite composition, the fluoropolymer coated surface texture maintains both the nano-scale and micro-scale roughness features. Each micro sized bump has a very small surface roughness which resembles raspberry-like dual-scale structured surfaces. Particularly for surfaces which do not have well-defined re-entrant surface textures (required for oleophobicity) such as the ones made by lithographic techniques, continuation of random but self-similar dual-scale surface topography in combination with the right fluorochemistry is essential for creating oleophobicity. It is seen that the novel raspberry-like surface texture resulting simply from spraying hydrophobic silica nanoparticles also forms when the silica nanoparticles and the biopolymer are sprayed together. The biopolymer-silica nanocomposite coatings formed in this way can be made oleophobic by coating them with a sufficiently thin layer of C-6 fluoropolymer. Therefore, it is possible to find the right combination of surface texture (by adjusting the polymer-to-nanoparticle ratio in solution) and the top fluoropolymer coating thickness that collectively results in oil repellent coatings.

10.5 Conclusions

Plants and animals have developed intelligent ways to control wetting without using synthetic fluorinated materials. Of course being able to duplicate nanostructured natural surfaces is quite commonplace now with state-of-the-art microfabrication techniques, but fabrication of liquid repellent materials *made up of* natural polymers or extracts or their blends or composites is still quite challenging. Review of the literature clearly shows that one way or the other, a certain synthetic hydrophobic agent is needed even if biopolymers are used as substrates in the form of fibers or rough surfaces. However, there are many encouraging new ways to make functional liquid repellent materials from green bio-based resources and various practical applications have been demonstrated such as oil-water separation, tuning of drug delivery rates, etc. Use of silicone polymers and elastomers along with biopolymers could be one interesting future direction as silicone polymers and silicone fluids are non-toxic, biodegradable materials and do not pose alarming environmental concerns related to C-8 fluoro compounds. It is hoped that this chapter will stimulate further research interest in this direction; after all nature around us is full of various waterproof materials synthesized by plants or animals alike such as waxes, resins and polymerizable oils.

References

1. H. Ogihara, J. Xie, J. Okagaki, and T. Saji, Simple method for preparing superhydrophobic paper: Spray-deposited hydrophobic silica nanoparticle coatings exhibit high water-repellency and transparency, *Langmuir* 28, 4605–4608 (2012).
2. G. Chitnis, Z. Ding, Chun-Li Chang, C. A. Savran and B. Ziaie Laser-treated hydrophobic paper: An inexpensive microfluidic platform, *Lab Chip*, 11, 1161–1165 (2011).
3. H. Ogihara, J. Xie and T. Saji, Factors determining wettability of superhydrophobic paper prepared by spraying nanoparticle suspensions, *Colloids Surfaces A*, 434, 35–41 (2013).
4. D. R. Lu, C. M. Xiao and S. J. Xu, Starch-based completely biodegradable polymer materials *Express Polymer Letters*, 3, 366–375 (2009).
5. X. Z. Tang, P. Kumar, S. Alavi, and K.P. Sandeep, Recent advances in biopolymers and biopolymer-based nanocomposites for food packaging materials. *Critical Rev. Food Sci. Nutrition*, 52, 426–442 (2012).
6. E. Ruiz-Hitzky, M. Dardera and P. Aranda, Functional biopolymer nanocomposites based on layered solids *J. Mater. Chem.*, 15, 3650–3662 (2005).
7. A. G. Cunha and A. Gandini, Turning polysaccharides into hydrophobic materials: A critical review. Part 1, *Cellulose*, 17, 875–889 (2010).
8. P. Samyn, Wetting and hydrophobic modification of cellulose surfaces for paper applications *J Mater. Sci.*, 48, 6455–6498 (2013).
9. B. Balu, J. S. Kim, V. Breedveld and D. W. Hess, Tunability of the adhesion of water drops on a superhydrophobic paper surface via selective plasma etching, *J. Adhesion Sci. Technol.* 23, 361–380, (2009)
10. I. S. Bayer, D. Fragouli, A. Attanasio, B.Sorce, G. Bertoni, R. Brescia, R.Di Corato, T. Pellegrino, M. Kalyva, S.Sabella, P. P. Pompa, R. Cingolani, and A. Athanassiou, Water-repellent cellulose fiber networks with multifunctional properties *ACS Appl. Mater. Interfaces* 3 , 4024–4031 (2011).
11. S. Li, S. Zhang, and X. Wang Fabrication of superhydrophobic cellulose-based materials through a solution-immersion process *Langmuir* 24, 5585–5590 (2008).
12. H. Zhou, H. Wang, H. Niu, A. Gestos, X. Wang, and T. Lin, Fluoroalkyl silane modified silicone rubber/nanoparticle composite: A super durable, robust superhydrophobic fabric coating *Adv. Mater.*, 24, 2409–2412 (2012).
13. H. Teisala, M. Tuominen, and J. Kuusipalo, Superhydrophobic coatings on cellulose-based materials: Fabrication, properties, and applications, *Adv. Mater. Interfaces*, 1, 1300026–46 (2014).
14. G. Gonçalves, P. A.A.P. Marques , T. Trindade, C. P. Neto, and A. Gandini, Superhydrophobic cellulose nanocomposites, *J. Colloid Interface Sci.* 324, 42–46 (2008).
15. L. Li, V. Breedveld, and D. W. Hess Design and fabrication of superamphiphobic paper surfaces *ACS Appl. Mater. Interfaces* 5, 5381–5386 (2013).

16. H. Jin , M. Kettunen, A. Laiho, H. Pynnönen, J. Paltakari, A. Marmur, O. Ikkala, and R. H. A. Ras, Superhydrophobic and superoleophobic nanocellulose aerogel membranes as bioinspired cargo carriers on water and oil, *Langmuir*, 27, 1930–1934 (2011).
17. I. S. Bayer, A. Steele, P. J. Martorana, E. Loth, and L. Miller, Superhydrophobic cellulose-based bionanocomposite films from Pickering emulsions, *Appl. Phys. Lett.*, 94, 163902 (2009).
18. I. S. Bayer, A. Steele, P. Martorana, E. Loth, S. J. Robinson and D. Stevenson, Biolubricant induced phase inversion and superhydrophobicity in rubber-toughened biopolymer/organoclay nanocomposites. *Appl. Phys. Lett.* 95, 063702 (2009).
19. S. Anitha, B. Brabu, D. John Thiruvadigal, C. Gopalakrishnan, and T.S. Natarajan, Optical, bactericidal and water repellent properties of electrospun nano-composite membranes of cellulose acetate and ZnO, *Carbohydrate Polymers* 97, 856–863 (2013).
20. B. Ding, C. Li, Y. Hotta, J. Kim, O. Kuwaki and S. Shiratori, Conversion of an electrospun nanofibrous cellulose acetate mat from a super-hydrophilic to super-hydrophobic surface, *Nanotechnology* 17, 4332–4339 (2006).
21. M. N. Kavalenka, A. Hopf, M. Schneider, M. Worgull and H. Holscher, Wood-based microhaired superhydrophobic and underwater superoleophobic surfaces for oil/water separation *RSC Adv.*, 4, 31079–31083 (2014).
22. Y. Yang, Y. Deng, Z. Tong, and C. Wang , Renewable lignin-based xerogels with self-cleaning properties and superhydrophobicity, *ACS Sustainable Chemistry & Engineering* 2, 1729–1733 (2014).
23. C. G. Obeso, M. P. Sousa, W. Song, M. A. Rodriguez-Perez, B. Bhushan and J. F. Mano, Modification of paper using polyhydroxybutyrate to obtain biomimetic superhydrophobic substrates, *Colloids Surfaces A*, 416, 51–55 (2013).
24. Z. Xue, Z. Sun, Y. Cao, Y. Chen, L. Tao, K. Li, L. Feng, Q. Fu and Y. Wei, Superoleophilic and superhydrophobic biodegradable material with porous structures for oil absorption and oil–water separation, *RSC Adv.*, 3, 23432–23437 (2013).
25. S.T. Yohe, Y. L. Colson, and M. W. Grinstaff, Superhydrophobic materials for tunable drug release: Using displacement of air to control delivery rates, *J Amer. Chem. Soc.* 134, 2016–2019 (2012).
26. A. Milionis, R. Ruffilli, and I. S. Bayer Superhydrophobic nanocomposites from biodegradable thermoplastic starch composites (Mater-Bi®), hydrophobic nano-silica and lycopodium spores, *RSC Adv.*, 4, 34395–34404 (2014).

Part 2

WETTABILITY MODIFICATION

Laser Ablated Micro/Nano-Patterned Superhydrophobic Stainless Steel Substrates

Sona Moradi¹, Saeid Kamal² and Savvas G. Hatzikiriakos^{1,*}

¹*Department of Chemical and Biological Engineering,
The University of British Columbia, Vancouver BC, Canada*

²*Laboratory for Advanced Spectroscopy and Imaging research (LASIR),
Chemistry Department,
The University of British Columbia, Vancouver BC, Canada*

Abstract

In order to produce long-lasting, non-wettable, micro-nano patterned metallic surfaces, femtosecond laser ablation process has been used. The effects of femtosecond laser irradiation process parameters (fluence, scanning speed and laser beam overlap) on the hydrophobicity of the resulted micro/nano-patterned morphologies on stainless steel are studied in detail. First, depending on the laser parameters, seven distinctly different nano-patterns were produced, namely nano-rippled, paraboloidal, sinusoidal, triple roughness, cauliflowered, tulip-flowered, and scaly nanostructures. These were classified according to the amount of energy absorbed by the surface that is a function of the laser intensity and scanning speed. Subsequently, the various fabricated substrates were chemically treated by silanization to reduce their surface energy and make them intrinsically hydrophobic with Young's water contact angle higher than 105°. Analysis of the wettability revealed superhydrophobicity for most of these structures, particularly of the cauliflowered and scaly patterns with contact angles in excess of 160° and hysteresis of less than 10°.

Keywords: Superhydrophobicity, laser ablation, micro/nano pattern, surface wettability, contact angle hysteresis, stainless steel.

*Corresponding author: savvas.hatzi@ubc.ca

11.1 Introduction

The ability to control surface wettability has attracted significant attention in the open literature from both the academic and industrial points of view. Numerous micro/nano systems such as Micro Electromechanical Systems (MEMS), lab-on-a-chip, or microfluidic systems require surfaces with low adhesion and friction [1]. Due to the small size of these devices, the surface forces tend to dominate over the volume forces, and, therefore, control of the adhesion and friction becomes a challenging problem for good operation of these systems. In order to reduce the surface adhesion for such applications, development of non-wettable and non-adhesive surfaces seems to be crucial.

Nature is full of biological organisms that exhibit amazing properties for low-adhesive surfaces such as plant leaves [2] and parts of insect bodies [3,4]. Most of these surfaces exhibit high water repellency and they are referred to as superhydrophobic surfaces. They exhibit water contact angle (CA) of more than 150° and contact angle hysteresis (CAH) of typically less than 10° . The surface of the lotus leaf is such an example, where water droplets readily roll off and remove contaminant particles from the surfaces, leading to a self-cleaning property. Study of the details of the surface of the lotus leaf has revealed that the poor wettability of surface is attributed to the combined effects of surface micro/nano asperities and surface chemistry. The surface of the lotus leaf is made up of a certain dual scale roughness structure, where randomly distributed asperities of micrometer scale are covered with a dense coating of agglomerated wax tubules in nano-scale [5].

Superhydrophobic surfaces have a number of potential applications such as dust-free and self-cleaning surfaces for solar cells and satellite dishes, corrosion-resistant surfaces for heat transfer devices, transparent and antireflective surfaces, anti-freezing and anti-snow surfaces [1]. The fact that liquid in contact with such surface slides with low friction suggests applications such as the fabrication of microfluidics and medical devices. The non-wettable character has been claimed in biomedical applications ranging from blood vessel replacement to wound management [6]. Other unexpected applications will emerge as the technology of making non-wettable surfaces matures.

As stated before, the surface chemistry and roughness are two crucial parameters that significantly affect surface wettability. The maximum contact angle corresponding to flat surfaces is obtained for surfaces covered with $(-\text{CF}_3)$ groups, which is 119° [7], so that to fabricate superhydrophobic surfaces, controlled roughness should be added onto the surface.

In recent years, due to a plethora of potential applications of superhydrophobicity in daily life, many efforts have been taken to fabricate artificial superhydrophobic surfaces. Depending on the application and material, different methods have been employed to create superhydrophobic surfaces [8]. Most of these methods involve either creating a micro/nano-structure on an inherently hydrophobic material [9,10] or treating a specific micro/nano-structure with a hydrophobic coating [11–14]. For instance, for metallic materials, roughened surfaces have to be coated with low surface energy materials.

Among all surface modification techniques, laser patterning using an ultrashort pulse laser source is a unique, noncontact technique that can modify the surface morphology to complex patterns with limited distortion of the bulk material. Laser processing has been proven to be an effective technique to create dual-scale roughness structures in noncontact material processing for industrial applications. According to well-established experimental [15] and theoretical works [16], pulsed lasers, especially ultra-short pulses (picosecond or femtosecond), can deposit energy into a material in a short period of time, before thermal diffusion occurs. Thus, the heat-affected zone, where melting and solidification can occur, is significantly reduced. Therefore, decreasing the pulse duration below a few picoseconds, it increases the machining precision and quality of the material. Due to high intensity and short pulse duration resulting in evaporation without noticeable melting, ultra-short laser pulse leads to high accuracy and precise patterns.

Laser ablation applied on different materials may have various effects depending mainly on the laser energy released to the target (parameters of laser beam and the physical and chemical properties of the target [17]). Laser parameters are the wavelength, intensity, spatial and temporal coherence, polarization, angle of incidence, and the dwell time (illumination time at a particular site). Higher energy released to the target generally produces higher atomic, molecular and electron removal and ionisation and photon emission from the plasma generated at the surface. The ablation process shows that below a minimum energy, the ablation threshold, no significant material removal is possible. In order to understand the effect of different laser processing parameters on the surface morphology, several studies have been performed in recent years. For instance, the effects of laser fluence [18], number of incident pulses [19], scanning overlap [20], focus position [21], laser pulse repetition rate [22] for metallic surfaces have been investigated. The application of femtosecond laser ablation in achieving hydrophobic surface has also attracted attention recently [14,23–26]. However, all of the fabricated morphologies, especially those produced to

reduce surface wettability, have been produced with low laser fluence (less than 10 J/cm^2) and low scanning speed (less than $250 \text{ }\mu\text{m/s}$) [23]. Thus, the produced structures are only nano-rippled or small parabolic pillared ones. By increasing the laser fluence or varying the laser scanning speed (number of laser pulses) and overlap, the type and size of the obtained structure may significantly change affecting the surface wettability as shown in the present work.

11.2 Materials and Experimental Methods

11.2.1 Materials

Disks of stainless steel 316L, 1 mm in thickness, were used as substrates in this work. They were polished using sandpapers (grit P60 to P1200) to an average roughness value (R_a) of about 500 nm. This is defined as the average length of protrusions above their mean value, a measure of roughness standard in literature. To modify the surface chemistry in order to render the metallic substrate a low surface energy material, trichloro (1H,1H,2H,2H-perfluorooctyl) silane, FTS (97%, Sigma-Aldrich, USA) was applied onto the surface.

In order to prepare hydrophobic and superhydrophobic surfaces, femtosecond laser was used to pattern the metallic surface and after irradiation the surface was subjected to silanization using dip coating in order to reduce its surface energy and make it inherently hydrophobic. Details on the silanization method used can be found elsewhere [27].

11.2.2 Surface Laser Irradiation

Ultra-short laser pulses to irradiate various substrates were generated by an amplified all solid-state Ti:Sapphire laser. The laser system includes a Ti:Sapphire seed laser (Coherent Mira HP) and an amplifier (Coherent Legend) to produce amplified femtosecond laser pulses with center wavelength of 800 nm. The repetition rate of laser pulses (f) was 1 kHz with pulse duration of 120 fs and the maximum output power of about 2W. The beam profile from this regenerative amplifier system has a Gaussian distribution with a beam waist of 10mm. A set of neutral density (ND) filters were used to attenuate and adjust the energy of the laser beam and a lens with 300 mm focal length was used to focus the beam on the sample. The spot size of beam at the focal point ($2\omega_0$) was $30\mu\text{m}$. A schematic diagram of the laser patterning set-up is shown in Figure 11.1.

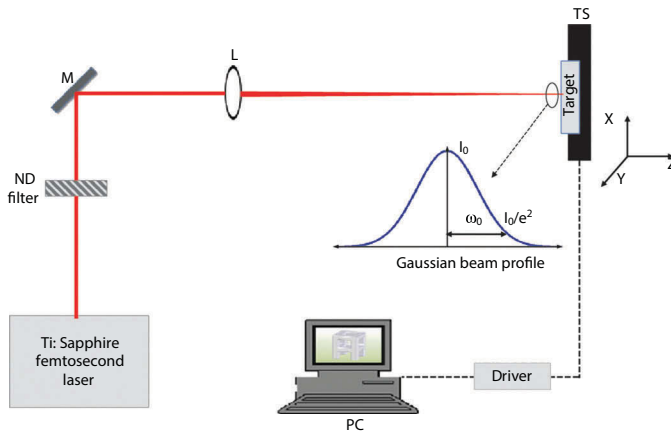


Figure 11.1 Schematic of the laser irradiation set-up.

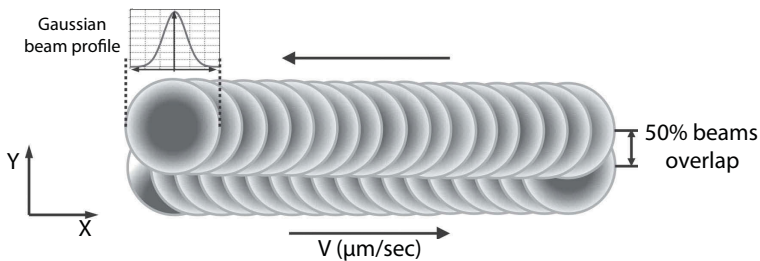


Figure 11.2 One pass of surface ablation experiment with a 50% beams overlap.

In order to move the samples under the laser beam, the stainless steel (SS) disks were mounted on a precise, computer-controlled ZABER T-LS80 X-Y translation stage. The power of the incident laser beam was adjusted in the range of 5 to 1700 mW and the scanning speed varied from 250 to 1850 $\mu\text{m/s}$. The samples were irradiated at normal incidence in air and then subjected to an ultrasonic bath for 2 min in acetone to remove all the debris off the patterned surface.

The translation of the sample under the laser beam in the X-Y direction is depicted schematically in Figure 11.2. Each pass (scan) of ablation with scanning speed, V , includes translation of the stage forward and backward in the X direction and forward in the Y direction. The amount of sample translation in the Y direction (between two consecutive scans in the X direction) depends on the specified overlap, which is defined as the ratio of forward Y-distance to the laser beam spot size ($2\omega_0$). Most of the

experiments in this work were performed with 50% (translation of 15 μm in the Y direction between two consecutive X direction scans).

11.2.3 Surface Analysis

The wetting behavior of the treated/irradiated samples was evaluated by measuring their CAs with distilled, deionized water. Droplets of water of volume 4 μL were dispensed on the respective surfaces with a piston-driven air displacement pipette. Digital images of the water droplets on the surfaces were taken with a Nikon D90 digital camera. The CAs were determined by analyzing droplet images with the image processing methods of MATLAB. Measurements of the advancing and receding CAs of a growing and shrinking droplet on the surface were performed to obtain the contact angle hysteresis (CAH).

The morphology of the surface structures was studied with a variable-pressure Scanning Electron Microscope (Hitachi S-3000N SEM) and a profilometer (Brüker, Dektak XT) in order to map the geometrical characteristics of the patterned surfaces as accurately as possible. The geometric information in the plane such as the length scale of periodicity of the asperities was obtained by Fast Fourier Transform (FFT) analysis of the SEM images using ImageJ software.

11.3 Experimental Details

As mentioned before there are two important parameters that are required for the fabrication of superhydrophobic surfaces, namely, surface roughness and low surface energy. In order to roughen metallic surfaces in a controlled manner, particularly stainless steel surfaces, the laser ablation method has been used in this work. The stainless steel substrates were mounted on a precise, computer-controlled translation stage capable of moving in front of a fixed laser beam.

The effects of laser parameters such as laser power (fluence), number of laser pulses induced to the surface (scanning speed) and laser beam overlap on the surface structure and wettability were examined. The various fabricated substrates were analyzed in terms of their geometrical characteristics. After laser irradiation, certain samples were subjected to silanization in order to reduce their surface energy. These surfaces were also analyzed in terms of their geometrical characteristics in order to determine the influence of silanization.

All experiments were done using stainless steel substrate. Due to the dependency of laser ablation method on the thermo-physical properties of the substrate, the morphology of surface for other metallic surfaces is expected to be different.

11.4 Results and Discussion

11.4.1 Surface Morphology

SEM images of laser irradiated samples have shown that the geometrical details of the morphologies of the obtained micro/nano-structures strongly depend on the laser parameters. Namely, they depend on the laser power, the number of laser pulses per spot, the scanning speed, and overlap. In this study, the laser power and the scanning speed have been varied in the range of 5 to 1700 mW (peak fluence: 1.5 to 480 J/cm² and 250 to 1850 μm/s, respectively). It is noted that the laser power is defined in terms of laser peak fluence, $\Phi_o \equiv 2E_p / \pi\omega_o^2$, where E_p is the laser beam pulse energy, which is ratio of power to beam frequency (f). The scanning overlap was 50% for all irradiation experiments and it was set to 15 μm. By varying the effective variables within the mentioned ranges, seven types of nano and micro-patterns were identified. These are described in detail below.

The first geometrical type of structure is a nano-pattern and forms at very low laser fluence with moderate to high scanning speed. Figure 11.3(a) shows SEM image of one sample with nano-scale pattern at different magnifications created by low laser fluence of 1.5 J/cm² and scanning speed of 250 μm/s. This image shows that the structure of the pattern is a periodic one, possessing regular ripples with a characteristic diameter in the submicrometer (nanometer) scale. The period of ripples (approximately hemi-cylindrical) is around 400-500 nm and their length is about 2-3 μm. The ripples are oriented perpendicularly to the polarization of the incident light (or electric field vector of incident light). In general, the periodicity of the ripples depends on the laser beam wavelength and is equal or less than the laser wavelength [17]. The possible explanation for this effect is based on the interference of incident and scattered laser radiation or excited surface waves [28].

By increasing the laser fluence at a constant scanning speed or decreasing the scanning speed at constant laser fluence, additional different micro-patterns are obtained. The first type is a pillared morphology with paraboloidal shapes shown in Figure 11.3(b) fabricated with a scanning speed of 930 μm/s and laser fluence of 16 J/cm². A higher magnification

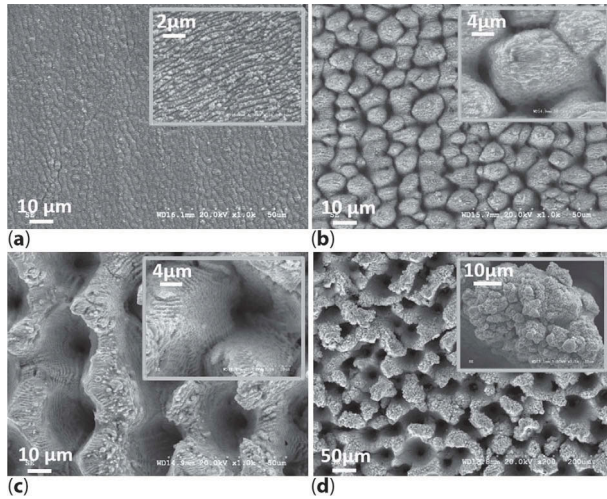


Figure 11.3 SEM images of the variously fabricated SS substrates (a). Nano-pillared pattern created by $\Phi_o = 1.5 \text{ J/cm}^2, V = 250 \mu\text{m/s}$ (b). Parabolic-pillared patterns formed by $\Phi_o = 16 \text{ J/cm}^2, V = 930 \mu\text{m/s}$, (c). Sinusoidal structure made by $\Phi_o = 185 \text{ J/cm}^2, V = 1850 \mu\text{m/s}$, (d). Triple pattern formed by $\Phi_o = 480 \text{ J/cm}^2$ and $V = 1850 \mu\text{m/s}$.

of the sample depicted as inset in Figure 11.2(b) reveals that the laser induced surface structures consisting of micro-paraboloids are covered with approximately hemi-cylindrical nano-scaled ripples.

Further increase of the laser power or decrease of the scanning speed implies a higher laser energy absorbed by the surface. Increasing the absorbed energy results in formation of elongated sinusoidal-pillared pattern covered with dual roughness presented in Figure 11.3(c) and tripled pattern depicted in Figure 11.3(d). As shown in the inset of Figure 11.3(d), triple pattern consists of coarse micro-asperities of irregular shape covered by small spheres with characteristic diameter of 2-3 μm as second level of roughness. Furthermore on top of these microspheres, there seem to exist smaller randomly distributed nano-scaled ripples.

In order to classify the various patterns as a function of the laser energy absorbed by the surface, the Laser Intensity Factor (LIF), is defined [11]:

$$LIF \equiv \frac{\Phi_o}{(V / 4\omega_o f)^n} \quad (11.1)$$

where, V is scanning speed and Φ_o is the peak fluence of laser beam defined above. It was empirically found that with the choice of exponent n of 0.5,

the modulation period of microstructures becomes a monotonically increasing function with increase of LIF.

Accordingly, using laser parameters (fluence and scanning speed) with LIF less than 150 J/cm^2 , the most dominant structure on the SS surface is the nano-rippled. Above 150 J/cm^2 and below 800 J/cm^2 , paraboloidal micro-structure forms, which becomes sinusoidal before turning into a triple roughness pattern once LIF exceeds 1500 J/cm^2 . Higher levels of laser energy absorption lead to formation of other patterns shown in Figure 11.4. The pattern depicted in Figure 11.4(a), micro/nano resembling the surface of cauliflower, referred to as cauliflowered pattern, has been produced with LIF of 3050 J/cm^2 , laser fluence, Φ_o , of 240 J/cm^2 and scanning speed, V , of $370 \mu\text{m/s}$. At the higher LIF value of 3950 J/cm^2 and scanning speed of $370 \mu\text{m/s}$, a more fractal and re-entrant cauliflowered structure has been formed on the surface (Figure 11.4(b)). The cauliflowered structure is an essentially triple roughness structure with micro-pillar size in the range of 50 to $100 \mu\text{m}$.

Further increase of LIF beyond 3950 J/cm^2 , produces two more patterns shown in Figure 11.4(c)-(d). The tulip-flowered structure shown in Figure 11.4(c) is a transition from the previous cauliflowered to the next scaly pattern depicted in Figure 11.4(d). The scaly flat micro-asperities

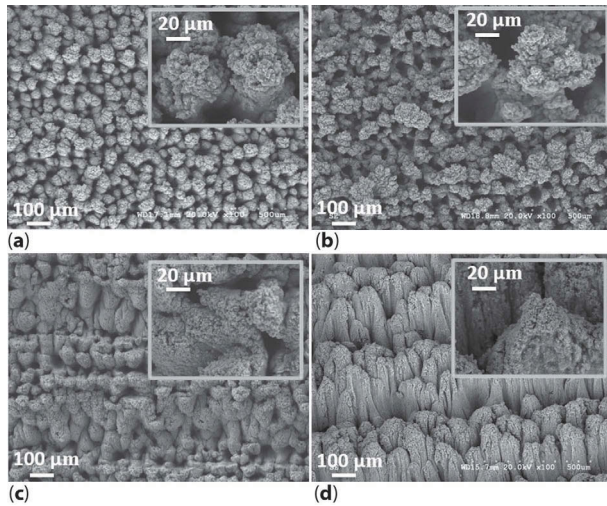


Figure 11.4 (a) Cauliflowered pattern produced with $\text{LIF} = 3050 \text{ J/cm}^2$, $\Phi_o = 240 \text{ J/cm}^2$ and $V = 370 \mu\text{m/s}$, (b). $\text{LIF} = 3950 \text{ J/cm}^2$, $\Phi_o = 310 \text{ J/cm}^2$ and $V = 370 \mu\text{m/s}$, (c). Tulip-flowered pattern fabricated with $\text{LIF} = 4790 \text{ J/cm}^2$, $\Phi_o = 375 \text{ J/cm}^2$ and $V = 370 \mu\text{m/s}$, (d). Scaly pattern produced with $\text{LIF} = 4600 \text{ J/cm}^2$, $\Phi_o = 300 \text{ J/cm}^2$ and $V = 250 \mu\text{m/s}$.

with periodicity in range of 300 to 400 μm covered with nano patterns is seen in inset image in Figure 11.4(d).

Figure 11.5 summarizes the various patterns fabricated in terms of the different laser parameters, namely the laser fluence, Φ_0 and scanning speed, V . Figure 11.5 also implies that by increasing the LIF to higher than 2000 J/cm^2 , the formation of more than one pattern is possible. For example, for ablation with LIF of 3500 J/cm^2 , depending on the laser fluence, and scanning speed, scaly, cauliflowered or triple roughness structures may possibly form on the stainless steel substrates. Therefore, instead of using the LIF, the values of laser fluence and scanning speed must be used to determine the expected pattern configuration.

Depending on the laser parameters, the height and periodicity of the micro/nano structures vary. The order of roughness is a function of the amount of absorbed energy by the surface. Roughly, the higher the absorbed energy by the surface is, the coarser the pattern formed. Since the LIF represents the amount of absorbed energy, it should be related with the periodicity and height of the asperities. This can be seen in Figure 11.6,

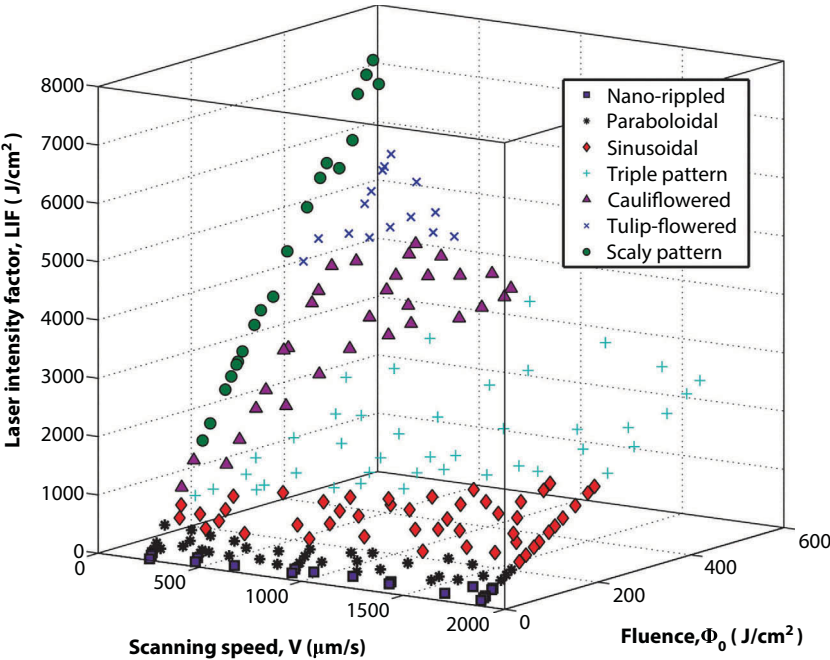


Figure 11.5 A 3-D diagram summarizing the various micro/nano structures formed in terms of the LIF parameter as a function of the laser fluence and scanning speed.

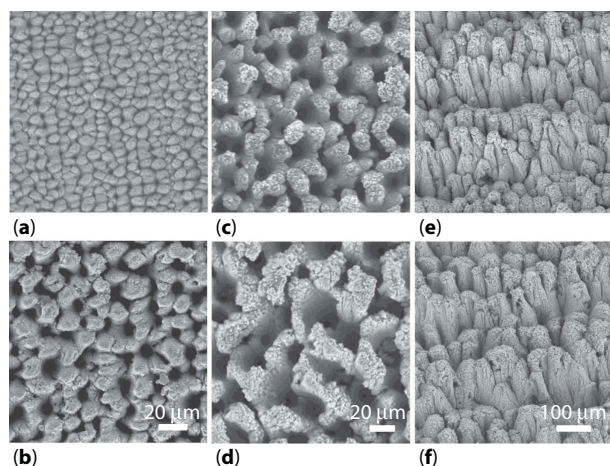


Figure 11.6 Micro/nano patterns produced with different LIF values to demonstrate the relationship between LIF and the characteristic dimensions of the patterns (a). Paraboloidal with $\text{LIF}=230 \text{ J/cm}^2$, $\Phi_o = 20 \text{ J/cm}^2$ and $V = 465 \text{ }\mu\text{m/s}$ (b). Paraboloidal with $\text{LIF}=434 \text{ J/cm}^2$, $\Phi_o = 38 \text{ J/cm}^2$ and $V = 465 \text{ }\mu\text{m/s}$ (c). Triple pattern with $\text{LIF} = 1700 \text{ J/cm}^2$, $\Phi_o = 240 \text{ J/cm}^2$ and $V = 1200 \text{ }\mu\text{m/s}$, (d). Triple pattern with $\text{LIF} = 2750 \text{ J/cm}^2$, $\Phi_o = 480 \text{ J/cm}^2$ and $V = 1850 \text{ }\mu\text{m/s}$. (e) Scaly pattern with $\text{LIF} = 4600 \text{ J/cm}^2$, $\Phi_o = 297 \text{ J/cm}^2$ and $V = 250 \text{ }\mu\text{m/s}$ and (f). Scaly pattern with $\text{LIF} 7450 \text{ J/cm}^2$, $\Phi_o = 480 \text{ J/cm}^2$ and $V = 250 \text{ }\mu\text{m/s}$.

starting with the parabolic patterns in Figures 11.6(a) and 11.6(b) which were produced using $\text{LIF} = 230 \text{ J/cm}^2$ and 434 J/cm^2 , respectively. As this Figure explains, the diameter and height of the pillars created using laser parameters that correspond to a higher LIF (Figure 11.6(b)) are larger than those fabricated using parameters that correspond to a lower LIF (Figure 11.6(a)). The same trend is true for all other patterns shown in the images of Figure 11.6, namely 11.6(c) to 11.6(f).

11.4.2 Surface Wettability

The water contact angle on flat stainless steel surface, after coating with fluorinated alkylsilane, FTS, is about $105^\circ \pm 3^\circ$ [11,29]. The morphologies of various structures were analyzed using SEM before and after silanization, and the thin layer of fluorinated alkylsilane did not affect the surface morphology. The contact angle (CA) and contact angle hysteresis (CAH) of various structures were measured as discussed above.

The nano-rippled pattern has the minimum CA, usually less than 120° with high CAH, more than 60° . The CAs of paraboloidal patterns are typically higher than those of the nano-rippled ones, ranging from 130° to

170° with CAH in range of 70° to 10° respectively. The paraboloidal pattern exhibits the petal effect that possesses a high CA and also high CAH, which results in sticking of droplet to the surface [29].

The wettability of the surface decreases with increase of the surface coarseness as demonstrated by the images in Figure 11.7, namely 11.7(a) to 11.7(d). For example compare the two samples with the paraboloidal structures depicted in Figures 11.7(a)-(b). A similar trend is noticed as well when Figures 11.7(c) and 11.7(d) are compared. In general increase of the aspect ratio of height (H) to diameter (D), (H/D), leads to increase of CA and decrease of the CAH (increase of hydrophobicity). The diameter of asperities (or pattern periodicity) in Figure 11.7(c) is about 28 μm and the height is 12 μm . The corresponding values of pattern in Figure 11.7(d) are 35 μm and 45 μm , respectively. As higher surface coarseness corresponds to a higher LIF, increasing the LIF parameter increases monotonically the CA and monotonically decreases the CAH. The same trend of surface wettability has been observed for all other patterns.

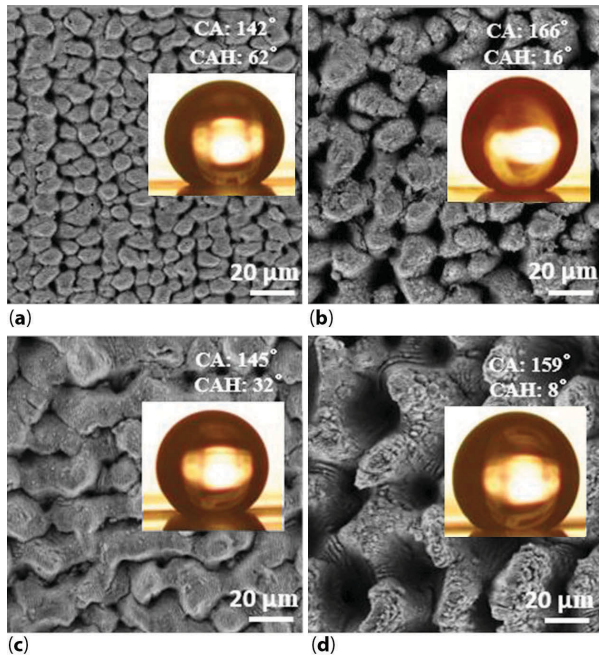


Figure 11.7 SEM image and wettability of paraboloidal pattern fabricated using (a). LIF = 186.5 J/cm², Φ_0 = 16 J/cm², and V = 460 $\mu\text{m/s}$, (b). LIF = 591.7 J/cm², Φ_0 = 38.2 and V = 250 $\mu\text{m/s}$, and sinusoidal pattern created by (c). LIF = 770 J/cm², Φ_0 = 135 J/cm², V = 1850 $\mu\text{m/s}$ and, (d). LIF = 1848 J/cm², Φ_0 = 214 J/cm², V = 1850 $\mu\text{m/s}$.

The surface hydrophobicity increases from patterns possessing dual-scale roughness (paraboloidal and sinusoidal patterns) to patterns possessing triple structures (triple pattern, cauliflowered, tulip-flowered, and scaly patterns). Addition of small micro-scale spherical bumps (2–5 μm) onto large micro-pillars ($>50\text{ }\mu\text{m}$) enhances the possibility of forming a stable Cassie-Baxter state. Figures 11.8(a)–(c) show this enhancement in surface hydrophobicity, as they all are superhydrophobic with CA much greater than 150° and CAH much less than 10° . Comparing the wettability of various structures reveals that the most superhydrophobic structure in terms of the highest CA and lowest CAH is the scaly pattern (Figure 11.8(d)). The CA of this pattern always is higher than 160° and the CA hysteresis along the direction of scaly pattern (perpendicular to the laser scanning direction) is less than 5° . Therefore, all scaly nano-patterns produced were highly superhydrophobic.

The wettability results of various microstructures are summarized in Table 11.1, where the ranges of contact angle (CA) and contact angle

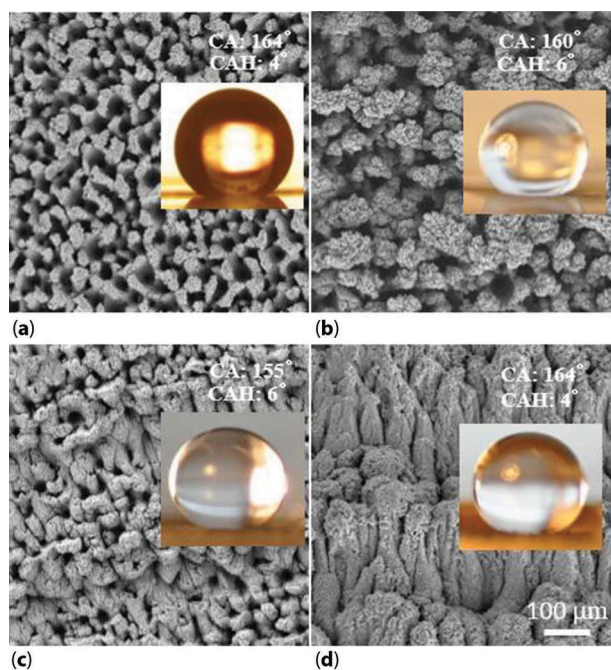


Figure 11.8 SEM images and wettability of various patterns (a). Triple pattern fabricated by $\text{LIF} = 2730\text{ J/cm}^2$, $\Phi_o = 480\text{ J/cm}^2$, $V = 1850\text{ }\mu\text{m/s}$ (b). Cauliflowered pattern created by $\text{LIF} = 3950\text{ J/cm}^2$, $\Phi_o = 310\text{ J/cm}^2$ and $V = 370\text{ }\mu\text{m/s}$ and (c). Tulip-flowered structure produced by $\text{LIF} = 4750\text{ J/cm}^2$, $\Phi_o = 340\text{ J/cm}^2$ and $V = 310\text{ }\mu\text{m/s}$, and (d). Scaly pattern produced by $\text{LIF} = 4600\text{ J/cm}^2$, $\Phi_o = 297\text{ J/cm}^2$ and $V = 250\text{ }\mu\text{m/s}$.

Table 11.1 Contact angle (CA) and Contact Angle Hysteresis (CAH) for all types of micro/nano-patterns fabricated on stainless steel substrates.

Pattern	CA (°)	CAH (°)
Nano-rippled	< 120	> 60
Paraboloidal	130–170	10–70
Sinusoidal	140–160	5–35
Triple roughness	> 145	< 20
Cauliflowered	> 150	5–20
Tulip-flowered	> 150	5–20
Scaly	> 160	< 5

hysteresis (CAH) are listed. The results of this work show that the pattern wettability decreases from the simply nano-rippled to the scaly pattern, in other words, it decreases in terms of increasing order of the LIF parameter. In addition, details of the geometrical parameters show that the pillar height to diameter (H/D) also increases in the following order, which coincides with the increasing order of the LIF parameter, that is:

$$\text{Paraboloidal} < \text{Sinusoidal} < \text{Triple} < \text{Cauliflowered} \\ < \text{Tulip-flowered} < \text{Scaly}$$

The pillar aspect ratio and the coverage of pillars with structures such as simple ripples or bumps of characteristic lengths of one order of magnitude smaller decrease significantly the wettability as simple thermodynamic analysis has shown [29,30].

11.4.3 The Effect of Overlap on Surface Wettability

All patterns presented above were produced using 50% overlap of the Gaussian beam diameter ($2\omega_0 = 30\mu\text{m}$). Increasing the overlap roughly increases the amount of energy applied on the surface. Figure 11.9 depicts the effect of decreasing overlap from 50% to 0% for three different sets of laser peak fluences and scanning speeds. Due to reduction of the intensity of incident light at a fixed point with overlap reduction, the crater height decreases. It is noted that the beam of the incident light at a fixed point decreases by decreasing the percentage of scanning overlap. Decrease of pillar height results in a reduction of surface hydrophobicity. Thus,

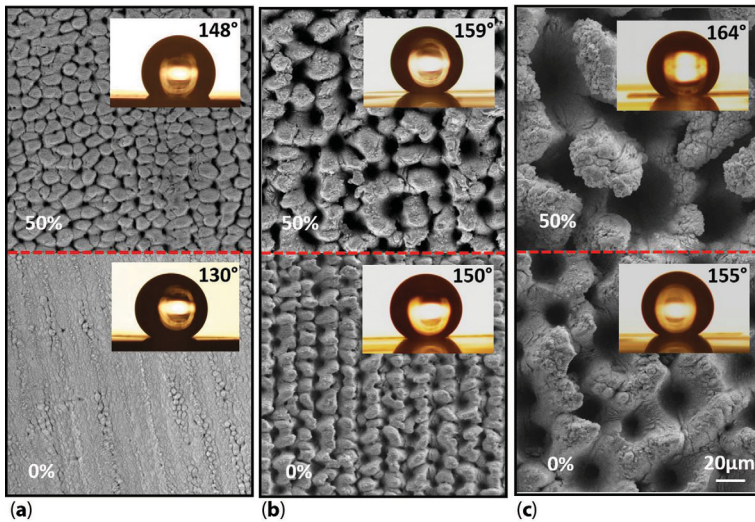


Figure 11.9 Wettability of patterned surfaces with 50% and 0% scanning overlap for (a). $\Phi_o = 16.5 \text{ J/cm}^2$ and $V = 460 \text{ } \mu\text{m/s}$; (b). $\Phi_o = 38.2 \text{ J/cm}^2$ and $V = 460 \text{ } \mu\text{m/s}$; (c). $\Phi_o = 480 \text{ J/cm}^2$ and $V = 1860 \text{ } \mu\text{m/s}$. In all cases decrease of overlap from 50 to 0% causes a decrease of contact angle.

increasing the scanning overlap decreases the surface wettability as shown in Figure 11.9 from the reported contact angles in the images.

11.5 Conclusions

The effects of laser parameters such as laser fluence, scanning speed and overlap on the generated micro/nano patterns on stainless steel substrates were examined in detail. First, femtosecond laser irradiation was applied to stainless steel substrates using a wide range of laser energy densities and scanning speeds to produce various patterns. Depending on the laser parameters, seven distinctly different nano-patterns were produced, namely nano-rippled, paraboloidal, sinusoidal, triple roughness, cauliflowered, tulip-flowered, and scaly nanostructures. These were classified according to the Laser Intensity Factor (*LIF*) that is related to the laser fluence and the scanning speed. A chemical treatment (silanization) was used to reduce the surface energy of all fabricated substrates to the same value and make them intrinsically hydrophobic with Young's contact angle of about 105° . Analysis of the wettability revealed enhanced superhydrophobicity for most of these structures, particularly of the cauliflowered

(re-entrant pattern) and scaly pattern with contact angles in excess of 160° and hysteresis less than 10° .

Acknowledgement

Financial assistance from NSERC, the federal funding agency of Canada, is acknowledged.

References

1. X. Yao, Y. Song, and L. Jiang, Applications of bio-inspired special wettable surfaces. *Adv. Mater.* 23, 719–734 (2011).
2. W. Barthlott, C. Neinhuis, H. Verlot, and C. L. Schott, Purity of the sacred lotus, or escape from contamination in biological surfaces. *Planta* 202, 1–8 (1997).
3. D. L. Hu, B. Chan, and J. W. M. Bush, The hydrodynamics of water strider locomotion. *Nature* 424, 663–666 (2003).
4. L. Gao and T. J. McCarthy, How Wenzel and Cassie were wrong. *Langmuir* 23, 3762–3765 (2007).
5. Y. T. Cheng, D. E. Rodak, C. A. Wong, and C. A. Hayden, Effects of micro- and nano-structures on the self-cleaning behaviour of lotus leaves. *Nanotechnology* 17, 1359–1362 (2006).
6. X. Wang, N. Yang, Q. Xu, C. Mao, X. Hou, and J. Shen, Preparation of a novel superhydrophobic PMMA surface with nanostructure and its blood compatibility. *e-polymers* 81, 1–8 (2012).
7. A. Nakajima, K. Hashimoto, and T. Watanabe, Invited Review Recent studies on super-hydrophobic films. *Monatshefte für Chemie-Chemical Monthly* 132, 31–41 (2001).
8. A. Carré and K. L. Mittal (Eds.), *Superhydrophobic Surfaces*, CRC Press, Boca Raton, FL (2009).
9. E. Bormashenko, R. Pogreb, G. Whyman, and M. Erlich, Cassie-Wenzel wetting transition in vibrating drops deposited on rough surfaces: Is the dynamic Cassie-Wenzel transition a 2D or 1D affair? *Langmuir* 23, 6501–6503 (2007).
10. G. Azimi, R. Dhiman, H.-M. Kwon, A. T. Paxson, and K. K. Varanasi, Hydrophobicity of rare-earth oxide ceramics. *Nature Mater.* 12, 315–320 (2013).
11. S. Moradi, S. Kamal, P. Englezos, and S. G. Hatzikiriakos, Femtosecond laser irradiation of metallic surfaces: Effects of laser parameters on superhydrophobicity. *Nanotechnology* 24, 415302–415313 (2013).

12. B. Liu and F. F. Lange, Pressure induced transition between superhydrophobic states: Configuration diagrams and effect of surface feature size. *J. Colloid Interface Sci.* 298, 899–909 (2006).
13. M. Nosonovsky and B. Bhushan, Multiscale effects and capillary interactions in functional biomimetic surfaces for energy conversion and green engineering., *Philos. Trans. A* 367, 1511–39 (2009).
14. M. N. W. Groenendijk and J. Meijer, Surface microstructures obtained by femtosecond laser pulses. *CIRP Annals - Manuf. Technol.* 55, 183–186 (2006).
15. T.-H. Her, R. J. Finlay, C. Wu, S. Deliwala, and E. Mazur, Microstructuring of silicon with femtosecond laser pulses. *Appl. Phys. Lett.* 73, 1673–1675 (1998).
16. S. I. Dolgaev, S. V. Lavrishev, A. A. Lyalin, A. V. Simakin, V. V. Voronov, and G. A. Shafeev, Formation of conical microstructures upon laser evaporation of solids. *Appl. Phys. A* 73, 177–181 (2001).
17. D. Bauerle, *Laser Processing and Chemistry*, 2nd ed., p. 32, Springer, Berlin, (1996).
18. K. Kuršelis, T. Kudrius, D. Paipulas, O. Balachninaite, and V. Sirutkaitis, Experimental study on femtosecond laser micromachining of grooves in stainless steel. *Lith. J. Phys.* 50, 95–103 (2010).
19. B. Raillard, L. Gouton, E. Ramos-Moore, S. Grandthyll, F. Müller, and F. Mücklich, Ablation effects of femtosecond laser functionalization on steel surfaces. *Surf. Coatings Technol.* 207, 102–109 (2012).
20. K. Kuršelis, R. Kiyas, and B. N. Chichkov, Formation of corrugated and porous steel surfaces by femtosecond laser irradiation. *Appl. Surf. Sci.* 258, 8845–8852 (2012).
21. W. Wang, X. Mei, G. Jiang, S. Lei, and C. Yang, Effect of two typical focus positions on microstructure shape and morphology in femtosecond laser multipulse ablation of metals. *Appl. Surf. Sci.* 255, 2303–2311 (2008).
22. D. Bruneel, G. Matras, R. Le Harzic, N. Huot, K. König, and E. Audouard, Micromachining of metals with ultra-short Ti-Sapphire lasers: Prediction and optimization of the processing time. *Opt. Lasers Eng.* 48, 268–271 (2010).
23. T. Baldacchini, J. E. Carey, M. Zhou, and E. Mazur, Superhydrophobic surfaces prepared by microstructuring of silicon using a femtosecond laser. *Langmuir* 22, 4917–4919 (2006).
24. V. Zorba, L. Persano, D. Pisignano, A. Athanassiou, E. Stratakis, R. Cingolani, P. Tzanetakis, and C. Fotakis, Making silicon hydrophobic: Wettability control by two-lengthscale simultaneous patterning with femtosecond laser irradiation. *Nanotechnology* 17, 3234–3238 (2006).
25. V. Zorba, E. Stratakis, M. Barberoglou, E. Spanakis, P. Tzanetakis, and C. Fotakis, Tailoring the wetting response of silicon surfaces via fs laser structuring. *Appl. Phys. A* 93, 819–825 (2008).
26. T. O. Yoon, H. J. Shin, S. C. Jeoung, and Y.-I. Park, Formation of superhydrophobic poly(dimethylsiloxane) by ultrafast laser-induced surface modification. *Opt. Express* 16, 12715–12725 (2008).

27. S. Moradi, S. G. Hatzikiriakos, and P. Englezos, Super-hydrophobic Nanopatterned Interfaces: Optimization and Manufacturing, PhD thesis, University of British Columbia, Canada (2014).
28. D. C. Emmony, R.P. Howson, and L.J. Willis, Laser mirror damage in germanium at 10.6 μm . *Appl. Phys. Lett.* 23, 598-600 (1973).
29. S. Moradi, P. Englezos, and S. G. Hatzikiriakos, Contact angle hysteresis of non-flattened-top micro/nanostructures. *Langmuir* 30, 3274-3284 (2014).
30. S. Moradi, S. G. Hatzikiriakos, and P. Englezos, Contact angle hysteresis: Surface morphology effects. *Colloid Polym. Sci.* 291, 317-328 (2012).

RF Plasma Treatment of Neptune Grass (*Posidonia oceanica*): A Facile Method to Achieve Superhydrophilic Surfaces for Dye Adsorption from Aqueous Solutions

Hernando S. Salapare III^{1,2,*}, Ma. Gregoria Joanne P. Tiquio³ and Henry J. Ramos¹

¹*Plasma Physics Laboratory, National Institute of Physics, College of Science, University of the Philippines Diliman, Philippines*

²*Laboratoire de Physique de la Matière Condensée, UMR 7336, CNRS, Université de Nice-Sophia Antipolis, France*

³*Ecosystèmes Côtiers Marins et Réponses aux Stress (ECOMERS) - EA 4228, Université de Nice-Sophia Antipolis, France*

Abstract

Neptune grass (*Posidonia oceanica*) samples were treated using argon and oxygen plasmas at varying plasma energies that ranged from 6 kJ to 180 kJ. The characterizations done on the samples were weight loss analysis, wettability studies, surface roughness measurements, determination of the surface chemical functionalities, and methyl red dye adsorption studies. As previously reported in Appl. Surface Sci., 273, 444–447 (2013), a greater weight loss was observed on oxygen plasma treatment than on argon plasma treatment. Superhydrophilic surface property (water contact angle, $\theta < 5^\circ$ within 1 second of drop deposition) was achieved at high-energy argon-plasma (180 kJ) and low-energy oxygen-plasma (6 kJ) treatments. The surface roughness increased for the high-energy argon-plasma treatments; however, an opposite trend was seen for the oxygen-plasma treatments. The aliphatic $-\text{CH}_2$ and C-H groups were absent from the FT-IR spectra of the superhydrophilic samples. Superhydrophilic surfaces were achieved from changes in both the surface roughness and the chemical functionalities of the samples after

*Corresponding author: hssalapare@up.edu.ph

the plasma treatment. Enhanced dye adsorption was found for superhydrophilic samples, which is attributed primarily to the creation of appropriate chemical functionalities of the treated materials.

12.1 Introduction

12.1.1 Surfaces and Wetting

Water droplets resting on a solid surface can show either wetting or non-wetting effect. Consider a sessile drop on an ideal homogeneous solid surface as shown in Figure 12.1. Three different interfaces exist and they are described by the corresponding surface free energies: γ^{sl} is the solid-liquid interfacial free energy, γ^{sv} is the solid-vapor interfacial free energy, and γ^{lv} is the liquid-vapor interfacial free energy. The liquid is attached to the solid surface at an equilibrium contact angle, θ . Each of the interfaces describes the contact line in a manner so that the corresponding interfacial area is minimized [1].

By looking at the balance of forces along the x-direction, we obtain the following relation:

$$\sum F_x = \gamma^{sv} - \gamma^{sl} - \gamma^{lv} \cos \theta = 0, \quad (12.1)$$

by re-arranging equation (12.1), we can derive the Young's equation as follows:

$$\gamma^{lv} \cos \theta = \gamma^{sv} - \gamma^{sl}. \quad (12.2)$$

The Young equation shows the relationship between the equilibrium contact angle with the surface free energies. If water contact angle $\theta < 90^\circ$,

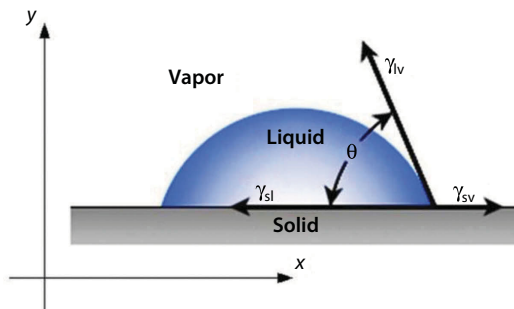


Figure 12.1 Surface free energies in case of a liquid drop residing on a solid surface [2].

the surface is hydrophilic which indicates that it has a wetting effect and if $\theta > 90^\circ$, then the surface is hydrophobic which indicates that it has a non-wetting effect [1, 3]. There are surfaces that possess extraordinary wettabilities. In this article, we will call them super-surfaces that may be either superhydrophilic or superhydrophobic.

Surfaces that possess water contact angles less than 5° within 1 second of drop deposition are called superhydrophilic surfaces. Materials with superhydrophilic surfaces have the highest water wetting property [4–6]. Surfaces that exhibit water contact angles of greater than 150° are called superhydrophobic surfaces [3, 7].

In general, the super-surface properties are mainly due to the surface chemistry and surface roughness. Surfaces with low surface energy are usually hydrophobic, and surfaces with high surface energy are usually hydrophilic. Also, as the surface roughness increases, surfaces that are hydrophobic tend to be even more hydrophobic, and surfaces that are hydrophilic tend to be even more hydrophilic [3, 4–6, 8–13]. For example, Table 12.1 and Figure 12.2 show the values of the water contact angles for various surface structures as reported in the literature [3, 14].

Artificial fabrication of super-surfaces used in most industries is inspired from nature, different plant and animal surfaces which exhibit super-surface properties. Figure 12.3 shows a Lotus leaf that exhibits superhydrophobic property. The right image in Figure 12.3 shows that the superhydrophobic property of the leaf is due to the rough surface nanostructures [21–22]. Figure 12.4 shows water spreading on the reptiles' superhydrophilic surfaces. These reptiles also possess specialized rough microstructures on surfaces [23].

Table 12.1 Values of the water contact angles for various surface structures [3, 14].

Surface Structure	Contact Angle (degrees)
Vertical pillars [15]	~ 160
Fractal structure [16]	~ 165
Cassie's wire gratings [17]	~ 150
Electrospun fiber surface [18]	~ 165
Lotus leaf [14]	~ 155
Micro-hoodoos [18]	~ 165
Nanonails [19]	~ 150

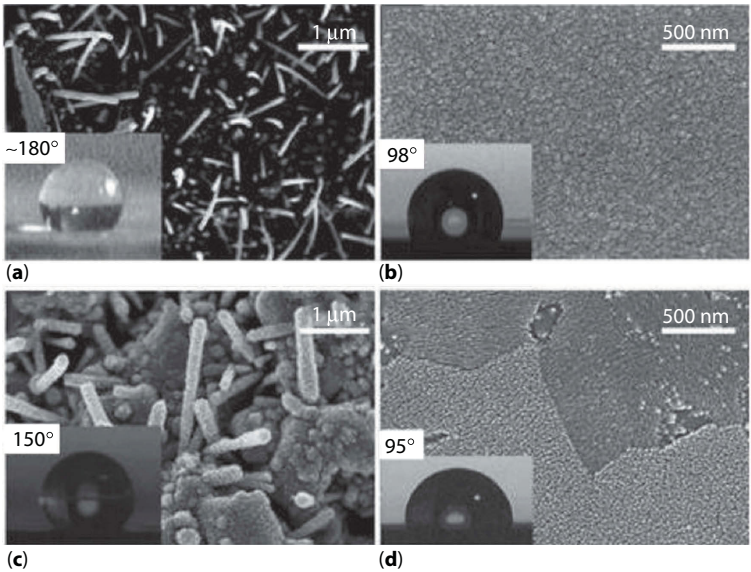


Figure 12.2 Values and images of the water contact angles for various surface structures [3, 14]. The nanostructures in (a) and (c) exhibit superhydrophobic property.

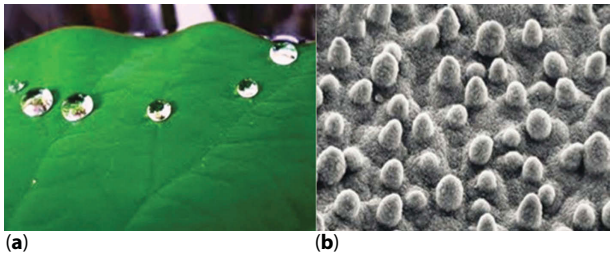


Figure 12.3 (a) Water drops on a Lotus leaf [20]. (b) SEM image showing the surface structure of a Lotus leaf [21–22].

The Young equation cannot be used directly to explain the effect of surface roughness on the wettability of a material because it is valid only for ideal smooth solid surfaces. There are two wetting models that are proposed when a water droplet sits on rough surfaces, these are the Wenzel model and the Cassie-Baxter model.

Figure 12.5 shows a water droplet in a homogeneous wetting state. The liquid in this state follows the solid surface and penetrates into the grooves caused by the protrusions [3]. This wetting state is called the Wenzel state. It is described by the following equation:

$$\cos \theta_w = r \cos \theta, \tag{12.3}$$

where θ_w is the apparent contact angle which corresponds to the stable equilibrium state (i.e., minimum free energy state for the system), θ is the equilibrium contact angle, and r is the roughness ratio. The roughness ratio r is the quotient between the real surface area and the projected surface area and the value is always greater than 1 since every surface has roughness at the molecular level [24–25].

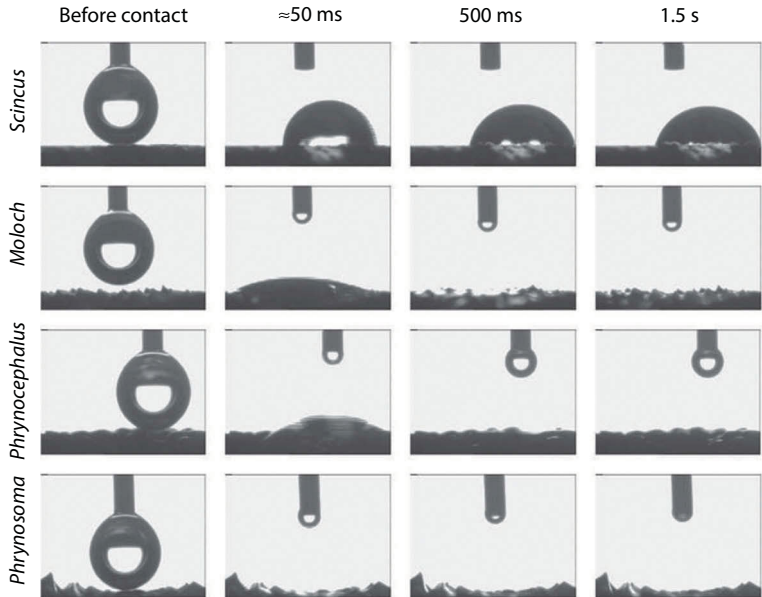


Figure 12.4 Water spreading on the reptiles’ superhydrophilic surfaces [23].

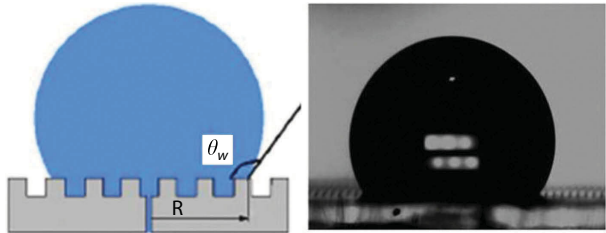


Figure 12.5 Water droplet in a homogeneous wetting state showing the apparent contact angle (left). The liquid in this state follows the solid surface and penetrates into the grooves caused by the protrusions [1, 3]. Image of a water droplet on a surface that exhibits Wenzel wetting state (right).

The Wenzel state explains why hydrophobic surfaces tend to be even more hydrophobic (when $\theta > 90^\circ$, θ_w is always greater than θ) when surface roughness increases and why hydrophilic surfaces tend to be even more hydrophilic (when $\theta < 90^\circ$, θ_w is always less than θ) when surface roughness increases [24–25].

Figure 12.6 shows a water droplet in a heterogeneous wetting state. The liquid in this state only contacts the top of the protrusions, leaving air trapped into the grooves [3]. This wetting state is called the Cassie-Baxter state. It is described by the following equation:

$$\cos \theta_{CB} = \phi_s \cos \theta + \phi_s - 1, \quad (12.4)$$

where θ_{CB} is the apparent contact angle which corresponds to the stable equilibrium state (i.e., minimum free energy state for the system), θ is the equilibrium contact angle, and ϕ_s is the areal fraction of the liquid-solid interface occluded by the texture [1, 17].

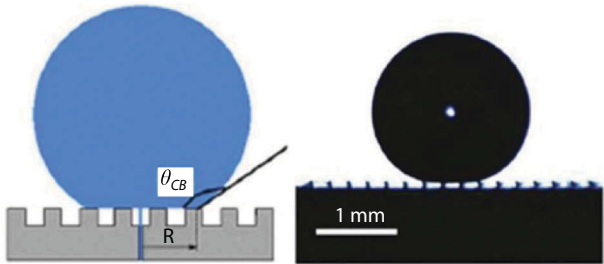


Figure 12.6 Water droplet in a heterogeneous wetting state showing the apparent contact angle (left). The liquid in this state only contacts the top of the protrusions, leaving air below into the grooves [1, 3]. Image of a water droplet on a surface that exhibits Cassie-Baxter wetting state (right).

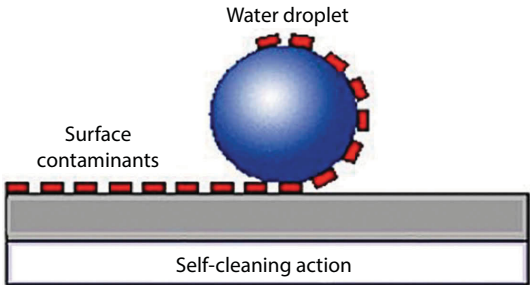


Figure 12.7 Self-cleaning action of a superhydrophobic surface [26].

When ϕ_s approaches the value of 0, θ_{CB} also approaches 180° , this means that there is a maximum air trapping into the surface's grooves. This scenario is true for a very robust surface and the material would possess a self-cleaning surface as shown in Figure 12.7. Water droplets would only bounce or roll-off on these surfaces [1, 17].

12.1.2 Plasma Surface Modification

Wettability of different surfaces can be modified by employing different techniques and examples are plasmas, UV-activation, ion-beams, corona discharge, flame, and chemicals [29–35]. Plasma treatment is a promising technique because of its superior ability to modify the chemistry and the morphology of a surface since it uses complex mixtures of ions, electrons, atoms, and radicals in the plasma [4, 36–43]. In Figure 12.8, it is shown that the composition of plasma is due to the fragmentation, ionization, and electrical excitation of the working gas when energy is applied to it [27]. As an example, Figure 12.9 shows that oxygen plasma may contain free radicals (highly reactive), ozone, negative ions, ultraviolet light photons, positive ions, and electrons [28].

Figure 12.10 shows how the surface of a material like polymer can be modified by plasma [27]. When the oxygen plasma reacts with the surface it modifies the surface chemically and physically and consequently producing mainly carbon dioxide and water by-products that can be pumped out of the system, leaving a modified surface with tailored properties.

In general plasma treatment can have the following effects on the material's surface: cleaning, activation, etching, and coating [1].

In Figure 12.11, plasma cleaning of a metal surface is done when ion bombardment causes the contaminants on the surface to be evaporated or sputtered and pumped out of the system [44]. This is done by carefully

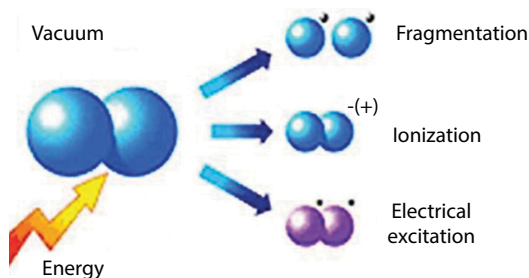


Figure 12.8 Reactions in a low-pressure plasma [27].

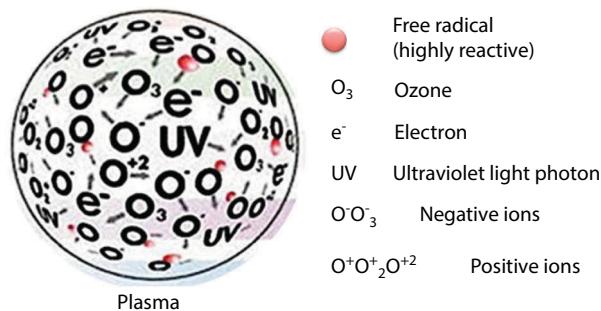


Figure 12.9 Composition of oxygen plasma [28].

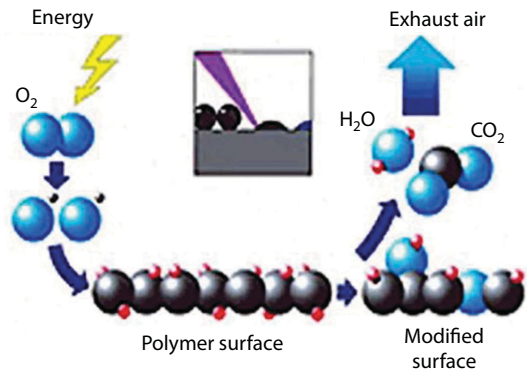


Figure 12.10 Surface modification of a polymer surface by oxygen plasma [27].

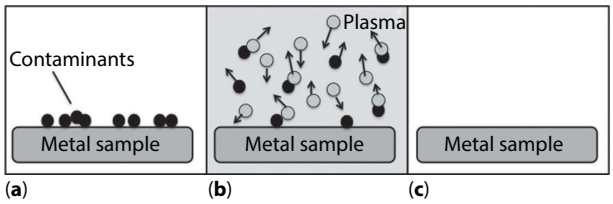


Figure 12.11 Plasma cleaning of a metal surface. (a) Contaminants on the surface of the metal sample. (b) Plasma particles interact with the contaminants. (c) Cleaned metal surface where the contaminants are evaporated or sputtered and pumped out of the system.

choosing the working gas for the plasma. There are varied applications for this effect, for example, in removing fats, oils or oxides on the substrate, or a pre-treatment for welding.

Figure 12.12 shows how plasma activation works for a polymer surface. The plasma produces high-energy particles that lead to chain-scission and the creation of active sites on the surface. These active sites, or radicals, can cause a change in the surface properties by the introduction of new functional groups.

Figure 12.13 shows how plasma can etch a silicon substrate with an etching mask. It is important to determine the proper working gas for etching to occur. The material that is etched is usually removed by vaporization or by pumping it out of the system. Etching is usually done to improve the adhesion performance of the surface.

Figure 12.14 shows an example of a polymer showing the effects of plasma etching. Etching normally increases the roughness of the material.

Figure 12.15 shows how plasma was used to coat or deposit new layers on the surface of a substrate. It is normally due to plasma polymerization. Among its various applications include the deposition of thin hydrophilic or hydrophobic layers.

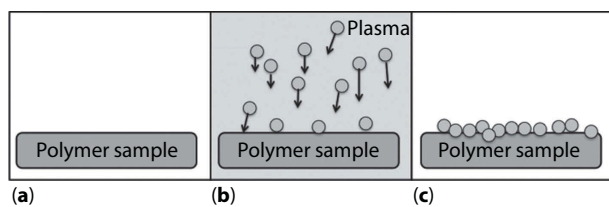


Figure 12.12 Plasma activation of a polymer surface. (a) Polymer sample before exposure to plasma. (b) Polymer sample during exposure to plasma. (c) Plasma particles create new functionalities or active sites on the surface of the polymer sample.

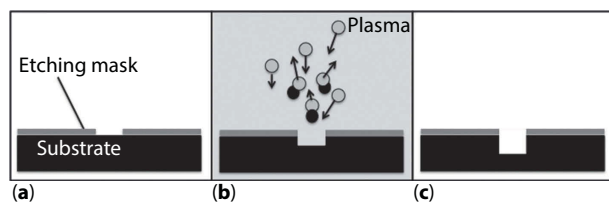


Figure 12.13 Plasma etching of a silicon substrate with an etching mask. (a) The substrate with an etching mask before exposure to plasma. (b) During exposure to plasma, the reactive particles in the plasma etch the substrate not covered with the etching mask. (c) The etched material after exposure to plasma.

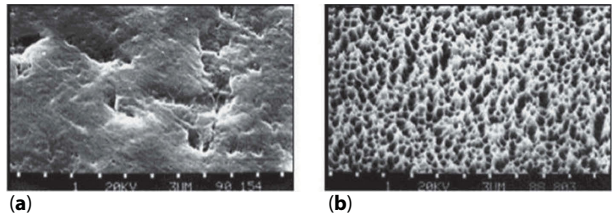


Figure 12.14 SEM images of a polymer surface showing the effects of plasma etching [39]. (a) Polymer surface before plasma etching. (b) Polymer surface after plasma etching.

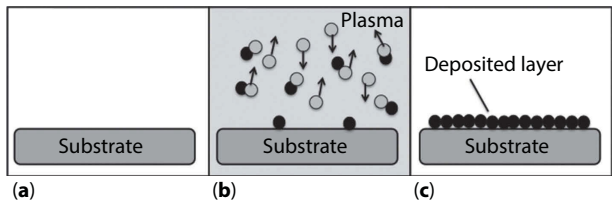


Figure 12.15 Plasma coating on a substrate. (a) Substrate before exposure to plasma. (b) During exposure to plasma, some plasma particles are attached to the surface of the substrate. (c) Substrate showing a deposited layer from the plasma exposure.

12.1.3 *Posidonia oceanica* [45]

Posidonia oceanica (commonly known as Neptune Grass or Mediterranean tapeweed) is the dominant lignocellulosic seagrass in the Mediterranean Sea. It is widely used as an ideal biological indicator in assessing the quality of water bodies [46]. It is highly important because of its efficiency in removing different dyes and heavy metals, including but not limited to textile dyes, phenol, methylene blue, ammonium, phosphorus, and copper from aqueous solutions [47–52]. The primary cause of the removal of these materials from aqueous solutions (especially for heavy metals) is the presence of oxygen functional groups in *Posidonia oceanica* [47]. The heavy metal biosorption property of *Posidonia oceanica* makes it as an efficient and environmental-friendly technique in wastewater treatment [47]. Studies show that the high wetting property of a material favors heavy metal biosorption [53].

Posidonia oceanica materials are also used for making artisanal handicrafts and to enhance the dyeability of these materials requires a change in their wettability. In this article, we will show how to alter the wettability

of *Posidonia oceanica* surfaces from being hydrophilic to superhydrophilic using oxygen and argon plasmas. The stability of the resulting superhydrophilic *Posidonia oceanica* surfaces was also studied. We also investigated the dye adsorption capability of untreated and treated *Posidonia oceanica* to particularly determine if a high wetting property would favor the adsorption of dye from aqueous solutions.

12.2 Experimental Details

12.2.1 Materials and Experimental Procedures

Posidonia oceanica samples (Figure 12.16) were collected from Golfe-Juan, Vallauris, France. They were cleaned by scraping with a glass slide to remove the attached epiphytes, and then rinsed with deionized water (Milli-Q water, 18 M Ω). The samples of size 3.0 cm x 0.5 cm were dried in an oven at 70°C to constant weight.

The cleaned and dried *Posidonia oceanica* samples were treated using argon and oxygen plasmas (Figure 12.17) using varying discharge powers and plasma exposure times. The discharge power was varied from 100 W to 600 W and the plasma exposure time was varied from 1 min to 5 min, which represents plasma discharge energies ranging from 6 kJ to 180 kJ. Table 12.2 summarizes the experimental parameters.

The plasmas were produced using a BSET EQ NT-1 plasma device (Digit Concept Microelectronics and High Tech Equipment, France) operating at an excitation frequency of 13.56 MHz. The power and ground electrodes were placed parallel to each other at 50 mm distance, the samples were

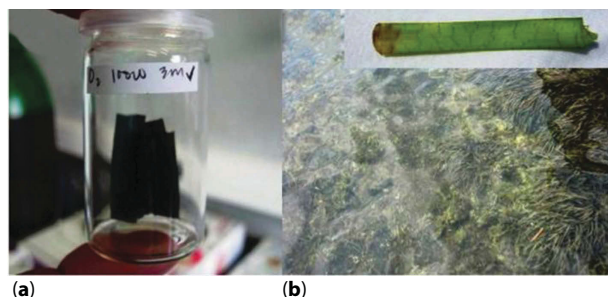


Figure 12.16 (a) Cleaned and dried *Posidonia oceanica* samples. (b) *Posidonia oceanica* in its natural habitat, inset shows a freshly collected sample.

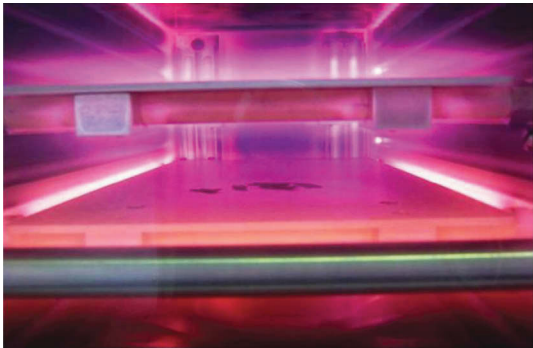


Figure 12.17 *Posidonia oceanica* samples on the ground electrode exposed to oxygen plasma with energy equal to 6 kJ.

Table 12.2 Summary of the experimental parameters for the plasma treatment of *Posidonia oceanica* samples.

Gas	Plasma Power and Exposure Time	Plasma Energy (kJ)
Argon	100W, 1min	6
Argon	100W, 3min	18
Argon	100W, 5min	30
Argon	600W, 1min	36
Argon	600W, 3min	108
Argon	600W, 5min	180
Oxygen	100W, 1min	6
Oxygen	100W, 3min	18
Oxygen	100W, 5min	30
Oxygen	600W, 1min	36
Oxygen	600W, 3min	108
Oxygen	600W, 5min	180

placed at the ground electrode. A 20 m³/h rotary pump evacuated the system and the base pressure was set at 100 mTorr. Argon and oxygen gases were fed into the chamber at a rate of 20 sccm. Figure 12.18 shows the image of the BSET EQ NT-1 plasma device and its schematic diagram.

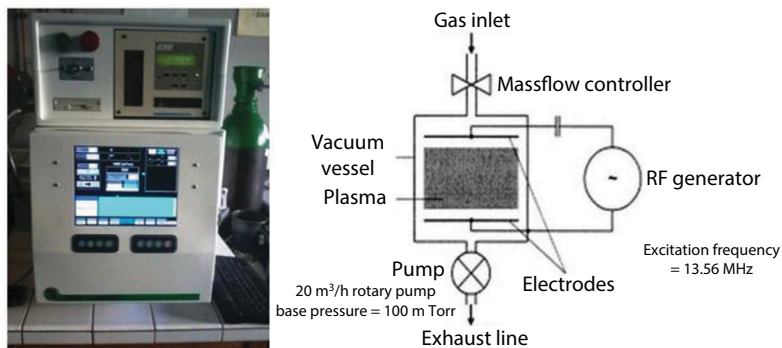


Figure 12.18 BSET EQ NT-1 plasma device (left). Schematic diagram of the plasma device (right).

12.2.2 Characterizations

12.2.2.1 Weight Loss

A Kern EW precision balance (Kern & Sohn GmbH, Germany) was used to determine the changes in the weight of the samples before and after the plasma treatment. The weight loss was calculated as follows:

$$\text{weight loss (\%)} = \frac{W_{\text{before treatment}} - W_{\text{after treatment}}}{W_{\text{before treatment}}} \times 100, \quad (12.5)$$

where $W_{\text{before treatment}}$ is the weight of the sample before the plasma treatment and $W_{\text{after treatment}}$ is the weight of the sample after the plasma treatment.

12.2.2.2 Contact Angle Measurements

A DSA 30S goniometer (Krüss GmbH, Germany) was used to study the changes in the wettability. The sessile drop method was used to determine static contact angles. About 2 μL of deionized water (Milli-Q water, 18 M Ω) was dropped vertically onto the samples using a motorized syringe mechanism; a drop shape analysis software was used to determine the contact angles. For each sample, contact angles were measured 5 times, at 5 different sites; the standard deviations of the contact angle measurements were all statistically the same. To study the stability of the surfaces, the samples were exposed to air and the water contact angles were measured after 24 h., 72 h., and 144 h.

12.2.2.3 Surface Roughness

A Wyko NT1100 Optical Profiling System (Veeco, Philippines) was used to measure the surface roughness. The experiment was carried out in VSI mode using a 20x objective lens and a 0.5x field of view lens. The effective field of view was 0.62 mm x 0.47 mm. 5 spots on the surface were measured for each sample. The surface roughness was reported as root-mean-squared (rms) roughness calculated over the entire area measured.

12.2.2.4 FT-IR Analysis

A Perkin Elmer Paragon 100 FT-IR spectrometer equipped with an MKII Golden Gate Single Reflection ATR system with a diamond ATR top plate was used to determine the changes in the chemical functionalities. The samples were clamped on the stage and scanned 4 times at 4 cm⁻¹ spectral resolution. The measurements were repeated at three locations and the collected spectra were averaged.

12.2.3 Dye Adsorption

The dye adsorption experiment was adapted from the studies of Tumlos *et al* [54]. A stock solution, 500 mg/L, was prepared by mixing a methyl red dye (C₁₅H₁₅N₃O₂) with distilled water. Serial dilution process was used to attain the desired concentration of the stock solution.

For each adsorption experiment, *Posidonia oceanica* materials of varying size but of the same mass per set-up were placed inside a circular flat-bottomed flask and mixed with a 100 mL of dye stock solution of known concentration and pH. The flask was agitated at different contact times ranging from 20 min to 120 min. The adsorbent was separated and the remaining solution was centrifuged at 4000 rpm, the absorbance values were then measured. Methyl red concentration was determined from the absorbance values from a Perkin Elmer UV/Vis Spectrophotometer before and after treatment using the following equation:

$$\frac{\text{Initial Concentration}}{\text{Initial Absorbance}} = \frac{\text{Final Concentration}}{\text{Final Absorbance}}. \quad (12.6)$$

The amount of dye adsorbed (Q_A) on the sample was calculated from the following equation:

$$Q_A = (C_i - C_f)V / M, \quad (12.7)$$

where C_i and C_f are the initial and final equilibrium concentrations of dye, respectively, V is the volume of the aqueous solution and M is the mass of the adsorbent used. The following parameters were varied for each set-up: initial dye concentration, pH, amount of adsorbent, and contact time.

12.3 Results and Discussion

12.3.1 Plasma Treatment of *Posidonia oceanica*

Figure 12.19 shows the influence of different plasma treatments on weight loss. In general, it can be observed that there is a weight loss after plasma treatment; however, a larger weight loss was seen for oxygen-plasma treatment than the argon-plasma treatment. The discharge gas is seen to play a vital role in the possible etching of the surface of the samples.

Based on the graph, the plasma discharge power and the plasma exposure times (as expressed in terms of plasma energy) have no clear relationship with the weight loss of the samples for the argon-plasma treatment. For the oxygen-plasma treatment, in general, an increase in weight loss is observed as the plasma discharge power and the plasma exposure time are increased. This leads to chain scission reactions at the surface of the samples; consequently, there is a continued appearance of new surfaces during the etching of the sample [32].

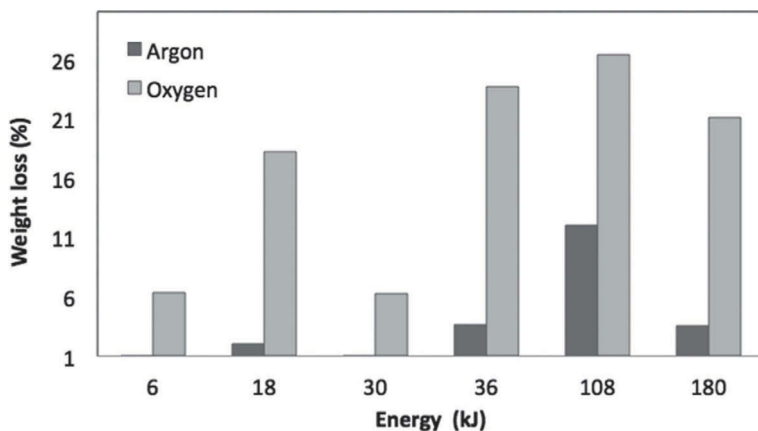


Figure 12.19 Influence of different plasma treatments on weight loss. In general, it can be observed that there is weight loss after plasma treatment; however, a larger weight loss is seen for oxygen-plasma treatment than the argon-plasma treatment [45].

Table 12.3 Summary of the experimental parameters and their effects on the water contact angle and surface roughness of argon and oxygen plasma-treated *Posidonia oceanica* samples [45].

Gas	Plasma Power and Exposure Time	Plasma Energy (kJ)	Contact Angle (°)				R _{rms} (nm)
			0h	24h	72h	144h	
	Untreated		67.4 ± 2.3				120.4
Argon	100W, 1min	6	25.2 ± 1.4	26.7 ± 1.9	36.3 ± 2.3	40.6 ± 2.1	178.5
Argon	100W, 3min	18	24.5 ± 1.5	27.9 ± 2.1	39.6 ± 3.1	43.1 ± 1.3	203.4
Argon	100W, 5min	30	22.2 ± 0.8	24.3 ± 1.0	36.1 ± 2.1	41.3 ± 0.2	234.8
Argon	600W, 1min	36	19.1 ± 1.1	22.9 ± 0.5	31.6 ± 2.0	38.0 ± 1.0	276.2
Argon	600W, 3min	108	10.8 ± 2.0	15.5 ± 1.2	19.7 ± 1.4	28.3 ± 1.9	377.5
Argon	600W, 5min	180	Spreading	10.6 ± 1.1	16.4 ± 2.3	17.5 ± 0.3	384.3
Oxygen	100W, 1min	6	Spreading	8.6 ± 0.7	12.5 ± 1.2	15.3 ± 0.7	404.4
Oxygen	100W, 3min	18	Spreading	10.1 ± 1.2	12.6 ± 1.4	14.2 ± 0.1	354.9
Oxygen	100W, 5min	30	12.8 ± 1.4	13.3 ± 0.9	19.3 ± 0.2	26.3 ± 1.4	270.0
Oxygen	600W, 1min	36	13.1 ± 0.5	14.9 ± 0.2	20.5 ± 0.9	27.8 ± 2.1	236.0
Oxygen	600W, 3min	108	16.3 ± 0.2	18.0 ± 1.3	24.4 ± 2.3	32.6 ± 3.5	179.5
Oxygen	600W, 5min	180	17.1 ± 0.6	25.7 ± 2.1	34.4 ± 1.8	38.4 ± 0.5	159.4

Table 12.3 summarizes the changes in the water contact angle as a function of time, and the surface rms roughness of argon and oxygen plasma-treated *Posidonia oceanica*. For both the argon-plasma and oxygen-plasma treatments, the water contact angle decreased right after treatment. Superhydrophilic surface was observed at 180 kJ argon-plasma treatments. Superhydrophilic surfaces were also observed for low plasma discharge energies (6 kJ and 18 kJ) for oxygen-plasma treatment. Figure 12.20 shows a water droplet on the *Posidonia oceanica*'s surface; (a) untreated sample shows a contact angle of 67.4°; (b) a sample treated with 6 kJ of oxygen plasma showing the spreading of a water droplet within 1 second of drop deposition.

The stability of the surface wettability was studied by measuring the water contact angles at 24 h., 72 h., and 144 h. after the plasma treatment. There was a general increase in the water contact angle as a function of time after the plasma treatment. The rate of increase in the water contact angle as a function of time after the plasma treatment for the superhydrophilic surfaces was found to be significantly smaller ($p < 0.05$) than the hydrophilic surfaces ($\theta \leq 10^\circ$).

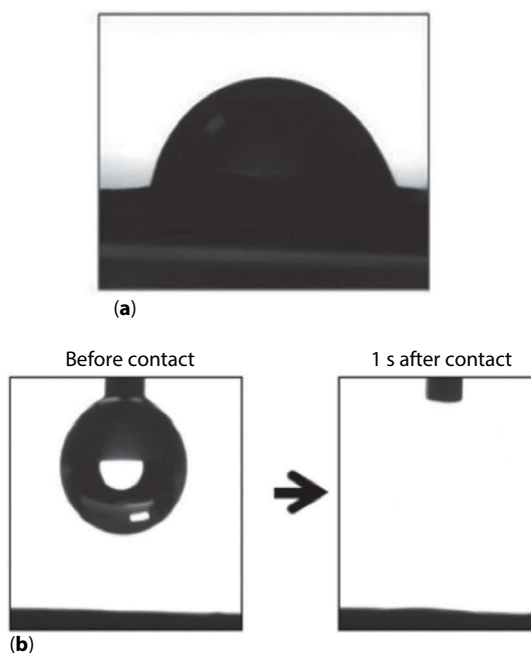


Figure 12.20 A water droplet on the *Posidonia oceanica*'s surface; (a) untreated sample showing a contact angle of 67.4°; (b) a sample treated with 6 kJ of oxygen plasma showing spreading of a water droplet within 1 second of drop deposition.

There is a decreasing trend for the water contact angle (just after plasma treatment) of argon-plasma treated samples as the plasma discharge power and the plasma exposure times (as expressed in terms of plasma energy) are increased. An opposite trend was seen for the oxygen-plasma treated samples. It is interesting to note that for both the argon and oxygen plasma-treated samples, the surface rms roughness increases as water contact angles decreases.

Figure 12.21 shows 2D surface profiles of the (a) untreated; (b) 180 kJ argon plasma-treated; and (c) 6 kJ oxygen plasma-treated *Posidonia oceanica* samples. The literature explains that an increase in the surface roughness can result in either a superhydrophobic surface or a superhydrophilic surface [5, 9–10, 55]; in this study, superhydrophilic surfaces were obtained due to the increase in the surface roughness.

Figure 12.22 shows a typical FTIR spectrum of untreated *Posidonia oceanica*. Table 12.4 summarizes the peak assignments of the FTIR spectrum of untreated *Posidonia oceanica*. The presence of -OH , -CH_2 and C-H groups shows that it is mainly composed of cellulose materials.

Figure 12.23 shows the representative FTIR-spectra of differently treated *Posidonia oceanica* samples. Low plasma discharge power and

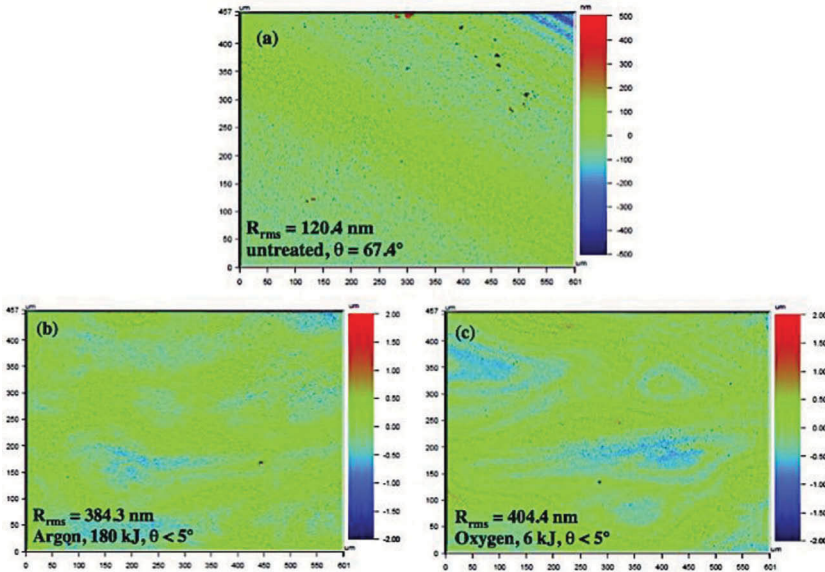


Figure 12.21 2D surface profiles of the (a) untreated; (b) 180 kJ argon plasma-treated; and (c) 6 kJ oxygen plasma-treated *Posidonia oceanica* samples.

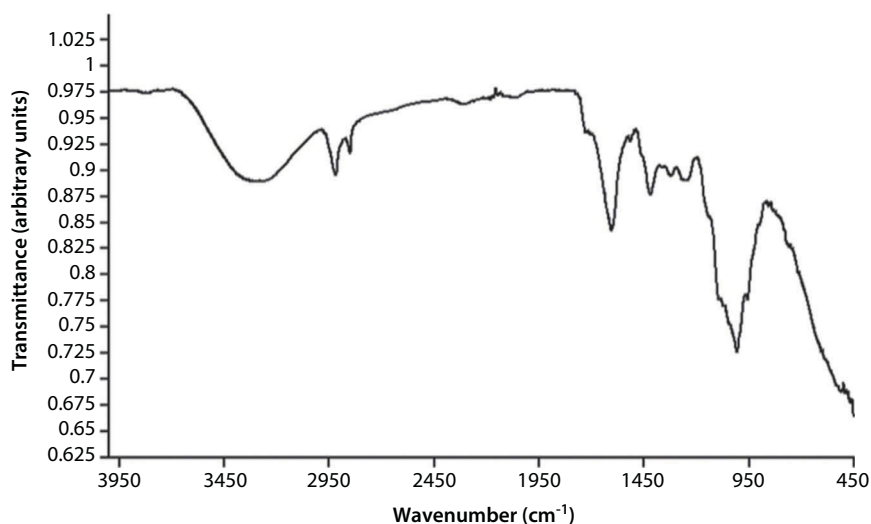


Figure 12.22 Typical FTIR spectrum of untreated *Posidonia oceanica* [45].

Table 12.4 Peak assignments of the FTIR spectrum of untreated *Posidonia oceanica* [45].

Group frequency, wave-number (cm^{-1})	Assignment
3600–3100 (with maximum absorption at 3298)	hydroxyl (-OH) groups
2920	-CH ₂ group
2850	asymmetric stretching of aliphatic C-H
1606	carbonyl (C=O) group stretching
1417	stretching of phenolic -OH and C-O
1160	PO stretching (phosphate group)
1033	aliphatic C-O bands
< 1000	fingerprint zone (phosphate and sulfur groups)

plasma exposure time (6 kJ) and high plasma discharge power and plasma exposure time (18 kJ) were considered for both the argon and oxygen plasma treatments to represent the extreme values of contact angles shown in Table 12.3. All the FTIR spectra for treated samples recorded lower

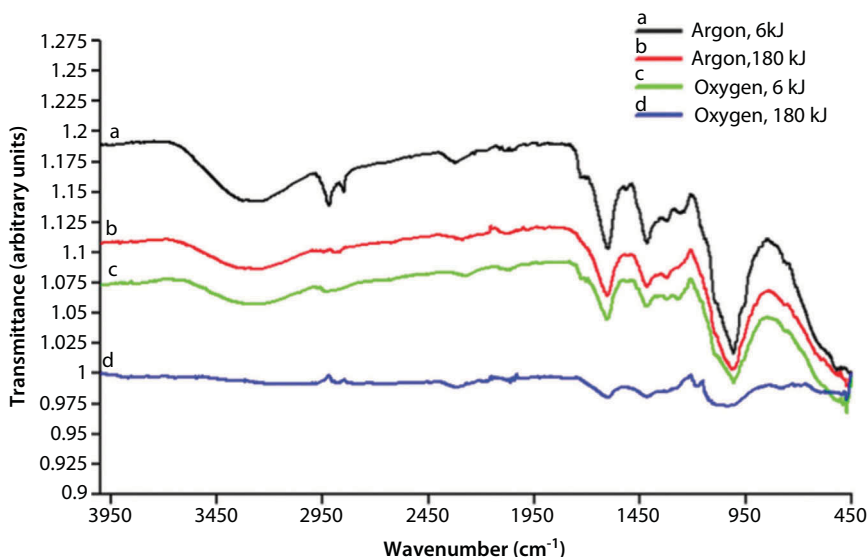


Figure 12.23 FTIR spectra of treated *Posidonia oceanica*. For argon 180 kJ and oxygen 6 kJ treatments, the aliphatic $-\text{CH}_2$ and C-H groups are absent in the spectra, all other peaks still exist in the spectra [45].

absorbance intensities for all the peaks as compared to the untreated sample. For argon, 6 kJ treatments, a spectrum with all peaks similar to the peaks in the spectrum in Figure 12.22 was recorded. For the oxygen, 180 kJ treatment, the $-\text{OH}$ group, and the aliphatic $-\text{CH}_2$ and C-H groups are not seen in the spectrum. Treatment with samples exposed to high energy plasma led to the disappearance of the $-\text{OH}$ groups.

For superhydrophilic surfaces (argon 180 kJ and oxygen 6 kJ), the aliphatic $-\text{CH}_2$ and C-H groups, which are hydrophobic groups, are absent in the spectra, all other peaks, which are hydrophilic still exist in the spectra. The aliphatic $-\text{CH}_2$ and C-H groups reacted with the plasma that resulted into combustion by-products, mainly water and carbon dioxide which were pumped out from the system. For the oxygen 180 kJ treatment, the $-\text{OH}$ groups are almost absent because the plasma temperature may have been too high and the water and alcohol already evaporated; the aliphatic $-\text{CH}_2$ and C-H groups also reacted with the oxygen plasma and the products of the combustion, mainly water and carbon dioxide, were pumped out from the system.

12.3.2 Dye Adsorption by *Posidonia oceanica* from Aqueous Solutions

Figure 12.24 shows the dye adsorption capability of untreated and treated samples when the adsorbent mass is varied and the initial dye

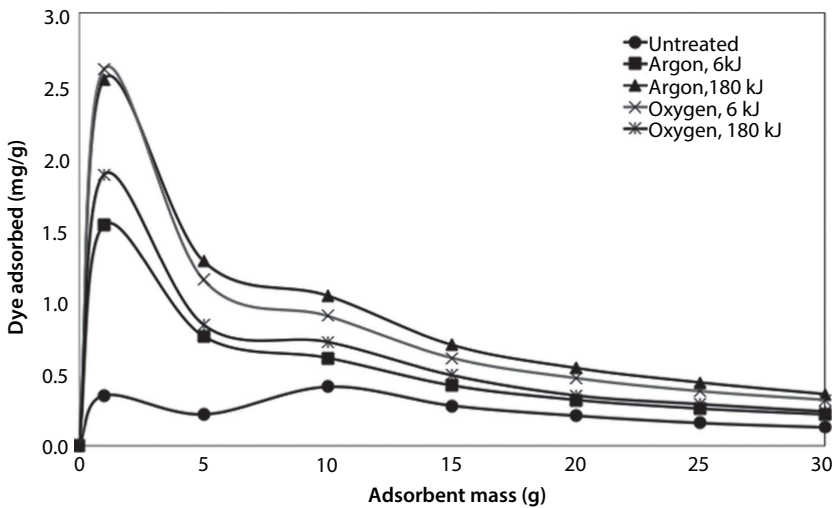


Figure 12.24 Dye adsorption by untreated and treated samples of varying adsorbent mass and fixed dye concentration of 150 mg/L, pH of 7 and contact time of 40 min.

concentration, pH, and contact time are fixed at 150 mg/L, 7, and 40 min, respectively. It can be observed from the graph that there is enhanced dye adsorption when the adsorbent material was treated with different plasmas of different energies. The highest recorded dye adsorption can be seen for samples treated with argon plasma of 180 kJ energy and oxygen plasma of 6 kJ energy, which are both superhydrophilic in nature. The dye adsorption for all the untreated and treated samples stabilizes at a certain amount of adsorbent and which in this case is when the adsorbent mass is 10 g. This means that the material has a limited adsorption capacity based on its mass when the initial dye concentration is fixed at a certain amount. The effect of varying the surface area of the adsorbent cannot be determined from the presented data as the size can vary since the mass is held constant.

Figure 12.25 shows the dye adsorption capability of untreated and treated samples when the contact time with the methyl red stock solution is varied and the initial dye concentration, pH, and adsorbent mass are fixed at 150 mg/L, 7, and 10g, respectively. It can be observed from the graph that there is enhanced dye adsorption when the adsorbent material was treated with different plasmas of different energies. The highest recorded dye adsorption can be seen for samples treated with argon plasma of 180 kJ energy and oxygen plasma of 6 kJ energy, which are both superhydrophilic in nature. The dye adsorption for all the untreated and treated samples stabilizes at a certain contact time and in this case when the contact time with the methyl red stock solution is 40 minutes. This

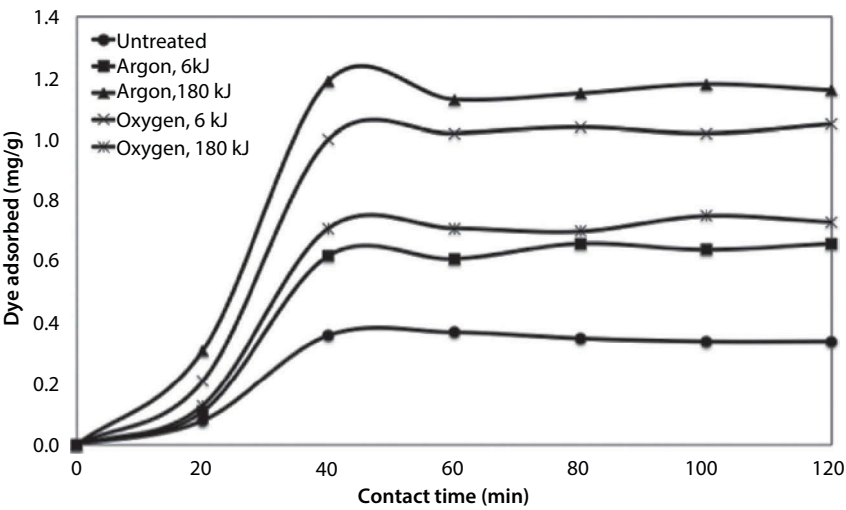


Figure 12.25 Dye adsorption by untreated and treated samples as a function of contact time and fixed dye concentration of 150 mg/L, pH of 7 and adsorbent mass of 10 g.

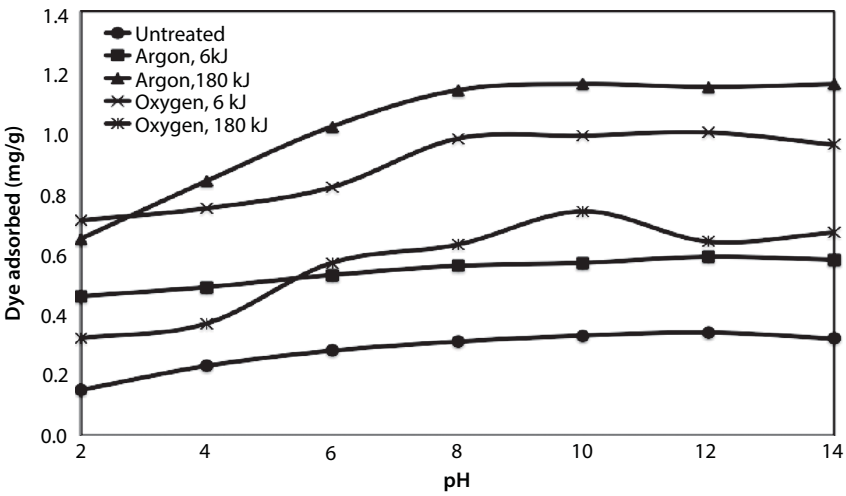


Figure 12.26 Dye adsorption by untreated and treated samples with varying pH and fixed dye concentration of 150 mg/L, adsorbent mass of 10 g and contact time of 40 min.

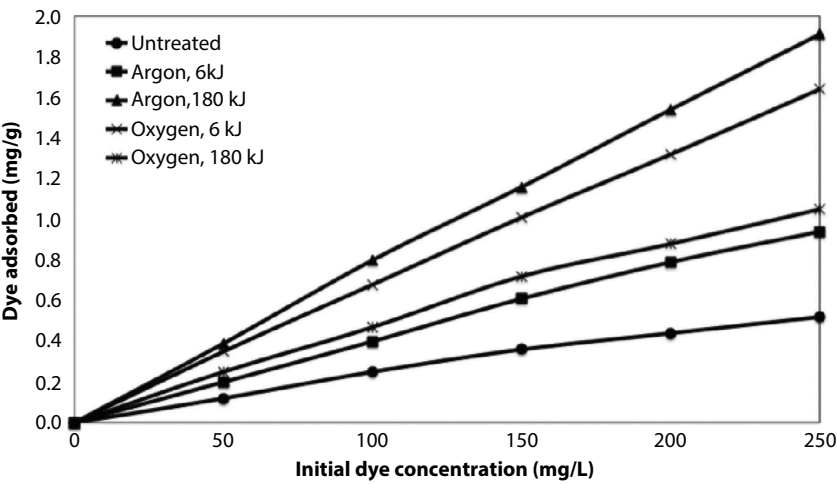


Figure 12.27 Dye adsorption by untreated and treated samples with varying initial dye concentration (mg/L) and fixed adsorbent mass of 10 g, pH of 7 and contact time of 40 min.

means that the material has a relatively fixed adsorption rate whether it is untreated or treated.

Figure 12.26 shows the dye adsorption capability of untreated and treated samples when the pH is varied and the initial dye concentration, contact time, and adsorbent mass are fixed at 150 mg/L, 40 min, and 10 g, respectively. It can be observed from the graph that there is enhanced dye adsorption when the adsorbent material was treated with different plasmas of different energies. The highest recorded dye adsorption can be seen for samples treated with argon plasma of 180 kJ energy and oxygen plasma of 6 kJ energy, which are both superhydrophilic in nature. The dye adsorption capability of the material is seen to increase with the increase in pH. This can be attributed to the increase in the number of available protons at higher pH that adsorb higher amount of methyl red on the adsorption surfaces [54].

Figure 12.27 shows the dye adsorption capability of untreated and treated samples when the initial dye concentration is varied and the pH, contact time, and adsorbent mass are fixed at 7, 40 min, and 10 g, respectively. It can be observed from the graph that there is enhanced dye adsorption when the adsorbent material was treated with different plasmas of different energies. The highest recorded dye adsorption can be seen for samples treated with argon plasma of 180 kJ energy and oxygen plasma of 6 kJ energy, which are both superhydrophilic in nature. The adsorbed dye

Table 12.5 Summary of the R^2 -values for both Langmuir and Freundlich adsorption isotherm models for the different dye adsorption rates for the different sample treatments.

Sample Treatment	Langmuir (R^2 -value)	Freundlich (R^2 -value)
Untreated	0.987	0.863
Argon Plasma, 6 kJ	0.992	0.882
Argon Plasma, 180 kJ	0.990	0.781
Oxygen Plasma, 6 kJ	0.989	0.880
Oxygen Plasma, 180 kJ	0.994	0.890

increased directly with the initial dye concentration, this result is expected as explained by Ncibi *et al.* [48].

Both Langmuir and Freundlich adsorption equilibrium isotherm models were used to determine the adsorption equilibrium of the samples treated using different types of plasma [56–57]. The correlation coefficient, R^2 -value was determined from the model curve and the results are shown in Table 12.5.

The R^2 -values of the untreated and treated samples show that the Langmuir equilibrium adsorption isotherm model best describes the *Posidonia oceanica* adsorbents. This means physisorption is the most likely mechanism that explains the adsorption of methyl red on the samples. This also means that most of the adsorption sites of the material are of homogeneous type as shown in Figure 12.21 [57–58]. Chemisorption may also be responsible for the high dye adsorption especially for the samples with superhydrophilic surfaces since the R^2 -value for the Freundlich model is just slightly lower than the Langmuir model. Adsorption is still affected by both changes in chemistry and morphology of the surfaces of the samples. Further experiments must be performed in order to explain the complex nature of chemisorption on the samples, and different functional groups of *Posidonia oceanica* may play role in the adsorption process.

12.4 Conclusions

Superhydrophilic surface property ($\theta < 5^\circ$ within 1 second of droplet contact) was achieved at high-energy argon-plasma (180 kJ) and low-energy

oxygen-plasma (6 kJ) treatments. The surface roughness increased for the high-energy argon-plasma treatments; however, an opposite trend was seen for the oxygen-plasma treatments. The decrease in the –OH bands (hydrophilic in nature) was observed for the treated samples, but for the superhydrophilic samples, the aliphatic –CH₂ and C–H groups which are hydrophobic in nature were absent from the FT-IR spectra. Superhydrophilic surfaces were achieved from changes in both the surface roughness and in the chemical functionalities of the samples after the plasma treatment. Enhanced dye adsorption was found for superhydrophilic samples, which can also be attributed to the changes in the surface chemistry and the surface morphology. Adsorption data for *Posidonia oceanica* materials fitted the Langmuir equilibrium isotherm adsorption model.

References

1. M. Callies and D. Quéré, On water repellency, *Soft Matter*, 1, 55–61 (2005).
2. ramé-hart Information on Contact Angle. <http://www.ramehart.com/contact-angle.htm> (2014).
3. Y.Y. Yan, N. Gao and W. Barthlott, Mimicking natural superhydrophobic surfaces and grasping the wetting process: A review on recent progress in preparing superhydrophobic surfaces, *Adv. Colloid Interface Sci.*, 169, 80–105 (2011).
4. E. Celia, E. Taffin de Givenchy, S. Amigoni and F. Guittard, Three steps to organic–inorganic hybrid films showing superhydrophilic properties, *Soft Matter*, 7, 10057–10062 (2011).
5. A. Lafuma and D. Quéré, Superhydrophobic states, *Nature Materials*, 2, 457–460 (2003).
6. T. Darmanin, F. Guittard, S. Amigoni, E. Taffin de Givenchy, X. Noblin, R. Kofman and F. Celestini, Superoleophobic behavior of fluorinated conductive polymer films combining electropolymerization and lithography, *Soft Matter*, 7, 1053–1057 (2011).
7. A. Carré and K.L. Mittal (Eds.), *Superhydrophobic Surfaces*, CRC Press, Boca Raton, FL (2009).
8. H. Bellanger, T. Darmanin and F. Guittard, Surface structuration (micro and/or nano) governed by the fluorinated tail lengths toward superoleophobic surfaces, *Langmuir*, 28, 186–192 (2012).
9. Y.C. Sheen, Y.C. Huang, C.S. Liao, H.Y. Chou and F.C. Chang, New approach to fabricate an extremely super-amphiphobic surface based on fluorinated silica nanoparticles, *J. Polym. Sci. B*, 46, 1984–1990 (2008).
10. D.K. Sarkar and N. Saleema, One-step fabrication process of superhydrophobic green coatings, *Surf. Coat. Technol.*, 204, 2483–2486 (2010).
11. X. Zhang, F. Shi, J. Niu, Y. Jiang and Z.J. Wang, Superhydrophobic surfaces: From structural control to functional application, *J. Mater. Chem.*, 18, 621–633 (2008).

12. S. Amigoni, E. Taffin de Givenchy, M. Dufay and F. Guittard, Covalent layer-by-layer assembled superhydrophobic organic–inorganic hybrid films, *Langmuir*, 25, 11073–11077 (2009).
13. M.E. Ryan and J.P.S. Badyal, Surface texturing of PTFE film using nonequilibrium plasmas, *Macromolecules*, 28, 1377–1382 (1995).
14. A. Tuteja, W. Choi, G.H. McKinley, R.E. Cohen and M.F. Rubner, Design parameters for superhydrophobicity and superoleophobicity, *MRS Bulletin*, 33, 752–758 (2008).
15. N.A. Patankar, On the modeling of hydrophobic contact angles on rough surfaces, *Langmuir*, 19, 1249–1253 (2003).
16. K. Tsujii, T. Yamamoto, T. Onda and S. Shibuichi, Super oil-repellent surfaces, *Angew. Chem. Int. Ed. Engl.*, 36, 1011–1012 (1997).
17. A.B.D. Cassie and S. Baxter, Wettability of porous surfaces, *Trans. Faraday Soc.*, 40, 546–551 (1944).
18. A. Tuteja, W. Choi, M.L. Ma, J.M. Mabry, S.A. Mazzella, G.C. Rutledge, G. H. McKinley and R.E. Cohen, Designing superoleophobic surfaces, *Science*, 318, 1618–1622 (2007).
19. A. Ahuja, J.A. Taylor, V. Lifton, A.A. Sidorenko, T.R. Salamon, E.J. Lobaton, P. Kolodner and T.N. Krupenkin, Nanonails: A simple geometrical approach to electrically tunable superhydrophobic surfaces, *Langmuir*, 24, 9–14 (2008).
20. Biomimetics: clingy as an octopus or slick as a lotus leaf? <http://www.science-inschool.org/2011/issue18/biomimetics> (2011).
21. J. Bico, C. Marzolin and D. Quéré, Pearl drops, *Euro. Phys. Lett.*, 47, 220–226 (1999).
22. L. Feng, S. Li, Y. Li, H. Li, L. Zhang, J. Zhai, Y. Song, B. Liu, L. Jiang and D. Zhu, Super-hydrophobic surfaces: From natural to artificial, *Adv. Mater.*, 14, 1857–1860 (2002).
23. P. Comanns, C. Effertz, F. Hischen, K. Staudt, W. Böhme and W. Baumgartner, Moisture texturing and water transport through specialized micro-structures on the integument of lizards, *Beilstein J. Nanotechnol.*, 2, 204–214 (2011).
24. R.N. Wenzel, Resistance of solid surfaces to wetting by water, *Ind. Eng. Chem.*, 28, 988–994 (1936).
25. R.N. Wenzel, Surface roughness and contact angle, *J. Phys. Colloid Chem.*, 53, 1466–1467 (1949).
26. Vecdör Nanocoatings are Anti-Scratch & Self-Cleaning. <http://www.nano-clear.co.nz/technical-information/vecdoer-nanocoatings-are-anti-scratch-self-cleaning.html> (2014).
27. Changing Surfaces: Functional Principle. <http://www.plasma-electronic.de/en/Funktionsprinzip/funktionsprinzip.php>
28. BioZone Europe, Purifying Plasma. <http://www.biozone-europe.eu/v2/en/technologies/cold-plasma> (2012).
29. M. Strobel, N. Sullivan, M. C. Branch, J. Park, M. Ulsh, R. S. Kapaun and B. Leys, Surface modification of polypropylene film using N₂O-containing flames, *J. Adhesion Sci. Technol.*, 14, 1243–1264 (2000).

30. E. Y. Kim, J. S. Kong, S. K. An and H. D. Kim, Surface modification of polymers and improvement of the adhesion between evaporated copper metal film and a polymer. I. Chemical modification of PET, *J. Adhesion Sci. Technol.*, 14, 1119–1130 (2000).
31. C. Mao, C. Zhang, Y. Qiu, A. Zhu, J. Shen and S. Lin, Introduction of anti-coagulation group to polypropylene film by radiation grafting and its blood compatibility, *Appl. Surface Sci.*, 228, 26–33 (2006).
32. J. M. Grace and L. J. Gerenser, Plasma treatment of polymers, *J. Dispersion Sci. Technol.*, 24, 305–341 (2003).
33. S. Nakata and S. Hiromatsu, Intermittent motion of a camphor float, *Colloids Surfaces A*, 224, 157–163 (2003).
34. M. Strobel, C.S. Lyons and K.L. Mittal (Eds.), *Plasma Surface Modification of Polymers: Relevance to Adhesion*, CRC Press, Boca Raton, FL (1994).
35. Michael Thomas and K.L. Mittal (Eds.), *Atmospheric Pressure Plasma Treatment of Polymers: Relevance to Adhesion*, Wiley-Scrivener, Beverly, MA (2013).
36. M.N. Acda, E.E. Devera, R.J. Cabangon, K.G. Pabeliña and H.J. Ramos, Effects of dielectric barrier discharge plasma modification on surface properties of tropical hardwoods at low pressure, *J. Tropical Forest Sci.*, 24, 416–425 (2012).
37. H.V. Boenig, *Plasma Science and Technology*, Cornell University Press, Ithaca, NY (1982).
38. N. Inagaki, Surface modification of ethylene-co-tetrafluoroethylene copolymer (ETFE) by plasma, *Nucl. Instrum. Methods B*, 208, 277–280 (2003).
39. PICO Low Pressure Plasma System. <http://www.plasma.de/pdfs/pico-eng-lich.pdf> (2015).
40. H.S. Salapare III, G.Q. Blantocas, V.R. Noguera and H.J. Ramos, Low-energy hydrogen ion shower (LEHIS) treatment of polytetrafluoroethylene (PTFE) materials, *Appl. Surface Sci.*, 255, 2951–2957 (2008).
41. M. Morra, E. Occhiello and F. Garbassi, Contact angle hysteresis in oxygen plasma treated poly(tetrafluoroethylene), *Langmuir*, 5, 872–876 (1989).
42. H.S. Salapare III, G.Q. Blantocas, V.R. Noguera and H.J. Ramos, The porosity and wettability properties of hydrogen ion treated poly(tetrafluoroethylene), in: *Contact Angle, Wettability, and Adhesion*, Vol. 6, K.L. Mittal (Ed.), pp. 207–216, CRC Press, Boca Raton, FL (2009).
43. H.S. Salapare III, G.Q. Blantocas, W.L. Rivera, V.A. Ong, R.S. Hipolito and H.J. Ramos, Anti-bacterial property of hydrogen-ion and oxygen-ion treated polytetrafluoroethylene (PTFE) materials, *Plasma Fusion Res.*, 6, 2406043 (2011).
44. D.F. O’Kane and K.L. Mittal, Plasma cleaning of metal surfaces, *J. Vac. Sci. Technol.*, 11, 567–569 (1974).
45. H.S. Salapare III, M.G.J.P. Tiquio and H.J. Ramos, Superhydrophilic properties of plasma-treated *Posidonia oceanica*, *Appl. Surface Sci.*, 273, 444–447 (2013).
46. C.F. Boudouresque, G. Bernard, P. Bonhomme, E. Charbonnel, G. Diviacco, A. Meinesz, G. Pergent, C. Pergent-Martini, S. Ruitton and L. Tunesi, *Protection*

- and Conservation of *Posidonia oceanica* Meadows, pp. 25–30, RAMOGE and RAC/SPA, Tunis, Tunisia (2012).
47. M. Izquierdo, P. Marzal, C. Gabaldón, M. Silvetti and P. Castaldi, Study of the interaction mechanism in the biosorption of copper (II) ions onto *Posidonia oceanica* and peat, *Clean: Soil, Air, Water*, 40, 428–437 (2012).
 48. M. C. Ncibi, B. Mahjoub and M. Seffen, Adsorptive removal of anionic and non-ionic surfactants from aqueous phase using *Posidonia oceanica* (L.) marine biomass, *J. Chem. Technol. Biotechnol.*, 83, 77–83 (2008).
 49. A. Chadlia and M.M. Farouk, Removal of basic blue 41 from aqueous solution by carboxymethylated *Posidonia oceanica*, *J. Appl. Polym. Sci.*, 103, 1215–1225 (2007).
 50. S. Jellali, M.A. Wahab, M. Anane, K. Riahi and N. Jedidi, Biosorption characteristics of ammonium from aqueous solutions onto *Posidonia oceanica* (L.) fibers, *Desalination*, 270, 40–49 (2011).
 51. S. Cengiz, F. Tanrikulu and S. Aksu, An alternative source of adsorbent for the removal of dyes from textile waters: *Posidonia oceanica* (L.), *Chem. Eng. J.*, 189–190, 32–40 (2012).
 52. M.A. Wahab, R.B. Hassine and S. Jellali, Removal of phosphorus from aqueous solution by *Posidonia oceanica* fibers using continuous stirring tank reactor, *J. Hazard. Mater.*, 189, 577–585 (2011).
 53. A. Blanco, B. Sanz, M.J. Llama and J.L. Serra, Biosorption of heavy metals to immobilized *Phormidium laminosum* biomass, *J. Biotechnol.*, 69, 227–240 (1999).
 54. R. Tumlos, J. Ting, E. Osorio, L. Rosario, H. Ramos, A. Ulano, H. Lee and G. Regalado, Results of the study of chemical-, vacuum drying- and plasma-pretreatment of coconut (*Cocos nucifera*) lumber sawdust for the adsorption of methyl red in water solution, *Surface Coat. Technol.*, 205, S425–S429 (2011).
 55. K.L. Mittal and F.M. Etzler, Is the world basic? Lessons from surface science, in: *Contact Angle, Wettability, and Adhesion*, Vol. 6, K.L. Mittal (Ed.), pp. 111–123, CRC Press, Boca Raton, FL (2009).
 56. K.V. Kumar and S. Sivanesan, Isotherms for Malachite Green onto rubber wood (*Hevea brasiliensis*) sawdust: Comparison of linear and non-linear methods, *Dyes Pigments*, 72, 124–129 (2007).
 57. N.B. Douissa, L. Bergaoui, S. Mansouri, R. Khiari and M.F. Mhenni, Macroscopic and microscopic studies of methylene blue sorption onto extracted cellulose from *Posidonia oceanica*, *Indust. Crops Prod.*, 45, 106–113 (2013).
 58. I. Langmuir, The adsorption of gases on plane surfaces of glass, mica and platinum, *J. Am. Chem. Soc.*, 40, 1361–1403 (1918).

Highly Liquid Repellent Technical Textiles Obtained by Means of Combined Photo-chemical and Laser Surface Modifications

Thomas Bahnners^{1,*} and Jochen S. Gutmann^{1,2}

¹*Deutsches Textilforschungszentrum Nord-West gGmbH (DTNW),
Krefeld, Germany*

²*Universität Duisburg-Essen, Physikalische Chemie and CENIDE, Essen, Germany*

Abstract

In this chapter, innovative approaches making use of the synergy between subsequent surface processing steps to (a) introduce surface roughness and to (b) modify surface chemistry in order to decrease the surface free energy are discussed in view of their potential to attain high liquid repellence of technical textiles. In the context of growing interest in physical processes, the chapter focuses on the potential of combined photo-chemical and laser surface modifications, which were extensively studied by the authors over the last years. The concept is illustrated by experimental data from studies aimed to increase water repellence of technical fabrics made of poly(ethylene terephthalate) (PET) and p-aramid and the concept of highly oil repellent PET fabrics. In the reported experiments, surface roughening was attained by irradiation using pulsed UV (excimer) lasers, while the surface chemistry of the roughened fibers was modified by UV-induced graft-copolymerization of dienes or perfluorinated agents. In all investigated cases, the experiments showed a synergetic effect of the combined treatment, which amplified the effects of the individual treatments.

Keywords: Technical textiles, water repellence, oil repellence, surface roughness, surface chemistry, laser irradiation, photo-grafting

*Corresponding author: bahners@dtnw.de

13.1 Introduction

In contrast to common clothing and home textiles, technical textiles are a growing and important market for textile companies in Western countries. Nowadays, technical textiles are considered high performance products with well-defined functionalities, often attained by advanced surface modification concepts. They find application in fields as diverse as medical engineering, aerospace and automotive industries, modern architecture and construction, filtration, and transport systems. The functionalities addressed cover particle and coating adhesion, tailored surface mechanical properties, anti-bacterial or anti-fouling properties, promotion or prohibition of protein adsorption, (local) electrical conductivity, charge storage, or sensor functions, to name just a few.

A long-standing demand has been (super-)hydrophobic or oleophobic character, required to attain effective liquid repellence, self-cleaning, unidirectional liquid transport, or to create barrier coatings on fiber surfaces. A comprehensive overview of recent attempts in this exciting field can be found in [1]. Besides the modification of surface chemistry in order to minimize the surface free energy, biomimetic concepts to incorporate surface roughness by mimicking surfaces of animals or plants such as the well-known Lotus leaf have been utilized. Accordingly, there have been numerous attempts to either modify surface chemistry by finishing, chemical and physical grafting, etc., or (independently) to modify surface topography.

As has been known for many years, liquid repellence can also be increased through rendering a surface rough, if the substrate is basically repellent for the liquid in question with a contact angle $> 90^\circ$ [2–5]. From the basic concept, high repellence can also be achieved by decreasing the surface free energy (SFE) of a micro-rough surface, which is moderately hydrophilic or – phobic, and oleophilic, or – phobic.

It can be observed, however, that attempts to apply both types of surface modifications – i.e. modification of surface chemistry *and* modification of surface topography – in a combined processing concept have been increasingly reported in recent years. Based on the concepts of Wenzel or Cassie-Baxter, super- or at least high repellence can thus be achieved by (a) the increase of liquid repellence by chemical surface modification to reduce SFE and subsequent roughening, or (b) by introducing surface roughness and subsequent chemical modification of the rough surface to reduce SFE.

The scope of this chapter is to give a short overview of fundamentals and innovative approaches making use of this synergy of combined surface treatments for high liquid-repellence on technical surfaces. In recent

years, there has been a growing interest in physical processes, which open avenues for achieving the requisite physical, topographical and chemical surface properties with no or little consumption of chemicals and no or little need for wastewater or gas emission treatments. In this context, the chapter will focus on the potential of combined photo-chemical and laser surface modifications, which were extensively studied by the authors over the last years.

13.2 Background of the Conceptual Approach

13.2.1 Surface Free Energy and Liquid Repellence

The spreading of a liquid on a smooth surface is determined by the balance of interfacial energies at the solid-liquid interface, the solid-vapor interface, and the liquid-vapor interface. The relation between these quantities and the (static) contact angle Θ_Y of a droplet residing on top of the surface is described by the well-known Young's equation. Equilibrium – and thus the corresponding equilibrium contact angle – is reached, when the total energy has reached a minimum [6,7]. It can be deduced from the formalism of Young's equation that surfaces with high liquid repellence can be chemically attained through the reduction of the surface free energy (SFE) by introduction of non-polar groups. In view of both water and oil repellence, highest repellence can be expected by establishing CF_3 -groups on the surface. A complete coverage of the surface with CF_3 -groups will reduce its surface free energy to 6.7 mJ/m^2 .

Accordingly, textile substrates are conventionally finished with fluorocarbons in a wet-chemical process by padding, followed by thermal stabilization, for both water and oil repellence. While the general performance of these products is very good, disadvantages have to be considered as well. These refer to limited wash stability and abrasion resistance and wastewater and environmental issues associated with the use of long-chain (C8) fluorocarbons based on perfluorooctanoic acid (PFOA) derivatives in the finishing step that are known to be bio-persistent [8]. Recent developments in the field of wet-chemical finishing processes, predominantly by suppliers of auxiliaries for the textile industry, have therefore concentrated on the development of innovative short-chain (C6) fluorocarbons (see, e.g., [9]).

As has already been mentioned, a further major disadvantage of wet-chemical finishes is the potentially doubtful long-term wash or abrasion stability. This is an issue especially for technical textiles, which may be subjected to mechanical, thermal, or chemical stress from natural or industrial

environments, or are employed as components in machinery and technical processes. The growing interest in the modification of surface chemistry by means of physical processes aiming at covalent bonding and grafting of low energy functional groups and resulting durability of the finish has to be understood in this context.

Besides plasma-based grafting and thin-layer polymerization, photochemical processes have proven their potential for an effective and durable functionalization of polymers, if treatments are conducted in reactive media, which can be a gaseous atmosphere or a liquid agent [10–16]. The absorption of UV photons either at the surface of the substrate – i.e. at the interface between substrate and reactive medium – or in the bulk of the reactive medium leads to radical generation and subsequent reactions. Besides the recombination of radicals and cross-linking of polymer chains at the substrate surface, the addition of radicals from the reactive medium, and the addition of bi-functional molecules with ensuing cross-linking between the functional groups result in photo-induced grafting or thin-layer cross-linking.

In a number of papers, Bahnert and co-workers studied fundamental effects of the photochemical process designed to increase hydrophobicity [16–19]. By choosing the appropriate substance serving as the reactive medium during irradiation, the water contact angle could be altered significantly. Reactive media, applied as a liquid finish before UV exposure, were 1,5-hexadiene, 1,7-octadiene, diallylphthalate (DAP), perfluoro(4-methylpent-2-ene) (PFMP), or 1H,1H,2H,2H-perfluorodecyl acrylate (PFDA). High oil repellence obviously was attained from fluorinated substances such as PFMP and PFDA.

13.2.2 Enhancing Liquid Repellence through Surface Roughness

If a smooth material is repellent for the liquid in question with a contact angle $> 90^\circ$, liquid repellence is further increased by surface roughness. As is well-known, two potential cases have to be considered. If the liquid is able to penetrate the features of the rough structure, a close contact area between the droplet and the substrate is preserved. This situation is commonly described by a model first published by Wenzel [3]. Wenzel relates the apparent contact angle on the rough surface Θ_w and the contact angle on the planar surface Θ_Y (“Young angle”) with the simple expression

$$\cos \Theta_w = r \cdot \cos \Theta_Y, \quad (13.1)$$

where the features of the surface topography are described by a roughness factor r , which gives the ratio of the effective area of actual rough surface to the ideal flat surface, i.e. $r \geq 1$. In the case of a flat surface, r will be 1 and, accordingly, $\Theta_w = \Theta_Y$.

If the liquid, on the other hand, sits on top of the surface features without penetrating the ‘valleys’, air will be enclosed between the droplet and the substrate and the liquid/air interface increases (cf. [4,5]). In this “Cassie-Baxter state”, the solid/liquid interface approaches a minimum. The further increase of surface area (i.e. spreading of the droplet) is hindered for energetic reasons [5]. The apparent contact angle observed under these conditions is usually described by the simplified equation

$$\cos \Theta_{CB} = -1 + \Phi_s (1 + \cos \Theta_Y), \quad (13.2)$$

known as the Cassie-Baxter equation. Eq.(13.2) again relates the apparent contact angle on the rough surface and the contact angle on the planar surface. The geometric features are described by the factor Φ_s , which gives the ratio of the actual liquid-solid interface area to the apparent contact area ($\Phi_s \leq 1$). Again, given a perfectly flat surface, i.e. $\Phi_s = 1$, the contact angle is equal to the Young angle, $\Theta_{CB} = \Theta_Y$.

Besides the static contact angle itself, the contact angle hysteresis, i.e. the difference $\Delta\Theta$ between the advancing angle Θ_A and the receding angle Θ_R , which are observed in a *dynamic* measurement, is an important criterion to classify a surface as highly hydrophobic or super-hydrophobic. Generally, the latter state is connected to a complete roll-off of a droplet *already* at a slight tilt of the surface as is observed on, e.g., the Lotus leaf. This is given, if $\Delta\Theta \rightarrow 0$. In the case of high hysteresis, a droplet will stick to the surface in spite of a high static contact angle. It is generally assumed that zero contact angle hysteresis is given only in the Cassie-Baxter state.

Among the first to show super-hydrophobicity on rough artificial surfaces were Onda and co-workers [20,21] and later Miwa *et al.* [22]. A good overview presenting various related concepts is given in [23].

13.2.3 Peculiarities of Textile Substrates and their Relevance to Wetting

The characteristic and complex geometry of textile substrates has significant effects on the wetting behavior of a droplet as well as the appropriate method to characterize the wettability of a textile.

A technical textile may be constructed as a non-woven structure of fibers – usually fibers are directly spun on a moving belt and form an

irregular web – or in a regular geometry mostly produced by weaving. A woven fabric is formed by weft and warp threads, which might be a monofilament (monofil) – i.e. an isolated, rather thick fiber –, a multifilament yarn made of a number of endless fibers, or a spun yarn made of a number of short fibers. While monofilaments have diameters up to several hundred micrometers, fibers may have diameters from below 1 μm (micro-fiber) to 20 μm . Relevant examples of woven technical fabrics are shown in Figure 13.1. It should be noted that in some cases the mostly perfectly cylindrical synthetic fibers may be textured during the spinning process to exhibit non-circular cross sections.

According to the complex composition of fibers and yarns, four factors influence the wetting behavior of a droplet on a textile surface.

1. Primarily, spreading is defined by the surface chemistry of the synthetic fiber. The vast majority of technical textiles are made of poly(ethylene terephthalate) (PET), polyamide (Nylon or PA), and poly(propylene) (PP), which can be categorized as more or less hydrophobic.
2. Macroscopically, a textile fabric has a coarse, textured surface, which may have similar effects on the wetting behavior

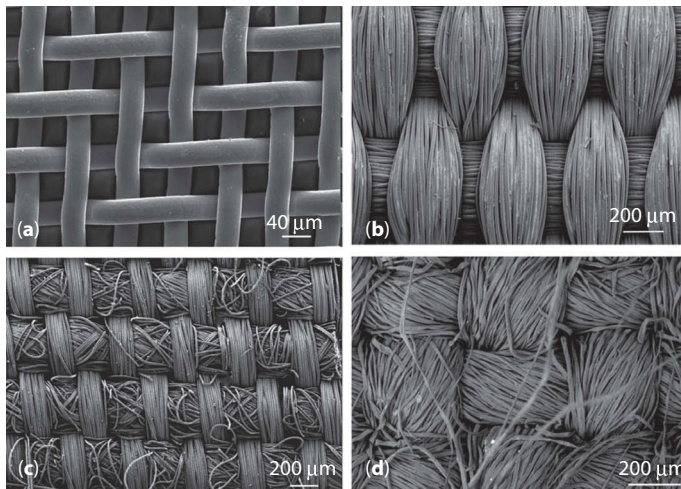


Figure 13.1 Elementary constructions of woven fabrics: (a) twill fabric made of monofilaments, (b) plain weave fabric made of multifilament yarn, (c) plain weave fabric made of multifilament (warp) and staple fiber yarn (weft), and (d) plain weave fabric made of a twisted multifilament yarn (from [24]).

of a sessile droplet as was discussed for the Wenzel or Cassie-Baxter cases.

3. Mesh openings act as pores allowing the liquid to penetrate the fabric in a direction perpendicular to the (macroscopic) surface.
4. Finally, the capillary system of multifilament yarn allows the liquid to penetrate and spread due to capillary effects. Due to this, lateral spreading may be more pronounced than would be the case for a planar substrate of identical surface chemistry.

An interesting observation related to the peculiar behavior of textiles was reported by Gao and McCarthy [25]. They used a silicone finish as hydrophobizing agent, which gave a contact angle of 110° on a flat surface. If applied to a fabric made from poly(ethylene terephthalate) (PET) microfiber yarn they observed contact angles of up to 170° . No further roughening of the fiber surfaces was carried out, the effect being brought about by the (existing) geometric structure of the fabric, which was composed of very fine fibers with diameters of only a few micrometers. While conventional yarns are composed of 30 to 40 filaments (fibers), a microfiber yarn of comparable titer¹ is composed by approximately 200 fine filaments and has a very pronounced surface structure in the micro-scale.

One important lesson is that measurement of the apparent contact angle of a sessile drop will not give a true measure of the wettability – or even surface free energy – of the fiber surface. The apparent contact angle will always be affected by microscopic surface property (i.e. fiber surface), macroscopic surface geometry (fabric), and capillary effects. In case of hydrophilic substrates the ‘sessile’ droplet will penetrate the porous textile, typically in seconds, and thus effectively prohibit the measurement. On a hydrophobic surface, the apparent contact angle will always differ from the ‘true’ contact angle on the fiber surface. Capillary effects occur even on hydrophobic substrates and compete with evaporation of the liquid.

In the context of the fundamental relation between surface topography and wetting behavior as modeled by Wenzel or Cassie and Baxter one has to consider the relevance of geometrical parameters for the complex porous and textured textile substrate. It is of interest in this context that a paper by Hsieh *et al.* [26], who studied the wetting of water and ethylene

¹ The quantity “titer”, often referred to as “fineness” or “linear density”, gives the weight of a yarn per unit length and is a measure of the thickness.

glycol on Si wafers which were coated with a perfluoroalkyl methacrylic co-polymer containing titanium dioxide nanoparticles, suggested that liquid repellence was mainly governed by the micropore structure, while mesopores – which obviously reflect in roughness factors – are unfavorable because they provoke capillary condensation.

It is not within the scope of the present chapter to derive appropriate – and maybe even analytical – models to describe the influence of geometrical parameters on the wetting behavior of textile fabrics. However, it is of interest at this point to mention two attempts to derive geometric parameters of the rough surfaces, which are more sensitive than the rather crude Wenzel factor to describe topographic peculiarities such as the two-scale roughness pattern of the Lotus leaf.

The well-known concept of fractal geometry was discussed in the context of wetting behavior as early as 1996 by the groups of Shibuichi and Onda [21,27] and Synytska and coworkers [28,29]. Different from a pure Euclidean approach, a rough surface is characterized by a dimension D_f , which is a real number greater than 2. This “fractal” dimension can be determined using a simple algorithm known as the “box-counting method”. Here, the surface profile, measured by laser profilometry, white-light interferometry (WLI), or atomic force microscopy (AFM), is approximated by a succession of boxes of size r and the number of boxes $N(r)$ is determined. This is repeatedly executed with decreasing box size and $\log N(r)$ plotted against $\log r$. It can be shown that $N(r)$ depends on r according to $N(r) \propto r^{-(D_f-1)}$. The logarithmic plot should therefore provide a linear dependence with slope $1 - D_f$ (cf. Figure 13.2). As Shibuichi *et al.* showed, $D_f > 2$ is obtained only in a range of r where the box approximation resolves the relevant topographic features [27]. If the parameters $l = \log r_{\min}$ and $L = \log r_{\max}$ denote the limits of this range, Shibuichi *et al.* derive a relation

$$\cos \Theta_f = \left(\frac{L}{l} \right)^{D_f-2} \cdot \cos \Theta_Y \quad (13.3)$$

between the apparent contact angle on the rough surface Θ_f and the Young contact angle from their measurements [27]. Experimental studies by Synytska *et al.* [29], who investigated the wetting behavior of textile fabrics decorated with Janus particles, indicated that super-hydrophobic behavior was observed only if D_f exceeded a certain threshold value.

Recently, a dimensionless quantity derived from the spatial frequency spectrum $PSD(f_x, f_y)$ (“power spectral density”) of a surface profile was proposed by Duparré and Coriand [30] and correlated with wetting properties

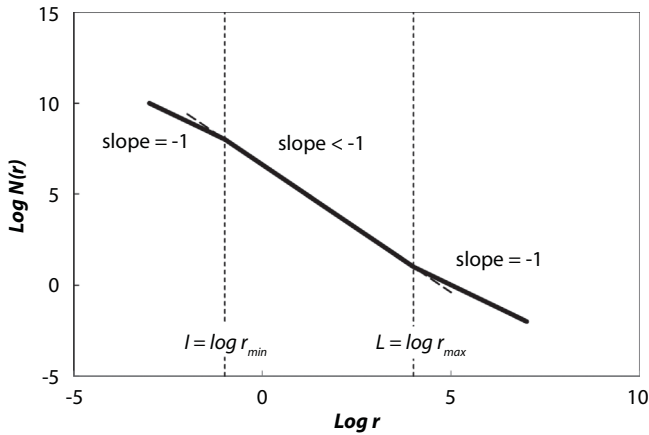


Figure 13.2 Determination of the fractal dimension of a surface using the box-counting method. The graph shows the number of boxes of size r necessary to approximate the measured surface profile. A planar surface would be precisely described independent of box size and the graph would be linear with slope -1. On a rough surface, the profile would be sufficiently resolved only within certain boundaries, which are denoted $l = \log r_{\min}$ and $L = \log r_{\max}$. The fractal dimension is derived from the slope within these boundaries.

of the respective surfaces. In a first step, $PSD(f_x, f_y)$ is calculated from the Fourier transform of the measured surface profile $z(x, y)$ through

$$PSD(f_x, f_y) = \lim_{L \rightarrow \infty} \frac{1}{L^2} |FT\{z(x, y)\}|^2 \quad (13.4)$$

where f_x and f_y are the spatial frequencies and L the size of the scanned area. Again, $z(x, y)$ can be determined by laser profilometry, white light-interferometry (WLI), or atomic force microscopy (AFM). As described in [30], transformation of $PSD(f_x, f_y)$ to give an amplitude spectrum according to

$$A(f) = 2 \sqrt{\pi \cdot \int_{f/\sqrt{1.5}}^{f\sqrt{1.5}} PSD(f') \cdot f' \cdot df'} \quad (13.5)$$

and subsequent integration

$$\kappa_B = \int_{\log(f_{\min} \times \mu m)}^{\log(f_{\max} \times \mu m)} A(f) \cdot f \cdot d(\log[f \times \mu m]) \quad (13.6)$$

provide a dimensionless factor κ_B characterizing the surface profile and its roughness. As Duparré and Coriand maintain, κ_B is sensitive to multi-scale roughness profile – such as exhibited by, e.g., the Lotus leaf – and indicates for surfaces of a given material the transition from hydrophobic to superhydrophobic behavior. Available data indicate that – regardless of chemical composition – a surface will only exhibit superhydrophobic behavior, if $\kappa_B > 0.4$ [30].

13.2.4 The Concept of Roughness Formation by Laser Irradiation

Many researchers try to mimic natural surface designs such as, e.g., the well-documented Lotus leaf, in order to attain roughness patterns in the nano- and micrometer scales and the fundamental conditions of the Cassie-Baxter state. A popular concept is to apply hybrid coatings of nanoparticles embedded in fluorinated or silane binders to textured technical surfaces in order to provide micro-/nano-roughness and low surface free energy simultaneously. An example of this concept is a hybrid coating for cotton fabrics based on silica nanoparticles and perfluorooctylated quaternary ammonium silane coupling agent (PFSC), which was reported by Yu *et al.* [31]. The water contact angle increased up to 145°, while oil repellence was also enhanced. An important issue with these types of hybrid coatings is their quite limited wash stability and abrasion resistance of particles and/or binders.

In the context of the scope of this chapter – to combine processes to attain surface roughness and chemical modification –, we shall discuss the use of laser radiation for the formation of roughness on a technical surface in the following paragraphs.

Various physical methods have been evaluated in recent years in reference to their potential to render metals and polymers rough in the nano- or micro-scale. In this context, high-power lasers have shown great potential. Already the first papers on laser ablation (or “dry etching”) of polymer films and photoresist by pulsed UV lasers (excimer lasers) in the early 1980s [32–34] reported the roughening of polymer surfaces as an unwanted side effect of irradiation. Later, Lazare *et al.* [35] studied the phenomenon in greater detail as a deliberate modification of PET film, while Bahnert and co-workers [36–39] developed the concept of controlled modification of the topography of polymer fibers.

The excimer laser irradiation of synthetic fibers made of highly absorbing polymers, e.g. aromatic polymers such as PET and aramids as well as aliphatic polymers such as polyamide-6 and -6.6 (PA), generates a

characteristic topography on fiber surfaces [38], which is exemplified in the SEM micrograph shown in Figure 13.3. The surface topography of excimer laser irradiated fibers can be described as a characteristic arrangement of ‘rolls’ at an average distance $\langle D \rangle$.

While Lazare *et al.* [35] proposed the formation of the rough surface as directly produced by the ablation process, a qualitative model suggesting a thermo-mechanical process was deduced from detailed analysis of the surface topography generated on fibers [38,39]. The major factors in this model are (I) the extremely strong absorption of the radiation with penetration depths of the order of $0.1 \mu\text{m}$, and (II) the time-scale involved in the energy deposition by a laser pulse of several nanosecond duration (see Table 13.1). In this time-scale, heat dissipation is considered to be negligible and hence a distinctive temperature profile is generated at the fiber surface. Under these far-from-equilibrium conditions the temperature at the surface of a PET fiber was estimated to be in excess of 2000 K [34].

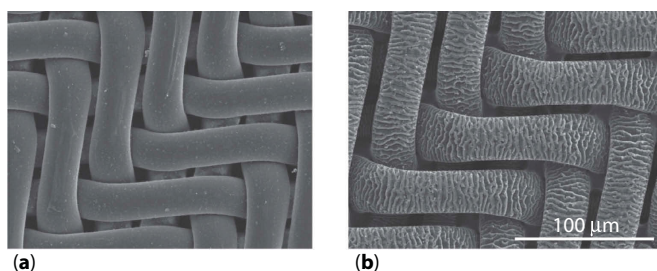


Figure 13.3 SEM micrographs of a technical fabric made of PET monofilaments as received (a) and laser irradiated at 248 nm (b). Irradiation was performed applying 10 pulses of 90 mJ/cm^2 fluence.

Table 13.1 Parameters describing the energy deposition by one excimer laser pulse at 248 nm and resulting effects to the substrate (PET).

absorption coefficient (PET at 248 nm)	$10^4 \text{ to } 10^5 \text{ cm}^{-1}$
penetration depth	$\sim 0.1 \mu\text{m}$
deposited energy per unit volume	$\sim 10 \text{ to } 20 \text{ kJ/cm}^3$
time-scale of energy deposition	$20 \text{ to } 30 \text{ ns}$
time-scale of bulk heating	0.1 s
estimated surface temperature	$\geq 2000 \text{ K}$
degradation temperature (PET)	$\sim 560 \text{ }^\circ\text{C}$

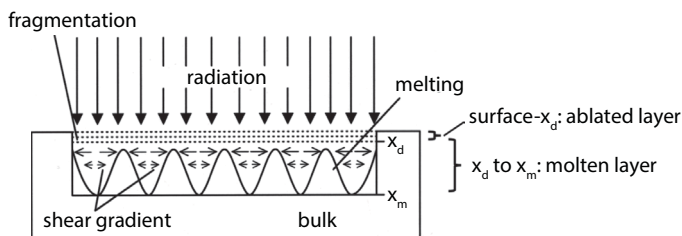


Figure 13.4 Schematic representation of the laser-induced processes according to the qualitative model proposed by Bahners and coworkers (cf. [36,38,39]).

Ablation will occur in the outermost surface layer, where the temperature is in excess of the degradation temperature T_d of the polymer, which is approximately 560 °C for PET. Where the temperature is lower than T_d but higher than the melting point T_m , a layer of molten material would form allowing relaxation of the very high internal stress fields present in commercial fibers and subsequent shrinkage (see sketch in Figure 13.4). A rough calculation gives a thickness of this layer of molten material of about 0.1 μm . In a “free-volume” theory of the polymer structure, this will only be possible in coordinated material transport leading to the self-organized formation of rolls. Accordingly, the overall orientation of the rolls is strictly perpendicular to the orientation of the fiber axis – ‘stress axis’ –, which is due to mechanical stress during the spinning process. Additional influential parameters in making rolls are the surface free energy and the viscosity of the molten material since the surface free energy has to overcome the viscous forces. It is notable that the model would predict the formation of random “pillars” on films with low orientation and a wavy structure on oriented films, which is consistent with the observations of Lazare *et al.* [35]. This was shown by experiments using partially oriented PET fibers and films as well as fibers made of a polyurethane elastomer [38,39].

Predicted by this physical model of the process and confirmed by experimental results, the mean roll distance $\langle D \rangle$ is governed by the material as well as process parameters. The material defines the extent of absorption at the given laser wavelength as well as the orientation of the macromolecules. The main laser parameter on the other hand is the number of laser pulses applied NP . As a matter of fact, the laser fluence, i.e. pulse energy per unit area, is of little influence.

At a given wavelength, the dependence of the mean roll distance $\langle D \rangle$ on NP , in all investigated cases, could be described by the logarithmic expression

$$\langle D \rangle = K_1 \cdot \log NP + K_2 \quad (13.7)$$

Table 13.2 Mean “roll distance” as a measure of the laser-generated surface topography on the filaments of the PET multifilament yarn (warp yarn).

No. of Laser Pulses	Mean Roll Distance [μm]
1	–
2	~ 1.0
5	1.4
10	1.8 – 1.9
15	2.4 – 2.5
20	2.5

where $\langle D \rangle$ was taken as the mean value over 10 to 20 rolls and K_1 and K_2 are constants for given conditions [39]. Characteristically $\langle D \rangle$ exhibits a strong dependence up to ten pulses applied with a saturation above approximately 20 pulses. Related dimensions for the exemplary PET fibers shown in Figure 13.3 are summarized in Table 13.2. The order of magnitude can be considered typical for the average technical PET fiber. K_1 is weakly dependent on laser fluence, but is sensitive to the given penetration depth, i.e. to absorption coefficient and wavelength of the laser and specific fiber properties (e.g. draw ratio as mentioned before). In this numerical expression, K_2 is equivalent to the roll distance $\langle D \rangle$ after the first laser shot.

Already in their early paper, Lazare *et al.* [35] studied the effect of the laser-induced formation of surface roughness on the wettability of PET film. They showed that depending on the crystallinity of the film, the roughness pattern affected contact angle, contact angle hysteresis, and the shape of the triple line.

An interesting observation, which is of relevance to this chapter, was reported by Kietzig *et al.*, who studied the wetting behavior of metal alloys treated with a pulsed femtosecond Ti:sapphire laser emitting at 800 nm [40]. Kietzig *et al.* reported a two-scale nano-/micro-structure, which initially rendered the surface superhydrophilic. However, after storage in air, nitrogen, or carbon dioxide for 10 to 20 days these samples turned superhydrophobic with contact angles in excess of 150° . Simultaneously, an increasing concentration of carbon was detected on the surface structures, which Kietzig *et al.* related to decomposition of carbon dioxide into zero valence carbon.

In the context of this chapter, however, Kietzig's observation indicates the potential of *deliberate* post-treatment of surfaces, which were artificially roughened.

13.2.5 Introducing Low Surface Energy to the Roughened Surface

Only few authors have reported on laser-based surface roughening and subsequent post-treatments to decrease SFE. Baldacchini *et al.* [41] coated the surfaces of silicon wafers, which had been roughened by Ti:sapphire femtosecond laser irradiation, with a layer of fluoroalkylsilane molecules to produce superhydrophobic silicon surfaces. The wetting behavior of the resultant two-scale surface topography in nano- and micro-scale could be controlled to some degree by the laser parameters.

An important aspect of the concept of roughening step followed by chemical modification is that the delicate topography of a nano-/micro-rough surface must not be affected by, e.g., the deposition of hydrophobic or oleophobic finish. Therefore, grafting or thin-layer deposition processes are more favorable. Physically driven processes such as plasma-based or UV induced grafting have the additional advantage of minimal use of chemicals for surface modification.

Making use of this concept, Wagterveld *et al.* modified epoxy-based photoresist (SU-8) by excimer laser irradiation (248 nm) and subsequent plasma-polymerization of a hydrophobic hexafluoropropene layer of only 30 nm thickness [42]. The surfaces showed water contact angles of approximately 165° and contact angle hysteresis values below the measurement limit. An interesting observation was that the plasma-polymerized layer – besides having low SFE – stabilized nano-scaled debris generated by the excimer laser process. According to Wagterveld *et al.* the nano-roughness of the debris was instrumental for the ultralow hysteresis of these surfaces. This latter observation is of high relevance for other laser-treated polymers, as the formation of debris with high carbon content namely in the case of aromatic polymers such as, e.g., PET and p-aramid is well known (see, e.g., [37]).

Though not employing laser for the initial roughening step, two additional papers shall be mentioned here because of their relevance to the concept. Tsuij *et al.* [43] reported super oil-repellent aluminum surfaces, where – in a first step – surface roughness was attained by anodically oxidizing plate material. The resulting super-wetting surface was rendered super-repellent by immersing the plate subsequently in fluorinated

monoalkylphosphates of different chain lengths (F_{m+1} -MAP, with $m = 7$ and 9). As far as oil repellence is concerned, best results are reported from F_8 -MAP with oil contact angles in excess of 150° and vanishing contact angle hysteresis.

Coulson *et al.* [44] report high repellence towards polar as well as non-polar liquids from micro-rough poly(tetrafluoroethylene) (PTFE) surfaces. In a first step, the samples were roughened by air plasma treatment, after which a thin-layer was polymerized from 1H,1H,2H,2H-heptadecafluorodecyl acrylate vapor in the same apparatus.

As a final remark, the concept of employing a post-treatment to increase SFE was applied to achieve super-*hydrophilic* surfaces, too. Bahnert *et al.* [45] report super-wetting properties of acrylate surfaces, which were roughened by photo-induced micro-folding, and subsequently modified by plasma-based grafting of p-toluenesulfonic acid (p-TSA) or by UV-induced grafting of the methacrylated poly(ethylene glycol) PEG300MA. Photo-induced micro-folding is based on a two-step UV curing process of a thin acrylate layer applied to substrates such as films, coated fabrics, or tiles (cf. [45,46]). In a first step, the acrylate is treated by vacuum ultraviolet (VUV) radiation and subsequently cured by conventional broadband UV irradiation. VUV photons are strongly absorbed and the relevant penetration depths are less than 100 nm. This results in a very fast curing of the thin surface layer on top of the still liquid bulk in the first step. Due to shrinkage occurring during polymerization and cross-linking, a wavy surface topography with pronounced roughness and small peak-to-peak distances is generated ('micro-folding'). This structure is frozen through the subsequent bulk curing. Surface analysis showed that plasma-aided grafting resulted in the lowest water contact angles and extremely wetting surfaces. Following the photo-chemical grafting of PEG300MA, on the other hand, the lowest contact angles obtained were of the order of 20° . In both cases, excellent stability of the layer and its wetting behavior was found.

13.3 Application of Combined Laser and Photo-chemical Modifications to Technical Textiles

The objective of the following sub-sections is to exemplify the synergetic effect of the combined processing by laser-induced surface roughening and subsequent UV-induced modification of surface chemistry and summarizes experimental results from earlier studies of the authors. The first example (sub-section 13.3.1) concerns the increase of water repellence of

technical fabrics made of PET and p-aramid (Kevlar®) while the second example (sub-section 13.3.2) is focused on highly oil repellent PET fabrics.

In both cases surface roughening was effected by irradiation with pulsed excimer laser emitting at 248 nm (Lambda LPX 215 iCC and Coherent COMPexPRO 50, respectively). This wavelength was chosen because of strong absorption in the spectral range from 220 to 250 nm by these aromatic polymers (cf. [18,39]). The photo-chemical modification of surface chemistry followed the concept of (a) finishing the textile samples with appropriate – i.e. hydrophobic or oleophobic – substances by conventional padding or simple immersion, (b) drying, and (c) irradiation using monochromatic (excimer) or broadband UV lamps as described in [16,18,19]. With regard to experimental details we refer to the original papers cited in the following sub-sections.

A comment has to be made on the methods to characterize wettability and the effect of the studied combined surface modifications. The conventional as well as convenient procedure is to measure the contact angle of specific liquids, which also allows to calculate the surface free energy (SFE) – and its polar and dispersion components - making use of formalisms such as Neumann or Owens-Wendt. It is worth mentioning that a critical survey of these methods was recently published by Etzler [47]. As has been discussed in section 13.2.3, texture, porosity, and capillarity of textile substrates have notable effects on the initial wetting behavior of a droplet and the dynamics of wetting as well as on the choice of an appropriate method to characterize the wettability of a textile. The authors refer to [24] for a detailed discussion on the effects of textile geometry and the significance of experimental methods for wettability characterization. Contact angles on textile substrates can be useful quantities for *comparative* measurements in order to characterize the effects of surface modifications, if the textile is distinctly hydrophobic and all other parameters, such as, e.g., micro-roughness, were not affected. The wide variation in the contact angles of droplets of water (in fact an aqueous dyestuff solution) on a technical fabric is clearly exemplified in the photograph shown in Figure 13.5. Experimentally, it is essential to avoid accidental distortions of the fabric. If a sample is rather wettable, the observation of the dynamics of wetting by means of drop penetration tests can be more informative (and significant). Drop penetration tests – characterizing either the penetration time, or the occurrence of penetration at all - are useful for comparative measurements meant to characterize the effects of fabric finishing, fiber surface modifications, etc. Various drop penetration tests such as the AATCC 118 oil repellence test rely on characterization by “repellency grades” ranging from 0 (fully wetting) to 8 (fully repellent). Obviously, differentiation is

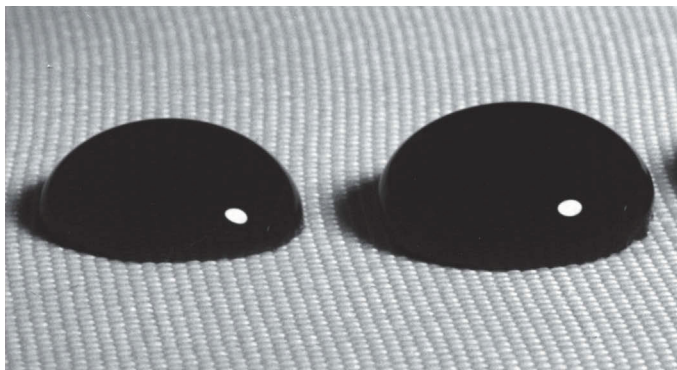


Figure 13.5 Droplets of aqueous dyestuff solution as employed for the TEGEWA drop penetration test on a hydrophobized PET fabric. The photographs clearly show a significant difference in the contact angles of the two droplets, which might be due to the clearly visible fabric distortion as well as local variations in microscopic features of the fabric geometry, i.e. pore sizes and capillary system.

limited. A quantitative measurement is based on the measurement of the time elapsed, until a defined droplet totally penetrates the fabric. The value determined is called “drop penetration time”. In the so-called TEGEWA² test, the droplet has a volume of 0.05 ml and is dropped from a height of 40 mm onto the sample. Mostly, an aqueous dyestuff solution is used instead of pure water for better visualization. In principle, the same elementary processes of penetration and spreading occur in the TEGEWA procedure as with contact angle measurements, and the recorded penetration time is determined by all contributing parameters at the same time.

13.3.1 Increasing Water Repellence of Technical Fabrics Made of PET and Aramids

For the majority of technical fabrics, high liquid repellence is seen in the context of, e.g., easy removal of products from transporting belts in the food or tobacco industry as well as reduction of adhesion of, e.g., dirt, particles, or process byproducts. The effect of high water repellence can be more complex, however, for very critical applications. An important example is the bullet-proof vests, which are constructed from fabric multi-layers

² TEGEWA is the German association of manufacturers of finishing agents, tanning agents and washing agents (TEGEWA = ‘TExtilhilfsmittel, Gerbstoffe, WAschrohstoffe’)

made of p-aramid. The reason to demand high water repellence is twofold in this case, one being the tendency of the fiber to take up water from the environment – common to polyamides – with the long-term danger of hydrolysis and loss in tensile strength, and second a water film on the fibers acts as a lubricant for a projectile and will significantly reduce the performance. In fact, standard test procedures by police forces include ballistic tests on both wet and dry vests.

In the context of these practical requirements the concept of combined laser and photo-chemical modifications has been applied in earlier studies to typical plain-weave fabrics made of PET and p-aramid (Kevlar®) and has been evaluated in view of high water repellence. Some of these results are unpublished as yet and reported for the first time, others were reported as early as in 2001 by Bahnert *et al.* [48].

As has been mentioned, surface roughening was effected by irradiation with a pulsed excimer laser emitting at 248 nm (Lambda LPX 215 iCC). In a first step, pulse energy per unit area – generally termed fluence – and number of pulses until (a) occurrence of the roll-structure and (b) saturation of the roll distance $\langle D \rangle$ were evaluated and optimized for each fiber polymer. Good results were achieved in both cases with a fluence of 90 mJ/cm² and 10 to 20 pulses. In most cases, samples were irradiated on both faces. SEM micrographs shown in Figure 13.3 and the geometric data given in Table 13.2 are representative for the generated surface topographies.

For the subsequent photo-chemical modification of surface chemistry, samples were immersed in 1,5-hexadiene, diallylphthalate (DAP), or perfluoro(4-methylpent-2-ene) (PFMP), dried and irradiated. A monochromatic (excimer) lamp emitting at 222 nm was employed and the irradiation performed for 5 or 10 min in an inert atmosphere. Samples were irradiated on both faces in all cases. In general, the samples were extracted for 4 hours in water/methanol and further 4 hours in petroleum ether before the treatments and washed after the photo-chemical modification in order to remove uncrosslinked residuals.

Drop penetration times of water droplets (in fact an aqueous dye-stuff solution) dropped onto the technical PET fabric are summarized in Table 13.3, the drop penetration characterized according to the TEGEWA procedure.

Various conclusions can be drawn from the table. With a slow drop penetration (elapsed time 80 s), the untreated fabric can be considered only modestly hydrophobic. One has to take into account that (a) the water contact angle on untreated PET film is of the order of 72° and (b) that capillary effects can be expected to be significant in the observed behavior.

Table 13.3 Water wetting behavior of technical PET fabrics following (a) laser-roughening, (b) photo-chemical modifications using different reactive media, and (c) combined laser roughening and photo-chemical modification. Both laser and photo-chemical modifications were performed on both faces of the fabrics. Water wettability was characterized by measurement of the drop penetration time of an aqueous dyestuff solution according to the TEGEWA procedure (see text).

Process	Condition of Laser Treatment	UV Exposure [min]	Drop Penetration Time [s]
untreated	-	-	80 ± 7
a) laser treatment (248 nm, 90 mJ/cm ²)	10 pulses	-	145 ± 5
	20 pulses	-	215 ± 10
b) photo-chemical modification with 1,5-hexadiene	-	5	185 ± 3
b) photo-chemical modification with PFMP	-	5	276 ± 10
	-	10	605 ± 13
c) laser treatment and subsequent photo-chemical modification with 1,5-hexadiene	10 pulses	5	649 ± 10
	20 pulses	5	677 ± 3
c) laser treatment and subsequent photo-chemical modification with PFMP	10 pulses	5	1371 ± 23
	10 pulses	10	1542 ± 15
	20 pulses	5	2040 ± 18
	20 pulses	10	2052 ± 25

The data show that the fabric becomes only slightly more repellent, if treated by the laser alone. If – for simplicity - a behavior following the formalism of the Wenzel equation is assumed, this is in full agreement with the prediction of the behavior of the apparent contact angle, if the Young contact angle is of the order of 90°. With $\cos\Theta_Y \rightarrow 0$, roughening will not yield significant effect towards repellence.

On the other hand, a photo-chemical treatment alone results in a decrease in SFE with the corresponding increase in contact angle. This has

consequences on initial wetting on the macroscopic surface as well as penetration into the pore system. However, it is rather unclear and difficult to assess with these technical samples, as to how far the inner surfaces of the multifilament yarn and the resulting capillary effects are affected by the treatment. Here, penetration of the reactive agent during the finishing step (itself governed by wetting behavior) and penetration of the UV radiation are important factors. Additionally, the graft-copolymerization may lead to layer formation, which obscures the pore system, especially following a very long UV exposure. The observed increase in drop penetration time may then well be an effect of obscured macro-, mesopores, and capillaries rather than “true” wetting effects.

Irrespective of the above discussion, the data summarized in Table 13.3 impressively show the synergetic effect of the combined treatment, which amplifies the effects of the individual treatments. This is also graphically shown in Figure 13.6. Whereas, e.g., a laser treatment with 10 pulses approximately doubles the drop penetration time, and functionalization with 1,5-hexadiene alone triples drop penetration time, the subsequent execution of both steps results in an eight-fold penetration time to more than 10 min. Using PFMP, drop penetration is not observed even after 35 min. It should be noted that the drop penetration behavior over this long period of time might be influenced by evaporation effects. Many

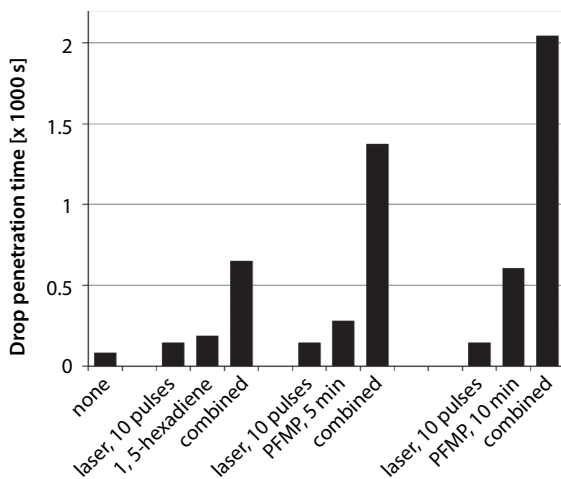


Figure 13.6 Drop penetration times according to the TEGEWA procedure on PET fabrics, which were laser irradiated (10 pulses of 90 mJ/cm²) and subsequently photochemically modified using 1,5-hexadiene and PFMP. UV exposure for chemical modification was 5 min in the case of 1,5-hexadiene, and 5 and 10 min in the case of PFMP.

researchers, therefore, stop the observation of the droplet in a TEGEWA measurement after 5 min (cf. [24]).

An interesting effect was observed when samples were *laser*-irradiated only from the front face. In spite of the photo-chemical modification being performed from both sides as before, this created a difference in wettability (gradient) of front and back faces. As a result, the droplet positioned on the hydrophobic front face remains unchanged for a certain time before being absorbed into the textile structure and is transferred to the more hydrophilic back face. At no time during this process does the droplet spread laterally on the front face.

This is illustrated in the context of data recorded on the p-aramid (Kevlar®) fabrics, which are summarized in Table 13.4. The first observation is that, again, extremely high water repellence is achieved by the combined process of laser-induced surface roughening and subsequent UV-induced modification of surface chemistry. The photo-chemical modification used

Table 13.4 Water wetting behavior of technical p-aramid fabrics following (a) laser-roughening, (b) UV-induced grafting of perfluoro(4-methylpent-2-ene) (PFMP) and (c) combined laser roughening and photo-chemical modification. Water wettability was characterized by measurement of the drop penetration time of an aqueous dyestuff solution according to the TEGEWA procedure (see text).

Process	Condition of Laser Treatment	UV Exposure [min]	Drop Penetration Time [s]
untreated	-	-	50 ± 4
a) laser treatment (248 nm, 90 mJ/cm ²)	10 pulses on front face	-	162 ± 5
	10 pulses on both faces	-	195 ± 10
b) photo-chemical modification with PFMP	-	5	1157 ± 50
c) laser treatment and subsequent photo-chemical modification with PFMP	10 pulses on front face	5	2601 ± 75
	10 pulses on both faces	5	> 3600*

* Measurement was stopped (see text)

PFMP as the reactive medium in this case. The data show that if the sample had been irradiated in both modification steps from both faces, the droplet was stable on the fabrics for one hour, after which the measurement was stopped. If, on the other hand, fibers were roughened only on the front face of the fabric, the droplets were stable for rather long periods of time (more than 40 min), after which they penetrated spontaneously

At this point, the paper by Wagterveld *et al.* shall be referred to once again who modified epoxy-based photoresist (SU-8) by excimer laser irradiation (248 nm) and subsequent plasma-polymerization of a hydrophobic hexafluoropropene layer [42] (see sub-section 13.2.5). Wagterveld *et al.* emphasized the role of nano-scaled debris generated by the excimer laser process. According to Wagterveld *et al.* the nano-roughness of the debris was instrumental for the ultralow contact angle hysteresis of these surfaces. The formation of debris with high carbon content in the case of aromatic polymers such as, e.g., PET and p-aramid was observed already in the first studies on laser-induced roughening of aromatic fibers (see, e.g., [31]) and was observed also in the experiments reported here.

Therefore, it was of interest to study the effect of debris formed on the p-aramid fibers on the wettability of the fabrics by determining drop penetration time on laser-treated samples, which were subjected to an extensive extraction procedure in order to remove as much of the debris as possible. In order to provoke debris formation, the samples were irradiated at significantly higher fluence (500 vs. 90 mJ/cm²) and pulse number (50 vs. 10). For cleaning, the samples were extracted for 4 hours in water/methanol and further 4 hours in petroleum ether. The effect of debris removal is summarized in Table 13.5 and can be described as rather significant. The drop penetration time on samples which were treated only by the laser dropped from 45 to 60 min to only 2 min after cleaning. Compared to the untreated fabrics this is only a very small increase in repellence, which may reflect the shallow – in comparison to the effect on the PET fibers – features of the surface topography (cf. Figure 13.7). Only following the combined treatment the effect on the cleaned fabrics is still quite prominent, although smaller than on samples where the debris was still in place.

13.3.2 Increased Oil Repellence of Technical PET Fabrics

The potential of discussed approaches for high *oil*-repellence of technical fabrics made of PET and its impact in the field of aerosol filtration was evaluated in a recent study by the authors [49]. The objective of this study was to assess the performance of technical fabrics as drainage media in compressed air filters. Drainage layers are designed to take up the oil from

Table 13.5 Effect of carbon-rich debris produced by the laser irradiation of p-aramid fabrics at 248 nm on their water wetting behavior. Data give the drop penetration time of an aqueous dyestuff solution measured according to the TEGEWA procedure (see text). For cleaning, the samples were extracted for 4 hours in water/methanol and further 4 hours in petroleum ether.

	No Cleaning After Laser Treatment	Extraction After Laser Treatment
laser irradiation (10 pulses, 90 mJ/cm ²)	1 4 min	-
laser irradiation (50 pulses, 500 mJ/cm ²)	45 60 min	2 min
laser irradiation (50 pulses, 500 mJ/cm ²) and subsequent graft-copolymerization of PFMP	> 60 min *	30 ... 40 min

* Measurement was stopped (see text)

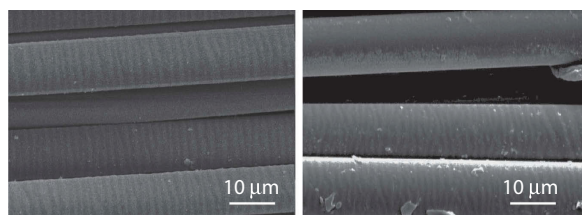


Figure 13.7 SEM micrographs of yarn made of p-aramid (Kevlar®) after laser irradiation (248 nm). The yarn was treated by application of 10 pulses at 90 mJ/cm² and analyzed without any further cleaning at various places. The micrographs indicate shallow surface features (in comparison to PET fibers, cf. Figure 13.3.) as well as residual particulates, which are assumed to be the debris generated by the laser-induced processes.

neighboring filter layers and transport it out of the airstream in order to keep the filter layer from blocking and secure a low pressure drop over the whole cartridge. While conventionally all layers of filter cartridges are made of non-wovens, the significant advantage of using woven fabrics composed of multifilament yarn for drainage layers is the auxiliary effect of capillary forces occurring in the yarn (cf. section 13.2.2).

Given its favorable material properties as, e.g., extremely strong absorption and high efficiency for bond breaking and radical generation, PET is a good candidate for the described photon-based processes for surface modification. As before an excimer laser treatment at 248 nm (Coherent COMPexPRO 50) was employed for surface roughening of the PET fibers. The number of applied pulses was 2, 10 or 20, and fabrics were irradiated from both faces. The pulse repetition rate was 1 Hz, and the fluence was

100 mJ/cm² throughout. Based on earlier work (cf. [17]), the subsequent photo-chemical treatment was UV induced grafting of 1H,1H,2H,2H-perfluoro-decyl acrylate (PFDA). PFDA was expected to be favorable for the oleophobic grafting modification on the basis of its terminal CF₃ groups. Also, a terminal double bond promotes the photo-induced grafting reaction. A broadband Hg lamp with a main emission band between 200 and 300 nm (UVACUBE 2000, Dr. Hönle, Munich, Germany) was used as the light source [49].

The effect of the excimer laser irradiation on fiber surface topography is exemplified by the SEM micrographs compared in Figure 13.8 (from [49]). As can be taken from the micrograph Figure 13.8a, the roughening effect occurs prominently on the fine and highly drawn fibers of the multifilament yarn, but is less pronounced on the thick monofilaments of the warp system. The effect is attributed to the different spinning conditions during fiber manufacture, which result in a higher macromolecular orientation and crystallinity of these “technical” fibers. The micrographs also mirror the high control of the attained topography by the number of applied laser pulses as exemplified by Figures 13.8b, 13.8c, and 13.8d.

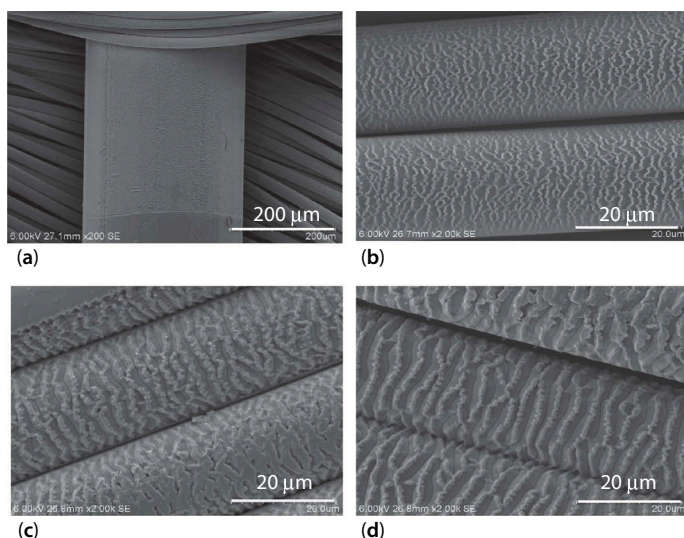


Figure 13.8 SEM micrographs of the PET drainage fabric after excimer laser irradiation at a wavelength of 248 nm and a laser fluence of 100 mJ/cm² in all cases (taken from Bahners *et al.* [49]). The micrographs (a) and (c) show the fabric following treatment with 10 pulses. The images indicate that roughening occurs prominently on the fibers of the highly oriented multifilament yarn, in contrast to the thick monofilaments, which are typically less drawn during manufacture. The micrographs (b) and (d) show the fibers of the multifilament yarn following treatments with 2 and 20 pulses, respectively.

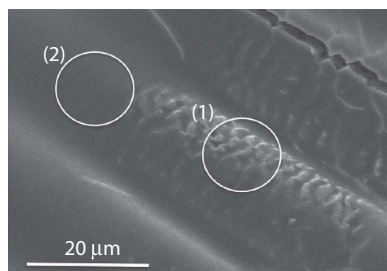


Figure 13.9 SEM micrograph of the PET fabric after combined laser and photo-chemical treatments. The layer formation following UV-induced copolymerization of PFDA is clearly seen. While the delicate laser-generated surface structure is conserved in certain places (1), it is obscured by a poly-PFDA layer elsewhere (2). The inhomogeneity of the treatment can be attributed to uneven take-up of the reactive medium in the course of the photo-chemical treatment.

SEM analysis after subsequent photo-chemical modification revealed that the process induces graft-copolymerization of PFDA and indeed affects the surface morphology to a certain degree and partly obscures the laser-generated surface pattern (Figure 13.9). The important property of PFDA is its absorption behavior in the UV range. Available data indicate that PFDA is nearly transparent in the spectral range above 220 nm. As the employed broadband lamp emits approximately from 200 to 300 nm, a certain part of the radiation is absorbed by the reactive medium and apparently induces cross-linking.

Oil contact angle measurements nevertheless indicated the synergetic effect of these two surface treatments. These measurements were performed following the sessile drop method using the industrial mineral oil Shell Corena D46. In view of the relevance for the underlying problem of pressurized air filtration, the tests concentrated on the wetting behavior of this highly refined mineral oil commonly used in compressors and vacuum pumps. The measured equilibrium contact angles summarized in Table 13.6 (from [49]) clearly show the increase in oil repellence following the grafting of PFDA as well as the synergetic effect of micro-roughening and grafting. The application of PFDA alone raises the contact angle of the oil on the previously wetting substrate to close to 100°. Making use of the combined effect of laser-induced surface roughening and subsequent grafting a highly oleophobic surface is created with oil contact angles as high as 130°. Obviously, the effect of the laser-generated patterns is significant in spite of the coverage by the grafted PFDA. This is especially noticeable in the long-term stability of the droplet, which does not spread

Table 13.6 Oil contact angle on technical PET fabric following UV initiated graft-copolymerization and combined laser roughening and subsequent graft-copolymerization. Test liquid was the industrial mineral oil Shell Cordena D46 commonly used in compressors and vacuum pumps (data from [49]).

	Oil Contact Angle[°]	Note
untreated fabric	spreads/ penetrates	
photo-grafting of PFDA	97 ± 17	droplet is semi-stable and has penetrated the fabric after 24 hours
laser irradiation (10 pulses) and subsequent photo-grafting of PFDA	131 ± 7	droplet is stable for more than 24 hours

or penetrate over a period of 24 hours. On all modified cases, pronounced pinning of the oil droplets was observed, with no roll-off up to 90° tilting angle. Experiments with a significant increase in droplet volume to 24 µl, and accordingly increased gravitational forces, provoke only slow (viscous) motion of the droplets and no real roll-off. Obviously, the contact angle hysteresis is high.

Results from filtration experiments (a detailed description is found in [49]) impressively show that the increased oil repellence improved the drainage efficiency significantly. The pressure drop after operation for one hour is reduced by approximately 10 % following a purely chemical surface modification and approximately 25 % following laser roughening and subsequent photo-grafting of PFDA. As would be expected from the rather small effect of surface roughening *without* chemical modification, the laser treatment alone could not increase drainage efficiency.

13.4 Summary

In the context of an increasing demand for application-related functionalities rendering technical textiles (super-)hydrophobic or oleophobic has been one of the major topics of research and development in recent years. Besides the modification of surface chemistry in order to

minimize the surface free energy, biomimetic concepts have shown the important role of surface roughness. In this framework several attempts to apply *both* types of surface modifications – i.e. chemical modification of surface *and* modification of surface topography – in a combined processing concept were reported. Based on the concepts of Wenzel or Cassie-Baxter, super- or at least high repellence can thus be achieved by (a) the increase of liquid repellence by chemical surface modification to reduce SFE and subsequent roughening, or (b) by introducing surface roughness and subsequent chemical modification of the rough surface to reduce SFE.

Given the increasing interest in physical processes with low consumption of chemicals, favorable environmental issues, and high controllability, the scope of this chapter was to give a short overview of fundamentals of combined photo-chemical and laser surface modifications and to exemplify the attainable effects by data obtained from experiments conducted by the authors.

Reported examples cover the increase of water repellence of technical fabrics made of PET and p-aramid and the concept of highly oil repellent PET fabrics. In all cases the experiments impressively showed the synergistic effect of the combined treatment, which amplified the effects of the individual treatments.

It should be emphasized that in all these considerations, one has to keep in mind how the characteristic and complex geometry of textile substrates affects the wetting behavior of a droplet. Liquid penetration and (apparent) spreading will *always* be governed simultaneously by microscopic – i.e. fiber – surface chemistry and roughness, by macroscopic surface properties – fabric texture –, but also by micro- and mesopores defined by fabric construction and the capillary system of the yarn(s) composing the fabric. An apparent contact angle will always mirror *all* these factors. Given this, the effects of surface modification techniques are not necessarily uniform, i.e. affect *all* surfaces of a porous textile in the same way. Photo-chemical grafting or laser roughening will, for instance, not necessarily affect the inner surfaces of a yarn, which define the wetting within the capillary system. In contrast, photo-chemical graft-copolymerization might obscure part of the pores and hinder water penetration into yarn capillaries. Thus, the treatment will reduce capillary effects as well as surface free energy of the outer, i.e. exposed, surfaces at the same time. In the context of these considerations, it can be concluded from the reported data that combined treatments have a marked potential for synergies and allow to attain significant overall effects.

Acknowledgement

Part of the reported research was conducted in the frame of the operational program “Regionale Wettbewerbsfähigkeit und Beschäftigung” of the State of Northrhine-Westfalia (NRW) and was funded by the European Regional Development Fund ERDF and the program Hightech.NRW under project no. 28 03 641 02.

References

1. T. Bahn timers, T. Textor, K. Opwis and E. Schollmeyer, Recent approaches to highly hydrophobic textile surfaces, in: *Superhydrophobic Surfaces*, A. Carré and K.L. Mittal (Eds.), pp.413–437, CRC Press, Boca Raton, FL (2009).
2. G.E. Fogg, Diurnal fluctuation in a physical property of leaf cuticle, *Nature* 154, 515–515 (1944).
3. R.N. Wenzel, Resistance of solid surfaces to wetting by water, *Ind. Eng. Chem.* 28, 988–994 (1936).
4. A.B.D. Cassie and S. Baxter, Wettability of porous surfaces, *Trans. Faraday Soc.* 40, 546–551 (1944).
5. A.B.D. Cassie and S. Baxter, Large contact angles of plant and animal surfaces, *Nature* 155, 21–22 (1945).
6. R.J. Good, Contact angle, wetting and adhesion: A critical review, in *Contact Angle, Wettability and Adhesion*, K.L. Mittal (Ed.), pp. 3–36, VSP, Utrecht (1993).
7. H. Kamusewitz and W. Possart, The static contact angle hysteresis and Young's equilibrium contact angle, in *Contact Angle, Wettability and Adhesion*, Vol 4, K.L. Mittal (Ed.), pp. 101–114, CRC Press, Boca Raton, FL (2006).
8. N. Yu, W. Shi, B. Zhang, G. Su, J. Feng, X. Zhang, S. Wei and H. Yu, Occurrence of perfluoroalkyl acids including perfluorooctane sulfonate isomers in Huai River Basin and Taihu Lake in Jiangsu Province, China, *Environ. Sci. Technol.* 47, 710–717 (2013).
9. B. Baghaei and F. Mehmood, Alternatives to Conventional Fluorocarbon based Soil Resistant Treatment for Automotive Interior Textiles-An Evaluative Study, M.Sc. thesis, University of Borås, Borås, Sweden (2011). <http://bada.hb.se/bitstream/2320/9247/1/2011.7.5.pdf>
10. S. Edge, S. Walker, W.J. Feast and W.F. Pacynko, Surface modification of polyethylene by photochemical grafting with 2-hydroxyethylmethacrylate, *J. Appl. Polym. Sci.* 47, 1075–1082 (1993).
11. K. Yamada, H. Tsutaya, S. Tatekawa and M. Hirata, Hydrophilic and adhesive properties of polyethylene plates grafted with hydrophilic monomers, *J. Appl. Polym. Sci.* 46, 1065–1085 (1992).

12. B. Ranby and F.Z. Guo, "Surface-photografting": New applications to synthetic fibers, *Polym. Adv. Technol.* 5, 829–836 (1994).
13. G.G. Bogoeva, N.Y. Pimonenko and G. Petrov, Photo-induced acrylamide graft polymerization onto polyamide-6, *Textile Res. J.* 63, 51–57 (1993).
14. E. Uchida, Y. Uyama and Y. Ikada, Grafting of water-soluble chains onto a polymer surface, *Langmuir* 10, 481–485 (1994).
15. M. Ulbricht, H. Matuschewski, A. Oechel and H.G. Hicke, Photo-induced graft polymerization surface modifications for the preparation of hydrophilic and low-protein-adsorbing ultrafiltration membranes, *J. Membrane Sci.* 115, 31–47 (1996).
16. D. Praschak, T. Bahnners and E. Schollmeyer, Excimer UV lamp irradiation induced grafting on synthetic polymers, *Appl. Phys. A* 71, 577–581 (2000).
17. T. Bahnners, T. Textor, K. Opwis and E. Schollmeyer, Recent approaches to highly hydrophobic textile surfaces, *J. Adhesion Sci. Technol.* 22, 285–309 (2008).
18. T. Bahnners, T. Textor and E. Schollmeyer, Photon-based processes for the surface modification of synthetic fibers, in: *Polymer Surface Modification: Relevance to Adhesion*, Vol. 3, K. L. Mittal (Ed.), pp. 97–124, CRC Press, Boca Raton, FL (2004).
19. T. Bahnners, K. Opwis, T. Textor and E. Schollmeyer, Highly hydrophobic textile surfaces following thin-layer deposition, in: *Contact Angle, Wettability and Adhesion*, Vol. 4, K. L. Mittal (Ed.), pp. 307–320, CRC Press, Boca Raton, FL (2006).
20. T. Onda, S. Shibuichi, N. Sato and K. Tsuji, Super-water-repellent fractal surfaces, *Langmuir* 12, 2125–2127 (1996).
21. S. Shibuichi, T. Yamamoto, T. Onda and K. Tsujii, Super water-repellent surfaces resulting from fractal structure, *J. Colloid Interface Sci.* 208, 287–294 (1998).
22. M. Miwa, A. Nakajima, A. Fujishima, K. Hashimoto and T. Watanabe, Effects of the surface roughness on sliding angles of water droplets on superhydrophobic surfaces, *Langmuir* 16, 5754–5760 (2000).
23. A. Carré and K.L. Mittal (Eds.), *Superhydrophobic Surfaces*, CRC Press, Boca Raton, FL (2009).
24. T. Bahnners, The "dos" and "don'ts" of wettability characterization in textiles, *J. Adhesion Sci. Technol.* 25, 2005–2021 (2011).
25. L. Gao and T.J. McCarthy, "Artificial Lotus Leaf" prepared using a 1945 patent and a commercial textile, *Langmuir* 22, 5998–6000 (2006).
26. C.-T. Hsieh, J.-M. Chen, R.-R. Kuo, T.-S. Lin and C.-F. Wu, Influence of surface roughness on water- and oil-repellent surfaces coated with nanoparticles, *Appl. Surf. Sci.* 240, 318–326 (2005).
27. S. Shibuichi, T. Onda, N. Satoh and K. Tsuji, Super water-repellent surfaces resulting from fractal structure, *J. Phys. Chem.* 100, 19512–19517 (1996).
28. A. Synytska, L. Ionov, K. Grundke and M. Stamm, Wetting on fractal superhydrophobic surfaces from "core-shell" particles: A comparison of theory and experiment, *Langmuir* 25, 3132–3136 (2009).

29. A. Synytska, R. Khanum, L. Ionov, C. Cherif and C. Bellmann, Water-repellent textile via decorating fibers with amphiphilic Janus particles, *ACS Appl. Mater. Interfaces* 3, 1216–1220 (2011).
30. A. Duparré and L. Coriand, Assessment criteria for superhydrophobic surfaces with stochastic roughness, in: *Advances in Contact Angle, Wettability and Adhesion*, Vol. 1, K.L. Mittal (Ed.), pp193–201, Wiley-Scrivener, Beverly, MA (2013).
31. M. Yu, G. Guotuan, W.D. Meng and F.L. Qing, Superhydrophobic cotton fabric coating based on a complex layer of silica nanoparticles and perfluorooctylated quaternary ammonium silane coupling agent, *Appl. Surf. Sci.* 253, 3669–3673 (2007).
32. Y. Kawamura, K. Toyoda and S. Namba, Effective deep ultraviolet photoetching of polymethylmethacrylate by an excimer laser, *Appl. Phys. Lett.* 40, 374–375 (1982).
33. R. Srinivasan and V. Mayne-Baynton, Self-developing photoetching of poly(ethylene terephthalate) films by far-ultraviolet excimer laser radiation, *Appl. Phys. Lett.* 41, 576–578 (1982).
34. J.E. Andrew, P.E. Dyer, D. Forster and P.H. Key, Direct etching of polymeric materials using a XeCl laser, *Appl. Phys. Lett.* 43, 717–719 (1983).
35. S. Lazare, V. Granier, P. Lutgen and G. Feyder, Controlled roughening of poly(ethylene terephthalate) by photoablation: Study of wetting and contact angle hysteresis, *Revue Phys. Appl.* 23, 1065–1070 (1988).
36. T. Bahniers and E. Schollmeyer, Morphological changes of the surface structure of polymers due to excimer laser radiation - A synergetic effect?, *J. Appl. Phys.* 66, 1884–1886 (1989).
37. T. Bahniers, D. Knittel, F. Hillenkamp, U. Bahr, C. Benndorf and E. Schollmeyer, Chemical and physical properties of laser treated poly(ethylene terephthalate), *J. Appl. Phys.* 68, 1854–1858 (1990).
38. W. Kesting, T. Bahniers and E. Schollmeyer, Controlled structuring of polymer surfaces by UV-laser irradiation, *Appl. Surf. Sci.* 46, 326–329 (1990).
39. T. Bahniers, Excimer laser irradiation of synthetic fibers as a new process for the surface modification for textiles - A review, *Opt. Quant. Electron.* 27, 1337–1348 (1995).
40. A.-M. Kietzig, S.G. Hatzikiriakos and P. Englezos, Patterned superhydrophobic metallic surfaces, *Langmuir* 25, 4821–4827 (2009).
41. T. Baldacchini, J.E. Carey, M. Zhou and E. Mazur, Superhydrophobic surfaces prepared by microstructuring of silicon using a femtosecond laser, *Langmuir* 22, 4917–4919 (2006).
42. R.M. Wagterveld, C.W. J. Berendsen, S. Bouaidat and J. Jonsmann, Ultralow hysteresis superhydrophobic surfaces by excimer laser modification of SU-8, *Langmuir* 22, 10904–10908 (2006).
43. K. Tsujii, T. Yamamoto, T. Onda and S. Shibuichi, Super oil-repellent surfaces, *Angew. Chem. Int. Ed. Engl.* 36, 1011–1012 (1997).

44. S.R. Coulson, I. Woodward, J.P.S. Badyal, S.A. Brewer and C. Willis, Super-repellent composite fluoropolymer surfaces, *J. Phys. Chem. B* 104, 8836–8840 (2000).
45. T. Bahn timers, L. Prager, A. Pender and J.S. Gutmann, Super-wetting surfaces by plasma- and UV-based grafting of micro-rough acrylate coatings, *Prog. Org. Coat.* 76, 1356–1362 (2013).
46. T. Bahn timers, L. Prager, and J.S. Gutmann, Controlling the wettability of acrylate coatings with photo-induced micro-folding, in: *Advances in Contact Angle, Wettability and Adhesion*, Vol. 1, K.L. Mittal (Ed.), pp259–277, Wiley-Scrivener, Beverly, MA (2013).
47. F.M. Etzler, Determination of the surface free energy of solids: A critical review, *Rev. Adhesion Adhesives* 1, 3–45 (2013).
48. T. Bahn timers, D. Praschak and E. Schollmeyer, Super repellent properties created by photonic surface treatment, *Melliand Textilber. Intern. Text. Reports* 82, 613–614 (2001).
49. T. Bahn timers, W. Mölter-Siemens, S. Haep and J.S. Gutmann, Control of oil-wetting on technical textiles by means of photo-chemical surface modification and its relevance to the performance of compressed air filters, *Appl. Surf. Sci.* 313, 93–101 (2014).

Modification of Paper/Cellulose Surfaces to Control Liquid Wetting and Adhesion

Victor Breedveld and Dennis W. Hess*

School of Chemical & Biomolecular Engineering, Georgia Institute of Technology, Atlanta, GA, USA

Abstract

Cellulose is a biodegradable, renewable, flexible, inexpensive biopolymer that is abundant in nature. However, due to its hydrophilicity, applications of cellulose (paper) in the handling of liquids are severely limited. Appropriate plasma- or glow discharge-assisted processing sequences can be used to modify the surface of cellulose/paper so that the interaction of liquids with these surfaces can be altered. In particular, nanostructures associated with crystalline regions of cellulose fibers can be uncovered by plasma-enhanced etching; subsequent plasma-enhanced fluorocarbon film deposition (~100 nm) converts the surface into a superhydrophobic (static water contact angle >150°; receding contact angle <8°) state. Similar results can be obtained by depositing diamond-like carbon films on the plasma-etched surface, in spite of the inherently hydrophilic nature of diamond-like carbon itself. In addition, droplet adhesion and mobility can be controlled; depending on the etch cycle parameters, the paper surface can be rendered 'roll-off' or 'sticky' superhydrophobic. Use of a commercial printer to generate hydrophobic ink patterns on superhydrophobic paper surfaces allows controlled movement, transfer and storage of water or other aqueous liquids on the paper surface. These basic functionalities can be combined to design simple two-dimensional lab-on-paper (LOP) devices. Finally, by controlling both the cellulose fiber size and spacing, and depositing a fluorocarbon film, paper surfaces can be rendered superomniphobic, repelling both polar and apolar liquids.

*Corresponding author: dennis.hess@chbe.gatech.edu

14.1 Introduction

Paper has been used as a substrate for writing or recording information for ~2000 years. Continuation of its use to date is due to the fact that its primary component, cellulose, is a ubiquitous, biodegradable, flexible, renewable, and inexpensive biopolymer. Although paper has been used extensively for printing, writing, and packaging, alternative innovative uses have received much attention within the past 10 years. For instance, processes to fabricate transistors [1,2], batteries and supercapacitors [3,4], sensors [5,6], and microfluidic devices [7–10] on paper substrates have been reported. Unfortunately, the inherently hydrophilic and oleophilic properties of paper limit its ultimate usefulness in many potential applications.

Alteration of cellulose surface properties can be used to control (promote or inhibit) liquid interactions, while maintaining the advantageous properties of bulk paper, such as strength, flexibility and cost. Specifically, the ability to control the wettability and adhesion of liquid droplets on paper or cellulose surfaces offers the potential to expand use of paper in devices or technologies that currently use polymers or biomaterials.

Wettability control of paper surfaces has traditionally been achieved by the use of sizing techniques [11–12]. Internal sizing is accomplished by adding sizing agents (e.g., anhydrides) to pulp slurries before the paper sheet is formed, while surface sizing is performed by adding starch or waxes to the paper surface after the paper has been dried. Since the amount of additive may be substantial, such approaches can lead to problems in paper recycling. Surface/wetting modification using a thin (<300 nm) surface coating on the fabricated paper could offer advantages in this respect. A possible alternative to solution methods for surface modification of paper invokes vapor phase material deposition. Our studies in this arena use radio frequency (rf) or cold plasmas for surface etching and film deposition.

14.2 Plasma Processing

As used for low temperature film deposition and substrate processing, a plasma is a partially ionized gas that contains electrons, ions, photons, and neutral species in ground and excited states [13]. Electron impact reactions with gases in the plasma cause molecular dissociation and ionization at low temperature (typically <50°C), thereby promoting reaction rates that are appropriate for surface etching and deposition processes, while ensuring compatibility with temperature-sensitive surfaces such as cellulose. Ion, electron, photon, and neutral radical bombardment onto

surfaces exposed to the plasma leads to the breaking of surface chemical bonds, thereby causing etching -when volatile products are formed-, and film deposition -when non-volatile compounds are created. Plasma reactions typically affect only the surface layers (top few nm) of substrates, thereby leaving the properties of the bulk material unaltered. Numerous studies have demonstrated the ability to modify the wetting characteristics of cellulose by surface oxidation, atom grafting, and film deposition (see for instance, [14–20]). However, only a few studies have been reported wherein more extreme liquid wetting characteristics, for example superhydrophobicity, oleophobicity or superoleophobicity, have been achieved on paper by plasma processing. In the following sections, we describe recent work from our group to control wetting and adhesion of liquid droplets on paper surfaces along with approaches to allow controlled transport of these droplets for possible applications in two-dimensional microfluidic devices.

14.3 Sticky vs. Roll-off Superhydrophobic Surfaces

A superhydrophobic (SH) surface is defined as one that has a static contact angle (CA) with water greater than 150° . In order to fully describe the surface-liquid interactions, adhesion characteristics of a droplet to the surface should also be captured; this is generally quantified by measuring the contact angle hysteresis (difference between advancing and receding CAs) of a liquid droplet as it moves on a surface. Because no known material offers a water contact angle greater than 120° on a flat, non-porous substrate, superhydrophobicity requires a specific combination of surface roughness (with the correct size scale) in addition to a low surface energy [21]. These criteria regarding chemistry and morphology can be met by a variety of fabrication processes, including lithographic patterning or particle deposition, followed by the formation/deposition of a low surface energy material [22]. Our studies on the modification of paper surfaces have employed a different approach to generate the requisite roughness or physical heterogeneity: selective etching. In this process, cellulose is exposed to an oxygen plasma to preferentially remove amorphous material, and thereby uncover the crystalline nanofibrils [23]. This procedure creates roughness at the nano-scale that is in addition to the existing micro-scale roughness of the porous cellulose fiber network. Subsequent deposition of a thin (~ 100 nm) film of fluorocarbon from a fluorinated precursor such as pentafluoroethane (C_2F_5H) then renders the surface superhydrophobic. Most of the nanoscopic roughness generation occurs during the first 15 min. of etching; a minimal increase in roughness

occurs between 15 and 60 min. of etching, as shown in Figure 14.1 and demonstrated by AFM and optical profilometry [23, 24]. At these longer etch times, the micrometer-level structures in the paper are modified by the etch process as shown in Figure 14.2 [23, 24]. Interestingly, when the roughness is of the correct size scale, even deposition of a relatively hydrophilic coating material like diamond-like carbon, which displays a CA of 68° on a flat substrate (e.g. Si wafer), renders the etched paper surface superhydrophobic, with a contact angle of $\sim 160^\circ$ [24]. The results are similar to those wherein a fluorocarbon film is deposited, but with a film material that is inherently hydrophilic.

Control of contact angle hysteresis is more sensitive to the etch time than to the static contact angle. Adhesion of water droplets can be tuned by varying the etch time. Even the unetched paper, with nanoscopically smooth fibers, yields an advancing contact angle $>150^\circ$ when coated with a low surface energy material (e.g., fluorocarbon) due to the micro-scale roughness of the porous fiber network; this advancing CA remains virtually constant for etch times between 0 and 60 min [23]. However, the receding CAs vary considerably with etch time, yielding contact angle hysteresis values that drop from 147° to 3.5° as the etch time increases from 0 to >30 min. [23]. This change results in a continuously varying

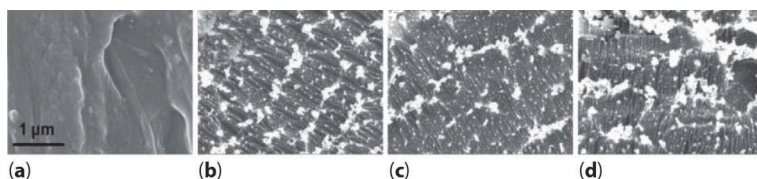


Figure 14.1 SEM images of (a) unetched paper fiber, and fibers that were plasma etched in O_2 for (b) 15 min, (c) 30 min, and (d) 60 min. Reproduced from Ref. 24 with permission from Springer.

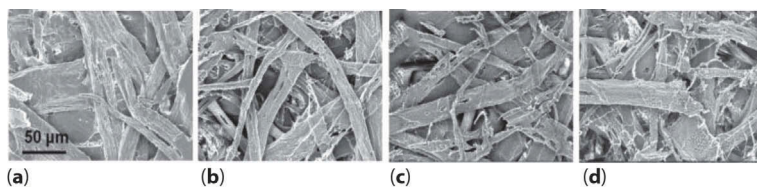


Figure 14.2 Low magnification SEM images of (a) unetched paper, and paper that was plasma etched in O_2 for (b) 15 min, (c) 30 min, and (d) 60 min. Reproduced from Ref. 24 with permission from Springer.

adhesion force or “stickiness” of the water droplet on the paper surface [23, 25]. Under the proper etch conditions (<5 min), the droplet shows SH behavior as indicated by the static CA, but the adhesion is so strong that the paper can be turned upside down and shaken without detaching the droplet from the surface. As the etch time increases, the adhesion force lessens, until at etch times >30 min., roll-off behavior of the droplet is observed; in this state even a low, less than a few degrees, tilt angle of the surface will induce droplet movement under the influence of gravity. These results can be ascribed to the extent of penetration of the droplet into the roughness created, with further penetration (but not yet a Wenzel state where complete wetting of the roughened surface occurs) yielding higher adhesion [25]. When droplet penetration is essentially nonexistent, indicating that the droplet sits on top of the nanofibrils, droplet roll-off is observed.

14.4 Local Wetting/Adhesion Control

The use of paper as a substrate for microfluidic devices is attractive in biomedical and analytical applications insofar as cost and flexibility are concerned. This approach has been used for 3-D devices [7–10] where the hydrophilic properties of paper allow water-based solutions to be absorbed into the paper and guided to desired locations by taking advantage of and manipulating capillary forces. Our efforts, in contrast, have focused on 2-D microfluidic approaches where patterns are created on the surface of paper so that required operations such as sampling, mixing, transfer, and storage of droplets can be realized without liquid penetration into the substrate [26, 27]. These operations are most easily implemented by using a desktop printer to create hydrophobic ink patterns on the SH paper [26]. Since the interactions of the water droplet with the SH surface surrounding the patterns is even less favorable than with the hydrophobic ink, the droplet is confined to the ink pattern and can be moved along the surface by simply tilting the paper. By printing line and dot segments, or combinations of these shapes in various patterns, anisotropic adhesion control and mobility of the droplets can be achieved. This fundamental principle can be harnessed to design building blocks and unit operations for functional microfluidic devices. Experimental results on paper substrates with ink patterns agree well with classical models that describe quantitatively both drag- and extensional-adhesion. Examples of the liquid-handling operations that can be performed with simple 2D print patterns (lines, dots) are shown in Figure 14.3 [26]. More intricate patterns such as semicircles

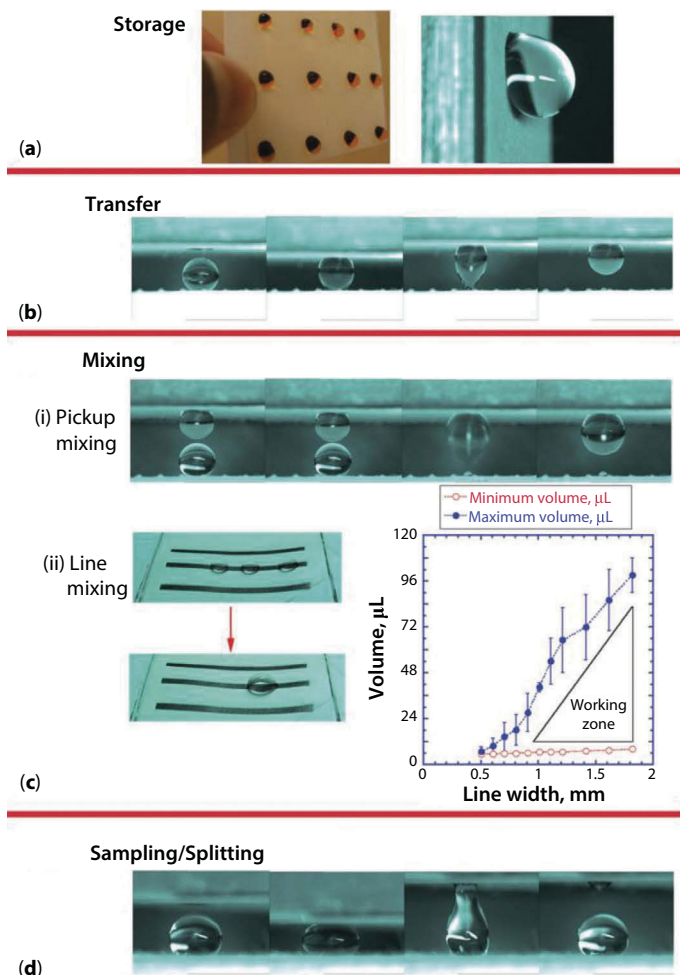


Figure 14.3 (a) Photographs of an array (left image) of water drops (food coloring was added to enhance contrast) and a high magnification image (right) of a single drop stored on a vertical substrate, (b) series of snapshots of a drop being transferred between two substrates, (c) photographs of merging and mixing: (i) pick-up mixing (two drops), (ii) line mixing (three drops) and graph that shows the working zone of drop volumes suitable for line mixing, (d) photographs of drop splitting between two substrates. Reproduced from Ref. 26 with permission from Royal Society of Chemistry.

or three-way junctions offer higher levels of directional mobility control of water droplets. For instance, a “mechanical diode” can be fabricated by printing a line segment that is interrupted by a semicircle; the mobilities of a droplet along the line in the convex and concave directions of the semicircle differ substantially [28].

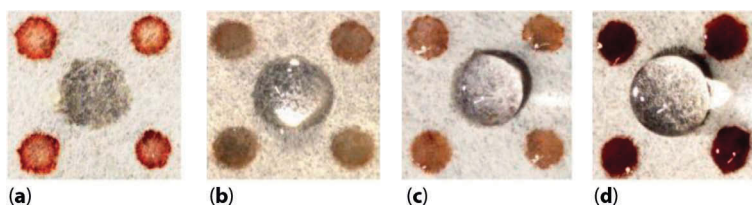


Figure 14.4 Colorimetric glucose test performed with high hysteresis wax islands on SH paper substrates; (a) dried reagents before exposure to test liquid; after sampling from bulk drops of (b) DI water, (c) 0.0015 M glucose solution, and (d) 0.005 M glucose solution. Reproduced from Ref. 27 with permission from Springer.

A potential application of the 2D microfluidic devices involves the creation of substrates that enable precise droplet manipulation, as required for medical testing of biofluid samples. A specific challenge is the generation of multiple small (e.g., 1-5 micro-liter) liquid samples with precise volumes for quantitative bio-assays from a single droplet of larger dimensions (~100 micro-liter) that could readily be obtained from a patient without the use of accurate and expensive tools, such as a finger prick. We have achieved this by taking advantage of the passive wetting properties of patterned SH paper substrates, which represent low-cost, point-of-use approaches. Droplet splitting has been achieved by the creation of contact angle hysteresis through the fabrication of heterogeneous paper surfaces [27]. SH, low hysteresis paper surfaces were prepared by the two-step plasma process (etching followed by fluorocarbon film deposition) described above. A thermal transfer stamping/printing process was then used to form wax patterns with high hysteresis on the SH paper. Use of different waxes allowed the surface chemistry to be altered, while the surface roughness was imparted and controlled independently by pressing the wax onto sandpapers of various grit sizes. Both wax chemistry and roughness enabled controlled variation of hysteresis and thus adhesion of water droplets. When a SH substrate with a 2 mm central wax dot surrounded by four 1 mm wax dots was pressed onto a large water droplet (100 micro-liter), multiple small droplet samples with precise volumes (and one large central droplet for stabilization of the capillary breakup) were transferred to the wax patterns on the test paper. Feasibility of this approach for the fabrication of a biomedically relevant test was demonstrated by functionalizing the perimeter wax drops with glucose colorimetric reagents. After bringing this test substrate in contact with aqueous droplets containing different glucose concentrations, identification of the glucose levels was apparent as shown in Figure 14.4.

14.5 Superamphiphobic/Superomniphobic Paper

Numerous applications can be envisioned for paper or cellulose surfaces that effectively repel oils and other non-polar liquids as well as aqueous solutions. For instance, liquids packaging and disposable clothing, medical apparel, and test strips would be possible using low cost, renewable materials. Little work has been reported for oleophobic and especially amphiphobic or superamphiphobic (repelling both high and low surface tension liquids) paper surfaces. When repellency of oil and grease is desired, cellulose-based substrates are generally overcoated; in this situation, the wetting properties are established by the coating rather than the properties of the fiber network (i.e., fiber size, shape, and chemistry). The exception to this statement is filter paper which has been designed specifically to repel liquids [29].

Attainment of superoleophobicity (SO), i.e. contact angles greater than 150° for multiple liquids, is difficult at best, since low surface tension liquids wet nearly any surface. Success in this area has depended on close control of the roughness geometry; in particular, re-entrant angles or undercut structures are required for stable SO surfaces [30–34]. The lower half of the cross section of a cylindrical fiber inherently displays a re-entrant angle; as a result, highly ordered woven fabrics and wire mesh substrates have successfully been designed with tightly controlled fiber spacing and surface chemistry to achieve SO behavior [30, 35–37]. Imparting SO properties to paper represents a considerable challenge, since fiber length, diameter, spacing and cross section are far from uniform; furthermore, the cross section of fibers is elliptical due to the pulp processing. Despite these complications, models formulated to describe/predict wetting behavior on uniform fiber-based substrates [34, 38] can be applied to paper to estimate the average fiber spacing and cross section needed to achieve SO characteristics. The fiber spacing in paper substrates can be adjusted by modification of the paper formation process, in particular by exchanging water as the suspending liquid of the pulp with less polar liquids such as sec-butanol. The (average) fiber diameter in the pulp can be modified prior to paper formation via a process known as refining, and further adjusted by plasma etching after the paper has been formed. When the desired fiber size and spacing are reached, deposition of a thin fluorocarbon layer to modify the surface chemistry will render even the highly heterogeneous and porous paper surface both superoleophobic and superhydrophobic (i.e., superamphiphobic) [39]. Control of fiber size and spacing is evident from the SEM images shown in Figure 14.5, where 10 HW signifies the number of revolutions (10,000) to which the hardwood fibers were subjected in a pulp

refiner (beater) to reduce fiber diameter. The porosity of the refined paper has been increased significantly and the fiber diameter reduced extensively relative to that of the unrefined paper. An image of the resulting paper surface (after fluorocarbon film deposition) with four different liquid droplets applied is shown in Figure 14.6 [39]. These liquids have widely different surface tensions (water: 72 mN/m; ethylene glycol: 48.4 mN/m; motor oil: 32.2 mN/m; n hexadecane: 27.5 mN/m). Yet, each displays a static contact angle $>150^\circ$ ($157 \pm 3^\circ$, $155 \pm 5^\circ$, $152 \pm 4^\circ$, and $154 \pm 2^\circ$ for water, ethylene glycol, motor oil, and hexadecane, respectively). The roll-off angles of these droplets, which are indicative of the contact angle hysteresis, vary widely, with water, ethylene glycol, and motor oil displaying roll-off at

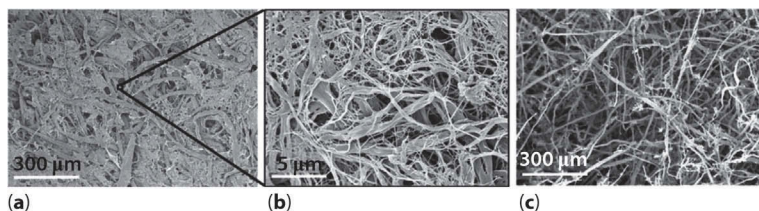


Figure 14.5 (a, b) Low- and high resolution SEM images of a 10 HW handsheet processed using sec-butanol before etching; (c) image of the same material after O_2 plasma etching for 30 min. Reproduced from Ref. 39 with permission from The American Chemical Society.



Figure 14.6 Droplets of four test liquids (water, dyed blue), ethylene glycol, motor oil, and n-hexadecane (dyed red) positioned on the handsheet depicted in Figure 14.5c; high ($>150^\circ$) contact angles are evident for all liquids. Reproduced from Ref. 39 with permission from The American Chemical Society.

$13 \pm 3^\circ$, $19 \pm 4^\circ$, and $34 \pm 6^\circ$, respectively. Hexadecane droplets adhere to the surface even when the paper sample is inverted. These results demonstrate that for heterogeneous fibrous materials, the fiber size, spacing and roughness must be balanced and optimized to achieve wetting control for a variety of liquids with different surface tensions. In order to achieve superamphiphobicity, the fiber spacing had to be increased over that of typical papers or handsheets where hydrogen bonding controls the spacing. For water-based paper, no plasma etch time could be identified that achieved the proper combination of fiber size and spacing for superamphiphobic behavior. Sec-butanol washing of the pulp was required to increase the fiber spacing by inhibiting hydrogen bonding between the fibers; subsequent plasma etching allowed the necessary fine-tuning of fiber spacing and size, and deposition of a fluorocarbon film supplied the hydrophobic surface properties needed to achieve superomphobicity. However, since these paper substrates have reduced fiber density and connectivity owing to the sec-butanol wash, the mechanical strength of the paper is reduced significantly. Optimization of the fiber spacing is being explored to ensure the wetting properties desired while maintaining paper strength.

14.6 Summary and Conclusions

Novel methods have been developed to create robust superhydrophobic paper or cellulose-based materials that display tunable wetting and droplet adhesion. These methods utilize plasma-enhanced etching and deposition techniques at moderate pressure (~ 1 Torr) to achieve independent control of nano- and micro-scale roughness, and surface chemistry. Such approaches are applicable to other fiber-based materials that, like paper, exhibit extensive heterogeneity with regards to fiber shape, size and orientation. If the proper nano-scale roughness level is incorporated via plasma etching, paper can be rendered superhydrophobic by depositing either a hydrophobic (fluorocarbon) or a more hydrophilic (diamond-like carbon) coating. A more hydrophilic material requires tighter control of the etch segment of this two-step process, while hydrophobic coating material permits a wider range of roughness conditions. Oil repellency is more difficult to achieve on paper than is water repellency. Specifically, fiber spacing, diameter, and surface geometry are all critical parameters for achieving superoleophobicity and, ultimately, superamphiphobicity of paper surfaces. Establishment of the necessary fiber spacing and size is possible by altering the manufacturing process of the paper, followed by plasma etching and hydrophobic film deposition.

Acknowledgments

The authors thank Drs. Balamurali Balu and Lester Li for their dedication and extensive accomplishments in modifying paper surfaces. Thanks are also due to the Institute for Paper Science and Technology (now Renewable Bioproducts Institute) at Georgia Tech for fellowships that supported B. Balu and L. Li during their PhD thesis work.

References

1. R. Martins, P. Barquinha, L. Pereira, N. Correia, G. Goncalves, I. Ferreira, and E. Fortunato, Write-erase and read paper transistor. *Appl. Phys. Lett.*, 93, 203501 (2008).
2. W. Lim, E. A. Douglas, S. H. Kim, D. P. Norton, S. J. Pearton, F. Ren, H. Shen, and W. H. Chang, High mobility InGaZnO₄ thin-film transistors on paper. *Appl. Phys. Lett.*, 94, 072103 (2009).
3. V. L. Pushparaj, M. M. Shaijumon, A. Kumar, S. Murugesan, L. Ci, R. Vajtai, R. J. Linhardt, O. Nalamasu, and P. M. Ajayan, Flexible energy storage devices based on nanocomposite paper. *Proc. Natl. Acad. Sci. (USA)*, 104, 13574-13577 (2007).
4. L. Hu, H. Wu, F. La Mantia, Y. Yang, and Y. Cui, Thin, flexible secondary Li-ion paper batteries. *ACS Nano*, 4, 5843-5848 (2010).
5. D. Nilsson, T. Kugler, P. O. Svensson, and M. Berggren, An all-organic sensor-transistor based on a novel electrochemical transducer concept printed electrochemical sensors on paper. *Sensors Actuator B*, 86, 193-197 (2002).
6. X. Li, J. Tian, G. Garnier, and W. Shen, Fabrication of paper-based microfluidic sensors by printing. *Colloids Surfaces B*, 76, 564570 (2010).
7. K. Abe, K. Suzuki, and D. Citterio, Inkjet-printed microfluidic multianalyte chemical sensing paper. *Anal. Chem.*, 80, 6928-6934 (2008).
8. D. A. Bruzewicz, M. Reches, and G. M. Whitesides, Low-cost printing of poly(dimethylsiloxane) barriers to define microchannels in paper. *Anal. Chem.*, 80, 3387-3392 (2008).
9. A. W. Martinez, S. T. Phillips, and G. M. Whitesides, Three-dimensional microfluidic devices fabricated in layered paper and tape. *Proc. Natl. Acad. Sci., (USA)*, 105, 19606-19611 (2008).
10. W. A. Zhao and A. van den Berg, Lab on paper. *Lab on a Chip*, 8, 1988-1991 (2008).
11. G. A. Smook, *Handbook for Pulp and Paper Technologists*, Angus Wilde Publications, Vancouver, Canada., (2002).
12. D. Barona and A. Amirfazli, Producing a superhydrophobic paper and altering its repellency through ink-jet printing. *Lab on a Chip*, 11, 936-940 (2011).

13. M. A. Lieberman and A. J. Lichtenberg, *Principles of Plasma Discharges and Materials Processing*, John Wiley & Sons, New York (2005).
14. M. R. Wertheimer, G. Suranyi, and D. A. I. Goring, Improvement in bonding properties of cellulose and polyethylene by treatment in a microwave discharge. *Tappi J*, 55, 1707-1714 (1972).
15. C. M. G. Carlsson and G. Strom, Reduction and oxidation of cellulose surfaces by means of cold plasma. *Langmuir*, 7, 2492-2497 (1991).
16. C. M. G. Carlsson, G. Strom, I. Eriksson, and E. Lindstrom, Improved wettability of chemithermomechanical pulp by oxygen plasma treatments. *Nord. Pulp Paper Res. J.*, 9, 72 (1994).
17. S. Sapiha, A. M. Wrobel, and M. R. Wertheimer, Plasma-assisted etching of paper. *Plasma Chem. Plasma Proc.*, 8, 331-346 (1988).
18. H. T. Sahin, S. Manolache, R. A. Young, and F. Denes, Surface fluorination of paper in CF_4 -RF plasma environments. *Cellulose*, 9, 171-181 (2002).
19. S. Vaswani, J. Koskinen, and D. W. Hess, Surface modification of paper and cellulose by plasma-assisted deposition of fluorocarbon films. *Surface Coat. Technol.*, 195, 121-129 (2005).
20. C. Gaiolas, M. N. Belgacem, L. Silva, W. Thielemans, A. P. Costa, M. Nunes, and M. J. S. Silva, Green chemicals and process to graft cellulose fibers. *J. Colloid Interface Sci.*, 330, 298-302 (2009).
21. X. M. Li, D. Reinhoudt, and M. Crego-Calama, What do we need for a superhydrophobic surface? A review on the recent progress in the preparation of superhydrophobic surfaces. *Chem. Soc. Rev.*, 36, 1350-1368 (2008).
22. A. Carré and K. L. Mittal (Eds.) *Superhydrophobic Surfaces*, CRC Press, Boca Raton, FL (2009).
23. B. Balu, V. Breedveld, and D. W. Hess, Fabrication of "roll-off" and "sticky" superhydrophobic cellulose surfaces via plasma processing. *Langmuir*, 24, 4785-4790 (2008).
24. L. Li, S. Roethel, V. Breedveld, and D. W. Hess, Creation of low hysteresis superhydrophobic paper by deposition of hydrophilic diamond-like carbon films. *Cellulose*, 20, 3219-3226 (2013).
25. B. Balu, J. S. Kim, V. Breedveld, and D. W. Hess, Tunability of the adhesion of water drops on a superhydrophobic paper surface via selective plasma etching. *J. Adhesion Sci. Technol.*, 23, 361-380 (2009).
26. B. Balu, A. D. Berry, D. W. Hess, and V. Breedveld, Patterning of superhydrophobic paper to control the mobility of micro-liter drops for two-dimensional lab-on-paper applications. *Lab on a Chip*, 9, 3066-3075 (2009).
27. L. Li, V. Breedveld, and D. W. Hess, Hysteresis controlled water droplet splitting on superhydrophobic paper. *Colloid Polym. Sci.*, 291, 417-426 (2013).
28. B. Balu, A. D. Berry, K. T. Patel, V. Breedveld, and D. W. Hess, Directional mobility and adhesion of water drops on patterned superhydrophobic surfaces. *J. Adhesion Sci. Technol.*, 25, 627-642 (2011).

29. C. F. Jin, Y. F. Jiang, T. Niu, and J. G. Huang, Cellulose-based material with amphiphobicity to inhibit bacterial adhesion by surface modification. *J. Mater. Chem.*, 22, 12562-12567 (2012).
30. A. Tuteja, W. Choi, M. L. Ma, J. M. Mabry, S. A. Mazzella, G. C. Rutledge, G. H. McKinley, and R. E. Cohen, Designing superoleophobic surfaces. *Science*, 318, 1618-1622 (2007).
31. A. Steele, I. Bayer, and E. Loth, Inherently superoleophobic nanocomposite coatings by spray atomization. *Nano Lett.*, 9, 501-505 (2009).
32. M. Liu, S. Wang, Z. Wei, Y. Song, and L. Jiang, Bioinspired design of a superoleophobic and low adhesive water/solid interface. *Adv. Mater.*, 21, 665-669 (2009).
33. T. Darmanin and F. Guittard, Super oil-repellent surfaces from conductive polymers. *J. Mater. Chem.*, 19, 7130-7136 (2009).
34. H. J. Lee, C. R. Willis, and C. A. Stone, Modeling and preparation of a superoleophobic non-woven fabric. *J. Mater. Sci.*, 46, 3907-3913 (2011).
35. H. F. Hoefnagels, D. Wu, G. de With, and W. Ming, Biomimetic superhydrophobic and highly oleophobic cotton textiles. *Langmuir*, 23, 13158-13163 (2007).
36. J. Yang, Z. Z. Zhang, X. H. Men, X. H. Xu, and X. T. Zhu, A simple approach to fabricate superoleophobic coatings. *New J. Chem.*, 35, 576-580 (2011).
37. A. K. Kota, Y. X. Li, J. M. Mabry, and A. Tuteja, Hierarchically structured superoleophobic surfaces with ultralow contact angle hysteresis. *Adv. Mater.*, 24, 5838-5843 (2012).
38. A. Marmur, Wetting on hydrophobic rough surfaces: To be heterogeneous or not to. *Langmuir*, 19, 8343-8348 (2003).
39. L. Li, V. Breedveld, and D. W. Hess, Design and fabrication of superamphiphobic paper surfaces. *ACS Appl. Mater. Interfaces*, 5, 5381-5386 (2013).

Part 3

SURFACE FREE ENERGY AND ADHESION

Surface Free Energy of Superhydrophobic Materials Obtained by Deposition of Polymeric Particles on Glass

Konrad Terpilowski

Department of Physical Chemistry-Interfacial Phenomena, Faculty of Chemistry, Maria Curie-Skłodowska University, Lublin, Poland

Abstract

Superhydrophobic surfaces were obtained by deposition of polymer particles on a glass plate. The polymers used were: Teflon, dimethacrylate of ethyl glycol, and copolymers of 2-methyl-2-propenoic acid with ethyl glycol and different amounts of hexane during polymerization. Hexane was used as a solvent and blowing agent during copolymerization. The surface covered with particles of the copolymer had the highest advancing and receding contact angles of $\theta_a=151.3^\circ$ and $\theta_r=117.9^\circ$. When (1:4) hexane was present during the copolymerization, the sliding angle was also measured and the droplet rolled down at 15° surface slope.

The apparent surface free energy calculated from the water contact angle hysteresis on the bare glass plate amounted to 65.7 mJ/m^2 . However with the deposited polymer (M1E4H4X) the apparent surface free energy was only 1.8 mJ/m^2 . Moreover, water advancing and receding contact angles were also used for calculating equilibrium contact angles using Tadmor's equation. Their values lie between the advancing and receding contact angles but closer to the advancing ones. The surface free energy calculated from the Tadmor's contact angles is higher in comparison to the surface free energy calculated from the contact angle hysteresis. For the bare glass plate it is higher by about 2 mJ/m^2 but for the surfaces with superhydrophobic property it is higher by 1.8 to 11.3 mJ/m^2 .

Keywords: Surface free energy, polystyrene layer, superhydrophobic surface, polymer particles

Corresponding author: terpil@umcs.pl

List of Notations

R_a – average roughness

R_{RMS} – root mean square roughness

R_t – peak-to-valley difference calculated over the entire measured area

γ – surface tension of liquid (water)

θ_a – advancing contact angle of water

θ_r – receding contact angle of water

θ_0 – equilibrium contact angle

15.1 Introduction

Superhydrophobicity is an important issue both for science and industry. Fabrication of such surfaces has been studied for more than ten years. Generally, there are some problems with obtaining stable superhydrophobic layers on solids. Many methods have been devised for such surface preparation [1].

Wang and Shu [2] obtained transparent superhydrophobic antireflective layers for solar cells. The layers were constructed on a glass substrate using layer-by-layer deposition of a polyelectrolyte. The superhydrophobic sol–gel system was prepared by hydrolyzing tetraethoxysilane and then reacting it with hexamethyldisilazane. The water contact angle measured on the layers obtained by the spin coating method was up to 163° on most superhydrophobic surfaces. Moreover, the transmittance of this layer was about 96%.

Chen *et al.* [3] prepared superhydrophobic Co-based powder using the electrodeposition method to fabricate a superhydrophobic layer on stainless steel. This method is characterized by a short preparation time, water contact angle larger than 160° , and roll-off angle smaller than 2° . The powder was crystalline as confirmed by FTIR and XRD methods.

A stable superhydrophobic effect was obtained by Guo *et al.* [4] using a stainless steel surface. Stainless steel plates after drying in pure N_2 were immersed in an aqueous $CuSO_4$ solution. Then, the plates were immersed into ethanol solution of perfluorooctyltriethoxysilane. After removal from the solution, the substrate was heated at $140^\circ C$ for 30 min. The water contact angle measured on these surfaces was 166° and the sliding angle for a $10\mu l$ water droplets was as low as 1° . After 100 days from the sample preparation, both the water contact angle and sliding angle increased by just one degree.

In our previous papers [5,6], the effects of PMMA poly(methyl methacrylate) and PS (polystyrene) layers with several different fillers deposited on a glass plate were investigated. First, we find the optimum concentration of PMMA or PS/chloroform solution for use as adhesive layer [5]. The problem with this method was covering the surface uniformly. The glass plates were covered with dispersions of the following fillers: TiO_2 , Al_2O_3 , silica, using spreading and spin coating techniques. On some samples, the water contact angles were larger than 150° and the sliding angles were about 5° .

Wettability of a rough surface can be described by the Wenzel [7] model if the surfaces are completely wetted by the liquid into the protrusions on the surface. The Cassie–Baxter [8,9] model gives an idea about wettability of rough hydrophobic surfaces. In the case of such surfaces, the air trapped into hierarchical roughness prevents water penetration into the surface protrusions.

In this study, it seemed interesting to us to investigate how certain polymers typically used as chromatographic column packing would act as the medium to create hierarchical structure on the surface. For this purpose, polystyrene powder was dissolved in chloroform and then spread on glass plates as glue layer, and then the polymer particles were sown on (Figure 15.1) After the surfaces were prepared, water advancing and receding contact angles were measured. The structures of deposited layers were observed using an optical microscope

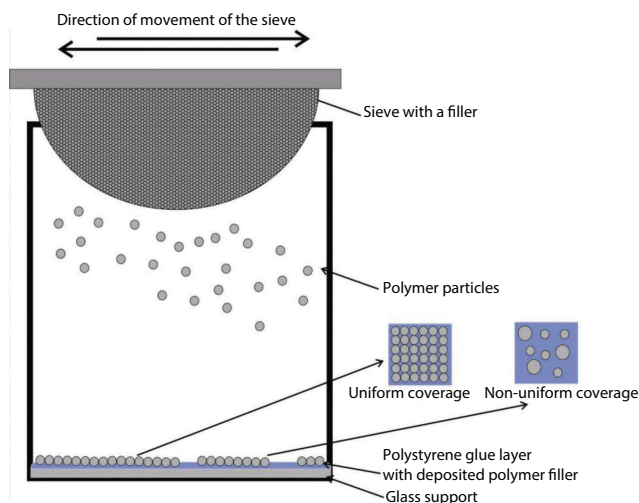


Figure 15.1 Method of surface preparation.

at different magnifications in transmitted light. For some samples, the surface topography was also determined using an optical profilometer. The apparent surface free energy was calculated using the contact angle hysteresis approach proposed by Chibowski [10–12]. The apparent surface free energy using this approach is determined from the probe liquid (water) advancing and receding contact angles and the liquid surface tension as:

$$\gamma_s = \frac{\gamma_L (1 + \cos \theta_a)^2}{(2 + \cos \theta_r + \cos \theta_a)} \quad (15.1)$$

where: γ_s is the apparent surface free energy, γ_L is the water surface tension (72.8 mN/m at 20°C), θ_a is the advancing contact angle, and θ_r is the receding contact angle of water.

To validate the values of surface free energy obtained from the hysteresis approach, Neumann [12,13], equation-of-state approach was also used. The apparent surface free energy in this approach is determined from the liquid advancing contact angle, its surface tension and constant β as:

$$\cos \theta_a = -1 + 2 \sqrt{\frac{\gamma_s}{\gamma_L}} e^{-\beta(\gamma_L - \gamma_s)^2} \quad (15.2)$$

Determination of equilibrium Young [14] contact angle is still an open problem [15]. Here, Tadmor's [16–18] equation (Eq. 15.3) was used for this purpose.

$$\begin{aligned} \text{(A)} \quad \Gamma_a &\equiv \left(\frac{\sin^3 \theta_a}{(2 - 3 \cos \theta_a + \cos^3 \theta_a)} \right)^{1/3}; \\ \text{(B)} \quad \Gamma_r &\equiv \left(\frac{\sin^3 \theta_r}{(2 - 3 \cos \theta_r + \cos^3 \theta_r)} \right)^{1/3}; \\ \text{(C)} \quad \theta_0 &= \arccos \left(\frac{\Gamma_a \cos \theta_a + \Gamma_r \cos \theta_r}{\Gamma_a + \Gamma_r} \right) \end{aligned} \quad (15.3)$$

where: Γ_a - the advancing angle weight coefficient, Γ_r - the receding angle weight coefficient

Using the contact angles calculated from (Eq. 15.3 C) and assuming that at the equilibrium contact angle θ_0 , $\theta_a = \theta_r = \theta_0$ [16–18] (Eq. 15.1) transforms to (Eq. 15.4).

$$\gamma_s = \frac{1}{2} \gamma_L (1 + \cos \theta_0) \quad (15.4)$$

15.2 Experimental

15.2.1 Materials and Methods

In order to determine the optimum concentration of the polystyrene solution, the layers were prepared with 0.5ml of the polystyrene solution in chloroform obtained by dissolving 0.1, 0.2, 0.3, 0.4, 0.5 and 0.6g of PS in 100ml chloroform and were spread on the glass surface. Then the plates were left for 12h in order to evaporate chloroform. On the surfaces prepared in this manner the advancing and receding contact angles of water droplets were measured and then the surface free energy was calculated. From these results, the optimum concentration of the polystyrene solution was selected. The contact angles on the polystyrene layer without any filler particles were measured using the sessile drop method. However, on the layers with the polymer filler the contact angles were measured with the tilting plate method.

15.2.2 Preparation of Superhydrophobic Layers Deposited on the Glass Surface

0.5ml of the polystyrene solution in chloroform were poured using a micropipette on a glass plate of size 2.55 cm \times 2.7 cm. Then 0.035g of powered polymers were sown on the plates using a sieve and left for 12h to evaporate the solvent (Figure 15. 1). Before measuring the advancing and receding angles of water, the prepared glass plates were kept in a desiccator. The contact angles were measured on three plates prepared with the same polymer filler. The polymers used were synthesized in the Department of Polymer Technology, Faculty of Chemistry, Maria Curie – Skłodowska University, Lublin. Also Teflon powder was used as a filler. The average particle diameter was measured using Zetasizer (Malvern, Great Britain) (Table 15.1)

Table 15.1 Polymer particles used to obtain superhydrophobic layers and their diameters.

Polymer	Diameter, μm
EGDMA	0.65
M1E4H4X	1.86
M1E4H4XS	2.50
M1E4H10X	1.41

The following polymers were used as the fillers:

- Dimethacrylate of ethyl glycol, EGDMA.
- Copolymer of methacrylic acid with dimethacrylate of ethylene glycol + 4ml of hexane, 1:4 M1E4H4X – washed with methanol after the synthesis.
- Copolymer of methacrylic acid with dimethacrylate of ethyl glycol + 4ml of hexane 1:4, M1E4H4XS – not washed with methanol after the synthesis.
- Copolymer of methacrylic acid with dimethacrylate of ethylene glycol + 10ml of hexane, 1:4 M1E4H10X – washed with methanol after the synthesis.
- Teflon powder from Azoty, Tarnów S.A., Poland

15.2.3 Contact Angle Measurements

The advancing and receding contact angles of water were measured using the GBX Contact Angle Meter (France) and the tilting plate method. A 6 μl water droplet was carefully deposited on the plate surface in the measuring chamber of the apparatus. Then the stage of the apparatus was inclined and the droplet was filmed until it started to slide. When analyzing the frames of the droplets the one just before the droplet started to slide was selected. The advancing contact angle was measured on the droplet front and the receding on its rear. Three glass plates covered with the PS layer and given fillers were produced and the contact angles of 10 water droplets on each layer were measured. Thus the mean values of 30 contact angles are plotted in the figures.

15.2.4 Photographs of PS Layers

Using an optical polarized microscope Eclipse E600 POL, Nikon, Japan, photographs of the PS layers deposited on a glass plate were taken in the

reflected light at 40 \times and 100 \times magnifications. However, the film transparency was sufficient to obtain good quality pictures also in the transmitted light.

15.2.5 Imaging the PS Layer Surface with an Optical Profilometer

Using an optical profilometer (Contour GT, Veeco) images of the most hydrophobic PS/M1E4H10X sample, selected as an example, and the surfaces roughness were analyzed.

15.3 Results and Discussion

15.3.1 Contact Angles Measured on Glass Plates Covered with Pure PS Layers

From the results in Figure 15.2, it follows that the largest advancing and receding angles of water were obtained on the pure PS layer prepared by dissolution of 0.2g of polystyrene in 100ml of chloroform and these were $91.7 \pm 1.0^\circ$ and $88.4 \pm 3.1^\circ$ respectively. However, at larger contents of PS, these angles were practically the same. The glass surface covered with polystyrene solution of concentration 0.1g/100ml appears to be covered inhomogeneously. For comparison, the values of advancing

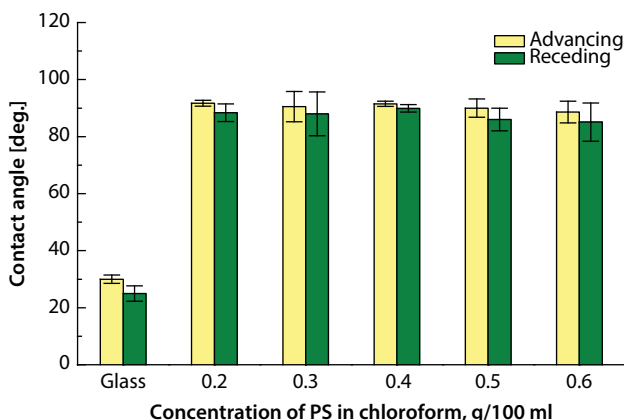


Figure 15.2 Advancing and receding contact angles of water measured on pure PS layers deposited on glass plates from PS in the chloroform solution. For comparison values on bare glass plate are also shown.

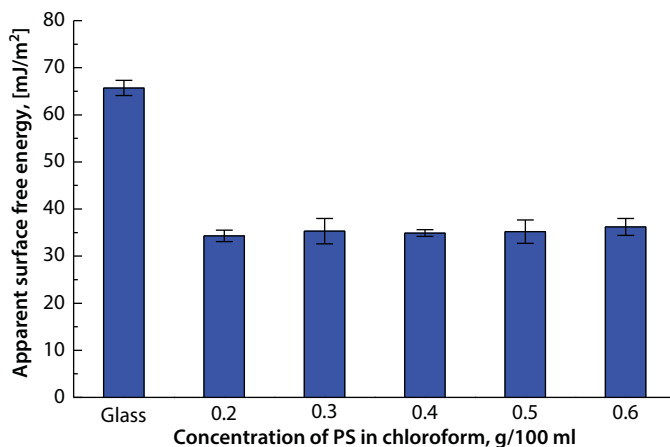


Figure 15.3 Apparent surface free energy of pure PS layers deposited on glass plates.

and receding contact angles on the bare glass surface are also shown in Figure 15.2. Then using the advancing and receding contact angles, the apparent surface free energy values of the studied layers were calculated from (Eq. 15.1).

15.3.2 Apparent Surface Free Energy Calculated for Glass Plates Covered with Pure PS Layers

Figure 15.3 shows that the apparent surface free energy value depends on the PS concentration in chloroform. It changes from 65 mJ/m² (bare glass) to 34.3–36.2 mJ/m² for deposited PS layers. As mentioned earlier in the case of the lowest concentration of the PS solution (0.2g/100ml) water forms the largest advancing and receding contact angles which results in the smallest surface free energy of 34.3±1.2 mJ/m². For higher concentrations of the PS solution, the surface free energy of the layers is about the same, i.e., from 35.3±2.7 to 36.2±1.8 mJ/m². Therefore, in further studies a polystyrene solution of concentration 0.2g in 100ml of chloroform was used to obtain the superhydrophobic surfaces.

15.3.3 Contact Angles Measured on Glass Plates Covered with the PS Layers with Embedded Polymer Fillers

As can be seen in Figure 15.4, the advancing contact angle of water droplets on the studied PS/polymer filler surfaces changes from 128.1° for

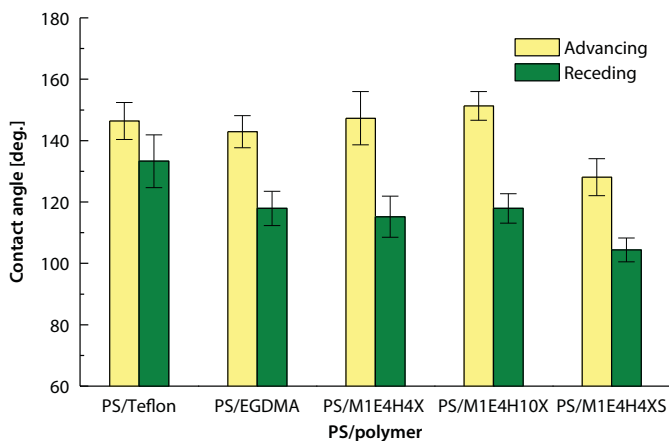


Figure 15.4 Advancing and receding contact angles of water measured on the PS layers with various embedded polymer particles on glass plate.

PS/M1E4H4XS to 151.3° for PS/M1E4H10X. The values of the receding contact angle are much lower and change from 104.4° for the PS/M1E4H4XS system to 133.3° for the PS/Teflon layer. Thus significant increase in the hydrophobic property was found for each system, except the PS/M1E4H4XS surface. In this case, the polymer powder was not washed with methanol after the synthesis and contained particles with the largest diameter (Table 15.1).

15.3.4 Apparent Surface Free Energy Calculated for the Glass Plates Covered with the PS/ Filler Layers

First, it should be mentioned that for the surfaces on which the contact angles were larger than 150° the Neumann [13] equation-of-state (Eq. 15.2) could not be applied because only mathematical solution was obtained without physicochemical meaning. For example, the surface covered with PS/M1E4H10X, the average advancing contact angle was 151.3° . Using 72.8 mJ/m^2 for the water surface tension and the constant $\beta=0.000125$, a value for apparent surface free energy as high as 237.2 mJ/m^2 was obtained. This value is too large to be considered to have a physicochemical meaning. Therefore, it can be concluded that the approach based on the Neumann [13] equation-of-state (Eq. 15.2) cannot be applied for superhydrophobic surfaces. Therefore, in the case of these surfaces the apparent surface free energy was calculated using only the contact angle hysteresis equation.

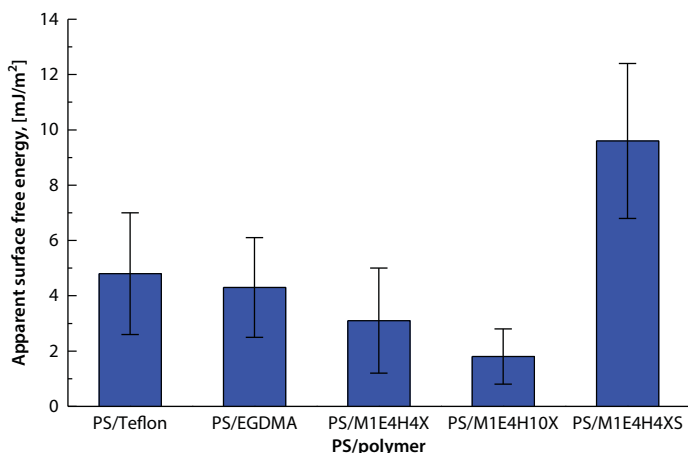


Figure 15.5 Apparent surface free energy of PS layers with various embedded polymer particles on glass plates.

The apparent surface free energy values calculated in this manner are plotted in Figure 15.5. The smallest value for PS/M1E4H10X is 1.8 ± 1.0 mJ/m² and the largest surface free energy is found for the PS/M1E4HXS layer, which is still relatively small and equals 9.6 ± 2.8 mJ/m². As it follows from the data in Figures 15.4 and 15.5 most of the studied surfaces are characterized by their superhydrophobic property. However, while analyzing the standard deviation from the average value, it can be seen that reproducibility of the water contact angle is not satisfactory because the measurement error varies between 4.7 and 8.7°. These differences result from a non-uniform coverage of the glass surface with the polymer layer because it was “sown” on the wet layer of PS solution in chloroform. This fact is confirmed by the images of the studied surfaces obtained from a polarization microscope Nikon (Type 120), Japan.

15.3.5 Optical Photographs of the PS Layers with Embedded Polymers Particles

As shown in Figure 15.6 the pictures at both magnifications show some “domains” which are due to a large variety of irregular roughness heights on the surface. The most homogeneous surface was obtained for the PS layer with the copolymer of methacrylic acid with dimethacrylate of ethyl glycol + 10ml hexane – M1E4H10X whose particle diameter is 1.4 μm (Figure 15.6 d and D’).

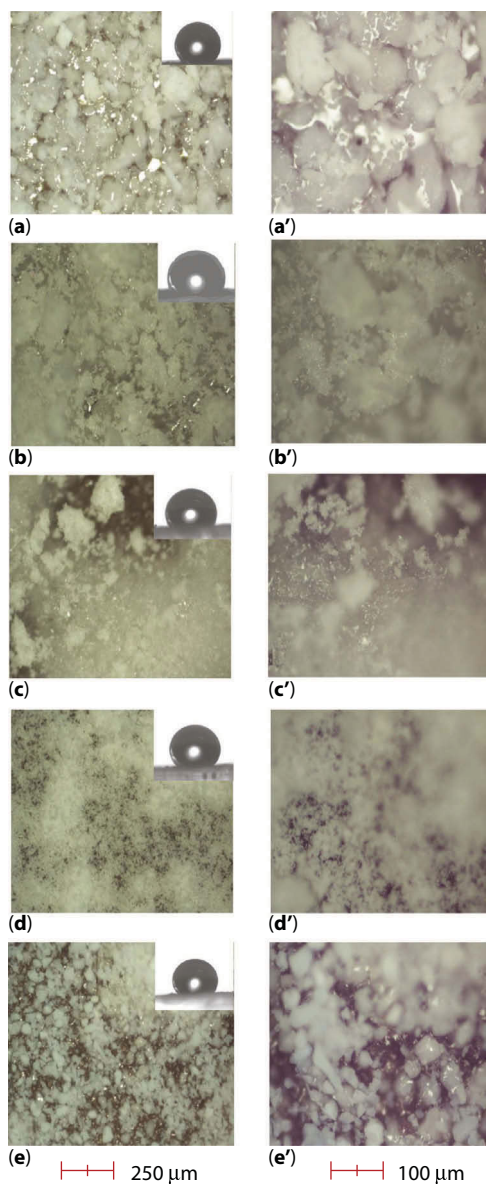


Figure 15.6 (a), (a') surface of PS/Teflon; (b), (b') surface of PS/EGDMA; (c), (c') surface of PS/M1E4H4X; (d), (d') surface of PS/M1E4H10X; (e), (e') surface of PS/M1E4H4XS layers deposited on glass plates. 40 \times and 100 \times magnifications. Additionally, pictures of water droplets are shown in the photographs.

15.3.6 Images of the Superhydrophobic Layers Using Optical Profilometry

To obtain more quantitative information about the differences in the surface topographies of the PS layers with different polymer fillers, optical profilometry images were obtained for the most superhydrophobic, i. e., the M1E4H10X sample (Figure 15.7 a)). The roughness parameters of the surfaces are listed in Table 15.2. The dominant feature on the surface is a microstructure but as shown in Figure 15.7 b) a nanostructure is also present on microstructure protrusions. It is helpful if the air is trapped beneath the water droplet as it causes an increase of the contact angle up to 150°.

15.3.7 Tadmor’s Equilibrium Contact Angles

Although the presented surfaces are rough, nevertheless it is possible to obtain in a reproducible manner the layers with superhydrophobic

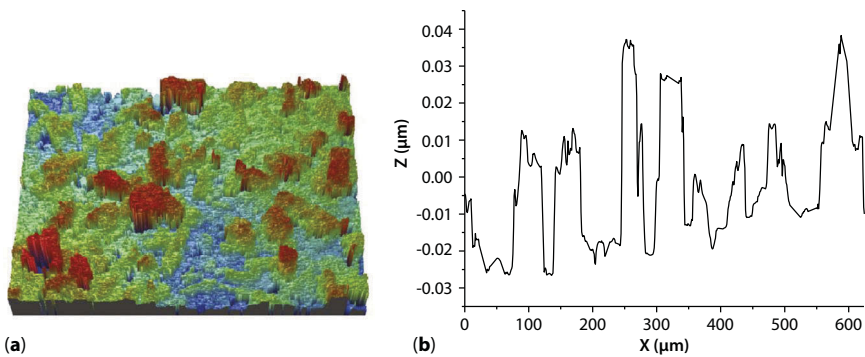


Figure 15.7 (a) 3D (468 $\mu\text{m} \times 624 \mu\text{m}$) profilometry image for PS/M1E4H10X surface
(b) Surface roughness along the (X) axis.

Table 15.2 Roughness parameters in [μm] for superhydrophobic layer of PS/M1E4H10X deposited on glass slide.

R_a	R_{RMS}	R_t
18.0 \pm 2.5	22.2 \pm 3.2	154.9 \pm 9.0

R_a – average roughness

R_{RMS} – root mean square roughness

R_t – peak – to – valley distance calculated over the entire measured area

property. The angle of water droplets rolling down on such surfaces was about 15° . As most of the surfaces presented in this paper possess superhydrophobic property, so Tadmor's [16–18] theory of equilibrium contact angle was used to calculate their surface free energy.

In all cases the equilibrium contact angle calculated from Tadmor's [16–18] equation (Eq. 15.3 C) lies between the advancing and receding contact angles. The largest contact angle value of $140.7 \pm 10.9^\circ$ was obtained for the glass surface covered with PS/Teflon. However, the surface covered with PS/M1E4H10X was characterized as having the largest contact angle value, with an equilibrium contact angle of $135.6 \pm 17.8^\circ$ (Figure 15.8). These differences result from differences in the contact angle hysteresis. In the case of the surface covered with PS/Teflon, the hysteresis is $13.1 \pm 2.5^\circ$, but for the surface covered with PS/M1E4H10X it is as large as $33.5 \pm 5.6^\circ$. Nevertheless, using these equilibrium contact angles from (Eq. 15.3 C), the surface free energy was also calculated.

When the surface free energy is calculated in this manner, it is smallest for the glass surface covered with PS/Teflon and is equal to $8.6 \pm 4.2 \text{ mJ/m}^2$. However, it is largest for the surface covered with PS/ M1E4H4XS and is equal to $19.0 \pm 7.0 \text{ mJ/m}^2$. Therefore, the theory proposed by Tadmor [16–18] to describe surfaces with large contact angle hysteresis is found to be applicable (Figures 15.5–9). The surface free energies thus obtained are marked with high standard deviation.

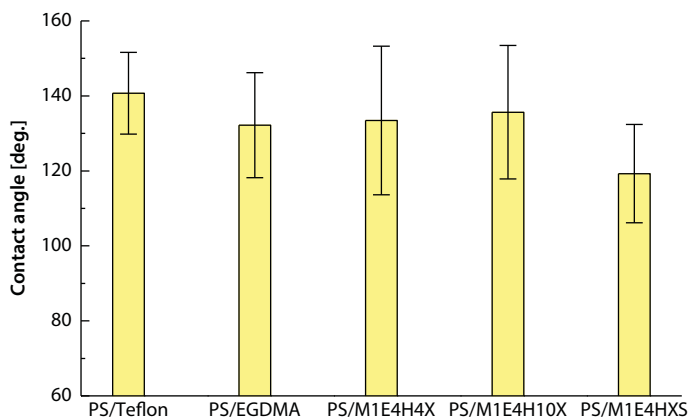


Figure 15.8 Tadmor's equilibrium water contact angles calculated for the PS layers with various embedded polymer fillers deposited on glass slides.

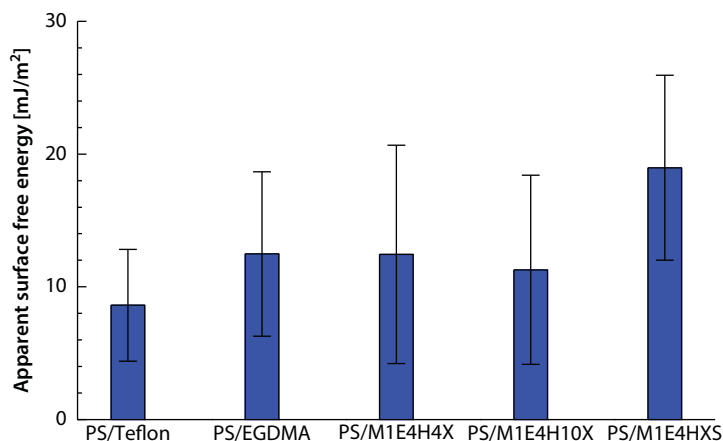


Figure 15.9 Apparent surface free energy for the PS layers with various embedded polymer fillers deposited on glass slides.

15.4 Conclusions

In summary, the incorporation of appropriate polymer powders on the glass plates covered first with polystyrene can be considered as an inexpensive and reliable method for preparing superhydrophobic layers. Practical application of this method requires further study. However, other types of substrate materials can also be considered using this method e.g. metals. In almost all cases the superhydrophobic effect was obtained on rough surfaces. Although a surface with hierarchical rough structure should be considered as a system with valleys and hills on the surface, the calculation of apparent surface free energy can also give interesting information about the wettability of superhydrophobic surfaces. The hysteresis approach proposed by Chibowski seems to be a good model for calculation of the apparent surface free energy in the case of rough hydrophobic surfaces. Also calculation of the equilibrium contact angles from Tadmor theory [16–18] can contribute to a better description of such surface wettability properties.

References

1. A. Carré and K.L. Mittal (Eds.) *Superhydrophobic Surfaces*, CRC Press, Boca Raton, FL (2009).

2. S.D. Wang and Y.Y. Shu, Superhydrophobic antireflective coating with high transmittance. *J. Coat. Technol. Res.* 10, 527–535 (2013).
3. Z. Chen, L. M. Hao, M.M. Duan and C. L. Chen, Electrodeposition fabrication of Co-based superhydrophobic powders coating in non-aqueous electrolyte. *Appl Phys A* 111, 581–585 (2013).
4. F. Guo, X. I. Su, G. L. Hou and P. Li, Bioinspired fabrication of stable and robust superhydrophobic steel surface with hierarchical flowerlike structure. *Colloids Surfaces. A* 401, 61–67 (2012).
5. E. Chibowski, L. Holysz, K. Terpilowski and M. Jurak, Investigation of superhydrophobic effect of PMMA layers with different fillers deposited on glass support. *Colloids Surfaces. A* 291, 181–190 (2006).
6. L. Holysz, K. Terpilowski, V. Zarko and E. Chibowski Superhydrophobic polystyrene layers filled with silica glass. *Surface Innovations*, 1, 52–59 (2013).
7. R. N. Wenzel, Resistance of solid surfaces to wetting by water, *Ind. Eng. Chem.* 28, 988–994 (1936).
8. A. Cassie and S. Baxter, Wettability of porous surfaces, *Trans. Faraday Soc.* 40, 546–551 (1944).
9. J. Drelich, E. Chibowski, D. D. Meng and K. Terpilowski, Hydrophilic and superhydrophilic surfaces and materials, *Soft Matter*, 7, 9804–9828 (2011).
10. E. Chibowski, Contact angle hysteresis due to a film present behind the drop, in: *Contact Angle, Wettability and Adhesion. Vol.2*, K.L. Mittal (Ed.), CRC Press, Boca Raton, FL, pp. 265–288 (2002).
11. E. Chibowski, On some relations between advancing, receding and Young's contact angles, *Adv. Colloid Interface Sci.* 133, 51–59 (2007).
12. F. M. Etzler, Determination of the surface free energy of solids: A critical review, *Rev. Adhesion Adhesives*, 1, 3–45 (2013).
13. A.W. Neumann, R.J. Good, C.J. Hope and M. Sejpal, An equation-of-state approach to determine surface tensions of low-energy solids from contact angles. *J. Colloid Interface Sci.* 49, 291–304 (1974).
14. T. Young, An essay on the cohesion of fluids. *Phil. Trans. R. Soc. Lond.*, 95, 65–87 (1805).
15. A. Marmur, Measures of wettability of solid surfaces. *Eur. Phys. J. Special Topics*, 197, 193–198 (2008).
16. R. Tadmor, Line energy and the relation between advancing, receding, and Young contact angles, *Langmuir* 20, 7659–7664 (2004).
17. R. Tadmor and P. S. Yadav, As-placed contact angles for sessile drops, *J. Colloid Interface Sci.*, 317, 241–246 (2008).
18. R. Tadmor, Line energy, line tension and drop size. *Surface Sci.*, 602, L108–L111 (2008).

Tablet Tensile Strength: Role of Surface Free Energy

Frank M. Etzler* and Sorana Pisano

Lake Erie College of Osteopathic Medicine, Erie, PA 16509, USA

Abstract

Tablets are the most common dosage form employed by the pharmaceutical industry. They are both inexpensive to produce and convenient to patients. Active pharmaceutical ingredients, particularly those incorporated into innovator company products, are new chemical substances whose chemical and physical properties are incompletely known and are sometimes present in large amounts in the manufactured products. Excipients present in the formulation can, at least partially, offset undesirable properties of active ingredients. Successful tablet formulation, in addition to having desirable medicinal properties, must be manufacturable. In order to be manufacturable tablets must have sufficient tensile strength to survive handling, processing and packaging. In this paper, a model based on adhesion science principles is discussed that allows the tensile strength of candidate formulations to be calculated from the Ryshkewitch-Duckworth parameters of the component materials. Both the model and the Ryshkewitch-Duckworth equation suggest that tablet porosity is the principal measure of the outcome of the tableting process. The model and available data further suggest a role for particle surface free energy in determining tablet tensile strength.

Keywords: Ryshkewitch-Duckworth equation, compaction, tableting, surface free energy, adhesion, tablet porosity

*Corresponding author: fetzler@lecom.edu

16.1 Introduction

16.1.1 Overview

Tablets are the most common dosage form employed by the pharmaceutical industry. They are both inexpensive to produce and convenient for patients. Active pharmaceutical ingredients, particularly those incorporated into innovator company products, are new chemical substances whose chemical and physical properties are incompletely known and are sometimes present in large amounts in the manufactured products. Excipients are often incorporated into tablet formulations to overcome at least some of the undesirable properties of the active ingredient. Successful formulations, in addition to having desirable medicinal properties and sufficient chemical and physical stability under environmental stress, must be manufacturable. In order to be manufacturable the powder from which tablets are formed must have adequate flow properties and tablets must have sufficient tensile strength to survive handling during manufacturing, packaging and subsequent handling during shipping and patient use.

Achieving adequate tensile strength can sometimes be a challenge, particularly when formulations contain large amounts of active ingredient or require special excipients to enhance dissolution or increase stability. Special excipients may have undesirable properties with regard to tableting.

During tableting, powder is uniaxially compressed in the die. During the compression process the powder is densified under the applied pressure. Densification of the powder occurs through particle rearrangement, particle fracture and particle deformation. The relative extent of each of the three identified densification mechanisms that occurs in a specific instance is determined by the applied pressure, the rate of the increase of pressure, the duration of the applied pressure, and the mechanical properties of the materials that are being compressed.

Adhesion strength depends on both the quality and quantity of intimate contact between the materials in question. The densification of the powder that occurs during tableting results in an increase in the contact area between the particles. The quality of interaction depends on the specific surface chemical properties and surface free energy of the materials in question.

The pharmaceutical literature has discussed the mechanical aspects of the tablet making process but has rarely discussed it from a surface chemistry or adhesion science perspective. In this paper, we discuss a model based on surface chemical principles that can be used to calculate the tensile strength of tablets from constituent components. Specifically, the role of surface free

energy is discussed. Understanding the fundamental nature of materials used in pharmaceutical manufacture is required for quality by design.

16.1.2 Densification of Powders under Pressure

Celik [1] has reviewed the literature concerning the densification of powders during compaction. Here only some of the highlights are discussed.

At least 19 different equations have been discussed in the literature in order to explain the densification of powders under compaction. At present, no universally accepted equation exists although some of the discussed equations are more popular than others. Further details regarding these models can be found in Celik's discussion.

All of the models discussed by Celik require knowledge of D , the packing density. $D = 1$ for a solid object and in general

$$D = \frac{\rho_b}{\rho_s} \quad (16.1)$$

Here, ρ_b is the bulk density of the powder under the applied pressure or the tablet density after removal from the die and after compaction. ρ_s is the true density of the material.

16.1.3 Measurement of Tablet Tensile Strength

The tensile strength of tablets is routinely tested as a measure of tablet quality [2]. It is possible to consider three types of tensile strength – radial, bending, and axial. Here we discuss only the radial tensile strength as it is by far the most common measurement.

The radial tensile strength is assessed by measuring the diametrical crushing force using what is commonly referred to as a “hardness tester”. The diametrical crushing force is dissimilar to indentation hardness and the use of “hardness” in the present context is erroneous but nonetheless conventional. Like other mechanical tests, the diametrical crushing force is dependent on the test speed; thus, results may vary between testers.

The speed of the tableting process can be expressed in a number of ways. The term speed may refer to the speed at which the tablet punches advance, the dwell time, the total contact time of the punches with the tablet or the rotational speed of the press. In a conventional tablet press, all of these terms are interrelated. The dwell time is usually defined as the time for the compression wheels to pass over the flat portion of the top of the tablet punch. For the Instron, discussed later in this work, it is the time that the

tablet punch remains in fixed position. This is not dissimilar to the case of the rotational press.

The radial tensile strength, τ , is calculated from the diametrical crushing force, F_c , for cylindrical tablets using the relation below [2–4].

$$\tau = \frac{2F_c}{\pi dh} \quad (16.2)$$

Here, d is the tablet diameter and h the tablet thickness. It is the radial tensile strength that is commonly determined to assess tablet quality. Procipio *et al.* [5] have discussed measurement of radial tensile strength.

16.1.4 The Ryshkewitch-Duckworth Equation

Ryshkewitch [6] and Duckworth [7] proposed an empirical equation to relate tablet tensile strength, τ , to porosity of the tablet, ε ($\varepsilon = 1 - D$). Thus,

$$\tau = \tau_0 e^{-k\varepsilon} \quad (16.3)$$

Here τ_0 is the tensile strength of the material at zero porosity ($D = 1$) and k a characteristic constant.

Differentiating Equation 16.3 with respect to ε and approximating the resultant exponential as a series results in the following relation.

$$\frac{d\tau}{d\varepsilon} \approx \tau_0 (1 - k\varepsilon) \quad (16.4)$$

This result suggests both k and τ_0 are related to adhesion quality. In other words, both quantities are related to $\frac{d\tau}{d\varepsilon}$

Over the past several decades the Ryshkewitch-Duckworth equation has been discussed a number of times. Recently, the Ryshkewitch-Duckworth equation has been discussed by Doelker [2], Barraleta *et al* [8], Nyongesa and Aduda [9] as well as by Tye *et al.* [10]. The literature suggests that the Ryshkewitch-Duckworth equation has been successfully applied to a variety of systems that have applications both to pharmaceutical science and to other disciplines.

The importance of the Ryshkewitch-Duckworth equation is that it suggests that porosity is a measure of the outcome of the tableting process. Tablets of the same porosity have the same mechanical properties even though they might have been made on vastly different tablet presses operating at different speeds.

The Ryshkewitch-Duckworth equation is an empirical equation. Andersson has, however, offered a theoretical explanation [11]. Knudsen [12] also comments on the Ryshkewitch-Duckworth equation and associates the increase in tensile strength with an increase in the surface area of contact and the k parameter to the difficulty of creating contact area. k is expected to be temperature dependent.

16.1.5 Surface Science of Adhesion

The thermodynamics of the surface free energy, γ , of solids has been reviewed by Etzler [13–14]. The ideal work of adhesion, W_A , between materials A and B is defined by the following relation.

$$W_A = \gamma_A + \gamma_B - \gamma_{AB} \quad (16.5)$$

where the subscripts A and B on the surface free energy terms refer to materials A and B, respectively. Similarly, if materials A and B are identical the work of cohesion, W_c , can be defined as:

$$W_c = 2\gamma_{A,B} \quad (16.6)$$

Fowkes [15–16] suggested that surface free energy and thus the work of adhesion could be considered as a sum of components resulting from various types of intermolecular interactions. At present, it is conventional to express the work of adhesion as a sum consisting of a term for Lifshitz-van der Waals interactions and second term resulting from Lewis acid-base interactions [13]. Frequently, Lifshitz-van der Waals interactions are dominant.

Intermolecular forces between molecules result from interactions between their corresponding electron orbitals. The principal non-bonding interactions result from induced dipole–induced dipole (London), dipole–induced dipole (Debye) and dipole–dipole (Keesom) interactions. The intermolecular potential energy function, U , for each of these three types of interactions is of the same form. Here, r is the separation distance between bodies.

$$U = \frac{-\beta_{12}}{r^6} \quad (16.7)$$

If only London dispersion forces are considered the constant in Equation (16.7) can be expressed as follows:

$$\beta_{12}^d = \left(\frac{2\sqrt{I_1 I_2}}{I_1 + I_2} \right) (\beta_{11}^d \beta_{22}^d)^{1/2} \quad (16.8)$$

Here the subscripts 11, 22 and 12 refer to interactions between like molecules (11, 22) and dissimilar molecules (12). β is the coefficient in Equation (16.7). I is the ionization potential. If $I_1 \approx I_2$ then

$$\beta_{12}^d = (\beta_{11}^d \beta_{22}^d)^{1/2} \quad (16.9)$$

Equation (16.9) forms the basis of the Berthelot principle [17–18] which states that dispersion interactions between dissimilar molecules can be estimated as the geometric mean of the interactions between like molecules.

The interaction potentials between molecules have been used to determine the interactions between macroscopic bodies. In this instance, the Hamaker constants, A , derived from β , also follow the geometric mean rule [13, 18–19]. Thus,

$$A_{12} = (A_{11} A_{22})^{1/2} \quad (16.10)$$

and assuming further that intermolecular distances, d , also follow the geometric mean rule [13]. The work of adhesion due to London dispersion forces may be expressed as follows.

$$W_{12}^d \approx \frac{(A_{11} A_{22})^{1/2}}{12\pi d_{11} d_{22}} = (W_{11}^d W_{22}^d)^{1/2} = 2(\gamma_{11}^d \gamma_{22}^d)^{1/2} \quad (16.11)$$

It has been further generalized that all of the Lifshitz-van der Waals (LW) components follow the same rule thus

$$W_A^{LW} = 2(\gamma_1^{LW} \gamma_2^{LW})^{1/2} \quad (16.12)$$

Berthelot's rule is widely accepted and is part of most models used to explain adhesion and contact angle phenomena.

16.1.6 A Model to Predict the Tensile Strength of Tablets from Individual Components

In an earlier paper, Wu *et al.* [20] proposed a model to calculate the radial tensile strength of tablets from the Ryshkewitch-Duckworth parameters of

the individual components of the powder being compressed. Tye *et al.* [10] and Sun [21] have also commented further on this approach. In particular, Tye *et al.* [10] have extended the application to quaternary mixtures. These studies establish the importance of the Ryshkewitch-Duckworth equation for understanding tensile strength of tablets composed of multiple components. Furthermore, they reiterate the importance of porosity as a measure of the outcome of the tableting process. Tablets even though produced by vastly different tablet presses operating at different speeds can be expected to have the same mechanical properties if they have the same porosity. The compaction force or compaction pressure may, however, not be the same if different presses are employed.

Here we propose a model which is similar to that proposed by Wu *et al.* [20] but which differs from that of the earlier authors by drawing more strongly from the principles of adhesion science. The form of the final equation also differs.

For a material the tensile strength, τ , is related to the surface free energy, γ [19]. Thus for two particles composed of the same material,

$$\tau \propto \gamma = (\gamma^{1/2})^2 \quad (16.13)$$

and if the particles are composed of different materials.

$$\gamma_{12} = \left(\gamma_1^{1/2} \gamma_2^{1/2} \right) \quad (16.14)$$

or

$$\tau_{12} = \left(\tau_1^{1/2} \tau_2^{1/2} \right) \quad (16.15)$$

Berthelot's rule is thus applied to the tensile strength between particles. We extend Berthelot's rule for an ensemble of particles assuming the geometric mean rule applies to an ensemble of adhesive contacts between particles and is weighted via the surface area fraction, ϕ_s , thus

$$\tau = \prod_i \tau_i^{\phi_s} \quad (16.16)$$

If the particles sizes of the components are similar then $\phi_s \propto \phi_v$ where ϕ_v is the volume fraction. Equation(16.16) is thus rewritten as:

$$\tau = \prod_i \tau_i^{\phi_v} \quad (16.17)$$

Combining Equation (16.17) and the Ryshkewitch-Duckworth equation (Equation (16.3)) yields the following relation.

$$\tau = \prod_i \left(\tau_{0_i} e^{-k_i \varepsilon} \right)^{\varphi_{vi}} \rightarrow \ln(\tau) = \sum_i \varphi_{vi} \left[\ln(\tau_{0_i}) - k_i \varepsilon \right] \quad (16.18)$$

$$= \ln(\tau_{0m}) - k_m \varepsilon$$

Equation (16.18) indicates that the Ryshkewitch-Duckworth parameters for a powder composed of several components may be calculated from the Ryshkewitch-Duckworth parameters of the individual components using the following relations.

$$\ln(\tau_{0m}) = \sum_i \varphi_{vi} \ln(\tau_{0_i}) \quad (16.19)$$

$$k_m = \sum_i \varphi_{vi} k_i \quad (16.20)$$

16.2 Applicability of the Proposed Model to Pharmaceutical Materials

Earlier [22], the applicability of the model proposed above (Section 1.6) to binary mixtures of common pharmaceutical excipients and sodium dodecyl sulfate (SDS) was investigated. SDS was chosen for study as its mechanical properties are vastly different from the other excipients – indeed more so than those selected by Wu *et al.* [20] and Tye *et al.* [10]. Secondly, SDS for various reasons is sometimes incorporated into pharmaceutical formulations and degrades the tableability of such formulations.

16.2.1 Experimental Details

Briefly the experimental details of the earlier study are summarized [22]. Tablets were prepared using an Instron fitted with a 9 mm punch (long dwell times) and an MCC Presster (short dwell times) was used with a 10mm punch. All tablets were flat faced so the tablets are cylindrical.

The tensile strength (τ) is calculated using the well-known relation that was previously introduced (Equation 16.2) and is again shown below (Equation 16.21) (Equation 16.12). Tablet porosity (ε) was calculated using Equation (16.22).

$$\tau = \frac{2F_c}{\pi dh} \quad (16.21)$$

$$\varepsilon = 1 - D = 1 - \frac{\rho_{\text{tablet}}}{\rho_{\text{true}}} \quad (16.22)$$

Where D is the relative density and ρ_{tablet} is the apparent density of the tablet and ρ_{true} is the material density determined using He pycnometry.

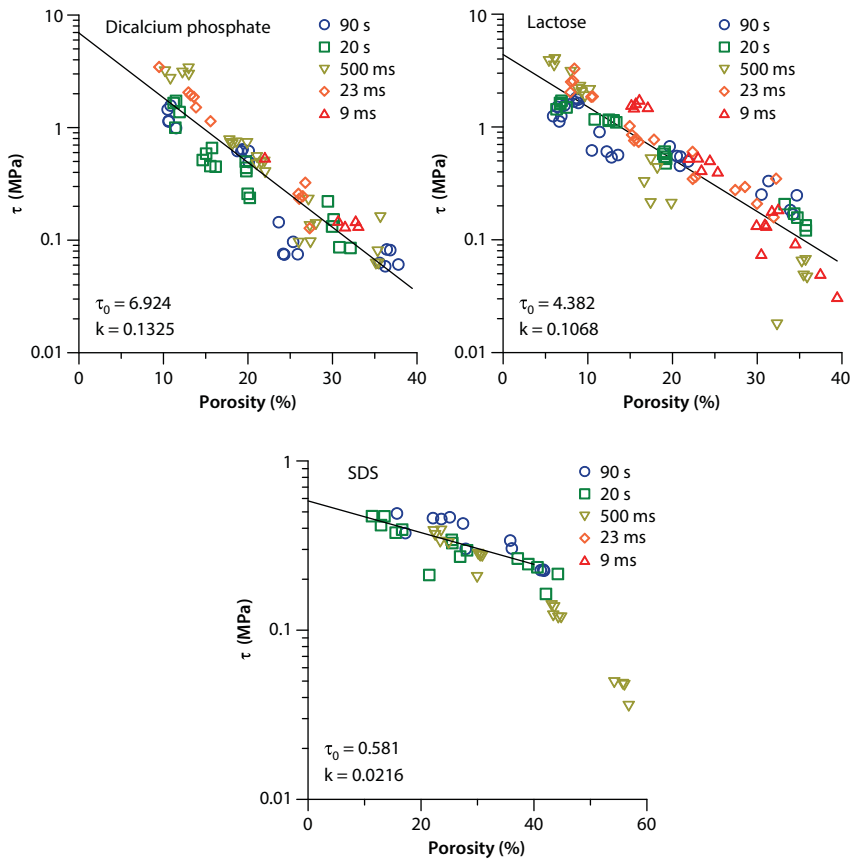


Figure 16.1 Ryshkewitch-Duckworth plots for dicalcium phosphate, lactose and sodium dodecyl sulfate (SDS) at several dwell times. As suggested in earlier publications [22] no dwell time dependence is noted. If data are missing for a given dwell time then tablets were not formed at this dwell time. Points represent data for individual tablets.

16.2.2 Ryshkewitch-Duckworth Equation as a Predictor of the Tensile Strength of Binary Mixtures

The tensile strengths of binary mixtures are shown in Figures 16.1-8. In general, the results conform to the proposed model and the Ryshkewitch-Duckworth equation. Specifically, the tensile strengths of tablets when plotted against porosity follow an exponential dependence. Furthermore, the dependences of k and τ_0 show the proper dependence on SDS volume fraction. k follows a linear dependence with volume fraction and τ follows an exponential dependence with volume fraction.

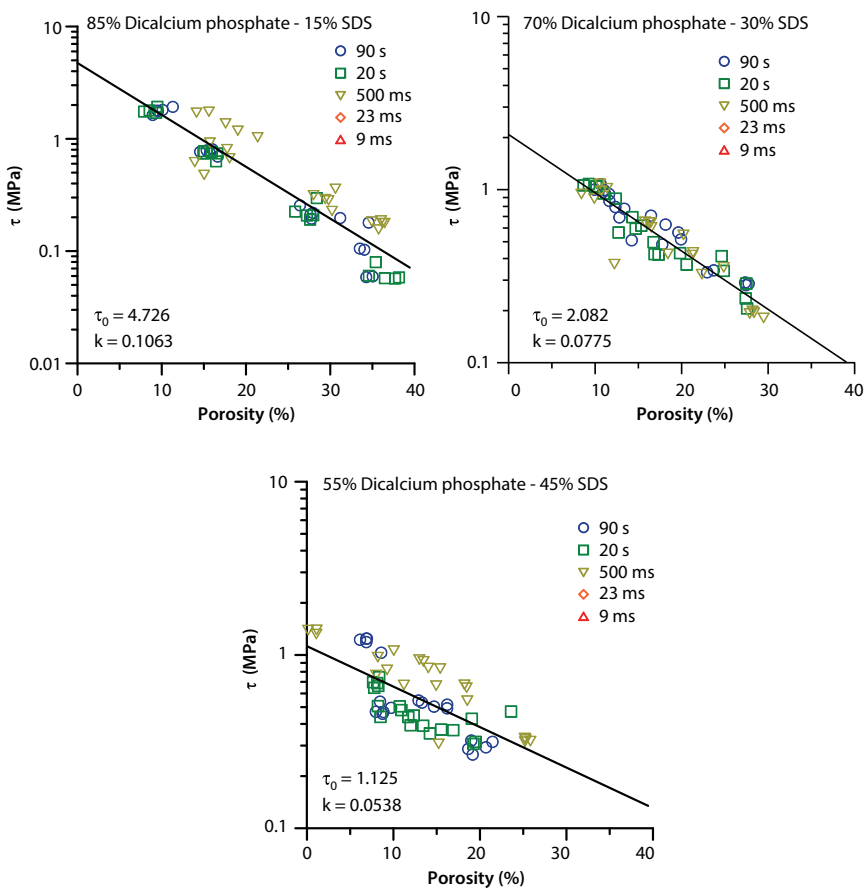


Figure 16.2 Ryshkewitch-Duckworth plots for dicalcium phosphate and sodium dodecyl sulfate (SDS) mixtures at several dwell times. As suggested in earlier publications [22] no dwell time dependence is noted. If data are missing for a given dwell time then tablets were not formed at this dwell time. Points represent data for individual tablets.

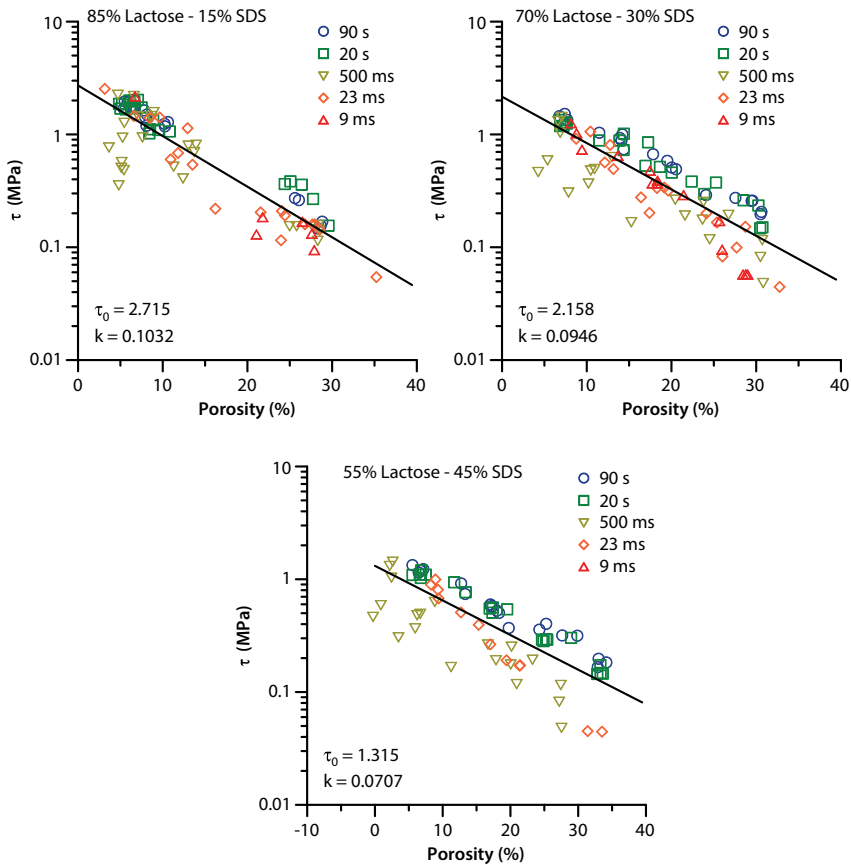


Figure 16.3 Ryshkewitch-Duckworth plots for lactose and sodium dodecyl sulfate (SDS) mixtures at several dwell times. As suggested in earlier publications [22] no dwell time dependence is noted. If data are missing for a given dwell time then tablets were not formed at this dwell time. Points represent data for individual tablets.

16.2.3 Dependence on Processing Parameters

Earlier a study was performed [23] using a formulation containing a drug compound (A), l-arginine, poly(ethylene glycol) 8000, SDS and mannitol. Tablets were made from the formulation by direct compaction and wet granulation. Plots of tensile strength versus porosity (Figure 16.9) show that the model presented above accurately predicts the tensile strength from the Ryshkewitch-Duckworth parameters of the individual components for direct compression but not for the formulation that was subject to wet granulation (The formulations are otherwise identical.). In the case

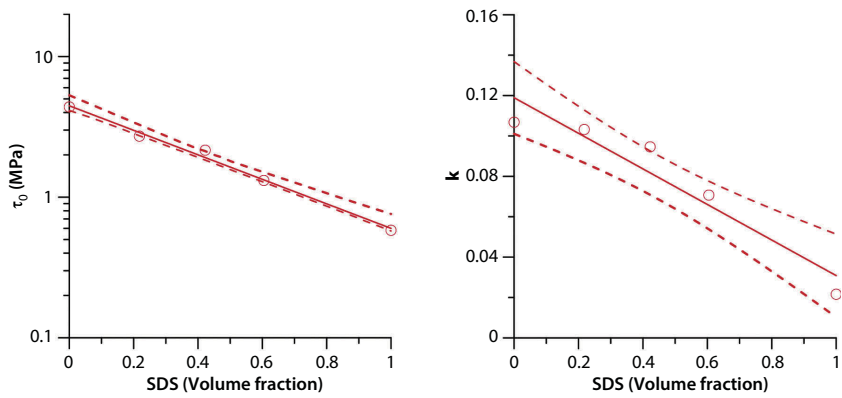


Figure 16.4 Ryshkewitch-Duckworth parameters for lactose and sodium dodecyl sulfate mixtures. Results conform to the proposed model and Equations (16.19) and (16.20). The 90% confidence interval of the least squares fit is indicated by the dashed lines. The solid line is the least squares fit to the data points.

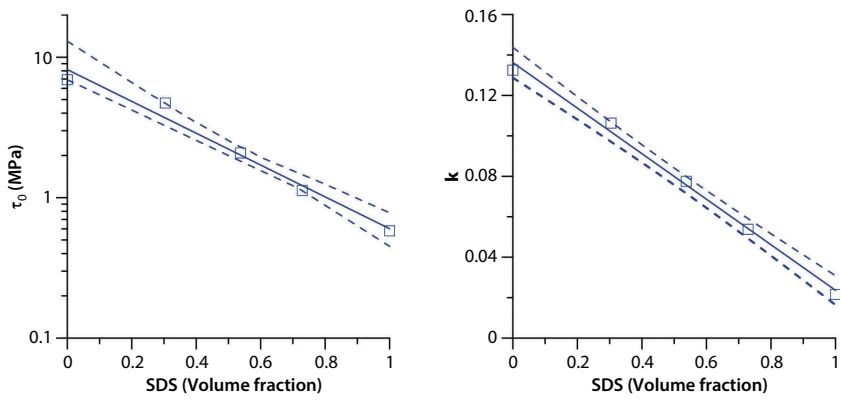


Figure 16.5 Ryshkewitch-Duckworth parameters for dicalcium phosphate and sodium dodecyl sulfate mixtures. Results conform to the proposed model and Equations (16.19) and (16.20). The 90% confidence interval of the least squares fit is indicated by the dashed lines. The solid line is a least squares fit to the data points.

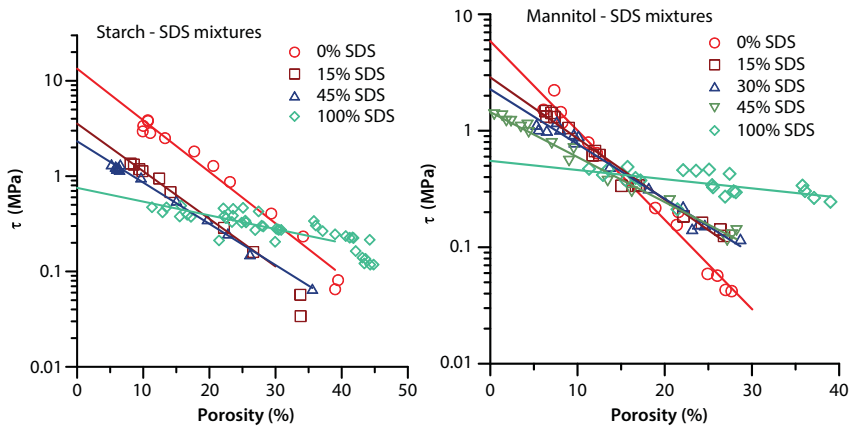


Figure 16.6 Ryshkewitch-Duckworth plots for starch and mannitol mixtures with sodium dodecyl sulfate (SDS)

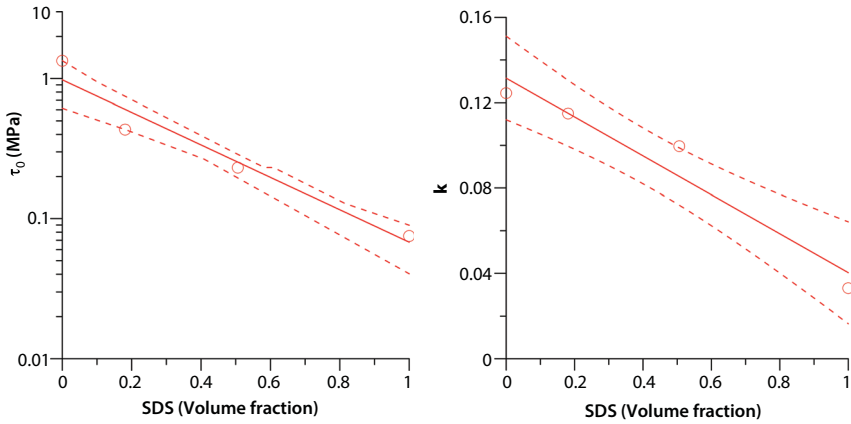


Figure 16.7 Ryshkewitch-Duckworth parameters for starch and sodium dodecyl sulfate mixtures. Results conform to the proposed model and Equations (16.19) and (16.20). The 90% confidence interval of the least squares fit is indicated by the dashed lines. The solid line is the least squares fit to the data points.

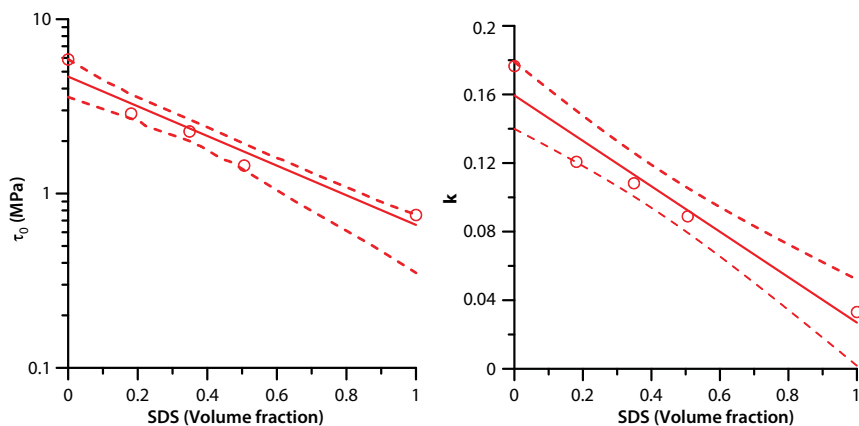


Figure 16.8 Ryshkewitch-Duckworth parameters for mannitol and sodium dodecyl sulfate mixtures. Results conform to the proposed model and Equations (16.19) and (16.20). The 90% confidence interval of the least squares fit is indicated by the dashed lines. The solid line is the least squares fit to the data points.

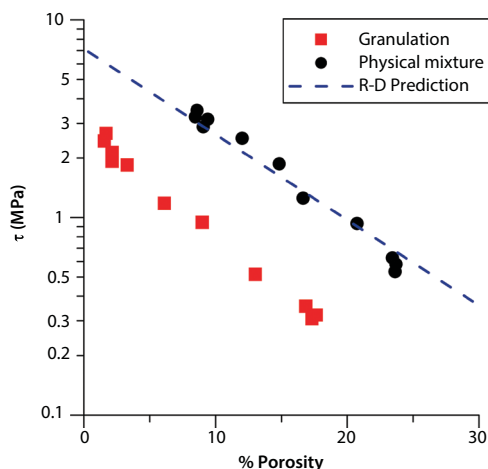


Figure 16.9 Tensile strength versus porosity for a drug formulation containing a drug compound, l-arginine, poly(ethylene glycol) 8000, SDS and mannitol [23]. Circles – tablets prepared using direct compression. Squares – tablets prepared using wet granulation. Wet granulation reduces tensile strength. Dashed line – Prediction using Ryshkewitch-Duckworth parameters for individual components.

of the wet granulated formulation, the tensile strength is less than that predicted by the model. (See Figure 16.9)

Further investigation indicated that the wet granulation had no effect on the tensile strength of tablets prepared from individual components except for l-arginine. (See Figure 16.10) Powder x-ray analysis showed that crystalline form for all but l-arginine was unaffected by wet granulation. L-arginine, in contrast, appears to form a hydrate. The deviation of the Ryshkewitch-Duckworth plot for wet granulated l-arginine from that predicted from the ungranulated material is, however, noticeable but small. As SDS is reasonably water soluble and is highly surface active it would appear reasonable to conclude that the surface free energy of the powder particles is lowered by adsorption of SDS.

Sun [24] has investigated the compaction of microcrystalline cellulose equilibrated to various water activities. Sun's investigation shows that compaction properties of moisture-sensitive polymers depend on water activity. The data also show that adhesion between microcrystalline cellulose particles is reduced by the presence of adsorbed moisture. Presumably the reduction in adhesion results from the corresponding reduction in direct bonding between powder particles. Some of the results contained in Sun's study are shown in Figure 16.11. More recently, Garcia -Mir *et al.* [25] have studied the compaction of both microcrystalline cellulose and chitin as a function of water activity. The tablets in this study were compressed to a constant pressure without regard to porosity so much of the power of

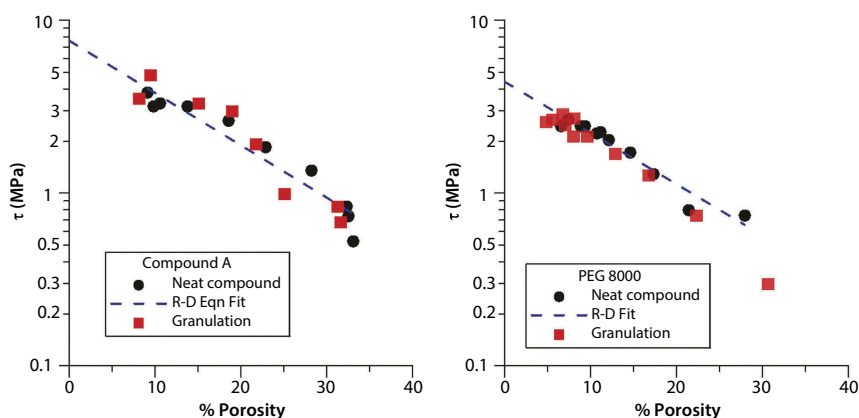


Figure 16.10 Tablet tensile strength versus porosity for two individual components (drug compound and PEG 8000) of the formulation discussed in Figure 16.9 [23]. Circles—neat compounds. Squares - wet granulations. Dashed line - prediction using Ryshkewitch-Duckworth parameters for neat compound.

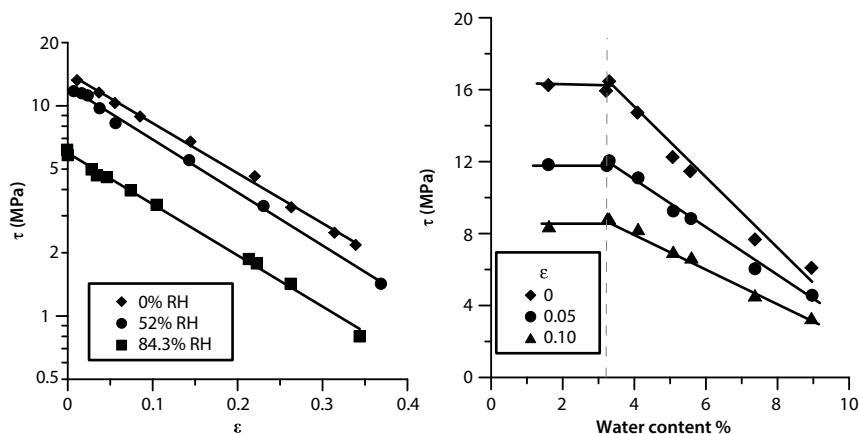


Figure 16.11 Left- tensile strength vs. porosity for microcrystalline cellulose at different water activities (%RH). Right – tensile strength versus water content for microcrystalline cellulose at different porosities. Water content is determined by water activity. Vertical dashed line represents monolayer coverage by water. Plots redrawn from data by Sun [24]. Data suggest that adsorbed water reduces adhesion between powder particles.

the study is lost as tablets at constant porosity cannot be compared. The data available for both chitin and microcrystalline cellulose are, however, consistent with Sun's earlier measurements. Chamrathy *et al.* [26] report a study on the compaction of microcrystalline cellulose that rather clearly demonstrates the relation between surface chemistry and mechanical property changes that occur with the sorption of water. The Ryshkewitch-Duckworth parameters for moisture sensitive- materials appear to be a function of water activity. Adsorbed water appears to affect both the surface chemistry of the particle surfaces as well as the mechanical properties of the material.

16.2.4 Direct Evidence for the Role of Surface Free Energy

Direct evidence for the role of surface free energy in determine tablet tensile strength is limited. Two studies , however, have been performed that suggest a role of surface free energy in determining tablet tensile strength. Tablet porosity was not carefully controlled or recorded in these studies so further confirmation is likely to be desirable.

El Gindy and Samara [27] measured the tensile strength of tablets composed of aspirin, indomethacin, magnesium stearate, potassium chloride and sodium chloride. The selection of materials used in this study allows

for a wide variation in surface free energy. Their results are seen in Figure 16.12. The figure clearly shows the relation between surface free energy and tablet tensile strength.

Luangtana-Anan and Fell [28] also studied the relation between surface free energy and tablet tensile strength. The correlation between the Lifshitz-van der Waals contribution to surface free energy, γ^{LW} , and tablet tensile strength is shown in Figure 16.13.

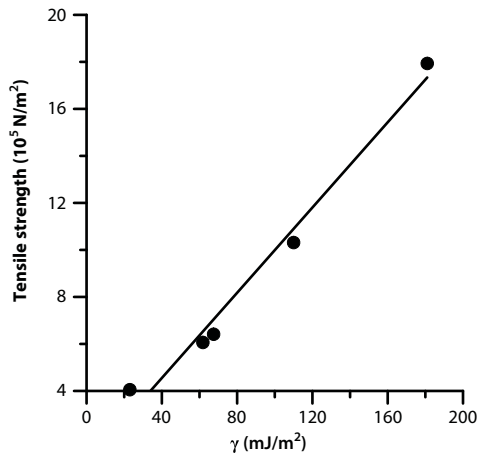


Figure 16.12 Tablet tensile strength versus surface free energy, γ , for several materials. Figure drawn from data by El Gindy and Samara [27].

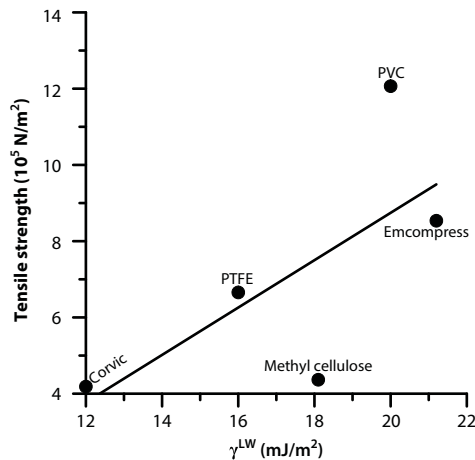


Figure 16.13 Tablet tensile strength versus γ^{LW} for several materials. Figure is drawn from data by Luangtana-Anan and Fell [28].

The two papers discussed above appear to be the only studies to date to relate surface free energy to tablet tensile strength. These authors appear not to have carefully controlled tablet porosity. Typical tablets have porosities between 0.1 and 0.2. Outside this range tablets are usually regarded as too hard or too soft for commercial use or sometimes even for laboratory handling. The range of porosities for tablets represented in the figures is thus likely to be limited thus minimizing the effect of porosity.

16.3 Discussion

Figures 16.1-3 show Ryshkewitch-Duckworth plots for dicalcium phosphate or lactose mixtures with sodium dodecyl sulfate as well as the Ryshkewitch-Duckworth plots for each of the pure components. As previously observed by Wu *et al.* [20] and Tye *et al.* [10] no dependence on dwell time was noted. We did note that tablets were not formed for some materials when short dwell times, comparable to production conditions, were used. Presumably, insufficient time is given for viscoelastic deformation of the materials that is, in part, responsible for adhesion. Viscoelastic recovery upon decompression may also contribute to lamination of tablets on decompression. Figures 16.1-3 and Figure 16.6 show the importance of tablet porosity to tablet tensile strength. Porosity should be considered a measure of the outcome of the tableting process.

For tablets to be commercially successful empirical experience suggests that tablets should have, at minimum, tensile strengths of 1–2 MPa with porosities of 10–20%. These properties ensure adequate strength for shipping and handling as well as appropriate dissolution times.

Figure 16.6 shows the effect on tensile strength caused by the addition of sodium dodecyl sulfate to mannitol and starch. It is interesting to note that at high porosities sodium dodecyl sulfate tablets are stronger than either mannitol or starch tablets. Sodium dodecyl sulfate requires little pressure to undergo deformation and tablet formation. At high porosities and low pressures, it appears that the deformation of sodium dodecyl sulfate allows it to act as an adhesive. As sodium dodecyl sulfate is a weak material as evidenced by its low τ_0 value, tablets at low porosities are weakened by increasing concentrations of sodium dodecyl sulfate. Figure 16.6 illustrates the mutual dependence of the Ryshkewitch-Duckworth k and τ_0 parameters with SDS concentration.

Figures 16.4, 16.5, 16.7 and 16.8 show the dependence of the Ryshkewitch-Duckworth parameters, τ_0 and k , on volume fraction of sodium dodecyl

sulfate. These plots are consistent with the model proposed in this work and Equations (16.19) and (16.20). The plots furthermore suggest that the tensile strength of tablets composed of multiple components can be calculated if the Ryshkewitch-Duckworth parameters are known for the component materials.

The work by Dudhedia *et al.* [23] suggests that processes, such as wet granulation, may sometimes alter the surface characteristics. In the instance described by Dudhedia *et al.* [23] the surface free energy of the materials appears to be reduced by spreading of SDS over particle surfaces during granulation. The study also suggests some materials may form hydrates during granulation. Hydrate formation alters the Ryshkewitch-Duckworth parameters for a compound.

Polymeric materials that adsorb water may show modified adhesion characteristics with the adsorption of water. The study by Sun [24] suggests that adsorption of water beyond 1 monolayer reduces adhesion between microcrystalline cellulose particles. Hydration of such polymers, of course, also alters the mechanical properties of a material.

More direct evidence for the role of surface free energy in determining tablet tensile strength is provided by the work of El Gindy and Samara [27] as well as that by Luangtana-Anan and Fell [28]. These studies also indicate the need for future more careful investigations that show the direct role of surface free energy in determining the Ryshkewitch-Duckworth parameters and tablet tensile strength.

16.4 Summary

In this paper the compaction of several common pharmaceutical excipients blended with sodium dodecyl sulfate is investigated. Furthermore, a model based on the principles of adhesion science is proposed for calculation of tablet radial tensile strength as a function of tablet porosity for powders composed of several materials. The data indicate that the model, indeed, allows for the calculation of tablet tensile strength from the Ryshkewitch-Duckworth parameters of the component materials.

The proposed model specifically suggests a role for surface free energy in determining tablet tensile strength. It is noted here that spreading of surfactants during wet granulation over powder particles reduces the tensile strength of tablets. In the case of water sorbing polymers (microcrystalline cellulose) it is found that sorption of water (at fixed tablet porosity) reduces tablet tensile strength.

The studies of El Gindy and Samara [27] as well as that by Luangtana-Anan and Fell [28] directly indicate relation between particle surface free energy and tablet tensile strength.

Here we have demonstrated the essential features of a proposed model for determining tablet tensile strength from the properties of the component materials. The dependence of the Ryshkewitch-Duckworth parameters with tablet composition is consistent with the proposed model. Furthermore, the relation between particle surface free energy and tablet tensile strength is consistent with the available data. Calculations of the type discussed can be used to improve the efficiency of the formulation process. The model presented here is a step toward achieving "quality by design" in the pharmaceutical industry.

Acknowledgements

The authors wish to thank Richard Deanne, Tommasina Bramante Svetlana Sinkiewicz, Dr. Sid Majumdar, Mayur Dudhedia, Doris (Chiappetta) Baker and George Gereg for their contributions to this work.

References

1. M. Celik, Overview of compaction data analysis techniques. *Drug Development and Industrial Pharmacy* 18, 767–810 (1992).
2. E. Doelker, Assessment of powder compaction, in: *Powder Technology and Pharmaceutical Processes*, D. Chulia, M. Deleul and Y. Pourcelot (Eds.), p. 403, Elsevier, New York (1994).
3. E. Doelker, D. Mordier and S. Kopp, Relevance of various mechanical strengths of pharmaceutical compressed tablets, in: *Powder and Grains*, J. Biarez and R. Gourves (Eds.), pp. 411–416, Balkema, Rotterdam (1989).
4. J. T. Fell and J. M. Newton, Determination of tablet strength by diametrical-compression test. *J. Pharm. Sci.* 59, 688–691 (1970).
5. A. T. Procipio, A. Zavaliangos and J. C. Cunningham, Analysis of the diametrical compression test and the applicability to plastically deforming materials. *J. Mater. Sci.* 38, 3629–3639 (2003).
6. E. Ryshkewitch, Compression strength of porous sintered alumina and zirconia, 9th communication to ceramography. *J. Amer. Ceramic Soc.* 36, 65–68 (1953).
7. W. Duckworth, Discussions of Ryshkewitch paper by Winston Duckworth. *J. Amer. Ceramic Soc.* 36, 68 (1953).

8. J. E. Barralet, L. Grover, T. Gaunt, A. J. Wright and I. R. Gibson, Preparation of macroporous calcium phosphate cement tissue engineering scaffold. *Biomaterials* 23, 3063–3072 (2002).
9. F. W. Nyongesa and B. O. Aduda, Fracture strength of porous ceramics: Stress concentration vs minimum solid area models. *African J. Sci. Technol. (AJST)* 5, 19–27 (2004).
10. C. K. Tye, C. Sun and G. E. Amidon, Evaluation of the effects of tableting speed on the relationships between compaction pressure, tablet strength and tablet solid fraction. *J. Pharm. Sci.* 94, 465–472 (2005).
11. C. A. Andersson, Derivation of the exponential relation for the effect of ellipsoidal porosity on elastic modulus. *J. Amer. Ceramic Soc.* 79 2181–2184 (1996).
12. F. P. Knudsen, Dependence of mechanical strength of brittle polycrystalline specimens on porosity and grain size. *J. Amer. Ceramic Soc.* 42, 376–387 (1959).
13. F. M. Etzler, Surface free energy of solids, in: *Contact Angle, Wettability and Adhesion*, Vol. 3, K. L. Mittal (Ed.), p. 219–264, CRC Press, Boca Raton, FL (2003).
14. F. M. Etzler, Determination of the surface free energy of solids: A critical review. *Rev. Adhesion Adhesives* 1, 3–45 (2013).
15. F. M. Fowkes, Calculation of work of adhesion by pair potential summation. *J. Colloid Interface Sci.* 28, 493–505 (1968).
16. F. M. Fowkes, Determination of interfacial tensions, contact angles, and dispersion forces in surfaces assuming additivity of intermolecular interactions in surfaces. *J. Phys. Chem.* 66, 382 (1962).
17. D. Berthelot, Sur le mélange des gaz. *Compt. Rend.* 126, 1857–1858 (1898).
18. W. V. Chang and X. Qin, Repulsive acid-base interactions: Fantasy or reality, in: *Acid-Base Interactions: Relevance to Adhesion Science and Technology*, vol 2., K. L. Mittal (Ed.), pp. 3–53, CRC Press, Boca Raton, FL (2000).
19. A. W. Adamson, *Physical Chemistry of Surfaces*, 4th ed., J. Wiley, New York (1990).
20. C.-Y. Wu, S. M. Best, A. Craig Bentham, B. C. Hancock and W. Bonfield, A simple predictive model for the tensile strength of binary tablets. *European J. Pharm. Sci.* 25, 331–336 (2005).
21. C. Sun, Critical roles of porosity in tableting properties characterization and solids formulation development. *Amer. Pharm. Rev.* 8, 105–108 (2005).
22. F. M. Etzler, T. Bramante, R. Deanne, S. Sienkiewicz and F. J. Chen, Tablet tensile strength: An adhesion science perspective. *J. Adhesion Sci. Technol.* 25, 501–519 (2011).
23. M. S. Dudhedia, D. K. Chippetta, S. K. Mujumdar and F. M. Etzler, Prediction of tensile strength of multicomponent physical mixture and multicomponent granulated system: A case study presented at the AAPS National Meeting (AAPS, New Orleans, LA, 2010).

24. C. C. Sun, Mechanism of moisture induced variations in true density and compaction properties of microcrystalline cellulose. *Int. J. Pharm.* 346, 93–101 (2008).
25. V. Garica-Mir, J. Heinamaki, O. Antikainen, A. I. Colarti, S. Airaksinen, M. Karljalainen, O. B. Revoredo, O. M. Nieto and J. Yliruusi, Effects of moisture on tablet compression of chitin. *Carbohydrate Polymers* 86, 477–483 (2011).
26. S. P. Chamarthy, F. X. Diringier and R. Pinal, The plasticization-antiplasticization threshold of water in microcrystalline cellulose: A prespective based on bulk free volume, in: *Water Properties in Food, Health, Pharmaceutical and Biological Sciences*, D. S. Reid, T. Sajjaanantakul, P. J. Lillford and S. Charoenrein (Eds.), pp. 297–314 Blackwell, New York (2010).
27. N. A. El Gindy and M. W. Samara, Tensile strength of some pharmaceutical compacts and their relation to surface free energy. *Int. J. Pharm.* 13, 35–46 (1983).
28. M. Luangtana-Anan and J. T. Fell, Bonding mechanisms in tableting. *Int. J. Pharm.* 60, 197–202 (1990).

Why Test Inks Cannot Tell the Whole Truth About Surface Free Energy of Solids

Ming Jin, Frank Thomsen, Thomas Skrivanek and Thomas Willers*

KRÜSS GmbH, Applications, Hamburg, Germany

Abstract

If information about a solid surface free energy (SFE) is needed, contact angle measurements and ink tests are two of the most frequently used methods. Here we present a comparative study of contact angle measurements and ink tests on 13 different materials. We observed major differences in the SFE values obtained by these two techniques and explained the differences on the basis of basic theoretical concepts of both methods. We found that test inks fail to monitor the efficiency of atmospheric plasma treatments on low surface energy solids. Moreover, we determined the polar and dispersion contributions to the test inks total surface tension (ST) in order to provide a more detailed understanding of these methods to determine a solid SFE.

Keywords: Surface free energy, test inks, dyne pens, plasma treatment, adhesion, contact angle

17.1 Introduction

The wetting characteristics of a liquid on a solid are largely driven by the relationship between the liquid surface tension (ST) and the solid surface free energy (SFE). Untreated plastics and materials with hydrophobic contamination have a low surface free energy and often low polarity. These characteristics lead to poor wetting and adhesion, particularly in contact with water-based varnishes and printing inks as well as adhesives and coatings. A cleaning or activation pre-treatment process is, therefore, necessary for

*Corresponding author: T. Willers@kruss.de

polymers and many other materials. Typical pretreatment processes include thermal or electrical methods, such as plasma, flame or corona treatment [1–3], and chemical treatment with oxidizing gases or conversion baths. Equally important are cleaning steps which remove hydrophobic substances from the surface. All these methods increase the substrate surface free energy (SFE) and therefore improve wettability and adhesion of liquids on the substrate. It is obvious that the success of these processes needs to be monitored by determining the solid SFE before and after such treatments. Contact angle measurements and ink tests are two of the most frequently used methods for this purpose. Both methods have been established for decades and are widely used. However, ink tests often fail to do the job in real-life applications letting the operator be at a loss with his particular wetting problem.

In this article we review the theoretical concepts of both methods on a basic level and compare their differences by presenting experimental data obtained by both techniques.

17.2 Background

In a **contact angle measurement**, a drop of a pure test liquid is dispensed onto the solid sample. The drop is recorded using a camera, and the video image is evaluated.

The contact angle θ is measured at the threephase point (liquid, solid, gas) between the lines describing the phase borders liquid-gas and solid-liquid. The better the wetting, the smaller this angle is; for complete wetting, it is 0° .

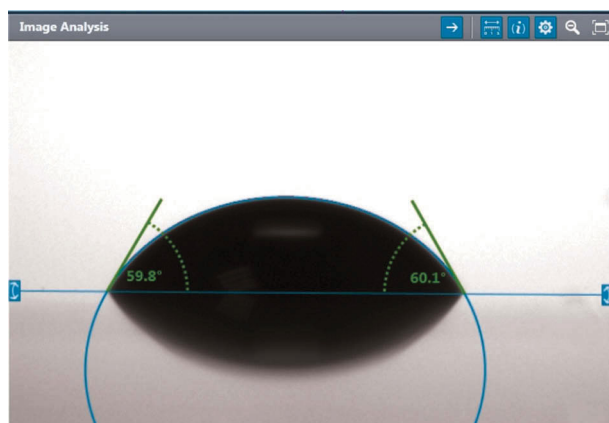


Figure 17.1 Evaluating the drop image to measure the contact angle

According to Young's equation [4], which has been used for over 200 years, there is a fundamental relationship between the contact angle θ , the SFE of the solid σ_s , the ST of the liquid σ_l and the interfacial tension (IFT) σ_{ls} between liquid and solid:

$$\sigma_s = \sigma_{ls} + \sigma_l \cos \theta \quad (17.1)$$

This equation can be heuristically understood as a balance of interfacial forces at the solid-liquid-gas three-phase point (see Figure 17.2). Here, $\sigma_l \cos(\theta)$ is the projection of the liquid surface tension onto the horizontal plane and in equilibrium θ adjusts such that for given interfacial forces the resulting net force vanishes. For the sake of completeness it should be noted that the upward capillary force of $\sigma_l \sin(\theta)$ is balanced by a strain field in the solid [5] that can be described by a force normal to the solid-liquid border line, and thus having a negligible effect on the contact angle, i.e. the wetting property. We also want to add here that from thermodynamic considerations the work of adhesion W_A of a liquid wetting a solid is

$$W_A = \sigma_s + \sigma_l - \sigma_{ls} \quad (17.2)$$

To determine solid SFE from Young's equation, knowledge about the liquid ST, the contact angle θ and the IFT σ_{ls} is required. The first two can be measured directly and the last can be calculated using different theories modeling the interactions between solid and liquid. Here, we will not illuminate all the different theories used to calculate the IFT, but we will review the common concepts of these different approaches. The different models find a mathematical description for the interfacial tension σ_{ls} which is solely a function of the solid SFE σ_s and the liquid ST σ_l . This is done by taking into account that the ST and SFE originate from different fundamental physical and chemical interaction forces and thereby ST and SFE are partitioned into several components. The most general and lump-sum way is to distinguish between Lifshitz-van der Waals (LW) forces and

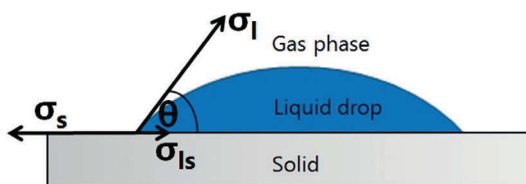


Figure 17.2 Equilibrium of forces, i.e. variables affecting the formation of the contact angle according to Young's equation.

Lewis acid-base (AB) interactions. Thus, the total ST of a liquid or SFE of a solid can be written as

$$\sigma^{\text{total}} = \sigma^{\text{LW}} + \sigma^{\text{AB}} \quad (17.3)$$

Lifshitz-van der Waals forces can be understood in the framework of quantum electrodynamics as the result of electron-density fluctuations causing electromagnetic waves between the interacting partners. This type of interaction is always present and thus might be understood as the *physical* reason for surface tension, IFT, and SFE.

In the term Lewis acid-base interaction virtually all other types of specific chemical interactions are lumped together. In the most general understanding a Lewis acid-base interaction between two participants is present whenever an electron pair is shared by the two. This can range from a covalent bonding in one extreme to an ionic interaction in the other. This type of interaction is related to certain functional groups and does not need to be present permanently. Thus, it could be taken as an additional chemical contribution to ST, SFE and IFT in addition to the always present Lifshitz-van der Waals interactions.

In a large part of the (current) literature the Lifshitz-van der Waals component (σ_i^{LW}) is simply termed “dispersion” component and the Lewis acid-base interactions (σ_i^{AB}) are interpreted as “*polar*” interactions even though the material’s dipole moments may be zero or the interactions originating from permanent dipoles are very small and can be easily associated with the dispersion part [6]. The misleading denominations go back to a historical misidentification of the acid-base interactions as “polar” interactions in the Owens-Wendt-Rabel-Kaelble [7–9] approach to calculate the IFT [6] (OWRK model). However, as an impact on the SFE calculation by this misinterpretation of this old theory occurs only when a monopolar base interacts with a monopolar acid, this nomenclature is still widely used. And here in this work we will also use the terms *dispersion* and *polar* interactions to differentiate the two major contributions to SFE, ST, and IFT. For a detailed discussion of the use of contact angles in determining SFE of solids and other methods of determining SFE, see Etzler [10].

Whereas the above mentioned OWRK model [7–9] assumes that SFE and ST consist of only the two components, namely the polar and the dispersion parts, there are also other models that use an even more elaborate distinction between the different types of interactions ending up with SFE, ST and thus IFT being a sum of more than just two components. Furthermore, all the different models to describe the IFT differ in their detailed descriptions (i.e. mathematical functions) of how the different parts of the liquid

ST interact with the different parts of the solid SFE. However, almost all of these make the same basic assumption that one specific part of the liquid ST solely and exclusively interacts with the corresponding part of the solid SFE. Thus, for the here used most basic distribution into dispersion and polar parts of SFE and ST, a simple rule of thumb describing the IFT is found: when a liquid gets in contact with a solid, the polar part of the liquid interacts only with the polar part of the solid and the dispersion part only with the dispersion one. Later in the text, it will be shown that this most basic assumption / model already helps to explain the major differences between test inks and contact angle measurements.

The **ink test** is based on the assumption that the SFE of the solid is equal to the ST of the liquid which just fully wets the solid. Test inks consist of a series of liquid mixtures, each with a set ST, usually in increments of 2 mN/m. During the test, one of the inks is applied to the sample with a brush stroke. If the applied film of the ink contracts, the ink with the next lower ST is used until the brush stroke produces a stable film on the solid. This corresponds to complete wetting of the sample. If the first stroke is stable, the ink with the next higher ST is applied until the brush stroke does not produce a stable film. The ST of the test ink which just forms a stable film is equated to the SFE of the material.

This concept is reminiscent of the idea of Zisman plots. Zisman and coworkers noted in 1964 [11,12] that for a given solid a plot of the cosine of the contact angle θ against the ST values of a series of liquids should result in a straight line. The extrapolation of this straight line to $\cos \theta = 1$ ($\theta = 0$) provides the so-called critical surface tension of the solid, which is normally considered as the solid SFE. However, Zisman already mentioned a number of prerequisites concerning the test liquids used: they must not swell or dissolve the solid, their vapors must not adsorb on the solid, and they must not interact specifically (H-bonding, acid-base interactions) with the solid. In particular, the importance of the last prerequisite is not considered in the ink test concept, which characterizes one major disadvantage of the ink test concept.

To summarize, in the ink test method, wetting experiments with liquids with different total ST are made to find the liquid with the highest SFT that just wets the solid. And in the contact angle methods the contact angles of at least two well-defined test liquids on the solid under investigation are determined. Knowing the polar and dispersion contributions to the test liquid's total SFT can provide further information about the polar and dispersion parts of the solid SFE. Making use of different models describing the solid-liquid IFT the total SFE and its polar and dispersion parts can be calculated from the contact angle data. Most of these models start from

the polar and dispersion components of the liquid ST and the solid SFE. The model according to Owens, Wendt, Rabel and Kaelble (OWRK) [7–9] assumes the most basic build-up of the total SFT, SFE, and IFT, because they are subdivided into only two main parts. Further, it is frequently used in the field of plastics analysis. We therefore also use this model for calculating IFT and SFE from the contact angle data in the present study.

17.3 Materials and Methods

17.3.1 Solid Samples Investigated

To make the study as broad as possible, we have investigated 13 materials including plastics, minerals and metals. We also chose very different material qualities, from almost ideally chemically homogeneous surfaces and technical raw materials to finished commercial products. With this selection we have covered a broad spectrum of possible scientific and industrial applications, where knowledge about the solid SFE is desired.

The change in SFE after plasma treatment was also investigated for PDMS, PVC and PET.

17.3.2 Sample Preparation

Before measurements were carried out, all samples (except mica) were cleaned with a degreasing detergent solution and then rinsed thoroughly with hot and cold tap water and finally with distilled water. Remaining water drops were subsequently removed with isopropanol. The samples were finally dried with clean compressed air. The mica samples were freshly cleaved using an adhesive tape.

17.3.3 Test Inks Used

We carried out tests with two different series of commercially available test inks for all samples:

- Series A (yellow): Colored mixture of ethanol and water (Tantec surface energy inks)
- Series B (blue): Colored mixture of formamide and ethylene glycol monomethyl ether (EGMM), according to ISO 8296 (Tantec surface energy inks)

Table 17.1 List of solid samples investigated.

Sample	Quality (type, source)	Designation
Acrylonitrile butadiene styrene	Technical (Arthur Krüger, Germany)	ABS
Aluminum	Finished product (foil)	Aluminum
Glass	Finished product (Microscope Slides, Carl Roth GmbH, Germany)	Glass
Mica	Chemically homogeneous mono-crystal, freshly cleaved (Highest Grade V1 Mica Discs, Ted Pella Inc., USA)	Mica
Polyamide 6 (Akulon® K222 D)	Technical	PA6
Polyamide 6 + 3% Cloisite® 30B	Technical	PA6 + 3% C30
Poly(dimethylsiloxane)	Pure, synthesized (Dow Corning Sylgard 184 Silicone Elastomer)	PDMS
Polyethylene	Finished product (film)	PE
Poly(ethylene terephthalate)	Finished product (bottle)	PET
Polypropylene	Technical	PP
Poly(tetrafluoroethylene)	Technical	PTFE
Poly(vinyl chloride)	Finished product (tablecloth)	PVC
Silicon wafer	Chemically homogeneous monocrystal	Si

The tests were carried out in accordance with the ASTM D 2578-84 standard.

Inks with ST values in 2 mN/m increments in the range between 30 and 56 mN/m were used for each test. Therefore, SFE values above 56 mN/m and below 30 mN/m could not be determined.

17.3.4 Contact Angle Measurement

The contact angle measurements were carried out using a KRÜSS Drop Shape Analyzer – DSA100. A software-controlled dosing system for several liquids was used for the dosing operation.

We chose three standard test liquids: water, diiodomethane and ethylene glycol for determining the SFE. This choice covers the range from purely dispersive to highly polar and is, therefore, particularly suitable for determining polar and dispersion components.

Static contact angles were measured (measurement using constant drop volume). The drops were produced at the tip of the needle of the dosing unit, carefully deposited on the sample and subsequently analyzed. There were no time-dependent changes in the contact angle for any of the samples.

17.3.5 Plasma Treatment

We used a Rheinhausen Plasma piezobrush® plasma pen (Regensburg, Germany) in air at atmospheric pressure for plasma treating PDMS, PVC and PET. The pen was positioned above the DSA100's software controlled x-y sample stage at a distance of 8 mm from the sample. The sample stage moved the solid substrate with a speed of 2 mm/sec in a direction vertical to the plasma source. The sample was moved over a distance of 40 mm and then back again so that the total exposure time for a treated strip of 40 mm was 40 seconds. Treatment with an exposure time of 60 s was also carried out for PDMS and PVC; in this case, the sample stage moved the sample under the pen one more time.

17.4 Results and Interpretation

17.4.1 SFE Determination for Untreated Samples

The following table contains the SFE results from the contact angle measurements and the ink tests for the materials which were not plasma treated:

In the case of the two very low surface free energy polymers, PDMS and PTFE, the SFE values were below 30 mN/m. This SFE range could not be probed with the test inks available in this study (starting from 30 mN/m). For the same reason we were unable to draw any conclusion regarding the correlation for glass, as the value of 64.6 mN/m determined by means of contact angles was above the range of the test inks used.

Table. 17.2 Results of comparative SFE determinations between contact angles and ink tests for all untreated samples. For the contact angle method the SFE was calculated following the OWRK approach.

Sample	SFE by OWRK Method Using Measured Contact Angles [mN/m*, Polar Component in %]	Test ink A [mN/m]	Test ink B [mN/m]
ABS	37.1 [16%]	34	34
Al	55.9 [46%]	≥56	≥56
Glass	64.6 [50%]	>56	>56
Mica	53.7 [24%]	>>56	>>56
PA 6	50.6 [19%]	≥56	≥56
PA 6+3% C30	52 [24%]	≥56	≥56
PDMS	21.6 [0%]	<<30	<<30
PE	32.2 [0%]	30	30
PET	44.2 [3%]	34	34
PP	29.6 [0%]	≤30	30
PTFE	16.1 [0%]	<<30	<<30
PVC	47.1 [3%]	30	32
Si	48.5 [39%]	46	42

*Note: SFE is generally expressed in mJ/m² unit. However, we think that both mN/m and mJ/m² are correct units for SFE as both are in SI units system and mN/m = mJ/m².

The results for PE and PP corresponded well. With all other samples, in many cases there were considerable differences between the contact angle and test ink results, and also sometimes differences between the test inks.

17.4.2 Interpretation Based on Interfacial Tension

It can be seen that for samples with a non-polar low SFE, i.e. PE and PP, the results obtained from test inks and contact angles correspond well. Deviations occur with higher surface free energy, polar samples. This can be explained by the fact that the ink test ignores a variable which is important for wetting, namely the IFT σ_{ls} (see Figure 17.2). According to the ink

test method, complete wetting occurs whenever the SFE is equal to the ST of the liquid. This is the case when the vectors σ_s and σ_l in Figure 17.2 are of equal length. The IFT σ_{ls} is not taken into account. In fact, the IFT can be greater than zero even when σ_s and σ_l are equal.

The following diagrams (see Figure 17.3) use Young's equation to illustrate the possibility of different wetting states in cases where the SFE and ST are equal in each case.

Accordingly, incomplete wetting can occur even when SFE and ST are equal; in fact, this is very likely.

The IFT depends on the interactions between solid and liquid. In the hypothetical absence of any attractive interactions between liquid and solid, the liquid tends to minimize its interface with the solid, i.e. it avoids wetting the solid. Accordingly, the IFT between solid and liquid is maximized in the absence of interactions and decreases with increasing interactions between solid and liquid.

As mentioned in the background section we apply a most basic model in that the total ST and SFE consist of two main components, the polar and the dispersion ones:

$$\sigma^{total} = \sigma^d + \sigma^p \quad (17.4)$$

Furthermore, as both contributions originate from physically different interaction processes, all theories applying this two-component model assume that the polar part of the solid SFE interacts solely with polar part of the liquid ST and dispersion part of the solid SFE interacts solely with the dispersion part of the liquid ST.

The following cartoon illustrates this behavior on an exemplary pair of solid and liquid. The Figure 17.4 shows a liquid with a total ST of 50 mN/m in contact with a solid with an SFE of also 50 mN/m. Thus, following the idea of test inks, the liquid should wet the solid completely. The large hands represent the (often stronger) polar parts and the small hands the (often weaker) dispersion parts of SFE and ST. The top panel shows a perfect match between the polar and dispersion parts: every polar hand of the solid grabs a polar hand of the liquid and every dispersive hand finds its dispersive partner. The interaction between solid and liquid is maximized and the interfacial tension vanishes. In this case of a vanishing interfacial tension, the contact angle becomes zero as illustrated in the bottom panel of Figure 17.3. However, in practice such a situation can only be found if totally dispersive liquids get in contact with totally dispersive solids.

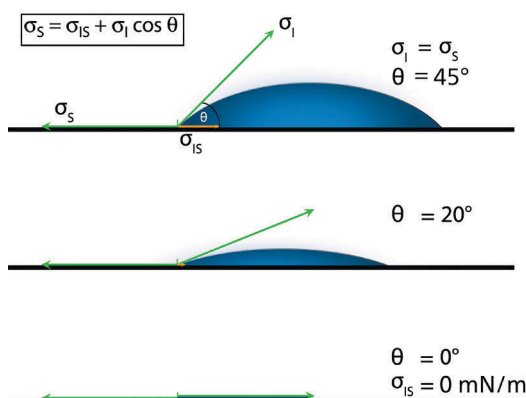


Figure 17.3 Different wetting states in spite of equality between SFE and ST. The smaller the contact angle, the smaller is the IFT (yellow arrow).

The bottom panel of Figure 17.4 shows the case in which the distribution into polar and dispersion parts of SFE and ST are different. In this case, there is only one corresponding pair of large polar hands and small dispersive hands. As a consequence, there is a remaining interfacial tension at the liquid-solid interface. This remaining interfacial tension results in a contact angle larger than zero degree as illustrated in the top and middle panels in Figure 17.3. Despite SFE and ST being equal, the liquid does not fully wet the solid as expected when following the test ink idea. This is exactly the case when a test ink is applied on a solid with a certain degree of polarity.

Finally, it is worthwhile to discuss a major intrinsic difference in the observed wetting processes when using static contact angle measurements and ink tests: a static contact angle measurement describes the result after a spontaneous wetting process, whereas an ink test rather monitors the result of a spontaneous dewetting process. Ink tests provide information related to the receding contact angle of the ink on the investigated substrate. As a result, for solids that exhibit a large contact angle hysteresis ink tests can only provide limited predictions about spontaneous wetting. For example, for a solid having a static water contact angle of 30° but a receding angle of 0° the yellow test inks would determine the SFE of this solid to be larger than 72 mN/m . This is because the test ink with a surface tension of 72 mN/m consists of pure water and thus forms a stable brush stroke on this solid. However, if water is sprayed on this surface it will not spread but rather form droplets with a contact angle of 30° .

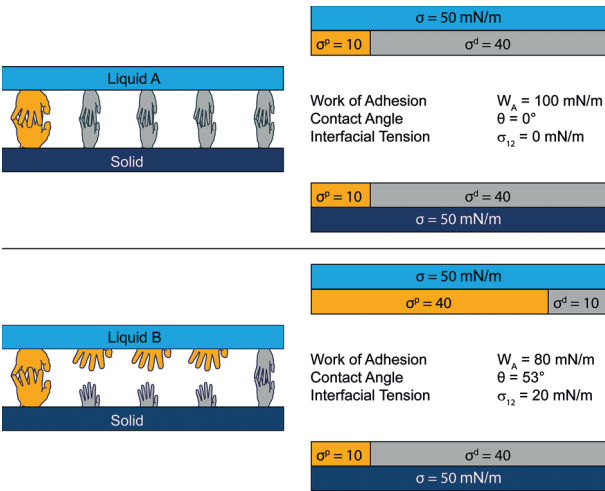


Figure 17.4 Schematic diagram of the interactions for the contact between a solid and a liquid with the SFE value being the same as the ST value, 50mN/m. The top panel illustrates the case of complete wetting as a result of liquid and solid having the same degree of polarity. The bottom panel shows the case of incomplete wetting. The values for IFT, contact angle and work of adhesion were calculated according to the OWRK approach.

17.4.3 Measurements on Plasma-treated Samples


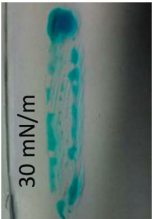
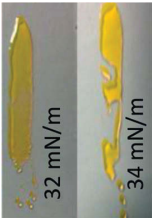


The difference between SFE values using contact angle measurements and test inks was most obvious in the case of plasma-treated samples. Tables 17.3a), b) and c) show the results for PDMS, PVC and PET before and after plasma treatment for different exposure times. We have documented the wetting patterns, i.e. images of brush strokes, for the test inks.

With plasma or corona treatments, polar groups are introduced into the surface structure due to oxidation [1–3]. The change in SFE is, therefore, based substantially on the increase in the polar component. This effect of treatment is shown throughout in the evaluations of contact angles according to OWRK. The very significant increase in SFE due to plasma treatment comes about almost entirely as a result of the increase in polar component.

The test inks do not reflect the increase in SFE for PDMS and PVC. With these two plastics, the test inks are, to a certain extent, blind to the effect of treatment.



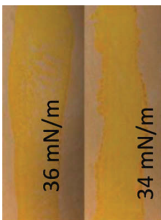
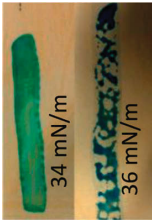

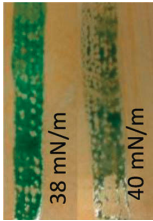
In the case of PET, the effect of pre-treatment is visible to a greater extent in the ink test, but here too, the values lead to an underestimation of the effect of plasma treatment.

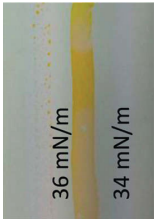
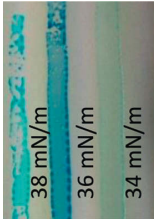
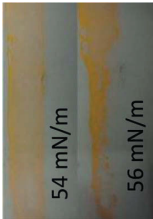

Table 17.3 a-c Results of comparative study between contact angles and ink tests for three untreated and plasma-treated plastics (PDMS, PVC, PET). As the interpretation of ink tests is partly user dependent this table also shows images of relevant brush strokes.

Treatment time	SFE by OWRK from contact angles	Test ink A	Test ink B
0 s	Total: 21.7 mN/m Polar component: 0.0 mN/m Dispersion component: 21.7 mN/m	Total: < 30 mN/m	Total: < 30 mN/m
40 s	Total: 40.3 mN/m Polar component: 14.2 mN/m Dispersion component: 26.1 mN/m	Total: < 30 mN/m 	Total: < 30 mN/m 
60 s	Total: 67.9 mN/m Polar component: 42.4 mN/m Dispersion component: 25.5 mN/m	Total: 32 mN/m  	Total: < 30 mN/m 
a) PDMS			

(Continued)

Table 17.3 a-c (Cont.)

Treatment time	SFE by OWRK from contact angles	Test ink A	Test ink B
0 s	Total: 47.1 mN/m Polar component: 1.4 mN/m Dispersion component: 45.7 mN/m	Total: 30 mN/m 	Total: 32 mN/m 
40 s	Total: 54.1 mN/m Polar component: 6.4 mN/m Dispersion component: 47.7 mN/m	Total: 34 mN/m 	Total: 34 mN/m 
60 s	Total: 61.7 mN/m Polar component: 14.3 mN/m Dispersion component: 47.4 mN/m	Total: 36 mN/m 	Total: 38 mN/m 
b) PVC			

0 s	Total: 47.2 mN/m Polar component: 1.6 mN/m Dispersion component: 45.6 mN/m	Total: 34 mN/m 	Total: 34 mN/m 
40 s	Total: 70.2 mN/m Polar component: 26.1 mN/m Dispersion component: 44.1 mN/m	Total: 54 mN/m 	Total: 54 mN/m 
c) PET			

17.4.4 Characterization of Test Inks

To support the above interpretation of the wetting of substrates by test inks we determined the polar and dispersion parts of the ST for some of the test inks for the series B. For that we applied the OWRK model. For this the total surface tension and the contact angles of the test inks on a totally non-polar reference substrate need to be known. As reference substrate we used PDMS from Dow Corning (Sylgard 184 Silicone Elastomer). As solid PDMS is produced via curing of the freshly mixed liquid the surface of this solid is intrinsically very smooth and it is reasonable to neglect any influence of physical roughness on the contact angle measurement. The SFE of the freshly produced and cleaned (see section 17.3.2) PDMS was determined to be 21.6 mN/m. The total ST of some test inks was checked by pendant drop measurements and was found to be in accord with the manufacturer's denomination of the different inks.

Figure 17.5 summarizes the mean contact angles of the test inks as determined from ten different sessile drops on the PDMS substrates and the deduced distribution into polar and dispersion components of the total ST for each test ink.

As illustrated in Figure 17.5, the degree of polarity increases with increasing total ST. This can be understood when knowing that these test

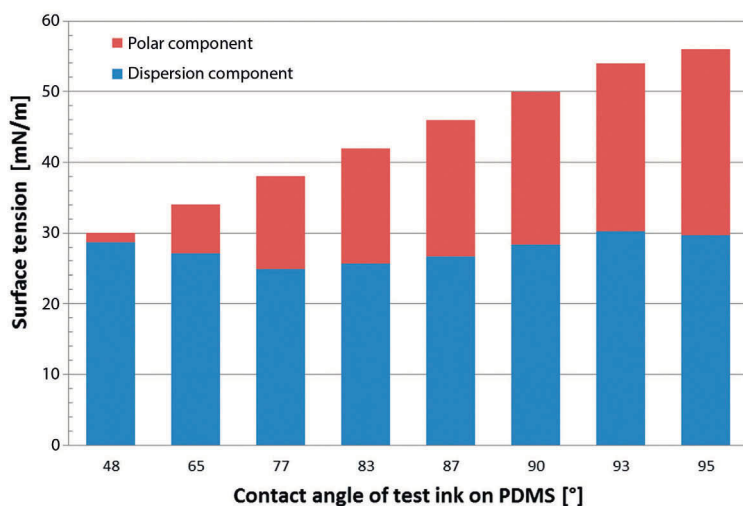


Figure 17.5 Surface tension values and equilibrium static contact angles of the blue test inks (series B, formamide based) on PDMS. The distribution into polar and dispersion parts was calculated from the contact angle data applying the OWRK approach.

inks are simple mixtures of a low value ST almost non-polar liquid with a high ST polar liquid. For the second series of test inks, the yellow ethanol based series A, we observed the same trend of an increasing degree of polarity with increasing total ST (not shown here). In conclusion, every test ink has a different degree of polarity. Thus, it becomes evident that the ink test method in most cases cannot provide even an approximate value about the total SFE of a particular solid. For example, the 50 mN/m ink only fully wets a solid with a total SFE of 50mN/m if its degree of polarity is ~43%, because only in this case the IFT between this particular ink and the solid vanishes. For any other degree of polarity of the solid there is a remaining IFT inhibiting a complete wetting of the ink on the solid (see Figure 17.4). However, an ink completely wetting a solid does not necessarily mean that both the total SFE of the solid and the degree of polarity are the same as for the ink. The ink might just have a smaller total ST than the solid SFE.

It is now simple to explain why only for PP and PE samples the contact angle method and the test ink method give comparable results. These two materials are totally non-polar low SFE (<32mN/m) solids. And the test inks with such low ST are also almost completely non-polar. Thus, for these materials the prerequisite of the test ink concept that the IFT between solid and ink vanishes is fulfilled. As a result, the ink having the same ST as the solid SFE completely wets the solid. However, these almost non-polar test inks are blind to monitor the effect of a plasma treatment on these particular solids, as a plasma treatment adds a polar part to the SFE keeping the dispersion part (almost) unchanged. This was observed, for example, in our measurements on plasma treated PDMS (see Table 17.3a).

17.5 Advantages and Drawbacks of Contact Angle Measurement in Practice

Of course, many users that need to monitor the SFE of solids tend towards using test inks, because the initial acquisition cost for a contact angle instrument is significantly higher than for a set of test inks. And whereas contact angle devices are larger, electrically powered and require a computer, test inks are small, non-powered and often a bit quicker to use. Further, as there are many different ways to measure contact angles (static versus dynamic contact angle and / or optical versus force measurement based methods) using test inks appears to be the simpler and thus straightforward method requiring less knowledge and / or experimental expertise. However, in

addition to the more reliable determination of the total SFE and the information gained about polarity of solid materials, there are also a number of other advantages of the contact angle method compared with the test ink method. For example, knowing the polar and dispersion parts of a solid substrate free energy and of the surface tension of a liquid coating that needs to be applied on the substrate allows calculating the work of adhesion (see Figure 17.5) and the IFT for that particular pair [13]. This provides insight into the quality of an interfacial contact which cannot be obtained from the ink test. The work of adhesion characterizes the driving force with which the two phases initially bond to one another. The IFT refers to the tension between adhesive or coating and substrate remaining at the interface. When the IFT is high, unwanted detachment of the phases from one another occurs more easily, for example, due to the penetration of moisture.

Some test inks, in particular the range obtained in accordance with ISO 8296, contain toxic liquids formamide and EGMM. As a result, the health of test personnel can be endangered during routine quality assurance. Contact angle measurements can be carried out with harmless liquids or with liquids which are less hazardous to health. In addition, significantly smaller amounts of liquids are required for the measurement than with the ink test.

Test inks made on ethanol basis, such as test inks A in our study, are also available as less harmful substitutes. In this case, however, the volatile alcohol content can partially evaporate, so that the composition of the ink changes if bottles are left open or are opened frequently. For the same reason, the wetting behavior can change when the ink is applied.

The risk of contaminating the whole ink supply in a test ink bottle after a measurement on a dirty sample is rather high. As a result the total ST of the test ink can change and thus falsify further measurements. This cannot happen to the test liquids used for contact angle measurements as the test liquid reservoir never gets in direct contact with the samples.

Many samples only offer a small area for carrying out a wetting test. However, test inks require a relatively large amount of space for applying several brush strokes. In contrast, the SFE can be determined on only a few square millimeters by means of contact angles. For some cases test inks can have the advantage to test the SFE of rather larger areas with one quick and very long brush stroke. But this works only as long as there is no contamination on the investigated surfaces, because this will change the ST of the test ink while it is applied on the surface and thus falsify the result.

Before the development of fast and manageable contact angle measuring instruments, test inks offered advantages for testing surfaces directly

and quickly on site. However, recent progress in contact angle measuring devices overcomes this drawback enabling to determine the solid SFE in less than a second using a small portable contact angle instrument.

Finally, with the ink test different interpretations of the wetting behavior are possible so that the results depend on the person carrying out the test. With the state of the art contact angle machines, the results are free from subjective assessment because of computerized automation and digital documentation of the measurement and evaluation.

17.6 Summary

A comparative study of contact angle measurements and ink tests on 13 materials found significant differences in the SFE values in many cases. A good correspondence was obtained only for two low-surface energy, non-polar plastics. We explained the differences taking into account the distribution of total SFE and ST into polar and dispersion parts using the OWKR model. For good wetting, this requires a compatibility of the phases with regard to the polar and dispersion fractions. However, it is highly probable that an ink, with a total ST equal in value to the SFE of the solid, has a different polarity and does not completely wet the sample.

In comparative measurements on three plasma-treated plastics the effect of treatment on two of the materials could be detected by means of contact angles but not by means of the ink tests. In the case of the third plastic, the SFE values from the contact angle evaluation were significantly higher than those from the ink tests.

We have determined the polar and dispersion parts for one type of test inks by means of contact angle measurements on a totally non-polar reference surface by applying the OWRK model. The degree of polarity of both series of inks increases with increasing total ST whereby the inks with the lowest ST are almost completely non-polar. With that we illustrated that the basic prerequisite for the ink test approach, i.e. that the IFT between ink and solid vanishes, is only fulfilled in rare cases.

In addition to the more detailed information that can be gained with contact angle measurement, we have also highlighted some benefits of this method in practice. These include reduced health hazard due to harmless liquids and a completely automated measurement which is independent of assessment by the user and enables proper documentation of raw data and results.

References

1. M. Strobel, C. S. Lyons and K. L. Mittal (Eds.), *Plasma Surface Modification of Polymers: Relevance to Adhesion*, CRS Press, Boca Raton, FL (1994).
2. K. L. Mittal (Ed.), *Polymer Surface Modification: Relevance to Adhesion*, Volume 5, CRC Press, Boca Raton, FL (2009).
3. M. Thomas and K. L. Mittal (Eds.), *Atmospheric Pressure Plasma Treatment of Polymers: Relevance to Adhesion*, Wiley-Scrivener, Beverly, MA (2013).
4. T. Young, On the cohesion of fluids, *Phil. Trans. Royal Soc. London*, 95, 65–87 (1805).
5. R. J. Good, Contact Angle, wetting, and adhesion: A critical review *J. Adhesion Sci. Technol.* 6, 1269–1302 (1992).
6. J. C. Berg, *An Introduction to Interfaces and Colloids*, World Scientific Publishing Co., (2010).
7. D. H. Kaelble, Dispersion-polar surface tension properties of organic solids, *J. Adhesion* 2, 66–81 (1970).
8. D. Owens and R. Wendt, Estimation of the surface free energy of polymers *J. Appl. Polym. Sci.* 13, 1741–1747 (1969).
9. W. Rabel, Einige Aspekte der Benetzungstheorie und ihre Anwendung auf die Untersuchung und Veränderung der Oberflächeneigenschaften von Polymeren, *Farbe und Lack* 77, 997–1005 (1971).
10. F. M. Etzler, Determination of the surface free energy of solids: A critical review, *Rev. Adhesion Adhesives*, 1, 3–45 (2013).
11. W. A. Zisman, Relation of the equilibrium contact angle to liquid and solid constitution, in: *Contact Angle, Wettability and Adhesion*, Adv. Chem. Ser., Vol. 43, pp. 1–51, American Chemical Society, Washington, DC, (1964).
12. H. W. Fox and W. A. Zisman, The spreading of liquids on low-energy surfaces. II. Modified tetrafluoroethylene polymers *J. Colloid Sci.* 7, 109–121 (1952).
13. K. L. Mittal, The role of the interface in adhesion phenomena, *Polym. Eng. Sci.*, 17, 467–473 (1977).

Index

- Ablation threshold, 289, 290
- Absorbed energy, 294, 296
- Adhesion, 288
- Adhesion force, 149–155, 157, 160–163
- Adsorption,
 - chemisorption, 328
 - dye, 305–306, 315, 318, 324–329
 - equilibrium, 319, 328–329
 - Freundlich, 328
 - Langmuir, 328–329
- Air,
 - bubble, 149–151, 155–157
 - layer, 150
- Alginate, 40, 41
- Aparrent contact angle, 216
- Apparent surface free energy
 - calculated for glass
 - plates covered with
 - pure PS layers, 388
- Apparent surface free energy
 - calculated for glass
 - plates covered with the
 - PS filler layers, 389
- Argon, 305, 315–316, 319–329
- Aspect ratio, 34, 39, 298, 300,
- Average friction length, 19
- Berthelot principal, 402, 403
- Biological liquids, 40
- Biolubricant, 270
- Biopolyester, 278
- Biopolymer, 260
- Blade test, 225
- Bond number, 149, 151, 155, 159
- Bubble,
 - contact width, 152–155, 158, 160–161
 - volume, 149–151, 153–154, 158–161
- Bulk superhydrophobic, 249–250
- Buoyancy force, 149, 151–152, 156, 159–161
- Capillarity, 79
- Capillary charge, 84, 92
- Capillary force, 157
- Capillary image force, 94
- Capillary length, 33, 77
- Capillary number, 11
- Capillary time, 11
- Capillary velocity, 23
- Captive bubble, 149
- Car engine oil, 165, 166, 168, 170–172, 174, 175
- Carreau-Yasuda law, 41
- Cassie contact angle, 5, 34
- Cassie-Baxter, 299, 212–214
- Cassie's equation, 112–115, 117–119, 122, 124
- Casson's law, 41
- Cellulose, 261, 365, 366, 374
- Cellulose acetate, 274
- Cheerio effect, 74

- Circular abrasion, 224
- Closest point projection, 136–137
- Composite channels, 12, 42
- Compression/tension test, 242
- Concus-Finn filaments, 4
- Contact angle, 420, 50, 53, 55, 62, 149–164
 - apparent, 309–310
 - Cassie-Baxter, 308, 310
 - equilibrium, 137–139, 306, 309
 - hysteresis, 149, 151, 153, 157–162
 - Wenzel, 308–310
 - Young, 306, 308
- Contact angle (CA), 288, 297, 298, 299, 300, 301
- Contact angle (CA),
 - advancing CA, 169, 292
 - apparent CA, 165, 166, 168, 170, 171, 174, 175
 - intrinsic CA, 168
 - metastable CA, 169
 - receding CA, 169, 292
 - Wenzel CA, 168
 - Young CA, 168
- Contact angle hysteresis (CAH), 288, 292, 297–301, 112, 119, 122, 124
- Contact angle measured on glass plates covered with pure PS Layers, 387
- Contact angle measured on glass plates covered with the PS Layers Embedded with polymer fillers, 388
- Contact angle measurements, 386
- Contaminant particle, 139, 142–145
- Cotton, 266
- Curvilinear coordinates, 130–132
- Cyanoacrylate, 263
- Cyclic olefin copolymer (COC), 16
- Depinning force, 150
- Deposition, 365, 366
- Detachment, 150
- Diamond-like carbon, 365, 368
- Differential geometry, 131–133
- Dip coating, 289, 290
- Dipole orientation, 51–52
- Drop contour analysis methods,
 - circle fitting, 169, 170
 - ellipse fitting, 169, 170
 - Laplace-Young fitting, 169, 170
 - tangent leaning, 169, 170
- Drop penetration test, 348, 349
- Droplet, 371
- Droplet impact, 236–237
- Dual scale roughness, 288, 289, 294, 299
- Dynamic contact angle, 29
- Dyne pens, 423
- Electrowetting-on-dielectric (EWOD), 102
- Equilibrium equation, 134
- Etching, 365, 366
- Ethanol, 47, 49, 61–66
- Evaporation, 6
- Evolver software, 11, 14, 35
- Excimer lamps, 350
- Excimer laser, 342
- Fanning coefficient, 23
- Femtosecond laser ablation, 289, 290
- Finger rubbing, 231
- Flame, 179
- Fluorinated alkylsilane, 297
- Fluorocarbon, 365, 367
- Foam, 192
- Free perimeter, 8, 34
- Friction, 150, 152–153, 157, 159, 161
- Friction and wear, 165, 166
- Friction force, 19
- Friction length, 19
- Friction reduction, 65
- Gas pressure impact, 238
- Gaussian distribution, 290, 300

- Gibbs free energy, 6, 32
- Glucose, 371
- Homogenization, 114
- Hydraulic diameter, 17
- Hydraulic jump, 205
- Hydraulic resistance, 22
- Hydrogen bonds, 47–48, 50–51, 53–55, 59–65
- Hydrophilic surface, 149–151, 154–163
- Hydrophilicity, 47, 66
- Hydrophobic material, 289
- Hydrophobicity, 47, 55, 66, 130, 146
- Hydrostatic pressure, 151
- Images of superhydrophobic layers using optical profilometry, 392
- Imaging of PS layers surface with an optical profilometer, 387
- Impenetrability constraint, 136
- Inertia, 20
- Jet impact, 236–237
- Laplace pressure, 21
- Laser energy density, 301
- Laser fluence, 289, 293, 296, 300, 301
- Laser Intensity Factor (LIF), 294, 298, 300, 301
- Laser power, 291, 292, 294
- Laser processing, 289
- Laser scanning overlap, 289, 291, 292, 293, 300
- Laser scanning speed, 290, 293, 294, 300, 301
- Laser surface modification, 335, 342 surface roughening, 342–346, 350
- Lateral adhesion, 150, 153
- Lateral capillary force, 74
- Lattice structure, 53, 64
- Laundry test, 243
- Lift-off force, 144–145
- Linear abrasion, 219–220
- Liquid filtration, 191
- Lotus, 288
- Lubrication effect, 157
- Lucas-Washburn-Rideal law (LWR), 15
- Mater-Bi, 280
- Measurement and analysis methodology, atomic force microscope, 165, 168, 175 contact angle measurement, 165, 169, 170, 173, 175 drop shape analysis, 169.17 white light interferometer, 165, 168, 175
- Medical testing, 371
- Micro Electromechanical Systems (MEMS), 288
- Micro/nano-structure, 289, 293, 296, 300
- Microfluidic, 369
- Modified Cassie's equation, 113, 118–119, 123–125
- Molecular dynamics simulation, 47–49, 59, 61–62, 66
- Molecular-scale hydrophilicity, 66
- Nanochannel, 28
- Nano-pattern, 293, 299
- Nano-scale, 298, 293, 294
- Newtonian fluids, 19, 20
- Newton's law, 36
- Non-Newtonian fluid, 41
- Optical photographs of the PS layers with embedded polymers particles, 390
- Ordered water monolayer that does not completely wet water, 47, 49, 51, 55–56, 61, 65–66
- Oscillating steel ball, 228
- Oscillating steel ring, 230–231
- OWRK theory, 422
- Oxygen, 305, 311–312, 314–316, 319–329
- Packing density, 399

- Paper, 268, 366, 368, 369, 371, 372, 374
- p-Aramid, 349
 - water repellence, 350–354
- Particle contact, 142–145
- Patterned surface, 291
- Peak fluence, 293, 294, 300
- Pencil hardness test, 227–228
- Periodicity, 293, 296, 298
- Photochemical surface
 - modification, 336, 350
 - graft-co-polymerization, 352
 - photo-grafting, 336
- Photographs of PS layers, 386
- Pickering emulsions, 270
- Plasma, 305–306, 311–317, 319–325, 327–329, 365, 366, 371, 374
- Plasma treatment, 430
- Point-of-care, 4
- Poiseuille number, 23
- Poiseuille profile, 36
- Poly methyl metacrylate (PMMA), 16
- Poly(ethylene terephthalate) (PET), 349
 - oil repellence, 354–358
 - water repellence, 350–354
- Porosity, 397, 403–415
- Porous nanocarbon, 180
- Posidonia oceanica*, 305, 314–316, 318–329
- Preparation of superhydrophobic layers deposited on the glass surface, 385
- Pressure force, 151–152
- Receding contact angle, 292
- Rectangular channel, 28
- Red blood cell (RBC), 41
- Refined paper, 373
- Resistor, 28
- Retentive force factor, 153–154, 160
- Reynolds number, 16
- Rods, 14
- Roll embossing, 30
- Roll-off angle, 216–217
- Roll-off behavior, 369
- Room temperature, 47–48, 49, 51, 56–57, 59–62, 64–66
- Rotary slurry test, 248–249
- Rough surface contact, 140–142
- Roughness,
 - Power Spectral Density (PSD), 165–167, 169, 172, 173
 - root mean square roughness (Rrms), 167, 173
 - roughness ratio (r), 168
 - spatial frequency, 166, 168, 172, 173, 175
 - surface roughness, 165–168, 171–175
- Ryshkewitch-Duckworth equation, 397, 400–416
- Self-cleaning, 288
- Self-healing, 216
- Shear-thinning fluid, 41
- Shedding angle, 217
- Silanization, 290, 292, 297
- Sliding angle, 149, 151–161, 216–217
- SLIPS, 212–213, 215
- Slope angle, 75
- Solid particle impact, 233–234
- Soot, 181
- Stabilization, 136, 141
- Stainless steel / metal surface, 166–168, 170, 172–176
- Starch, 279
- Stickiness, 369
- Stokes equation, 22
- Superamphiphobic, 372
- Superhydrophilic surface, 149–151, 154–161
- Superhydrophobic, 367, 368, 374, 212
- Superhydrophobic medium, 42
- Superhydrophobic surface, 288, 289, 290, 292, 299, 301
- Superoleophobic, 372, 374, 212
- Superomniphobic, 212

- Surface,
 - chemistry, 288, 290
 - energy, 289, 290, 292
 - morphology, 289, 297
 - pattern, 150
 - roughness, 288, 292
 - wettability, 288, 290, 298, 300, 301, 150, 153–154, 161
- Surface curvature, 133, 135
- Surface defect, 55–56, 61, 65
- Surface free energy, 397, 398, 401, 403, 411–413, 419
- Surface modification, 289
- Surface roughness, 367
- Surface tension, 419, 434, 150–151, 159
- Surface treatment,
 - lapping, 166, 167, 172
 - polishing, 166, 167, 172
- Surfaces,
 - chemical functionalities, 305–306, 318, 329
 - surface free energies, 306
 - surface modification, 311–312
 - surface roughness, 305, 307–308, 310, 318, 320, 322, 329
- Suspended channels, 31, 35
- Tadmor's equilibrium contact angles, 392
- Tape peeling, 239–240
- Teflon, 195
- Tensile strength, 397–418
- Test inks, 423, 434
- Textiles, 334
 - capillary effects, 339
 - fabric, 338, 339
 - fiber, 338
 - pore system, 339
 - technical textiles, 334
 - wetting behavior, 337–339
 - yarn, 338
- Thermal conductivity, 57–59
- Thermal property, 49, 56, 58
- Thermal transfer printing, 371
- Tomotika time, 11
- Trapezoidal channel, 30
- Tribological system, 165
- Ultrashort pulse laser, 289
- Ultrasonication, 247
- Underwater superoleophobicity, 275
- V-groove, 38
- Viscosity, 42
- Water activity, 411, 412, 415, 418
- Water droplet, 47–53, 55–56, 59–61, 64
- Water film, 156–157
- Water jet, 199
- Water strider, 269
- Water-oil separation, 186
- Wenzel, 212–214
- Wenzel equation, 168.173
- Wenzel's equation, 112–115, 117–118, 124
- Wettability, , 149–151, 153–154, 158, 161, 164
 - hydrophilic, 307, 310, 313, 315, 321, 324, 329
 - hydrophobic, 307, 310, 313, 324, 329
 - superhydrophilic, 305–307, 309, 315, 321–322, 324–325, 327–329
 - superhydrophobic, 307–308, 310, 322
 - wetting, 306–310, 314–315
- Wetted perimeter, 8, 34
- Wetting, 150–151, 156, 161
- Wetting behavior,
 - complete wettability, 166.169
 - effect of pre-wetted surface, 170, 171
 - heterogeneous, 168
 - homogeneous, 168
 - hydrophilic, 165, 168, 174
 - hydrophobic, 165, 168, 169, 174
 - influence of temperature, 170, 171, 175

- oleophilic, 165, 166, 168–171, 174–176
- roughness effect, 171–173
- Wetting parameter (kB), 167, 172–175
- Wetting time, 169, 170, 171, 174, 175
- Work of adhesion, 421
- Xerogel, 277
- Young contact angle, 6
- Young theory, 168
- Young-Laplace equation, 76, 77, 82
- Young-Laplace pressure, 151, 152, 157

Also of Interest

Check out these published and forthcoming related titles from Scrivener Publishing

Reviews of Adhesion and Adhesives

Editor: K.L. Mittal

Quarterly publication. ISSN 2168-0965

www.scrivenerpublishng.com

Laser Technology: Applications in Adhesion and Related Areas

K.L. Mittal and Wei-Sheng Lei

Forthcoming spring 2016. ISBN 978-1-119-18493-5

Adhesion in Polymer Nanocomposites

Edited by Anil Netravali and K.L. Mittal

Forthcoming spring 2016. ISBN 978-1-119-18491-1

**Advances in Contact Angle, Wettability and Adhesion
Volume 2**

Edited by K.L. Mittal

Published 2015. ISBN 978-1-119-11698-1

Particle Adhesion and Removal

Edited by K.L. Mittal and Ravi Jaiswal

Published 2015. ISBN 978-1118-83153-3

Laser Surface Modification and Adhesion

Edited by K.L. Mittal and Thomas Bahners

Published 2014. ISBN 978-1-118-83163-2

Adhesion in Microelectronics

Edited by K.L. Mittal and Tanweer Ahsan

Published 2014. ISBN 978-1-118-83133-5

**Advances in Contact Angle, Wettability and Adhesion
Volume 1**

Edited by K.L. Mittal

Published 2013. ISBN 978-1-118-47292-7

Advances in Modeling and Design of Adhesively Bonded Systems

Edited by S. Kumar and K.L. Mittal

Published 2013. ISBN 978-1-118-68637-9

Atmospheric Pressure Plasma Treatment of Polymers

Edited by Michael Thomas and K.L. Mittal

Published 2013. ISBN 978-1-118-59621-0

Atomic Layer Deposition

Principles, Characteristics, and Nanotechnology Applications

By Tommi Kääriäinen, David Cameron, Marja-Leena Kääriäinen and Arthur Sherman

Published 2013. ISBN 978-1-118-06277-7

Encapsulation Nanotechnologies

Edited by Vikas Mittal

Published 2013. ISBN 978-1-118-34455-2

Atmospheric Pressure Plasma for Surface Modification

By Rory A. Wolf

Published 2012. ISBN 9781118016237

Introduction to Surface Engineering and Functionally Engineered Materials

By Peter Martin

Published 2011. ISBN 978-0-470-63927-6

WILEY END USER LICENSE AGREEMENT

Go to www.wiley.com/go/eula to access Wiley's ebook EULA.